Springer Series in Materials Science 227

Michael Kneissl
Jens Rass *Editors*

III-Nitride Ultraviolet Emitters

Technology and Applications

Springer

Springer Series in Materials Science

Volume 227

Series editors

Robert Hull, Charlottesville, USA
Chennupati Jagadish, Canberra, Australia
Richard M. Osgood, New York, USA
Jürgen Parisi, Oldenburg, Germany
Tae-Yeon Seong, Seoul, Korea, Republic of (South Korea)
Shin-ichi Uchida, Tokyo, Japan
Zhiming M. Wang, Chengdu, China
Yoshiyuki Kawazoe, Sendai, Japan

The Springer Series in Materials Science covers the complete spectrum of materials physics, including fundamental principles, physical properties, materials theory and design. Recognizing the increasing importance of materials science in future device technologies, the book titles in this series reflect the state-of-the-art in understanding and controlling the structure and properties of all important classes of materials.

More information about this series at http://www.springer.com/series/856

Michael Kneissl · Jens Rass
Editors

III-Nitride Ultraviolet Emitters

Technology and Applications

Springer

Editors
Michael Kneissl
Institute of Solid State Physics
Technische Universität Berlin
Berlin
Germany

and

Ferdinand-Braun-Institut
Leibniz-Institut für Höchstfrequenztechnik
Berlin
Germany

Jens Rass
Institute of Solid State Physics
Technische Universität Berlin
Berlin
Germany

and

Ferdinand-Braun-Institut
Leibniz-Institut für Höchstfrequenztechnik
Berlin
Germany

ISSN 0933-033X ISSN 2196-2812 (electronic)
Springer Series in Materials Science
ISBN 978-3-319-24098-5 ISBN 978-3-319-24100-5 (eBook)
DOI 10.1007/978-3-319-24100-5

Library of Congress Control Number: 2015952531

Springer Cham Heidelberg New York Dordrecht London
© Springer International Publishing Switzerland 2016
This work is subject to copyright. All rights are reserved by the Publisher, whether the whole or part of the material is concerned, specifically the rights of translation, reprinting, reuse of illustrations, recitation, broadcasting, reproduction on microfilms or in any other physical way, and transmission or information storage and retrieval, electronic adaptation, computer software, or by similar or dissimilar methodology now known or hereafter developed.
The use of general descriptive names, registered names, trademarks, service marks, etc. in this publication does not imply, even in the absence of a specific statement, that such names are exempt from the relevant protective laws and regulations and therefore free for general use.
The publisher, the authors and the editors are safe to assume that the advice and information in this book are believed to be true and accurate at the date of publication. Neither the publisher nor the authors or the editors give a warranty, express or implied, with respect to the material contained herein or for any errors or omissions that may have been made.

Printed on acid-free paper

Springer International Publishing AG Switzerland is part of Springer Science+Business Media (www.springer.com)

Preface

In the past two decades, group III-nitride-based ultraviolet light-emitting diodes (UV-LEDs) and their applications have undergone a progressively accelerating development. This can be demonstrated by many metrics. For example, the number of published articles in the area of UV-LEDs is steadily increasing and has reached nearly 1.000 journal articles per year in 2014 (see Fig. 1). However, we have found that the fast progress in this field makes it difficult to obtain or maintain a comprehensive overview of all these very rapidly developing research areas. Many times when researchers in the field of semiconductor materials and optoelectronics devices describe the applications of UV emitters, large gaps in information are revealed. On the other hand, developers and engineers who are working in various areas of applications of UV emitters and detectors often do not comprehend the complexities in materials and device development. In order to put all these developments into a context, various chapters in this book aim to provide a comprehensive examination of the state of the art in group III-nitride-based materials, ultraviolet emitters, and their applications. It is intended for researchers and graduate-level students in the area of electrical engineering, material science, and physics as well as scientists, developers, and engineers in various application fields of UV emitters and detectors. The book provides an overview of group III-nitride materials including their structural, optical, and electronic properties as well as key

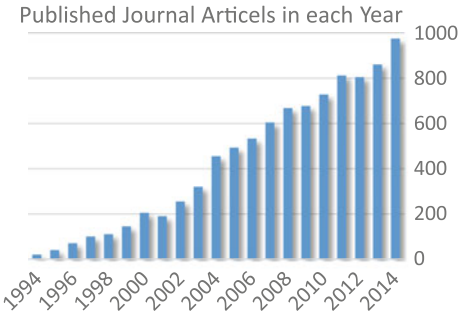


Fig. 1 Journal articles in each year for publications under the keywords "ultraviolet" and "light emitting diode" (*Source* Web of Science. Retrieved 17 July 2015 from apps.webofknowledge.com)

features of various optoelectronic components, like UV-LEDs, ultraviolet lasers, and photodetectors. It also offers an introduction to a number of key applications for UV emitters and detectors, including water purification, phototherapy, gas sensing, fluorescence excitation, plant growth lighting, and UV curing. Although each chapter stands on its own and can be understood without the knowledge of the others, the organization of the chapters has been deliberately chosen to start with chapters focusing on basic materials properties, followed by chapters on ultraviolet devices, and to conclude with several chapters describing key applications for UV emitters and detectors. In the first chapter, Michael Kneissl provides an introduction to group III-nitride UV emitter technologies and their applications. This is followed by Matthias Bickermann's review of the growth and structural properties of bulk AlN substrates. In the third chapter, Eberhard Richter, Sylvia Hagedorn, Arne Knauer, and Markus Weyers review the use of sapphire as a substrate for nitride-based light emitters in the UV range, especially the growth of low defect density AlGaN templates by hydride vapor phase epitaxy. In Chap. 4 Hideki Hirayama discusses crystal growth techniques for low defect density AlN and AlGaN layers on sapphire and presents state-of-the-art performance characteristic of UVC-LEDs on sapphire. In Chap. 5 Shigefusa F. Chichibu, Hideto Miyake, Kazumasa Hiramatsu, and Akira Uedono provide an in-depth discussion of the effects of dislocations and point defects on the internal quantum efficiency of the near-band-edge emission in AlGaN-based DUV light-emitting materials. Understanding the role of defects on the IQE of UV-LEDs is critical for improving the efficiency and output power of UV-LEDs. In the area of devices, the optical polarization and light extraction from UV-LEDs is reviewed by Jens Rass and Neysha Lobo-Ploch. The homoepitaxial growth of UVC-LEDs on bulk AlN substrates and their application in water disinfection is examined by James R. Grandusky, Rajul V. Randive, Therese C. Jordan, and Leo J. Schowalter in Chap. 7. Noble Johnson, John Northrup, and Thomas Wunderer discuss optical gain in AlGaN quantum well laser heterostructures and present the state of the art in the development of AlGaN-based UV laser diodes in Chap. 8, and in Chap. 9 solar and visible blind UV photodetectors are reviewed by Moritz Brendel, Enrico Pertzsch, Vera Abrosimova, and Torsten Trenkler. In Chap. 10 Martina Lange, Tim Kolbe, and Martin Jekel examine the application of UVC-LEDs for water purification and in Chap. 11 Uwe Wollina, Bernd Seme, Armin Scheibe, and Emmanuel Gutmann describe the application of UV emitters in dermatological phototherapy. In Chap. 12 Hartmut Ewald and Martin Degner review the role of UV emitters in gas-sensing applications and in Chap. 13 Emmanuel Gutmann, Florian Erfurth, Anke Drewitz, Armin Scheibe, and Martina Meinke discuss UV fluorescence detection and spectroscopy systems for applications in chemistry and life sciences. In Chap. 14 Monika Schreiner, Inga Mewis, Susanne Neugart, Rita Zrenner, Melanie Wiesner, Johannes Glaab, and M.A.K. Jansen examine the application of UV-LEDs for plant growth lighting, especially the triggering of the secondary plant metabolism with UVB light. In the final chapter, the application of LEDs for UV curing is reviewed by Carsten Dreyer and Franziska Mildner.

We like to thank all the authors of the various chapters for their timely and well-prepared contributions. This book would not have been possible without their commitment, hard work, and perseverance. We would especially like to thank Claus Ascheron at Springer Science for presenting us with the opportunity to edit this book and for his continued support during the process.

Berlin, Germany

Michael Kneissl
Jens Rass

Contents

1 A Brief Review of III-Nitride UV Emitter Technologies and Their Applications 1
Michael Kneissl
1.1 Background 1
1.2 UV Light Emitters and Their Applications 3
1.3 UV-LEDs—State of the Art and the Challenges Ahead 4
1.4 UV-LEDs—Key Parameters and Device Performance 7
1.5 The Role of Defects on the IQE of UV-LEDs 10
1.6 Current-Injection Efficiency and Operating Voltages of UV-LEDs 12
1.7 Light Extraction from UV-LEDs 13
1.8 Thermal Management and Degradation of UV-LED 14
1.9 Outlook 16
1.10 Summary 17
References 18

2 Growth and Properties of Bulk AlN Substrates 27
Matthias Bickermann
2.1 Properties and History of AlN Crystals 27
2.2 AlN Bulk Growth by the PVT Method: Theory 29
2.3 AlN Bulk Growth by the PVT Method: Technology 31
2.4 Seeded Growth and Crystal Enlargement 34
2.5 Structural Defects in PVT-Grown AlN Bulk Crystals 36
2.6 Impurities and Resulting Properties of AlN Substrates 38
2.7 Conclusions and Outlook 41
References 42

3 Vapor Phase Epitaxy of AlGaN Base Layers on Sapphire Substrates for Nitride-Based UV-Light Emitters 47
Eberhard Richter, Sylvia Hagedorn, Arne Knauer and Markus Weyers
3.1 Introduction 47
3.2 Growth of Al(Ga)N Buffer Layers by MOVPE. 49
3.3 Techniques for MOVPE of Al(Ga)N Base Layers with Reduced TDD 51
3.4 Growth of AlGaN Layers by HVPE 54
3.4.1 Fundamentals of the HVPE Technique 54
3.4.2 The Choice of Substrate 58
3.4.3 Selected Results from Growth of AlGaN Layers by HVPE 58
3.5 Summary 70
References. 70

4 Growth Techniques of AlN/AlGaN and Development of High-Efficiency Deep-Ultraviolet Light-Emitting Diodes 75
Hideki Hirayama
4.1 Introduction 75
4.2 Research Background of DUV LEDs 76
4.3 Growth Techniques of High-Quality AlN on Sapphire Substrate 81
4.4 Marked Increase in Internal Quantum Efficiency (IQE) 85
4.5 222–351 nm AlGaN and InAlGaN DUV LEDs 90
4.6 Increase in Electron Injection Efficiency (EIE) by MQB 97
4.7 Future LED Design for Obtaining High Light Extraction Efficiency (LEE) 104
4.8 Summary 111
References. 112

5 Impacts of Dislocations and Point Defects on the Internal Quantum Efficiency of the Near-Band-Edge Emission in AlGaN-Based DUV Light-Emitting Materials 115
Shigefusa F. Chichibu, Hideto Miyake, Kazumasa Hiramtsu and Akira Uedono
5.1 Introduction 116
5.2 Experimental Details 118
5.3 Impacts of Impurities and Point Defects on the Near-Band-Edge Luminescence Dynamics of AlN. 120
5.4 Effective Radiative Lifetime of the Near-Band-Edge Emission in $Al_xGa_{1-x}N$ Films. 125

5.5 Impacts of Si-Doping and Resultant Cation Vacancy Formation on the Luminescence Dynamics of the Near-Band-Edge Emission in $Al_{0.6}Ga_{0.4}N$ Films Grown on AlN Templates 127
5.6 Summary 133
References 133

6 Optical Polarization and Light Extraction from UV LEDs 137
Jens Rass and Neysha Lobo-Ploch
6.1 Light Extraction from UV LEDs 138
6.2 Optical Polarization 140
6.2.1 Factors Influencing the Light Polarization Switching in AlGaN Layers 143
6.2.2 Optical Polarization Dependence on Substrate Orientation 147
6.2.3 Influence of the Optical Polarization on the Light Extraction Efficiency 149
6.3 Concepts for Improved Light Extraction 152
6.3.1 Contact Materials and Design 152
6.3.2 Surface Preparation 157
6.3.3 Packaging 164
References 166

7 Fabrication of High Performance UVC LEDs on Aluminum-Nitride Semiconductor Substrates and Their Potential Application in Point-of-Use Water Disinfection Systems 171
James R. Grandusky, Rajul V. Randive, Therese C. Jordan and Leo J. Schowalter
7.1 Introduction 172
7.1.1 Types of UVC Light Sources 172
7.1.2 What Is UVC Light? 173
7.1.3 How Does Germicidal UV Work 174
7.2 Fabrication of UVC LEDs on AlN Substrates 175
7.3 Leveraging Performance Gains in UVC LEDs for POU Water Disinfection 183
7.3.1 Effect of UVT 183
7.3.2 Design Flexibility 186
7.3.3 Modeling Flow Cells 186
7.3.4 Example Flow Analysis 187
7.3.5 Working with UVC Light 189
References 191

8 AlGaN-Based Ultraviolet Laser Diodes 193
Thomas Wunderer, John E. Northrup and Noble M. Johnson
8.1 Introduction 194
8.2 Growth on Bulk AlN for Highest Material Quality 196
8.2.1 Bulk AlN Substrate 196
8.2.2 Homoepitaxial AlN 197
8.2.3 AlGaN Laser Heterostructure 198
8.2.4 Multiple Quantum Well Active Zone 199
8.3 High Current Capability in High Band Gap AlGaN Materials 201
8.4 High Injection Efficiency at High Current Levels 205
8.5 Optically Pumped UV Lasers 208
8.6 Alternative Concepts for Compact Deep-UV III-N Lasers 211
8.6.1 Electron-Beam Pumped Laser 212
8.6.2 InGaN-Based VECSEL + Second Harmonic Generation 213
8.7 Summary and Conclusion 214
References 215

9 Solar- and Visible-Blind AlGaN Photodetectors 219
Moritz Brendel, Enrico Pertzsch, Vera Abrosimova, Torsten Trenkler and Markus Weyers
9.1 Introduction 219
9.2 Basics of Photodetectors 222
9.2.1 Characteristic Parameters and Phenomena 222
9.2.2 Various Types of Semiconductor Photodetectors 232
9.3 III-Nitrides for Solid-State UV Photodetection 242
9.3.1 AlGaN-Based Photoconductor 244
9.3.2 AlGaN-Based MSM Photodetector 245
9.3.3 AlGaN-Based Schottky Barrier Photodiode 247
9.3.4 AlGaN-Based p-i-n Photodiode 248
9.3.5 AlGaN-Based Avalanche Photodetector 250
9.3.6 AlGaN-Based Photocathode 252
9.3.7 III-Nitride-Based Devices of High Integration Level 254
9.4 Present Status of Wide Bandgap Photodetectors 255
9.5 Summary and Conclusions 257
References 258

10 Ultraviolet Light-Emitting Diodes for Water Disinfection 267
Martina A. Lange, Tim Kolbe and Martin Jekel
10.1 Introduction 267
10.2 Basic Principles of UV Disinfection 268
10.2.1 Factors Influencing UV Fluence 271

10.2.2 Modeling and Validation of UV Reactor Performance . . . 273
10.3 Case Study . . . 274
10.3.1 Proposal for an Experimental Setup to Test UV LEDs . . . 275
10.3.2 Test Conditions . . . 278
10.3.3 Results of Tests Conducted with UV LEDs . . . 282
10.4 Potential of UV LEDs for Water Disinfection . . . 287
References . . . 288

11 Application of UV Emitters in Dermatological Phototherapy . . . 293
Uwe Wollina, Bernd Seme, Armin Scheibe and Emmanuel Gutmann
11.1 Introduction . . . 293
11.2 Sources for UV Phototherapy . . . 294
11.2.1 Natural Sunlight . . . 295
11.2.2 Gas Discharge Lamps . . . 296
11.2.3 Lasers . . . 298
11.2.4 UV-LEDs . . . 299
11.3 Variants of Dermatological UV Phototherapy . . . 300
11.3.1 Psoralen Plus UVA (PUVA) Therapy . . . 300
11.3.2 Broadband UVB (BB-UVB) Therapy . . . 302
11.3.3 Narrowband UVB (NB-UVB) Therapy . . . 302
11.3.4 UVA-1 Therapy . . . 303
11.3.5 Targeted UV Phototherapy . . . 303
11.3.6 Extracorporeal Photochemotherapy (ECP) . . . 304
11.4 Mechanisms of Action for Major Dermatological Indications . . . 306
11.4.1 Psoriasis . . . 307
11.4.2 Atopic Dermatitis . . . 307
11.4.3 Vitiligo . . . 308
11.4.4 Cutaneous T-Cell Lymphomas . . . 308
11.4.5 Lichen Planus and Alopecia Areata . . . 309
11.4.6 Systemic Sclerosis and Morphoea . . . 309
11.4.7 Graft-Versus-Host Disease . . . 309
11.4.8 Polymorphic Light Eruption . . . 310
11.5 Clinical Studies with Novel UV Emitters . . . 310
11.5.1 Study with an Electrodeless Excimer Lamp . . . 310
11.5.2 Study with UV-LEDs . . . 312
11.6 Summary and Outlook . . . 313
References . . . 314

12 UV Emitters in Gas Sensing Applications 321
Martin Degner and Hartmut Ewald
12.1 Introduction 321
12.2 Light Absorption Spectroscopy 324
12.3 Absorption Spectroscopic Systems 329
12.4 Light Sources for UV Spectroscopy 333
12.5 Optical and Electrical Properties of the LEDs for Spectroscopy Application 337
12.6 Application of UV-LED Absorption Spectroscopy 342
12.6.1 Ozone Sensor 342
12.6.2 Ozone Sensor Design 342
12.6.3 Measurement Arrangement 343
12.6.4 Results 343
12.6.5 SO_2 and NO_2 Sensor 343
12.6.6 Sensor Design for SO_2/NO_2 Exhaust Gas Sensor 344
12.6.7 Measurement Setup 345
12.7 Conclusion and Outlook 348
References 348

13 UV Fluorescence Detection and Spectroscopy in Chemistry and Life Sciences 351
Emmanuel Gutmann, Florian Erfurth, Anke Drewitz, Armin Scheibe and Martina C. Meinke
13.1 Introduction 351
13.2 Fundamentals and Apparative Aspects of Fluorescence Detection and Spectroscopy 353
13.3 Fluorescence in Lab-Based Instrumental Analysis 359
13.4 Fluorescence Chemical Sensing for Environmental Monitoring and Bioanalytics 361
13.5 Detection of Microorganisms Using Autofluorescence 369
13.6 Fluorescence in Medical Diagnosis of Skin Diseases 374
13.7 Summary and Outlook 378
References 378

14 UV-B Elicitation of Secondary Plant Metabolites 387
Monika Schreiner, Inga Mewis, Susanne Neugart, Rita Zrenner, Johannes Glaab, Melanie Wiesner and Marcel A.K. Jansen
14.1 Nature and Occurrence of Secondary Plant Metabolites 388
14.2 Nutritional Physiology of Secondary Plant Metabolites 389
14.3 Association Between Fruit and Vegetable Consumption and Chronic Diseases 390
14.4 Secondary Plant Metabolites Within the Plant–Environment Interaction 391
14.4.1 UV-B Perception and Signaling in the Plant 391

14.4.2 UV-B as Stressor and Plant Regulator 393
14.5 Structure-Differentiated Response to UV-B 394
14.5.1 Flavonoids and Other Phenolics 395
14.5.2 Glucosinolates 399
14.6 Tailor-Made UV-B Induction of Secondary Plant Metabolites by UV-B LEDs 402
14.6.1 Current State of Research: UV-B Light-Emitting Diodes for Plant Lightning 402
14.6.2 Advantages of UV-B LEDs for Targeted Triggering of Plant Properties 402
14.6.3 Experimental Setup for Targeted Triggering of Plant Properties by UV-B LEDs 404
14.7 Outlook 405
References 406

15 Application of LEDs for UV-Curing 415
Christian Dreyer and Franziska Mildner
15.1 Introduction 415
15.2 Light Source 417
15.3 Chemistry and Mechanisms 419
15.4 Kinetics 422
15.5 Medical Applications 424
15.6 Coatings, Inks, and Printing 427
15.7 Stereolithography 430
15.8 Conclusion and Outlook 431
References 432

Index 435

Contributors

Vera Abrosimova JENOPTIK Polymer Systems GmbH, Berlin, Germany

Matthias Bickermann Leibniz Institute for Crystal Growth (IKZ), Berlin, Germany; Institute for Chemistry, Technische Universität, Berlin, Germany

Moritz Brendel Ferdinand-Braun-Institut, Leibniz-Institut für Höchstfrequenztechnik, Berlin, Germany

Shigefusa F. Chichibu Institute of Multidisciplinary Research for Advanced Materials, Tohoku University, Sendai, Japan

Martin Degner Institute of General Electrical Engineering, University of Rostock, Rostock, Germany

Anke Drewitz Department Photonics and Sensorics, Gesellschaft zur Förderung von Medizin-, Bio- und Umwelttechnologien e.V. (GMBU), Jena, Germany

Christian Dreyer Fraunhofer-Einrichtung für Polymermaterialien und Composite PYCO, Teltow, Germany

Florian Erfurth Department Photonics and Sensorics, Gesellschaft zur Förderung von Medizin-, Bio- und Umwelttechnologien e.V. (GMBU), Jena, Germany

Hartmut Ewald Institute of General Electrical Engineering, University of Rostock, Rostock, Germany

Johannes Glaab Ferdinand-Braun-Institut, Leibniz-Institut für Höchstfrequenztechnik, Berlin, Germany

James R. Grandusky Crystal IS, Green Island, NY, USA

Emmanuel Gutmann Department Photonics and Sensorics, Gesellschaft zur Förderung von Medizin-, Bio- und Umwelttechnologien e.V. (GMBU), Jena, Germany

Sylvia Hagedorn Ferdinand-Braun-Institut, Leibniz-Institut für Höchstfrequenztechnik, Berlin, Germany

Kazumasa Hiramtsu Department of Electrical and Electronic Engineering, Mie University, Tsu, Japan

Hideki Hirayama RIKEN, Quantum Optodevice Laboratory, Saitama, Japan

Marcel A.K. Jansen School of Biological, Environmental and Earth Sciences, University College Cork, Distillery Field, Cork, Ireland

Martin Jekel Technische Universität Berlin, Fachgebiet Wasserreinhaltung, Berlin, Germany

Noble M. Johnson PARC Palo Alto Research Center, Inc., Palo Alto, CA, USA

Therese C. Jordan Crystal IS, Green Island, NY, USA

Arne Knauer Ferdinand-Braun-Institut, Leibniz-Institut für Höchstfrequenztechnik, Berlin, Germany

Michael Kneissl Institute of Solid State Physics, Technische Universität, Berlin, Germany; Ferdinand-Braun-Institut, Leibniz-Institut für Höchstfrequenztechnik, Berlin, Germany

Tim Kolbe Ferdinand-Braun-Institut, Leibniz-Institut für Höchstfrequenztechnik, Berlin, Germany

Martina A. Lange Technische Universität Berlin, Fachgebiet Wasserreinhaltung, Berlin, Germany

Neysha Lobo-Ploch Ferdinand-Braun-Institut, Leibniz-Institut für Höchstfrequenz technik, Berlin, Germany

Martina C. Meinke Center of Experimental and Applied Cutaneous Physiology (CCP), Department of Dermatology, Venerology and Allergology, Charité – Universitätsmedizin Berlin, Berlin, Germany

Inga Mewis Department Plant Quality, Leibniz-Institute of Vegetable and Ornamental Crops Großbeeren and Erfurt e. V., Großbeeren, Germany

Franziska Mildner Fraunhofer-Einrichtung für Polymermaterialien und Composite PYCO, Teltow, Germany

Hideto Miyake Department of Electrical and Electronic Engineering, Mie University, Tsu, Japan

Susanne Neugart Department Plant Quality, Leibniz-Institute of Vegetable and Ornamental Crops Großbeeren and Erfurt e. V., Großbeeren, Germany

John E. Northrup PARC Palo Alto Research Center, Inc., Palo Alto, CA, USA

Enrico Pertzsch JENOPTIK Polymer Systems GmbH, Berlin, Germany

Rajul V. Randive Crystal IS, Green Island, NY, USA

Jens Rass Ferdinand-Braun-Institut, Leibniz-Institut für Höchstfrequenztechnik, Berlin, Germany; Institute of Solid State Physics, Technische Universität Berlin, Berlin, Germany

Eberhard Richter Ferdinand-Braun-Institut, Leibniz-Institut für Höchstfrequenz technik, Berlin, Germany

Armin Scheibe Department Photonics and Sensorics, Gesellschaft zur Förderung von Medizin-, Bio- und Umwelttechnologien e.V. (GMBU), Jena, Germany

Leo J. Schowalter Crystal IS, Green Island, NY, USA

Monika Schreiner Department Plant Quality, Leibniz-Institute of Vegetable and Ornamental Crops Großbeeren and Erfurt e. V., Großbeeren, Germany

Bernd Seme Department Photonics and Sensorics, Gesellschaft zur Förderung von Medizin-, Bio- und Umwelttechnologien e.V. (GMBU), Jena, Germany

Torsten Trenkler JENOPTIK Polymer Systems GmbH, Berlin, Germany

Akira Uedono Division of Applied Physics, Faculty of Pure and Applied Science, University of Tsukuba, Tsukuba, Ibaraki, Japan

Markus Weyers Ferdinand-Braun-Institut, Leibniz-Institut für Höchstfrequenztechnik, Berlin, Germany

Melanie Wiesner Department Plant Quality, Leibniz-Institute of Vegetable and Ornamental Crops Großbeeren and Erfurt e. V., Großbeeren, Germany

Uwe Wollina Department of Dermatology and Allergology, Hospital Dresden-Friedrichstadt, Academic Teaching Hospital of the Technical University of Dresden, Dresden, Germany

Thomas Wunderer PARC Palo Alto Research Center, Inc., Palo Alto, CA, USA

Rita Zrenner Department Plant Quality, Leibniz-Institute of Vegetable and Ornamental Crops Großbeeren and Erfurt e. V., Großbeeren, Germany

Chapter 1
A Brief Review of III-Nitride UV Emitter Technologies and Their Applications

Michael Kneissl

Abstract This chapter provides a brief introduction to group III-nitride ultraviolet light emitting diode (LED) technologies and an overview of a number of key application areas for UV-LEDs. It covers the state of the art of UV-LEDs as well a survey of novel approaches for the development of high performance UV light emitters.

1.1 Background

More than two decades have passed since a series of fundamental breakthroughs in the area of gallium nitride (GaN) semiconductor materials led to the first demonstration of high efficiency and high brightness blue LEDs [1–4]. Today, GaN-based blue and white LEDs have achieved efficiencies surpassing that of any conventional light source and billions of LEDs are fabricated every week. This tremendous progress has been accompanied by increasing penetration of blue and white LEDs into new applications and larger markets, starting with backlighting of LCD displays in mobile phones, computer screens, and TVs, followed by automotive and street lighting, and finally conquering lighting applications in all places. Therefore, it is only fitting that in 2014 the Royal Swedish Academy of Sciences awarded the Nobel Prize for Physics to Isamu Akasaki, Hiroshi Amano, and Shuji Nakamura "for the invention of efficient blue light emitting diodes which has enabled bright and energy-saving white light sources" [5]. This example shows how breakthroughs in development of new semiconductor materials and device technologies can lead to a paradigm shift of a complete industry, in this case solid-state lighting. The Royal Swedish Academy of Sciences stated in their press release "in the spirit of Alfred

M. Kneissl (✉)
Institute of Solid State Physics, Technische Universität, Berlin, Germany
e-mail: kneissl@physik.tu-berlin.de

M. Kneissl
Ferdinand-Braun-Institut, Leibniz-Institut für Höchstfrequenztechnik, Berlin, Germany

© Springer International Publishing Switzerland 2016

M. Kneissl and J. Rass (eds.), *III-Nitride Ultraviolet Emitters*,
Springer Series in Materials Science 227, DOI 10.1007/978-3-319-24100-5_1

Nobel the Prize rewards an invention of greatest benefit to mankind; using blue LEDs, white light can be created in a new way" [5]. Despite these tremendous achievements, we have to date only utilized a very narrow sliver of the emission spectrum that gallium nitride devices are capable of generating. By adding aluminum nitride (AlN) to the GaN alloy system, the emission wavelength of AlGaN-based LEDs can be tuned over almost the entire UVA (400–320 nm), UVB (320–280 nm), and UVC (280–200 nm) spectral range with emission wavelength as short as 210 nm. Although the efficiencies and power levels of AlGaN-based UV-LEDs today are still modest (see Fig. 1.1) compared to their visible wavelength counterparts, another paradigm shift in the area of semiconductor-based UV sources is just around the corner. Without doubt the efficiencies and output powers of UV-LEDs will continue to improve over the coming years and at the same time the costs per milliwatt of UV light from LEDs will drop significantly. For many high-end applications, e.g., in the area of medical diagnostics, phototherapy, and sensing, UV-LEDs are already competitive since they enable major advances in system design and performance and only contribute a small fraction of the overall cost. As the UV-LED performance improves over time it is clear that many more application areas will follow.

In order to put all these developments into a context, this chapter will provide a comprehensive overview of the state of the art in group III-nitride-based materials,

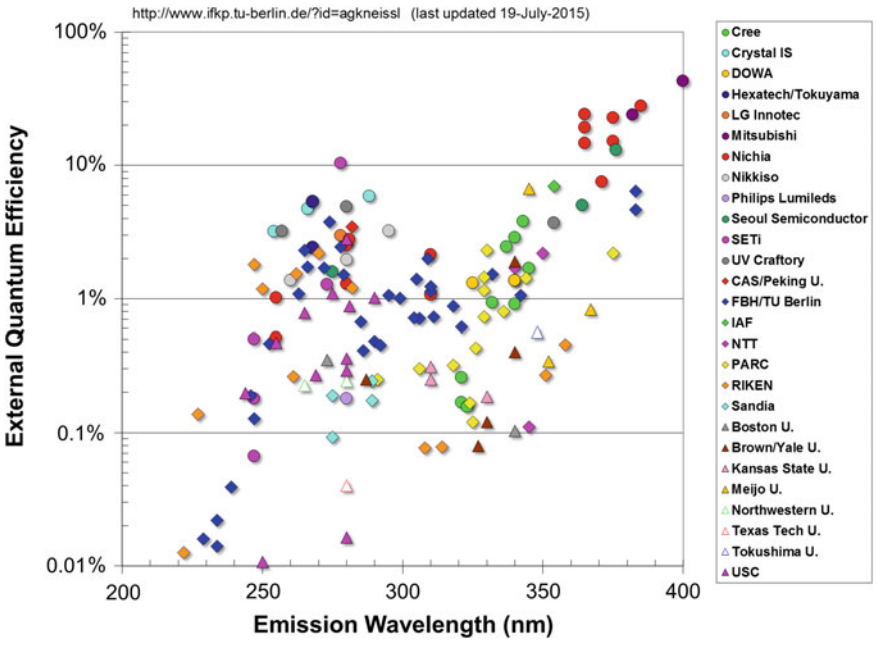


Fig. 1.1 Reported external quantum efficiencies for AlGaN, InAlGaN-, and InGaN quantum well LEDs emitting in the UV spectral range [6–32]

ultraviolet emitters, and their applications. Several key applications for UV emitters and detectors will be discussed, including water purification, phototherapy, gas sensing, fluorescence excitation, plant growth lighting, and UV curing. In addition, the optical, electronic, and structural properties of group III-nitride materials as well as the design and key performance parameters of UV-LEDs will be reviewed. Furthermore, the most important technological challenges for the realization of high efficiency, high power UV light emitters will be examined and a number of approaches to overcome these hurdles will be presented.

1.2 UV Light Emitters and Their Applications

Compared to conventional UV sources, such as low and medium pressure mercury lamps [33], ultraviolet LEDs offer a number of advantages. UV-LEDs are extremely robust, compact, environmentally friendly, and can exhibit very long lifetimes. They do not require any warm-up times and can be switched on and off within a few tens of nanoseconds or even faster. These unique properties designate UV-LEDs as a key enabling component for a number of new applications that cannot be realized with conventional UV sources. For example, the ability to rapidly turn UV-LEDs on and off gives rise to advanced measuring detection algorithms and improved baseline calibrations that can significantly enhance the sensitivity of the system. By closely spacing different UV-LEDs, it is also possible to realize multi-wavelength modules, which may be able to identify specific gases, biomolecules, or organisms. UV-LEDs are operated at moderate DC voltages, which make them ideally suited for battery operation or solar cell powering. They are also easily electronically dimmable, which can be an important energy saving feature, e.g., in water purification applications, where the required UV radiation dose strongly depends on the volume of the water flow. But most importantly, their emission can be tuned to cover any wavelength in the UVA (400–320 nm), UVB (320–280 nm), and UVC (280–200 nm) spectral range. A compilation of different applications for UV-LEDs is shown in Fig. 1.2. Important applications in the UVA spectral range include UV curing of inks, paints, coatings, resins, polymers, and adhesives as well as 3D-printing for rapid prototyping and lightweight construction. Additional applications can be found in the area of sensing, e.g., whitening agents or so-called blankophores, detection of security features, e.g., in ID cards and banknotes, and medical applications like blood gas analysis. Key applications in the UV-B are phototherapy [34, 35], especially the treatment of psoriasis and vitiligo, as well as plant growth lighting, e.g., for the targeted triggering of secondary plant metabolites [36]. High volume applications in the UVC are water purification [37–42], e.g., point-of-use systems, wastewater treatment, and recycling as well as disinfection of medical equipment and food. There are also a number of sensing applications [42–44] for UVB- and UVC-LEDs since many gases (e.g., SO_2, NO_x, NH_3) and biomolecules exhibit absorption bands in these spectral regions, including tryptophan, NADH, tyrosine, DNA, and RNA. UVC-LEDs can also be used for non-line-of-sight communication

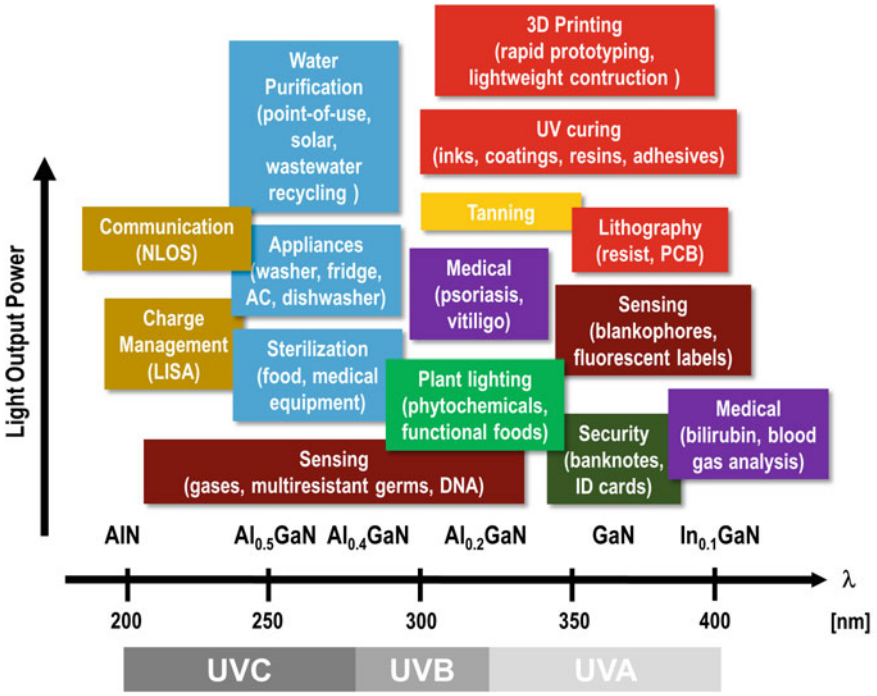


Fig. 1.2 Applications of UVA (400–320 nm), UVB (320–280 nm), and UVC (280–200 nm) LEDs

[45] and are also of interest for basic science experiments in the area of gravitational sensors, e.g., for enabling the charge management systems in the ESA/NASA laser interferometer space antenna (LISA) mission [46]. The foundation of all these applications, however, is the development of high-efficiency and high power AlGaN-based LEDs emitting in the UVA, UV-B, and UVC spectral range.

Thus, the economic and societal benefits resulting from the development of a wide range of applications that require UV-LED technologies are perfectly obvious. Latest market studies predict rapid technological advances in the development of semiconductor-based UV-LED sources. For the world market of UV-LED components alone an annual growth rate of more than 28 % is being forecasted by Yole Développement, reaching a total volume of US$ 520 million by 2019 [47].

1.3 UV-LEDs—State of the Art and the Challenges Ahead

A large number of research groups have reported AlGaN-based light emitting diodes in the ultraviolet spectral range [6–32] and several companies have started to commercialize UV-LED devices. In the 365–400 nm spectral range, many

companies are already offering UVA-LEDs with excellent performance. Companies include for example, Nichia (Japan), Nitride Semiconductors (Japan), Epitex (Japan), UVET Electronics (China), Tekcore (Taiwan), Seoul Opto Device (Korea), SemiLEDs (USA), Luminus Devices (USA), Lumex (USA), and LED Engine (USA). Access to commercial UVB-LEDs is much sparser with companies SETi (USA), Dowa (Japan), Nikkiso (Japan), and UVphotonics (Germany) offering devices in the 320–280 nm range. Similarly in the UVC, only a few companies are currently selling LED devices, including SETi (USA), Nitek (USA), Crystal-IS/Asahi-Kasei (USA/Japan), Hexatech (USA), UVphotonics (Germany), Nikkiso (Japan), and LG Electronics (Korea). Whereas the performance for UVA-LEDs, especially in the wavelength range 365–400 nm is already suitable for many applications, the external quantum efficiencies (EQE) of most UVB and UVC emitters are still in the single digit percentage range. Currently, most UVB- and UVC-LEDs provide only a couple of milliwatts of output power and lifetimes are often limited to less than a thousand hours [30, 41]. There are multiple reasons which limit the performance of group III-nitride-based deep UV-LEDs and nearly every layer in the heterostructure poses a different challenge as illustrated in Fig. 1.3.

Most UV-LED heterostructures are grown on (0001) oriented c-plane sapphire substrates. Sapphire substrate are readily available in various sizes with diameters ranging from 2 to 8-in. for commercial wafers and 12-in. diameter sapphire substrates already being demonstrated as R&D samples [49]. Due to the large volumes of sapphire substrates that are being used for blue LED production, sapphire wafers have become very inexpensive. Most importantly, sapphire is fully transparent across the entire UVA, UVB, and UVC spectral range due its large bandgap energy of 8.8 eV. Most AlGaN-based LED heterostructures are grown by metalorganic

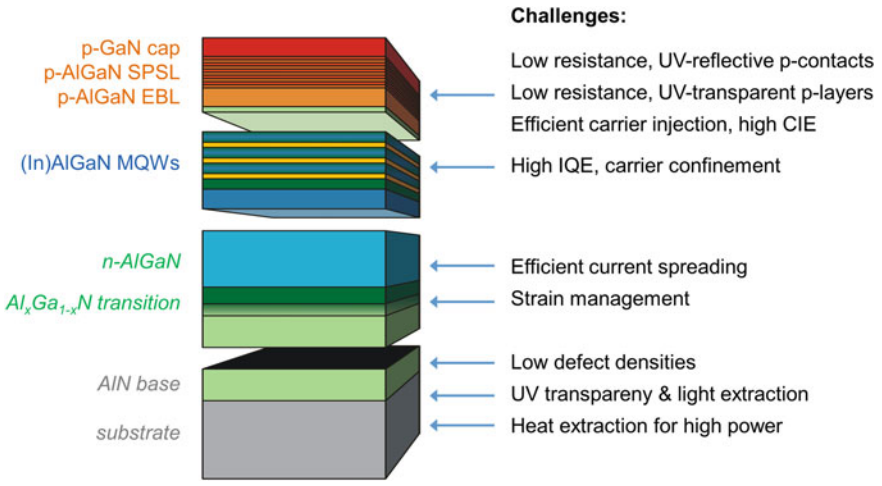


Fig. 1.3 Schematic of an (In)AlGaN MQW UV-LED heterostructure [48]

vapor phase epitaxy (MOVPE) using trimethylgallium (TMGa), triethylgallium (TEGa), trimethyaluminum (TMAl), and trimethylindium (TMIn) as group-III precursor, as well as ammonia (NH3) for the group-V element. Silane (SiH_4) and di (cyclopentadienyl)magnesium (Cp_2Mg) are used as n- and p-doping sources and hydrogen or nitrogen as carrier gas. Typical growth temperatures for the deposition of AlGaN layers are in the range of 1000–1200 °C, but can be as high as 1500 °C for the deposition of the AlN base layer [50–52]. Since the sapphire substrate is electrically insulating an Si-doped n-AlGaN current spreading layer is subsequently deposited to enable uniform lateral current-spreading and injection of electrons into the AlGaN multiple quantum well (MQW) active region. In order to accommodate the difference in the a-lattice constants of AlGaN and AlN (see Fig. 1.6), an $Al_xGa_{1-x}N$ transition layer is inserted between the AlN base and the AlGaN current spreading layer for strain management. The light emitting active region typically comprises a few nanometer thick AlGaN or InAlGaN quantum wells (QWs) separated by (In)AlGaN quantum barriers. The emission wavelength of the LEDs is primarily determined by the aluminum and indium mole fractions in the AlGaN or InAlGaN quantum wells as can be seen in Fig. 1.4a.

Additional contributions to the transition energies and consequently the emission wavelength arise from the electron and hole confinement energies in the quantum well and depend on the QW width as well as the quantum barrier height, i.e., the barrier composition. Figure 1.4b shows the emission wavelength of $Al_{0.72}Ga_{0.28}N$ triple quantum well LEDs with $Al_{0.82}Ga_{0.18}N$ barriers and different QW widths. Since almost all UV-LEDs are grown on the polar c-plane of the wurtzite crystal, strong spontaneous and piezoelectric polarization charges arise at AlGaN heterostructure interfaces, leading to polarization fields in the QWs and consequently to a redshift in emission wavelength. This is effect is commonly known as

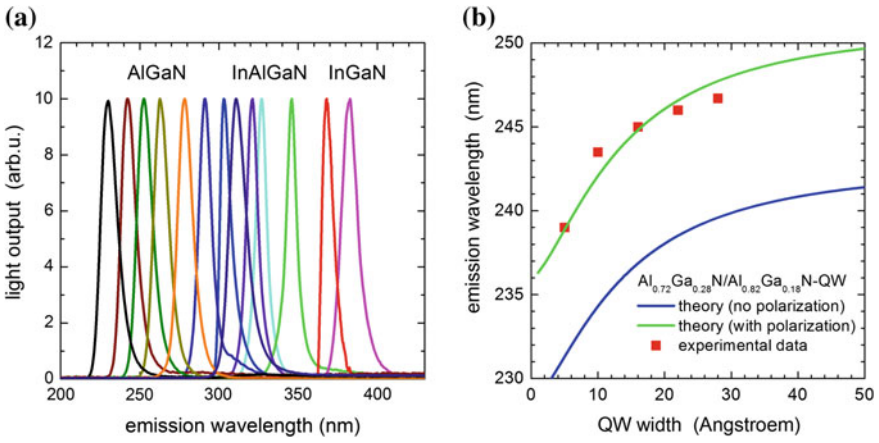


Fig. 1.4 **a** Emission spectra of AlGaN, InAlGaN, and InGaN quantum well LEDs emitting in the UVA, UVB, and UVC spectral range. **b** Emission wavelength of $Al_{0.72}Ga_{0.28}N$ quantum well LEDs for different QW width

the quantum confined Stark effect (QCSE) [53]. The magnitude of the polarization field will largely depend on the difference in the aluminum mole fractions between the AlGaN quantum wells and AlGaN barriers as well as the strain state with the QW stack.

The active region is capped with an Mg-doped p-AlGaN electron blocking layer (EBL), followed by an Mg-doped p-AlGaN short period superlattice layer (SPSL) and a highly Mg-doped p-GaN ohmic contact layer. The function of the p-AlGaN electron blocking layer (EBL) is to facilitate efficient hole injection into the QW active region while preventing electron leakage from the AlGaN QW active region into the p-layers. Ideally, the Mg-doped p-AlGaN SPSL is UV-transparent in order to prevent the absorption of UV photons. Looking at the different implementations of UV-LEDs in the literature, of course, there are many deviations from this basic UV-LED structure. For example, instead of a p-AlGaN short period superlattice layer, an Mg-doped bulk p-AlGaN layer can also be used. Some LED heterostructure designs utilize a gradient of the aluminum mole fraction in the p-AlGaN layer in order to enhance the hole carrier concentrations through polarization doping [54]. Nevertheless, the key elements described above and in Fig. 1.3 can be found in most UV-LEDs. While metalorganic vapor phase epitaxy (MOVPE) is the dominant growth technique for the realization of UV-LEDs, AlGaN-based UV light emitters have also been demonstrated using molecular beam epitaxy (MBE) [55] or hydride vapor phase epitaxy (HVPE) [56].

1.4 UV-LEDs—Key Parameters and Device Performance

There are several key parameters that characterize the performance characteristics of UV-LEDs. The conversion efficiency by which the electrical input power is converted into UV light output is described by the so-called wall plug efficiency (WPE) or power conversion efficiency (PCE). In general, the wall plug efficiency of light emitting diodes is defined as the ratio of the total UV output power to the input electrical power, i.e., the drive current times the operating voltage of the device. This can be described by the following relationships:

$$\mathrm{WPE} = \frac{P_{\mathrm{out}}}{I \cdot V} = \eta_{\mathrm{EQE}} \frac{\hbar\omega}{e \cdot V},$$

where P_{out} denotes the output power of the UV emission, I the drive current of the LED, V the operating voltage for the LED, $h\omega$ the photon energy, and η_{EQE} the external quantum efficiency (EQE) of the LED. The external quantum efficiency of the UV-LED can be easily determined by measuring the total UV output power P_{out} and dividing this by the drive current I and the photon energy $h\omega$ according to the following equation:

$$\eta_{\mathrm{EQE}} = \frac{e \cdot P_{\mathrm{out}}}{I \cdot \hbar\omega}$$

In other words, the EQE can also be described as the ratio of the number of UV photons emitted from the LED to the number of charge carriers injected into the device. The external quantum efficiency itself can be described as a product of the injection efficiency η_{inj}, the radiative recombination efficiency η_{rad}, and the light extraction efficiency η_{ext} as also shown in the following formula:

$$\eta_{\mathrm{EQE}} = \eta_{\mathrm{inj}} \cdot \eta_{\mathrm{rad}} \cdot \eta_{\mathrm{ext}} = \eta_{\mathrm{IQE}} \cdot \eta_{\mathrm{ext}}$$

Therefore, the injection efficiency η_{inj} describes the ratio of charge carriers, i.e., electrons and holes that reach the QW active region versus the total current being injected into the device. The radiative recombination efficiency η_{rad} is the fraction of all electron–hole pairs that recombine radiatively in the QW active region, i.e., producing UV photons. The internal quantum efficiency η_{IQE} (or IQE) can be calculated as the product of the radiative recombination efficiency η_{rad} and the injection efficiency η_{inj}. It is possible to determine the IQE by temperature and excitation power-dependent photoluminescence measurements [57], although great care has to be taken in the interpretation of the data. The light extraction efficiency η_{ext} is defined as the fraction of UV photons that can be extracted from the LED compared to all the UV photons that are generated in the active region. The radiative recombination efficiency η_{rad} can be expressed as the ratio of the radiative recombination rate R_{sp} versus the sum of radiative and nonradiative recombination R_{nr} rates and is described by the following equation:

$$\eta_{\mathrm{rad}} = \frac{R_{\mathrm{sp}}}{R_{\mathrm{sp}} + R_{\mathrm{nr}}}$$

The nonradiative recombination rate can be expressed as the sum of the Shockley–Read–Hall recombination term and the Auger recombination term as follows:

$$R_{\mathrm{nr}} = A \cdot n + C \cdot n^3,$$

where A represents the Shockley–Read–Hall (SRH) recombination coefficient, C the Auger recombination coefficient, and the parameter n the charge carrier density in QW. The Shockley–Read–Hall recombination coefficient A is inverse proportional to the SRH recombination lifetime, which strongly depends on the defect density in the materials. Nonradiative recombination lifetimes as short as a few tens of ps have been measured for highly defective AlGaN layers. In contrast, nonradiative recombination lifetimes in the ns range have been demonstrated for AlGaN quantum well emitters on low defect density bulk AlN substrates [58, 59]. The magnitude of the Auger recombination coefficient C for III-nitride materials is still being heavily debated [60–65] and values for the C coefficient for blue-violet

LEDs range between 1×10^{-31} and 2×10^{-30} cm^6 s^{-1}. Measurements to determine the C coefficient for UV emitter are even more rudimentary [66]; also theoretical models suggest that the Auger coefficient should become smaller and smaller for shorter emission wavelength [67].

Finally, the radiative recombination or spontaneous recombination rate R_{sp} can be expressed as

$$R_{sp} = B \cdot n^2,$$

with B representing the bimolecular recombination coefficient and n the charge carrier density in QW. The B coefficient will strongly depend on the design of the active region, e.g., the quantum well width, quantum barrier height, the strain state of the AlGaN QWs, and the magnitude of the polarization field in the QW. Typical values for the B coefficient are in the range of 2×10^{-11} cm^3 s^{-1} [66, 68].

Today, the best InGaN-based blue LEDs boast external quantum efficiencies (EQE) of 84 % and wall plug efficiencies (WPE) of 81 % [69] and commercial blue LEDs exhibit EQEs of 69 % and WPEs of 55 %, respectively [70]. These extraordinary values can only be achieved by perfecting all constituents that contribute to the WPE and EQE. Due the development of thin film LED technologies, highly reflective metal contacts, and advanced packaging methods, light extraction efficiencies in modern blue LEDs exceed 85 %. Furthermore, low defect density GaN/sapphire templates and highly efficient InGaN quantum well active regions lead to internal quantum efficiencies near 90 % [70]. Mg-doped GaN AlGaN electron blocking layers and low resistance n-GaN current spreading layers lead to injection efficiencies well beyond 90 % [70]. And finally, refined Mg- and Si-doping profiles and optimized ohmic contacts guarantee very low operating voltages, which translate into high WPE. However, the extraordinary characteristics of blue LEDs do not translate into similar performance for shorter wavelength LEDs. Whereas UVA-LEDs near 365 nm still exhibit EQEs beyond 30 %, at least in research prototypes, typical LEDs in the UV-B and UVC spectral range exhibit external quantum efficiencies of 1–3 %, as can be seen in Fig. 1.1. A number of factors contribute to this overall small value, including poor radiative recombination efficiencies and modest injection efficiencies, resulting in low internal quantum efficiencies as well as inferior light extraction and high operating voltages. From the analysis of state-of-the-art UVC-LED one can estimate the light extraction efficiency to be below 10 %, and the radiative and injection efficiencies to be somewhere around 50 %, respectively. In the following section the main causes contributing to these behaviors will be explained and different options to overcome these deficiencies will be discussed.

1.5 The Role of Defects on the IQE of UV-LEDs

A significant contribution to the low IQE in UV emitters can be attributed to the relatively high defect densities in AlN and AlGaN materials. For example, growth of AlN layers on (0001) sapphire substrates typically yields dislocation densities in the range of 10^{10} cm^{-2} [50–52]. These threading dislocations form nonradiative recombination pathways for the injected carriers leading to significantly reduced internal (IQE) and external quantum efficiencies (EQE) [57, 70, 71]. Different approaches to reduce the dislocation densities in AlGaN and AlN layers on sapphire substrates have been demonstrated, including epitaxial lateral overgrowth (ELO) yielding defect densities in the mid 10^8 cm^{-2} range [72–76]. Other approaches to reduce the defect density include the growth on nano-patterned sapphire substrates [29, 77], the use of short period AlGaN superlattices [78] as well as low temperature AlN or SiN_x interlayers [18, 79]. To estimate the effect of dislocations on the internal quantum efficiency of UV-LEDs the IQE was simulated based on a model initially published by Karpov et al. [71]. In order to compute the IQE, the radiative and noradiative recombination rates are calculated as a function of the threading dislocation density and injection current density [23]. The model assumes that threading dislocations form deep levels within the band gap that act as nonradiative recombination centers for electrons and holes. There are a number of potential defects in AlGaN wurtzite semiconductor materials that form deep levels, e.g., screw, edge, or mixed type threading dislocations as well as N- or Ga-vacancies [80–83]. Although the nature of the dislocation and its electronic properties is not part of the model, the parameter S in the simulation characterizes the fraction of electrically active sites on the dislocation core. In addition, the IQE is governed by the electron and hole mobilities, nonequilibrium carrier concentrations, and consequently the minority carrier diffusion lengths. As can be seen from the results of the simulation in Fig. 1.5a, dislocation densities in the range of 10^7 cm^{-2} are required in order to provide internal quantum efficiencies close to unity. By utilizing advanced dislocation filtering techniques, one could expect to realize dislocation densities in this range even for heteroepitaxial growth on sapphire substrates. As can also be seen from Fig. 1.5b, for a fixed threading dislocation density, the IQE also strongly depends on the electron mobility and current density. This dependency is most pronounced for dislocation densities ranging between mid 10^8 and 10^{10} cm^{-2}, when the carrier diffusion lengths and the spacing of the dislocations are approximately the same size (Fig. 1.6).

Even lower defect densities can be achieved by homoepitaxial growth on bulk AlN substrates. For example, bulk AlN substrates grown by sublimation recondensation have yielded dislocation densities as low as 10^4 cm^{-2} [84–87], although the availability of these substrates is still limited and currently typical substrates sizes are 1-in. diameter or even smaller. In addition bulk AlN substrates exhibit strong absorption bands in the UVC spectral range [88, 89], which poses a serious challenge for the light extraction, since this is normally achieved by extracting the UV light through the substrate. As various studies show, the origin of these UVC

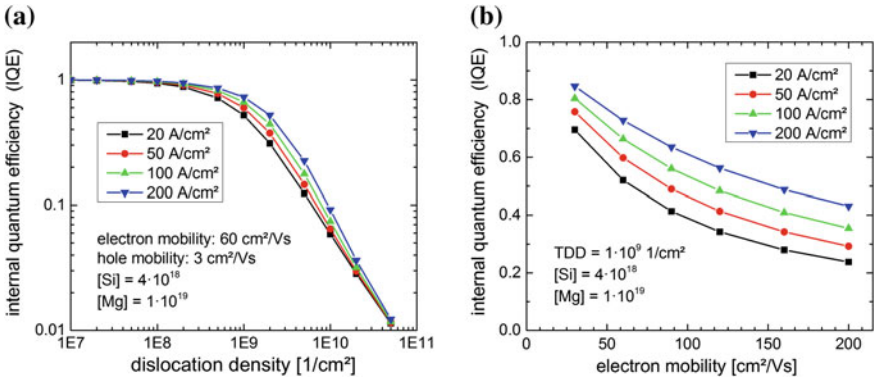


Fig. 1.5 Simulated internal quantum efficiencies (IQE) for an AlGaN MQW LED emitting near 265 nm. **a** IQE versus threading dislocation density in the active region for different current densities. **b** IQE versus the electron mobility for different current densities (simulations are courtesy of Martin Guttmann and Christoph Reich, Institute of Solid State Physics, TU Berlin)

absorption bands can be traced back to carbon impurities and the formation of complexes [88–90]. Therefore these UVC absorption bands appear to be not a fundamental problem, but a materials research challenge that can be solved by optimizing the purity of the sources in order to reduce the carbon impurity concentrations either by clever co-doping schemes, or by inserting a thick hydride vapor epitaxy grown AlN base layer [91]. UVC-LED heterostructures pseudomorphically grown on bulk AlN substrate have been demonstrated by two groups [22, 92] with external quantum efficiencies of more than 5 % at emission wavelength near 270 nm and first steps to commercialize these devices have been undertaken.

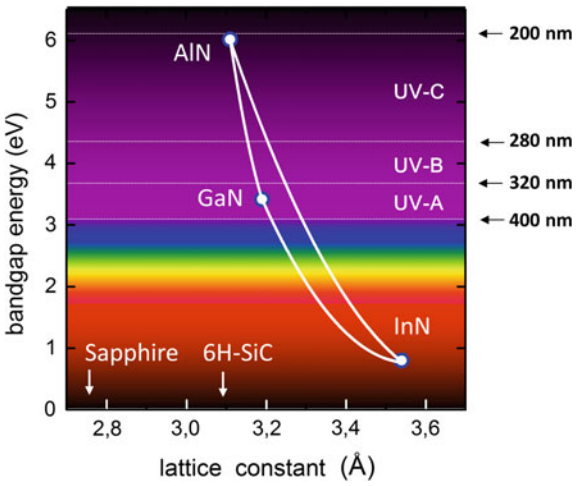


Fig. 1.6 Bandgap energies and emission wavelength of InN, GaN, AlN and other III–V and II–VI compound semiconductor materials plotted versus their lattice spacing

1.6 Current-Injection Efficiency and Operating Voltages of UV-LEDs

Very often UV-LEDs suffer from poor injection efficiencies and high operation voltages that originate from the relatively low conductivities of Mg-doped p-AlGaN layers. This is due to the fact that the ionisation energy for the Mg acceptor increases steadily with the aluminum mole fraction in the Mg-doped p-AlGaN layer [93, 94]. For Mg-doped AlN layers the acceptor level has been determined to be about 510 meV above the valence band edge [70]. Therefore, in Mg-doped bulk AlGaN layers only a small fraction of the Mg acceptors are ionized at room temperature, resulting in very low free hole concentrations. But even the silicon doping on n-AlGaN layers becomes increasingly more challenging at high aluminum mole fractions [95–97]. Both n- and p-AlGaN layer resistances as well as the ohmic contact resistances of the n- and p-metals contribute to the relatively high operating voltages of UV light emitting devices. Various approaches to improve the conductivity of p-AlGaN layers have been explored, e.g., utilizing short period $Al_xGa_{1-x}N/Al_yGa_{1-y}N$ superlattices [98, 99], polarization doping of graded $Al_xGa_{1-x}N$ layers [100], and alternative p-layer materials like Mg-doped boron nitride (hBN) [101]. Also, the limits of silicon doping of n-AlGaN layers at very high aluminum mole fractions have been explored and record low resistivity AlGaN: Si current-spreading layers in the composition range between 60 and 96 % have been demonstrated [102, 103]. A number of studies have looked at ohmic metal contact formation to n-AlGaN layers and lowering the contact resistances [104–108] with very promising results in the medium aluminum composition range. Since sapphire and AlN substrates are electrically insulating, electrons are normally laterally injected through the n-AlGaN layer. In order to reduce the n-layer series resistance and to facilitate homogeneous current injection often interdigitated finger contact geometries are employed in the chip design. Figure 1.7 shows a photograph of an

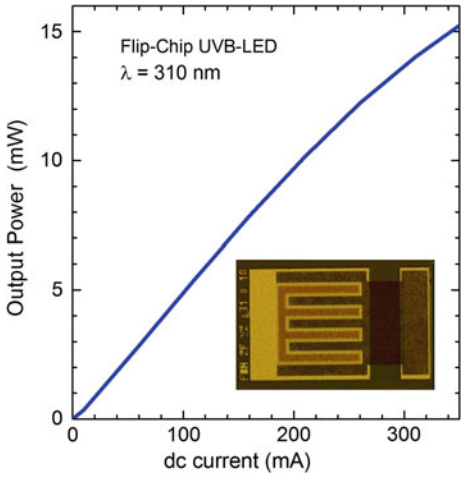


Fig. 1.7 Light-output versus current (*L–I*) characteristic of a flip-chip mounted UVB-LED on a ceramic package. The *inset* shows a photograph of the LED chip with interdigitated finger contacts before mounting

UVB-LED chip with interdigitated finger contacts and its light-output versus current (*L–I*) characteristic after flip-chip mounting.

Another key challenge is efficient hole injection into the AlGaN quantum wells as well as electron leakage from the active region. Injection efficiency and electron leakage are two properties that are difficult to determine in a UV-LED and can range from less than 10 % for deep UV emitters to more than 90 % for UVA-LEDs near 400 nm [70, 109]. Especially for UVB- and UVC-LEDs, the development of novel injection schemes is critical in order to reduce electron leakage while improving hole-injection efficiencies into the active region. On this topic, various approaches have been demonstrated, e.g., Mg-doped AlGaN electron blocking layers, AlN/AlGaN electron blocking heterostructures [28, 31], and AlGaN/AlGaN multi-quantum-barriers [19].

1.7 Light Extraction from UV-LEDs

Improving light extraction from UV-LEDs is a key challenge in order to increase the EQE and WPE of UV-LEDs. Currently, most UV-LED chips do not include any features for advanced light extraction. As can be seen from Table 1.1, the light extraction efficiency for a single square LED chip on a UV-transparent sapphire substrate is only in the range of 8–10 % [110]. This is due to the fact that many of the light extraction methods that are state of the art for blue and near UV-LED cannot be applied to deep UV-LEDs. For example, highly reflective and low resistance silver-based metal contacts are typically employed in blue LEDs. Although Ag contacts provide excellent reflectors in the visible and near UV range, the reflectivity drops rapidly for wavelength below 350 nm (see e.g., Chap. 6). Aluminum, which would be a very good reflector in the entire UV range and possible alternative contact material does not normally form an ohmic contact to Mg-doped p-AlGaN due to its low work function. In addition, thin film technologies that are routinely applied to GaN-based LEDs have not yet been developed

Table 1.1 Estimated light extraction efficiencies (LEE) for different UV-LEDs chip technologies

UV-LED chip technology	LEE (%)
LED on-wafer	7–9
Single square LED chip	8–10
Single triangular LED chip	11–13
LED with reflective p-contact (R = 40 %)	~20
LED with reflective p-contact (R = 80 %)	~30
Thin film LED chip, incl. backside roughening	30–50
Thin film LED chip with reflective contacts and backside roughening	40–60
Thin film LED with reflective contacts and backside roughening and advanced packaging	50–90

for deep UV emitters. Ultraviolet light also poses an enormous challenge in finding suitable encapsulation and packaging materials. Many advanced packaging materials, i.e., high-index transparent silicones and polymers, that are state of the art for blue LEDs, are not stable when exposed to high energy UV photons. Therefore completely new solutions have to be developed for AlGaN-based deep UV emitters and several approaches to enhance light extraction have been investigated including photonic crystals, roughening of LED surfaces, patterning of substrates, shaping of LED dies, micro-pixel LEDs, and omnidirectional reflectors [111–115]. Another approach to realize ohmic and UV-reflective contacts are nano-pixel LEDs. In this case low resistance ohmic contacts are facilitated through closely spaced nano-pixel size Pd/p-GaN electrodes while the area between the nano-pixels is covered with UV-reflective aluminum reflectors [116].

An additional complication arises from the large negative crystal field splitting in AlGaN alloys. This causes a rearrangement of the valence bands at higher aluminum mole fraction resulting in a change in the polarization of light emission from TE to TM at shorter wavelength [117]. Consequently, fewer photons can be extracted from the light escape cone via the surface or the substrate of deep UV-LEDs. Although the basic properties of AlN materials cannot be changed, the optical polarization of the light emission can be controlled by the design of the AlGaN quantum well active region and the built-in compressive or tensile strain. Recent studies have shown that even at very short wavelengths below 250 nm the polarization of emission from LEDs can be switched to strongly TE-polarized emission by employing highly compressively strained AlGaN active regions [118–121] and by appropriately adjusting the quantum well width and barrier height [122]. In addition, by employing reflector and scattering structures in advanced UVC-LED chip designs, enhanced outcoupling of TM polarized emission was recently demonstrated [123, 124].

1.8 Thermal Management and Degradation of UV-LED

Since the UV-LED light output as well as LED degradation is highly temperature-dependent, thermal management is pivotal for high performance UV light emitters [125, 126, 127]. Many LED failure mechanisms can also be traced back to overheating. Therefore most high-power UV-LEDs are flip-chip mounted onto ceramic submounts or directly integrated into SMD (surface-mount device) packages. Flip-chip mounting allows for efficient light extraction through the UV-transparent sapphire substrate and at the same time provides excellent heat extraction for thermal management. Typical packaging materials, e.g., include AlN and BN ceramics as well as aluminum, CuW, and copper. In order to dissipate the power generated at the contacts and pn-junction of the LED, the excess heat must be extracted through the package. Since only a small fraction of the excess power can be dissipated by radiation or convection from the LED chip, the heat extraction is mostly conducted through the package. The thermal resistance of the package is

hereby given by the sum of the thermal resistance of the LED die, the die attach, the heatsink, and finally the solder attaching the package to the board. Of course for the total thermal resistance the thermal resistances of the solder pads and the mounting board (e.g., PCB) also have to be added. Package thermal resistance can vary greatly depending on the packaging technologies. Top-emitting low power UV-LEDs, where the heat is extracted through the sapphire substrate can exhibit thermal resistance in the range of 40 K/W to more than 200 K/W depending on the packaging technology [128]. On the other hand flip-chip mounted UV-LEDs in high power packages can yield thermal resistances from 15 K/W to less than 5 K/W [129].

Another complex issue is the degradation of UV-LEDs. Early devices exhibited rapid degradation and very short lifetimes, especially for UVB- and UVC-LEDs [39, 41]. In some cases the output power dropped by more than 50 % within the first 100 h of operation, rendering these LEDs impractical for real-world applications. Next to increasing the LED efficiencies, improving the lifetimes of UV-LEDs is one of the key issues to solve in order to enable a broader integration of UV-LEDs in many applications. Fortunately due to improvements in material quality, chip technology, and thermal management, significant improvements in UV-LED lifetimes can be observed as can be seen in Fig. 1.8. Today, state-of-the-art UVB-LEDs on sapphire emitting at 310 nm and near 280 nm exhibit L50 lifetimes of more than 10.000 h [130, 131] and 3.000 h [30]. For UVC-LEDs on bulk AlN substrates with emission below 270 nm L50 lifetimes well in excess of 1.000 h have been reported [132]. It is difficult to predict how fast progress in this area will be but a better understanding of the degradation mechanism of UV-LEDs will be pivotal in solving the lifetime issues [133, 134]. This, of course, is not only limited to the LED chip and the semiconductor materials, but also includes packaging and encapsulation materials.

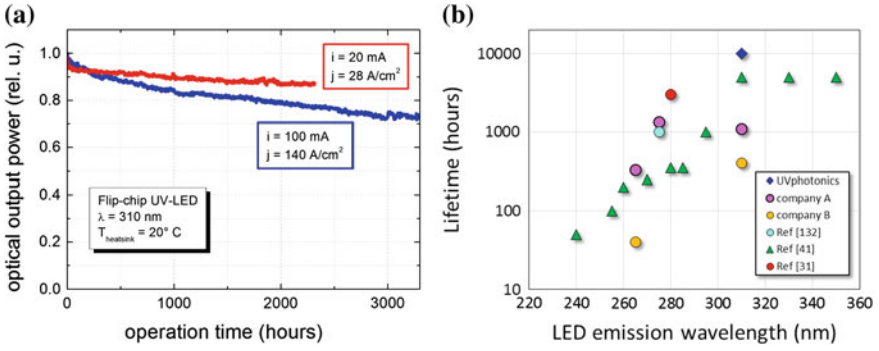


Fig. 1.8 **a** Normalized change in UVB-LED output power over time. L_{50} lifetimes of more than 10.000 h are expected. **b** Reported and measured lifetimes for UV-LEDs from different generations and emission wavelength

1.9 Outlook

Generally, it is a difficult undertaking to provide an accurate prognosis of the future performance of UV-LEDs. Nevertheless, by taking into account the rate of progress in the past decade as well as the potential improvements by implementing the different technological advances outlined in the earlier paragraphs, one can compile a roadmap for the future device performance. Based on these assumptions Fig. 1.9a, b displays the projected device performance for three wavelength bands around 310, 285, and 310 nm. Specifically, the past and future wall plug efficiencies and output power levels for single LEDs chips are plotted. The solid data points hereby represent the state of the art of commercially available UV-LED devices at different times up to 2015. It should be noted that these values have been obtained by measurements in our laboratory. In addition, the number of tested devices was limited due to the scant number of commercial sources for UVB- and UVC-LEDs and that devices were not readily available from all commercial sources. There are a number of factors that will lead to future improvement of the wall plug efficiency (WPE), including increases in internal quantum efficiency, reduced operating voltages, and enhancements in light extraction. As the WPE is improving, the output power per UV-LED chip will also increase. In addition to efficiency improvements larger chip areas, improved thermal management, and increases in the operating current will lead to further increases in the total output power per LED chip. For example, today most UVB- and UVC-LEDs are operated at 20 or 100 mA DC current and the footprint of the emitting area is typically limited to less than 0.1 mm^2. It is expected that the chip size of UV-LEDs will increase to 1 mm^2 and more, and operating currents of 350, 700 mA or even 1 A will become standard. The pace at which these improvements are implemented, will of course also depend on the amount of effort that goes into the research and development for these

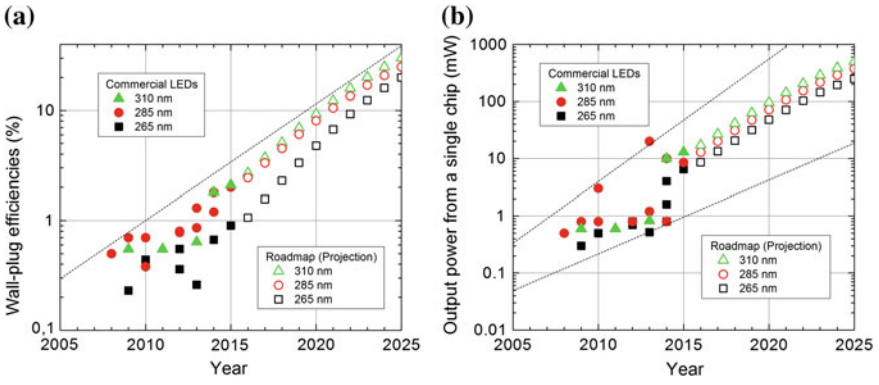


Fig. 1.9 Actual and projected wall plug efficiencies **a** as well as light output power **b** of production scale UV-LEDs in the wavelength band around 310, 285, and 265 nm. The *dotted lines* provide the upper and lower limits for the prognosis and are also an indicator for the uncertainty in the projection

devices. Fortunately, it appears that research efforts in the development of UV light emitters have significantly accelerated in the past few years and that more and more larger industry players (e.g., Nichia, LG Innotek, Panasonic) are getting involved.

1.10 Summary

Since the first demonstration of UV light emitting diodes in the early 1990s [135] and first AlGaN-based LEDs in early 2000 [136–138], steady progress has been made in the development of ultraviolet LEDs. For a number of reasons however, the rate of progress in UV emitter performances was much slower than for GaN-based blue and white LEDs. The various technological challenges have been discussed in this chapter. One additional reason is the enormous variety of applications for UV emitters. This makes UV-LEDs on the one hand extremely versatile, but on the other hand it hinders the rapid development of UV devices due to the strongly varying requirements (i.e., emission wavelength, power levels, lifetimes) depending on the application. Overall, the development of group III-nitride UV emitters can be divided into three stages. The first phase was characterized by fundamental materials breakthrough and basic proof of device operation. This stage was followed by steady progress in device technologies and UVB- and UVC-LED performance as well as maturing of UVA-LEDs and their widespread adoption in applications like UV curing. We have now entered the third phase, which is characterized by an increasing number of companies and especially larger players entering the commercial markets. This will accelerate the development pace of UVB- and UVC-LEDs and soon the performance level will reach the threshold to enable first applications in the area of sensing, medical diagnostics, phototherapy, and point-of-use water disinfection. It is not an overstatement to say that there are no fundamental technological roadblocks prohibiting the realization of long-lived, high power and high efficiency UV-LED in the entire UV spectral range. Without exaggeration one can state that AlGaN-based LEDs will prevail as UV emitter technology and that in the not too distant future we will see more and more applications that are enabled by UV-LEDs.

Acknowledgment This review would not have been possible without the commitment of numerous Ph.D. students, postdoctoral researchers, colleagues, and collaborators over many years resulting in a large number of joint publications, many of which are also referenced in this book chapter. Without emphasizing anyone in particular I would like to thank all of these individuals for their contributions. I also like to acknowledge the financial support by a number of funding agencies, starting with the DARPA "SUVOS" program that ran in the United States between 2002 and 2006. Since my return to Germany I gratefully acknowledge support by the German Research Foundation (DFG) within the Collaborative Research Center "Semiconductor Nanophotonics" (CRC 787) as well as funding by the Federal Ministry of Education and Research (BMBF) of Germany within the "Deep UV-LED" and "UltraSens" projects, the regional growth core "WideBaSe", and the consortium "Advanced UV for Life" within the "Twenty20 – Partnership for Innovation" initiative. Finally, I would like to take this opportunity to thank my family, in particular my wife Rebecca, for her encouragement, continued support, and patience.

References

1. I. Akasaki, H. Amano, K. Hiramatsu, N. Sawaki, High efficiency blue LED utilizing GaN film with AlN buffer layer grown by MOVPE. in *Proceedings of 14th International Symposium on Gallium Arsenide and Related Compounds 1987,* pp. 633–636 (1988)
2. S. Nakamura, T. Mukai, M. Senoh, High-power GaN p-n junction blue-light-emitting diodes. Jpn. J. Appl. Phys. **30**, L1998–L2001 (1991)
3. S. Nakamura, M. Senoh, T. Mukai, p-GaN/n-InGaN/n-GaN double-heterostructure blue-light-emitting diodes. Jpn. J. Appl. Phys. **32**, L8–L11 (1993)
4. S. Nakamura, T. Mukai, M. Senoh, Candera-class high-brightness InGaN/AlgaN double-heterostructure blue-light-emitting diodes. Appl. Phys. Lett. **64**, 1687–1689 (1994)
5. Press release of the The Royal Swedish Academy of Sciences. Retrieved 7 Oct 2014, www.nobelprize.org/nobel_prizes/physics/laureates/2014/press.html.
6. `UV LED Efficiency 2015 (last update 19-July-2015)'. Retrieved 6 Oct 2015, www.researchgate.net/publication/280131929
7. T. Nishida, N. Kobayashi, T. Ban, GaN-free transparent ultraviolet light-emitting diodes. Appl. Phys. Lett. **82**, 1 (2003)
8. J. Edmond, A. Abare, M. Bergman, J. Bharathan, K.L. Bunker, D. Emerson, K. Haberern, J. Ibbetson, M. Leung, P. Russel, D. Slater, High efficiency GaN-based LEDs and lasers on SiC. J. Cryst. Growth **272**, 242 (2004)
9. M. Kneissl, Z. Yang, M. Teepe, C. Knollenberg, N.M. Johnson, A. Usikov, V. Dmitriev, Ultraviolet InAlGaN light emitting diodes grown on hydride vapor phase epitaxy AlGaN/sapphire template. Jpn. J. Appl. Phys. **45**, 3905 (2006)
10. Y. Taniyasu, M. Kasu, T. Makimoto, An aluminium nitride light-emitting diode with a wave-length of 210 nanometres. Nature **441**, 325 (2006)
11. H. Tsuzuki, F. Mori, K. Takeda, T. Ichikawa, M. Iwaya, S. Kamiyama, H. Amano, I. Akasaki, H. Yoshida, M. Kuwabara, Y. Yamashita, H. Kan, High-performance UV emitter grown on high-crystalline quality AlGaN underlying layer. Phys. Status Solidi (a) **206**, 1199 (2009)
12. J.P. Zhang, A. Chitnis, V. Adivarahan, S. Wu, V. Mandavilli, R. Pachipulusu, M. Shatalov, G. Simin, J.W. Yang, M.A. Kahn, Milliwatt power deep ultra-violet light-emitting diodes over sapphire with emission at 278 nm. Appl. Phys. Lett. **81**, 4910 (2002)
13. V. Adivarahan, S. Wu, J.P. Zhang, R.A. Chitnis, M. Shatalov, V. Mandavilli, R. Gaska, M. A. Khan, High-efficiency 269 nm emission deep ultraviolet light-emitting diodes. Appl. Phys. Lett. **84**, 4762 (2004)
14. J. Zhang, X. Hu, A. Lunev, J. Deng, Y. Bilenko, T.M. Katona, M.S. Shur, R. Gaska, M.A. Khan, AlGaN deep-ultraviolet light-emitting diodes. Jpn. J. Appl. Phys. **44**, 7250 (2005)
15. H. Hirayama, T. Yatabe, N. Noguchi, T. Ohashi, N. Kamata, 231–261 nm AlGaN deep-ultraviolet light-emitting diodes fabricated on AlN multilayer buffers grown by ammonia pulse-flow method on sapphire. Appl. Phys. Lett. **91**, 071901 (2007)
16. A. Khan, K. Balakrishnan, T. Katona, Ultraviolet light-emitting diodes based on group three nitrides. Nat. Photonics **2**, 77 (2008)
17. S. Sumiya, Y. Zhu, J. Zhang, K. Kosaka, M. Miyoshi, T. Shibata, M. Tanaka, T. Egawa, AlGaN-based deep ultraviolet light-emitting diodes, grown on epitaxial AlN/sapphire templates. Jpn. J. Appl. Phys. **47**, 43 (2008)
18. H. Hirayama, S. Fujikawa, N. Noguchi, J. Norimatsu, T. Takano, K. Tsubaki, N. Kamata, 222–282 nm AlGaN and InAlGaN-based deep-UV LEDs fabricated on high-quality AlN on sapphire. Phys. Stat. Sol. (a) **206**, 1176 (2009)
19. H. Hirayama, Y. Tsukada, T. Maeda, N. Kamata, Marked enhancement in the efficiency of deep-ultraviolet AlGaN light-emitting diodes by using a multiquantum-barrier electron blocking layer. Appl. Phys. Express **3**, 031002 (2010)

20. A. Fujioka, T. Misaki, T. Murayama, Y. Narukawa, T. Mukai, Improvement in output power of 280-nm deep ultraviolet light-emitting diode by using AlGaN multi quantum wells. Appl. Phys. Express **3**, 041001 (2010)
21. C. Pernot, M. Kim, S. Fukahori, T. Inazu, T. Fujita, Y. Nagasawa, A. Hirano, M. Ippommatsu, M. Iwaya, S. Kamiyama, I. Akasaki, H. Amano, Improved efficiency of 255–280 nm AlGaN-based light-emitting diodes. Appl. Phys. Express **3**, 061004 (2010)
22. J.R. Grandusky, S.R. Gibb, M.C. Mendrick, C. Moe, M. Wraback, L.J. Schowalter, High output power from 260 nm pseudomorphic ultraviolet light-emitting diodes with improved thermal performance. Appl. Phys. Express **4**, 082101 (2011)
23. M. Kneissl, T. Kolbe, C. Chua, V. Kueller, N. Lobo, J. Stellmach, A. Knauer, H. Rodriguez, S. Einfeldt, Z. Yang, N.M. Johnson, M. Weyers, Advances in group III-nitride based deep UV light emitting diode technology. Semicond. Sci. Technol. **26**, 014036 (2011)
24. M. Shatalov, W. Sun, A. Lunev, X. Hu, A. Dobrinsky, Y. Bilenko, J. Yang, AlGaN Deep-ultraviolet light-emitting diodes with external quantum efficiency above 10 %. Appl. Phys. Express **5**, 082101 (2012)
25. V. Kueller, A. Knauer, C. Reich, A. Mogilatenko, M. Weyers, J. Stellmach, T. Wernicke, M. Kneissl, Z. Yang, C.L. Chua, N.M. Johnson, Modulated epitaxial lateral overgrowth of aln for efficient UV LEDs. IEEE Photonics Tech. Lett. **24**, 1603 (2012)
26. T. Kinoshita, T. Obata, T. Nagashima, H. Yanagi, B. Moody, S. Mita, S. Inoue, Y. Kumagai, A. Koukitu, Z. Sitar, Performance and reliability of deep-ultraviolet light-emitting diodes fabricated on AlN substrates prepared by hydride vapor phase epitaxy. Appl. Phys. Express **6**, 092103 (2013)
27. J.R. Grandusky, J. Chen, S.R. Gibb, M.C. Mendrick, C.G. Moe, L. Rodak, G.A. Garrett, M. Wraback, L.J. Schowalter, 270 nm pseudomorphic ultraviolet light-emitting diodes with over 60 mW continuous wave output power. Appl. Phys. Express **6**, 032101 (2013)
28. T. Kolbe, F. Mehnke, M. Guttmann, C. Kuhn, J. Rass, T. Wernicke, M. Kneissl, Improved injection efficiency in 290 nm light emitting diodes with Al(Ga)N electron blocking heterostructure. Appl. Phys. Lett. **103**, 031109 (2013)
29. P. Dong, J. Yan, J. Wang, Y. Zhang, C. Geng, T. Wei, P. Cong, Y. Zhang, J. Zeng, Y. Tian, L. Sun, Q. Yan, J. Li, S. Fan, Z. Qin, 282-nm AlGaN-based deep ultraviolet light-emitting diodes with improved performance on nano-patterned sapphire substrates. Appl. Phys. Lett. **102**, 241113 (2013)
30. A. Fujioka, K. Asada, H. Yamada, T. Ohtsuka, T. Ogawa, T. Kosugi, D. Kishikawa, T. Mukai, High-output-power 255/280/310 nm deep ultraviolet light-emitting diodes and their lifetime characteristics. Semicond. Sci. Technol. **29**, 084005 (2014)
31. F. Mehnke, C. Kuhn, M. Guttmann, C. Reich, T. Kolbe, V. Kueller, A. Knauer, T. Wernicke, J. Rass, M. Weyers, M. Kneissl, Efficient charge carrier injection into sub-250 nm AlGaN multiple quantum well light emitting diodes. Appl. Phys. Lett. **105**, 051113 (2014)
32. H. Hirayama, N. Maeda, S. Fujikawa, S. Toyoda, N. Kamata, Recent progress and future prospects of AlGaN-based high-efficiency deep-ultraviolet light-emitting diodes. Jpn. J. Appl. Phys. **53**, 100209 (2014)
33. Information on low and medium pressure mercury lamps. Retrieved 5 Oct 2015, www.heraeus-noblelight.com
34. W.L. Morison, *Phototherapy and Photochemotherapy of Skin Disease*, 2nd edn. (Raven Press, New York, 1991)
35. P.E. Hockberger, A history of ultraviolet photobiology for humans, animals and microorganisms. Photochem. Photobiol. **76**(6), 561–579 (2002)
36. M. Schreiner, J. Martínez-Abaigar, J. Glaab, M. Jansen, UVB induced secondary plant metabolites. Optik Photonik **9**(2), 34–37 (2014)
37. S. Vilhunen, H. Särkkä, M. Sillanpää, Ultraviolet light-emitting diodes in water disinfection. Environ. Sci. Pollut. Res. **16**(4), 439–442 (2009)
38. M.H. Crawford, M.A. Banas, M.P. Ross, D.S. Ruby, J.S. Nelson, R. Boucher, A.A. Allerman, Final LDRD report: ultraviolet water purification systems for rural environments and mobile applications. Sandia Report, SAND2005-7245 (2005)

39. M.A. Würtele, T. Kolbe, M. Lipsz, A. Külberg, M. Weyers, M. Kneissl, M. Jekel, Application of GaN-based deep ultraviolet light emitting diodes—UV-LEDs—for Water disinfection. Water Res. **45**(3), 1481 (2011)
40. W. Kowalski, *Ultraviolet Germicidal Irradiation Handbook* (Springer-Verlag, Berlin, Heidelberg, 2009)
41. G.Y. Lui, D. Roser, R. Corkish, N. Ashbolt, P. Jagals, R. Stuetz, Photovoltaic powered ultraviolet and visible light-emitting diodes for sustainable point-of-use disinfection of drinking waters. Sci. Total Environ. **493**, 185 (2014)
42. J. Mellqvist, A. Rosen, DOAS for flue gas monitoring—temperature effects in the UV/visible absorption spectra of NO, NO_2, SO_2, and NH_3. J. Quant. Spectrosc. Radiat. Transf. **56**(2), 187–208 (1996)
43. J. Hodgkinson, R.P. Tatam, Optical gas sensing: a review. Meas. Sci. Technol. **24**, 012004 (2013)
44. P.J. Hargis Jr, T.J. Sobering, G.C. Tisone, J.S. Wagner, Ultraviolet fluorescence detection and identification of protein, DNA, and bacteria. Proc. SPIE **2366**, 147 (1995)
45. Z. Xu, B.M. Sadler, Ultraviolet communications: potential and state-of-the-art. IEEE Commun. Mag. **67** (2008)
46. K.-X. Sun, B. Allard, S. Buchman, S. Williams, R.L. Byer, LED deep UV source for charge management of gravitational reference sensors. Class. Quantum Grav. **23**, S141–S150 (2006)
47. "UV-LED market to grow from $90 m to $520 m in 2019". Retrieved 5 Oct 2015, www.semiconductor-today.com Semicond. Today **10**(1), 80 (2015)
48. F. Mehnke, Institute of Solid State Physics, TU Berlin, private communication (2014)
49. T. Whitaker, Rubicon technology demonstrates 12-inch sapphire wafers. www.ledsmagazine.com/articles/2011/01/rubicon-technology-demonstrates-12-inch-sapphire-wafers.html
50. F. Brunner, H. Protzmann, M. Heuken, A. Knauer, M. Weyers, M. Kneissl, High-temperature growth of AlN in a Production Scale 11x2" MOVPE reactor. Phys. Stat. Sol. (c) **1** (2008)
51. O. Reentilä, F. Brunner, A. Knauer, A. Mogi-latenko, W. Neumann, H. Protzmann, M. Heuken, M. Kneissl, M. Weyers, G. Tränkle, Effect of the AlN nucleation layer growth on AlN material qual-ity. J. Cryst. Growth **310**(23), 4932 (2008)
52. V. Kueller, A. Knauer, F. Brunner, A. Mogilatenko, M. Kneissl, M. Weyers, Investigation of inversion domain formation in AlN grown on sapphire by MOVPE. Phys. Stat. Sol. (c) **9**(3–4), 496–498 (2012)
53. D.A.B. Miller, D.S. Chemla, T.C. Damen, A.C. Gossard, W. Wiegmann, T.H. Wood, C.A. Burrus, Band-edge electroabsorption in quantum Weil structures: the quantum-confined stark effect. Phys. Rev. Lett. **53**(22), 2173 (1984)
54. J. Simon, V. Protasenko, C. Lian, H. Xing, D. Jena, Polarization-induced hole doping in wide–band-gap uniaxial semiconductor heterostructures. Science **327**, 60 (2009)
55. Y. Liao, C. Thomidis, C. Kao, T.D. Moustakas, AlGaN based deep ultraviolet light emitting diodes with high internal quantum efficiency grown by molecular beam epitaxy. Appl. Phys. Lett. **98**, 081110 (2011)
56. S. Kurin, A. Antipov, I. Barash, A. Roenkov, A. Usikov, H. Helava, V. Ratnikov, N. Shmidt, A. Sakharov, S. Tarasov, E. Menkovich, I. Lamkin, B. Papchenko, Y. Makarov, Characterization of HVPE-grown UV LED heterostructures. Phys. Stat. Sol (c) **11**(3–4), 813 (2014)
57. S.F. Chichibu, A. Uedono, T. Onuma, B.A. Haskell, A. Chakraborty, T. Koyama, P.T. Fini, S. Keller, S.P. DenBaars, J.S. Speck, U.K. Mishra, S. Nakamura, S. Yamaguchi, S. Kamiyama, H. Amano, I. Akasaki, J. Han, T. Sota, Origin of defect-insensitive emission probability in In-containing (Al, In, Ga)N alloy semiconductors. Nat. Mater. **5**, 810–816 (2006)
58. T. Wunderer, C.L. Chua, Z. Yang, J.E. Northrup, N.M. Johnson, G.A. Garrett1, H. Shen1, M. Wraback, Pseudomorphically grown ultraviolet C photopumped lasers on bulk AlN substrates. Appl. Phys. Express **4**, 092101 (2011)

59. T. Wunderer, C.L. Chua, J.E. Northrup, Z. Yang, N.M. Johnson, M. Kneissl, G.A. Garrett, H. Shen, M. Wraback, B. Moody, H.S. Craft, R. Schlesser, R.F. Dalmau, Z. Sitar, Optically pumped UV lasers grown on bulk AlN substrates. Phys. Stat. Sol. (c) **9**, 822 (2012)
60. Y.C. Shen, G.O. Mueller, S. Watanabe, N.F. Gardner, A. Munkholm, M.R. Krames, Auger recombination in InGaN measured by photoluminescence. Appl. Phys. Lett. **91**, 141101 (2007)
61. M.-H. Kim, M.F. Schubert, Q. Dai, J.K. Kim, E. Fred Schubert, J. Piprek, Y. Park, Origin of efficiency droop in GaN-based light-emitting diodes. Appl. Phys. Lett. **91**, 183507 (2007)
62. J. Hader, J.V. Moloney, B. Pasenow, S.W. Koch, M. Sabathil, N. Linder, S. Lutgen, On the importance of radiative and Auger losses in GaN-based quantum wells. Appl. Phys. Lett. **92**, 261103 (2008)
63. A. Laubsch, M. Sabathil, W. Bergbauer, M. Strassburg, H. Lugauer, M. Peter, S. Lutgen, N. Linder, K. Streubel, J. Hader, J.V. Moloney, B. Pasenow, S.W. Koch, On the origin of IQE-'droop' in InGaN LEDs. Phys. Stat. Sol. (c) **6**(S2), S913 (2009)
64. J. Cho, E. Fred Schubert, J.K. Kim, Efficiency droop in light-emitting diodes: Challenges and countermeasures. Laser Photonics Rev. **7**(3), 408–421 (2013)
65. J. Iveland, L. Martinelli, J. Peretti, J.S. Speck, C. Weisbuch, Direct measurement of auger electrons emitted from a semiconductor light-emitting diode under electrical injection: identification of the dominant mechanism for efficiency droop. Phys. Rev. Lett. **110**, 177406 (2013)
66. J. Yun, J.-I. Shim, H. Hirayama, Analysis of efficiency droop in 280-nm AlGaN multiple-quantum-well light-emitting diodes based on carrier rate equation. Appl. Phys. Express **8**, 022104 (2015)
67. E. Kioupakis, P. Rinke, K.T. Delaney, C.G. Van de Walle, Indirect Auger recombination as a cause of efficiency droop in nitride light-emitting diodes. Appl. Phys. Lett. **98**, 161107 (2011)
68. K. Ban, J. Yamamoto, K. Takeda, K. Ide, M. Iwaya, T. Takeuchi, S. Kamiyama, I. Akasaki, H. Amano, Internal quantum efficiency of whole-composition-range AlGaN multiquantum wells. Appl. Phys. Express **4**, 052101 (2011)
69. Y. Narukawa, M. Ichikawa, D. Sanga, M. Sano, T. Mukai, White light emitting diodes with super-high luminous efficacy. J. Phys. D Appl. Phys. **43**, 354002 (2010)
70. Solid-state lighting research and development: multi-year program plan. U.S. Department of Energy, DOE/EE-1089 (2014)
71. S. Karpov, Y.N. Makarov, Dislocation effect on light emission in gallium nitride. Appl. Phys. Lett. **81**, 4721 (2002)
72. C. Reich, M. Feneberg, V. Kueller, A. Knauer, T. Wernicke, J. Schlegel, M. Frentrup, R. Goldhahn, M. Weyers, M. Kneissl, Excitonic recombination in epitaxial lateral overgrown AlN on sapphire. Appl. Phys. Lett. **103**, 212108 (2013)
73. V. Kueller, A. Knauer, F. Brunner, U. Zeimer, H. Rodriguez, M. Weyers, M. Kneissl, Growth of AlGaN and AlN on patterned AlN/sapphire templates. J. Cryst. Growth **315**(1), 200 (2011)
74. V. Kueller, A. Knauer, U. Zeimer, M. Kneissl, M. Weyers, Controlled coalescence of MOVPE grown AlN during lateral overgrowth. J. Cryst. Growth **368**, 83 (2013)
75. U. Zeimer, V. Kueller, A. Knauer, A. Mogilatenko, M. Weyers, M. Kneissl, High quality AlGaN grown on ELO AlN/sapphire templates. J. Cryst. Growth **377**, 32 (2013)
76. M. Martens, F. Mehnke, C. Kuhn, C. Reich, T. Wernicke, J. Rass, V. Küller, A. Knauer, C. Netzel, M. Weyers, M. Bickermann, M. Kneissl, Performance characteristics of UVC AlGaN-based lasers grown on sapphire and bulk AlN substrates. IEEE Photonics Tech. Lett. **26**, 342 (2014)
77. M. Kim, T. Fujita, S. Fukahori, T. Inazu, C. Pernot, Y. Nagasawa, A. Hirano, M. Ippommatsu, M. Iwaya, T. Takeuchi, S. Kamiyama, M. Yamaguchi, Y. Honda, H. Amano, I. Akasaki, AlGaN-based deep ultraviolet light-emitting diodes fabricated on patterned sapphire substrates. Appl. Phys. Express **4**, 092102 (2011)

78. J. Rass, T. Kolbe, N. Lobo Ploch, T. Wernicke, F. Mehnke, C. Kuhn, J. Enslin, M. Guttmann, C. Reich, J. Glaab, C. Stoelmacker, M. Lapeyrade, S. Einfeldt, M. Weyers, M. Kneissl, High power UV-B LEDs with long lifetime. Proc. SPIE **9363**, 93631K (2015)
79. K. Forghani, M. Klein, F. Lipski, S. Schwaiger, J. Hertkorn, R.A.R. Leute, F. Scholz, M. Feneberg, B. Neuschl, K. Thonke, O. Klein, U. Kaiser, R. Gutt, T. Passow, High quality AlGaN epilayers grown on sapphire using SiN_x interlayers. J. Cryst. Growth **315**, 216–219 (2011)
80. C.G. Van de Walle, J. Neugebauer, First-principles calculations for defects and impurities: applications to III-nitrides. J. Appl. Phys. **95**(8), 3851 (2004)
81. M.A. Reshchikova, H. Morkoç, Luminescence properties of defects in GaN. J. Appl. Phys. **97**, 061301 (2005)
82. S.F. Chichibu, T. Onuma, K. Hazu, A. Uedono, Major impacts of point defects and impurities on the carrier recombination dynamics in AlN. Appl. Phys. Lett. **97**, 201904 (2010)
83. T.A. Henry, A. Armstrong, A.A. Allerman, M.H. Crawford, The influence of Al composition on point defect incorporation in AlGaN. Appl. Phys. Lett. **100**, 043509 (2012)
84. J. Carlos Rojo, G.A. Slack, K. Morgan, B. Raghothamachar, M. Dudley, L.J. Schowalter, Report on the growth of bulk aluminum nitride and subsequent substrate preparation. J. Cryst. Growth **231**, 317 (2001)
85. Z.G. Herro, D. Zhuang, R. Schlesser, Z. Sitar, Growth of AlN single crystalline boules. J. Cryst. Growth **312**, 2519–2521 (2010)
86. M. Bickermann, B.M. Epelbaum, O. Filip, P. Heimann, S. Nagata, A. Winnacker, UV transparent single-crystalline bulk AlN substrates. Phys. Stat. Sol. (C) **7**(1), 21 (2010)
87. C. Hartmann, J. Wollweber, A. Dittmar, K. Irmscher, A. Kwasniewski, F. Langhans, T. Neugut, M. Bickermann, Preparation of bulk AlN seeds by spontaneous nucleation of freestanding crystals. Jpn. J. Appl. Phys. **52**, 08JA06 (2013)
88. R. Collazo, J. Xie, B.E. Gaddy, Z. Bryan, R. Kirste, M. Hoffmann, R. Dalmau, B. Moody, Y. Kumagai, T. Nagashima, Y. Kubota, T. Kinoshita, A. Koukitu, D.L. Irvine, Z. Sitar, On the origin of the 265 nm absorption band in AlN bulk crystals. Appl. Phys. Lett. **100**, 191914 (2012)
89. K. Irmscher, C. Hartmann, C. Guguschev, M. Pietsch, J. Wollweber, M. Bickermann, Identification of a tri-carbon defect and its relation to the ultraviolet absorption in aluminum nitride. J. Appl. Phys. **114**, 123505 (2013)
90. B.E. Gaddy, Z. Bryan, I. Bryan, J. Xie, R. Dalmau, B. Moody, Y. Kumagai, T. Nagashima, Y. Kubota, T. Kinoshita, A. Koukitu, R. Kirste, Z. Sitar, R. Collazo, D.L. Irving, The role of the carbon-silicon complex in eliminating deep ultraviolet absorption in AlN. Appl. Phys. Lett. **104**, 202106 (2014)
91. Y. Kumagai, Y. Kubota, T. Nagashima, T. Kinoshita, R. Dalmau, R. Schlesser, B. Moody, J. Xie, H. Murakami, A. Koukitu, Z. Sitar, Preparation of a freestanding AlN substrate from a thick AlN layer grown by hydride vapor phase epitaxy on a bulk AlN substrate prepared by physical vapor transport. Appl. Phys. Express **5**, 055504 (2012)
92. T. Kinoshita, K. Hironaka, T. Obata, T. Nagashima, R. Dalmau, R. Schlesser, B. Moody, J. Xie, S. Inoue, Y. Kumagai, A. Koukitu, Z. Sitar, Deep-ultraviolet light-emitting diodes fabricated on AlN substrates prepared by hydride vapor phase epitaxy. Appl. Phys. Express **5**, 122101 (2012)
93. K.B. Nam, M.L. Nakarmi, J. Li, J.Y. Lin, H.X. Jiang, Mg acceptor level in AlN probed by deep ultraviolet photoluminescence. Appl. Phys. Lett. **83**(5), 878 (2003)
94. M.L. Nakarmi, K.H. Kim, M. Khizar, Z.Y. Fan, J.Y. Lin, H.X. Jiang, Electrical and optical properties of Mg-doped $Al_{0.7}Ga_{0.3}N$ alloys. Appl. Phys. Lett. **86**, 092108 (2005)
95. X.T. Trinh, D. Nilsson, I.G. Ivanov, E. Janzén, A. Kakanakova-Georgieva, N.T. Son, Stable and metastable Si negative-U centers in AlGaN and AlN. Appl. Phys. Lett. **105**, 162106 (2014)

96. A. Kakanakova-Georgieva, D. Nilsson, X.T. Trinh, U. Forsberg, N.T. Son, E. Janzen, The complex impact of silicon and oxygen on the n-type conductivity of high-Al-content AlGaN. Appl. Phys. Lett. **102**, 132113 (2013)
97. J.R. Grandusky, J.A. Smart, M.C. Mendrick, L.J. Schowalter, K.X. Chen, E.F. Schubert, Pseudomorphic growth of thick n-type AlxGa1-xN layers on low-defect-density bulk AlN substrates for UV LED applications. J. Cryst. Growth **311**, 2864 (2009)
98. B. Cheng, S. Choi, J.E. Northrup, Z. Yang, C. Knollenberg, M. Teepe, T. Wunderer, C.L. Chua, N.M. Johnson, Enhanced vertical and lateral hole transport in high aluminum-containing AlGaN for deep ultraviolet light emitters. Appl. Phys. Lett. **102**, 231106 (2013)
99. A.A. Allerman, M.H. Crawford, M.A. Miller, S.R. Lee, Growth and characterization of Mg-doped AlGaN–AlN short-period superlattices for deep-UV optoelectronic devices. J. Cryst. Growth **312**, 756–761 (2010)
100. J. Simon, V. Protasenko, C. Lian, H. Xing, D. Jena, Polarization-induced hole doping in wide-band-gap uniaxial semiconductor heterostructures. Science **327**, 60 (2010)
101. R. Dahal, J. Li, S. Majety, B.N. Pantha, X.K. Cao, J.Y. Lin, H.X. Jiang, Epitaxially grown semiconducting hexagonal boron nitride as a deep ultraviolet photonic material. Appl. Phys. Lett. **98**, 211110 (2011)
102. R. Collazo, S. Mita, J. Xie, A. Rice, J. Tweedie, R. Dalmau, Z. Sitar, Progress on n-type doping of AlGaN alloys on AlN single crystal substrates for UV optoelectronic applications. Phys. Stat. Sol. (c) **8**(7–8), 2031 (2011)
103. F. Mehnke, T. Wernicke, H. Pinhel, C. Kuhn, C. Reich, V. Kueller, A. Knauer, M. Lapeyrade, M. Weyers, M. Kneissl, Highly conductive n-$Al_xGa_{1-x}N$ layers with aluminum mole fractions above 80 %. Appl. Phys. Lett. **103**, 212109 (2013)
104. S. Ruvimov, Z. Liliental-Weber, J. Washburn, D. Qiao, S.S. Lau, P.K. Chu, Microstructure of Ti/Al ohmic contacts for n-AlGaN. Appl. Phys. Lett. **73**, 2582 (1998)
105. J.H. Wang, S.E. Mohney, S.H. Wang, U. Chowdhury, R.D. Dupuis, Vanadium-based ohmic contacts to n-type $Al_{0.6}Ga_{0.4}N$. J. Electron. Mater. **33**, 418 (2004)
106. R. France, T. Xu, P. Chen, R. Chandrasekaran, T.D. Moustakas, Vanadium-based Ohmic contacts to n-AlGaN in the entire alloy composition. Appl. Phys. Lett. **90**, 062115 (2007)
107. M. Lapeyrade, A. Muhin, S. Einfeldt, U. Zeimer, A. Mogilatenko, M. Weyers, M. Kneissl, Electrical properties and microstructure of vanadium-based contacts on ICP plasma etched n-type AlGaN:Si and GaN:Si surfaces. Semicond. Sci. Technol. **28**, 125015 (2013)
108. M. Lapeyrade, F. Eberspach, N. Lobo Ploch, C. Reich, M. Guttmann, T. Wernicke, F. Mehnke, S. Einfeldt, A. Knauer, M. Weyers, M. Kneissl, Current spreading study in UVC LED emitting around 235 nm. Proc. SPIE **9363**, 93631P (2015)
109. I.E. Titkov, D.A. Sannikov, Y.-M. Park, J.K. Son, Blue light emitting diode internal and injection efficiency. AIP Adv. **2**, 032117 (2012)
110. N. Lobo-Ploch, Chip designs for high efficiency III-nitride based ultraviolet light emitting diodes with enhanced light extraction. Ph.D. Thesis (2015)
111. A. Khan, K. Balakrishnan, T. Katona, Ultraviolet light-emitting diodes based on group three nitrides. Nat. Photonics **2**, 77 (2008)
112. V. Adivarahan, A. Heidari, B. Zhang, Q. Fareed, S. Hwang, M. Islam, A. Khan, 280 nm deep ultraviolet light emitting diode lamp with an AlGaN multiple quantum well active region. Appl. Phys. Express **2**, 102101 (2009)
113. L. Zhou, J.E. Epler, M.R. Krames, W. Goetz, M. Gherasimova, Z. Ren, J. Han, M. Kneissl, N.M. Johnson, Vertical injection thin-film AlGaN/AlGaN multiple-quantum-well deep ultraviolet light-emitting diodes. Appl. Phys. Lett. **89**, 241113 (2006)
114. T.N. Oder, K.H. Kim, J.Y. Lin, H.X. Jiang, III-nitride blue and ultraviolet photonic crystal light emitting diodes. Appl. Phys. Lett. **84**, 466 (2004)
115. T. Gessmann, E.F. Schubert, J.W. Graff, K. Streubel, C. Karnutsch, Omnidirectional reflective contacts for light-emitting diodes. IEEE Electron Device Lett. **24**(10), 683 (2003)

116. N. Lobo, H. Rodriguez, A. Knauer, M. Hoppe, S. Einfeldt, P. Vogt, M. Weyers, M. Kneissl, Enhancement of light extraction in UV LEDs using nanopixel contact design with Al reflector. Appl. Phys. Lett. **96**, 081109 (2010)
117. K.B. Nam, J. Li, M.L. Nakarmi, J.Y. Lin, H.X. Jianga, Unique optical properties of AlGaN alloys and related ultraviolet emitters. Appl. Phys. Lett. **84**, 5264 (2004)
118. J.E. Northrup, C.L. Chua, Z. Yang, T. Wunderer, M. Kneissl, N.M. Johnson, T. Kolbe, Effect of strain and barrier composition on the polarization of light emission from AlGaN/AlN quantum wells. Appl. Phys. Lett. **100**, 021101 (2012)
119. T. Kolbe, A. Knauer, C. Chua, Z. Yang, V. Kueller, S. Einfeldt, P. Vogt, N.M. Johnson, M. Weyers, M. Kneissl, Effect of temperature and strain on the optical polarization of (In)(Al) GaN ultraviolet light emitting diodes. Appl. Phys. Lett. **99**, 261105 (2011)
120. T. Kolbe, A. Knauer, J. Stellmach, C. Chua, Z. Yang, H. Rodrigues, S. Einfeldt, P. Vogt, N. M. Johnson, M. Weyers, M. Kneissl, Optical polarization of UV-A and UV-B (In)(Al)GaN multiple quantum well light emitting diodes. Proc. SPIE **7939**, 79391G (2011)
121. T. Kolbe, A. Knauer, C. Chua, Z. Yang, H. Rodrigues, S. Einfeldt, P. Vogt, N.M. Johnson, M. Weyers, M. Kneissl, Optical polarization characteristics of ultraviolet (In)(Al)GaN multiple quantum well light emitting diodes. Appl. Phys. Lett. **97**, 171105 (2010)
122. J.J. Wierer, I. Montano, M.H. Crawford, A.A. Allerman, Effect of thickness and carrier density on the optical polarization of $Al_{0.44}Ga_{0.56}N/Al_{0.55}Ga_{0.45}N$ quantum well layers. J. Appl. Phys. **115**, 174501 (2014)
123. J.J. Wierer Jr, A.A. Allerman, I. Montano, M.W. Moseley, Influence of optical polarization on the improvement of light extraction efficiency from reflective scattering structures in AlGaN ultraviolet light-emitting diodes. Appl. Phys. Lett. **105**, 061106 (2014)
124. H.-Y. Ryu, I.-G. Choi, H.-S. Choi, J.-I. Shim, Investigation of light extraction efficiency in AlGaN deep-ultraviolet light-emitting diodes. Appl. Phys. Express **6**, 062101 (2013)
125. N. Lobo Ploch, H. Rodriguez, C. Stölmacker, M. Hoppe, M. Lapeyrade, J. Stellmach, F. Mehnke, T. Wernicke, A. Knauer, V. Kueller, M. Weyers, S. Einfeldt, M. Kneissl, Effective thermal management in ultraviolet light emitting diodes with micro-LED arrays. IEEE Trans. Electron Devices **60**(2), 782–786 (2013)
126. N. Lobo Ploch, S. Einfeldt, T. Kolbe, A. Knauer, M. Frentrup, V. Kueller, M. Weyers, M. Kneissl, Investigation of the temperature dependent efficiency droop in UV LEDs. Semicond. Sci. Technol. **28**, 125021 (2013)
127. M. Shatalov, W. Sun, R. Jain, A. Lunev, X. Hu, A. Dobrinsky, Y. Bilenko, J. Yang, G.A. Garrett, L.E. Rodak, M. Wraback, M. Shur, R. Gaska, High power AlGaN ultraviolet light emitters. Semicond. Sci. Technol. **29**, 084007 (2014)
128. P. Scheidt, Thermal management of LED technology in applications. LED Prof. Rev. **19** (2007), Retrieved 7 Oct 2014, www.led-professional.com.
129. R. Huber, Thermal management in high power LED systems. LED Prof. Rev. **22** (2007), Retrieved 7 Oct 2014, www.led-professional.com.
130. J. Glaab, C. Ploch, R. Kelz, C. Stölmacker, M. Lapeyrade, N. Lobo Ploch, J. Rass, T. Kolbe, S. Einfeldt, F. Mehnke, C. Kuhn, T. Wernicke, M. Weyers, M. Kneissl, Temperature induced degradation of InAlGaN multiple-quantum well UV-B LEDs. MRS Proc. **1792**, mrss15-2102646 (2015)
131. J. Glaab, C. Ploch, R. Kelz, C. Stoelmacker, M. Lapeyrade, N. Lobo Ploch, J. Rass, T. Kolbe, S. Einfeldt, F. Mehnke, C. Kuhn, T. Wernicke, M. Weyers, M. Kneissl, Degradation of (InAlGa)N-based UV-B LEDs stressed by current and temperature. J. Appl. Phys. **118**(9), 094504 (2015)
132. C.G. Moe, J.R. Grandusky, J. Chen, K. Kitamura, M.C. Mendrick, M. Jamil, M. Toita, S.R. Gibb, L.J. Schowalter, High-power pseudomorphic mid-ultraviolet light-emitting diodes with improved efficiency and lifetime. Proc. SPIE **8986**, 89861V (2014)
133. M. Meneghini, M. Pavesi, N. Trivellin, R. Gaska, E. Zanoni, G. Meneghesso, Reliability of deep-UV light-emitting diodes. IEEE Trans. Device Mater. Reliab. **8**(2), 248 (2008)

134. M. Meneghini, D. Barbisan, L. Rodighiero, G. Meneghesso, E. Zanoni, Analysis of the physical processes responsible for the degradation of deep-ultraviolet light emitting diodes. Appl. Phys. Lett. **97**, 143506 (2010)
135. H. Amano, I. Akasaki, GaN blue and ultraviolet light emitting devices. Solid State Phys. **25**, 399 (1990)
136. A. Chitnis, A. Kumar, M. Shatalov, V. Adivarahan, A. Lunev, J.W. Yang, G. Simin, M.A. Khan, R. Gaska, M. Shur, High-quality p-n junctions with quaternary AlInGaN/InGaN quantum wells. Appl. Phys. Lett. **77**, 3880–3882 (2000)
137. V. Adivarahan, S. Wu, A. Chitnis, R. Pachipulusu, V. Mandavilli, M. Shatalov, J.P. Zhang, M. Asif Khan, G. Tamulaitis, I. Yilmaz, M.S. Shur, R. Gaska, AlGaN single-quantum-well light-emitting diodes with emission at 285 nm. Appl. Phys. Lett. **81**(19), 3666 (2002)
138. A. Chitnis, J.P. Zhang, V. Adivarahan, W. Shuai, J. Sun, M. Shatalov, J.W. Yang, G. Simin, M. Asif Khan, 324 nm light emitting diodes with milliwatt powers. Jpn. J. Appl. Phys. **41** (Part 2), 4B, L450 (2002)

Chapter 2
Growth and Properties of Bulk AlN Substrates

Matthias Bickermann

Abstract Bulk crystal growth of aluminum nitride (AlN) comes into focus in order to provide substrates for deep-UV optoelectronics (LEDs, lasers, and sensors) which are typically based on Al-rich AlGaN epitaxial layers and structures. On AlN substrates, pseudomorphic AlGaN layers can be deposited with compressive strain and high structural quality [1–3]. In this context, the growth of AlN crystals by sublimation and recondensation (physical vapor transport method) at temperatures exceeding 2000 °C has proven to be the method of choice, as the boules and substrates show very high structural perfection at reasonable growth rates. Availability of AlN substrates as well as their useable area, structural quality, and electrical/optical properties are directly related to growth technology issues, including selection of set-up materials, seeding strategy, and pre-purification efforts. After a brief overview of history and applications of bulk AlN, the basic principles of AlN bulk growth by physical vapor transport (PVT) are reviewed. The formation of extended defects and the incorporation of impurities during growth as well as their impact on the material's optical and electrical properties are discussed in detail. The main target of this chapter is to provide readers with enough information about AlN substrate preparation to understand and make informed decisions about employing AlN substrates for deep-UV optoelectronics.

2.1 Properties and History of AlN Crystals

AlN is a binary compound crystallizing in the hexagonal wurtzite structure ($P6_3/mmc$). Each atom is surrounded by a regular tetrahedron of atoms of the other kind. The ionic fraction of the chemical bond is 42 % [4]. The sp^3 bonding in conjunction with

M. Bickermann (✉)
Leibniz Institute for Crystal Growth (IKZ), Berlin, Germany
e-mail: matthias.bickermann@ikz-berlin.de

M. Bickermann
Institute for Chemistry, Technische Universität, Berlin, Germany

© Springer International Publishing Switzerland 2016

M. Kneissl and J. Rass (eds.), *III-Nitride Ultraviolet Emitters*,
Springer Series in Materials Science 227, DOI 10.1007/978-3-319-24100-5_2

the low atomic mass of its constituents leads to extraordinary high chemical stability, phonon energies (around 100 meV), bulk acoustic wave velocities (11270 m/s), and thermal conductivity (about 320 W/mK) [5, 6]. AlN crystals are polar, birefringent, pyroelectric, and piezoelectric.

The high chemical stability imposes a considerable challenge to crystal growth. AlN decomposes before melting under technologically feasible conditions [7]. Thus, growth from the melt, as performed for most other III–V semiconductors, is not possible. On the other hand, the total pressure of gaseous species above the solid already reaches considerable values much below the decomposition temperature (about 2430 °C at 1 bar total pressure). This sublimation can be used to facilitate a species transport, mediated, e.g., by a concentration gradient which is induced by a temperature gradient, from the hotter source to the colder growth area, where the species condense to form a crystal. The corresponding process of high-temperature sublimation and recondensation is called physical vapor transport (PVT). The PVT method is employed also for bulk SiC growth, where it was developed into an industrial technique.

Today, bulk AlN crystals are almost exclusively grown by PVT. Alternative growth methods like high-temperature chemical vapor deposition (HT-CVD/HVPE) [8–11], thermal decomposition [12], PVT variations using the sandwich sublimation method [13], or liquid Al as precursor [14] as well as high-temperature solution, flux, and ammonothermal growth [15–20] are also investigated for bulk growth, but currently remain at a research level due to unresolved restrictions in crystal size, growth rate, or yield. On the other hand, preparation of an HVPE layer on an AlN bulk substrate with subsequent removal of that substrate is currently proposed to provide a UV-transparent template suitable for light out-coupling [21].

Aluminum nitride (AlN) was first synthesized in 1862 by reacting molten aluminum with nitrogen gas [22]. Today, AlN powder is mainly synthesized from alumina by carbothermal nitridation [23]

$$Al_2O_3 + 3\,C + N_2 \rightarrow 2AlN + 3\,CO. \tag{2.1}$$

AlN ceramics are used as refractory construction parts, heat sinks, and substrates where high thermal conductivity is required in conjunction with high mechanical and thermal robustness [24, 25]. However, due to the high preparation cost compared to alumina, the use of AlN ceramics remains restricted to high-end products and niche markets.

The first serious attempts to grow bulk AlN single crystals date back to the 1960s [26–30]. AlN, powder or liquid, Al were used as source materials in an atmosphere of nitrogen at temperatures exceeding 1700 °C. The experiments were conducted in carbon-containing set-ups, which led to highly contaminated crystals. In 1976, Slack and McNelly prepared mm-sized AlN single crystals with high purity [7, 31, 32] by using a Piper-Polich [33] growth technique in which a sealed rhenium/tungsten crucible with conical end was moved through a hot zone of an inductively heated furnace. However, research on AlN bulk single crystal growth

for epitaxial substrate preparation only started in the late 1990s [34–36] with the rising interest in wide band-gap semiconductors. The reactor design from the much more advanced SiC PVT technique [37], in which SiC sublimates and condenses at temperatures 2100–2500 °C in graphite crucibles was soon adopted for AlN growth. However, a lot of initial work was dedicated to find chemically stable and suitable hot-zone materials [38–41]. Also, the initial absence of AlN seeds led to different strategies to obtain large bulk of single crystals [42].

As of today, a few companies and research facilities have demonstrated AlN single crystals of up to 2 in. in diameter [43–49]. Worldwide AlN substrate production is still very small as compared to SiC or sapphire. While the main target is still to produce substrates for UV optoelectronics [50–56], other potential applications for AlN bulk crystals, including piezo- and pyroelectrics, electroacoustics [57], and substrates for AlGaN-based power devices [58, 59] are currently evaluated.

2.2 AlN Bulk Growth by the PVT Method: Theory

In the thermodynamic Al–N [60] system, the only stable compounds are Al, AlN, and N_2, see Fig. 2.1a. At temperatures and pressures relevant for crystal growth and under nitrogen excess, only gaseous Al and N_2 are at equilibrium with solid AlN. Other species are calculated to appear at much lower concentrations [61], and their

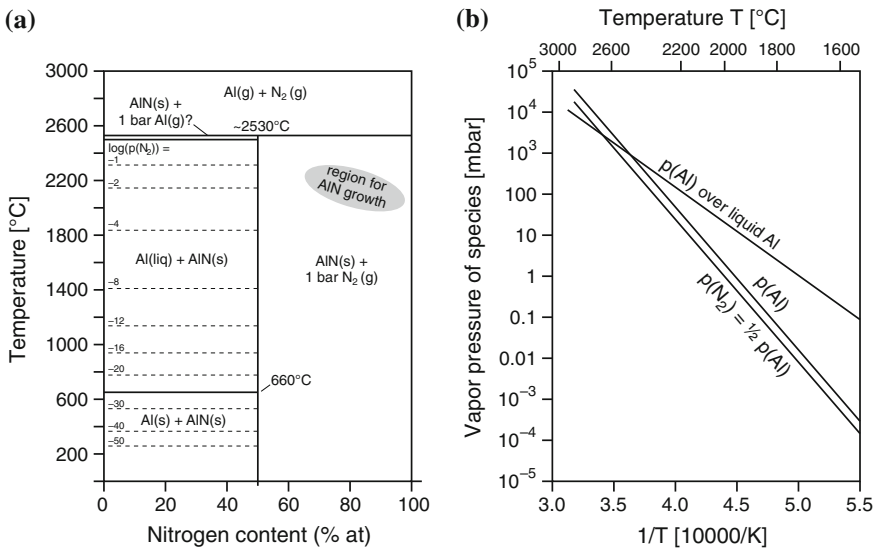


Fig. 2.1 **a** Phase diagram at 1 bar (with N_2 fugacities, after [60], and the region for AlN growth) and **b** partial pressure of vapor species under stoichiometric sublimation in the Al–N_2 system with Al partial pressure over liquid Al (after [7])

relevance for crystal growth is considered negligible. Thus, the sublimation–recondensation reaction can be written as

$$2\,\mathrm{AlN(s)} \rightleftharpoons 2\,\mathrm{Al(g)} + \mathrm{N_2(g)} \tag{2.2}$$

with the equilibrium constant $K = \mathrm{e}^{-\Delta G/RT} = p_{\mathrm{Al}} \cdot p_{\mathrm{N2}}^{1/2}$, $\log_{10} K = -32450/T + 16.08$ [62]. $\Delta G \approx 630$ kJ/mol [63] is the Gibbs free energy for sublimation, R is the universal gas constant, T is the temperature, and p_{Al} and $p_{\mathrm{N2}} = ½\, p_{\mathrm{Al}}$ are the temperature-dependent equilibrium partial pressures of the gaseous products [7], see Fig. 2.1b.

In contrast to melt growth where the growth temperature is determined by the melting temperature of the compound, sublimation growth can be performed generally at any temperature. In sublimation growth, a temperature difference ΔT between source and seed provides for a net mass flow rate of species J_{Transp} through the growth space due to the concentration gradients formed by the temperature-dependent partial pressures. The Al partial pressure over AlN provides sufficient evaporation for mass transport even at 1600 °C, but due to insufficient surface ad-atom mobility and/or N_2 chemical activity, only very thin needles form at this temperature [62]. Higher temperatures are beneficial for increasing both growth rate and surface kinetics, i.e., helping the atoms to properly arrange themselves at the surface. But in any case, the concentration of species in the gas phase is in the orders of magnitude lower than in melt growth, which restricts the achievable growth rate.

Stoichiometric sublimation ("into vacuum") results in very high deposition rates and polycrystalline growth due to lack of growth control. Instead, the transport and deposition during growth is regulated by buffering with N_2 "in excess," i.e., adding N_2 to the growth atmosphere so that the total pressure in the system p_{sys} is about 2–10 times higher than the total pressure of vapor species. As a consequence, in the gas phase, $N_{\mathrm{Al}}/N_{\mathrm{N}} = p_{\mathrm{Al}}/(2 \cdot p_{\mathrm{sys}})$ is in the order of 0.1. While excess N_2 does not necessarily lead to N-rich growth conditions, this is the commonly assumed growth regime for AlN growth (AlN–N_2 system). The growing AlN crystal still enforces stoichiometry, as its existence range is confined, but might form vacancies. The chemical activity of N_2 is most probably governed by kinetics of surface reactions such as [62]

$$\mathrm{Al(ads)} + \mathrm{N_2(ads)} \rightleftharpoons \mathrm{AlN(s)} + \mathrm{N(ads)}. \tag{2.3}$$

Additionally, nitrogen dissociation could be enhanced via reaction with impurities.

In AlN sublimation growth models, sublimation and recondensation are typically described by Hertz–Knudsen equations as

$$J_{\mathrm{Subl/Recond}} = \alpha \cdot (2\pi\, mRT)^{-1/2} \cdot \Delta p \tag{2.4}$$

with α as the (effective) sublimation/condensation coefficient, m as the molar mass, and Δp as the difference between the actual (super- or undersaturated) and the

equilibrium partial pressure of the transported species at the source or seed area, respectively. Assuming Al as the rate-limiting species, as N_2 is provided in excess [62], it is sufficient to regard only Al species, and α is typically set to unity for AlN growth.

It is commonly assumed that the mass transport in the gas phase is dominated by diffusion (Fick's law). Natural convection is typically absent at the given growth conditions (cf. [64]), and advection (Stefan flow) is insignificant due to the N_2 buffering. If the limiting step for bulk growth is indeed diffusive mass transport, i.e., sublimation or recondensation kinetics are considerably faster than diffusion in the vapor phase, the growth rate R_G can be approximated by [63, 65]

$$R_G = J_{Transp}\, m_{AlN}/\rho_{AlN} \propto (\Delta T/L) \cdot e^{-\Delta G/RT}/(T^{1.2} \cdot p_{sys}^{1.5}). \tag{2.5}$$

with m_{AlN} and ρ_{AlN} as the mass and density of solid AlN, and L as the source-to-seed distance.

The parameters governing the mass transport are thus T, p_{sys}, and $\Delta T/L$. The growth rate increases with increasing temperature gradient and temperature (due to the exponential term), while the increase with decreasing total pressure is in fact rather weak for typical growth conditions [66]. In the practical case, R_G is lower due to volatile species leaving the semi-open crucible and reacting with the crucible materials. Finally, the presence of impurities may significantly change growth behavior, e.g., via impurity-assisted transport of growth species, or by acting as surfactants, i.e., changing kinetic barriers at the growth surface [67–69]. As a consequence, preparation of highest purity source materials is not only mandatory in order to control the properties of the grown crystals, it is also necessary for achieving a stable and reproducible crystal growth.

As mentioned, AlN bulk growth is typically performed at temperatures T ranging from 1800 to 2300 °C and system pressures p_{sys} of 300–900 mbar. The process window for stable growth of AlN depends on the hot-zone and seed materials (see below) and the growth orientation (polarity). Higher temperatures and supersaturations seem to stabilize N-polar growth [70, 71]. As only a relatively low growth rate R_G (typically lower than 200 µm/h) will allow for single-crystalline growth without deterioration of structural quality, the axial thermal gradients $\Delta T/L$ are typically in the range of only 2–10 K/cm.

2.3 AlN Bulk Growth by the PVT Method: Technology

The hot-zone of the typically used vertical set-up consists of a cylindrical crucible with removable upper lid where a seed can be mounted, a surrounding susceptor, and thermal insulation, see Fig. 2.2. The crucible has to be porous or semi-closed to allow gas and pressure exchange with the environment, often provided already by the nonideal closure between the lid and the crucible. It is filled with solid AlN source material (as powder, sintered bodies, or lumps from previous growth

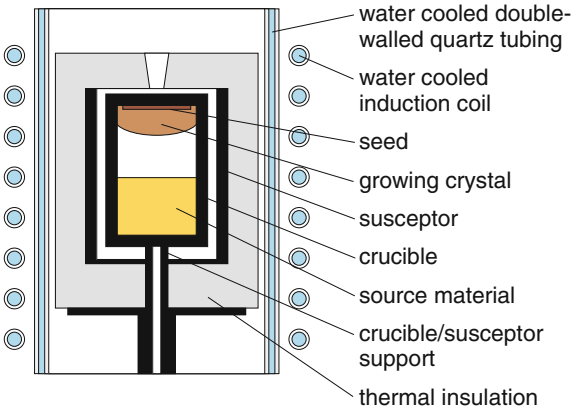


Fig. 2.2 Crucible and reactor set-up for AlN bulk growth

experiments) to 50–80 % of its total height. The hot-zone geometry has to be carefully designed to provide the proper thermal gradients at growth temperatures, where heat is dominantly transferred by radiation.

Electrical power is used to heat the crucible either by induction (at 8–50 kHz frequency, depending on the susceptor material) or by resistive heating, whereas the former is much more established. The use of a susceptor is advantageous in that it remits the heat to the crucible via radiation, providing a more homogeneous temperature field in the growth cell compared to direct crucible heating. As shown in Fig. 2.2, the set-up is located inside a water-cooled growth vessel which provides the gas-tight enclosure, a loading port, and connections for pyrometer access and gas inlet/outlet. Some reactors allow for a controlled movement of the coil relative to the crucible to affect the axial temperature gradient in the crucible; this can be also facilitated by separate control of several heaters.

The growth procedure typically includes the following steps: The hot-zone is assembled and loaded into the reactor. After purging and pre-heating steps, the vessel is filled with N_2 gas, and the growth cell is heated to growth temperature. During heating up, the seed is kept at a slightly higher temperature than the source material to prevent early growth, clean the seed surface, and further remove volatile impurities. If the growth temperature is reached, a soft growth start is achieved by inverting the axial temperature gradient, i.e., providing a higher temperature at the source compared to the seed. During growth, the system pressure is kept constant by maintaining a constant inert gas input flow while controlling the exhaust flow.

As the temperature inside the growth cell is inaccessible, the "growth temperature" is obtained by pyrometers measuring the temperatures of crucible outer surfaces (e.g., on the upper and lower lid) and controlled by adjusting the heating power. Note that maintaining the temperature gradients at the growth interface during growth is crucial in order to obtain crystals with high chemical and structural homogeneity. Thus, the thermal gradients near the growing surface during growth are derived by numerical modeling. The gradients depend on the complete hot-zone geometry including radiation shields and thermal insulation (for which accurate

material data at growth temperatures is rarely available) and on the growth rate (due to release of latent heat), and transient simulations are needed to account for the move of the growth interface while the boule grows.

Considering the typical growth rates of 50–300 µm/h, it takes several days to grow 10–30 mm thick crystals. Mass transport yields exceeding 80 % are possible if the evaporation losses through the semi-open crucible are kept at a low level. The end of growth is initiated by decreasing the heater power, optionally with inverting the gradient again. A controlled cooling is demanded to mitigate strain-induced defect formation.

As will be shown below, the selection of hot-zone materials has a decisive impact on AlN growth behavior and properties. Typically, the crucible is made from either tungsten (W) or tantalum carbide (TaC). Graphite and boron nitride lead to considerable contamination of the crystal with carbon or boron, respectively; a few more materials have been positively evaluated (Re [7], TaN, HfN, TaB_2), but are not currently used [38–41]. Tungsten is long-term stable against Al vapor in the presence of sufficient N_2, and chemical erosion is negligible up to temperatures of about 2250 °C [31]. However, it will readily react with oxygen, carbon, and silicon. Only purified source materials can be used and the preheating step must be performed under high vacuum conditions to remove residual oxygen. Thermal insulation is provided by tungsten heat shields; graphite insulation can be employed if not in direct contact, but severely degrades the crucible lifetime.

TaC is available as ceramic powder and can be sintered to 96 % vol density without sintering aids [38, 72]. TaC is chemically stable under AlN growth conditions at temperatures well exceeding 2300 °C. TaC elements are compatible with graphite (for susceptor and insulation elements), tungsten (possible use of TaC as susceptor) and SiC (as seeds), even if in direct contact. Long-term stability is generally limited by cracking due to internal grain growth [38]. To prevent structural failure, the crucible is commonly enclosed in graphite cylinders which also act as a susceptor [49]. As a variant, carburized tantalum crucibles can be employed [73]. However, as they are typically used with graphite parts, the crucibles continue to carburize and finally become brittle; this process is accelerated at growth temperatures exceeding 2100 °C. TaC coatings are no alternative as they tend to crack and spall off due to differences in thermal expansion and chemical attack.

The AlN source material is prepared from commercially available ceramic powder material by carbothermal reduction [74], sintering, or sublimation [75], while direct synthesis from high-purity elements [31] is less common. The purification process should remove the most important impurities and condense the source material to mitigate moisture adsorption during handling in air. Typical contamination of purified stating material is less than 100 ppm wt for oxygen and carbon, and about 2 ppm wt of silicon [75]. On the other hand, tungsten acts as a getter material for carbon and silicon. In contrast, TaC acts as a source of carbon, which leads to carbon contamination of the crystal and at the same time to a lower oxygen incorporation due to carbothermal reduction of residual oxides.

2.4 Seeded Growth and Crystal Enlargement

In the past, different technologies for seed preparation and crystal enlargement have been evaluated by different research groups [42]. In unseeded growth, crystals nucleate on the crucible lid, and a polycrystalline boule grows from which large grains can be separated. Grain selection is possible using a conical lid [31] or repeated regrowth [70]. However, grains are often strained or structurally deteriorated due to direct contact to their neighbors. Several groups reported growth of free-standing single crystals that spontaneously nucleated on crucible parts under conditions close to thermodynamic equilibrium and low nucleation density. Typically, tungsten grids are placed above the source material and the axial temperature gradients are lowered to the lowest possible value to yield optimum nucleation and growth conditions [76–78].

The growth rate of AlN is the slowest on prismatic facets for all but the highest growth temperatures, thus the crystal habit changes from needles to almost equiaxed (isometric) crystals [62, 78] with increasing temperature. The spontaneously nucleated crystals grown in carbon-free tungsten set-ups preferentially grow in Al-polar direction and show an unfinished habit, governed by pyramidal facets on the Al-polar side [76] and with only small (0001) basal plane facets (Fig. 2.3a). In contrast, crystals grown in TaC crucibles grow preferentially in N-polar directions, forming dominant (000-1) basal plane as well as prismatic side facets [78] (Fig. 2.3b, c). In each case, crystals nucleating in "wrong" directions become stunted and are easily overgrown by their neighbors. Single crystals with dimensions of up to 15 × 15 × 10 mm^3 have been obtained, which can be cut and used as seeds in subsequent growth runs. However, this process is not very reproducible and the yield of large and well-formed crystals is low.

Thick layers of AlN can be grown on SiC seeds, which are commercially available at industrial relevant sizes (4–6 in. in diameter). The fundamental disadvantage is the partial decomposition of SiC in the presence of AlN already at temperatures of 2000 °C, which contaminates the growing crystal with up to several atomic percent of silicon and carbon [79, 80]. Additionally, the mismatch of lattice

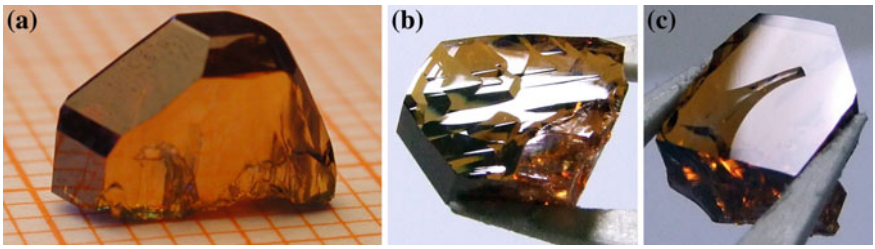


Fig. 2.3 Spontaneously nucleated, free-standing AlN bulk crystals; **a** grown in a tungsten crucible (on mm grid), the (0001)Al facet is upwards; **b**, **c** grown in a TaC crucible, crystal dimensions about 8 mm. **b** the Al-polar face is upwards but note that the (0001)Al-polar facet does not appear; **c** the flat (000-1)N facet is upwards

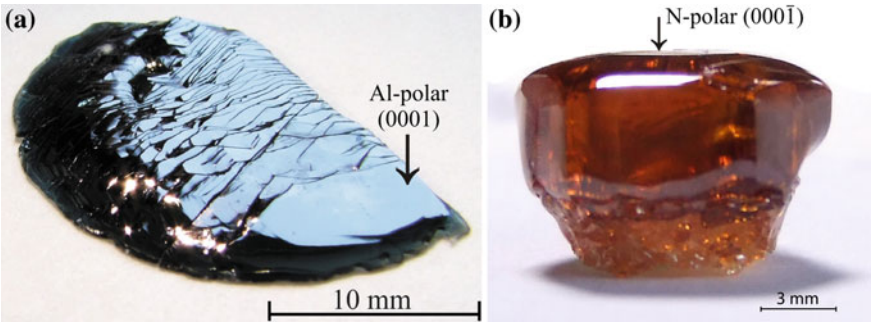


Fig. 2.4 **a** AlN crystal (Al-polar) grown on a SiC seed with 7° off-orientation with respect to the (0001) plane [82]; **b** AlN crystal (N-polar) grown on an N-polar (000-1) AlN seed [78]. Growth was performed in a TaC set-up, the crystals are turned so that the as-grown surface is upwards

parameters between AlN and SiC results in a formation of tilted domains, and the different thermal expansion coefficients lead to partial stress relaxation by dislocation formation during cooling, often resulting in a network of cracks originating at the interface [44, 81]. Nevertheless, the threading dislocation density between the domain boundaries may be as low as 10^5 cm^{-2} [82, 83]. A sample crystal is shown in Fig. 2.4a. AlN always grows Al-polar on polar SiC planes. These layers can be separated from the SiC seed and are used as seeds in subsequent AlN bulk growth [44, 45].

The main advantage of bulk crystal growth—steady improvement in diameter and structural quality—is only achieved in "homoepitaxial growth," i.e., wafers cut from the grown crystal are used as seeds in subsequent growth runs. Unfortunately, to grow a single crystal of a particular diameter, the seed must have roughly the same diameter. Seeded growth of AlN crystals has been successfully attempted from AlN seeds cut from spontaneously nucleated crystals as well as from AlN layers separated from SiC seeds. While in the former case, the main task is to perpetuate the high structural quality while providing for crystal enlargement, the latter approach is concerned with the defect density inherited from the seed and the impending diameter decrease due to formation of pyramidal side facets during Al-polar growth. Figure 2.4b shows a crystal grown on an N-polar basal plane seed with typical habit.

AlN growth is best performed on polar basal plane (c-plane) surfaces, because these planes possess isotropic in-plane properties. The ideal interface shape in sublimation growth is slightly convex, to allow the step flow from a single growth center (e.g., a screw dislocation to enable spiral growth) to spread across the whole surface area. AlN growth in other orientations has been reported [84–86], but the lower symmetry of the growth surface leads to anisotropic growth and formation of macrosteps and extended defects.

The major current issues in seeded growth of AlN are seed fixation, mitigation of seed backside evaporation, and preventing adjacent ("parasitic") grain growth. A rigid connection between the seed and the lid may lead to considerable strain,

formation of cracks, and potential seed separation from the lid during the heating-up stage due to the differences in thermal expansion. If the connection is too soft, the seed may move or fall down during the heating-up stage, and outer parts of the seed may evaporate due to the gap between the fixation rim and the lid. In any case, pores or gaps between the seed and the lid lead to seed backside evaporation. Material from the seed sublimes toward the colder crucible lid to close the void, and as a consequence, they travel through the seed and eventually through the growing crystal (negative crystal growth, cf. [87]) to locally degrade the crystal quality [86]. Seed backside plating [88] is a possible means to mitigate both backside evaporation and cracking. Nucleation and growth of parasitic grains, which also lead to strain and crystal cracking during cooling due to anisotropic thermal expansion of AlN, can be prevented by proper tailoring of the thermal field, i.e., increasing the temperature around the seed area.

2.5 Structural Defects in PVT-Grown AlN Bulk Crystals

As for any bulk growth method, the structural quality of the resulting bulk single crystals decisively depends on the seed quality and growth conditions. Defects from the seed volume and its surface as well as from backside areas of improper seed fixation penetrate into the growing crystal. A number of defects originate at the seed surface or form during initial stages of growth when the growth conditions are not yet stable. Defect formation during growth is caused by growth instabilities such as local variations of the supersaturation at the growth interface and thermal stress, and promoted by high temperatures and gradients, low pressures, and high growth rates. Finally, thermal stress during cooling may lead to formation of slip bands (consisting of straight rows of basal plane dislocations) [89] or even cracks [90] in the outer parts of the crystal.

Piercing points of dislocations, low angle grain boundaries (LAGBs), and inversion domains can be visualized by KOH–NaOH wet chemical etching on the Al-polar basal crystal surfaces and polished wafers [91, 92], see Fig. 2.5a. Another valuable detection method is X-ray topography [77, 93, 94], see Fig. 2.5b. In some samples, also cathodoluminescence imaging was successfully used [95]. Some of the threading screw dislocations act as growth centers for spiral growth. If their density is low, the resulting spirals may extend over several square millimeters and form hexagonal hillocks or round plateaus on the growth surface [45].

Spontaneously nucleated and free-standing crystals can be virtually unstrained and show highest structural perfection, i.e., overall dislocation densities below 10^3 cm^{-2} without any micropipes or volume defects [77, 78]. Rocking curve full width at half maximum (FWHM) values of 12–20 arcsecs are achieved even for large areas and in open detector measurements. The dislocation density in the crystals is typically very inhomogeneous, as basal plane dislocations mainly form due to local deformation, e.g., at the crystal border or at macrosteps (cf. Fig. 2.5b), while threading dislocations generally nucleate at growth instabilities or defects.

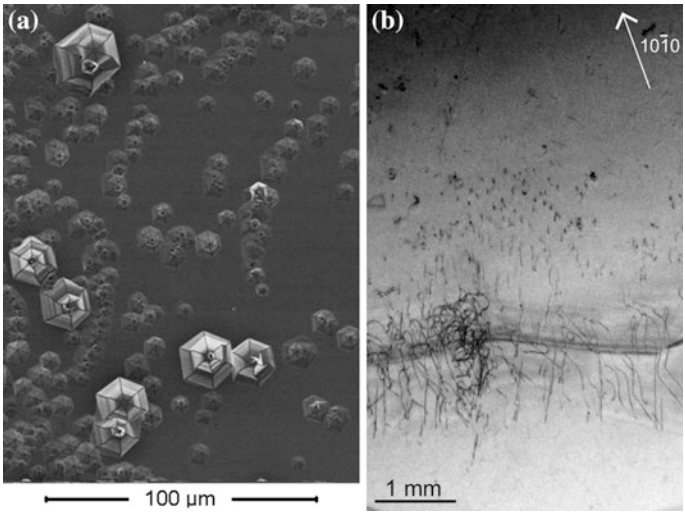


Fig. 2.5 Dislocations in AlN bulk crystals; **a** scanning electron microscope image of an Al-polar (0001) surface (seeded growth) after wet chemical etching. Bigger and smaller etch pits denote threading screw and mixed/edge dislocations, respectively; **b** X-ray transmission Lang topography image of a 1 mm thick basal plane wafer (spontaneously nucleated crystal) showing dark contrast from threading dislocations (*black dots*) and basal plane dislocations (*black curved lines*) partially entering a strained area (wavy interference contrast) caused by a macrostep formation at the growing surface. Note that the areas on the *bottom* and *top* of the image are virtually dislocation free

Additionally, in some of the earlier crystals a high density of microscopic inclusions were found, and these inclusions also decorated grown-in dislocations [93].

AlN bulk crystals often feature a mosaic structure, in particular when they were grown on defect-containing or foreign seeds. Several growth centers appearing at initial stages of growth lead to tilted domains after coalescence, eventually forming sub-grains bound by LAGBs composed of threading edge dislocations [94, 95]. If present, a mosaic structure of the seed also propagates into the growing crystal. The tilt between domains is typically below 100 arcsecs [1, 3], while growth on SiC seeds can lead to tilt values of up to 0.5° [83] and the formation of macroscopic hexagonal hillocks on the surface [45, 81]. Additional LAGBs may form in the outer crystal area during diameter enlargement where lateral expansion by growth on prismatic facets is accompanied by polygonization [96, 89]. The dislocation densities in AlN crystals grown on AlN seeds are typically in the 10^3–10^5 cm^{-2} range.

Inversion domains may be observed in particular in AlN crystals grown on SiC seeds [86, 97]. They nucleate probably due to growth instabilities and expand in size during further growth.

Finally, AlN bulk crystals exhibit a so-called zonar structure. Crystallographically different facets feature a different incorporation of impurities and thus, the corresponding crystal zones—i.e., crystal volume parts that were

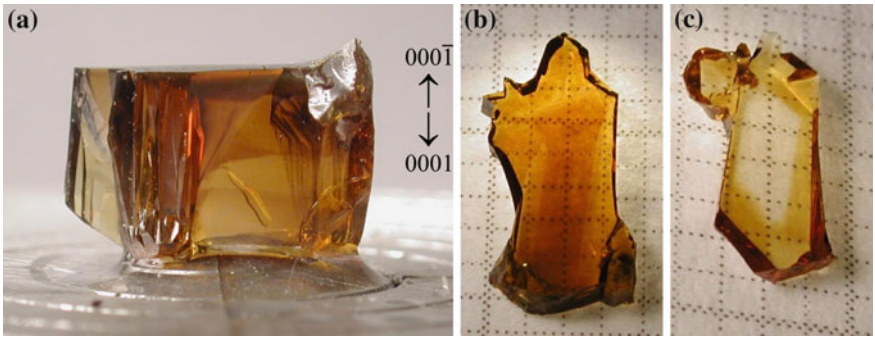


Fig. 2.6 Spontaneously nucleated, free-standing bulk AlN crystal with zonar structure, grown in a tungsten crucible; **a** side view, the N-polar basal plane is upwards; **b** top basal plane cut (on mm grid) showing crystal parts grown on the N-polar basal plane facet (*center region*) and on prismatic facets (*outer regions*); **c** bottom cut (on mm grid) showing crystal parts grown on the Al-polar basal facet (*center region*) and on Al-polar pyramidal facets (*outer regions*)

grown on the respective facets—show different optical (e.g., transmission and luminescence) and electrical properties. Due to obvious differences in coloration, the zones are easily distinguished in polished wafers [45, 78, 98] as shown in Fig. 2.6. Crystal zones are not bounded by LAGBs or other structural defects.

2.6 Impurities and Resulting Properties of AlN Substrates

Apart from size and structural quality, the key requirement for using AlN substrates for UV optoelectronics is high optical transmittance at the emission/detection wavelength. While AlN should be transparent for radiation above approximately 210 nm due to its band-gap of about 6.015 eV at room temperature [99], optical transitions involving deep levels lead to broad absorption bands in the blue and UV wavelength range. While it is recognized that these optical properties are induced by residual impurities such as carbon, silicon, and oxygen, the underlying mechanisms are still under discussion [31, 75, 100, 101, 102, 103, 104]. Apart from chemical analysis, the concentration of electrically active impurities of AlN bulk crystals has been evaluated from bound exciton luminescence [105, 106], electron paramagnetic resonance [104, 107, 108], infrared spectroscopy [103], and high-temperature resistivity measurements [75].

Due to the unavoidable contamination during high-temperature sublimation growth, the effects of different impurities can be hardly separated in optical absorption or luminescence spectra. Furthermore, intrinsic defects (such as vacancies) and defect clusters will enable additional optical transitions. The formation of such defects and their dependence on impurity incorporation is barely understood [109], and only a few techniques exist [110, 111] to evidence their concentrations. As a consequence, efforts to influence electrical and optical

properties of bulk AlN crystals are still focused on reducing contamination from both feedstock and set-up materials, rather than on controlled doping.

Oxygen is the main contamination of the source material and introduced to the growth chamber during loading/unloading in air. Silicon also occurs in the source material, although at lower levels compared to oxygen, and probably in the TaC hot-zone materials. Carbon is mainly introduced by the hot-zone materials such as the TaC crucible, the graphite susceptor, and graphite insulation parts. On the other hand, the impurity content in the crystals is strongly influenced by the materials in the hot-zone, by the crystal zone, i.e., the facet on which the impurity was incorporated. As a consequence, the oxygen and carbon concentrations of crystals grown in Al-polar direction in pure tungsten set-ups are considerably lower as compared to crystals grown in N-polar direction in TaC crucibles, see Table 2.1. Note that the formation of a zonar structure poses a problem when aiming at substrates with homogeneous absorption properties. Finally, the impurity content also depends on the growth temperature [75].

Figure 2.7 shows optical absorption (OA) spectra of the AlN crystals listed in Table 2.1. The broad OA band at around 2.8 eV which causes the yellowish coloration of the crystals is most dominant on the N-polar (000-1) zones. As it does not seem to correlate directly to a concentration of a single impurity, involvement of intrinsic defects is suspected [31, 100, 101]. A steep OA band at 4.7 eV, presumably consisting of several sub-peaks [112], dominates the spectra of crystals grown in TaC crucibles (and in particular crystals grown on SiC seeds, cf. [44, 79]). While this peak is clearly related to the carbon concentration in the crystal, the exact optical transitions that form this band are still under debate [45, 103, 113]. The band is absent in samples where the oxygen or silicon concentration clearly exceeds the carbon contamination, pointing toward a Fermi level effect. A monotonic OA increase above 5.3 eV is correlated to the 4.7 eV band, but in any case, the onset of near band-gap features limits the deep-UV transparency of AlN substrates effectively to wavelengths above about 220 nm. Finally, in some brownish areas, a broad band peaking around 4.0 eV is observed, presumably caused by oxygen and/or intrinsic defects [112].

Table 2.1 Typical values of impurity concentrations (in 10^{18} cm^{-3}) in different zones of bulk AlN crystals as measured by calibrated secondary ion mass spectrometry [123]

No.	Crucible	Zone	[O]	[Si]	[C]	References
1	W	Al-polar (0001)	0.4	0.20	0.7	[45]
2	W	Al-polar {10-13}	5.5	0.25	0.2	[45]
3	W	Al-polar {11-25}	5.0	0.7	3.5	[45]
4	W	Al-polar (0001)	2.0	0.01	0.5	[112]
5	W	Al-polar {10-12}	3.5	0.10	0.6	[112]
6	TaC	prismatic {10-10}	7.0	0.03	6.0	[78]
7	TaC	N-polar (000-1)	30	0.1	5.0	[78]
8	TaC	N-polar (000-1)	20	5.0	30	[114]

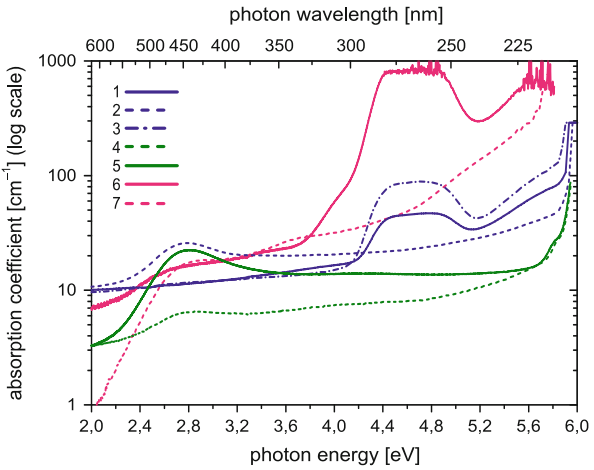


Fig. 2.7 Room temperature optical absorption spectra of selected bulk AlN crystals; the sample numbers correspond to the entries of Table 2.1 [122]

Especially the 4.7 eV absorption peak is detrimental to the light out-coupling of deep-UV (250–280 nm) emitters through the substrate. The best optical absorption values (without reflection corrections) for PVT-grown AlN published so far [112] are about 8 cm^{-1} on a local spot and about 13 cm^{-1} on a full wafer with yellowish coloration, both from a crystal grown in a pure tungsten set-up (No. 4 and 5 of Table 2.1, respectively). In contrast, AlN grown in TaC crucibles hardly shows absorption coefficients lower than 50 cm^{-1} at 265 nm (No. 7 of Table 2.1) [78]. As a consequence, the AlN substrate is thinned down to 20 µm after processing [50], or a HVPE thick layer (typically 250 µm) is deposited on the substrate and the substrate is subsequently removed by mechanical polishing [21]. The best reported optical absorption value for HVPE-grown AlN at 265 nm is 6.6 cm^{-1}, measured on a sample with the carbon and oxygen concentrations of below 0.2×10^{18} cm^{-3} and below 0.4×10^{18} cm^{-3}, respectively [114].

Using the above band-gap excitation, e.g., by an ArF excimer laser at 193 nm or by electron irradiation in an electron microscope, near band-gap emission can be observed. Excitonic luminescence recorded at low temperatures reveal valuable information about the material quality, e.g., strain and dislocation density. Furthermore, the intensity of the donor bound exciton emission corresponds to the respective donor (silicon, oxygen) concentration. However, as significant compensation by carbon quenches the excitonic luminescence, this technique has been successfully applied so far only to AlN bulk crystals grown pure in tungsten set-ups [106] or on homoepitaxial HPVE layers [105].

Below band-gap luminescence is very interesting for AlN ceramics in UV and ionization radiation dosimetry applications, but could also provide unwanted side effects in deep-UV emission devices. Ceramic samples, which are highly contaminated with oxygen and trace metals, show major luminescence bands at around 2.1 and 2.8 eV [115]. These bands are also observed in bulk AlN crystals, together with a band at 3.9 eV [45, 116]. The bands at 2.8 and 3.9 eV correlate to the carbon contamination in the samples [45, 113, 117]. The luminescence at 2.1 eV is found

in samples of very different provenance, and its origin currently remains unclear. On the other hand, luminescence in the 3.3–3.6 eV range clearly dominates the spectra of AlN either grown with SiC addition [79, 118] or in pure tungsten set-ups [98, 101, 119]. The common interpretation is that this band correlates to transitions of shallow donors (silicon or oxygen) to aluminum vacancies or their complexes [118, 120]. Obviously, these transitions are quenched as the carbon concentration exceeds that of the shallow donors.

AlN crystals and substrates are generally not electrically conductive. Measurements of the temperature-dependent conductivity show that the crystals are strongly compensated by deep levels with activation energies in the range of 0.6–1.0 eV [75, 121]. However, the different zones of the crystals show significant differences in charging after electron irradiation, e.g., in a scanning electron microscope [119]. Measurements of the temperature-dependent free carrier absorption indicate that carbon contamination may lead to semi-insulating behavior, while oxygen-dominated yellowish samples might show some very weak conductivity at elevated temperatures.

2.7 Conclusions and Outlook

Within the last 15 years, the growth of AlN bulk single crystals by the PVT method has matured from basic transport experiments yielding polycrystalline boules into an industrially applicable technique. Fueled by the interest in UV optoelectronics, the research has always aimed at providing material for substrates, with a clear focus on crystal size, process stability, and yield. Consequently, this progress was almost completely driven by appreciation of experimental work, i.e., solving technological issues such as finding compatible hot-zone materials, proper techniques for purification of the AlN starting material, and optimum growth conditions, as well as mitigating defect formation, backside evaporation, and parasitic nucleation.

While possible solutions to these issues are outlined in this chapter, important details remain proprietary technology based on the researchers' experimental knowledge. Each research team is bound to its developed technology, in particular the crucible material and the seeding/enlargement strategy. Teams that developed AlN on SiC seeds [44, 45, 49] have already demonstrated single crystals with 2 in. in diameter, but are faced with inhomogeneities and structural defects in the crystals, as well as problems in keeping the diameter in subsequent growth runs. On the other hand, teams that focused on AlN grain enlargement while perpetuating the high structural quality [77, 78] have been able to increase the single-crystalline diameter by only about 3 mm/year on average.

This poses at least two serious implications for future development of AlN crystals and substrates: First, the number of parties able to provide state-of-the-art substrates will remain limited, as newcomers lack the experimental experience. Second, technology convergence as well as further progress and commercial

breakthrough will decisively depend on further improvements in understanding the AlN growth technology, in particular regarding the influence of contaminants and dopants on crystal growth. Finally, the high temperatures and low growth rates of AlN PVT growth will limit the use of AlN substrates to applications which clearly benefit from the unique properties of this material. As it stands, deep-UV opto-electronics is one of them.

Acknowledgments The author acknowledges contributions of J. Wollweber, C Hartmann, A. Dittmar, K. Irmscher, T. Schulz, F. Langhans, S. Kollowa, C. Guguschev, M. Pietsch, A. Kwasniewski, M. Albrecht, M. Naumann, T. Neugut, and U. Juda from the Leibniz Institute for Crystal Growth. The author also thanks B.M. Epelbaum, O. Filip, P. Heimann, and A. Winnacker for the joint work on bulk AlN growth at the Department of Materials Science 6, University of Erlangen-Nuremberg, Germany, now continued in the company CrystAl-N.

References

1. R. Dalmau, B. Moody, R. Schlesser, S. Mita, J. Xie, M. Feneberg, B. Neuschl, K. Thonke, R. Collazo, A. Rice, J. Tweedie, Z. Sitar, J. Electrochem. Soc. **158**, H530 (2011)
2. J. Tweedie, R. Collazo, A. Rice, J. Xie, S. Mita, R. Dalmau, Z. Sitar, J. Appl. Phys. **108**, 043526 (2010)
3. R.T. Bondokov, S.G. Mueller, K.E. Morgan, G.A. Slack, S. Schujman, M.C. Wood, J.A. Smart, L.J. Schowalter, J. Cryst. Growth **310**, 4020 (2008)
4. L.H. Dreger, V.V. Dadape, J.L. Margrave, J. Phys. Chem. **66**, 1556 (1962)
5. M. Levinshtein, S. Ruymantsev, M. Shur (eds.), *Properties of Advanced Semiconductor Materials, GaN, AlN, InN, BN, SiC, SiGe* (Wiley, New York, 2001). ISBN 978-0-471-35827-5
6. G.A. Slack, J. Phys. Chem. Solids **34**, 321 (1973)
7. G.A. Slack, T.F. McNelly, J. Cryst. Growth **34**, 263 (1976)
8. T. Baker, A. Mayo, Z. Veisi, P. Lu, J. Schmitt, Phys. Status Solidi C **11**, 373 (2014)
9. O. Kovalenkov, V. Soukhoveev, V. Ivantsov, A. Usikov, V. Dmitriev, J. Cryst. Growth **281**, 87 (2005)
10. Y. Katagiri, S. Kishino, K. Okuura, H. Miyake, K. Hiramatu, J. Cryst. Growth **311**, 2831 (2009)
11. Y. Kumagai, J. Tajima, M. Ishizuki, T. Nagashima, H. Murakami, K. Takada, A. Koukitu, Appl. Phys. Express **1**, 045003 (2008)
12. J.A. Freitas Jr, G.C.B. Braga, E. Silveira, J.G. Tischler, M. Fatemi, Appl. Phys. Lett. **83**, 2584 (2003)
13. T. Furusho, S. Ohshima, S. Nishino, Mater. Sci. Forum **389–393**, 1449 (2002)
14. R. Schlesser, Z. Sitar, J. Cryst. Growth **234**, 349 (2002)
15. K. Kamei, Y. Shirai, T. Tanaka, N. Okada, A. Yauchi, H. Amano, Phys. Status Solidi C **4**, 2211 (2007)
16. M. Bockowski, Cryst. Res. Technol. **36**, 771 (2001)
17. M. Yano, M. Okamoto, Y.K. Yap, M. Yoshimura, Y. Mori, T. Sasaki, Diam. Relat. Mater. **9**, 512 (2000)
18. Y. Kangawa, R. Toki, T. Yayama, B.M. Epelbaum, K. Kakimoto, Appl. Phys. Express **4**, 095501 (2011)
19. B.T. Adekore, K. Rakes, B. Wang, M.J. Callahan, S. Pendurti, Z. Sitar, J. Electron. Mater. **35**, 1104 (2006)

20. R. Dwilinski, R. Doradzinski, J. Garczynski, L. Sierzputowski, M. Palczewska, A. Wysmolek, M. Kaminska, MRS Internet J. Nitride Semicond. Res. **3**, 1 (1998)
21. T. Kinoshita, K. Hironaka, T. Obata, T. Nagashima, R. Dalmau, R. Schlesser, B. Moody, J. Xie, S.-I. Inoue, Y. Kumagai, A. Koukitu, Z. Sitar, Appl. Phys. Express **5**, 122101 (2012)
22. Fr. Briegleb, A. Geuther, Justus Liebigs Ann. Chem. **123**, 228 (1877)
23. W. Nakao, H. Fukuyama, K. Nagata, J. Am. Ceram. Soc. **84**, 889 (2002)
24. W. Werdecker, F. Aldinger, I.E.E.E. Trans, Hybrids Manuf. Technol. **7**, 399 (1984)
25. L.M. Sheppard, Am. Ceram. Soc. Bull. **69**, 1801 (1990)
26. G.A. Slack, M.R.S. Symp, Proc. **512**, 35 (1998)
27. K.M. Taylor, C. Lenie, J. Electrochem. Soc. **107**, 308 (1960)
28. H.-D. Witzke, Phys. Status Solidi **2**, 1109 (1962)
29. J. Pastrnak, L. Roskovcova, Phys. Status Solidi **7**, 331 (1964) (in German)
30. G.A. Cox, D.O. Cummins, K. Kawabe, R.H. Tredgold, J. Phys. Chem. Solids **28**, 543 (1967)
31. G.A. Slack, T.F. McNelly, J. Cryst. Growth **42**, 560 (1977)
32. G.A. Slack, *Aluminum Nitride Crystal Growth,* U.S. Air Force Office of Scientific Research (1979). DTIC document ADA085932 (http://www.dtic.mil)
33. W.W. Piper, S.J. Polich, J. Appl. Phys. **32**, 1278 (1961)
34. C.M. Balkas, Z. Sitar, T. Zheleva, L. Bergman, R. Nemanich, R.F. Davis, J. Cryst. Growth **179**, 363 (1997)
35. M. Tanaka, S. Nakahata, K. Sogabe, H. Nakata, M. Tobioka, Jpn. J. Appl. Phys. **36**, L1062 (1997)
36. J.C. Rojo, G.A. Slack, K. Morgan, B. Raghothamachar, M. Dudley, L.J. Schowalter, J. Cryst. Growth **231**, 317 (2001)
37. Yu.M. Tairov, Mater. Sci. Eng. B **29**, 83 (1995)
38. R. Schlesser, R. Dalmau, D. Zhuang, R. Collazo, Z. Sitar, J. Cryst. Growth **281**, 75 (2005)
39. R. Dalmau, B. Raghothamachar, M. Dudley, R. Schlesser, Z. Sitar, MRS Symp. Proc. **798**, Y2.9 (2004)
40. B. Liu, J.H. Edgar, Z. Gu, D. Zhuang, B. Raghothamachar, M. Dudley, A. Sarua, M. Kuball, H.M. Meyer III, MRS Internet J. Nitride Semicond. Res. **9**, 6 (2004)
41. G.A. Slack, J. Whitlock, K. Morgan, L.J. Schowalter, MRS Symp. Proc. **798**, Y10.74 (2004)
42. B.M. Epelbaum, M. Bickermann, A. Winnacker, J. Cryst. Growth **275**, e479 (2005)
43. S.G. Mueller, R.T. Bondokov, K.E. Morgan, G.A. Slack, S.B. Schujman, J. Grandusky, J.A. Smart, L.J. Schowalter, Phys. Status Solidi A **206**, 1153 (2009)
44. R.R. Sumathi, P. Gille, Jpn. J. Appl. Phys. **52**, 08JA02 (2013)
45. M. Bickermann, B.M. Epelbaum, O. Filip, B. Tautz, P. Heimann, A. Winnacker, Phys. Status Solidi C **9**, 449 (2012)
46. Z.G. Herro, D. Zhuang, R. Schlesser, Z. Sitar, J. Cryst. Growth **312**, 2519 (2010)
47. I. Nagai, T. Kato, T. Miura, H. Kamata, K. Naoe, K. Sanada, H. Okumura, J. Cryst. Growth **312**, 2699 (2010)
48. M. Miyanaga, N. Mizuhara, T. Kawase, S. Fujiwara, M. Shimazu, H. Nakahata, T. Kawase, J. Cryst. Growth **300**, 45 (2007)
49. Yu.N. Makarov, O.V. Avdeev, I.S. Barash, D.S. Bazarevskiy, T.Yu. Chemekova, E.N. Mokhov, S.S. Nagalyuk, A.D. Roenkov, A.S. Segal, Yu.A. Vodakov, M.G. Ramm, S. Davis, G. Huminic, H. Helava, J. Cryst. Growth **310**, 881 (2008)
50. J.R. Grandusky, J. Chen, S.R. Gibb, M.C. Mendrick, C.G. Moe, L. Rodak, G.A. Garrett, M. Wraback, L.J. Schowalter, Appl. Phys. Express **6**, 032101 (2013)
51. R. Collazo, S. Mita, J. Xie, A. Rice, J. Tweedie, R. Dalmau, Z. Sitar, Phys. Status Solidi C **8**, 2031 (2011)
52. T. Wunderer, C.L. Chua, Z. Yang, J.E. Northrup, N.M. Johnson, G.A. Garrett, H. Shen, M. Wraback, Appl. Phys. Express **4**, 092101 (2011)
53. M. Kneissl, Z. Yang, M. Teepe, C. Knollenberg, O. Schmidt, P. Kiesel, N.M. Johnson, S. Schujman, L.J. Schowalter, J. Appl. Phys. **101**, 123103 (2007)

54. M. Martens, F. Mehnke, C. Kuhn, C. Reich, V. Kueller, A. Knauer, C. Netzel, C. Hartmann, J. Wollweber, J. Rass, T. Wernicke, M. Bickermann, M. Weyers, M. Kneissl, IEEE Photonics Lett. **26**, 342 (2014)
55. J. Xie, S. Mita, Z. Bryan, W. Guo, L. Hussey, B. Moody, R. Schlesser, R. Kirste, M. Gerhold, R. Collazo, Z. Sitar, Appl. Phys. Lett. **102**, 171102 (2013)
56. T. Erlbacher, M. Bickermann, B. Kallinger, E. Meissner, A.J. Bauer, L. Frey, Phys. Status Solidi C **9**, 968 (2012)
57. G. Bu, D. Ciplys, M. Shur, L.J. Schowalter, S. Schujman, R. Gaska, IEEE Trans. Ultrasonics Ferroelectr. Freq. Control **53**, 251 (2006)
58. X. Hu, J. Deng, N. Pala, R. Gaska, M.S. Shur, C.Q. Chen, J. Yang, G. Simin, M.A. Khan, J. C. Rojo, L.J. Schowalter, Appl. Phys. Lett. **82**, 1299 (2003)
59. A. Dobrinsky, G. Simin, R. Gaska, M. Shur, ECS Trans. **58**(4), 129 (2013)
60. L. Siang-Chung, Mater. Sci. Lett. **16**, 759 (1997)
61. Y. Li, D.W. Brenner, Phys. Rev. Lett. **92**, 075503 (2004)
62. B.M. Epelbaum, M. Bickermann, S. Nagata, P. Heimann, O. Filip, A. Winnacker, J. Cryst. Growth **305**, 317 (2007)
63. V. Noveski, R. Schlesser, S. Mahajan, S. Beaudoin, Z. Sitar, J. Cryst. Growth **264**, 369 (2004)
64. Q.-S. Chen, V. Prasad, H. Zhang, M. Dudley, in: K. Byrappa, T. Ohachi (eds.), *Crystal Growth Technology* (Springer, Berlin, 2005). ISBN 978-3-540-00367-0, chap. 7
65. S.Yu. Karpov, D.V. Zimina, Yu.N. Makarov, E.N. Mokhov, A.D. Roenkov, M.G. Ramm, Yu.A. Vodakov, Phys. Status Solidi A **176**, 435 (1999)
66. A.S. Segal, S.Yu. Karpov, Yu.N. Makarov, E.N. Mokhov, A.D. Roenkov, M.G. Ramm, Yu. A. Vodakov, J. Cryst. Growth **211**, 68 (2000)
67. P. Heimann, B.M. Epelbaum, M. Bickermann, S. Nagata, A. Winnacker, Phys. Status Solidi C **3**, 1575 (2006)
68. S.Yu. Karpov, A.V. Kulik, I.N. Przhevalskii, M.S. Ramm, Yu.N. Makarov, Phys. Status Solidi C 0 1989 (2003)
69. M. Albrecht, J. Wollweber, M. Rossberg, M. Schmidbauer, C. Hartmann, R. Fornari, Appl. Phys. Lett. **88**, 211904 (2006)
70. Z.G. Herro, D. Zhuang, R. Schlesser, R. Collazo, Z. Sitar, J. Cryst. Growth **286**, 205 (2006)
71. M. Bickermann, B.M. Epelbaum, A. Winnacker, Phys. Status Solidi C **2**, 2044 (2005)
72. A. Dittmar, C. Guguschev, C. Hartmann, S. Golka, A. Kwasniewski, J. Wollweber, R. Fornari, J. Eur. Ceram. Soc. **31**, 2733 (2011)
73. C. Hartmann, J. Wollweber, M. Albrecht, I. Rasin, Phys. Status Solidi C **3**, 1608 (2006)
74. C. Guguschev, A. Dittmar, E. Moukhina, C. Hartmann, S. Golka, J. Wollweber, M. Bickermann, R. Fornari, J. Cryst. Growth **360**, 185 (2012)
75. M. Bickermann, B.M. Epelbaum, A. Winnacker, J. Cryst. Growth **269**, 432 (2004)
76. B.M. Epelbaum, C. Seitz, A. Magerl, M. Bickermann, A. Winnacker, J. Cryst. Growth **265**, 577 (2004)
77. B. Raghothamachar, J. Bai, M. Dudley, R. Dalmau, D. Zhuang, Z. Herro, R. Schlesser, Z. Sitar, B. Wang, M. Callahan, K. Rakes, P. Konkapaka, M. Spencer, J. Cryst. Growth **287**, 349 (2006)
78. C. Hartmann, J. Wollweber, A. Dittmar, K. Irmscher, A. Kwasniewski, F. Langhans, T. Neugut, M. Bickermann, Jpn. J. Appl. Phys. **52**, 08JA06 (2013)
79. M. Bickermann, O. Filip, B.M. Epelbaum, P. Heimann, M. Feneberg, B. Neuschl, K. Thonke, E. Wedler, A. Winnacker, J. Cryst. Growth **339**, 13 (2012)
80. R.R. Sumathi, P. Gille, Cryst. Res. Technol. **47**, 237 (2012)
81. O. Filip, B.M. Epelbaum, M. Bickermann, P. Heimann, S. Nagata, A. Winnacker, Mater. Sci. Forum **615–617**, 983 (2009)
82. C. Hartmann, M. Albrecht, J. Wollweber, J. Schuppang, U. Juda, Ch. Guguschev, S. Golka, A. Dittmar, R. Fornari, J. Cryst. Growth **344**, 19 (2012)
83. M. Bickermann, B.M. Epelbaum, O. Filip, P. Heimann, S. Nagata, A. Winnacker, Phys. Status Solidi C **5**, 1502 (2008)

84. B.M. Epelbaum, M. Bickermann, A. Winnacker, Mater. Sci. Forum **433–436**, 983 (2003)
85. D. Zhuang, Z.G. Herro, R. Schlesser, Z. Sitar, J. Cryst. Growth **287**, 372 (2006)
86. O. Filip, B.M. Epelbaum, M. Bickermann, P. Heimann, A. Winnacker, J. Cryst. Growth **318**, 427 (2011)
87. D. Hofmann, M. Bickermann, W. Hartung, A. Winnacker, Mater. Sci. Forum **338–342**, 445 (2000)
88. H. Helava, E.N. Mokhov, O.A. Avdeev, M.G. Ramm, D.P. Litvin, A.V. Vasiliev, A.D. Roenkov, S.S. Nagalyuk, Yu.N. Makarov, Mater. Sci. Forum **740–742**, 85 (2013)
89. R. Dalmau, B. Moody, J. Xie, R. Collazo, Z. Sitar, Phys. Status Solidi A **208**, 1545 (2011)
90. R.T. Bondokov, K.E. Morgan, R. Shetty, W. Liu, G.A. Slack, M. Goorsky, L.J. Schowalter, MRS Symp. Proc. **892**, FF30-03 (2006)
91. D. Zhuang, J.H. Edgar, Mater. Sci. Eng. R **48**, 1 (2005)
92. M. Bickermann, S. Schmidt, B.M. Epelbaum, P. Heimann, S. Nagata, A. Winnacker, J. Cryst. Growth **300**, 299 (2007)
93. B. Raghothamachar, M. Dudley, J.C. Rojo, K. Morgan, L.J. Schowalter, J. Cryst. Growth **250**, 244 (2003)
94. B. Raghothamachar, Y. Yang, R. Dalmau, B. Moody, S. Craft, R. Schlesser, M. Dudley, Z. Sitar, Mater. Sci. Forum **740–742**, 91 (2013)
95. M. Bickermann, S. Schimmel, B.M. Epelbaum, O. Filip, P. Heimann, S. Nagata, A. Winnacker, Phys. Status Solidi C **8**, 2235 (2011)
96. R.T. Bondokov, K.E. Morgan, R. Shetty, W. Liu, G.A. Slack, M. Goorsky, L.J. Schowalter, MRS Symp. Proc. **892**, FF30-03 (2006)
97. R. Dalmau, R. Schlesser, Z. Sitar, Phys. Status Solidi C **2**, 2036 (2005)
98. M. Bickermann, P. Heimann, B.M. Epelbaum, Phys. Status Solidi C **3**, 1902 (2006)
99. M. Feneberg, R.A.R. Leute, B. Neuschl, K. Thonke, M. Bickermann, Phys. Rev. B **82**, 075208 (2010)
100. G.A. Slack, L.J. Schowalter, D. Morelli, J.A. Freitas Jr, J. Cryst. Growth **246**, 287 (2002)
101. M. Bickermann, B.M. Epelbaum, O. Filip, P. Heimann, S. Nagata, A. Winnacker, Phys. Status Solidi B **246**, 1181 (2009)
102. L. Gordon, J.L. Lyons, A. Janotti, C.G. Van de Walle, Phys. Rev. B **89**, 085204 (2014)
103. K. Irmscher, C. Hartmann, C. Guguschev, M. Pietsch, J. Wollweber, M. Bickermann, J. Appl. Phys. **114**, 123505 (2013)
104. N.T. Son, M. Bickermann, E. Janzén, Appl. Phys. Lett. **98**, 092104 (2011)
105. B. Neuschl, K. Thonke, M. Feneberg, S. Mita, X. Xie, R. Dalmau, R. Collazo, Z. Sitar, Phys. Status Solidi B **249**, 511 (2012)
106. M. Feneberg, R.A.R. Leute, B. Neuschl, K. Thonke, M. Bickermann, Phys. Rev. B **82**, 075208 (2010)
107. S.B. Orlinskii, J. Schmidt, P. Baranov, M. Bickermann, B.M. Epelbaum, A. Winnacker, Phys. Rev. Lett. **100**, 256404 (2008)
108. S.M. Evans, N.C. Giles, L.E. Halliburton, G.A. Slack, S.B. Shujman, L.J. Schowalter, Appl. Phys. Lett. **88**, 062112 (2006)
109. C. Stampfl, C.G. van de Walle, Phys. Rev. B **65**, 155212 (2002)
110. N.T. Son, A. Gali, Á. Szabó, M. Bickermann, T. Ohshima, J. Isoya, E. Janzén, Appl. Phys. Lett. **98**, 242116 (2011)
111. F. Tuomisto, J.-M. Mäki, T.Yu. Chemekova, Yu.N. Makarov, O.V. Avdeev, E.N. Mokhov, A.S. Segal, M.G. Ramm, S. Davis, G. Huminic, H. Helava, M. Bickermann, B.M. Epelbaum, J. Cryst. Growth **310**, 3998 (2008)
112. M. Bickermann, B.M. Epelbaum, O. Filip, P. Heimann, S. Nagata, A. Winnacker, Phys. Status Solidi C **7**, 21 (2010)
113. R. Collazo, J. Xie, B.E. Gaddy, Z. Bryan, R. Kirste, M. Hoffmann, R. Dalmau, B. Moody, Y. Kumagai, T. Nagashima, Y. Kubota, T. Kinoshita, A. Koukitu, D.L. Irving, Z. Sitar, Appl. Phys. Lett. **100**, 191914 (2012)
114. T. Nagashima, Y. Kubota, T. Kinoshita, Y. Kumagai, J. Xie, R. Collazo, H. Murakami, H. Okamoto, A. Koukitu, Z. Sitar, Appl. Phys. Express **5**, 125501 (2012)

115. L. Trinkler, B. Berzina, in: *Advances in Ceramics: Characterization, Raw Materials, Processing, Properties, Degradation and Healing*, C. Sikalidis (ed.), InTech Open Access Book (2011). ISBN 978-953-307-504-4, chap. 4
116. A. Sedhain, L. Du, J.H. Edgar, J.Y. Lin, H.X. Jiang, Appl. Phys. Lett. **95**, 262104 (2009)
117. B.E. Gaddy, Z. Bryan, I. Bryan, R. Kirste, J. Xie, R. Dalmau, B. Moody, Y. Kumagai, T. Nagashima, Y. Kubota, T. Kinoshita, A. Koukitu, Z. Sitar, R. Collazo, D.L. Irving, Appl. Phys. Lett. **103**, 161901 (2013)
118. T. Schulz, M. Albrecht, K. Irmscher, C. Hartmann, J. Wollweber, R. Fornari, Phys. Status Solidi B **248**, 1513 (2011)
119. M. Bickermann, B.M. Epelbaum, O. Filip, P. Heimann, M. Feneberg, S. Nagata, A. Winnacker, Phys. Status Solidi C **7**, 1743 (2010)
120. T. Mattila, R.M. Nieminen, Phys. Rev. B **55**, 9571 (1997)
121. K. Irmscher, T. Schulz, M. Albrecht, C. Hartmann, J. Wollweber, R. Fornari, Phys. B **401–402**, 323 (2007)
122. Note that the absorption spectra for samples 6 and 7 differ to the ones shown in [78], as they were measured on similar crystals with virtually the same impurity concentrations. Furthermore, absorption coefficients above 700 cm^{-1} (sample 6) contain measurement artifacts
123. The silicon concentrations of samples 1 through 7 are corrected to reflect a calibration error which was found after the values cited in the references [75,78,112] had been published

Chapter 3
Vapor Phase Epitaxy of AlGaN Base Layers on Sapphire Substrates for Nitride-Based UV-Light Emitters

Eberhard Richter, Sylvia Hagedorn, Arne Knauer and Markus Weyers

Abstract UV transparent lattice matched substrates, e.g., AlN and AlGaN, with low dislocation densities are required for the epitaxial growth of UV-LED structures. In the absence of inexpensive high-quality UV transparent AlN bulk substrates, the heteroepitaxial growth of AlN base layers on relatively cheap and readily available sapphire substrates is the commonly used approach for most UV-B and UV-C LEDs. This chapter provides an insight into growth, strain management, and dislocation reduction techniques in metalorganic vapor phase epitaxy (MOVPE) of AlN and hydride vapor phase epitaxy (HVPE) of AlGaN layers. For both MOVPE and HVPE epitaxial lateral overgrowth of patterned substrate surfaces is an important technique to enhance the thickness of crack-free layers. This opens the route to UV-LEDs with improved performance.

3.1 Introduction

The choice of a suitable substrate is always a fundamental point for group III nitride technologies because of the lack or limited availability of wafers for homoepitaxy from conventional bulk growth techniques and the rather large differences of lattice constants between the binaries AlN, GaN, and InN. For example, emission wavelengths due to recombination of electron-hole pairs with near band-gap energy of

E. Richter (✉) · S. Hagedorn · A. Knauer · M. Weyers
Ferdinand-Braun-Institut, Leibniz-Institut für Höchstfrequenztechnik,
Gustav-Kirchhoff-Str. 4, 12489 Berlin, Germany
e-mail: eberhard.richter@fbh-berlin.de

S. Hagedorn
e-mail: sylvia.hagedorn@fbh-berlin.de

A. Knauer
e-mail: arne.knauer@fbh-berlin.de

M. Weyers
e-mail: markus.weyers@fbh-berlin.de

© Springer International Publishing Switzerland 2016

M. Kneissl and J. Rass (eds.), *III-Nitride Ultraviolet Emitters*,
Springer Series in Materials Science 227, DOI 10.1007/978-3-319-24100-5_3

AlN at 210 nm and GaN at 365 nm comprise a major part of the UV spectrum, but the difference of in-plane lattice constants is as huge as 2.4 %. Thus, homoepitaxial and pseudomorphic growth of device layer structures is limited to the range of 210 nm to about 280 nm for use of AlN substrates and of about 340 nm to above 400 nm with the drawbacks of absorption and tensile strain below 365 nm for use of GaN substrates. The generation of considerable densities of threading dislocations (TDD) due to lattice relaxation has to be dealt with in the remaining wavelength range, i.e., the UV-B part, or in case of thicker relaxed layer structures. Therefore, nowadays, the use of sapphire (instead of AlN or GaN) as substrate material despite the large lattice mismatch and the additional drawback of strongly different thermal expansion coefficient yields similar TDD but offers the advantage of nearly unlimited availability. Sapphire and heteroepitaxial growth thereon will be in the main focus of the following chapter. In the first part, growth of templates for UV device layer structures by metalorganic vapor phase epitaxy (MOVPE) is discussed and the second part comprises attempts to grow thick AlGaN layers by hydride vapor phase epitaxy (HVPE), especially for the UV-B wavelength region. In the UV region, the high TDD results in a strong decrease of internal quantum efficiency (IQE) due to non-radiative recombination of excited carriers at dislocations. Additionally, dislocations can trap carriers and impede carrier transport. For high Al content, a low TDD is prerequisite to obtain reasonable n-type doping [1]. This behavior leads to the strong decrease of external quantum efficiency (EQE) with emission wavelength from the UV-A to the UV-B as shown in Fig. 3.1. It has been shown by simulation and experiments that the TDD has to be below 7×10^8 cm^{-2} to avoid limitations of EQE by IQE to below 50 % [2, 3]. In the UV-C range, pseudomorphic growth on AlN or relaxed AlN buffer layers with low TDD first leads to a higher IQE/EQE than in the UV-B, but for higher Al content the EQE decreases again caused by the decreasing carrier confinement in the quantum wells as well as by the lower extraction efficiency of the increasing part of TM polarized light.

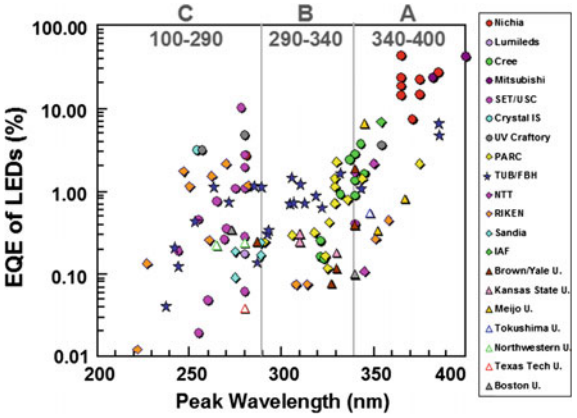


Fig. 3.1 External quantum efficiency of UV-LEDs versus emission wavelength collected from published data of UV-LEDs [4]

3.2 Growth of Al(Ga)N Buffer Layers by MOVPE

The majority of device layer structures for UV-light emitters are fabricated by MOVPE [5] and thus it is straightforward to use this technique also for the heteroepitaxial growth of buffer layers on sapphire [3]. MOVPE reactors designed for high throughput are offered by several vendors. Growth rates are typically in the range of up to 10 µm/h depending on reactor design, growth conditions, and semiconductor material. Metalorganic precursors like tri(m)ethylgallium (TMG, TEG) and tri(m)ethylaluminum (TMAl, TEAl) are used for group III supply and react after pyrolysis with the group V source gas ammonia which is usually supplied in excess. However, the direct start of growth with the desired composition of the ternary compound semiconductor AlGaN would mean to add the complication of local variations in Al/Ga concentrations [6] to the basic problems of heteroepitaxy like large lattice mismatch and difference in thermal expansion coefficients. The lattice mismatch between AlN and (0001) sapphire would be 35 % if there was not a better coincidence of the two lattices by a 30° rotation resulting in only 13 % mismatch [7, 8]. Thus, the critical thickness of AlN on c-plane sapphire is below one monolayer and misfit dislocations are formed in high densities at the interface immediately (Fig. 3.2). In practice, after thermal annealing of the sapphire substrate in hydrogen, AlN growth is started typically at low to medium temperatures of about 600–1000 °C with high V/III ratio >1000 and buffer layer thickness of up to 200 nm or directly at high temperatures above 1100 °C. Using an AlN buffer layer [9], the subsequent high temperature growth of an AlN layer is

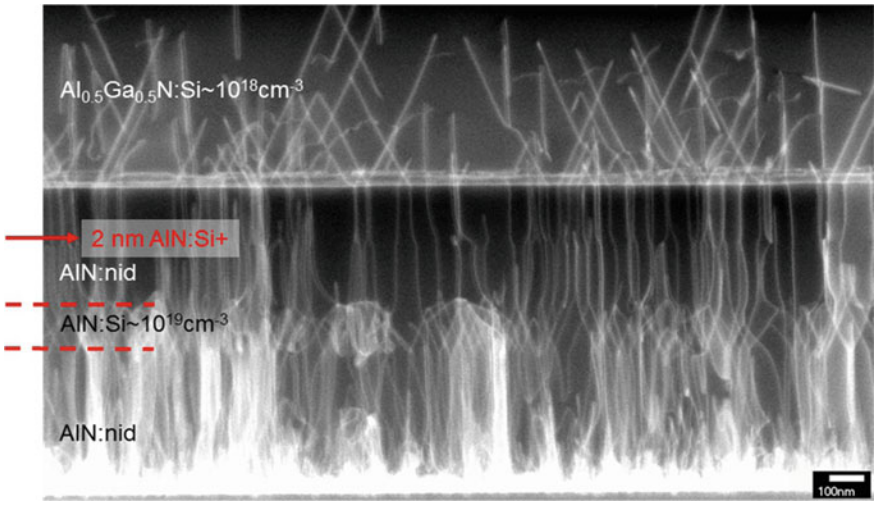


Fig. 3.2 Cross-sectional micrograph recorded by transmission electron microscopy in annular dark field mode (TEM-ADF) of *n*-$Al_{0.5}Ga_{0.5}N$/AlN/sapphire grown by MOVPE containing two Si-doped interlayers with Si concentrations of 1×10^{19} and 4×10^{19} cm^{-3} [12]

characterized by a low lateral growth rate compared to, e.g., GaN [10]. Thus, the merging of the high number of isolated small seeds is poor resulting in mosaicity with tilt and twist and threading dislocations with a density above 10^{10} cm^{-2} originating from boundaries between different domains. These dislocations due to different seed orientation remain after most of the misfit dislocations have annihilated after some tens to hundreds of nm. The introduction of pulsed NH_3 growth for higher lateral growth rates and development of MOVPE setups allowing high temperatures of 1200–1400 °C led to more homogeneously oriented and larger AlN domains in recent years helping to reduce the TDD [11]. In addition, it was found, that the usually oxygen-terminated sapphire surface is stable until it is heated above 1050 °C under hydrogen resulting in Al–H termination and a reconstructed surface. Such a surface is found to allow for growth according to the epitaxial law:

$$(0001)_{AlN} \parallel (0001)_{\alpha-Al_2O_3} \text{ and } [2\bar{1}\bar{1}0]_{AlN} \parallel [1\bar{1}00]_{\alpha-Al_2O_3}$$

but small additional rotation which leads to small angle grain boundaries between domains twisted by 3–4 ° and arrays of equidistant edge dislocations [13] were observed. These low-angle grain boundaries are proposed to be avoidable by use of precisely step-bunched sapphire substrates or weakening of the epitaxial law by disturbing the sapphire surface reconstruction by proper miscut [13], or surface roughening [14], or preconditioning the surface before growth. For the latter, a pre-flow of TMAl was found to support a homogeneously Al-terminated surface for subsequent Al-polar growth of AlN layers [15–17]. Coexistence of Al- and N-polar domains yields rough morphology since the growth rate in N-polar direction is significantly lower than in the metal-polar direction [18, 19]. After growth of the AlN buffer in first step, the wafer is heated up to growth temperatures of about 1200–1400 °C with usually reduced V/III, e.g., 50–250 to enhance lateral growth and seed coalescence. Smoothing of the surface at the end of growth can be achieved by reduced growth temperature of about 1100 °C and use of low V/III ratio [17]. The reduction of the TDD with thickness due to dislocation annihilation is the reason for tensile strain being built up in the AlN layer [21]. This strain leads to an increase of curvature with layer thickness, whereas the starting concave shape of the sapphire is mainly determined by the temperature difference between the hot sapphire backside and the gas cooled frontside of the sapphire (Fig. 3.3). The typical critical layer thickness for cracking of AlN layers on sapphire is about 1 to 1.5 μm and the TDD is then in the range of 10^9–10^{10} cm^{-2} [17]. A further reduction of the TDD to 10^8 cm^{-2} or less is needed to improve the internal quantum efficiency in Al(Ga)N quantum well structures [22]. However, growing a nonpseudomorphic $Al_xGa_{1-x}N$ layer above the critical thickness on an AlN buffer leads to the generation of new dislocation with a density of about 10^{10} cm^{-2} due to the lattice mismatch. The TDD can again be reduced by annihilation by growth of several μm of AlGaN but remains in the range of some 10^9 cm^{-2} [23]. Hence, different growth concepts are required.

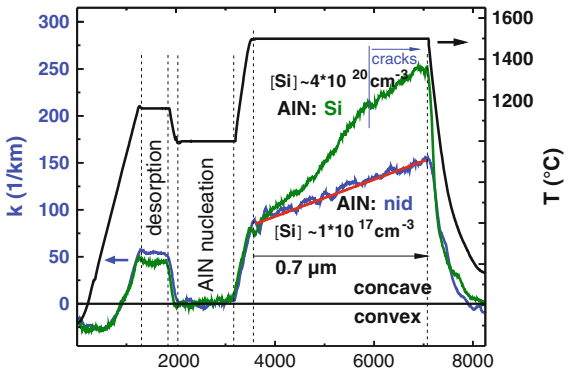


Fig. 3.3 In-situ data of curvature k and process temperature T recorded by EpiCurveTT™ (LayTec AG) of MOVPE growth of non-intentionally and Si-doped AlN on sapphire [20]

3.3 Techniques for MOVPE of Al(Ga)N Base Layers with Reduced TDD

In the UV-A range GaN and in the UV-C range transparent AlN templates, as well as in the UV-B range AlGaN templates with AlN fraction of 50–80 % in the alloy and with mid 10^8 cm^{-2} TDD are currently reasonable values for use in epitaxy of UV-LEDs. A useful figure of merit that also comprises evaluation of overall crystal quality is the widths of X-ray rocking curves taken at different reflections [24]. Large area footprints of several mm^2 and use of double axis diffraction geometry are suited to get meaningful data. Values of full width at half maximum of symmetric reflections at (0002) planes and skew-symmetric reflections at $(30\bar{3}2)$ planes should be below 150 and 450 arcsec, respectively. For future high-end devices, higher demands are already being discussed with dislocation density generally below 10^6 cm^{-2} and a resulting FWHM below 40 arcsec in (0002) and $(10\bar{1}2)$ reflection [25].

The use of in situ SiN_x masks formed by decomposition of silane and ammonia is common for defect reduction in GaN [26]. These in situ masks can partially block the vertical propagation of dislocations by lateral epitaxial overgrowth [6]. This approach can also be useful in the UV-A range with $Al_xGa_{1-x}N$ compositions x below 0.4 [27], but there are no reports on successful application for the Al content necessary for the UV-B. Another useful approach for the UV-A range exploits the coherent coincidence of surface meshes between (0001) sapphire and c-plane $Al_xGa_{1-x}N$ layers at $x \approx 0.22$ at growth temperature which could be used to reduce the TDD in such layers [28]. Other successful approaches use low temperature AlN layers or grooved AlGaN layers for subsequent overgrowth with $Al_xGa_{1-x}N$ to reduce the TDD [29–32]. For UV-B devices, the reduction can be achieved by subsequent growth of a thick, compressively strained $Al_xGa_{1-x}N$ layer ($x \approx 0.4$–0.7) on the AlN buffer [20] or patterned AlGaN [31] on sapphire. If doped,

this AlGaN buffer may also serve as contact layer for the device. Short period superlattices of alternating Al(Ga)N/(Al)GaN layers have been demonstrated to accommodate the strain in the pseudomorphically grown thin layers of the superlattice by inclination of dislocations and partial dislocation annihilation. Thus, AlGaN thicknesses of several µm TDD of few 10^9 cm^{-2} have been realized [33]. Another approach of TDD reduction taking benefit from an enhanced annihilation due to dislocation inclination is to use Si-doped AlN interlayers with doping levels of some 10^{19} cm^{-3} as shown in Fig. 3.2. This approach can only be applied for layers with high TDD in the range of 10^{10} cm^{-2}. However, the reduction of the TDD by a factor of two also reduces the critical layer thickness for cracking due to increase of tensile strain as can be seen in Fig. 3.3.

For UV-C devices, bulk AlN substrates offer a low dislocation density that is beneficial for device performance as long as the device layer structure is grown pseudomorphically without generation of new dislocations. However, substrate cost and absorption bands in AlN substrates are challenges for this approach. Dislocation annihilation with increasing thickness promises lower dislocation densities in thick buffer layers on sapphire. However, crack generation due to tensile strain is a challenge here [11, 34]. One approach for obtaining a thick AlN layer with low TDD on sapphire is to create a rough surface by pulsed NH_3 flow growth and to reduce TDD and roughness by coalescence in a continuous flow mode at high growth rate and moderate temperature. A stable Al-face +c polarity is achieved by the use of Al-rich growth conditions. By repetition of this process, a TDD below 8×10^8 cm^{-2} was achieved in around 5 µm thick AlN [35]. However, roughening as well as smoothing seems to only have small parameter windows making a general application in different reactors difficult. Another approach uses mainly trench patterned AlN/sapphire substrates [36–39] or self-assembled patterned AlN nanorods [40]. Reduction of the TDD and increase of the critical thickness is achieved by epitaxial lateral overgrowth over trenches or rods creating bridges over voids (ELO or bridge growth). Patterned AlN instead of mask material is used to prevent polycrystalline growth on the mask due to high-adhesion of Al-species. Stripes along $\langle 11\bar{2}0\rangle_{\text{sapphire}}$ or $\langle 1\bar{1}00\rangle_{\text{AlN}}$ direction were used with 1–4 µm wide ridges and 0.5–7 µm wide trenches as typical pattern. Lateral overgrowth takes place into a-direction resulting in smooth c-plane-oriented surfaces (Fig. 3.4). Inclined dislocations can terminate at the free inner surfaces of voids or annihilate. A sapphire offcut in the direction of lateral growth supports the reproducible coalescence of the AlN layer [41, 42]. If the offcut is ≥0.15°, macro-steps originate at the point of coalescence. Transmission electron microscopy reveals inclined threading dislocations starting at the points of coalescence and ending at macro-steps. The macro-steps generated during coalescence propagate over the surface and kinetically trap most of the dislocations in the kink of the step (Fig. 3.4a). In the samples with smaller offcut (Fig. 3.4b) or off-orientation to a-direction, the dislocations cannot be trapped due to too small step heights. The occurrence of inclined grain boundaries at the point of coalescence is often observed. Vertically propagating dislocations can bend into such grain boundaries

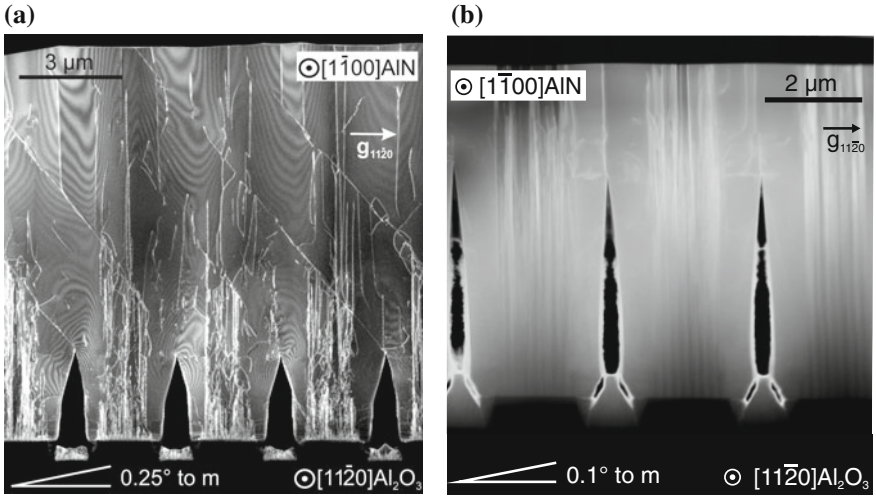


Fig. 3.4 Cross-sectional TEM-ADF micrographs revealing the behavior of threading dislocations (TD) including inclined and vertically oriented boundaries between coalescing grains in an ELO-AlN layer grown on sapphire with an offcut of 0.25° to m (**a**) and 0.1° to m (**b**) [42]

and an additional reduction of the TDD down to 10^7 cm^{-2} can be achieved for layers, where the macro-steps cross over the dislocation-rich area [42] as seen in Fig. 3.4a. A stripe-like TDD distribution with enrichments over the ridges will be observed for trench patterned AlN templates. More homogeneous TDD distribution and avoidance of macro-steps can be achieved by use of nanorods. In both cases, the TDD is in the middle 10^8 cm^{-2} range for the typically used 4–5 µm AlN total thickness. The high AlN thickness leads to strong convex bow during the cooling down from growth temperatures of 1100–1400 °C of the AlN/sapphire templates due to their different thermal expansion coefficients. The AlN layer thickness at the point of coalescence and size of the voids can be controlled by the growth temperature and V/III ratio. Lower lateral growth rates resulting in delayed coalescence are observed for lower temperatures, higher V/III ratios [37, 41, 43], or by addition of the anti-surfactant silicon [44]. Starting from 5 to 15 µm thick AlN layers with TDD in the mid 10^8 cm^{-2} range, the growth of $Al_{0.8}Ga_{0.2}N$ layers, and quantum well structures with similar TDD [45] and emission with improved internal quantum efficiency in the UV-B and -C range [43, 46, 47] was achieved. The thick AlN base layer is beneficial for the thermal impedance of high power devices deposited on it because of the much better thermal conductivity of AlN in comparison to sapphire. Even for flip-chipped devices at least 20 % of heat is removed through the substrate [47].

3.4 Growth of AlGaN Layers by HVPE

Hydride vapor phase epitaxy (HVPE) offers high growth rates which in metalorganic vapor phase epitaxy (MOVPE) of AlGaN are limited by pre-reactions [48] and thus HVPE is a promising technique for thick buffer layers. However, the future role of HVPE for AlGaN growth is not yet completely clear because growth of this ternary compound by HVPE is still a challenge and commercial equipment is not available. Only few groups currently deal with this topic with different objectives starting from growth of Mg-doped AlGaN shells for nanowires [49], AlGaN intermediate layers to improve subsequent growth of semipolar GaN [50], growth of UV-LED heterostructures [51], LED heterostructures with direct white emission eliminating the need for phosphors [52], AlGaN-based vertical LEDs [53], AlGaN buffer layers for UV-B-LED heterostructures with reduced dislocation density [52, 54], Al(Ga)N buffer layers for UV-C-LED heterostructures [55], or highly transparent AlN substrates for such devices [56–61]. Not only the objectives but also growth technology and used substrates differ between the groups active in this field. These issues will briefly be summarized, but most of the following part will concentrate on growth behavior and challenges by using conventional quartz equipment and c-plane sapphire as starting substrate. Experimental conditions have basically not changed since early pioneering work of HVPE of GaN [62] and of AlN [63]. At least with respect to GaN and AlN, the hope that large-scale and homogeneous deposition of structurally high-quality layers is possible by HVPE has already been fulfilled, while the ternary compound AlGaN is still challenging.

3.4.1 Fundamentals of the HVPE Technique

In contrast to MOVPE, in HVPE a gaseous halide serves as group III reactant which is usually formed from a metal and a halogen within the process. In case of nitride HVPE, NH_3 is the group V source. The gaseous reactants are transported by a carrier gas in an open hot-wall reactor enabling continuous growth with minimized wall deposits. The process usually contains the formation of group III halides in a source zone and the targeted crystalline layer in a substrate zone with different temperatures. HVPE usually permits control of growth rate over several orders of magnitude mainly by group III supply and temperature. However, gas switching is often sluggish compared to MOVPE due to the large volume in the source zone. The purity of the grown layers depends not only on the purity of the sources (metals and gases) but also on the stability of substrate and reactor materials in a growth environment containing halides. The conventional reactor material is quartz. However, since a long time quartz is known to be rather sensitive against aluminum compounds.

A conventional HVPE reactor for the growth of AlGaN layers is shown in Fig. 3.5.

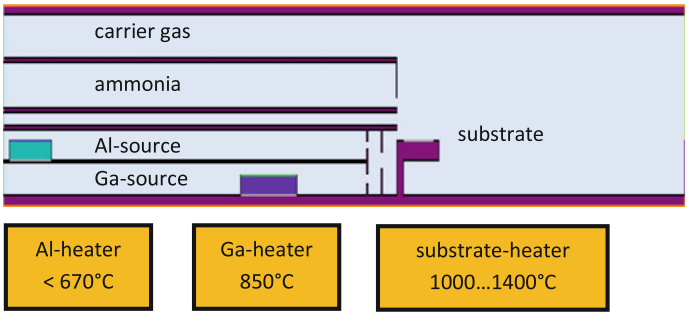


Fig. 3.5 Cross-sectional sketch of conventional horizontal HVPE reactor for the growth of AlGaN layers. Note, for the sake of depiction, vertical dimensions are stretched by a factor of 4

Practically, reactors similar to Fig. 3.5 are made from tubes which then contain metallic sources of high purity like gallium (≥6 N) and aluminum (≥5 N). Gaseous hydrogen chloride flows over the metals and the resulting metal halides have to be mixed before reacting with ammonia at the surface of the substrate. Reactor geometry, total pressure, reactant and carrier gas flows and their resulting partial pressures at the substrate surface, temperatures of different heaters, and time sequence of the process play a crucial role for the growth result. It has been shown by means of elementary thermodynamic treatment that the chemical processes can be described with a small number of reaction equations [64]. The most important processes for formation of metal halides are described as

$$\mathrm{Al(s)} + 3\mathrm{HCl(g)} \rightarrow \mathrm{AlCl_3(g)} + 3/2\mathrm{H_2(g)} \tag{3.1}$$

$$\mathrm{Ga(l)} + \mathrm{HCl(g)} \rightarrow \mathrm{GaCl(g)} + 1/2\mathrm{H_2(g)} \tag{3.2}$$

Growth of AlN and GaN in the AlGaN alloy can be described by

$$\mathrm{GaCl(g)} + \mathrm{NH_3(g)} \leftrightarrow \mathrm{GaN(s)} + \mathrm{HCl(g)} + \mathrm{H_2(g)} \tag{3.3}$$

$$\mathrm{AlCl_3(g)} + \mathrm{NH_3(g)} \leftrightarrow \mathrm{AlN(s)} + 3\mathrm{HCl(g)} \tag{3.4}$$

The findings lead already to a fundamental understanding of this growth process. The formation of metal halides is very efficient at elevated temperatures of around 750 °C or above for liquid gallium and at temperatures of 500 °C up to the melting point of about 670 °C for aluminum. This was shown experimentally for the formation of GaCl [65] or can be concluded from high equilibrium partial pressures of $AlCl_3$ compared to HCl above a solid Al source at 550 °C [66] as shown in Fig. 3.6 for experimental conditions according to Fig. 3.5. Formation of AlN by HVPE is in principle not restricted to the use of solid Al, but use of molten Al has the disadvantages of huge material stress on the crucible during re-hardening when cooled down and the dominant formation of AlCl at temperatures above 790 °C

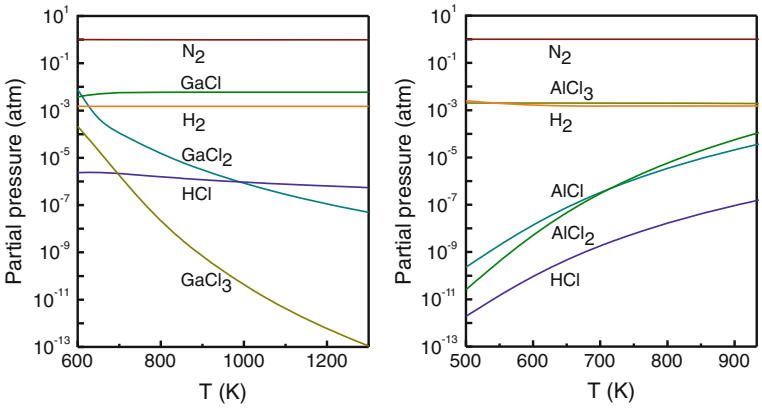


Fig. 3.6 Calculated equilibrium partial pressures above the Ga (*left*) and Al source (*right*) revealing GaCl and $AlCl_3$ as most prominent and thus determining reactants for HVPE of AlGaN (calculated after [67, 68])

which is more damaging to quartz than $AlCl_3$ [66]. Furthermore, from (3.3) and (3.4) and comparison of thermodynamic calculations and experimental data it was concluded that the growth processes of GaN and AlN are mass transport type II limited processes [64, 67, 68]. That means that the growth rate r_g is limited by diffusion through a boundary layer at the growth surface and can hence be described by the difference of incoming partial pressure of group III at the outer face of this boundary layer and the equilibrium partial pressure at the substrate surface ΔP_{III} and a proportionality factor which is called the mass transfer coefficient K_g.

$$r_g = K_g \Delta P_{III} \tag{3.5}$$

Although the thermodynamic description is usually performed in terms of equilibrium equations for convenience, this result for the driving force, which is the basis for the possible high growth rates, clearly proves that the HVPE process is in general neither at nor near thermodynamic equilibrium [69]. However, the ratio of reactants and reaction products can dramatically be changed by addition of HCl(g) or H_2(g) in the formation process of GaN according to (3.3) [65, 67] or by addition of HCl(g) in the AlN formation according to (3.4) [68]. Hence, addition of hydrogen into the carrier gas reduces Ga incorporation in the AlGaN alloy [64].

Unfortunately, the description given so far is not complete. Surface kinetic effects cause different growth or incorporation rates for different crystal orientations. The growth process is thus not strictly mass transport limited type II [70] and a more accurate description would require different mass transfer coefficients for different orientations. Such an anisotropic description then leads to kinetic Wulff plots [71]. Prediction of growth habit can be complex due to the parameter-dependent growth rates of GaN and AlN on different facets and additional geometrical effects which also requires taking into account temporal evolution [72].

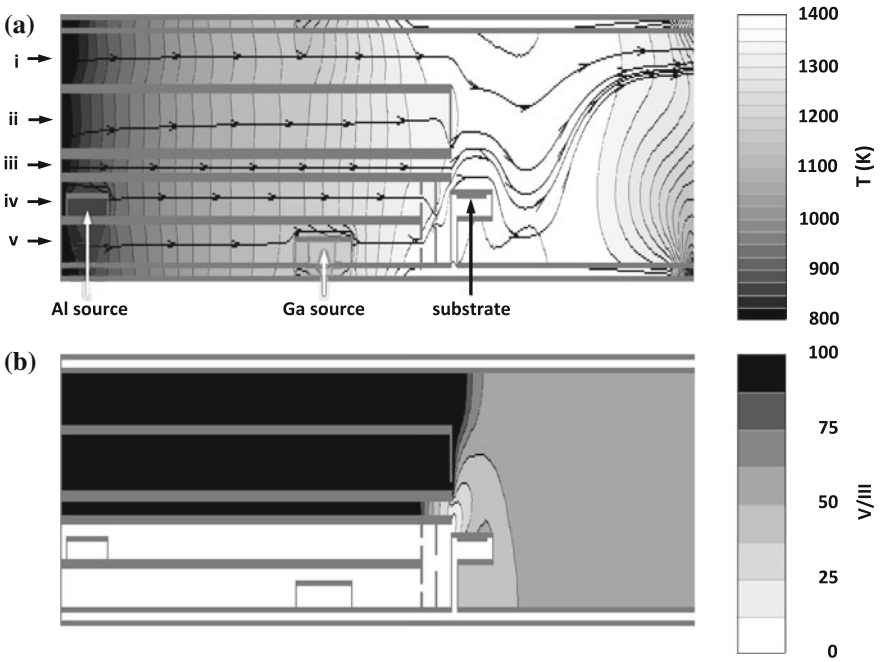


Fig. 3.7 Scheme of a horizontal HVPE reactor according to Fig. 3.5 with 2D-simulated distribution of temperature and flow pattern (**a**) and distribution of the ratio of group V to group III elements. P_{total} = 400 hPa with incoming fluxes at the *left side* from *top* to *bottom* as indicated in (**a**) *i* Q_{N_2} = 5 slm, *ii* Q_{NH_3} = 0.9 slm in Q_{N_2} = 0.9 slm, *iii* Q_{N_2} = 1 slm, *iv* Q_{HCl} over Al = 0.19 slm in Q_{N_2} = 0.71 slm, *v* Q_{HCl} over Ga = 0.05 slm in Q_{N_2} = 0.85 slm) (calculated with [76])

Such considerations open the possibility of a comprehensive numerical simulation of the growth process for an arbitrary reactor geometry including computation of fluid dynamics (CFD), heat transfer, mass transport and a quasi-thermodynamic model for heterogeneous reaction at surfaces. Simulation tools with a unique mass transfer coefficient have been developed and experimentally verified [73, 74]. 3D simulation has been successfully demonstrated [75] and 2D simulators with time evolution are available [76].

Assuming that the reactor of Fig. 3.5 would be continued to infinity perpendicular to the image plane, a 2D simulation using a virtual reactor can be performed. In Fig. 3.7a, temperature and flow patterns and in Fig. 3.7b, the distribution of the V/III ratio are shown for a typical parameter set used for AlGaN growth. Such simulation helps to optimize growth parameters and is necessary to understand the effects resulting from variations of these parameters.

There are some variants of AlGaN HVPE. Apart from HVPE of AlGaN [77] with mixed mono- and tri-metal halides (the latter also called THVPE [78, 79]) as group III reactants formed from separated source lines [53], there are also

approaches where MOVPE and HVPE are successively performed in a hybrid growth system, where the HVPE mode is used for thick buffer layers and the MOVPE mode for the active layer stack [80].

3.4.2 The Choice of Substrate

Native nitride substrates of satisfactory size are hardly available. Recently, HVPE growth of GaN on large area GaN substrates supplied by ammonothermal growth [81] and of AlN on large area AlN substrates [56] was successfully demonstrated. In these cases, the HVPE-grown layers are of high structural perfection since issues in heteroepitaxy like lattice bending do not play a role and homoepitaxy on a low-TDD substrate yields low-TDD layers with no need of dislocation annihilation by thickness [70, 82, 83]. In case of AlN HVPE-grown material is of higher purity than PVT AlN and has considerably less absorption. A combination of the high crystalline perfection of PVT bulk AlN and the high optical quality of HVPE AlN thus appears attractive for UV-C devices [56].

Despite these recent developments, epitaxial growth of AlGaN layers relies on foreign substrates. (0001) sapphire belongs to the most studied among the various starting substrates [84]. Challenges associated with heteroepitaxial growth are high dislocation densities and strain due to lattice mismatch, bending and cracking during cool-down due to different thermal expansion coefficients especially in case of sapphire, meltback etching of the substrate by solution of Ga in case of silicon substrates [85]. Additionally, often one wants to get rid of the foreign substrate after growth. However, once these drawbacks are overcome the heteroepitaxial HVPE technique offers fast and affordable scalability. Whatever is used as starting substrate, the aim of many research and development efforts is focused on achieving a competitive material quality and leverage the advantage of HVPE like purity and high growth rate for fabrication of buffer layers and substrates with reduced threading dislocation density (TDD). Thus, HVPE promises to be an excellent technique for fabrication of substrates for subsequent homoepitaxial growth of high-end device structures. Most of the aforementioned disadvantages have been solved for the binary GaN using sapphire [86], silicon [87], and other substrates [88], leaving productivity and a price reduction as remaining issues.

3.4.3 Selected Results from Growth of AlGaN Layers by HVPE

The following results were obtained during academic proof-of-concept studies by addition of an Al source to an existing HVPE reactor for GaN. Growth was performed in a quartz reactor similar to Fig. 3.5 on single-side polished, epiready

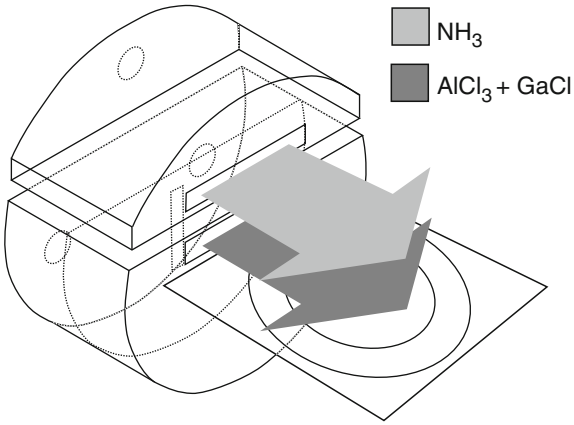


Fig. 3.8 Scheme of the mixing system for introducing the reactants through horizontal slits at the front side into the growth zone. Circular openings at the backside are inlets for GaCl and $AlCl_3$ into the lower chamber and ammonia into the *upper* chamber. The *lower* chamber contains a baffle for effective mixing of Ga and Al precursors. All parts are made of quartz

sapphire substrates with (0001) surface. The mixing of the group III source gases was realized in a mixing chamber as shown in Fig. 3.8. The lower slit acts as gas inlet for the group III mixture, the upper slit as inlet for ammonia, and in the open space between the chambers a separating purge flow is injected to avoid pre-reactions of group III sources with ammonia before reaching the substrate. The inlet geometry yields a laminar flow pattern over the substrate. In the experiment, the sample holder can be moved by gas foil rotation. AlGaN layers can be grown in the entire composition range and the composition can be adjusted by choice of the ratio of hydrogen chloride gas reacting with Ga and Al. Sapphire substrates of 16 × 16 mm^2 were overgrown with AlGaN layers of about 2 µm thickness. An optimized sequence of $AlCl_3$ pretreatment, nitridation, and growth of an AlN starting layer were used. Basic growth conditions with the above described reactor include a total pressure of 400 hPa, main carrier gas flow of 9 slm nitrogen, 900 sccm ammonia mixed with 900 sccm nitrogen, 50 sccm HCl mixed with 850 sccm nitrogen for reaction with liquid Ga at about 850 °C, 90 sccm HCl mixed with 710 sccm nitrogen for reaction with solid Al at about 520 °C, and a growth temperature of 1085 °C. The layer composition was determined by X-ray diffraction from the distance between the two positions of the reflections at (0006) of c-plane sapphire and at (0002) of the c-plane $Al_xGa_{1-x}N$ layers which were found to be completely relaxed. Growth rates were determined gravimetrically. Results are shown in Figs. 3.9, 3.10 and 3.11. In addition, results from variation of the ammonia flow and with hydrogen chloride gas flow over only one of the metal sources for growth of pure AlN or GaN are shown.

It is found that the growth rate of the $Al_xGa_{1-x}N$ layer does not depend remarkably on the ammonia flow (Fig. 3.9). The sum of the growth rates of the AlN layer and of the GaN layer exceeds the growth rate of the $Al_xGa_{1-x}N$ layer only

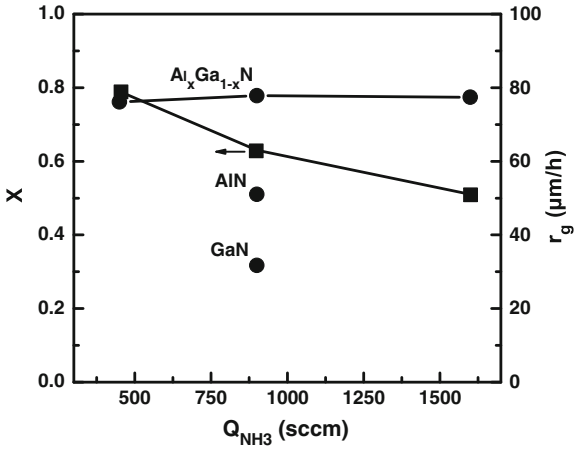


Fig. 3.9 Dependencies of growth rate r_g and composition x of $Al_xGa_{1-x}N$ layers grown with different ammonia flows Q_{NH_3} and with hydrogen chloride passing either only over the Al source or only over the Ga source

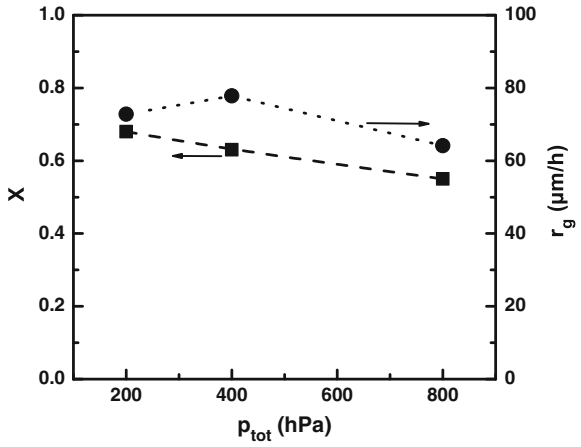


Fig. 3.10 Dependencies of growth rate r_g and composition x of $Al_xGa_{1-x}N$ layers grown at different reactor pressures

slightly and would result in a similar composition. However, the AlN fraction of the $Al_xGa_{1-x}N$ layer decreases with increasing ammonia flow. A slight reduction of the AlN fraction in the $Al_xGa_{1-x}N$ layer is also observed for a higher reactor pressure (Fig. 3.10). It is probable that under our conditions less $AlCl_3$ reaches the sample due to the lower gas velocities for higher reactor pressures. The nearly linear dependence of the growth rate of the $Al_xGa_{1-x}N$ layer from the group III supply in Fig. 3.11 is in agreement with (3.5). The growth of $Al_xGa_{1-x}N$ layers can be understood as superposition of the growth processes for AlN and GaN. According to (3.5) the composition of the $Al_xGa_{1-x}N$ layer should be constant as long as the ratio of the HCl flow rates across Al and Ga source is constant. It can be seen in

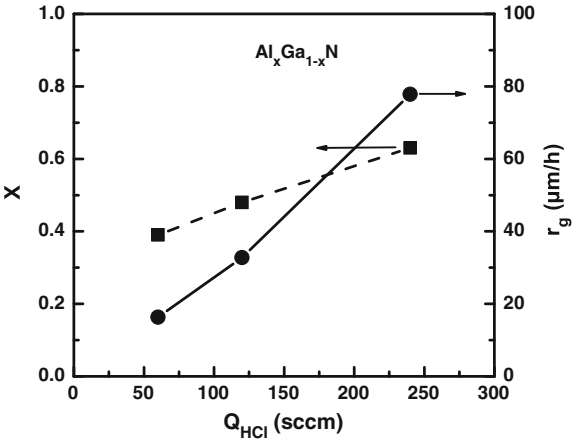


Fig. 3.11 Dependencies of growth rate r_g and composition x of $Al_xGa_{1-x}N$ layers grown with different flows of hydrogen chloride. The ratio 19:5 of flows over the Al source and the Ga source is constant and Q_{HCl} is the sum of the HCl flow rates

Fig. 3.11 that experimentally an increase of the Al content with increasing group III supply is observed. This tendency is similar to the V/III ratio effect in Fig. 3.9, i.e., in the case of a lower V/III the formation of AlN is favored against the formation of GaN. This observation is supposed to indicate the impact of homogenous pre-reactions between ammonia and Al-species in the gas phase.

3.4.3.1 Lateral Homogeneity

In case of a ternary compound, substrate rotation does not only affect the lateral uniformity of the growth rate but if the incorporation rates of the individual species are different it also alters the homogeneity of the composition. In order to investigate the influence of substrate rotation, AlGaN layers in a medium composition range with about 4 µm thickness were grown on quarter 2 inch c-plane sapphire samples without substrate rotation and with substrate rotation of about 30 rpm. The result for the stationary sample is shown in Fig. 3.12a. The AlN fraction drops by a factor 2 across the sample from the gas inlet downstream. The higher chemical reactivity of Al compared to Ga result in this faster depletion of Al than of Ga in the gas phase above the sample. The radial distribution of composition on the rotated sample is depicted in Fig. 3.12b with the rotation axis indicated in the inset. The AlN fraction determined by XRD across the sample is approximately constant at about $x = 0.5$. The lateral composition homogeneity across one inch diameter could be improved by rotation to ±2 % in our case (Fig. 3.12b). Taking into account the findings of the stationary sample, graded superlattices of more Al-rich and more Ga-rich layers can be expected and were indeed found by cross-sectional TEM in a sample in a distance of about 5 mm from its center (Fig. 3.13). Vertical compositional changes of up to ±15 % for a sample diameter of one inch with the period of the graded superlattice depending on radial distance and rotation speed were observed. The periodicity of the graded superlattice is 20 nm which fits well with

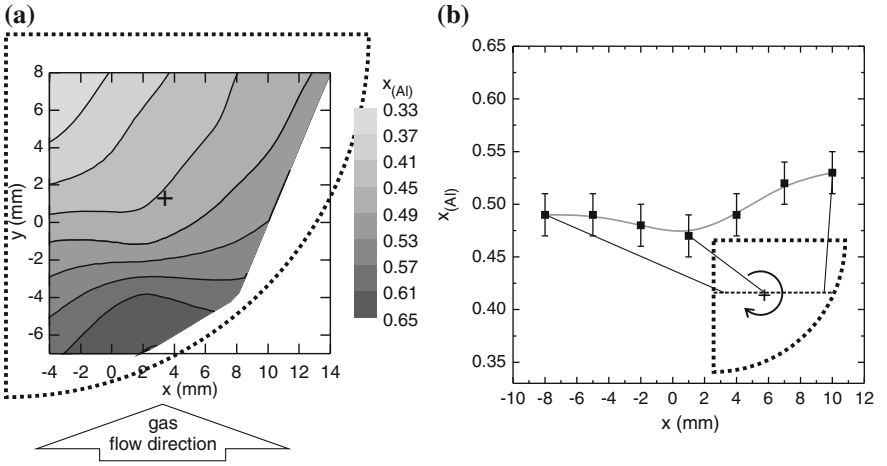


Fig. 3.12 Lateral homogeneity of the composition measured by XRD of 4 μm thick AlGaN layers grown on a stationary (**a**) and a rotating sample (**b**)

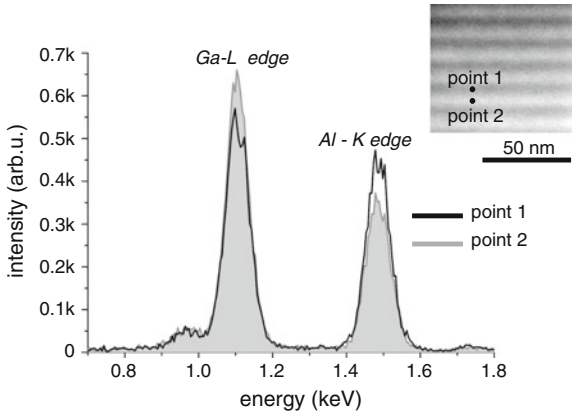


Fig. 3.13 TEM image and EDX spectra of an AlGaN layer which rotated during growth. Point 1 and point 2 indicates the position in cross-sectional TEM micrograph where the corresponding EDX spectra were recorded. The superlattice formed by the different depletion of the precursors is clearly visible

the growth rate of 36 μm h^{-1}. Thus, the different depletion behavior of the group III species leads in general to compositional inhomogeneity in geometrical setups with flow pattern parallel to the sample surface.

3.4.3.2 Use of MOVPE-Grown AlN/Sapphire Templates

Templates consisting of MOVPE-grown AlN-layers of 500 nm thickness on sapphire wafers were used to investigate formation of macroscopic defects in comparison. An optical Nomarski micrograph of a 600 nm thick $Al_{0.47}Ga_{0.53}N$ layer grown on such a template is shown in Fig. 3.14a. The surface is disturbed by polycrystalline material which appears darker when more of the facets are inclined to the surfaces. These crystallites were observed for a wide range of growth conditions. These surface defects consist mostly of three tilted crystallites which are typically arranged like triangles as shown in the SEM micrographs of Fig. 3.15a, b. The threefold symmetry of these crystallites suggests a relation to the threefold symmetry of the sapphire substrate (Fig. 3.15c). Possibly, these crystallites start to grow on n-plane sapphire facets [89, 90] which are offered unintentionally during the growth process. It was found that use of MOVPE-grown starting layers is not mandatory. As shown in Fig. 3.14b $Al_{0.47}Ga_{0.53}N$ directly grown on sapphire exhibits much less polycrystalline regions but local layer separation.

3.4.3.3 Direct Growth Start in HVPE

An optimized starting procedure in HVPE comprises (i) exposure of the surface to $AlCl_3$, (ii) exposure of the surface to NH_3, and (iii) growth of a thin AlN buffer layer. $AlCl_3$ pre-flow across the wafer for 1/4 h effectively reduced misaligned crystallites protruding from the surface of AlGaN layers. It is assumed that $AlCl_3$ changes the nucleation conditions on c-plane sapphire possibly by creating tiny nucleation centers similar to the effect of GaCl pretreatment prior to GaN growth on sapphire by HVPE [92].

Subsequent to the $AlCl_3$ pretreatment a nitridation step is performed. Figure 3.16 shows Nomarski micrographs of two $Al_{0.98}Ga_{0.02}N$ layers grown without and with NH_3 pre-flow across the sapphire substrate prior to growth. The surface of the layer

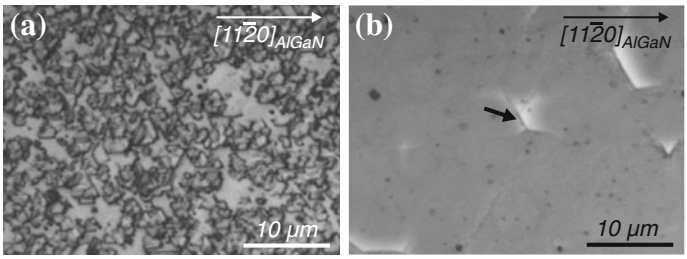


Fig. 3.14 Nomarski micrographs of 600 nm thick $Al_{0.47}Ga_{0.53}N$ layers grown by HVPE under identical conditions on MOVPE-grown AlN/sapphire template (**a**) and directly on sapphire (**b**). The surface is partly disturbed by polycrystalline materials (darker features). Local separation of the layer from the sapphire is indicated by brighter regions (*arrow*) in case of direct growth on sapphire

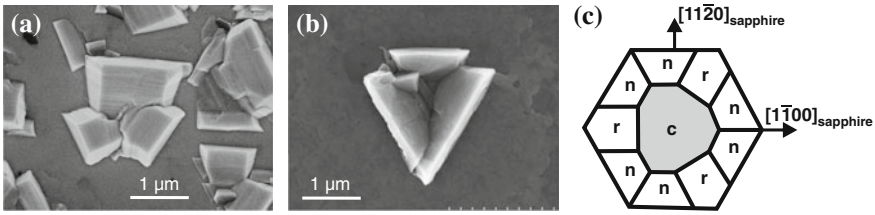


Fig. 3.15 SEM micrographs of typically oriented crystallites taken on the surface of the samples in Fig. 3.14a, b. Defects on the surfaces of the AlGaN layers grown on the AlN template (**a**) and directly on the sapphire wafer (**b**) look similar. On the template, the density of non-c-plane crystallites is much higher than on the sapphire wafer. Stable facets of sapphire with its threefold symmetry are depicted in the scheme (**c**) [91]

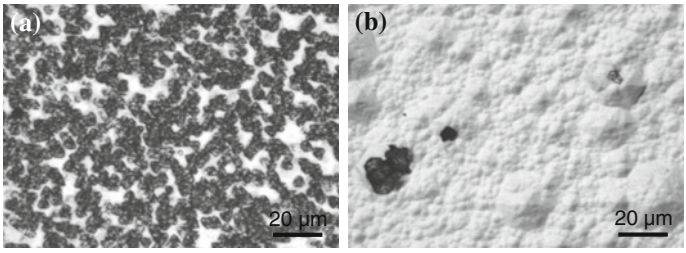


Fig. 3.16 Nomarski surface micrograph of $Al_{0.98}Ga_{0.02}N$ layers of 680 nm in thickness grown without nitridation (**a**) and of 2.5 µm in thickness grown with nitridation by NH_3 prior to growth (**b**)

grown without nitridation exhibits polycrystalline material already after a thickness of 680 nm (Fig. 3.16a). In contrast, the layer grown with nitridation is still mostly free of crystallites (Fig. 3.16b) for a layer thickness of 2.5 µm. X-ray omega-rocking curves measured for the symmetric 002 AlGaN and skew-symmetric 302 AlGaN reflections showed FWHM of 1129 and 3472 arcsec for the layer grown without nitridation and of 626 and 1454 arcsec for the layer grown with nitridation, respectively. Nitridation thus allows for thicker c-plane-oriented AlGaN layers with improved structural and morphological quality.

The surface of an $Al_{0.45}Ga_{0.55}N$ layer with a thickness of 5 µm is shown in the SEM micrograph of Fig. 3.17a revealing overgrown cracks. The CL-spectrum recorded by integration across the area of Fig. 3.17a is plotted in b. It exhibits two peaks that can be assigned to near band edge emissions of Al-rich (284 nm, $x = 0.47$) and of Ga-rich (343 nm, $x = 0.07$) regions. The 284 nm luminescence originates from almost the whole area as revealed by the CL topogram in Fig. 3.17c. The 343 nm luminescence is found along overgrown cracks and at some steps of surface hillocks (Fig. 3.17d). Reasons for this composition inhomogeneity at cracks and steps could be the higher mobility of Ga compared to Al on the growing surface and the higher Ga incorporation probability of Ga at non-c-plane facets. Consequently, composition inhomogeneity can easily be introduced in the ternary

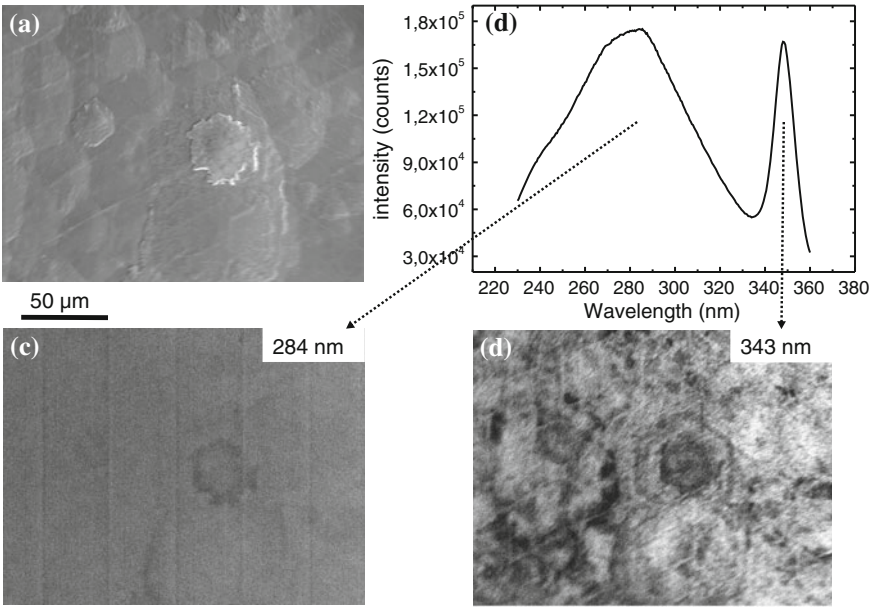


Fig. 3.17 SEM micrograph of $Al_{0.45}Ga_{0.55}N$ layer of 5 µm thickness grown on sapphire by the use of $AlCl_3$ and NH_3 pretreatment (**a**), corresponding CL-spectrum at 90 K (**b**), monochromatic CL image at 284 nm (**c**), and monochromatic CL image at 343 nm (**d**)

system already during the early stage of nucleation on the sapphire surface. With regard to the preparation of pseudosubstrates for subsequent growth of UV-LEDs, composition inhomogeneity is not desired since it may decrease the transmittance.

A thin AlN buffer layer was expected to facilitate the homogenous growth start and to reduce cracking by lowering tensile strain in the subsequently grown $Al_{0.45}Ga_{0.55}N$ layer. Therefore, the impact of an AlN buffer layer grown by HVPE after the $AlCl_3$ and NH_3 pretreatment was investigated. A 5 µm thick $Al_{0.45}Ga_{0.55}N$ layer was grown for comparison on a AlN buffer of 500 nm thickness (Fig. 3.18). The FWHM of omega-rocking curves decreased from 2310 to 1500 arcsec for the 002 $Al_{0.45}Ga_{0.55}N$ reflections and from 2200 to 1640 arcsec for the 302 AlGaN reflections indicating an enhanced crystal quality. The improvement could be due to a reduced crack density in the sample. In addition, XRD $\omega/2\theta$-scans did not show additional peaks caused by inhomogeneous Al-distribution as found in the sample grown without AlN buffer layer. The AlN buffer layer also did not decrease transmittance for wavelengths between 365 and the cutoff wavelength of the $Al_{0.45}Ga_{0.55}N$ layer at 290 nm. Although the material quality was improved by the AlN buffer layer, it unfortunately led to some new misaligned crystals disturbing the c-plane AlGaN surface as shown in Fig. 3.18. These misaligned crystallites were found to originate from micro-cracks in the AlN buffer layer. Thus, further means for strain release during the growth of AlGaN layers are needed to increase

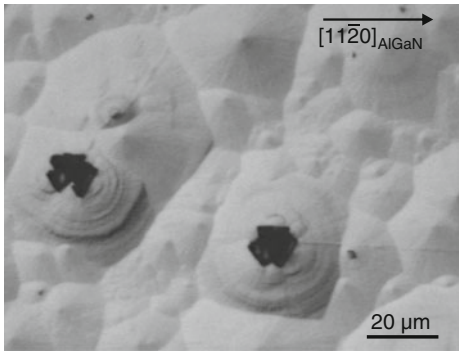


Fig. 3.18 Nomarski surface micrograph of HVPE-grown AlGaN layer of 5 µm thickness grown with an AlN buffer layer

the crack-free layer thickness and in consequence the crystalline quality by natural annihilation of dislocations with increasing thickness. A commonly applied method in heteroepitaxial growth consists in the reduction of contact area at the substrate-layer interface by epitaxial lateral overgrowth (ELOG) of masked areas or of voids using patterned sapphire substrates (PSS). Mask materials like SiO_2, SiN_x, TiN, and WSiN which are successfully used to grow freestanding GaN by HVPE [13] tend to be covered by polycrystalline AlGaN due to the low mobility of Al-species when Al chlorides were added to the process. Thus, masked ELOG was found unsuitable for AlGaN.

3.4.3.4 Growth on PSS with Trenches Along $[11\bar{2}0]_{sapphire}$

To achieve maskless ELOG, PSS with 4 µm deep trenches along $[11\bar{2}0]_{sapphire}$ were fabricated using a thick photoresist for high aspect ratios in ICP etching. Parameter studies on these PSS focused on the influence of an in situ AlN buffer layer, substrate offcut, input V/III ratio, total pressure, and growth temperature in HVPE growth of AlGaN layers of medium composition.

The growth from the bottom of the trenches was successfully suppressed due to the large depth and the already described AlN buffer layer was found to promote c-plane growth on the c-plane sapphire facets on top of the ridges. However, additional growth of $(11\bar{2}2)$ oriented AlGaN occurred from the trench sidewalls and generated a saw tooth like surface structure as shown in Fig. 3.19a.

The orientation of this semipolar grown material was deduced by XRD measurements under different sample rotations around a $[11\bar{2}0]_{sapphire}$ axis (Fig. 3.19b–d). The epitaxial relationship for the growth on the $(1\bar{1}00)$ oriented sapphire sidewalls was determined to:

$$(1\bar{1}00)_{sapphire} \parallel (11\bar{2}2)_{AlGaN} \text{ and } [11\bar{2}0]_{sapphire} \parallel [1\bar{1}00]_{AlGaN}$$

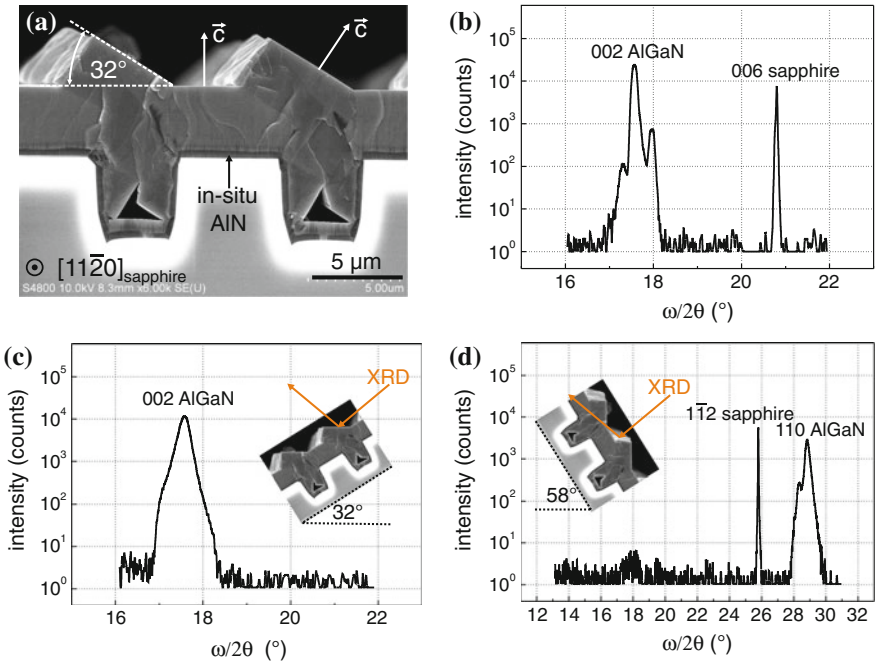


Fig. 3.19 $Al_{0.45}Ga_{0.55}N$ layer grown on PSS with a 500 nm thick AlN buffer layer. Semi-polar growth on the sidewalls and c-plane growth on the ridges cause formation of differently oriented AlGaN surfaces (**a**). XRD $\omega/2\theta$ measurements of the symmetric 002 AlGaN and 006 sapphire reflections to show c-plane AlGaN on c-plane sapphire (**b**), of 002 AlGaN reflection at a sample rotation around a $[11\bar{2}0]_{sapphire}$ aligned axis by 32° (**c**), and of $1\bar{1}0$ AlGaN reflection at a sample rotation around a $[11\bar{2}0]_{sapphire}$ aligned axis by 58° (**d**)

It was found that this semipolar growth occurred on just-oriented or PSS misoriented toward a-plane but not on PSS with miscut toward m-plane. It is assumed that additional surface steps parallel to the stripes accelerate the lateral growth rate of the c-plane-oriented material. The degree of substrate miscut toward the m-plane was varied in the range of 0.15°–4°. The best material quality of the c-plane-oriented closed AlGaN layers was determined by the shape of XRD ω-rocking curves for miscuts of 0.25° and 2°. C-plane sapphire with a miscut of 0.25° toward m-plane was used in the following to obtain c-plane-oriented AlGaN layers.

Parameter studies of the input V/III ratio and the reactor pressure resulted in homogeneously c-plane-oriented $Al_{0.45}Ga_{0.55}N$ layers on such striped PSS without differently oriented or polycrystalline defects on the surface. It was found that high V/III ratios (≈40), high total pressures (≈800 hPa) and high growth temperatures (≈1085 °C, limited by use of quartz components) favor the formation of flat AlGaN layers with homogeneous composition and hence allow for deposition of thick layers. $Al_{0.45}Ga_{0.55}N$, grown under optimized growth conditions on PSS, shows transparency in the UV region above a cutoff wavelength of 280 nm [93].

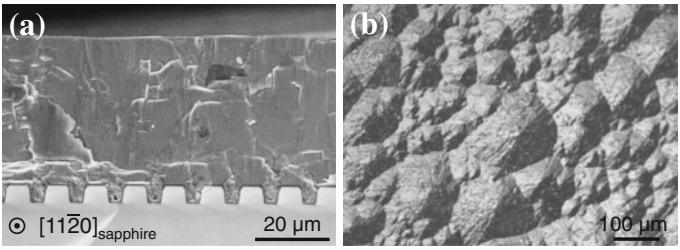


Fig. 3.20 Cross-sectional SEM image of 40 µm thick $Al_{0.45}Ga_{0.55}N$ on PSS (**a**), Nomarski micrograph of the surface (**b**) [94]

A cross sectional SEM image and a Nomarski micrograph of a 40 µm thick $Al_{0.45}Ga_{0.55}N$ layer are shown in Fig. 3.20. At thicknesses exceeding 5 µm, AlGaN layers suffer again from buried crack networks and partly overgrown surface cracks. One reason for cracking, especially perpendicular to the PSS stripe direction is an insufficient release of tensile strain in the direction of stripes during growth. It is expected that the observed anisotropic crack formation perpendicular to the stripes can be reduced by more isotropic patterns like hexagonally arranged columns or honeycombs and by narrower ridges. Another issue is the continuous repetition of cracking with increasing layer thickness. A reasonable explanation would be the continuous formation of tensile strain due to the interaction of silicon and dislocations which became only understood in recent years [95]. To avoid this either the dislocation density needs to be reduced to the low 1×10^7 cm^{-2} range or the Si incorporation needs to be suppressed to below 1×10^{17} cm^{-3}. The threading dislocation density at the surface of the 5 µm thick $Al_{0.45}Ga_{0.55}N$ layer on PSS was determined by TEM to be up to 8×10^9 cm^{-2} in regions above the ridges and up to 5×10^9 cm^{-2} in regions above the trenches. The Si incorporation determined by SIMS in our AlN layers is about 1×10^{19} cm^{-3}. This high Si incorporation most probably is introduced due to corrosion of quartz by $AlCl_n$.

3.4.3.5 Growth on PSS with Isotropic Motifs

Hexagonally arranged columns and honeycomb-like pattern were fabricated on c-plane sapphire wafers and used to determine the different AlGaN crystal orientations which grow on the sapphire sidewalls and to achieve coalesced AlGaN layers with reduced and more isotropic in-plane strain.

Depending on the NH_3 supply during nitridation, AlGaN growth on the sidewalls of the columns can change from mostly semipolar to mostly nonpolar with respect to the c-plane sapphire surface. ELOG on columns with 20 µm AlGaN layer thickness was performed (Fig. 3.21). However, a coalescence barrier is observed for vis-á-vis aligned m-plane AlGaN facets.

$Al_xGa_{1-x}N$ layers with different AlN fractions x of 0.3 (Fig. 3.22c), 0.5, or 0.7 and thicknesses in the range of 10 to 20 µm were grown on honeycomb patterned

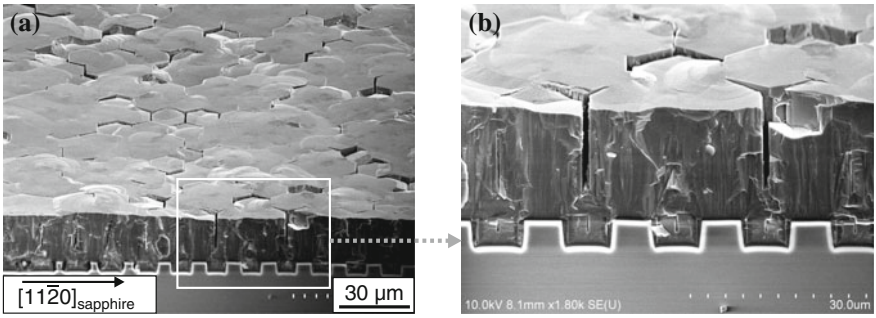


Fig. 3.21 Bird's-eye view on a cleavage plane and surface of 20 µm thick AlGaN layer grown on PSS with hexagonally arranged columns (**a**) and detail with higher magnification (**b**) showing that opposing m-facets do often not coalesce

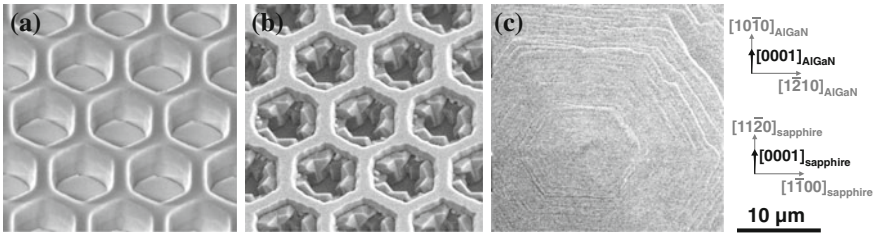


Fig. 3.22 Honeycomb pattern in sapphire (**a**), growth of $Al_{0.3}Ga_{0.7}N$ on ridges and at sidewalls after 15 min (**b**), and surface of completely coalesced $Al_{0.3}Ga_{0.7}N$ layer of 20 µm thickness after 120 min (**c**)

sapphire. In Fig. 3.22, different stages of the growth are depicted for layers with $x = 0.3$. Proper pretreatment and nitridation favor growth of crystallites (Fig. 3.22b) within the honeycombs which can easily be overgrown. This concept works independent of the alloy composition. The aforementioned formation of tensile strain by interaction of Si and dislocations leads to formation of cracks for thicknesses exceeding 10–20 µm. Grading of the AlGaN layer can partly compensate the tensile strain during growth and may allow for AlGaN layer structures which are thick enough for subsequent polishing and demonstration of devices.

With ongoing research and commercialization of HVPE for GaN and AlN further improvements of simulation, reactors, and processes can be expected. Therefore, the search for a more sustainable reactor material is a prerequisite to make further progress in the growth of AlGaN with high crystalline quality.

3.5 Summary

For the growth of UV-C LEDs, in principle bulk AlN substrates are available but still suffer from high price, small dimensions, and limited transparency. Thick AlN buffers with a sufficiently low defect density can be grown by MOVPE using techniques for defect elimination like ELOG. Such buffers with low defect density then allow for pseudomorphic growth of UV-C emitters. Layers structures for UV-B emitters require AlGaN base layers with low defect density since pseudomorphic growth on AlN is not possible for high Ga content. Such thick layers of AlGaN have been grown by HVPE on patterned substrates but currently the reduction of the defect density is still a challenge to be solved before ternary pseudosubstrates can make inroads into UV-B LED fabrication.

Acknowledgements The work on AlGaN was supported by the German Research Foundation in Project RI1224/1-1 and in the Collaborative Research Center 787 Semiconductor Nanophotonics.

References

1. F. Mehnke, T. Wernicke, H. Pingel, C. Kuhn, C. Reich, V. Kueller, A. Knauer, M. Lapeyrade, M. Weyers, M. Kneissl, Appl. Phys. Lett. **103**(21), 212109 (2013)
2. M. Kneissl, T. Kolbe, C. Chua, V. Kueller, N. Lobo, J. Stellmach, A. Knauer, H. Rodriguez, S. Einfeldt, Z. Yang, N.M. Johnson, M. Weyers, Semicond. Sci. Technol. **26**, 014036 (2011)
3. H. Hirayama, S. Fujikawa, N. Noguchi, J. Norimatsu, T. Takano, K. Tsubaki, N. Kamata, Phys. Status Solidi A **206**(6), 1176 (2009)
4. J. Rass, T. Kolbe, N. Lobo-Ploch, T. Wernicke, F. Mehnke, C. Kuhn, J. Enslin, M. Guttmann, C. Reich, A. Mogilatenko, J. Glaab, C. Stoelmacker, M. Lapeyrade, S. Einfeldt, M. Weyers, M. Kneissl, Proc. SPIE **9363**, 93631K (2015)
5. J.E. Ayers, *Heteroepitaxy of Semiconductors: Theory, Growth, and Characterization* (Taylor & Francis Group LCC, 2007)
6. O. Klein, J. Biskupek, K. Forghani, F. Scholz, U. Kaiser, J. Cryst. Growth **324**, 63 (2011)
7. C.J. Sun, P. Kung, A. Saxler, H. Ohsato, K. Haritos, M. Razeghi, J. Appl. Phys. **75**(8), 3964 (1994)
8. F.A. Ponce, J.S. Major, W.E. Plano, D.F. Welch, Appl. Phys. Lett. **65**(18), 2302 (1994)
9. H. Amano, N. Sawaki, I. Akasaki, Y. Toyoda, Appl. Phys. Lett. **48**(5), 353 (1986)
10. H. Amano, I. Akasaki, K. Hiramatsu, N. Koide, N. Sawaki, Thin Solid Films **163**, 415 (1988)
11. H. Hirayama, T. Yatabe, N. Noguchi, T. Ohashi, N. Kamata, Appl. Phys. Lett. **91**(7), 071901 (2007)
12. Ferdinand-Braun-Institut Berlin (unpublished)
13. Y. Hayashi, R.G. Banal, M. Funato, Y. Kawakami, J. Appl. Phys. **113**(18), 183523 (2013)
14. K. Ueno, J. Ohta, H. Fujioka, H. Fukuyama, Appl. Phys. Express **4**(1), 015501 (2011)
15. K. Kawaguchi, A. Kuramata, Jpn. J. Appl. Phys. **44**(11L), L1400 (2005)
16. O. Reentilä, F. Brunner, A. Knauer, A. Mogilatenko, W. Neumann, H. Protzmann, M. Heuken, M. Kneissl, M. Weyers, G. Tränkle, J. Cryst. Growth **310**(23), 4932 (2008)
17. H. Li, T.C. Sadler, P.J. Parbrook, J. Cryst. Growth **383**, 72 (2013)
18. Q.S. Paduano, D.W. Weyburne, J. Jasinski, Z. Liliental-Weber, J. Cryst. Growth **261**, 259 (2004)
19. V. Kueller, A. Knauer, F. Brunner, A. Mogilatenko, M. Kneissl, M. Weyers, Phys. Status Solidi C **9**, 496 (2012)

20. A. Knauer, F. Brunner, T. Kolbe, V. Kueller, H. Rodrigues, S. Einfeldt, M. Weyers, Kneissl. Proc. SPIE **7231**, 72310G (2009)
21. N.A. Fleck, M.F. Ashby, J.W. Hutchinson, Scripta Mater. **48**, 179 (2003)
22. M. Iwaya, S. Terao, T. Sano, S. Takanami, T. Ukai, R. Nakamura, S. Kamiyama, H. Amano, I. Akasaki, Phys. Status Solidi A **188**(1), 117 (2001)
23. H. Amano, K. Nagamatsu, K. Takeda, T. Mori, H. Tsuzuki, M. Iwaya, S. Kamiyama, I. Akasaki, Proc. SPIE **7216**, 72161B (2009)
24. M.A. Moram, M.E. Vickers, Rep. Progr. Phys. **72**, 036502 (2009)
25. T. Wunderer, C.L. Chua, Z. Yang, J.E. Northrup, N.M. Johnson, G.A. Garrett, H. Shen, M. Wraback, Appl. Phys. Express **4**(9), 092101 (2011)
26. P. Vennéguès, B. Beaumont, S. Haffouz, M. Vaille, P. Gibart, J. Cryst. Growth **187**(2), 167 (1998)
27. K. Forghani, M. Klein, F. Lipski, S. Schwaiger, J. Hertkorn, R.A.R. Leute, F. Scholz, B. Feneberg, M. Neuschl, K. Thonke, O. Klein, U. Kaiser, R. Gutt, T. Passow, J. Cryst. Growth **315**, 216 (2011)
28. A. Krost, J. Bläsing, F. Schulze, O. Schön, A. Alam, M. Heuken, J. Cryst. Growth **221**, 251 (2000)
29. M. Iwaya, S. Terao, N. Hayashi, T. Kashima, H. Amano, I. Akasaki, Appl. Surf. Sci. **159160**, 405 (2000)
30. H. Tsuzuki, F. Mori, K. Takeda, M. Iwaya, S. Kamiyama, H. Amano, I. Akasaki, H. Yoshida, M. Kuwabara, Y. Yamashita, H. Kan, J. Cryst. Growth **311**, 2860 (2009)
31. A.A. Allerman, M.H. Crawford, S.R. Lee, B.G. Clark, J. Cryst. Growth **388**, 76 (2014)
32. K. Iida, T. Kawashima, M. Iwaya, S. Kamiyama, H. Amano, I. Akasaki, A. Bandoh, J. Cryst. Growth **298**, 265 (2006)
33. H.M. Wang, J.P. Zhang, C.Q. Chen, Q. Fareed, J.W. Yang, M.A. Khan, Appl. Phys. Lett. **81** (4), 604 (2002)
34. J.R. Grandusky, J. Chen, S.R. Gibb, M.C. Mendrick, C.G. Moe, L. Rodak, G.A. Garrett, M. Wraback, L.J. Schowalter, Appl. Phys. Express **6**(3), 032101 (2013)
35. H. Hirayama, T. Yatabe, N. Noguchi, T. Ohashi, N. Kamata, Phys. Status Solidi C **5**(9), 2969 (2008)
36. K. Nakano, M. Imura, G. Narita, T. Kitano, Y. Hirose, N. Fujimoto, N. Okada, T. Kawashima, K. Iida, K. Balakrishnan, M. Tsuda, M. Iwaya, S. Kamiyama, H. Amano, I. Akasaki, Phys. Status Solidi A **203**(7), 1632 (2006)
37. H. Hirayama, S. Fujikawa, J. Norimatsu, T. Takano, K. Tsubaki, N. Kamata, Phys. Status Solidi C **6**(S2), S356 (2009)
38. R. Dalmau, B. Moody, R. Schlesser, S. Mita, J. Xie, M. Feneberg, B. Neuschl, K. Thonke, R. Collazo, A. Rice, J. Tweedie, Z. Sitar, J. Electrochem. Soc. **158**(5), H530 (2011)
39. V. Kueller, A. Knauer, F. Brunner, U. Zeimer, H. Rodriguez, M. Kneissl, M. Weyers, J. Cryst. Growth **315**(1), 200 (2011)
40. M. Conroy, V.Z. Zubialevich, H. Li, N. Petkov, J.D. Holmes, P.J. Parbrook, J. Mater. Chem. C **3**, 431 (2015)
41. V. Kueller, A. Knauer, U. Zeimer, M. Kneissl, M. Weyers, J. Cryst. Growth **368**, 83 (2013)
42. A. Mogilatenko, V. Küller, A. Knauer, J. Jeschke, U. Zeimer, M. Weyers, G. Tränkle, J. Cryst. Growth **402**, 222 (2014)
43. V. Kueller, A. Knauer, C. Reich, A. Mogilatenko, M. Weyers, J. Stellmach, T. Wernicke, M. Kneissl, Z. Yang, C. Chua, N. Johnson, IEEE **24**(18), 1603 (2012)
44. G. Nishio, S. Yang, H. Miyake, K. Hiramatsu, J. Cryst. Growth **370**, 74 (2013)
45. U. Zeimer, V. Kueller, A. Knauer, A. Mogilatenko, M. Weyers, M. Kneissl, J. Cryst. Growth **377**, 32 (2013)
46. A. Knauer, V. Kueller, U. Zeimer, M. Weyers, C. Reich, M. Kneissl, Phys. Status Solidi A **210**(3), 451 (2013)
47. V. Adivarahan, Q. Fareed, S. Srivastava, T. Katona, M. Gaevski, Khan, Jap. J. Appl. Phys. **46**, L537 (2007)

48. J. Han, J. Figiel, M. Crawford, M. Banas, M. Bartram, R. Biefeld, Y. Song, A. Nurmikko, J. Cryst. Growth **195**(14), 291 (1998)
49. G. Jacopin, L. Rigutti, S. Bellei, P. Lavenus, F.H. Julien, A.V. Davydov, D. Tsvetkov, K.A. Bertness, N.A. Sanford, J.B. Schlager, M. Tchernycheva, Nanotechnology **23**(32), 325701 (2012)
50. A. Usikov, V. Soukhoveev, L. Shapovalov, A. Syrkin, V. Ivantsov, B. Scanlan, A. Nikiforov, A. Strittmatter, N. Johnson, J.G. Zheng, P. Spiberg, H. El-Ghoroury, Phys. Status Solidi A **207** (6), 1295 (2010)
51. S. Kurin, A. Antipov, I. Barash, A. Roenkov, A. Usikov, H. Helava, V. Ratnikov, N. Shmidt, A. Sakharov, S. Tarasov, E. Menkovich, I. Lamkin, B. Papchenko, Y. Makarov, Phys. Status Solidi C **11**(3–4), 813 (2014)
52. G.S. Lee, H. Jeon, S.G. Jung, S.M. Bae, M.J. Shin, K.H. Kim, S.N. Yi, M. Yang, H.S. Ahn, Y. M. Yu, S.W. Kim, H.J. Ha, N. Sawaki, Jpn. J. Appl. Phys. **51**(1S), 01AG06 (2012)
53. S.M. Bae, H. Jeon, S.G. Lee, G.S. Jung, K.H. Kim, S.N. Yi, M. Yang, H.S. Ahn, Y.M. Yu, S. W. Kim, S.H. Cheon, H.J. Ha, N. Sawaki, J. Ceram. Proc. Res. **13**, s75 (2012)
54. E. Richter, S. Fleischmann, D. Goran, S. Hagedorn, W. John, A. Mogilatenko, D. Prasai, U. Zeimer, M. Weyers, G. Tränkle, J. Electronic Mater. **49**, 814 (2014)
55. H.C. Chen, I. Ahmad, B. Zhang, A. Coleman, M. Sultana, V. Adivarahan, A. Khan, Phys. Status Solidi C **11**(3–4), 408 (2014)
56. T. Kinoshita, T. Obata, T. Nagashima, H. Yanagi, B. Moody, S. Mita, S. Ichiro Inoue, Y. Kumagai, A. Koukitu, Z. Sitar, Appl. Phys. Express **6**(9), 092103 (2013)
57. T. Baker, A. Mayo, Z. Veisi, P. Lu, J. Schmitt, Phys. Status Solidi C **11**(3–4), 373 (2014)
58. T. Nagashima, A. Hakomori, T. Shimoda, K. Hironaka, Y. Kubota, T. Kinoshita, R. Yamamoto, K. Takada, Y. Kumagai, A. Koukitu, H. Yanagi, J. Cryst. Growth **350**(1), 75 (2012)
59. T. Nomura, K. Okumura, H. Miyake, K. Hiramatsu, O. Eryu, Y. Yamada, J. Cryst. Growth **350**(1), 69 (2012)
60. Y. Kumagai, Y. Enatsu, M. Ishizuki, Y. Kubota, J. Tajima, T. Nagashima, H. Murakami, K. Takada, A. Koukitu, J. Cryst. Growth **312**(18), 2530 (2010)
61. H. Helava, T. Chemekova, O. Avdeev, E. Mokhov, S. Nagalyuk, Y. Makarov, M. Ramm, Phys. Status Solidi C **7**(7–8), 2115 (2010)
62. H.P. Maruska, J.J. Tietjen, Appl. Phys. Lett. **15**, 327 (1969)
63. F. Bugge, A.N. Efimov, I.G. Pichugin, A.M. Tsaregorodtsev, M.A. Chernov, Cryst. Res. Technol. **22**(1), 65 (1987)
64. A. Koukitu, J. Kikuchi, Y. Kangawa, Y. Kumagai, J. Cryst. Growth **281**, 47 (2005)
65. W. Seifert, G. Fitzl, E. Butter, J. Cryst. Growth **52**, 257 (1981)
66. Y. Kumagai, T. Yamane, T. Miyaji, H. Murakami, Y. Kangawa, A. Koukitu, Phys. Status Solidi C **0**, 2498 (2003)
67. A. Koukitu, S. Hama, T. Taki, H. Seki, Jpn. J. Appl. Phys. **37**, 762 (1998)
68. Y. Kumagai, K. Takemoto, J. Kikuchi, T. Hasegawa, H. Murakami, A. Koukitu, Phys. Status Solidi B **243**, 1431 (2006)
69. D.W. Shaw, *Crystal Growth* (Plenum, New York, 1978)
70. E. Richter, U. Zeimer, S. Hagedorn, M. Wagner, F. Brunner, M. Weyers, G. TrÃ¤nkle. J. Cryst. Growth **312**(18), 2537 (2010)
71. B. Leung, Q. Sun, C.D. Yerino, J. Han, M.E. Coltrin, Semicond. Sci. Technol. **27**, 024005 (2012)
72. D. Du, D.J. Srolovitz, M.E. Coltrin, C.C. Mitchell, Phys. Rev. Lett. **95**, 155503 (2005)
73. A. Segal, A.V. Kondratyev, S.Y. Karpov, D. Martin, V. Wagner, M. Ilegems, J. Cryst. Growth **270**, 384 (2004)
74. A.S. Segal, D.S. Bazarevskiy, M.V. Bogdanov, E.V. Yakovlev, Phys. Status Solidi C **6**(S2), S329 (2009)
75. E. Richter, C. Hennig, M. Weyers, F. Habel, J.D. Tsay, W.Y. Liu, P. Brückner, F. Scholz, Y. Makarov, A. Segal, J. Kaeppeler, J. Cryst. Growth **277**, 6 (2005)
76. http://www.str-soft.com/products/Virtual_Reactor/hepigans/ (2014)

77. Y. Kumagai, T. Yamane, A. Koukitu, J. Cryst. Growth **281**, 62 (2005)
78. T. Yamane, K. Hanaoka, H. Murakami, Y. Kumagai, A. Koukitu, Phys. Status Solidi C **8**, 1471 (2011)
79. K. Eriguchi, T. Hiratsuka, H. Murakami, Y. Kumagai, A. Koukitu, J. Cryst. Growth **310**(17), 4016 (2008)
80. G.S. Solomon, D.J. Miller, M. Ramsteiner, A. Trampert, O. Brandt, K.H. Ploog, Appl. Phys. Lett. **87**(18), 181912 (2005)
81. T. Sochacki, Z. Bryan, M. Amilusik, M. Bobea, M. Fijalkowski, I. Bryan, B. Lucznik, R. Collazo, J.L. Weyher, R. Kucharski, I. Grzegory, M. Bockowski, Z. Sitar, J. Cryst. Growth **394**, 55 (2014)
82. S. Mathis, A. Romanov, L. Chen, G. Beltz, W. Pompe, J. Speck, Phys. Status Solidi A **179**(1), 125 (2000)
83. Y. Kumagai, T. Nagashima, H. Murakami, K. Takada, A. Koukitu, Phys. Status Solidi C **5**(6), 1512 (2008)
84. O. Kovalenkov, V. Soukhoveev, V. Ivantsov, A. Usikov, V. Dmitriev, J. Cryst. Growth **281**, 87 (2005)
85. A. Krost, A. Dadgar, Mater. Sci. Eng. B **93**, 77 (2002)
86. T. Yoshida, Y. Oshima, T. Eri, K. Ikeda, S. Yamamoto, K. Watanabe, M. Shibata, T. Mishima, J. Cryst. Growth **310**(1), 5 (2008)
87. M. Lee, D. Mikulik, J. Kim, Y. Tak, J. Kim, M. Shim, Y. Park, U. Chung, E. Yoon, S. Park, Appl. Phys. Express **6**(12), 125502 (2013)
88. K. Motoki, T. Okahisa, R. Hirota, S. Nakahata, K. Uematsu, N. Matsumoto, J. Cryst. Growth **305**(2), 377 (2007)
89. M. Takami, A. Kurisu, Y. Abe, N. Okada, K. Tadatomo, Phys. Status Solidi C **8**, 2101 (2011)
90. N. Goriki, H. Miyake, K. Hiramatsu, T. Akiyama, T. Ito, O. Eryu, Jpn. J. Appl. Phys. **52**, 08JB31 (2013)
91. O. Ambacher, J. Phys. D Appl. Phys. **31**, 2653 (1998)
92. K. Naniwae, S. Itoh, H. Amano, K. Itoh, K. Hiramatsu, I. Akasaki, J. Cryst. Growth **99**, 381 (1990)
93. S. Hagedorn, E. Richter, U. Zeimer, D. Prasai, W. John, M. Weyers, J. Cryst. Growth **353**, 129 (2012)
94. S. Hagedorn, E. Richter, U. Zeimer, M. Weyers, Phys. Status Solidi C **10**, 355 (2013)
95. D.M. Follstaedt, S.R. Lee, A.A. Allerman, J.A. Floro, J. Appl. Phys. **105**, 083507 (2009)

Chapter 4
Growth Techniques of AlN/AlGaN and Development of High-Efficiency Deep-Ultraviolet Light-Emitting Diodes

Hideki Hirayama

Abstract Recent advances in the performance of AlGaN-based deep-ultraviolet (DUV) light-emitting diodes (LEDs) and the development of crystal growth techniques for wide-bandgap AlN and AlGaN materials are discussed. DUV LEDs in the spectral range between 222 and 351 nm have been demonstrated. Significant increases in the internal quantum efficiency (IQE) of AlGaN quantum wells (QWs) have been achieved by growth on low-threading dislocation-density (TDD) AlN obtained by ammonia pulsed-flow multilayer growth. Electron Injection efficiency (EIE) in DUV LEDs was significantly improved by introducing a multi-quantum barrier (MQB) and light-extraction efficiency (LEE) was enhanced by developing transparent p-AlGaN contact layers. The maximum external quantum efficiency (EQE) obtained was 7 % for a 279 nm DUV LED. EQEs in the double-digit ranges are anticipated in the near future by further improving LEE, e.g., by utilizing transparent contact layers and pillar array buffer layers.

4.1 Introduction

In this chapter, growth techniques of AlN/AlGaN semiconductors and recent advances in AlGaN-based deep-ultraviolet (DUV) light-emitting diodes (LEDs) are reviewed. 220–350 nm-band DUV LEDs have been realized by developing crystal growth techniques for wide-bandgap AlN and AlGaN semiconductors. Significant increases in internal quantum efficiency (IQE) have been achieved for AlGaN DUV emissions by developing low-threading-dislocation-density (TDD) AlN buffer layers grown on sapphire substrates. The electron injection efficiency (EIE) of the LEDs was also significantly increased by introducing a multi-quantum barrier (MQB). We also discuss light extraction efficiency (LEE), which is the most important parameter for achieving high-efficiency DUV LEDs. We succeeded in

H. Hirayama (✉)
RIKEN, Quantum Optodevice Laboratory, 2-1 Hirosawa, Wako, Saitama 351-0198, Japan
e-mail: hirayama@riken.jp

© Springer International Publishing Switzerland 2016

M. Kneissl and J. Rass (eds.), *III-Nitride Ultraviolet Emitters*,
Springer Series in Materials Science 227, DOI 10.1007/978-3-319-24100-5_4

improving LEE by developing a transparent p-AlGaN contact layer. The maximum external quantum efficiency (EQE) obtained was 7 % for a 279 nm DUV LED. EQE could be increased by up to several tens of percent through the improvement of LEE by utilizing transparent contact layers and photonic nanostructures.

In Sect. 4.2, the research background including device applications, history and the current status of DUV LEDs are described. We will describe the development of crystal growth techniques for obtaining high-quality AlN and AlGaN crystals in Sect. 4.3. We will describe the achievement of high IQE for AlGaN DUV emission and the realization of DUV LEDs in Sects. 4.4 and 4.5, respectively. We will go on to discuss several issues for increasing the efficiencies of DUV LEDs, i.e., EIE and LEE, in Sect. 4.6. Finally, the future prospects of DUV LEDs are discussed in Sect. 4.7.

4.2 Research Background of DUV LEDs

The development of semiconductor light sources operating in the DUV region, such as DUV LEDs and laser diodes (LDs), is quite an important subject because they are required for a wide variety of applications. Figures 4.1 and 4.2 summarize the image of sterilization application and wide potential application fields of high-efficiency DUV LEDs and LDs, respectively. DUV LEDs and LDs with emission wavelengths in the range of 230–350 nm are expected to be used in applications such as sterilization, water purification, medicine, and biochemistry, light sources for high density optical recording, white light illumination, fluorescence analytical systems, and related information sensing fields. They are also very important for air purification equipment and for zero-emission automobiles [1, 2].



Fig. 4.1 Image of sterilization applications of deep-ultraviolet (DUV) LEDs

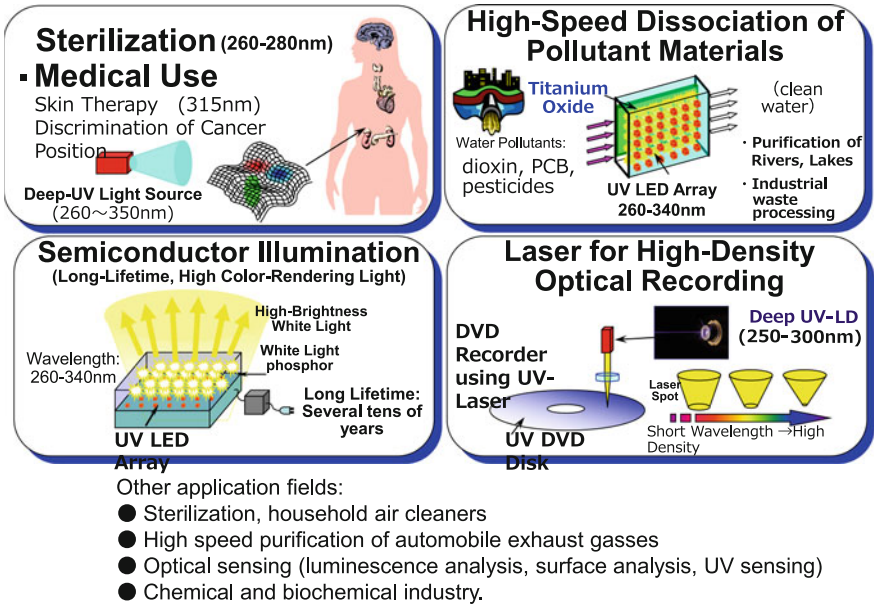


Fig. 4.2 Potential applications of DUV LEDs and LDs

Figure 4.3 shows the classification of UV light and the wavelength range achieved by AlGaN DUV LEDs. For applications involving sterilization or water purification with direct UV-light treatment, UVC light with the wavelength range between 260–280 nm is most suitable. For the UV purification process using a titanium-oxide (TiO_2) catalyst, the wavelength range between 320–380 nm is also

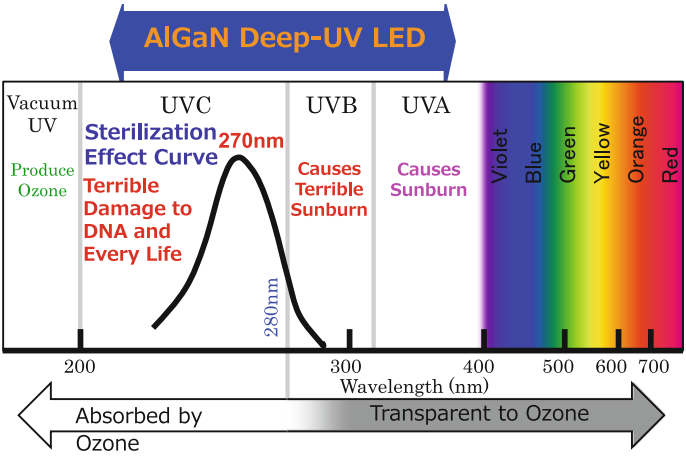


Fig. 4.3 Classification of UV light and the wavelength range achieved by AlGaN DUV LEDs

useful. For application to white LED illumination produced by a mixture of RGB phosphors excited by a UV-LED, wavelengths around 340 nm (UVA) are considered to be most suitable, taking into account both the efficient absorption by phosphors (<350 nm) and the high-efficiency operation wavelength range of AlGaN UV-LEDs. The wavelength range achieved by AlGaN LED covers from UVA and UVC as shown in Fig. 4.3.

Because of their wide direct transition energy range in the UV, covering the region between 6.2 eV (AlN) and 3.4 eV, AlGaN and quaternary InAlGaN are attracting considerable attention as candidate materials for the realization of DUV LEDs and LDs [2]. Figure 4.4 shows the relationship between the direct transition bandgap energy and the lattice constant of the wurtzite (WZ) InAlGaN material system and the lasing wavelengths of various gas lasers. The main advantages of using AlGaN or InAlGaN for DUV light sources are (1) the possibility of obtaining high-efficiency optical emission from quantum wells (QWs), (2) the possibility of producing both p- and n-type semiconductors in the wide-bandgap spectral region, (3) their physical properties, i.e., nitrides are mechanically hard and the devices

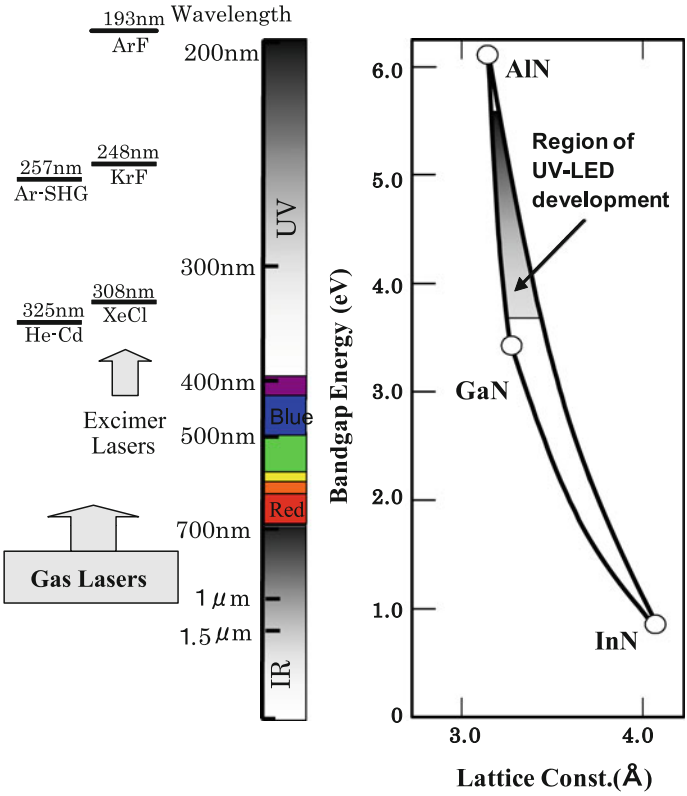


Fig. 4.4 Relationship between the direct transition bandgap energy and the lattice constant of the wurtzite (WZ) InAlGaN material system and the lasing wavelengths of various gas lasers

have long life-times, and (4) the fact that the materials are free from harmful arsenic, mercury and lead [2].

Research into AlGaN-based UV LEDs for wavelengths shorter than 360 nm was initiated by several research groups between 1996 and 1999 [3–5]. In the US, the effort directed at DUV light sources was driven by DARPA's Semiconductor Ultraviolet Optical Sources (SUVOS) program. A group at the University of South Carolina reported the first 250 280 nm AlGaN-based DUV LEDs between 2002 and 2006 [6–8]. A group at NTT reported the shortest wavelength (210 nm) LED using an AlN emitting layer in 2006 [9]. We started research into AlGaN-based DUV LEDs in 1997, and reported the first efficient DUV (230 nm) photoluminescence (PL) from AlGaN/AlN QWs [10], and a 333 nm AlGaN-QW UV LED on SiC in 1999 [4]. We have also developed high-efficiency UV LEDs using In-incorporation effects into AlGaN [2, 11, 12]. We have demonstrated several mW cw operation from 340 350 nm InAlGaN-QW UV LEDs on both GaN single-crystal substrates [13] and sapphire substrates [14].

Figure 4.5 shows the current status of the external quantum efficiency (EQE) of nitride UV LEDs, especially for UVA and UVC, as measured at room temperature (RT). The development of 280 nm-band AlGaN DUV LEDs to achieve high-efficiency and high-power operation has become extremely competitive recently, because they are expected to have a huge market for sterilization applications. We developed a growth method for low-threading-dislocation-density (TDD) AlN templates on sapphire substrates in 2007 [15], and achieved high IQE (>60 %) for AlGaN and quaternary InAlGaN QWs in the DUV region [16, 17]. We also achieved high electron injection efficiency (EIE) by introducing a multi-quantum barrier (MQB) design as an electron-blocking layer (EBL) [18], and demonstrated AlGaN and InAlGaN-based UV LEDs with a wide emission range (222 351 nm) [17–21]. We have also improved the light extraction efficiency (LEE) of DUV LED by developing a transparent p-AlGaN contact layer and a highly reflective p-type electrode [22, 23], and have recently achieved an external quantum efficiency (EQE) of 7 % [24]. RIKEN and Panasonic have started to

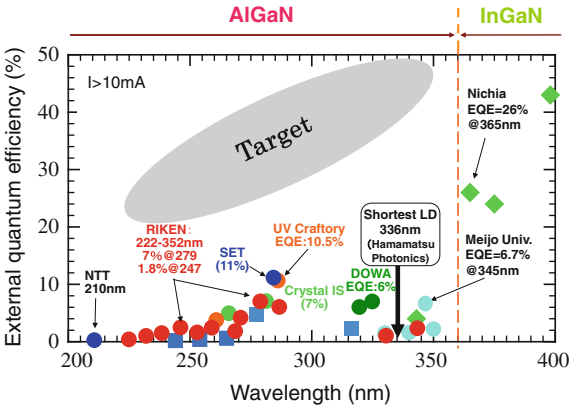


Fig. 4.5 Current status of the external quantum efficiency (EQE) of nitride UV LEDs, especially for UVA and UVC, measured at room temperature

provide commercially available DUV LED modules for sterilization use (270 nm, 10 mW LED module with lifetime longer than 10,000 h, EQE of 2 3 %) [25, 26].

The recent progress in high-efficiency DUV LEDs with wavelength between 260 and 300 nm developed by several companies is summarized in Table 4.1. sensor electronic technology (SET) has developed commercially valuable UV LEDs with wavelengths ranging between 240 and 360 nm [27–29], and they have reported a maximum EQE of 11 % for 278 nm LED [29]. Crystal IS and Tokuyama have developed DUV LED on single-crystal AlN substrates fabricated by a sublimation method [30, 31] and hydride vapor phase epitaxy (HVPE) [32, 33], respectively, and have reported 5–7 % EQE. Also, UV Craftory, Nitek, and Nichia have developed high-efficiency DUV LEDs [34–37]. UV Craftory has reported record high EQE of 14.3 % for a DUV LED, though it was obtained at very low injection current [27]. The shortest wavelength achieved for a UV-LD is 336 nm [38], which was achieved by Hamamatsu Photonics.

The next targets in UV device research are to develop EQEs of several tens of percent for 220 350 nm LEDs and to achieve 250–330 nm LDs. However, the realization of high EQE UV LEDs with wavelengths below 360 nm is still challenging owing to some major problems. The sudden drop in efficiency of UV-LEDs below 360 nm is mainly due to the following three factors:

Table 4.1 Recent progress of high-efficiency DUV LEDs with wavelength between 260 and 300 nm developed by several companies

Group	Year	References	Structures and techniques	Maximum EQE (%)	Wavelength (nm)
UV craftory	2014	[37]	Sapphire/AlN/AlGaN-QW (encapsulated)	14.3 at 2 mA	280–300
				10.5 at 20 mA	
Sensor electric technology	2012	[29]	Sapphire/AlN/AlGaN-QW (encapsulated) using p-AlGaN contact layer	11 at 10 mA	278
RIKEN	2014	[24]	Sapphire/AlN/AlGaN-QW using highly transparent p-AlGaN contact layer	7 at 25 mA	279
Crystal IS	2013	[30]	Single-crystal AlN (sublimation method)/ AlGaN-QW	7 at 50 mA	280
				5.4 at 50 mA	266
Tokuyama	2013	[33]	Single crystal AlN (grown by HVPE)/AlGaN-QW	3.1 at 250 mA	265
				5.3 at 250 mA (With PhC)	265
Nichia	2010	[36]	Sapphire/AlN/AlGaN-QW	2.8 at 20 mA	281

1. IQE of AlGaN is more sensitive to TDD than that of InGaN.
2. The hole concentration of p-AlGaN is low, resulting in low injection efficiency (IE).
3. LEE is low because of the absorption of UV light in p-GaN contact layers.

The development of low-TDD AlN templates is most important, because IQE of AlGaN-QWs is as low as 1 % if we use conventional templates with high TDD. To obtain high IQE of more than 60 %, the reduction of TDD to below 5×10^8 cm^{-2} is required [16, 17]. To fabricate such a low-TDD AlN template on sapphire, it is necessary to introduce some special growth conditions. Low-TDD AlN single-crystal wafers have advantages for high IQE [30–33], although they are expensive for use as commercially available DUV LEDs. We are using the 'ammonia (NH_3) pulsed-flow multilayer (ML) growth' method to fabricate AlN templates on sapphire, and we have obtained IQE of approximately 60 % from AlGaN QWs [15–17]. Also, for the realization of high IQE DUV emission, the use of quaternary InAlGaN with a few percent of indium (In) is effective [2, 17].

The device properties of AlGaN DUV LEDs strongly depend on the properties of the p-AlGaN. The hole concentration of p-AlGaN with high Al content (Al > 60 %) is low (as low as 10^{14} cm^{-3}) owing to its deep acceptor level, i.e., 240 (GaN) 590 meV (AlN). EIE of a DUV LED is reduced owing to the leakage of electrons to the p-side layers. The high series resistance of p-type layers also becomes a problem for the device properties.

Owing to the lack of high-hole-density p-type AlGaN, we must use p-GaN contact layers. The use of a p-GaN contact layer results in a significant reduction in LEE owing to the strong absorption of DUV light. LEE of a DUV LED is typically below 8 %. Transparent p-AlGaN contact layers and highly reflective p-type electrodes are desirable for realizing high LEE devices.

The current EQE of 270 nm DUV LEDs in our group is approximately 7 %, which is determined by 60 % IQE, 80 % EIE, and 15 % LEE. Further improvements in EQE are expected as we start the production of commercially available DUV LEDs. Techniques for increasing each of these efficiencies are described in the following sections.

4.3 Growth Techniques of High-Quality AlN on Sapphire Substrate

In order to realize high-efficiency DUV LEDs, it is necessary to develop a low TDD AlGaN/AlN template. The TDD of a conventional AlN buffer layer on a sapphire substrate, which was fabricated using a low-temperature (LT)-AlN buffer, was greater than 2×10^{10} cm^{-2}. On the other hand, TDD of 10^8–10^9 cm^{-2} is required in order to obtain high IQE values of several tens % from AlGaN QWs. Several fabrication methods have been reported for obtaining high-quality AlN buffers; for example, the use of AlN/AlGaN superlattices (SLs) grown with alternating gas

feeds [6], AlGaN buffer layers deposited by epitaxial lateral overgrowth (ELO) [39], and a combination of GaN/AlN SLs and AlGaN produced by alternate source-feeding epitaxy (ASFE) on SiC [40].

In the former experiments, we grew AlN layers directly onto sapphire substrates at high-growth temperature (HT) after an initial nitridation treatment using NH_3. The growth temperature was around 1300 °C, and the V/III ratio was a relatively low value. Figure 4.6 shows the relationship between the full width at half maximum (FWHM) of X-ray diffraction (10–12) and (0002) ω-scan rocking curves (XRCs) and the nitridation time of AlN layers grown on sapphire substrates. As the nitridation time was increased from 5 to 10 min, the FWHM of (10–12) XRC was reduced to 560 arcsec. The value of the FWHM of (10–12) XRC corresponds to the edge-type threading-dislocation density. We found that larger AlN nuclei are formed in the initial stages of the growth process by introducing longer nitridation times, and that edge dislocations are reduced by embedding them in a thick AlN layer. However, heavy nitridation on sapphire become the cause of a polarity inversion from Al to N polarity, which leads to the generation of abnormal large nuclei on the AlN surface. We also found that a long nitridation time leads to cracks on the AlN surface.

It is necessary to satisfy several conditions to achieve high-quality AlGaN/AlN templates that are applicable to DUV emitters, i.e., low-TDD, crack-free, atomically flat surfaces and stable Al (+c) polarity. To obtain all of the conditions mentioned above, we have introduced an 'ammonia (NH_3) pulsed-flow multilayer (ML) growth' method for fabricating AlN layers on sapphire [15]. Figure 4.7 shows the typical gas flow sequence and a schematic view of the growth control method using pulsed- and continuous-flow gas feeding growth that is used for the NH_3 pulsed-flow ML-AlN growth.

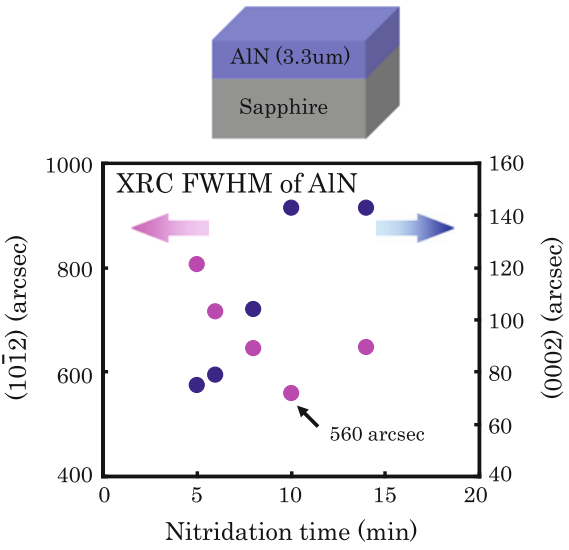


Fig. 4.6 Full width at half maximum (FWHM) of X-ray diffraction (10–12) ω-scan rocking curves (XRC) as a function of initial nitridation time for AlN layers grown on sapphire substrates using a direct high-growth temperature low V/III growth method

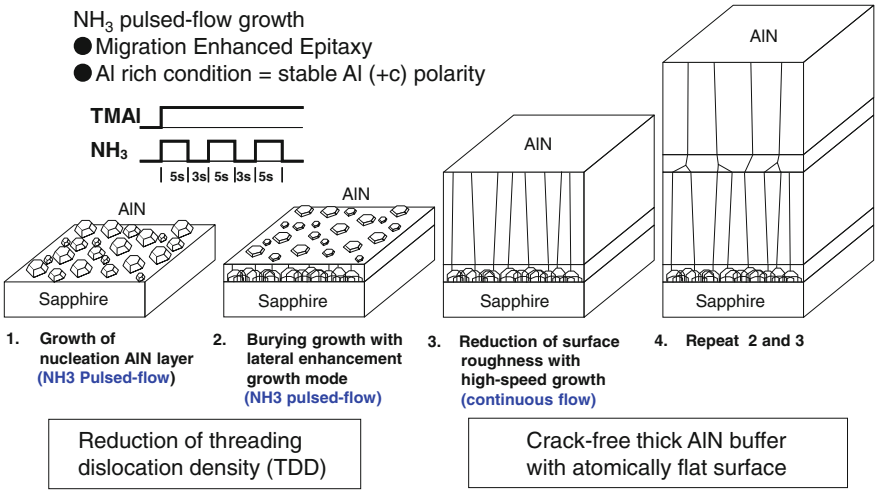


Fig. 4.7 Gas flow sequence and schematic view of the growth control method used for 'an NH_3 pulsed-flow multilayer (ML)-AlN growth technique'

The samples were grown on sapphire (0001) substrates by low-pressure metal-organic chemical vapor deposition (LP-MOCVD). First, an AlN nucleation layer and a 'burying' AlN layer was deposited, both by NH_3 pulsed-flow growth. The trimethylaluminum (TMAl) flow was continuous during the NH_3 pulsed-flow sequence, as shown in Fig. 4.7. Low-TDD AlN can be achieved by promoting the coalescence of the AlN nucleation layer. After the growth of the first AlN layer, the surface is still rough because of the low growth rate by the pulsed-flow mode growth. We introduced a high-growth rate continuous-flow mode to reduce the surface roughness. By repeating the pulsed- and continuous-flow modes, we can obtain crack-free, thick AlN layers with atomically flat surfaces. NH_3 pulsed-flow growth is effective for obtaining high-quality AlN because of the enhancement of precursor migration. Furthermore, it is effective for obtaining stable Al (+c) polarity, which is necessary for suppressing polarity inversion from Al to N by maintaining Al-rich growth conditions.

As described above, we used three different growth conditions in this method, i.e., the initial deposition in order to fabricate an AlN nucleation layer, migration enhancement epitaxy for decreasing TDD, and a high-growth rate using a conventional continuous flow mode. The detailed growth conditions were described in [15, 19]. The typical growth rates in the pulsed- and continuous-flow modes were approximately 0.6 and 6 μm/h, respectively. We found recently that a low V/III ratio and higher growth temperature ($\sim$400 °C) is more suitable for obtaining a low TDD AlN growth on sapphire.

The advantage of using ML-AlN for the DUV LED is that low TDD AlN can be obtained without the need for AlGaN layers, yielding a device structure with minimal DUV absorption. An AlGaN-free buffer is believed to be important for realizing sub-250 nm-band high-efficiency LEDs.

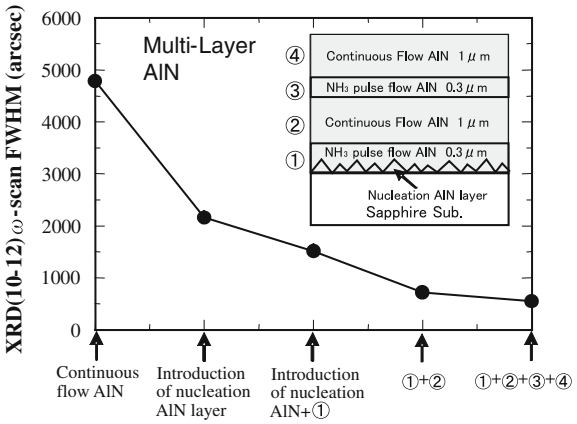


Fig. 4.8 Reduction of FWHM of X-ray diffraction (10–12) ω-scan rocking curve (XRC) for various stages of ML-AlN growth

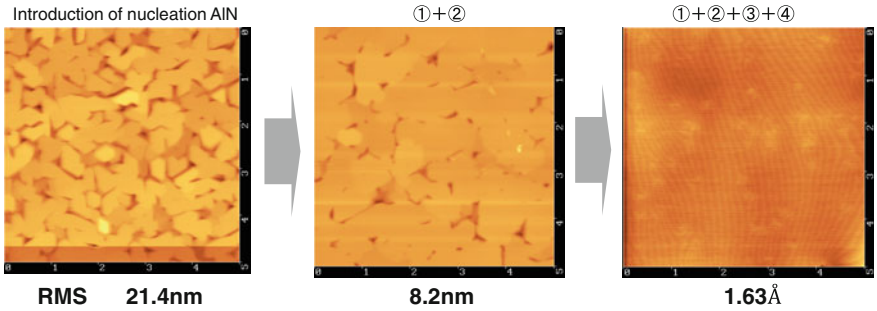


Fig. 4.9 AFM images of the surface of ML-AlN with an area of 5 × 5 μm^2 square for various stages of growth

Figure 4.8 shows the FWHM of the X-ray diffraction (10–12) ω-scan rocking curves (XRC) for various stages of the ML-AlN growth. The FWHM of XRC (10–12) for AlN was reduced from 2160 to 550 arcsec by introducing 'two-times repetition' of the NH_3 pulsed-flow ML-AlN growth. Figure 4.9 shows atomic-force microscope (AFM) images of the surface of ML-AlN on sapphire at various stages of the ML-AlN growth. We can observe that the surface was improved by growing the multilayers of AlN, and we can finally confirm an atomically flat surface, as demonstrated in Fig. 4.9. The root-mean-square (RMS) value of the surface roughness of the ML-AlN obtained from the AFM image was 0.16 nm.

Figure 4.10 shows (a) a schematic structure and (b) a cross-sectional transmission electron microscope (TEM) image of an AlGaN/AlN template with a 5-step ML-AlN buffer layer grown on a sapphire substrate. The total thickness of the ML-AlN buffer was typically 4 μm. The typical full widths at half maximum

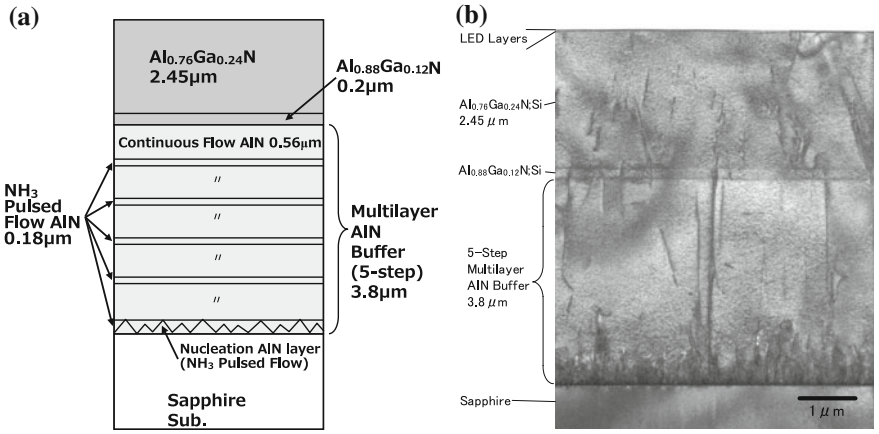


Fig. 4.10 **a** Schematic structure and **b** cross-sectional TEM image of an AlGaN/AlN template including a 5-step ML-AlN buffer layer grown on a sapphire substrate

(FWHMs) of X-ray diffraction (10–12) and (0002) ω-scan rocking curves (XRCs) of the ML-AlN were approximately 370 and 180 arcsec, respectively, which were achieved by a highly uniform 3 × 2 in. reactor MOCVD [25]. The minimum FWHMs obtained for a 1 × 2 in. reactor MOCVD were approximately 290 and 180 arcsec, respectively. The minimum edge- and screw-type dislocation densities of the ML-AlN were below 5×10^8 and 4×10^7 cm^{-2}, respectively, as observed by a cross-sectional TEM image.

4.4 Marked Increase in Internal Quantum Efficiency (IQE)

We observed a remarkable enhancement of the DUV emission of AlGaN-QWs by fabricating them on low TDD AlN templates [16, 17]. Figures 4.11 show a cross-sectional TEM image of the quantum-well region of an AlGaN multi-(M)QW DUV-LED with an emission wavelength of 227 nm fabricated on a ML-AlN buffer. We used a thin quantum well in order to obtain a high IQE by suppressing the effects of the polarization field spontaneously applied in the well. This is believed to be particularly important for obtaining the atomically smooth hetero-interfaces that are necessary in order to achieve a high IQE from such a thin QW. The atomically flat hetero-interfaces of the 1.3 nm-thick three-layer QWs are confirmed as observed in the cross-sectional TEM image shown in Fig. 4.11.

Figure 4.12 shows photoluminescence (PL) spectra of AlGaN QWs fabricated on ML-AlN templates with various values of XRC (10–12) FWHM, as measured at room temperature (RT). The peak emission wavelengths of the QWs were around

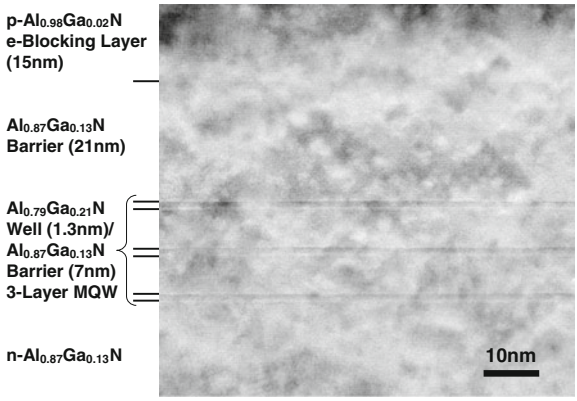


Fig. 4.11 Cross-sectional TEM image of the quantum well region of an AlGaN-MQW DUV-LED

254 nm. The QWs were excited with 244 nm Ar-ion second harmonics generation (SHG) laser. The excitation power density was fixed at 200 W/cm^2. The PL emission intensity of the AlGaN QW was significantly increased by improving the XRC (10–12) FWHM, as shown in Fig. 4.12. We can see from Fig. 4.12 that the emission efficiency of AlGaN depends strongly on the edge-type TDD.

Figure 4.13 shows the PL peak intensity as measured at RT for 254 nm-emission AlGaN-QWs as a function of XRC (10–12) FWHM. The PL intensity was increased by approximately 80 times by reducing the XRC (10–12) FWHM from 1400 to 500 arcsec. The PL intensity increased rapidly when the FWHM of the XRC was reduced to 500–800 arcsec. The rapid increase in PL intensity can be explained by a reduction of a non-radiative recombination rate as the distance between TDs becomes greater compared with the carrier diffusion length in the QW. We obtained similar enhancement of the emission from AlGaN QWs with various wavelengths QWs. The relationships between IQE and TDD in DUV emission AlGaN-QWs were also investigated in [27, 41].

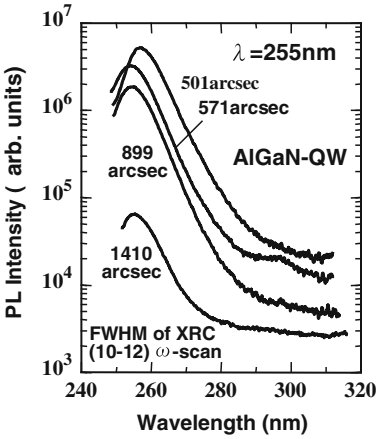


Fig. 4.12 Photoluminescence (PL) spectra of AlGaN QWs on multilayer (ML) AlN templates with various values of XRC (10–12) FWHM

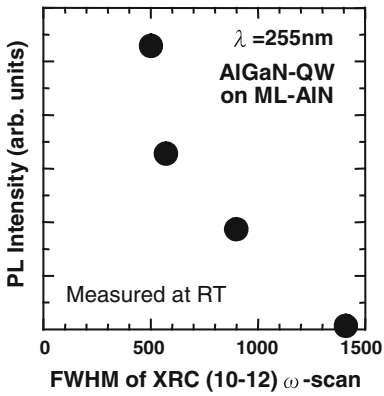


Fig. 4.13 PL intensity of AlGaN-QWs as a function of XRC (10–12) FWHM of AlGaN buffers

Figure 4.14 shows an example of a temperature dependence of the integrated PL intensity measured for an AlGaN MQW with an emission wavelength at 288 nm fabricated on a ML-AlN template. The IQE can be roughly estimated from the temperature-dependence of the integrated PL intensity if we assume that the non-radiative recombination rate is quite low at low temperature. The estimated IQE at RT for the 288 nm-emission AlGaN QW was observed to be approximately 30 % for this sample.

The quaternary alloy InAlGaN is attracting considerable attention as a candidate material for realizing DUV LEDs, since efficient UV emission as well as higher hole concentrations can be realized due to In-incorporation effects. The incorporation of a few percent of In into AlGaN is considered to be quite effective for obtaining high IQE, because an efficient DUV emission can be obtained due to the In segregation effect, which has already been investigated for the ternary InGaN alloy. We have described the advantages of the use of the quaternary InAlGaN alloy in [2, 11, 12, 17].

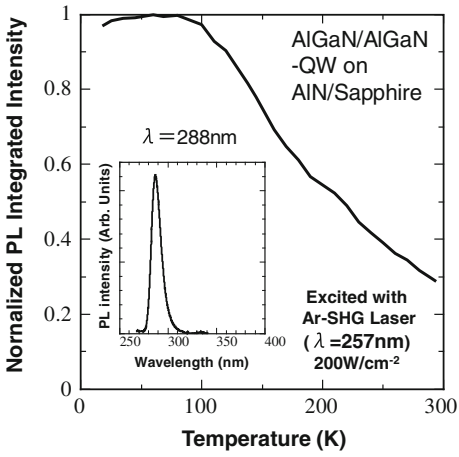


Fig. 4.14 Temperature dependence of integrated PL intensity for an AlGaN 3-layer MQW grown on a ML-AlN template

Figure 4.15 shows a cathodoluminescence (CL) image obtained from a quaternary InAlGaN layer [2] and a schematic image of carrier recombination in an InAlGaN alloy. Emission fluctuations in the submicron region were clearly observed in the CL image. The emission fluctuation is considered to be due to carrier localization in the In-segregation area. The CL images obtained for quaternary InAlGaN were very similar to those obtained for InGaN films. Electron-hole pairs localized in the low-potential valley emit before they are trapped in non-radiative centers induced by dislocations. Therefore, the advantage of the In incorporation is that the emission efficiency is less sensitive to TDD.

Figure 4.16 shows the temperature dependence of the integrated PL intensity measured for an InAlGaN/InAlGaN MQW with an emission wavelength of 338 nm fabricated on a high-temperature (HT)-AlN buffer on sapphire. The TDD of the HT-AlN was approximately 2×10^{10} cm^{-2}. The estimated IQE was approximately 47 % at RT, from Fig. 4.16. We found that high IQE can be obtained for InAlGaN QWs in the wavelength range between 310–380 nm, even when using a high-TDD template [2, 11, 12].

Then we took up the challenge of developing crystal growth for high-quality InAlGaN alloys emitting at the 'sterilization' wavelength (280 nm) [17]. The crystal growth of high Al-composition quaternary InAlGaN is relatively difficult, because In-incorporation becomes more difficult with increasing growth temperature, which

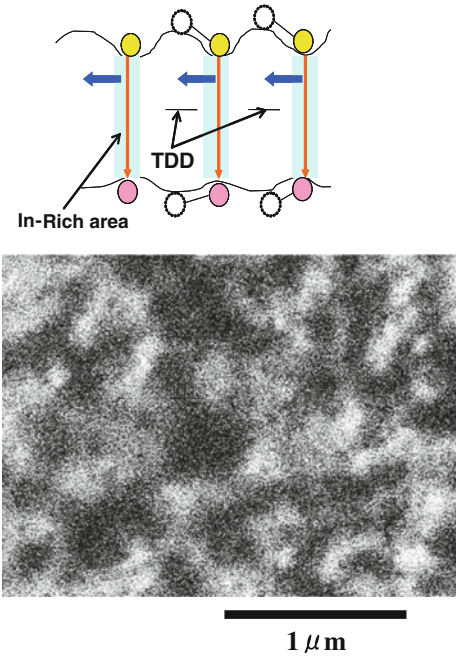


Fig. 4.15 Cathodeluminescence (CL) image obtained from a quaternary InAlGaN layer and a schematic image showing carrier recombination in an InAlGaN alloy

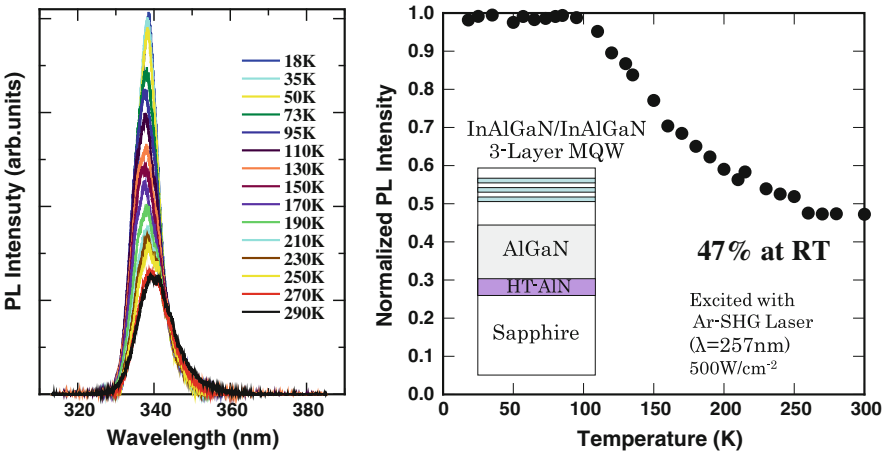


Fig. 4.16 Temperature dependence of integrated PL intensity measured for an InAlGaN/InAlGaN MQW with an emission wavelength of 338 nm fabricated on a high-temperature (HT)-AlN buffer on sapphire

is required in order to maintain the crystal quality of high-Al-content AlGaN. We achieved high-quality quaternary InAlGaN layers with high-Al-content (>45 %) by using relatively low growth-rate epitaxy, i.e., 0.03 μm/h. The emission intensity of a 280 nm-band quaternary InAlGaN QW at RT was increased by five times by reducing the growth rate from 0.05 to 0.03 μm/h. Figure 4.17 shows the PL spectra of a quaternary InAlGaN QW measured at 77 K and at RT. We obtained extremely high intensity PL emission at RT. The ratio of the integrated intensity of the RT–PL

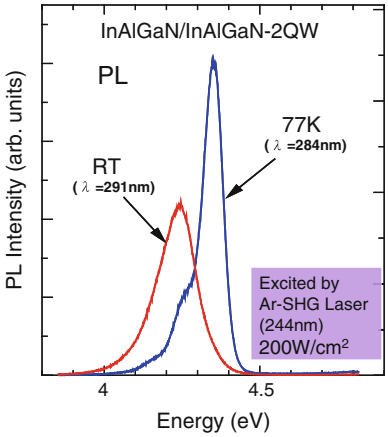


Fig. 4.17 PL spectra of a quaternary InAlGaN/InAlGaN QW emitting at 282 nm measured at 77 K and at RT

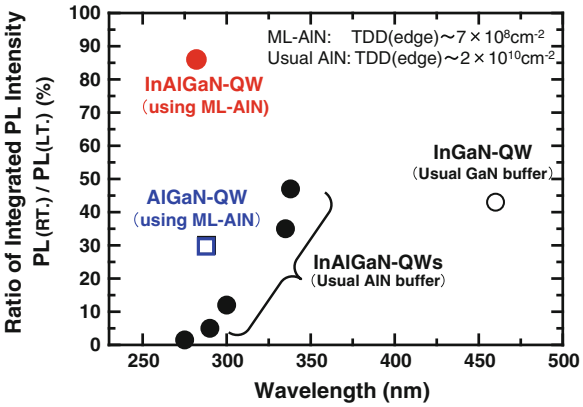


Fig. 4.18 Wavelength dependence of the ratio of the integrated PL intensity (PL measured at RT against PL measured at low temperature) for AlGaN and quaternary InAlGaN QWs fabricated on conventional high-TDD AlN and on low-TDD ML-AlN templates on sapphire substrates

against the 77 K–PL was 86 %. Thus, high IQE was obtained from the quaternary InAlGaN QW at RT.

Figure 4.18 summarizes the wavelength dependence of the ratio of the integrated PL intensity [PL measured at room temperature (RT) against PL measured at low temperature (usually below 20 K)] investigated in 2008 [17], which is related to IQE. IQE of 340 nm InAlGaN QW was estimated to be 30 50 %, even when we use a high-TDD template (TDD $\sim 2\times10^{10}$ cm^{-2}). However, IQE was reduced to below 2 % for short wavelength (280 nm) QWs, even we use quaternary InAlGaN QWs. On the other hand, we achieved high IQE by introducing low-TDD ML-AlN templates. The ratios of the integrated PL intensity obtained for 280 nm QWs were approximately 30 and 86 % for an AlGaN QW and an InAlGaN QW, respectively, when we use low-TDD ML-AlN templates (TDD $\sim 7 \times 10^8$ cm^{-2}). The IQE at RT can also be estimated from the PL intensity observed at RT. We observed higher IQE values (50–60 %) for AlGaN QWs by realizing a further reduction of the TDD and by optimizing the AlGaN QW growth conditions.

4.5 222–351 nm AlGaN and InAlGaN DUV LEDs

AlGaN and quaternary InAlGaN MQW DUV LEDs were fabricated on low-TDD ML-AlN templates [15–25]. Figure 4.19a, b show a schematic of the structure and emission images taken by a digital camera, respectively, of an AlGaN-based DUV LED fabricated on a sapphire substrate. Table 4.2 shows the typical design values of the Al compositions (x) in the $Al_xGa_{1-x}N$ wells, the buffer and barrier layers, and the electron-blocking layers (EBLs) that were used for the 222–273 nm AlGaN-MQW LEDs. High-Al-composition AlGaN layers were used in order to

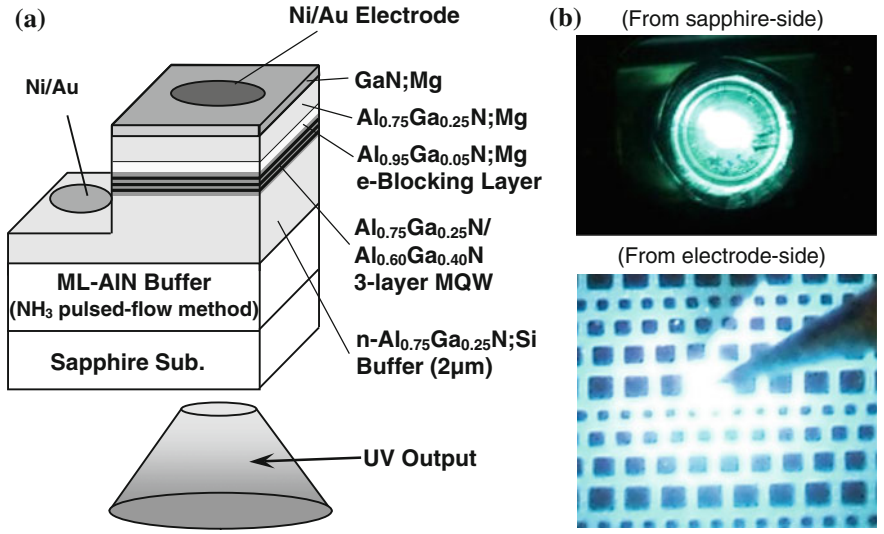


Fig. 4.19 **a** Schematic structure and **b** emission images taken by a digital camera of a typical AlGaN-based DUV LED fabricated on a sapphire substrate

Table 4.2 Typical design values of Al compositions (x) in $Al_xGa_{1-x}N$ wells, buffer and barrier layers, and electron-blocking layers (EBLs) used for 222–273 nm AlGaN-MQW LEDs

Wavelength (nm)	Well	Barrier and buffer	Electron blocking layer
222	0.83	0.89	0.98
227	0.79	0.87	0.98
234	0.74	0.84	0.97
248	0.64	0.78	0.96
255	0.60	0.75	0.95
261	0.55	0.72	0.94
273	0.47	0.67	0.93

obtain short-wavelength DUV emissions, as shown in Table 4.1. A typical LED structure consisted of an approximately 4 μm-thick undoped ML-AlN buffer layer grown on sapphire, a 2 μm-thick Si-doped AlGaN buffer layer, followed by a 3-layer undoped MQW region consisting of approximately 1.5 nm-thick AlGaN wells and 7 nm-thick AlGaN barriers, an approximately 20 nm-thick undoped AlGaN barrier, a 15 nm-thick Mg-doped AlGaN electron-blocking layers (EBLs), a 10 nm-thick Mg-doped AlGaN p-layer, and an approximately 20 nm-thick Mg-doped GaN contact layer. The quantum well thickness was varied within the range between 1.3 and 2 nm. Thin quantum wells are preferable for AlGaN QWs in order to suppress the effects of large piezoelectric fields in the well. Ni/Au electrodes were used for both n-type and p-type electrodes. The typical size of the

p-type electrode was 300 × 300 μm^2. The output power that radiated into the back of the LED was measured using a Si photodetector located behind the LED sample, which was calibrated to measure the luminous flux so that the output power of a fabricated flip-chip LED device gives an accurate value. The output power of the flip-chip LED was measured precisely using an integrated sphere system [25]. The LEDs were measured under 'bare wafer' or 'flip-chip' conditions. The forward voltages (Vf) of the bare wafer and the flip-chip samples with an injection current of 20 mA were approximately 15 and 8.3 V, respectively.

Figure 4.20 shows the electroluminescence (EL) spectra of the fabricated AlGaN and InAlGaN-MQW LEDs with emission wavelengths between 222 and 351 nm, all measured at room temperature (RT) with an injection current of approximately 50 mA. As can be seen in Fig. 4.20, single-peak operation was obtained for every sample. The deep-level emissions were two orders of magnitude smaller than that of the main peak.

Figure 4.21 shows the EL spectra of a 227 nm AlGaN LED on a log scale [19]. We obtained single-peaked EL spectra, even for sub-230 nm wavelength LEDs. The deep-level emissions with wavelengths at around 255 and 330–450 nm were more than two orders of magnitude smaller than the main peak. These peaks may correspond to deep-level emissions associated with Mg-acceptors or other impurities. The output power of the 227 nm LED was 0.15 mW at an injection current of 30 mA, and the maximum EQE was 0.2 % under RT pulsed operation. The pulse width and the repetition frequency were 3 μs and 10 kHz, respectively.

Figure 4.22 shows (a) the EL spectra for various injection currents and (b) current versus output power (I-L) and EQE (η_{ext}) characteristics for a 222 nm AlGaN-MQW LED measured under RT pulsed operation [20]. Single-peaked

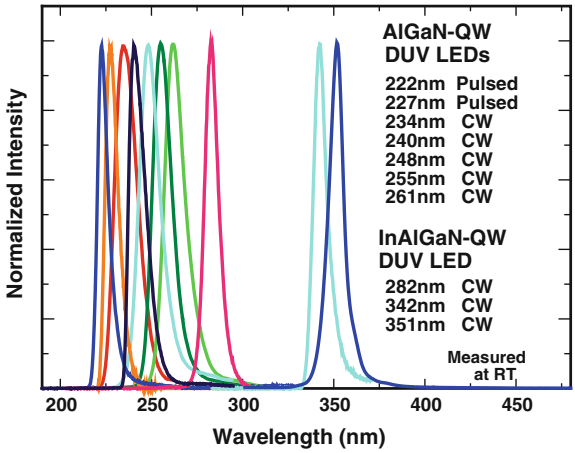


Fig. 4.20 Electroluminescence (EL) spectra of fabricated AlGaN and quaternary InAlGaN MQW LEDs with emission wavelengths between 222 and 351 nm, all measured at room temperature (RT) with injection currents of around 50 mA

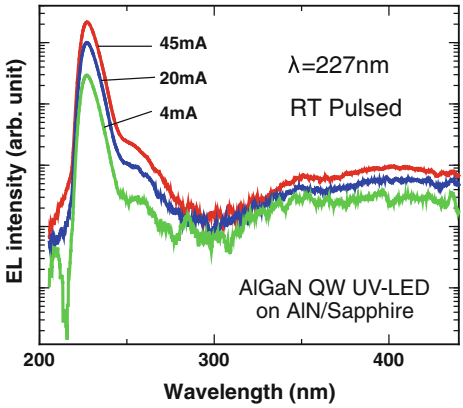


Fig. 4.21 EL spectra on a log scale of a 227 nm AlGaN DUV LED for various injection currents

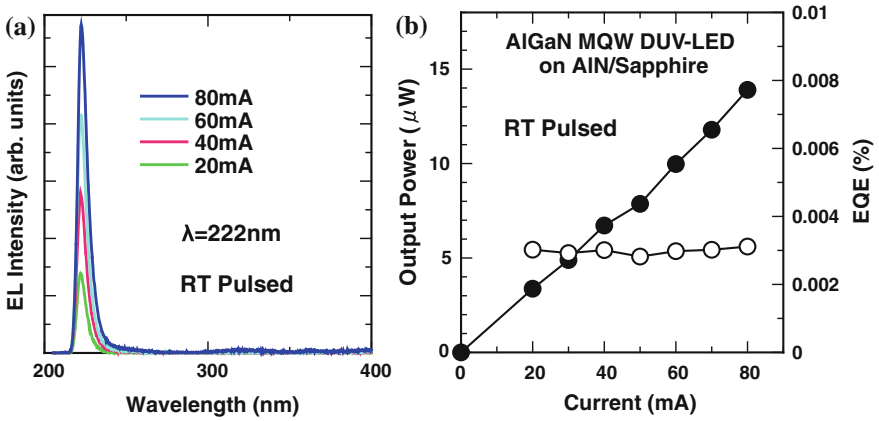


Fig. 4.22 **a** EL spectra for various injection currents and **b** current versus output power (I-L) and EQE (η_{ext}) characteristics for a 222 nm AlGaN-MQW LED measured under RT pulsed operation

operation of a 222 nm DUV AlGaN-MQW LED was realized, which is the shortest record wavelength ever reported for a QW LED. The output power of the 222 nm LED was 0.14 μW at an injection current of 80 mA, and the maximum EQE was 0.003 % under RT pulsed operation.

Figure 4.23 shows (a) current versus output power (I-L) and (b) current versus EQE (η_{ext}) characteristics for 250 nm-band AlGaN-MQW LEDs under RT continuous-wave (cw) operation. We fabricated two types of samples with different Al-composition AlGaN EBLs, i.e., one at 90 % and the other at 95 %. The corresponding barrier heights of the EBLs in the conduction band were 280 and 420 meV, respectively. As seen in Fig. 4.23, the EQE of the LED was significantly increased by using a higher electron-blocking height. This fact indicates that

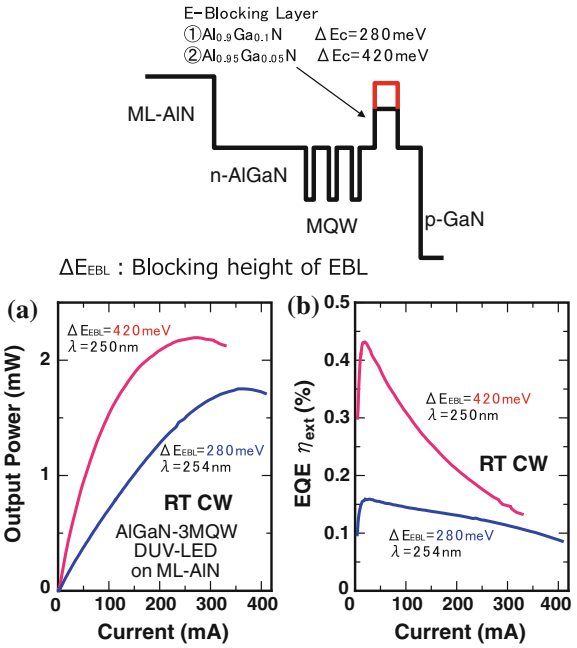


Fig. 4.23 **a** Current versus output power (I-L) and **b** current versus EQE (η_{ext}) characteristics for 250 nm-band AlGaN-MQW LEDs under RT continuous-wave (cw) operation

electron overflow is significantly reduced due to the electron reflection by the EBL, and therefore the electron injection efficiency (EIE) into the QW is increased. The maximum output power and EQE obtained by optimizing the height of the EBL were 2.2 mW and 0.43 %, respectively, for an LED with an emission wavelength of 250 nm under RT cw operation [17].

Figure 4.24 shows the wavelength dependence of the output powers of 245–260 nm AlGaN-MQW LEDs, varying the edge-type TDD of the AlN templates and the electron barrier height of the EBLs obtained in 2007 [17]. A marked

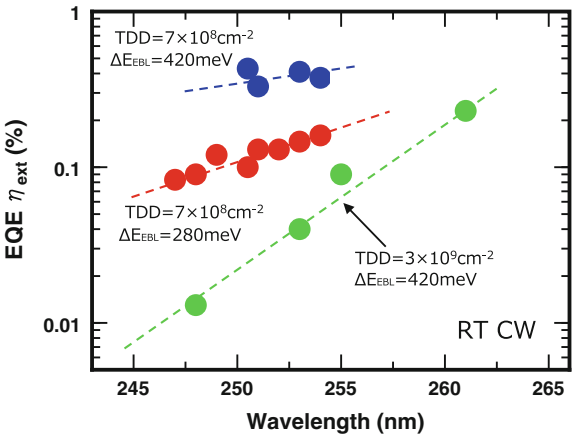


Fig. 4.24 Wavelength dependence of output power of 245–260 nm AlGaN MQW LEDs varying the edge-type TDD of AlN template and the electron barrier height of the EBL

increase in cw output power was observed by reducing the TDD and by increasing the EBL height. The 250 nm-band output power was increased by more than 30 times by reducing the TDD from 3×10^9 cm^{-2} to 7×10^8 cm^{-2}. We also found that a higher electron-blocking height is effective for obtaining high-output-power.

Figure 4.25 shows the EL spectra of 225 nm AlGaN QW DUV LEDs with various quantum well thicknesses, as measured under RT pulsed operation. The well thickness was changed in the range between 1.6 and 4 nm. Intense emission was obtained in the case of thin QWs. From this experiment, we confirmed that thin well thicknesses are suitable for AlGaN QWs in order to suppress the effects of large Piezoelectric fields. We found that the emission efficiency is reduced by approximately two orders of magnitude by increasing the well thickness from 1.6 to 4 nm.

It has been reported that 'normal' c-axis direction emission (vertical emission) is difficult to obtain from an AlN (0001) or a high-Al-content AlGaN surface, because the optical transition between the conduction band and the top of the valence band is mainly only allowed for light that has its electric field parallel to the c-axis direction of AlN (E//c) [9]. The suppression of the vertical emission is a quite severe problem for AlGaN-based DUV LEDs, because it results in a significant reduction in the light extraction efficiency. Several groups have reported that vertical c-axis emission is suppressed for high-Al content AlGaN QWs [42, 43]. Banal et al. reported that the critical Al composition for 'polarization switching' could be expanded to approximately 0.82 by using a very thin (1.3 nm) quantum well, when AlGaN-QW was fabricated on an AlN/sapphire template [42].

Figure 4.26 shows the radiation angle dependence of emission spectra of a 222 nm AlGaN QW LED. The radiation angle was measured under bare wafer

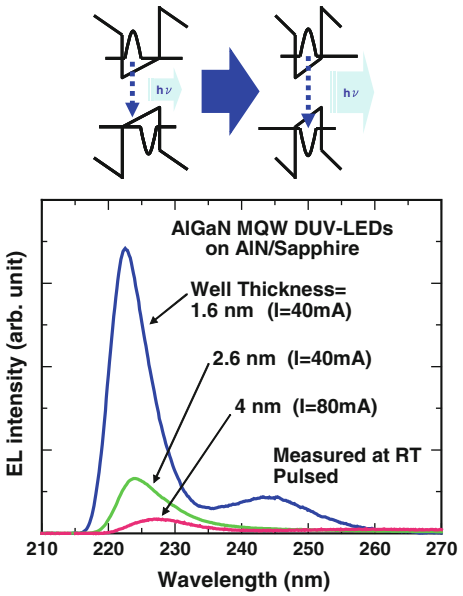


Fig. 4.25 EL spectra of 225 nm AlGaN-QW DUV LEDs with various quantum well thicknesses, measured under RT pulsed operation

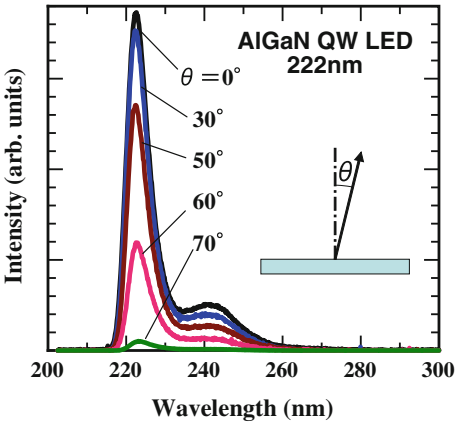


Fig. 4.26 Radiation angle dependence of emission spectra of a 222 nm AlGaN QW DUV LED

condition, not using flip-chip-mounted sample. The backside of the substrate was not polished and was just left with rough surface. We demonstrated that 'normal' c-axis-direction emission (vertical emission) can be obtained, even for short-wavelength (222 nm) LEDs with a high-Al-composition AlGaN QW, as shown in Fig. 4.26 [20]. It was found that vertical c-axis emission can be obtained for an AlGaN-QW LED on AlN/sapphire, even when the Al-composition range of the AlGaN QW is as high as 83 %.

We fabricated quaternary InAlGaN-based DUV LEDs in order to increase IQE and EIE of the DUV LEDs. Figure 4.27 shows a schematic structure and a

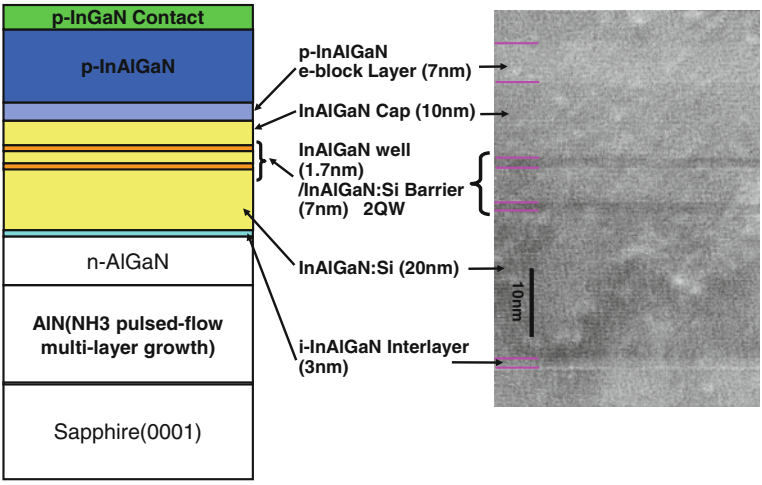


Fig. 4.27 Schematic structure and the cross-sectional TEM image of a quaternary InAlGaN QW DUV LED with emission wavelength at 282 nm

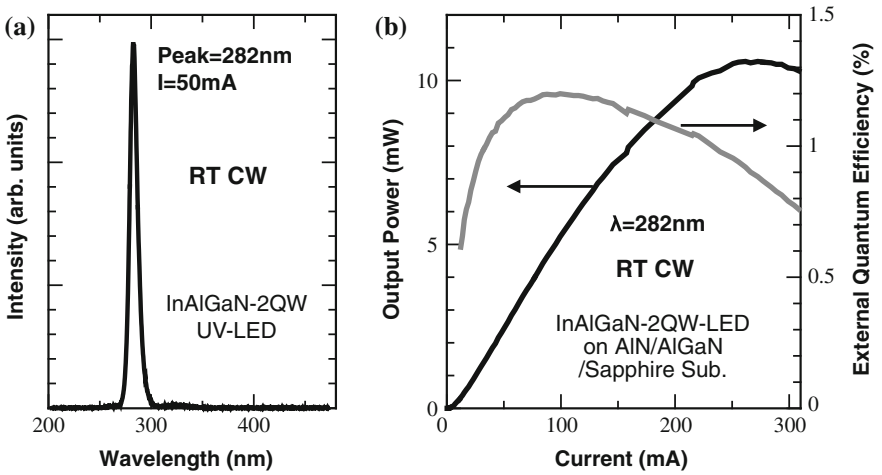


Fig. 4.28 **a** EL spectrum and **b** current versus output power (I-L) and EQE characteristics of the quaternary InAlGaN QW DUV-LED with emission wavelength at 282 nm

cross-sectional TEM image of an InAlGaN-QW DUV LED. We confirmed that the surface roughness of the InAlGaN layer was significantly improved by introducing a Si-doped InAlGaN buffer layer. The InAlGaN-based DUV LED is considered to be attractive for achieving high EQE due to the higher-IQE and higher hole-concentration obtained by In-segregation effects. Figure 4.28 shows (a) an EL spectrum and (b) the current versus output power (I-L) and EQE characteristics of an InAlGaN-based QW DUV-LED with an emission wavelength of 282 nm. The maximum output power and EQE were 10.6 mW and 1.2 %, respectively, under RT cw operation. From these results, we found that quaternary InAlGaN QWs and p-type InAlGaN are quite useful for achieving high-efficiency DUV LEDs [17].

4.6 Increase in Electron Injection Efficiency (EIE) by MQB

Despite achieving high IQE in DUV as mentioned above, EQE of the LED was still as low as 1–2 % [17]. The low EQE figures for AlGaN DUV LEDs compared with those for InGaN blue LEDs are a result of low electron injection efficiency (EIE) into the QW due to electron leakage caused by low hole concentrations in the p-type AlGaN layers, as well as inferior light extraction efficiencies (lower than 8 %) due to strong UV absorption in the p-GaN contact layer and the p-side electrode. The values of EIE for 250–280 nm-band AlGaN-based DUV LEDs were roughly estimated to be 10–30 % [17]. We have introduced a MQB as an EBL in an AlGaN-QW LED, and have consequently achieved a marked increase in EIE [18].

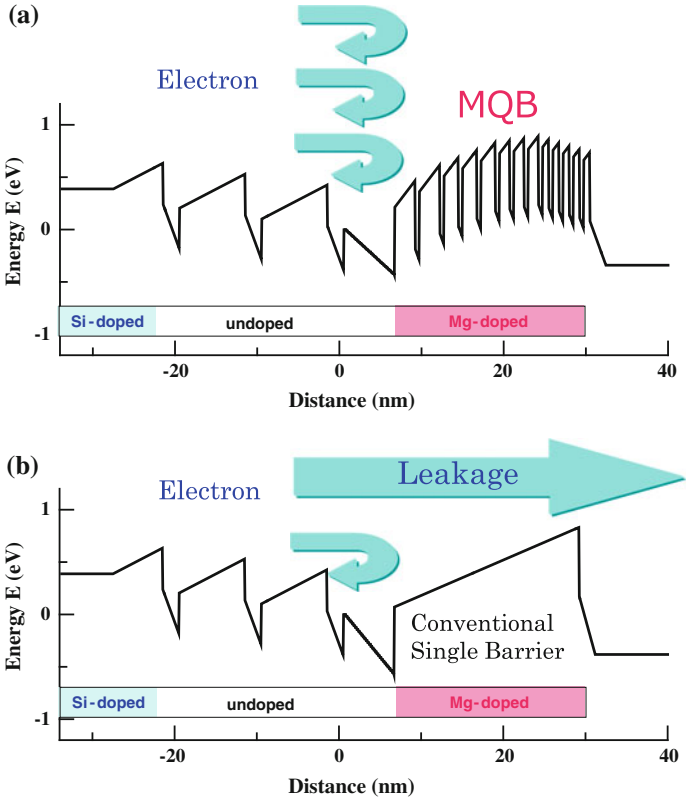


Fig. 4.29 Schematic images of the electron flow for AlGaN DUV LEDs with **a** a MQB EBL and **b** a conventional single-barrier EBL

Figure 4.29 shows schematic images of the electron flow for AlGaN DUV LEDs with (a) a MQB EBL and (b) a conventional single-barrier EBL. A large barrier height is required for the EBL to obtain a sufficiently high EIE for the suppression of overflow electrons above the QW into the p-type AlGaN layers. We have tried using AlN or high-Al-composition (Al > 0.95) AlGaN layers for the EBL [17, 19, 20], however, the barrier heights of these EBLs were still not sufficient high to obtain the desired high EIE. Indeed, EIE is estimated to be particularly low (<20 %) for short-wavelength AlGaN LEDs (<250 nm).

Such a material limitation can be overcome by enhancing the 'effective' barrier height through the introduction of an MQB, which causes multi-reflection effects in the wavefunctions. The MQB was predicted theoretically by Iga et al. in 1986 [44], and the effects were demonstrated experimentally in GaInP/AlInP red laser diodes (LDs) [45]. It has been reported that the effective electron barrier height of an MQB in comparison with a bulk potential barrier is increased by as much as 30 % for GaAs/AlAs and by 50 % for GaInAs/InP MQBs. It is believed that the use of

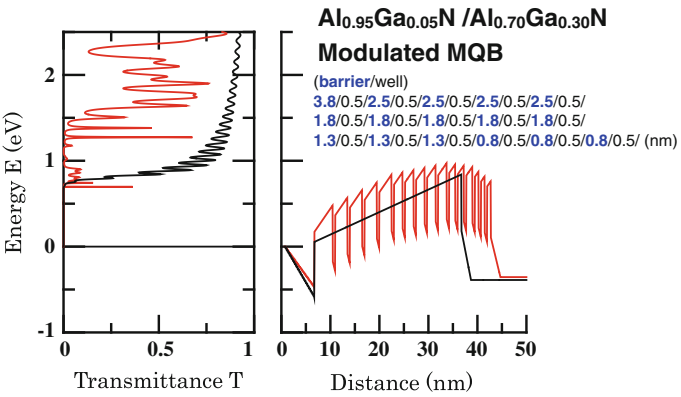


Fig. 4.30 Electron transmittance through AlGaN/AlGaN MQB (*red-line*) and conventional single-barrier EBL (*black-line*) calculated for a 250 nm-band AlGaN-QW LED

AlN/AlGaN or AlGaN/AlGaN MQBs would be quite effective for increasing the 'effective' barrier height of an EBL and, as a result, would contribute to the realization of high EQE AlGaN DUV LEDs.

Figure 4.30 shows electron transmittance through an AlGaN/AlGaN MQB (red-line) and a conventional single-barrier EBL (black-line) calculated for a 250 nm AlGaN QW LED. The multi-reflection effects in the heterostructures are analyzed by a transfer-matrix method. It was shown that the 'effective' electron barrier height of an MQB in comparison with a conventional single-barrier EBL is increased by maximally 2 times for an AlGaN/AlGaN MQB by using barriers with thickness modulation.

Figure 4.31 shows a schematic structure and a cross-sectional TEM image of a fabricated 250 nm AlGaN QW DUV LED with an MQB EBL. We investigated an appropriate MQB structure experimentally for use with 250 nm DUV LEDs. We found that the insertion of an initial thick-barrier is important for obtaining the reflection of lower energy electrons. We also found that thin barriers contribute to the reflection of higher-energy electrons. The optimized MQB structure for a 250 nm AlGaN QW LED was a 5-layer $Al_{0.95}Ga_{0.05}N/Al_{0.77}Ga_{0.23}N$ MQB with thicknesses of **7**/4/**5.5**/4/**4**/2.5/**4**/2.5/**4** nm, in which the bold letters are for barriers and the normal letters are for valleys). We should design the total thickness of the MQB to be within 40 nm, because a coherent length exists for obtaining the multi-reflection effect of an MQB.

Figure 4.32 shows (a) a current versus output power (I-L) and (b) a current versus EQE (η_{ext}) characteristics for a 250 nm AlGaN MQW LED with an MQB and with a single-barrier EBL, both measured under RT cw operation. Significant increases in output power and EQE were observed when the single-EBL was replaced by the MQB. The maximum output powers of the 250 nm LED with the MQB and with the single-barrier EBL were 15 and 2.2 mW, respectively. The EQE of a 250 nm LED was increased by approximately 4 times by the introduction of the

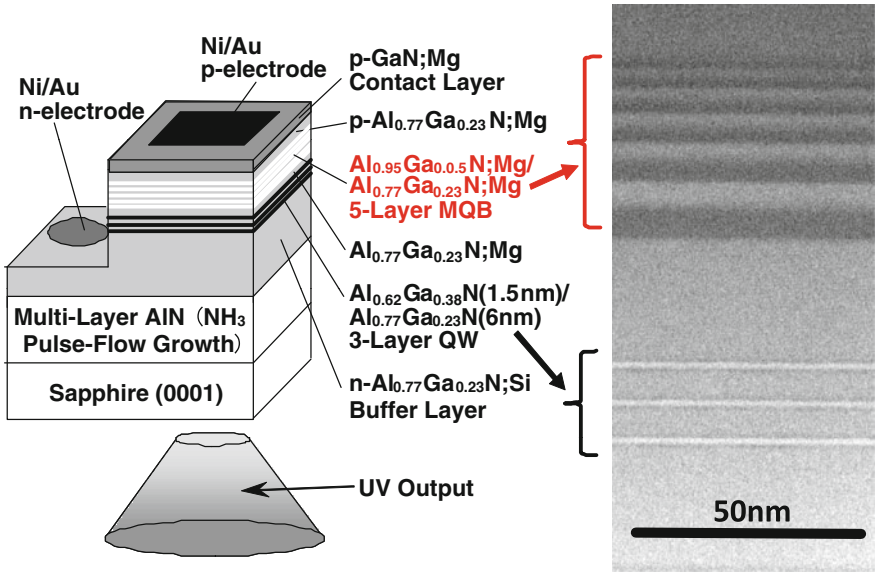


Fig. 4.31 Schematic structure and cross-sectional TEM image of a 250 nm AlGaN QW DUV LED with an MQB

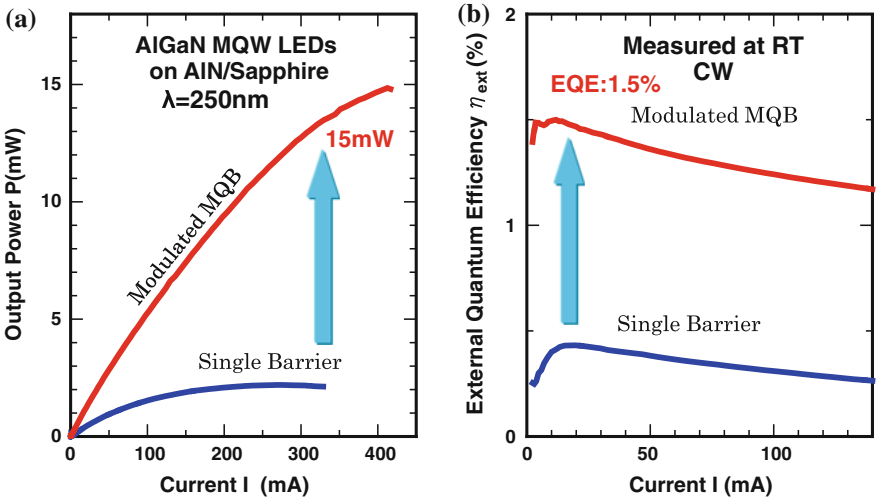


Fig. 4.32 **a** Current versus output power (I-L) and **b** current versus EQE (η_{ext}) characteristics for 250 nm AlGaN-MQW LEDs with an MQB and with a single-EBL

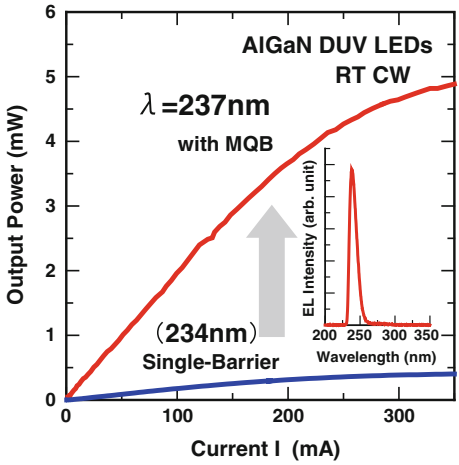


Fig. 4.33 Current versus output power (I-L) characteristic for the 237 nm AlGaN-MQW LEDs with an MQB and with a single-EBL

MQB. From Fig. 4.32, we have estimated that the EIE of the 250 nm LED was improved from approximately 25 % to more than 80 % by introducing the MQB.

Figure 4.33 shows current versus output power (I-L) characteristic for a 237 nm AlGaN-MQW LED with an MQB and with a single-barrier EBL, both measured under RT cw operation. The enhancement of EIE when using the MQW was found to be extremely high for short-wavelength DUV LEDs, as seen in Fig. 4.33. The output power of the 234 nm LED was increased by approximately 12 times by replacing a single-barrier EBL by a MQB.

Figure 4.34 summarizes the wavelength dependence of EQE of AlGaN DUV LEDs with MQBs and single-barrier EBLs. The enhancement factors of the value of EQE by introducing the MQB are approximately 10, 4, and 3 times for 235, 250, and 270 nm AlGaN LEDs, respectively. Figure 4.35 shows the current versus output power (I-L) and the EQE (η_{ext}) characteristics for a high-output-power 270 nm AlGaN-MQW LED with an MQB, as measured under RT cw operation.

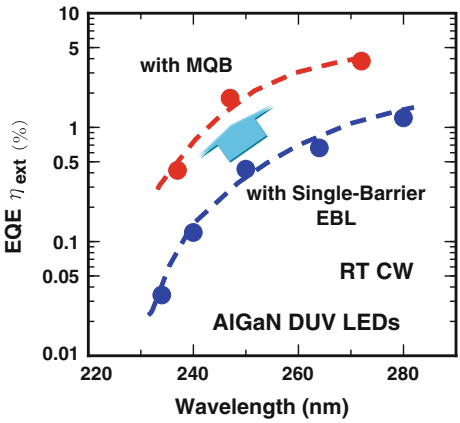


Fig. 4.34 Wavelength dependence of EQE of AlGaN DUV LEDs with MQBs and single-EBLs

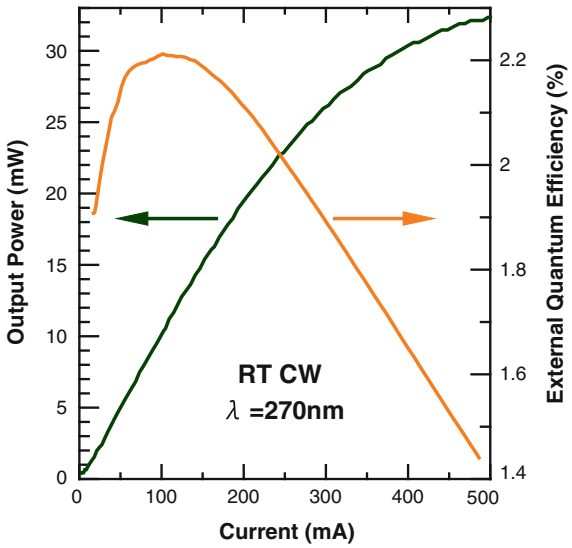


Fig. 4.35 Current versus output power (I–L) and EQE (η_{ext}) characteristics for the high-output-power 270 nm AlGaN MQW LED with an MQB, measured under RT cw operation

A cw output power of 33 mW was obtained for a bare-chip sample. Higher output power may be obtained by performing heat-dissipation by using a flip-chip geometry. The value of the EQE for a 270 nm AlGaN DUV LED with a MQB was 3.8 % without using any structures for increasing LEE [21].

Figure 4.36 summarizes the maximum output powers of AlGaN and InAlGaN-based DUV LEDs fabricated on low-TDD ML-AlN templates that were

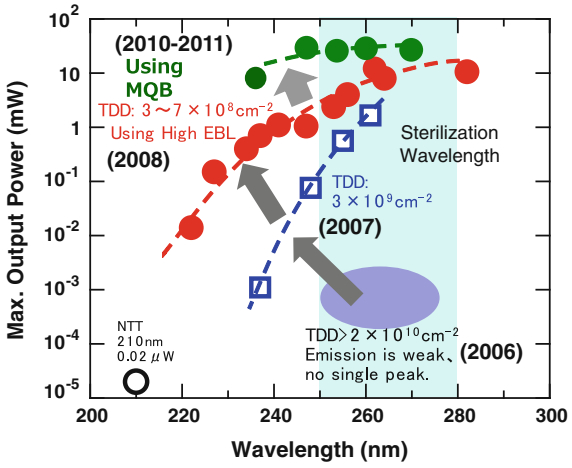


Fig. 4.36 Maximum output powers of AlGaN and InAlGaN-based DUV LEDs fabricated on low-TDD ML-AlN templates that were achieved by RIKEN between 2007 and 2012 [16–22]

achieved by the RIKEN between 2007 and 2012 [16–22]. We have achieved significant increases in the EQE and output powers of AlGaN-based DUV LEDs by introducing low-TDD AlN templates and MQB electron-blocking layers. The maximum output powers obtained were 15–33 mW for 245–270 nm single-chip LEDs. These achievements will contribute to accelerating the practical application of DUV LED, and to expanding them to a wide range of applications.

RIKEN and Panasonic have developed commercially available DUV LED modules for sterilization use. For developing a commercially available device, the reproducibility, the uniformity of an AlN template and an AlGaN LED layer are required for obtaining a constant high EQE and a long device lifetime. To obtain the reproducibility for an AlN and an AlGaN layer is particularly difficult because the growth condition is very sensitive for a vapor-reaction between NH_3 and TMAl which are induced by a high-growth temperature (1200–1400 °C). Figure 4.37 shows (a) the location of 3 × 2 in. wafer on the carbon susceptor and (b) the uniformity of the FWHM of (0002) and (10–12) XRCs observed for an AlN template grown by a NH_3 pulsed-flow ML growth method on sapphire using a product type MOCVD. The fluctuation of the FWHM of XRCs in an AlN template on sapphire was within 5 %. Technique to obtain such a highly uniform template wafer is suitable for a product of commercial DUV LEDs. Figure 4.38 shows (a) a bird's eye view and (b) operating properties of a 270 nm 10 mW DUV LED module for an application to sterilization. We integrated 6 chips for the DUV LED module. A lifetime longer than 10,000 h under 30 % reduction condition has been already achieved for devices with EQE of 2 3 % [25, 26]. Figure 4.39 shows the digital camera image during operation of the DUV LED module shown in Fig. 4.38a. We can see the copy paper emits blue exited by the 270 nm DUV light from the LED.

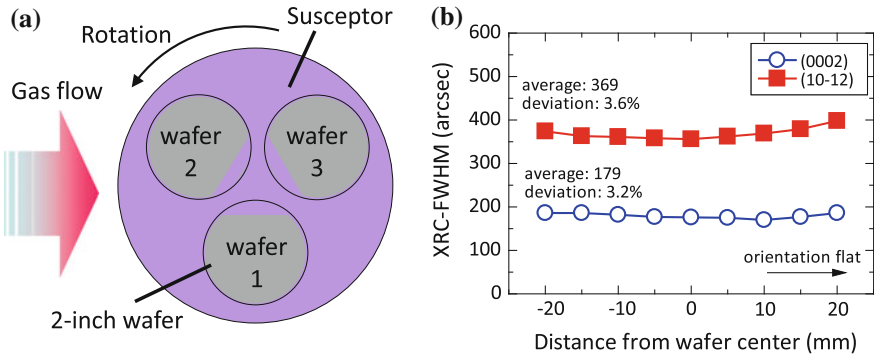


Fig. 4.37 **a** Location of 3 × 2 in. wafer on the carbon susceptor and **b** the uniformity of the FWHM of (0002) and (10–12) XRCs observed for an AlN template grown by a NH_3 pulsed-flow ML growth method on sapphire using a product type MOCVD

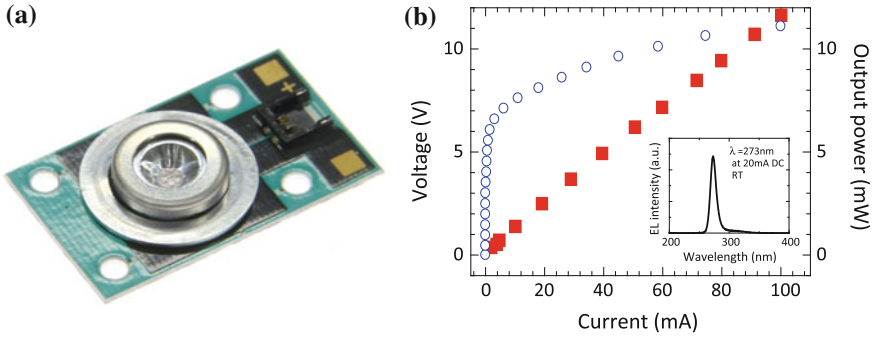


Fig. 4.38 **a** A bird's eye view and **b** operating properties of a commercially available 270 nm 10 mW DUV LED module for an application to sterilization developed by RIKEN and Panasonic

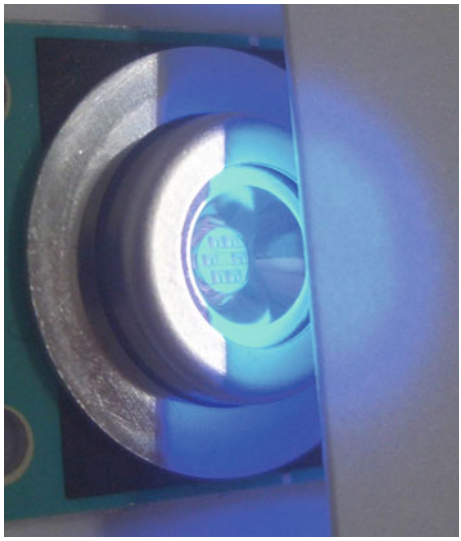


Fig. 4.39 A digital camera image during operation of the DUV LED module with a copy paper near the LED

4.7 Future LED Design for Obtaining High Light Extraction Efficiency (LEE)

The improvement in LEE is a particularly important for AlGaN DUV LEDs, because the LEE of AlGaN DUV LEDs is quite low (8–20 %) and efforts to improve the LEE are critical for future applications. However, increasing the LEE is quite challenging because of the lack of suitable transparent p-type contact layers, transparent p-type electrodes, and lack of highly reflective p-type electrodes in the DUV wavelength range.

Figure 4.40 shows schematic images of the improvement in LEE of an AlGaN DUV LED that can be achieved by replacing the conventional p-GaN

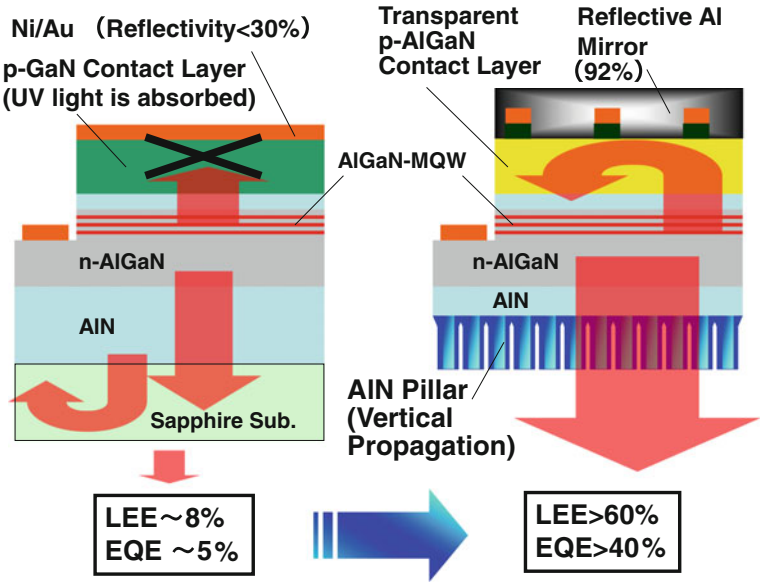


Fig. 4.40 Schematic images of the improvement in LEE of an AlGaN DUV LED by introducing a transparent p-AlGaN contact layer, a highly reflective p-type electrode, and a vertical light-propagation AlN pillar array

contact-layer structure by the novel LED structure proposed in this work [24]. In a conventional DUV LED, the QW top emission is completely absorbed by the p-GaN contact layer. The DUV emission toward the substrate is reflected by the sapphire/air interface (<16 % of the downward light is extracted and >84 % of the downward light is reflected mainly by a total internal reflection). As a result, the LEE of a conventional DUV LED is typically smaller than 8 %. Although we use an encapsulating technique, photonic nanostructures on the surface of sapphire substrates, and growth on patterns sapphire substrate (PSS), the LEE improvement is still limited (maximum LEE is expected to be around 20 %) due to the strong absorption of UV light in the p-GaN contact layer.

To realize high LEE, the combination of a transparent contact layer, a highly reflective p-type electrode, and a vertical light-propagation photonic structure is desirable. Recently, we have fabricated a DUV LED with a high-Al-content p-AlGaN contact layer. We found that the p-AlGaN can act as a highly transparent p-type contact layer. The reflectance of a conventional Ni/Au p-electrode is low (~25 %) and is not suitable as a highly reflective mirror. The reflectance of Al in DUV is 92 %, but ohmic contacts are difficult to obtain. The introduction of a mesh-type electrode with Al mirror windows is one of the solutions for a highly reflective p-type electrode, as shown on the right of Fig. 4.40. If the reflectivity of the p-type electrode is not sufficiently high (~80 %), a photonic structure with a vertical light-propagation property is required to extract the light with the minimum

number of reflections. In other words, an efficient light coupling into a photonic structure such as a pillar array is important for obtaining an efficient light extraction.

The LEE of an AlGaN DUV LED similar to our proposed structure was investigated by Ryu et al. [46] using finite-difference time-domain (FDTD) simulations. They also concluded from the calculation that the combination of a vertical LED geometry with a photonic nanostructure and a transparent p-AlGaN contact layer is important for obtaining high LEE in AlGaN DUV LEDs. They demonstrated that LEE of the vertical AlGaN DUV LED can be improved by an order of magnitudes, when the thickness of the p-GaN contact layer is reduced from 25 nm to zero. They also showed in their simulation that a maximum LEE as high as 72 % can be obtained for the transverse-electric (TE) mode, if a transparent p-AlGaN contact layer is introduced in the vertical LEDs. These simulation results are in good agreement with the LED structure that we propose.

We will demonstrate a very simple estimation of LEE for a proposed DUV LED. We assume that the equivalent reflectance for the upward-direction light is 80 %, which is determined by the reflectivity of a p-electrode and the absorption through a p-AlGaN contact layer. We also assume that the equivalent coupling coefficient of the downward light into a pillar array is 40 %. In other words, 40 % of the downward light can be extracted through the pillar array. Of course, they are average values taking into account all propagating light into every direction. At first, 50 % light is emitted from the QW toward the downward direction and 40 % light is reflected and returned by the p-electrode, then 90 % light reaches in front of a pillar array. The amount of light extraction through the pillar array in the first attempt is calculated to be 90 % × 0.4 = 36 %, whereas 54 % of the light is reflected by the pillar array. The amount of light extraction through the pillar array in the second attempt is calculated to be 54 % × 0.8 × 0.4 = 17.3 %. With the same approach, the percentages of light extraction are calculated for the third and fourth attempt to be 8.3 and 4 %, respectively. By integrating the amounts of the first- to the third-time extraction light, we can obtain a very high LEE of more than 61.6 %. The equivalent coupling coefficient of 40 % is considered to be reasonable by comparing with FDTD results. Through the above estimations, we can obtain high LEE with the minimum number of reflections.

We demonstrated a DUV LED with a highly transparent p-AlGaN contact layer. The LED structure used for the experiment is shown in Fig. 4.41. The emission wavelength of the QW was 277 nm, and the Al composition of the p-AlGaN contact layer was varied between 60 and 63 % (corresponding compositional wavelengths were 270 265 nm). Figure 4.42 shows the transparency of a high-Al-content Mg-doped p-AlGaN layer, grown on an AlGaN/AlN/sapphire template usually used for a DUV LED. We confirmed that the transparency of a 120 nm-thick p-AlGaN layer with an Al composition of 60 % is higher than 94 % for 279 nm DUV light, as measured using a spectrophotometer. The transparency of the p-AlGaN contact layer used for an actual DUV LED was estimated to be approximately 97 % taking into account the contact layer thickness (70 nm).

Figure 4.43 shows the current versus EQE (η_{ext}) characteristics of 277 nm AlGaN-MQW DUV LEDs with transparent p-AlGaN contact layers and a

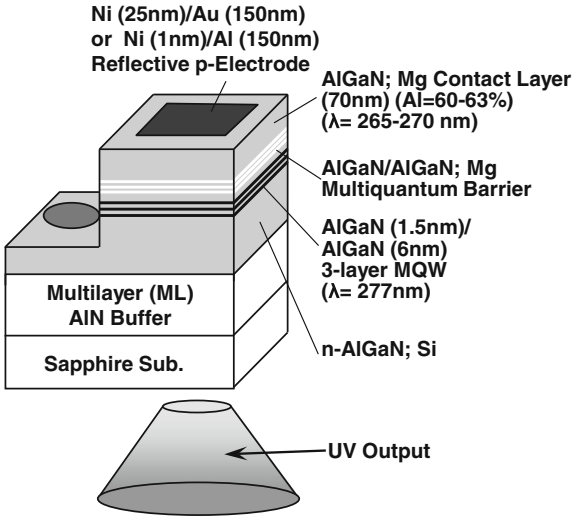


Fig. 4.41 Schematic structure of an AlGaN-QW DUV LED with a transparent p-AlGaN contact layer and a highly reflective Ni/Al p-electrode

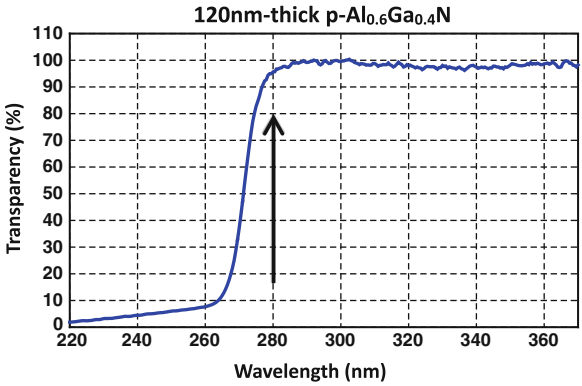


Fig. 4.42 Transparency of a high-Al-content Mg-doped p-AlGaN layer, grown on an AlGaN/AlN/sapphire template

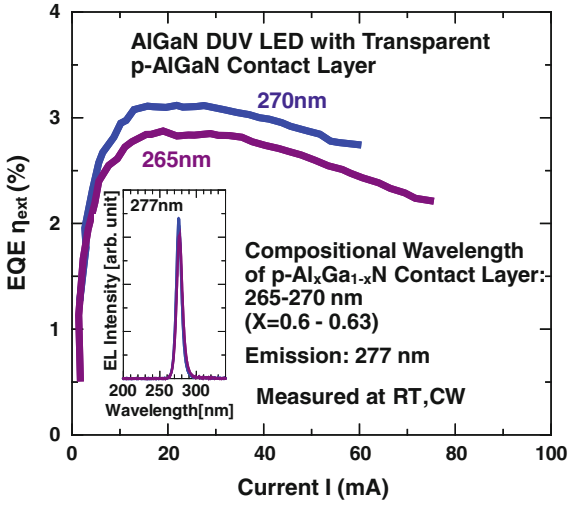


Fig. 4.43 Current versus EQE (η_{ext}) characteristics of 277 nm AlGaN-MQW DUV LEDs with transparent p-AlGaN contact layers and a conventional Ni/Au p-electrode, measured under RT cw operation

conventional Ni/Au p-electrode, measured under RT cw operation. We achieved the operation of DUV LEDs with high-Al-composition (60 63 %) p-AlGaN contact layers. The maximum EQEs that we obtained were 3.1 and 2.8 % for Al compositions of 60 and 63 %, respectively, of the p-AlGaN contact layer. We found that direct contact between high-Al-content p-AlGaN and a Ni/Au or a Ni/Al electrode is suitable for DUV LEDs, despite the very low hole concentration in p-AlGaN layers.

As a p-type electrode, we replaced the conventional Ni(25 nm)/Au(150 nm) with a highly reflective Ni(1 nm)/Al(150 nm). Current injection was made possible by inserting a very thin Ni layer (<1 nm) between the Al layer and the p-AlGaN layer. Figure 4.44 shows the wavelength dependent of the reflectivity for various type p-type electrodes used for AlGaN DUV LEDs. In the actual 270 nm DUV LED devices, the reflectivity of the p-type electrode was increased from 30 to 64 % by replacing the conventional Ni(25 nm)/Au(150 nm) electrode with a Ni(1 nm)/Al (150 nm) electrode.

Figure 4.45 shows the current vs EQE (η_{ext}) characteristics of 279 nm AlGaN-MQW DUV LEDs with transparent p-AlGaN contact layers, comparing them with conventional Ni(25 nm)/Au(150 nm) and highly reflective Ni(1 nm)/Al (150 nm) p-electrodes measured under RT cw operation. EQE was significantly increased from 4 to 7 % (by 1.7 times) owing to the increase in LEE induced by replacing the conventional Ni/Au p-electrode with a highly reflective Ni/Al electrode. We can estimate that the transparency of the p-AlGaN contact layer is higher than 95 % from the enhancement factor of LEE. The LEE enhancement factors that were achieved in 265 279 nm DUV LEDs by replacing the Ni/Au p-electrode with the highly reflective Ni/Al electrode were approximately 1.3 1.7.

The increase in the forward voltage (Vf) when a Ni/Au p-electrode was replaced with a Ni/Al electrode was negligibly small.

We observed an increase in the Vf when p-GaN was replaced with a transparent p-AlGaN contact layer. Vf at an injection current of 5 mA increased from 11 V to 17 V for a bare wafer DUV LED when the contact layer was changed from p-GaN

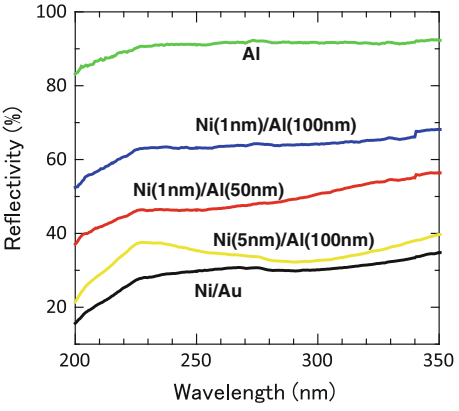


Fig. 4.44 Wavelength dependent of the reflectivity for various type p-type electrodes for AlGaN DUV LEDs

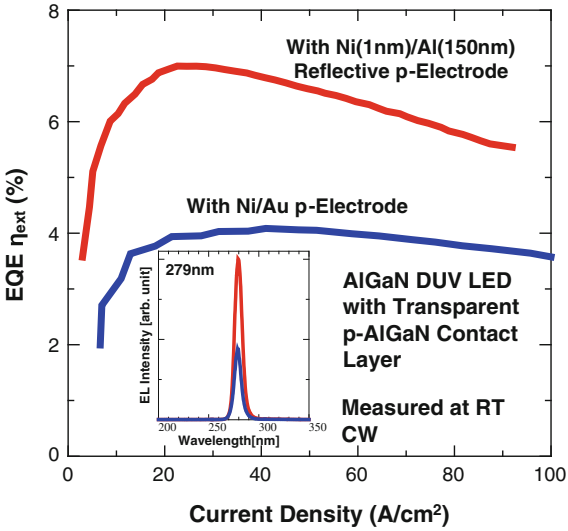


Fig. 4.45 Current versus EQE (η_{ext}) characteristics of 279 nm AlGaN-MQW DUV LEDs with transparent p-AlGaN contact layers in comparison with conventional Ni/Au and highly reflective Ni/Al p-electrodes, measured under RT cw operation

to p-AlGaN. Therefore, the high resistivity of p-contacts caused by the low hole concentration is still a problem for the use of p-AlGaN contact layers. The increase in Vf causes a reduction in the wall-plug efficiency (WPE) of the device. We aim to improve Vf by using mesh-type p-electrodes, as we proposed in Fig. 4.40.

To achieve high LEE, we are developing a connected pillar AlN buffer on a patterned sapphire substrate (PSS). Figure 4.46 shows (a) a scanning electron microscopy (SEM) image of the surface of the PSS, (b) an optical microscopy surface image and (c) an SEM bird's-eye view of an AlN pillar array, and (d) an SEM bird's-eye view of a connected pillar AlN buffer layer. The period of the triangular lattice of the PSS used in this experiment was around 3 μm. The PSS was fabricated by nano-imprinting and an inductively coupled plasma (ICP) dry-etching technique. We have succeeded in growing high-aspect-ratio hexagonal AlN pillar arrays on PSS under high-temperature and low-V/III-ratio growth conditions. The use of such a pillar array structure would be quite effective for obtaining high LEE in DUV LEDs. The AlN pillar array was embedded in a flat surface by an over-growth process under low-V/III-ratio growth conditions, as shown in Fig. 4.46d. We have fabricated a 270 nm DUV LED on a connected pillar AlN buffer, and obtained a maximum EQE of 0.4 % and a cw output power of 5 mW. We are trying to improve the efficiency of the LEDs by improving the surface roughness of the pillar buffer.

We need the remove the sapphire wafer to fabricate the high LEE LED structure shown in Fig. 4.40. The process of removing the sapphire from the AlN layer by a laser lift-off (LLO) method is not very suitable for high-efficiency devices because of the damage it induces in the epitaxial layers. However, for AlGaN-based DUV LEDs on silicon, the Si substrate can be easily removed from nitride epilayers by

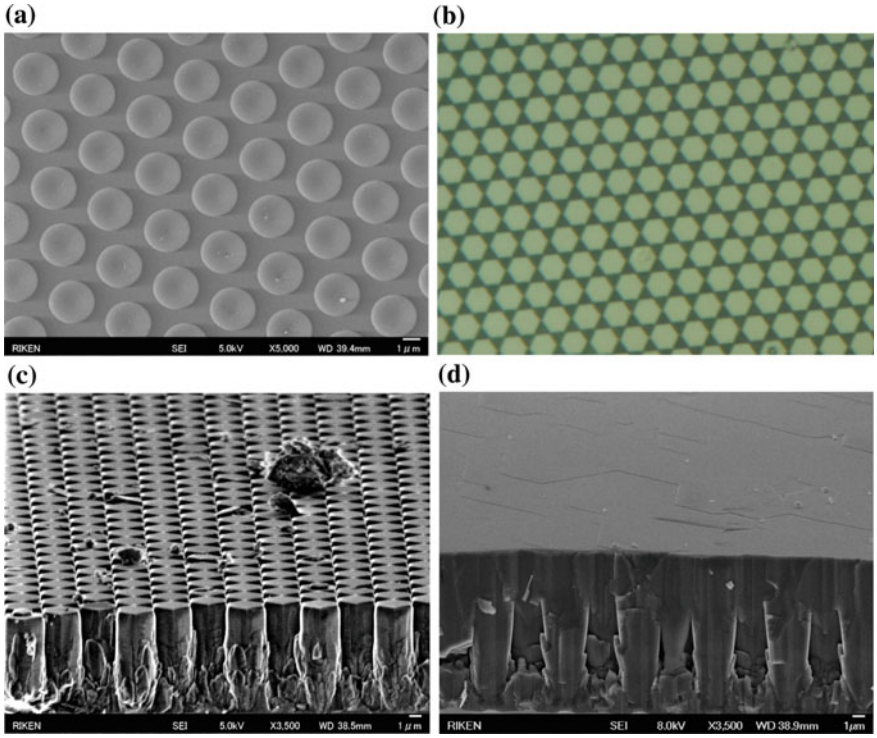


Fig. 4.46 **a** SEM image of the surface of a PSS, **b** optical microscopy surface image and **c** SEM bird's-eye view of an AlN pillar array grown on the PSS, and **d** SEM bird's-eye view of a pillar AlN buffer layer fabricated by lateral overgrowth

wet-chemical etching. The use of a Si substrate is one of the solutions for the damage-free removal of the substrate. The fabrication of a DUV LED on a Si wafer has also other advantages, i.e., large-area and low-cost devices are possible, and a vertical LED structure is easily fabricated by removing the Si substrate. However, the crystal growth of AlN buffer layers on Si substrates is relatively difficult owing to the generation of surface cracks caused by the fact that the thermal expansion coefficient of Si is much smaller than that of AlN.

We have developed AlGaN and quaternary InAlGaN DUV LEDs on Si substrates [47, 48]. To obtain a crack-free AlN buffer layer on a Si substrate, we fabricated AlN layers by the ELO method [48]. Figure 4.47 shows (a) a cross-sectional SEM image of an ELO AlN buffer layer on Si and (b) the structure and spectrum of a DUV LED fabricated on an ELO AlN-on-Si substrate. We have succeeded in the first demonstration of a DUV LED fabricated on a Si substrate. The emission wavelength of the LED was 256 nm under RT cw operation [48]. We are planning to realize the proposed structure as shown in Fig. 4.40 by introducing these techniques, with the aim of achieving a marked improvement in LEE for

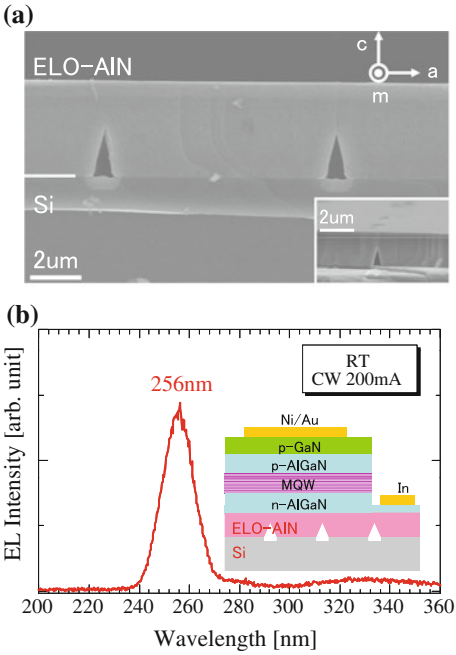


Fig. 4.47 **a** Cross-sectional SEM image of an ELO AlN buffer layer on Si and **b** structure and spectrum of a DUV LED fabricated on ELO AlN on a Si substrate

DUV LEDs. We hope that the application of such devices to fields involving sterilization will be widely expanded through the achievement of high-efficiency DUV LEDs in the near future.

4.8 Summary

We reported on the recent progress in the performance of AlGaN-based DUV LEDs, which has been achieved by the development of crystal growth techniques for wide-bandgap AlN and AlGaN. Significant increases in IQE have been accomplished for AlGaN-QW DUV emissions by using low-TDD AlN on sapphire grown by an NH_3 pulsed-flow multilayer growth method. 222 351 nm DUV LEDs have been demonstrated using the high IQE emission layers. The EIE of DUV LEDs was significantly increased by controlling the electron flow using an MQB. We also demonstrated the improvement of LEE by using a transparent p-AlGaN contact layer and a highly reflective p-electrode. The maximum EQE obtained was 7 % for a 279 nm DUV LED. EQE could be increased up to several tens of percent in the near future by improving LEE by utilizing transparent contact layers and pillar array buffer layers.

References

1. A. Zukauskas, M.S. Shue, R. Gaska, *Introduction to Solid-State Lighting* (Wiley, New York, 2002)
2. H. Hirayama, J. Appl. Phys. **97**, 091101 (2005)
3. J. Han, M.H. Crawford, R.J. Shul, J.J. Figiel, M. Banas, L. Zhang, Y.K. Song, H. Zhou, A.V. Nurmikko, Appl. Phys. Lett. **73**, 1688 (1998)
4. A. Kinoshita, H. Hirayama, M. Ainoya, A. Hirata, Y. Aoyagi, Appl. Phys. Lett. **77**, 175 (2000)
5. T. Nishida, H. Saito, N. Kobayashi, Appl. Phys. Lett. **78**, 711 (2001)
6. W.H. Sun, V. Adivarahan, M. Shatalov, Y. Lee, S. Wu, J.W. Yang, J.P. Zhang, M.A. Khan, Jpn. J. Appl. Phys. **43**, L1419 (2004)
7. V. Adivarahan, S. Wu, J.P. Zhang, A. Chitnis, M. Shatalov, V. Madavilli, R. Gaska, M.A. Khan, Appl. Phys. Lett. **84**, 4762 (2004)
8. V. Adivarahan, W.H. Sun, A. Chitnis, M. Shatalov, S. Wu, H.P. Maruska, M. Asif Khan, Appl. Phys. Lett. **85**, 2175 (2004)
9. Y. Taniyasu, M. Kasu, T. Makimoto, Nature **444**, 325 (2006)
10. H. Hirayama, Y. Enomoto, A. Kinoshita, A. Hirata, Y. Aoyagi, Appl. Phys. Lett. **80**, 37 (2002)
11. H. Hirayama, A. Kinoshita, T. Yamabi, Y. Enomoto, A. Hirata, T. Araki, Y. Nanishi, Y. Aoyagi, Appl. Phys. Lett. **80**, 207 (2002)
12. H. Hirayama, Y. Enomoto, A. Kinoshita, A. Hirata, Y. Aoyagi, Appl. Phys. Lett. **80**, 1589 (2002)
13. H. Hirayama, K. Akita, T. Kyono, T. Nakamura, K. Ishibashi, Jpn. J. Appl. Phys. **43**, L1241 (2004)
14. S. Fujikawa, T. Takano, Y. Kondo, H. Hirayama, Jpn. J. Appl. Phys. **47**, 2941 (2008)
15. H. Hirayama, T. Yatabe, N. Noguchi, T. Ohashi, N. Kamata, Appl. Phys. Lett. **91**, 071901 (2007)
16. H. Hirayama, T. Yatabe, T. Ohashi, N. Kamata, Phys. Status Solidi C **5**, 2283 (2008)
17. H. Hirayama, N. Noguchi, S. Fujikawa, J. Norimatsu, T. Takano, K. Tsubaki, N. Kamata, Phys. Status Solidi A **206**, 1176 (2009)
18. H. Hirayama, Y. Tsukada, T. Maeda, N. Kamata, Appl. Phys. Express **3**, 031002 (2010)
19. H. Hirayama, N. Noguchi, T. Yatabe, N. Kamata, Appl. Phys. Express **1**, 051101 (2008)
20. H. Hirayama, N. Noguchi, N. Kamata, Appl. Phys. Express **3**, 032102 (2010)
21. S. Fujikawa, H. Hirayama, N. Maeda, Phys. Status Solidi C **9**(3–4), 790–793 (2012)
22. N. Maeda, H. Hirayama, Phys. Status Solidi C **10**, 1521 (2014)
23. H. Hirayama, N. Maeda, S. Fujikawa, S. Toyoda, N. Kamata, Optronics **2**, 58 (2014)
24. H. Hirayama, N. Maeda, S. Fujikawa, S. Toyota, N. Kamata, Recent progress and future prospects of AlGaN-based high-efficiency deep-ultraviolet light-emitting diodes. Jap. J. Appl. Phys. (Selected Topic) **53**, 100209 1–10 (2014)
25. T. Mino, H. Hirayama, T. Takano, N. Noguchi, K. Tsubaki, Phys. Status Solidi C **9**, 749 (2012)
26. T. Mino, H. Hirayama, T. Takano, K. Tsubaki, M. Sugiyama, Proc. SPIE **8625**, 59 (2013)
27. M. Shatalov, W. Sun, Y. Bilenko, A. Sattu, X. Hu, J. Deng, J. Yang, M. Shur, C. Moe, M. Wraback, R. Gaska, Appl. Phys. Express **3**, 062101 (2010)
28. J. Mickevičius, G. Tamulaitis, M. Shur, M. Shatalov, J. Yang, R. Gaska, Appl. Phys. Lett. **103**, 011906 (2013)
29. M. Shatalov, W. Sun, A. Lunev, X. Hu, A. Dobrinsky, Y. Bilenko, J. Yang, Appl. Phys. Express **5**, 082101 (2012)
30. J.R. Grandusky, J. Chen, S.R. Gibb, M.C. Mendrick, C.G. Moe, L. Rodak, G.A. Garrett, M. Wraback, L.J. Schowalter, Appl. Phys. Express **6**, 032101 (2013)
31. J.R. Grandusky, S.R. Gibb, M.C. Mendrick, C. Moe, M. Wraback, L.J. Schowalter, Appl. Phys. Express **4**, 082101 (2011)

32. T. Kinoshita, K. Hironaka, T. Obata, T. Nagashima, R. Dalmau, R. Schlesser, B. Moody, J. Xie, S. Inoue, Y. Kumagai, A. Koukitu, Z. Sitar, Appl. Phys. Express **5**, 122101 (2012)
33. T. Kinoshita, T. Obata, T. Nagashima, H. Yanagi, B. Moody, S. Mita, S. Inoue, Y. Kumagai, A. Koukitu, Z. Sitar, Appl. Phys. Express **6**, 092103 (2013)
34. C. Pernot, M. Kim, S. Fukahori, T. Inazu, T. Fujita, Y. Nagasawa, A. Hirano, M. Ippommatsu, M. Iwaya, S. Kamiyama, I. Akasaki, H. Amano, Appl. Phys. Express **3**, 061004 (2010)
35. S. Hwang, D. Morgan, A. Kesler, M. Lachab, B. Zhang, A. Heidari, H. Nazir, I. Ahmad, J. Dion, Q. Fareed, V. Adivarahan, M. Islam, A. Khan, Appl. Phys. Express **4**, 032102 (2011)
36. A. Fujioka, T. Misaki, T. Murayama, Y. Narukawa, T. Mukai, Appl. Phys. Express **3**, 041001 (2010)
37. M. Ippommatsu, Optronics **2**, 71 (2014)
38. H. Yoshida, Y. Yamashita, M. Kuwabara, H. Kan, Appl. Phys. Lett. **93**, 241106 (2008)
39. K. Iida, T. Kawashima, A. Miyazaki, H. Kasugai, A. Mishima, A. Honshio, Y. Miyake, M. Iwaya, S. Kamiyama, H. Amano, I. Akasaki, Jpn. J. Appl. Phys. **43**, L499 (2004)
40. T. Takano, Y. Narita, A. Horiuchi, H. Kawanishi, Appl. Phys. Lett. **84**, 3567 (2004)
41. K. Ban, J. Yamamoto, K. Takeda, K. Ide, M. Iwaya, T. Takeuchi, S. Kamiyama, I. Akasaki, H. Amano, Appl. Phys. Express **4**, 052101 (2011)
42. R.G. Banal, M. Funato, Y. Kawakami, Phys. Rev. B **79**, 121308(R) (2009)
43. H. Kawanishi, M. Senuma, M. Yamamoto, E. Niikura, T. Nukui, Appl. Phys. Lett. **89**, 081121 (2006)
44. K. Iga, H. Uenohara, F. Koyama, Electron. Lett. **22**, 1008 (1986)
45. K. Kishino, A. Kikuchi, Y. Kaneko, I. Nomura, Appl. Phys. Lett. **58**, 1822 (1991)
46. H.Y. Ryu, I.G. Choi, H.S. Choi, J.I. Shim, Appl. Phys. Express **6**, 062101 (2013)
47. S. Fujikawa, H. Hirayama, Appl. Phys. Express **4**, 061002 (2011)
48. T. Mino, H. Hirayama, T. Takano, K. Tsubaki, M. Sugiyama, Appl. Phys. Express **4**, 092104 (2011)

Chapter 5
Impacts of Dislocations and Point Defects on the Internal Quantum Efficiency of the Near-Band-Edge Emission in AlGaN-Based DUV Light-Emitting Materials

Shigefusa F. Chichibu, Hideto Miyake, Kazumasa Hiramtsu and Akira Uedono

Abstract In this chapter, we show the impact of point defects rather than threading dislocations (TDs) on the emission dynamics of the near-band-edge (NBE) excitonic luminescence in AlN and high AlN mole fraction (x) $Al_xGa_{1-x}N$ alloy films using deep ultraviolet (DUV) time-resolved luminescence and positron annihilation measurements. The extreme radiative nature of excitons in AlN is identified, as the radiative lifetime (τ_R) for a free excitonic emission was determined to be as short as 11 ps at 7 K and 180 ps at 300 K, which are the shortest ever reported for the spontaneous emission in bulk semiconductors. However, apparent τ_R increased to 530 ps at 7 K with increasing impurity and Al-vacancy (V_{Al}) concentrations irrespective of the TD density. The result reflects the contribution of bound exciton components. A continuous decrease in τ_R with increasing temperature up to 200 K of heavily impurity-doped samples reflects a carrier release from band-tail states. The room temperature (RT) τ_R of $Al_xGa_{1-x}N$ alloys of high x was

S.F. Chichibu (✉)
Institute of Multidisciplinary Research for Advanced Materials,
Tohoku University, 2-1-1 Katahira, Aoba, Sendai 980-8577, Japan
e-mail: chichibulab@yahoo.co.jp

H. Miyake · K. Hiramtsu
Department of Electrical and Electronic Engineering, Mie University,
Tsu 514-8507, Japan
e-mail: miyake@elec.mie-u.ac.jp

K. Hiramtsu
e-mail: hiramatu@elec.mie-u.ac.jp

A. Uedono
Division of Applied Physics, Faculty of Pure and Applied Science,
University of Tsukuba, Tsukuba, Ibaraki 305-8573, Japan
e-mail: uedono.akira.gb@u.tsukuba.ac.jp

© Springer International Publishing Switzerland 2016

M. Kneissl and J. Rass (eds.), *III-Nitride Ultraviolet Emitters*,
Springer Series in Materials Science 227, DOI 10.1007/978-3-319-24100-5_5

nevertheless as short as a few ns at 300 K. The results essentially indicate an excellent radiative performance. Finally, the impact of Si-doping and the resulting cation vacancy formation on the nonradiative lifetime (τ_{NR}) of the NBE emission in $Al_{0.6}Ga_{0.4}N$ films are discussed.

5.1 Introduction

High AlN mole fraction (x) $Al_xGa_{1-x}N$ alloys have attracted considerable interest for applications in UV-C ($\lambda \leq 280$ nm) deep ultraviolet (DUV) light-emitting diodes (LEDs) [1–3], e-beam pumped UV sources [4, 5], and laser diodes. Recently, epitaxial growths of low threading dislocation (TD) density ($\leq 10^8$ cm^2) $Al_xGa_{1-x}N$ films have become possible, even for x higher than 0.6, using a variety of AlN templates on (0001) Al_2O_3 [1–6] and freestanding AlN substrates [7, 8]. However, the external quantum efficiency (η_{ext}) of DUV LEDs is still limited at the maximum of 10 % [1–3].

As η_{ext} is a product of internal quantum efficiency (η_{int}), carrier injection efficiency (η_{inj}), and light extraction efficiency (η_{lee}), all of them must be improved. Among these, η_{int} is a fraction of radiative rate over the sum of radiative and nonradiative rates, i.e., $\eta_{int} = (1 + \tau_R/\tau_{NR})^{-1}$, where τ_R and τ_{NR} are the radiative and nonradiative lifetimes, respectively. To increase η_{int}, short τ_R and long τ_{NR} are preferable. In general, quantum well (QW) structures are used to shorten τ_R by increasing the wavefunction overlap of electron–hole (e–h) pairs. In addition, the concentration of nonradiative recombination centers (NRCs) must be decreased to elongate τ_{NR} at elevated temperatures.

The authors have studied the impacts of point defects on the emission dynamics in (Al, Ga, In)N compounds and alloys using a combination of time-resolved photoluminescence (TRPL) and positron annihilation spectroscopy (PAS), and the origin of NRCs in GaN has been assigned to defect complexes containing Ga vacancies (V_{Ga}) such as V_{Ga}–X, where X is unidentified yet [9, 10]. In particular for $Al_xGa_{1-x}N$ alloys, Polyakov et al. [11], Bradley et al. [12], Onuma et al. [13], and Hashizume et al. [14] have independently investigated electrically and optically active native defects having midgap states using photoluminescence (PL) [11, 13], cathodoluminescence (CL) [12, 13], TRPL [13], PAS [13], and the combination of X-ray photoelectron spectroscopy and junction capacitance method [14, 15].

Meanwhile, η_{inj} to an active region can be increased by increasing conductivities of p- and n-type layers keeping a balance between the electron and hole concentrations. Accordingly, high-concentration doping of donor- or acceptor impurities with minimal defect formation is mandatory, because impurity doping is known to generate certain native defects having their counter-charge due to the Fermi-level effect [16–22], and such defects may diffuse into the active region. To obtain low resistivity n-type $Al_xGa_{1-x}N$ by Si-doping, extensive studies have been carried out with emphasis on the growth conditions of metalorganic vapor phase epitaxy

(MOVPE) [23, 24], exciton localization [25], changes in the RT PL spectra [26, 27], PAS [28, 29], and estimation of η_{int} [30]. One of the additional serious problems of heavy impurity doping is the overcompensation, which will be discussed later.

As very low TD and structural defect density AlN templates and substrates became available, exploring intrinsic influences of point defects on the nonradiative carrier recombination and positron annihilation became possible. Consistent with the calculated results that the formation energy (E_{Form}) of Al vacancies (V_{Al}) in AlN is very low and even negative [31] in *n*-type materials; V_{Al} has been found to be the major vacancy defect in AlN [32] and $Al_xGa_{1-x}N$ alloys ($x \neq 0$) [29]. Therefore, impacts of point defects introduced by impurity doping on the recombination dynamics of the NBE emission in AlN and $Al_xGa_{1-x}N$ must be studied carefully, as V_{Al}-complexes may also act as NRCs. However, due to limited availability of a desirable DUV femtosecond excitation source, only a few papers [33–39] have dealt with the emission dynamics of (Al, Ga, In)N in UV-C range. The authors have been studying the recombination dynamics of excitons in unintentionally doped (UID) AlN and AlGaN alloys using DUV TRPL [34–38] and time-resolved cathodoluminescence (TRCL) measurements [35–39].

Although electron concentrations *n* exceeding 10^{19} cm^{-3} without deactivation have been reported for Si- or Ge-doped GaN [40], the overcompensation issue of Si is significant in $Al_xGa_{1-x}N$ alloys. Shimahara et al. [24] have reported that *n* in $Al_{0.6}Ga_{0.4}N$ films first increased with the increase in the doping concentration of Si, [Si], up to approximately 10^{18} cm^{-3}, then saturated, and eventually decreased to 5×10^{17} cm^{-3} for [Si] = 4×10^{18} cm^{-3}. Uedono et al. [29] have studied these samples by PAS using a monoenergetic positron (e^+) beam line to detect V_{Ga}, V_{Al}, and their complexes. They have observed simultaneous increase in cation vacancy (V_{III}) concentration, [V_{III}], with [Si], and reported that the major defect species was V_{Al} [29]. Such an overcompensation phenomenon is commonly seen in III–V and II–VI semiconductors. For example, overcompensation of heavily doped Si donors on Ga sites (Si_{Ga}) in GaAs has been attributed to the formation of a defect complex with V_{Ga}, such as V_{Ga}–Si_{Ga} [41–43]. Therefore, it is likely that V_{III}–Si_{III} defect complexes, especially on Al site (V_{Al}–Si_{III}), are formed in $Al_{0.6}Ga_{0.4}N$:Si.

In this chapter, we show the impact of point defects rather than TDs on the emission dynamics of the NBE excitonic luminescence in AlN and $Al_xGa_{1-x}N$ alloy films with high *x* using DUV TRPL, TRCL, and PAS measurements. Extremely radiative nature of AlN is identified, as the radiative lifetime (τ_R) under weak excitation regime for a free excitonic emission was determined to be as short as 180 ps at 300 K, which is the shortest ever reported for the spontaneous emission in bulk semiconductors. However, apparent τ_R increased with the increase in impurity and V_{Al} concentrations up to 530 ps at 7 K, irrespective of the TD density. The result may reflect the contribution of bound exciton components. Continuous decrease in τ_R with temperature rise up to 200 K of heavily impurity-doped samples reflects a carrier release from band-tail states. The τ_R values at RT of $Al_xGa_{1-x}N$ alloys with high *x* were nevertheless as short as a few ns at 300 K. The results essentially indicate an excellent radiative performance. Finally, impacts of

Si-doping and resultant cation vacancy formation on the nonradiative lifetime (τ_{NR}) of the NBE emission in $Al_{0.6}Ga_{0.4}N$ films are discussed.

5.2 Experimental Details

For studying the emission dynamics in AlN [34, 35, 37], approximately 2-μm-thick epilayers were grown by low-pressure MOVPE using trimethylaluminium (TMAl) and ammonia (NH_3). The *c*-plane AlN films (sample ID numbers A1–A5) were grown on a *c*-plane Al_2O_3 substrate, and an *m*-plane AlN film (ID number A6) was grown on an *m*-plane freestanding GaN (FS-GaN) substrate [44]. The TD densities having edge components (N_E) were 2×10^8 cm^{-2} for A1, 1×10^9 cm^{-2} for A2 and A6, 3×10^9 cm^{-2} for A4 and A5, and 1×10^{10} cm^{-2} for A3. The growth temperatures (T_g) were 1500 °C for A1 and 1350 °C for A2 and A3. These samples are classified as high-temperature (HT) grown (HTG) samples. Their Si, C, and O concentrations were below the detection limit of secondary-ion-mass spectrometry (SIMS) ([Si] < 5×10^{17}, [C] < 10^{17}, and [O] < 5×10^{17} cm^{-3}, respectively). The low-temperature (LT) grown (LTG) samples A4 and A5 were grown at 1200 °C. The sample A6 was grown at 1120 °C to prevent FS-GaN from decomposing. Among these, A5 contained high-concentration impurities ([Si] = [C] = 4×10^{19} cm^{-3} and [O] = 2×10^{19} cm^{-3}). Those concentrations in A4 and A6 were an order of magnitude lower than A5 [35, 37]. All AlN epilayers exhibited monolayer or bilayer atomic step lines on their surface (Table 5.1).

Table 5.1 List of AlN samples (after [35, 37])

ID#	T_g (°C)		Substrate	N_E (cm^{-2})	Impurity concentrations (cm^{-3})	Remarks
A1	>1500	HTG	*c*-plane Al_2O_3	2×10^8	Lower than detection limits	Strong compressive stress
					[Si] < 5×10^{17}	
A2	1350		*c*-plane Al_2O_3	1×10^9	[C] < 10^{17}	
A3	1350		*c*-plane Al_2O_3	1×10^{10}	[O] < 5×10^{17}	Mostly relaxed high TD density
A4	1200	LTG	*c*-plane Al_2O_3	3×10^9	Lower than A5	
A5	1200		*c*-plane Al_2O_3	3×10^9	[Si] = 4×10^{19}	High impurity concentration
					[C] = 4×10^{19}	
					[O] = 2×10^{19}	
A6	1120		*m*-plane GaN	1×10^9	Lower than A5	*m*-plane

For studying the emission dynamics in $Al_xGa_{1-x}N$ alloys of high x [36], approximately 1.3-μm-thick (0001) epilayers (x = 0.65, 0.89, and 0.97) were grown at T_g = 1120–1200 °C and 2.0 × 10^4 Pa by MOVPE on a 1-μm-thick AlN epitaxial template [6], which was grown on a (0001) Al_2O_3 substrate. They can be classified as LTG samples. Trimethylgallium (TMGa), TMAl, and NH_3 were used as the precursors. The N_E values were estimated from the full-width at half-maximum (FWHM) for the {10–12} X-ray ω-rocking curve (1200–1500 arcsec) using the relation given in [45] to be 2–3 × 10^9 cm^{-2}. The TD densities having pure screw components (N_S) were estimated to be lower than 2–6×10^7 cm^{-2}. The epilayers were characterized using the X-ray reciprocal space mapping (X-RSM) method to be partially relaxed against the AlN template. The x values were calculated from the in-plane and out-of-plane lattice parameters and the degree of relaxation using the relation similar to that given in [46].

For studying the impact of Fermi-level effects [16–22] on the emission dynamics in $Al_xGa_{1-x}N$ alloys of high x, approximately 0.8-μm-thick (0001) Si-doped $Al_{0.6}Ga_{0.4}N$ epilayers ($Al_{0.6}Ga_{0.4}N$:Si) were grown at T_g = 1180–1200 °C and 6.7 × 10^3 Pa by MOVPE on a 0.8-μm-thick AlN epitaxial template [6]. Monomethylsilane (CH_3SiH_3) gas was used to control [Si] in the solid phase from 2 × 10^{16} to 4 × 10^{18} cm^{-3}, the values being quantified by SIMS measurement. All the samples were confirmed by X-RSM method to be coherently grown on the template. The N_E values have been estimated to be about 3 × 10^8 cm^{-2}. Details of the growth have been given in [24].

Steady-state wide-area CL was excited using an electron beam (e^--beam) operated at 3.5 kV acceleration voltage (V_{acc}) and 1.0 × 10^{-2} A/cm^2 probe current density. Corresponding excited carrier concentration is estimated to be 2 × 10^{18} cm^{-3}. Approximately 200 fs pulses of a frequency-quadrupled (4ω) mode-locked Al_2O_3:Ti laser [34–37] were used for the TRPL measurement. The wavelength and power density were approximately 200 nm and 40 nJ/cm^2 a pulse, respectively. The maximum electron–hole (e–h) pair concentration is estimated to be 4 × 10^{15} cm^{-3} during the pulse. For measuring macro-area TRCL signals, we constructed a femtosecond excitation photoelectron gun (PE-gun) similar to [47]. It was composed of a 15-nm-thick rear-excitation configuration Au film, extraction electrodes, and acceleration electrodes to give V_{acc}, as shown in Fig. 5.1. The Au film was excited using the frequency-tripled (3ω) pulses of the Al_2O_3:Ti laser (240–260 nm, 100 fs, 1 μJ/cm^2 per pulse). The distance between the PE-gun and the sample was 52.5 mm. The quantum efficiency of the PE-gun was approximately 2.5 × 10^{-6} electrons/photon for V_{acc} = 10 kV, and the current density was 1.8 pA/cm^2 during the pulse. The corresponding excitation density for TRPL case was approximately 10 nJ/cm^2.

The spatio-time-resolved cathodoluminescence (STRCL) system [48, 49] equipped with a PE-gun driven by 200 fs pulses of a 3ω mode-locked Al_2O_3:Ti laser was used to measure micro-area CL lifetimes for the NBE emission as a function of temperature, T. Typical V_{acc} was 6.5 kV and approximately 1.5 electrons per pulse were injected. Using these conditions, about 650 e–h pairs were generated in case of $Al_{0.6}Ga_{0.4}N$ alloy films. The excitation intensities for both TRPL and TRCL were low enough to maintain weak excitation conditions. The

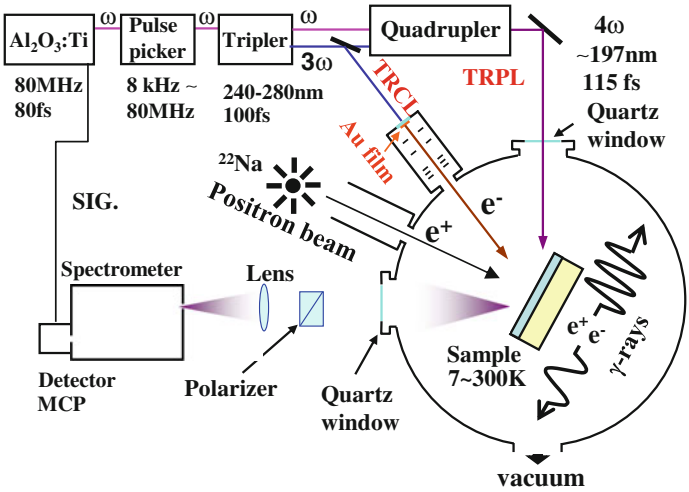


Fig. 5.1 Schematic drawing of TRPL, TRCL, and PAS measurement system (after [35, 37]. Copyright 2010 and 2013, AIP Publishing LLC)

energy-resolved TRPL and TRCL signals were acquired using a streak camera, of which temporal resolution was 7–10 ps.

In order to correlate τ_R and τ_{NR} with [V_{III}], PAS [50, 51] was carried out using the monoenergetic e^+-beam line [29, 32]. Here, S parameter [9, 10, 13, 28, 29, 32, 35, 38, 43, 50, 51] for the Doppler-broadening spectrum of e^+–e^- annihilating γ-rays is used as the measure of concentration or size of negatively charged V_{III}-defects [29, 32, 50, 51]. Details of the measurement and analysis are given in [29].

5.3 Impacts of Impurities and Point Defects on the Near-Band-Edge Luminescence Dynamics of AlN

Room temperature and low temperature macro-area CL spectra of the AlN epilayers (A1–A6) are shown in Fig. 5.2a, b, respectively. As shown, the spectra for HTG samples are characterized [52] by sharp excitonic peaks and weak broad emission bands between 2.5 and 4.2 eV that are originating from V_{Al}-impurity complexes [53–56]. The spectra for LTG samples, in contrast, are characterized by intense deep-state emission bands and a broad NBE emission band. The NBE peak energies for A5 and A6 were approximately 200 meV lower than the bandgap energy (E_g) [57]. Because LTG samples are contaminated with Si, O, and C, the results suggest the formation of a band tail. However, we note that their spectral feature was not really characterized by N_E.

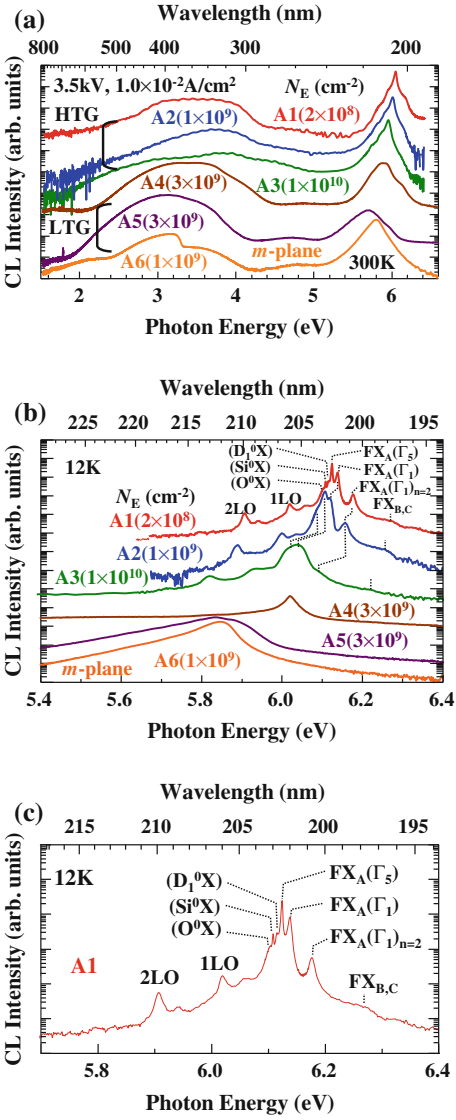


Fig. 5.2 Steady-state CL spectra of AlN epilayers measured at **a** 300 and **b, c** 12 K. The N_E values are shown in parentheses. FX, I_2, and LO mean-free exciton, neutral donor bound exciton, and LO phonon replica, respectively (after [34, 35]. Copyright 2010, AIP Publishing LLC)

As shown in the magnified CL spectrum in Fig. 5.2c, the best quality sample A1 exhibited four free excitonic peaks or shoulders. The sample A1 has been measured to have strong in-plane compressive stress [34, 52], and the blue-shifted emissions are assigned to the recombination of free B- and C-excitons ($FX_{B,C}$) at 6.27 eV, the first excited states of free A-excitons of irreducible representation Γ_1 [$FX_A(\Gamma_1)_{n=2}$] at 6.1768 eV, the ground state free A-excitons of Γ_1-symmetry [$FX_A(\Gamma_1)$] at 6.1383 eV, and free A-excitons of Γ_5-symmetry [$FX_A(\Gamma_5)$] at 6.1243 eV, in order of decreasing photon energy. In addition, three emission peaks due to the

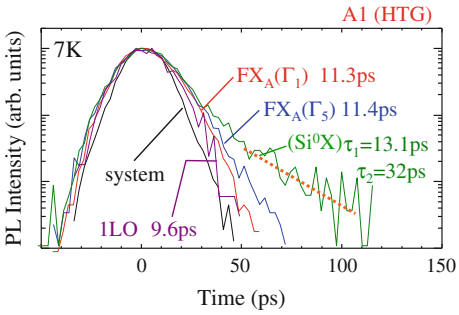


Fig. 5.3 Energy-resolved TRPL signals for FX$_A$(Γ_1), FX$_A$(Γ_5), (Si^{0}X), and an LO phonon replica of FX$_A$(Γ_5) peaks in A1 at 7 K (after [34]. Copyright 2010, AIP Publishing LLC)

recombination of excitons bound to an unknown neutral donor (D_1^0X), those bound to neutral silicon (Si^{0}X) [58], and bound to neutral oxygen (O^{0}X) [59] were observed at 6.1153, 6.1087, and 6.1040 eV, respectively. The longitudinal optical (LO) phonon replicas of free excitons were found energetically lower than 6.05 eV. We note that these CL peak energies were higher by 95 meV than the strain-free values. The strongest FX$_A$(Γ_5) peak exhibited the narrowest FWHM value being 2.9 meV, which indicates excellent crystal homogeneity. The crystal perfection was also inspected by PAS. The Doppler broadening S parameter for the annihilation γ-ray spectrum, which reflects the size or concentration of negatively charged cation vacancies (V_{Al} and V_{Al}-complexes in this case [32]), was 0.458. This value is close to the characteristic S for nearly V_{Al}-free AlN [32].

The energy-resolved TRPL signals of A1 at 7 K are shown in Fig. 5.3. The signals exhibited a single or a double exponential decay shape with very fast initial lifetimes (τ_1). Here, the energy-resolved decay signals were fitted with a single exponential function for the FX$_A$(Γ_1), FX$_A$(Γ_5), and their LO phonon peaks and a double exponential function for the (Si^{0}X) peak. The value of τ_1 for the two free excitonic peaks FX$_A$(Γ_1) and FX$_A$(Γ_5) was commonly as short as 11 ps. It is well known that measuring the lifetime of an LO phonon replica, instead of zero phonon line, is preferable to determine the PL lifetime (τ_{PL}) in the bulk region. This is because the energies of LO phonon replicas are lower than E_g and they can be extracted from the bulk, where any possible effects due to surface nonradiative recombination can be excluded. As shown in Fig. 5.3, τ_1 of FX$_A$-1LO peak at 6.016 eV was 9.6 ps. Nam et al. [33] have attributed the measured τ_{PL} of 50 ps to FX$_A$ and 80 ps to I$_2$ at 10 K. The discrepancy between the present result and theirs [33] may originate from different overall crystalline quality, judging from the broader spectral lineshape of the emissions in [33]; the FWHM value of the I$_2$ peak was 15.5 meV, which is five times broader than that of the present A1 sample. We note that the slower lifetime component (τ_2) of (Si^{0}X) peak at 7 K being 38 ps is close to their τ_{PL} value for FX$_A$ [33].

In general, τ_{PL} at LT is governed by τ_R, because NRCs are frozen. Therefore, τ_{PL} at 7 K can be used as a representative intrinsic τ_R for the first approximation.

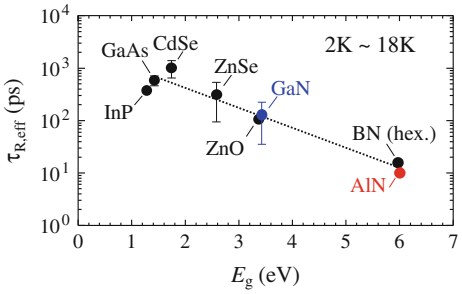


Fig. 5.4 Low-temperature (effective radiative) PL lifetimes ($\tau_{R,eff}$) for the NBE emissions in III–V and II–VI compound semiconductors as a function of E_g. The $\tau_{R,eff}$ values for GaN, ZnO, GaAs, CdSe, InP, ZnSe, and BN are from [61–66], respectively (after [34]. Copyright 2010, AIP Publishing LLC)

Apparently, τ_{PL} of the $FX_A(\Gamma_1)$ and $FX_A(\Gamma_5)$ peaks (and their 1LO) approximately 10 ps is much shorter than that of GaN (35–220 ps) [60] and ZnO (106 ps) [61]. The effective radiative lifetime $\tau_{R,eff}$ for the NBE emission at LT in III–V and II–VI semiconductors [60–66] is plotted as a function of E_g in Fig. 5.4. The value of τ_R is generally described [67] as $\tau_R = 2\pi\varepsilon_0 m_0 c^3/(ne^2\omega^2 f)$, where f is the oscillator strength, n the refractive index, ε_0 the dielectric constant in vacuum, and m_0 the electron mass in vacuum. Using the values $n = 2.79$ (2.67) and $\omega = 9.3 \times 10^{15}$ s^{-1} (5.3×10^{15} s^{-1}), we obtain $\tau_R = 220/f_{AlN}$ ($717/f_{GaN}$) ps for FX_A of AlN (GaN). According to the effective-mass approximation, f is represented as $f = E_p V/(\pi\hbar\omega a_B^{*3})$, where E_p is the Kane matrix element, V the volume of unit cell (1.25×10^{-22} cm^3 for AlN and 1.37×10^{-22} cm_3 for GaN), and a_B^* the effective Bohr radius of a free exciton (1.7 nm for AlN and 3.4 nm for GaN). Assuming the same E_p value (18.8 eV [68]), f_{AlN} and f_{GaN} are calculated to be 2.6×10^{-2} and 6.0×10^{-3}, respectively. Using these values, τ_R of FX_A in AlN is calculated to be 8.4 ns, which is shorter by a factor of 14 than that of GaN (120 ns). This trend is consistent with Fig. 5.4. However, absolute values are three orders of magnitude longer than the measured ones.

The discrepancy can be partially explained considering the formation of exciton polaritons [69, 70]. Right after the excitation, electrons and holes lose their excess energy and momentum within the bands, which usually take sub-picosecond [71]. Subsequently excitons are formed and they relax to an exciton-polariton bottleneck in a quite pure, high-quality bulk semiconductor material, especially at LT. An exciton-polariton is a manifold of an exciton and a light wave that can propagate in a material, and thereby the polariton lifetime is the time-of-flight to the surface [71]. This is very dependent on energy, in particular around the bottleneck, due to the strong variation of the group velocity. It also depends strongly where the polariton has been created. Then, what one measures could be space-averaged time-of-flight. Also, the time-of-flight lifetime is only true if polaritons propagate without collisions. As we have thick samples, elastic collisions may dominate the polariton lifetime. Assuming that the polariton lifetime near the bottleneck in AlN is close to

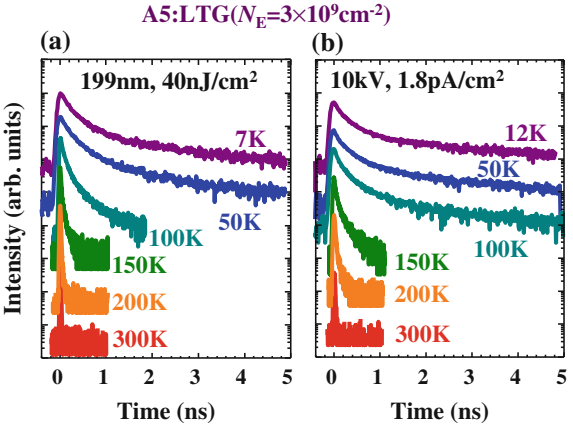


Fig. 5.5 Comparison of **a** TRPL and **b** TRCL signals for the NBE emission of heavily impurity-doped LTG AlN (A5) (after [35]. Copyright 2010, AIP Publishing LLC)

that calculated for GaN being a few picosecond [72], the measured lifetime of approximately 10 ps may reflect whole processes. Nevertheless, AlN has the shortest $\tau_{R,eff}$ at LT among the semiconductors displayed in Fig. 5.4, indicating that the material itself is quite radiative in nature.

Different from such HTG samples, TRPL signals of LTG samples at LT commonly exhibited a *stretched exponential* decay with slower lifetimes, as shown in Fig. 5.5a, which is characteristic of the emission processes in amorphous or defective semiconductors [73]. To confirm if TRCL gives similar data as TRPL, temperature variations of the those signals for an LTG sample A5 are compared in Fig. 5.5. As shown, the data are quite similar. To systematically compare τ_R and τ_{NR} for various quality AlN, effective PL (CL) lifetime $\tau_{PL(CL),eff}$ was defined [10] as the time after excitation when $\int_0^{\tau_{PL(CL),eff}} I(t)dt / \int_0^{t_{lim}} I(t)dt$ becomes 1–1/*e*, where I(t) is the intensity at time t and t_{lim} is defined as the time when $I(t_{lim})$ becomes $0.01I(0)$. The effective lifetimes $\tau_{R,eff}$ and $\tau_{NR,eff}$ were deduced from $\eta_{int} = (1 + \tau_{R,eff}/\tau_{NR,eff})^{-1}$ and $\tau_{PL(CL),eff}^{-1} = \tau_{R,eff}^{-1} + \tau_{NR,eff}^{-1}$, where η_{int} was approximated [10] as the spectrally integrated PL (CL) intensity at given temperature T over that at around 10 K. Because donor doping such as Si (and O) increases V_{Al} concentration through the Fermi-level effect [18], S of A4–A6 (>0.463) were higher than the HTG series (<0.462). Low temperature $\tau_{R,eff}$ for the NBE emission are plotted as a function of S in Fig. 5.6, in which characteristic S for AlN having V_{Al} concentration lower than the detection limit (<10^{15} cm^{-3}) is shown by the arrow on the horizontal axis (S_{free} = 0.458 [32]). Considering the fact that $V_{Al}(O_N)_x$ complexes exhibit smaller characteristic S than isolated V_{Al} [32], the result shown in Fig. 5.6 indicates that $\tau_{R,eff}$ of excitons bound to neutral donors (A4) and *e*–*h* pairs bound in impurity-induced band tail (A5 and A6) are much longer than intrinsic $\tau_{R,eff}$ of free excitons (FX) in HTG AlN (A1–A3) being 10 ps [34]. However, TD itself (N_E) showed negligible influence on $\tau_{R,eff}$ (and $\tau_{NR,eff}$).

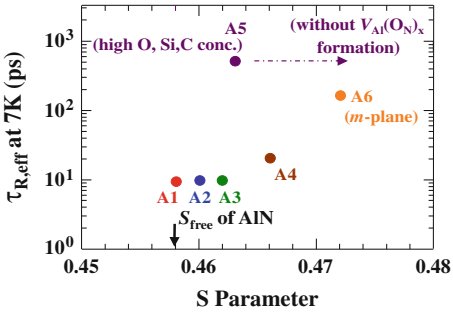


Fig. 5.6 Low-temperature $\tau_{R,eff}$ for the AlN epilayers as a function of S parameter. Characteristic S for defect-free AlN (0.458) is shown by the arrow on the horizontal axis (after [34]. Copyright 2010, AIP Publishing LLC.) The S value for A5 is lessened in comparison with other samples due to the formation of V_{Al}-$(O_N)_x$ complexes ([32])

Temperature variations of $\tau_{R,eff}$ and $\tau_{NR,eff}$ of A1 and A5 are compared in Fig. 5.7. For A1, $\tau_{R,eff}$ monotonically increased according to approximately $T^{1.5}$ above 130 K, reflecting the characteristic of quantum particles in three-dimensional (3D) free space [74]. The $\tau_{R,eff}$ value reaches 183 ps at 300 K, which is still the shortest among the semiconductors shown in Fig. 5.4. Conversely, $\tau_{NR,eff}$ decreases with T due to the thermal activation of NRCs. On the other hand, $\tau_{R,eff}$ of A5 first decreased with T up to 200 K. The result may reflect the recovery of oscillator strength of e–h pairs, which were spatially separated in conduction band minima and valence band maxima formed due to charged impurities and counter-charged point defects at LT, as shown schematically in Fig. 5.7b. As T was increased, the carriers may be released to 3D space to gain the wave function overlap, and finally, $\tau_{R,eff}$ increased with $T^{1.5}$ above 230 K. The decrease in $\tau_{NR,eff}$ with T due to the activation of NRCs for A5 was much remarkable than A1, reflecting enhanced carrier capture by NRCs due to the carrier release. Because $\tau_{NR,eff}$ at 300 K showed little decrease from 10 to 7 ps with the increase in S, which are close to the resolution, assertive conclusion cannot be drawn on the relation between $\tau_{NR,eff}$ and V_{Al} concentration at this stage. However, similar to GaN [9, 10] and ZnO [61], identification of NRCs in AlN may be V_{Al}-complexes.

5.4 Effective Radiative Lifetime of the Near-Band-Edge Emission in $Al_xGa_{1-x}N$ Films

Steady-state PL or CL spectra of (0001) $Al_xGa_{1-x}N$ epilayers of high x measured at LT are shown in Fig. 5.8. They were grown at 1200 °C on an AlN epitaxial template [6] and are classified as LTG samples (A4 in the case of AlN) because T_g

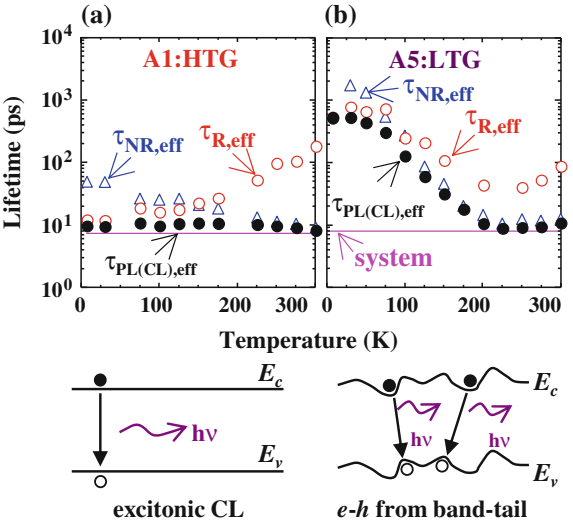


Fig. 5.7 Temperature variations of measured $\tau_{PL(CL),eff}$ (*closed circles*) and calculated $\tau_{R,eff}$ (*open circles*) and $\tau_{NR,eff}$ (*open triangles*) for **a** HTG sample A1 and **b** LTG sample A5. Schematic representations of carrier recombination are also given (after [35]. Copyright 2010, AIP Publishing LLC)

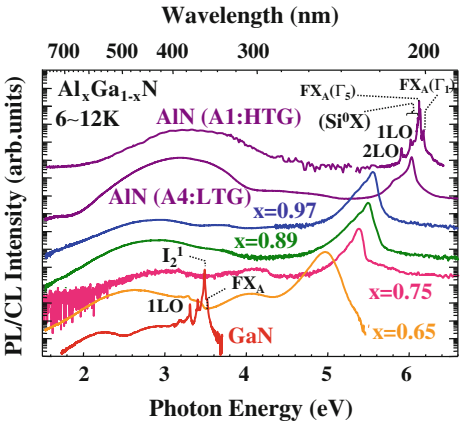


Fig. 5.8 Steady-state PL and CL spectra at 6–12 K of the $Al_xGa_{1-x}N$ alloy epilayers grown by MOVPE (after [36]. Copyright 2011, AIP Publishing LLC)

was far lower than what is appropriate for high-quality AlN film growth [34–39]. The spectra for good quality end-point compounds, namely, GaN and HTG AlN (A1), are characterized by the NBE excitonic lines originating from neutral-donor bound excitons (I_2), FX_A, and their LO phonon replicas. The spectra for the alloys exhibited a broad but reasonably intense NBE emission peak. The peak energies were lower by approximately 200 meV than the bandgap energies, similar to the previous reports [13, 75, 76]. Different from LTG AlN, peak intensities for the deep-state emission bands below 4.4 eV were two or three orders of magnitude weaker than the NBE peak, although the samples must contain high-concentration C, O, and Si impurities [35] and V_{III}-defects [35, 36]. As the formation energy of

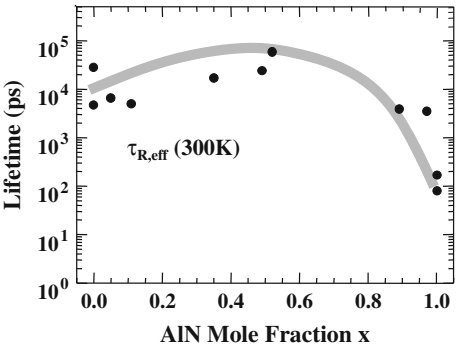


Fig. 5.9 Values of $\tau_{R,eff}$ at 300 K for the NBE emission of $Al_xGa_{1-x}N$ epilayers (after [36]. Copyright 2011, AIP Publishing LLC)

V_{Al} in AlN is far lower than that of V_{Ga} in GaN and even negative in *n*-type sample [16–22], major V_{III}-defect in $Al_xGa_{1-x}N$ is assigned to V_{Al}.

As $\tau_{R,eff}$ at RT reflects the radiative performance of a material, $\tau_{R,eff}$ values for the NBE emission in $Al_xGa_{1-x}N$ alloys at 300 K are plotted as a function of x in Fig. 5.9. We note that the samples of $x < 0.64$ were grown at 1150 °C on a (0001) Al_2O_3 substrate [13]. The $\tau_{R,eff}$ value slightly increased with x for $x < 0.5$, then had a maximum of a few tens of ns at around $x = 0.5$, and decreased to approximately 200 ps at $x = 1$. This result is consistent with the fact that f for 3D e–h pairs (excitons) in AlN is approximately 4–10 times that of GaN [34, 35, 77]. As a matter of fact, $\tau_{R,eff}$ values for the HTG AlN are as short as 10 ps at 8 K and 180 ps at 300 K [34, 35]. Therefore, $\tau_{R,eff}$ at RT being in the order of a few ns for the present $Al_xGa_{1-x}N$ alloys of high x is reasonably short, being comparable to or even shorter than that of GaN and InGaN films [10].

5.5 Impacts of Si-Doping and Resultant Cation Vacancy Formation on the Luminescence Dynamics of the Near-Band-Edge Emission in $Al_{0.6}Ga_{0.4}N$ Films Grown on AlN Templates

Figure 5.10a shows a representative temperature dependency of the CL spectra for the $Al_{0.6}Ga_{0.4}N$:Si film, of which [Si] is 1.9×10^{17} cm^{-3}. The spectra are characterized by a predominant NBE peak at around 5 eV and recognizable but very weak deep-state emission band ranging from 3 to 4 eV. In contrast, as shown in Fig. 5.10b, CL spectra at elevated temperatures of heavily Si-doped ([Si] = 4×10^{18} cm^{-3}), overcompensated film exhibited a predominant deep-state emission band in the green color region at around 2.4 eV, in addition to the NBE emission peak. The result implies that the heavily doped sample contains high-density V_{III}, because these deep-state emission centers have been ascribed to contain V_{III} with deferent charge states [9, 11–13, 26–28, 32].

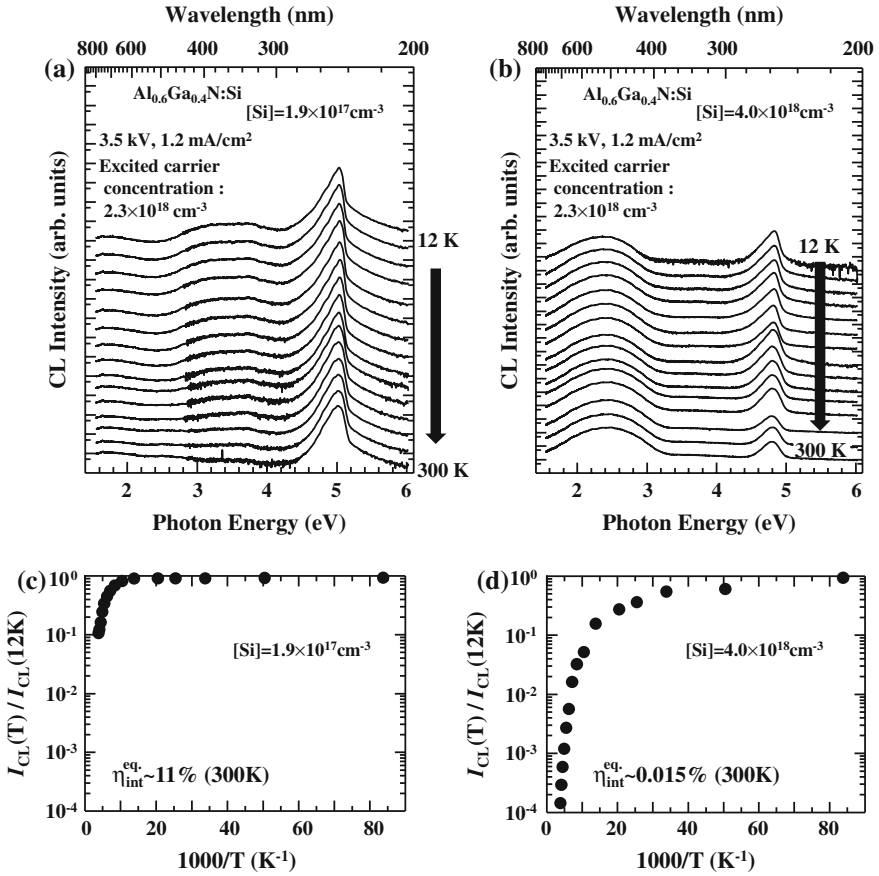


Fig. 5.10 Representative CL spectra of the $Al_{0.6}Ga_{0.4}N$:Si films for **a** [Si] = 1.9×10^{17} cm^{-3} and **b** [Si] = 4.0×10^{18} cm^{-3} as a function of T. Temperature dependencies for the ratios of spectrally integrated CL intensities at given T [I_{CL}(T)] to those at 12 K [I_{CL}(12 K)] for the NBE emission at around 5 eV, which are used as the equivalent value of $\eta_{int}(T)[\eta_{int}^{eq}(T)]$, for the $Al_{0.6}Ga_{0.4}N$:Si films of **c** [Si] = 1.9×10^{17} cm^{-3} and **d** [Si] = 4.0×10^{18} cm^{-3} (after [38]. Copyright 2013, AIP Publishing LLC)

Figure 5.10c, d shows the temperature dependencies for the ratios of spectrally integrated CL intensities at given T [I_{CL}(T)] to those at 12 K [I_{CL}(12 K)] for the NBE emission, which are used as the equivalent values for $\eta_{int}(T)$ $[\eta_{int}^{eq}(T)]$ in this article. For the films with [Si] = 1.9×10^{17} and 4.0×10^{18} cm^{-3}, η_{int}^{eq} (300 K) were 11 and 0.015 %, respectively. The former value was the highest among the present samples.

Room temperature PL spectra and the PL decay signals for the NBE emission of the $Al_{0.6}Ga_{0.4}N$ films are shown as a function of [Si] in Fig. 5.11a, b, respectively. The signal decay is seen to be abruptly shortened when [Si] exceeds 10^{18} cm^{-3} at

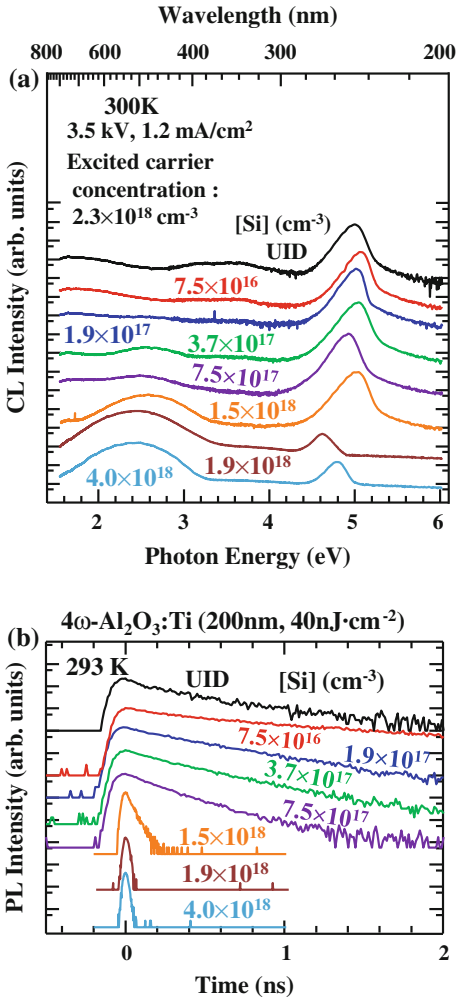


Fig. 5.11 **a** Room-temperature PL spectra and **b** PL decay signals for the NBE emission of the $Al_{0.6}Ga_{0.4}N$:Si films at various [Si] (after [38]. Copyright 2013, AIP Publishing LLC)

which concentration of the relative intensity of the green CL band increased. We fit the decay curves by a double exponential function to extract the characteristic lifetimes of the fast decay components (τ_1), because this value essentially determines the NBE emission intensity at elevated temperatures. The results are shown in Fig. 5.12d.

Figure 5.12a–c summarize room temperature values of n, S, and I_{deep}/I_{NBE} for the $Al_{0.6}Ga_{0.4}N$:Si films, respectively, as a function of [Si]. The values of τ_1 and η_{int}^{eq} for the NBE emission are plotted in Fig. 5.12d, e, respectively. The values of n and S are taken from [24, 29], respectively. As shown in Fig. 5.12b, S for the films of

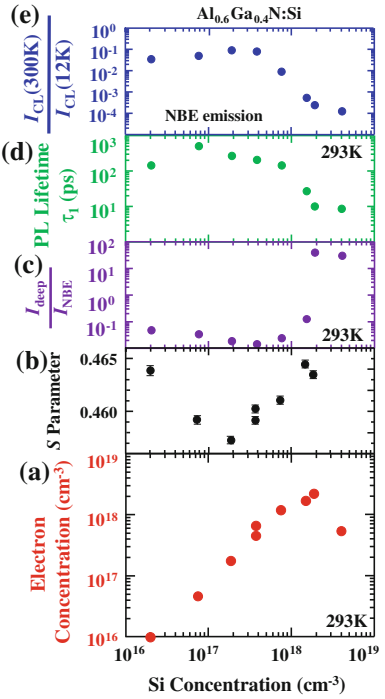


Fig. 5.12 Room temperature values of **a** electron concentration, n, **b** S parameter, **c** I_{deep}/I_{NBE}, and **d** τ_1 and **e** η_{int}^{eq} for the NBE emission, of the $Al_{0.6}Ga_{0.4}N$:Si films plotted as a function of [Si]. The values of n and S are taken from [24] and [29], respectively (after [38]. Copyright 2013, AIP Publishing LLC)

[Si] < 10^{17} cm^{-3} was larger than that for the smallest S being 0.457 at [Si] = 1.9 × 10^{17} cm^{-3}. The result means that the presence of certain amount of Si suppresses the introduction of vacancy-type defects, possibly at the growing surface. There are several plausible explanations for this. One is that Si acts as a surfactant and provides wetting conditions to improve the surface morphology of the epilayer [78], which reduces [V_{III}], although n-type doping decreases E_{Form} of V_{Ga} and V_{Al} in the bulk. Another explanation is the presence of doping reactants that give lower surface and internal energies when incorporated on the growing surface. It is well known for MOVPE of Si-doped GaAs (GaAs:Si) using TMGa–AsH_3–SiH_4 and TMGa–$C_4H_9AsH_2$–SiH_4 systems that the reaction between SiH_4 and AsH_3 or $C_4H_9AsH_2$ forms H_3SiAsH_2 in the gas phase (boundary layer), and H_3SiAsH_2 acts as the major doping reactant [79, 80]. In the present TMGa–TMAl–NH_3–CH_3SiH_3 system, H_3SiNH_2 is most likely effective on Si-doping, because CH_3SiH_3 decomposes into SiH_3 faster than SiH_4 does and reacts with NH_3 to form H_3SiNH_2 [81]. Then, Si is expected to be incorporated in a form of metastable N–Si bond, which decreases the internal energy of isolated Si_{III} donor [43] forming $Si_{Ga}^{(+)} - N_N^{(0)}$ (or $Si_{Al}^{(+)} - N_N^{(0)}$) and a free e^- at the surface and in the bulk. We note that the N–Si bond would give less chance for Si to occupy N sites forming a Si_N acceptor. Under the presence of N–Si bond, [V_{III}] could be lower than the UID case, although E_{Form} of isolated V_{Al} in AlN is very low and even negative in n-type materials [31]. On the other hand, the increase in S with further increase in

[Si] (>10^{17} cm^{-3}) is most likely due to the decrease in E_{Form} of V_{III} due to the Fermi-level effect [16–22, 31].

As shown in Fig. 5.12a, n increased linearly with [Si] up to approximately 10^{18} cm^{-3}. However, n saturated to increase for higher [Si] and then decreased to 5×10^{17} cm^{-3} for further increase in [Si] to 4.0×10^{18} cm^{-3}; i.e., electrical overcompensation is significant. The results shown in Fig. 5.12a, b are similar to what were observed for MOVPE of heavily Si-doped GaAs [80] in which the overcompensation of Si and steep increase in S were significant for [Si] > 10^{19} cm^{-3}. It is apparent that I_{deep}/I_{NBE} abruptly increased while τ_1 and η_{int}^{eq} rapidly decreased for [Si] > 10^{18} cm^{-3} in the present case, as shown in Fig. 5.12c–e, respectively. Because N_E for all the $Al_{0.6}Ga_{0.4}N$ films have been confirmed to be nearly the same [24, 29], the changes in I_{deep}/I_{NBE}; τ_1, and η_{int}^{eq} are purely correlated with the increase in S, namely the increase in [V_{III}] and the concentration of V_{III}-complexes. Consistently, deep-state emission bands commonly observed in GaN (2.2 eV), AlN (3.1 eV), and AlGaN (between 2.2 and 3.1 eV) have been assigned to originate from V_{III} or V_{III}–O_N complexes [9, 29, 32]. In the case of GaAs:Si, such an overcompensation due to heavy doping has been attributed to the formation of defect complexes such as V_{Ga}–Si_{Ga} ([41–43]. By analogy, complex defects such as V_{III}–Si_{III} (V_{Al}–Si_{Al}, V_{Al}–Si_{Ga}, etc.) are major culprits for the present $Al_{0.6}Ga_{0.4}N$:Si films.

It is noteworthy that significant correlations between τ_1 and S (τ_1–S relation) and between I_{CL}(300 K)/I_{CL}(12 K) and τ_1 ($\eta_{int}^{eq} - \tau_1$ relation) seen in GaN [9, 10, 82–84] are also remarkable in the $Al_{0.6}Ga_{0.4}N$:Si films, as shown in Fig. 5.13a, b, respectively. Almost linear τ_1–S relation indicates that the major NRCs in the $Al_{0.6}Ga_{0.4}N$:Si films are most likely [9, 10, 82–84] composed of defect complexes incorporated with V_{III}, such as V_{Al}–X (and V_{Ga}–X), because τ_1 at RT is generally dominated by τ_{NR} that decreases with increasing the concentration of NRCs. As

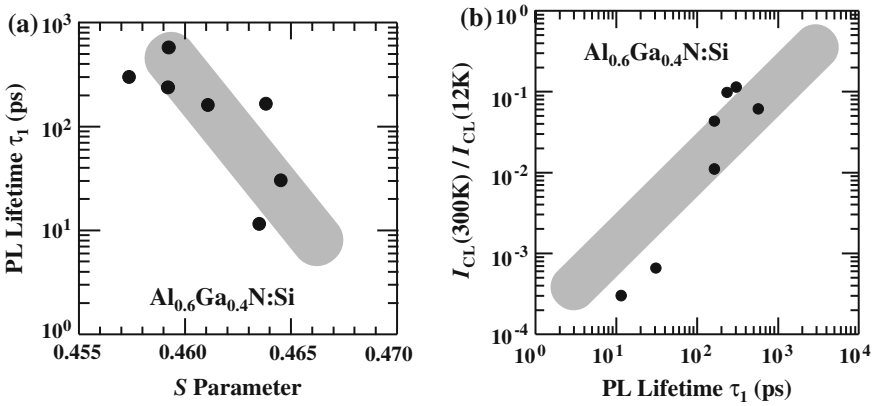


Fig. 5.13 **a** τ_1–S and **b** $\eta_{int}^{eq} - \tau_1$ relations for the $Al_{0.6}Ga_{0.4}N$:Si films at various [Si], which are derived from Fig. 5.12 (after [38]. Copyright 2013, AIP Publishing LLC)

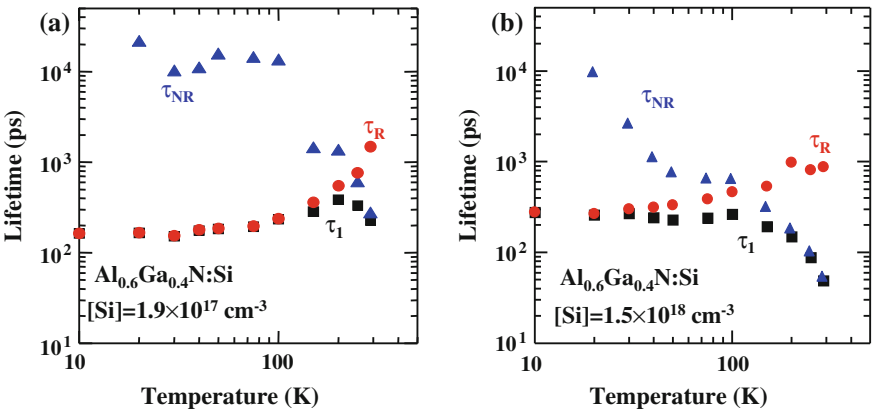


Fig. 5.14 Measured τ_1 (*squares*), derived τ_R (*circles*), and derived τ_{NR} (*triangles*) values as a function of T for the $Al_{0.6}Ga_{0.4}N$:Si films with [Si] of **a** 1.9×10^{17} and **b** 1.5×10^{18} cm^{-3}. Corresponding η_{int}^{eq} (300 K) were 11 and 0.07 %, respectively (after [38]. Copyright 2013, AIP Publishing LLC

shown in Fig. 5.13b, η_{int}^{eq} increases linearly with increasing τ_1. The result is quite reasonable because $\eta_{int}^{eq} = (1 + \tau_R/\tau_{NR})^{-1}$, τ_R is an intrinsic value to a particular material, and τ_1 is dominated by τ_{NR} at room temperature with the relation $\tau_1^{-1} = \tau_R^{-1} + \tau_{NR}^{-1}$. Very similar trends have been found in GaN and ZnO [9, 10, 61, 82–86].

By measuring τ_1 and η_{int}^{eq} for the NBE emission of the $Al_{0.6}Ga_{0.4}N$:Si films as a function of T, τ_R and τ_{NR} are derived. Representative data for the films of [Si] = 1.9×10^{17} and 1.5×10^{18} cm^{-3} are plotted in Fig. 5.14a, b, respectively. Corresponding η_{int}^{eq} (300 K) were 11 and 0.07 %, respectively. The value of τ_1 at low T, which mostly represents τ_R, for the former lightly doped sample (150 ps) was shorter than that for the latter highly doped sample ($\sim$300 ps), reflecting better overlapping of electron and hole wavefunctions due most likely to the small potential inhomogeneity; i.e., shallower band tail [36]. The values of τ_R increase with T for both the samples, reflecting the decrease in the oscillator strengths of excitons. Because of the larger potential inhomogeneity (deeper band tail), τ_R of the latter highly doped sample shows small change with T, being about 1 ns at 300 K. However, absolute τ_R values for both the samples are similar, and distinct difference between the two is the change in τ_{NR} with the increase in T: i.e., τ_{NR} of the latter sample decreases really rapidly than the former does due to the presence of high-concentration NRCs (V_{III}–complexes).

We mention here that the Fermi-level control method [87] using an UV light irradiation during MOVPE growth gave rise to higher maximum electron concentration in $Al_{0.65}Ga_{0.35}N$:Si epitaxial films. The concept was to modify the locations of quasi Fermi-levels during doping, in order to increase E_{Form} of V_{Al} defects. They finally obtained n approximately 4×10^{18} cm^{-3} [87], which is twice that obtained in this work.

5.6 Summary

The role of point defects on the emission dynamics of the NBE excitonic luminescence in AlN and high AlN mole fraction $Al_xGa_{1-x}N$ alloy films has been studied using DUV-TRPL and TRCL measurements and comparing it with the results of PAS measurements. The extreme radiative nature of excitons in high-quality AlN was identified, as τ_R for a free excitonic emission was determined to be as short as 11 ps at 7 K and 180 ps at 300 K, which are the shortest values as the spontaneous emission in bulk semiconductors. However, apparent τ_R increased with the increase in impurity and V_{Al} concentrations up to 530 ps at 7 K, irrespective of the TD density. The result reflects the contribution of bound exciton components. Continuous decrease in τ_R with temperature rise up to 200 K of heavily impurity-doped samples reflects a carrier release from the band-tail states. The τ_R values at RT of $Al_xGa_{1-x}N$ alloys of high x were as short as a few ns at 300 K. The results essentially indicate an excellent radiative performance of the present wide bandgap AlGaN alloys. Finally, the impact of Si-doping and the resulting V_{III} formation on τ_{NR} of the NBE emission in $Al_{0.6}Ga_{0.4}N$ films was shown. Therefore, controlling the concentration of point defects is a key instrument to increase the quantum efficiencies and to improve the device performance.

Acknowledgments The authors thank Prof. T. Sota of Waseda Univ., Prof. B. Gil of Univ. Montpellier II, Prof. C. Weisbuch of Univ. California Santa Barbara, Dr. M. Tanaka, and Prof. S. Nakamura of Univ. California Santa Barbara for fruitful discussions. The first author is thankful to Dr. K. Furusawa for help with the experiments. This work was supported in part by NEDO programs under METI, Grant-in-Aids for Scientific Research Nos. 23656206 and 18069001 under MEXT, Japan, and AFOSR/AOARD Grant Nos. FA2386-11-1-4013 and FA2386-11-1-4108 monitored by Dr. G. Jessen. We finally thank Prof. Michael Kneissl for giving us a chance to contribute to this issue.

References

1. C. Pernot, M. Kim, S. Fukahori, T. Inazu, T. Fujita, Y. Nagasawa, A. Hirano, M. Ippommatsu, M. Iwaya, S. Kamiyama, I. Akasaki, H. Amano, Appl. Phys. Express **3**, 061004 (2010)
2. M. Shatalov, W. Sun, A. Lunev, X. Hu, A. Dobrinsky, Y. Bilenko, J. Yang, M. Shur, R. Gaska, C. Moe, G. Garrett, M. Wraback, Appl. Phys. Express **5**, 082101 (2012)
3. M. Kneissl, T. Kolbe, C. Chua, V. Kueller, N. Lobo, J. Stellmach, A. Knauer, H. Rodriguez, S. Einfeldt, Z. Yang, N.M. Johnson, M. Weyers, Semicond. Sci. Technol. **26**, 014036 (2011)
4. Y. Shimahara, H. Miyake, K. Hiramatsu, F. Fukuyo, T. Okada, H. Takaoka, H. Yoshida, Appl. Phys. Express **4**, 042103 (2011)
5. T. Oto, R.G. Banal, K. Kataoka, M. Funato, Y. Kawakami, Nat. Photonics **4**, 767 (2010)
6. T. Shibata, K. Asai, S. Sumiya, M. Mouri, M. Tanaka, O. Oda, H. Katsukawa, H. Miyake, K. Hiramatsu, Phys. Status Solidi C **0**, 2023 (2003)
7. A. Rice, R. Collazo, J. Tweedie, R. Dalmau, S. Mita, J. Xie, Z. Sitar, J. Appl. Phys. **108**, 043510 (2010)
8. J.R. Grandusky, Z. Zhong, J. Chen, C. Leung, L.J. Schowalter, Solid-State Electron. **78**, 127 (2012)

9. S.F. Chichibu, A. Uedono, T. Onuma, T. Sota, B.A. Haskell, S.P. DenBaars, J.S. Speck, S. Nakamura, Appl. Phys. Lett. **86**, 021914 (2005)
10. S.F. Chichibu, A. Uedono, T. Onuma, B.A. Haskell, A. Chakraborty, T. Koyama, P.T. Fini, S. Keller, S.P. DenBaars, J.S. Speck, U.K. Mishra, S. Nakamura, S. Yamaguchi, S. Kamiyama, H. Amano, I. Akasaki, J. Han, T. Sota, Nat. Mater. **5**, 810 (2006); Philos. Mag. **87**, 2019 (2007)
11. A.Y. Polyakov, M. Shin, J.A. Freitas, M. Skowronski, D.W. Greve, R.G. Wilson, J. Appl. Phys. **80**, 6349 (1996)
12. T. Bradley, S.H. Goss, L.J. Brillson, J. Hwang, W.J. Schaff, J. Vac. Sci. Technol. B **21**, 2558 (2003)
13. T. Onuma, S.F. Chichibu, A. Uedono, T. Sota, P. Cantu, T.M. Katona, J.F. Keading, S. Keller, U.K. Mishra, S. Nakamura, S.P. DenBaars, J. Appl. Phys. **95**, 2495 (2004)
14. T. Kubo, H. Taketomi, H. Miyake, K. Hiramatsu, T. Hashizume, Appl. Phys. Express **3**, 021004 (2010)
15. K. Ooyama, K. Sugawara, S. Okuzaki, H. Taketomi, H. Miyake, K. Hiramatsu, T. Hashizume, Jpn. J. Appl. Phys., Part 1 **49**, 101001 (2010)
16. J. Neugebauer, C.G. Van de Walle, Phys. Rev. B **50**, 8067 (1994)
17. J. Neugebauer, C.G. Van de Walle, Appl. Phys. Lett. **69**, 503 (1996)
18. C. Stampfl, C.G. Van de Walle, Appl. Phys. Lett. **72**, 459 (1998)
19. C.G. Van de Walle, J. Neugebauer, J. Appl. Phys. **95**, 3851 (2004)
20. A.F. Wright, U. Grossner, Appl. Phys. Lett. **73**, 2751 (1998)
21. K. Leung, A.F. Wright, E.B. Stechel, Appl. Phys. Lett. **74**, 2495 (1999)
22. A.F. Wright, J. Appl. Phys. **90**, 1164 (2001)
23. S. Keller, P. Cantu, C. Moe, Y. Wu, S. Keller, U.K. Mishra, J.S. Speck, S.P. DenBaars, Jpn. J. Appl. Phys. Part 1 **44**, 7227 (2005)
24. Y. Shimahara, H. Miyake, K. Hiramatsu, F. Fukuyo, T. Okada, H. Takaoka, H. Yoshida, Jpn. J. Appl. Phys. Part 1 **50**, 095502 (2011)
25. G.R. James, A.W.R. Leitch, F. Omnes, M. Leroux, Semicond. Sci. Technol. **21**, 744 (2006)
26. N. Nepal, M.L. Nakarmi, J.Y. Lin, H.X. Jiang, Appl. Phys. Lett. **89**, 092107 (2006)
27. K.X. Chen, Q. Dai, W. Lee, J.K. Kim, E.F. Schubert, W. Liu, S. Wu, X. Li, J.A. Smart, Appl. Phys. Lett. **91**, 121110 (2007)
28. J. Slotte, F. Tuomisto, K. Saarinen, C.G. Moe, S. Keller, S.P. DenBaars, Appl. Phys. Lett. **90**, 151908 (2007)
29. A. Uedono, K. Tenjinbayashi, T. Tsutsui, Y. Shimahara, H. Miyake, K. Hiramatsu, N. Oshima, R. Suzuki, S. Ishibashi, J. Appl. Phys. **111**, 013512 (2012)
30. H. Murotani, D. Akase, K. Anai, Y. Yamada, H. Miyake, K. Hiramatsu, Appl. Phys. Lett. **101**, 042110 (2012)
31. C. Stampfl, C.G. Van de Walle, Phys. Rev. B **65**, 155212 (2002)
32. A. Uedono, S. Ishibashi, S. Keller, C. Moe, P. Cantu, T.M. Katona, D.S. Kamber, Y. Wu, E. Letts, S.A. Newman, S. Nakamura, J.S. Speck, U.K. Mishra, S.P. DenBaars, T. Onuma, S.F. Chichibu, J. Appl. Phys. **105**, 054501 (2009)
33. K.B. Nam, J. Li, M.L. Nakarmi, J.Y. Lin, H.X. Jiang, Appl. Phys. Lett. **82**, 1694 (2003)
34. T. Onuma, K. Hazu, A. Uedono, T. Sota, S.F. Chichibu, Appl. Phys. Lett. **96**, 061906 (2010)
35. S.F. Chichibu, T. Onuma, K. Hazu, A. Uedono, Appl. Phys. Lett. **97**, 201904 (2010)
36. S.F. Chichibu, K. Hazu, T. Onuma, A. Uedono, Appl. Phys. Lett. **99**, 051902 (2011)
37. S.F. Chichibu, T. Onuma, K. Hazu, A. Uedono, Phys. Status Solidi (c) **10**, 501 (2013)
38. S.F. Chichibu, H. Miyake, Y. Ishikawa, M. Tashiro, T. Ohtomo, K. Furusawa, K. Hazu, K. Hiramatsu, A. Uedono, J. Appl. Phys. **113**, 213506 (2013)
39. S.F. Chichibu, K. Hazu, Y. Ishikawa, M. Tashiro, T. Ohtomo, K. Furusawa, A. Uedono, S. Mita, J. Xie, R. Collazo, Z. Sitar, Appl. Phys. Lett. **103**, 142103 (2013)
40. S. Nakamura, T. Mukai, M. Senoh, Jpn. J. Appl. Phys. **31**, 2883 (1992)
41. R.T. Chen, V. Rana, W.G. Spitzer, J. Appl. Phys. **51**, 1532 (1980)
42. N. Furuhata, K. Kakimoto, M. Yoshida, T. Kamejima, J. Appl. Phys. **64**, 4692 (1988)

43. S. Chichibu, A. Iwai, Y. Nakahara, S. Matsumoto, H. Higuchi, L. Wei, S. Tanigawa, J. Appl. Phys. **73**, 3880 (1993)
44. K. Fujito, K. Kiyomi, T. Mochizuki, H. Oota, H. Namita, S. Nagao, I. Fujimura, Phys. Status Solidi A **205**, 1056 (2008)
45. C.G. Dunn, E.F. Koch, Acta Metall. **5**, 548 (1957)
46. K. Hazu, M. Kagaya, T. Hoshi, T. Onuma, S.F. Chichibu, J. Vac. Sci. Technol., B **29**, 021208 (2011)
47. M. Merano, S. Collin, P. Renucci, M. Gatri, S. Sonderegger, A. Crottini, J.D. Ganiere, B. Deveaud, Rev. Sci. Instrum. **76**, 085108 (2005)
48. S.F. Chichibu, Y. Ishikawa, M. Tashiro, K. Hazu, K. Furusawa, H. Namita, S. Nagao, K. Fujito, A. Uedono, Electrochem. Soc. Trans. **50**(42), 1 (2013)
49. K. Furusawa, Y. Ishikawa, M. Tashiro, K. Hazu, S. Nagao, H. Ikeda, K. Fujito, S.F. Chichibu, Appl. Phys. Lett. **103**, 052108 (2013)
50. R. Krause-Rehberg, H.S. Leipner, *Positron Annihilation in Semiconductors, Solid-State Sciences*, vol. 127 (Springer, Berlin, 1999)
51. P.G. Coleman, *Positron Beams and Their Application* (World Scientific, Singapore, 2000)
52. T. Onuma, T. Shibata, K. Kosaka, K. Asai, S. Sumiya, M. Tanaka, T. Sota, A. Uedono, S.F. Chichibu, J. Appl. Phys. **105**, 023529 (2009)
53. G.A. Slack, L.J. Schowalter, D. Morelli, J.A. Freitas Jr, J. Cryst. Growth **246**, 287 (2002)
54. K.B. Nam, M.L. Nakarmi, J.Y. Lin, H.X. Jiang, Appl. Phys. Lett. **86**, 222108 (2005)
55. A. Dadgar, A. Krost, J. Christen, B. Bastek, F. Bertram, A. Krtschil, T. Hempel, J. Blasing, U. Haboeck, A. Hoffmann, J. Cryst. Growth **297**, 306 (2006)
56. T. Koyama, M. Sugawara, T. Hoshi, A. Uedono, J.F. Kaeding, R. Sharma, S. Nakamura, S.F. Chichibu, Appl. Phys. Lett. **90**, 241914 (2007)
57. H. Ikeda, T. Okamura, K. Matsukawa, T. Sota, M. Sugawara, T. Hoshi, P. Cantu, R. Sharma, J.F. Kaeding, S. Keller, U.K. Mishra, K. Kosaka, K. Asai, S. Sumiya, T. Shibata, M. Tanaka, J.S. Speck, S.P. DenBaars, S. Nakamura, T. Koyama, T. Onuma, S.F. Chichibu, J. Appl. Phys. **102**, 123707 (2007); **103**, 089901(E) (2008)
58. B. Neuschl, K. Thonke, M. Feneberg, S. Mita, J. Xie, R. Dalmau, R. Collazo, Z. Sitar, Phys. Status Solidi B **249**, 511 (2012)
59. Z. Bryan, I. Bryan, M. Bobea, L. Hussey, R. Kirste, Z. Sitar, R. Collazo, J. Appl. Phys. **115**, 133503 (2014)
60. G. Pozina, J.P. Bergman, T. Paskova, B. Monemar, Appl. Phys. Lett. **75**, 4124 (1999)
61. S.F. Chichibu, T. Onuma, M. Kubota, A. Uedono, T. Sota, A. Tsukazaki, A. Ohtomo, M. Kawasaki, J. Appl. Phys. **99**, 093505 (2006)
62. R. Hoger, E.O. Göbel, J. Kuhl, K. Ploog, H.J. Quiesser, J. Phys. C **17**, L905 (1984)
63. C. Gourdon, P. Lavallard, M. Dagenais, Phys. Rev. B **37**, 2589 (1988)
64. S. Charbonneau, L.B. Allard, A.P. Roth, T.S. Rao, Phys. Rev. B **47**, 13918 (1993)
65. Y. Yamada, T. Mishina, Y. Masumoto, Y. Kawakami, S. Yamaguchi, K. Ichino, S. Fujita, S. Fujita, T. Taguchi, Phys. Rev. B **51**, 2596 (1995)
66. K. Watanabe, T. Taniguchi, T. Kuroda, H. Kanda, Diam. Relat. Mater. **15**, 1891 (2006)
67. G.W. p't Hooft, W.A.J.A. van der Poel, L.W. Molenkamp, C.T. Foxon, Phys. Rev. B **35**, 8281 (1987)
68. S. Shokhovets, O. Ambacher, B.K. Meyer, G. Gobsch, Phys. Rev. B **78**, 035207 (2008)
69. H. Sumi, J. Phys. Soc. Jpn. **41**, 526 (1976)
70. C. Weisbuch, H. Benisty, R. Houdre, J. Lumin. **85**, 271 (2000)
71. J. Shah, *Ultrafast Spectroscopy of Semiconductors and Semiconductor Nanostructures* (Springer, Berlin, 1996)
72. K. Torii, T. Deguchi, T. Sota, K. Suzuki, S. Chichibu, S. Nakamura, Phys. Rev. B **60**, 4723 (1999)
73. R. Kohlrausch, Ann. Phys. **12**, 393 (1847)
74. J. Feldmann, G. Peter, E.O. Göbel, P. Dawson, K. Moore, C. Foxon, R.J. Elliot, Phys. Rev. Lett. **59**, 2337 (1987)

75. N. Teofilov, K. Thonke, R. Sauer, L. Kirste, D.G. Ebling, K.W. Benz, Diam. Relat. Mater. **11**, 892 (2002)
76. H. Murotani, Y. Yamada, H. Miyake, K. Hiramatsu, Appl. Phys. Lett. **98**, 021910 (2011)
77. H. Murotani, T. Kuronaka, Y. Yamada, T. Taguchi, N. Okada, H. Amano, J. Appl. Phys. **105**, 083533 (2009)
78. V. Lebedev, F.M. Morales, H. Romanus, S. Krischok, G. Ecke, V. Cimalla, M. Himmerlich, T. Stauden, D. Cengher, O. Ambacher, J. Appl. Phys. **98**, 093508 (2005)
79. M. Mashita, Jpn. J. Appl. Phys., Part 1 **28**, 1298 (1989)
80. S. Chichibu, A. Iwai, S. Matsumoto, H. Higuchi, Appl. Phys. Lett. **60**, 489 (1992); Erratum **60**, 2439 (1992)
81. B.T. Luke, J.A. Pople, M.K. Jespersen, Y. Apeloig, J. Chandrasekhar, P.R. Schleyer, J. Am. Chem. Soc. **108**, 260 (1986)
82. Y. Ishikawa, M. Tashiro, K. Hazu, K. Furusawa, H. Namita, S. Nagao, K. Fujito, S.F. Chichibu, Appl. Phys. Lett. **101**, 212106 (2012)
83. S.F. Chichibu, Y. Ishikawa, M. Tashiro, K. Hazu, K. Furusawa, H. Namita, S. Nagao, K. Fujito, A. Uedono, Electrochem. Soc. Trans. **50**(42), 1 (2013)
84. S.F. Chichibu, K. Hazu, Y. Ishikawa, M. Tashiro, H. Namita, S. Nagao, K. Fujito, A. Uedono, J. Appl. Phys. **111**, 103518 (2012)
85. S.F. Chichibu, A. Uedono, A. Tsukazaki, T. Onuma, M. Zamfirescu, A. Ohtomo, A. Kavokin, G. Cantwell, C.W. Litton, T. Sota, M. Kawasaki, Semicond. Sci. Technol. **20**, S67 (2005)
86. D. Takamizu, Y. Nishimoto, S. Akasaka, H. Yuji, K. Tamura, K. Nakahara, T. Onuma, T. Tanabe, H. Takasu, M. Kawasaki, S.F. Chichibu, J. Appl. Phys. **103**, 063502 (2008)
87. Z. Bryan, I. Bryan, B.E. Gaddy, P. Reddy, L. Hussey, M. Bobea, W. Guo, M. Hoffmann, R. Kirste, J. Tweedie, M. Gerhold, D.L. Irving, Z. Sitar, R. Collazo, Appl. Phys. Lett. **105**, 222101 (2014)

Chapter 6
Optical Polarization and Light Extraction from UV LEDs

Jens Rass and Neysha Lobo-Ploch

Abstract In solid-state devices, light is generated by radiative transitions between the lowest conduction band and the highest valence subband. In wurtzite group III-nitride compound materials, the valence band is split into three subbands (heavy hole band, light hole band, and crystal field split-off band) each having a unique polarization state for electronic transitions. The ordering of these bands and hence the optical polarization is determined by the strain state, the aluminum mole fraction x of the $Al_xGa_{1-x}N$ alloy, and the quantum confinement. This has consequences for the optical polarization properties and for the extraction efficiency of the spontaneously emitted light generated in light-emitting diodes (LEDs). Furthermore, the high refractive index of the semiconductor material and the presence of absorbing metal contacts and p-semiconductor layers result in UV LEDs having a low extraction efficiency. In this chapter, the basic mechanisms of light extraction and the generation of polarized light in UV LEDs are discussed. Different concepts for improving the light extraction efficiency are presented. This includes reflective contacts, contact design, surface patterning and surface roughening, photonic crystals, plasmonics, and encapsulation techniques.

J. Rass (✉) · N. Lobo-Ploch
Ferdinand-Braun-Institut, Leibniz-Institut für Höchstfrequenztechnik,
Gustav-Kirchhoff-Str. 4, 12489 Berlin, Germany
e-mail: jens.rass@fbh-berlin.de; jens.rass@physik.tu-berlin.de

N. Lobo-Ploch
e-mail: neysha.lobo-ploch@fbh-berlin.de

J. Rass
Institute of Solid State Physics, Technische Universität Berlin,
Hardenbergstr. 36, 10623 Berlin, Germany

© Springer International Publishing Switzerland 2016

M. Kneissl and J. Rass (eds.), *III-Nitride Ultraviolet Emitters*,
Springer Series in Materials Science 227, DOI 10.1007/978-3-319-24100-5_6

6.1 Light Extraction from UV LEDs

In order to maximize the external quantum efficiency η_{EQE} of light-emitting diodes, three key parameters have to be taken into account namely the internal quantum efficiency, the injection efficiency, and the light extraction efficiency.

The internal quantum efficiency η_{IQE}, also known as IQE, is the ratio of generated photons per charge carrier pair in the active region. It is mainly governed by the ratio between nonradiative and radiative recombination processes and it is therefore strongly related to the defect density in the semiconductor device. A typical loss mechanism that reduces the IQE is electrons overshooting the quantum well active region and recombining nonradioactively in the Mg-doped layers of the LED heterostructure. The injection efficiency, η_{inj}, is the ratio between the carriers injected into the active region and the carriers injected into the device. Concepts such as Mg-doped AlGaN electron blocking layers help to improve the injection efficiency. The extraction efficiency η_{extr} describes the ratio between the number of extracted photons from the device and the number of photons generated in the active region. The overall efficiency is the product of the three parameters described above:

$$\eta_{EQE} = \eta_{IQE}\eta_{inj}\eta_{extr} \tag{6.1}$$

In this chapter, we will focus on the extraction efficiency since this parameter strongly affects the overall device performance. Light extraction is a major challenge due to the high refractive index of the semiconductor/substrate which results in total internal reflection of the light at the semiconductor–air or substrate–air interface. The critical angle for total internal reflection (ϑ_{crit}) can be determined from Snell's law and is given by (6.2), where n_s is the refractive index of the semiconductor and n_0 is the refractive index of air or the surrounding medium. Only light incident on the surface at an angle, w.r.t. the normal, smaller than the critical angle can escape thus defining a light escape cone (see Fig. 6.1).

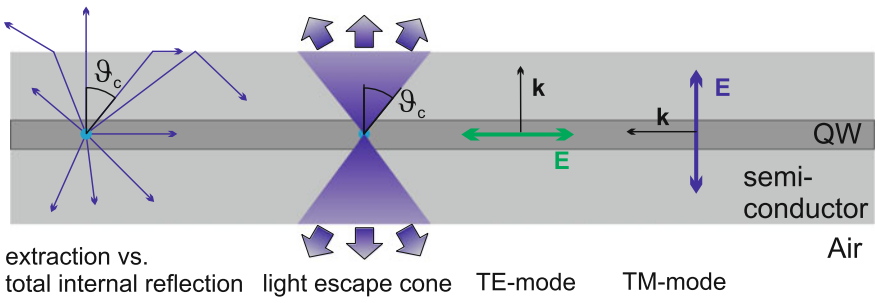


Fig. 6.1 Refraction and total internal reflection at interfaces in semiconductors, light escape cone, and polarization modes

$$\vartheta_{\text{crit}} = \arcsin\frac{n_0}{n_s} \tag{6.2}$$

In order to understand the difficulty in extracting light from an LED, we consider the fraction of light that is extracted into the escape cone. Assuming isotropic emission from the active region (which is strictly true only in devices with fully degenerated valence subbands as group III-arsenide or III-phosphide-based emitters, see Sect. 6.2), the fraction of light which is emitted into the escape cone and hence can be extracted is given by

$$\eta_{\text{extr}} = \frac{\int_0^{\vartheta_{\text{crit}}}\int_0^{2\pi}\sin(\vartheta)\mathrm{d}\vartheta\mathrm{d}\phi}{\int_0^{\pi}\int_0^{2\pi}\sin(\vartheta)\mathrm{d}\vartheta\mathrm{d}\phi} = \frac{1}{2}(1-\cos(\vartheta_{\text{crit}})) \tag{6.3}$$

Assuming an emission wavelength of 300 nm, the refractive index $n_{\text{Al}_2\text{O}_3} = 1.81$ of sapphire [1] leads to a maximum critical angle of $\vartheta_{\text{crit}} = 33.5^\circ$ and hence to an extraction efficiency of $\eta_{\text{extr}} = 8.3\,\%$. In case of AlN with a refractive index $n_{\text{AlN}} = 2.28$ [2], the maximum critical angle is $\vartheta_{\text{crit}} = 26.0^\circ$ and the extraction efficiency is $\eta_{\text{extr}} = 5.1\,\%$.

LED structures are conventionally quadrangular parallelepipeds which have six light escape cones, two perpendicular and four parallel to the plane of the active layer. In the case of rectangular parallelepiped nitride LEDs grown heteroepitaxially on sapphire substrates, the photons will be outcoupled based on their angle of emission (θ) from the active region with respect to the normal to the plane of the active region. The emission can be divided into various zones [3]:

1. Surface emission zone: $0 \le \theta < \theta_1 = \sin^{-1}(n_0/n_s)$
   The photons emitted within this zone will be extracted if the cladding layers and substrate are transparent and the ohmic contacts are transparent or reflective. For a GaN-based LED, $\theta_1 \approx 23^\circ$.
2. No escape zone: $\theta_1 \le \theta < \theta_2 = \sin^{-1}\frac{n_{\text{sub}}\cos[\sin^{-1}(n_0/n_{\text{sub}})]}{n_s}$
   where n_{sub} is the refractive index of the substrate. These photons are totally internally reflected at both the surface and the edge of the LED. For GaN LEDs grown on sapphire substrates $\theta_2 \approx 35^\circ$.
3. Substrate edge emission zone: $\theta_2 \le \theta < \theta_3 = \sin^{-1}(n_{\text{sub}}/n_s)$
   Photons emitted within this angular region can be coupled out from the side walls of the substrate. For GaN LEDs grown on sapphire substrates $\theta_3 \approx 44^\circ$. The light needs to undergo a number of reflections to reach the edge of the structure before being extracted.
4. Waveguide zone: $\theta_3 \le \theta < 90^\circ$. These photons are waveguided in the cladding layers and may be collected at the edge of the LED structure after multiple reflections.

The light which is guided within the LED structure may be reabsorbed by defects, contacts, the active region, or other absorbing layers (see Fig. 6.2). In UV

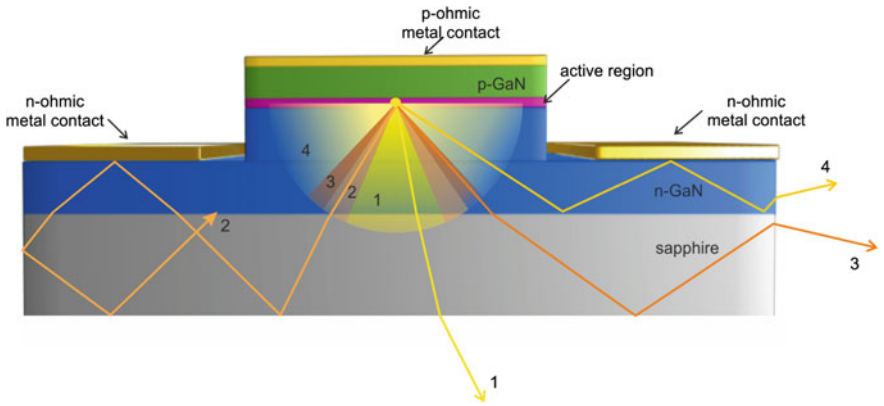


Fig. 6.2 Schematic of the propagation of the light emitted from a rectangular parallelepiped nitride LED. Based on the angle of emission (θ) from the active region with respect to the normal to the plane of the active region the four emission zones are depicted in the figure, namely, the surface emission zone (*1*), the no escape zone (*2*), the substrate edge emission zone (*3*), and the waveguide zone (*4*)

LEDs, the p-GaN contact layer and usually also the p-AlGaN layers are absorbing. 'Photon recycling,' i.e., the re-emission of photons absorbed in the active region, may occur which results in the randomization of angular distribution of the photons. However, the probability of re-emission is dependent on the IQE of the device, and hence is not a viable method to improve the outcoupling of light. Therefore, to increase the efficiency of the LEDs, it is necessary to suitably modify the geometry of the LED to outcouple the light which is guided within the structure.

6.2 Optical Polarization

Almost all visible and UV LEDs and optoelectronic devices are grown in the wurtzite (WZ) phase of the III-nitride crystal structure, and this is also the thermally stable form of the III-nitride crystals. Hence, in this section the band structure of the WZ phase of AlInGaN emitters will be discussed. The electrical and optical properties of WZ group III-nitrides are mainly determined by the band structure near the Brillouin zone center (wave vector $k \approx 0$). At the Γ point, GaN and AlN have one conduction band (CB), Γ_7, with states having atomic *s*-orbital character. The valence band (VB) states have atomic p_x, p_y, and p_z characters where the *z*-direction is defined parallel to the *c*-axis of the crystal. Transitions between the *s* and p_x-, p_y-, and p_z-like states involve *x*-, *y*-, and *z*-polarized light, respectively. Due to the reduced symmetry of the wurtzite crystal structure, III-nitride materials are anisotropic along and perpendicular to the direction of the *c*-axis. This anisotropy results in a crystal field splitting (Δ_{CF}) of the VBs. The top of the VB is split

into twofold and single degenerate states [4]. The twofold degenerate state has atomic p_x- and p_y-like character (wave form $|X \pm iY\rangle$ like), while the single degenerate state has a predominant atomic p_z-like character (wave form $|Z\rangle$ like). The order of the two energy levels depends on the kind of materials, the c/a ratio of the lattice constants and the relative displacement of the N sublattice with respect to the Al or Ga sublattice along the c-direction. If spin–orbit interaction Δ_{SO} is introduced, the degeneracy of the twofold degenerate state is lifted resulting in Γ_9 and Γ_7 states which are known as the heavy hole (HH) and light hole (LH) bands, respectively. The single degenerate state (Γ_7) is called the crystal field split-off hole band (CH).

Based on the quasi-cubic model [5], at the Γ point, the energetic position of the Γ_9 band with respect to the two (Γ_7) bands is given by

$$\Gamma_9 - \Gamma_{7\pm} = \frac{\Delta_{CF} + \Delta_{SO}}{2} \pm \frac{1}{2}\sqrt{(\Delta_{CF} + \Delta_{SO})^2 - \frac{8}{3}\Delta_{CF}\Delta_{SO}} \tag{6.4}$$

The spin–orbit splitting energies are positive for both GaN (17 meV) [6–8] and AlN (20 meV) [9]. However, the more ionic nature of AlN results in a crystal field splitting Δ_{CF} which is negative (−206 meV) instead of positive as in the case of GaN (10 meV) [6–9]. Due to the difference in the crystal field splitting, the order of the valence subbands at the Γ point in AlN is different from that in GaN (see Fig. 6.3). For GaN, the HH (Γ_9) band is the topmost valence subband closely followed in energy by the LH (Γ_7) band and CH (Γ_7) band [10]. On the other hand, in AlN, the topmost valence subband is the CH band (Γ_7) followed by the HH band (Γ_9) and the LH band (Γ_7). The valence subbands are named A, B, and C according to the order of their energetic positions from the highest to the lowest.

Chen et al. [10] and Li et al. [13] calculated the square of the transition matrix element (I_V) for the band-to-band transition involving the three valence subbands, in GaN and AlN, respectively, using the quasi-cubic model (see Table 6.1). The

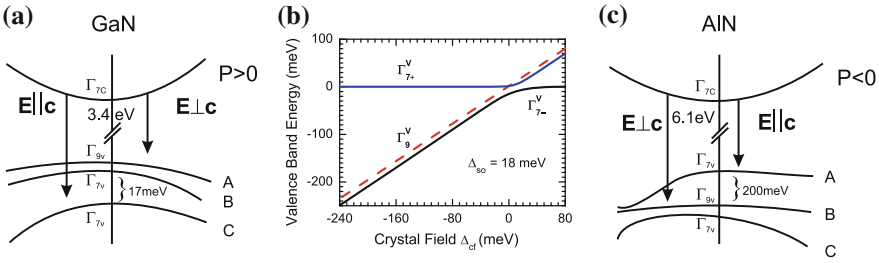


Fig. 6.3 **a** Schematic of the band structure of WZ GaN at the Γ point [6, 7, 11]. **b** Relative valence band energies at the Γ point as a function of the crystal field for a spin–orbit energy of 18 meV. Reprinted with permission from [12]. **c** Schematic of the band structure of WZ AlN at the Γ point [9, 11]

Table 6.1 Calculated values for the square of the transition matrix element (I_V) of WZ GaN [10] and WZ AlN [13] for light-polarized parallel and perpendicular to the c-axis

GaN			AlN		
Transition	$E\|\|c$	$E\perp c$	Transition	$E\|\|c$	$E\perp c$
$E_A(\Gamma_{7C} \leftrightarrow \Gamma_{9V})$	0	1	$E_A(\Gamma_{7C} \leftrightarrow \Gamma_{7V})$	0.4580	0.0004
$E_B(\Gamma_{7C} \leftrightarrow \Gamma_{7V})$	0.053	0.974	$E_B(\Gamma_{7C} \leftrightarrow \Gamma_{9V})$	0	0.2315
$E_C(\Gamma_{7C} \leftrightarrow \Gamma_{7V})$	1.947	0.026	$E_c(\Gamma_{7C} \leftrightarrow \Gamma_{7V})$	0.0007	0.2310

For WZ GaN, the values relative to E_A are listed

square of the transition matrix element (I_V) determines the polarization selection rules and is given by

$$I_V = \left|\left\langle \Psi_V \middle| H_{\text{dipole}} \middle| \Psi_C \right\rangle\right|^2 \tag{6.5}$$

where Ψ_V and Ψ_C are the hole and electron wave functions.

The dipole transition matrix calculations show that the recombination between the conduction band and the holes in the topmost valence subband Γ_7 in the case of AlN is almost prohibited for $E\perp c$ [13], i.e., the emitted light is TM polarized. On the other hand for GaN, with the topmost valence subband Γ_9, the recombination is almost forbidden for $E||c$ [10], i.e., the emitted light is strongly TE polarized.

In AlGaN alloys, as the concentration of Al increases, Δ_{CF} changes from positive to negative. Neuschl et al. [14] proposed a crystal field bowing between 0 and −0.18 eV for AlGaN alloys while Coughlan et al. [15] proposed a crystal field bowing of −23 meV. As Δ_{CF} decreases, the energy separation between the three valence bands is reduced until the Γ_7 band becomes the uppermost band when Δ_{CF} becomes negative. Goldhahn et al. [12] calculated the relative positions of the three valence bands as a function of Δ_{CF} for $\Delta_{SO} = 18$ meV (see Fig. 6.3b). Assuming a linear dependence of Δ_{CF} on the Al concentration in the alloy, a band crossing at 5 % Al concentration was predicted for strain-free AlGaN layers. Due to the dependence of the valence subband order on the Al concentration, the degree of polarization of light emitted from AlGaN layers is related to the composition of the alloy. The degree of polarization of the emitted light ρ (also denoted P) is defined as

$$\rho = \frac{I_{\text{TE}} - I_{\text{TM}}}{I_{\text{TE}} + I_{\text{TM}}} \tag{6.6}$$

where I_{TE} and I_{TM} are the integrated intensities of the in-plane emitted TE- and TM-polarized light, respectively. At a critical Al concentration, the optical polarization of the emitted light from AlGaN layers will switch from predominant TE polarization ($E\perp c$) to predominant TM ($E||c$) polarization. Light emitted from UV LEDs grown along the c-axis, which is polarized with the electric field vector lying in the quantum well plane ($E\perp c$), can be efficiently extracted from an LED, while the polarized light emitted with the electric field vector perpendicular to the plane of the quantum well ($E||c$) propagates within the LED and may be extracted or

reabsorbed in the LED structure. The value of the critical Al concentration is therefore important for the extraction of the spontaneously emitted light in UV LEDs and hence has been widely investigated.

6.2.1 *Factors Influencing the Light Polarization Switching in AlGaN Layers*

In literature, a large variation in the Al concentration, at which switching of polarization characteristics of light emitted from $Al_xGa_{1-x}N$ layers occurs, has been reported. Nam et al. [11] measured the change in the degree of polarization of the light emitted from 1-μm-thick undoped $Al_xGa_{1-x}N$ layers grown on sapphire templates. The emitted light was found to switch from mainly TE polarized, for low values of x ($x < 0.25$), to dominantly TM polarized for higher values of x (see Fig. 6.4). At $x = 0.25$, the degree of polarization was found to be zero as the three valence subbands become degenerate at the Γ point. Kolbe et al. [16] showed that for UV LEDs, the in-plane electroluminescence is polarized with the intensity ratio of TE-polarized light to TM-polarized light reducing with decreasing wavelength. The cross-over from mainly TE-polarized light to dominantly TM-polarized light was found to be near 300 nm (see Fig. 6.5). Banal et al. [17] reported polarization switching at an Al composition $x \approx 0.83$ for $Al_xGa_{1-x}N$/AlN multiple quantum wells (MQWs) grown on sapphire (0001) substrates. For AlGaN MQW lasers built on free-standing AlN template grown on SiC substrates, Kawanishi et al. [18] estimated a change in the lasing polarization from the TM mode to the TE mode at an Al concentration $x \approx 0.36 - 0.41$ based on experimental results. Netzel et al. [19] reported an optical polarization switching at an Al concentration of 8 % for AlGaN layers grown pseudomorphically on top of 4.4 μm GaN buffer layers on c-plane sapphire substrates.

To understand the discrepancies in the reported values of the critical Al concentration, i.e., the wavelength at which the polarization switching of the emitted

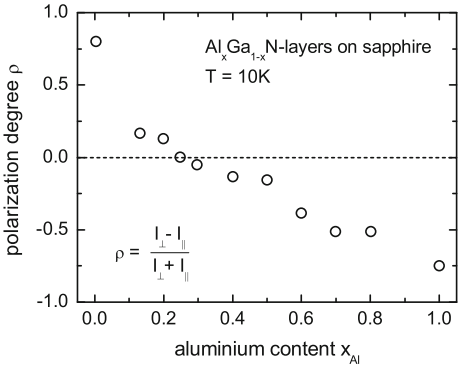


Fig. 6.4 Dependence of the degree of polarization of the emitted light on the Al concentration (x) for 1-μm-thick undoped $Al_xGa_{1-x}N$ layers grown on sapphire templates measured by photoluminescence spectroscopy. Based on [11]

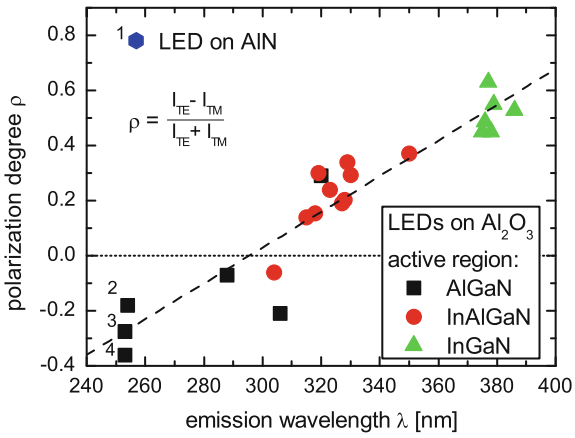


Fig. 6.5 Degree of polarization ρ of emission from LEDs fabricated on sapphire or AlN substrates. Device 1, in the *upper left hand corner*, was grown on AlN and emits highly polarized TE light at 253 nm. The quantum wells in devices 2, 3, and 4 are identical in design to device 1 but are grown on sapphire. The *dashed line* illustrates the trend for LEDs grown on sapphire. Based on [20]

light takes place, the influences of many factors such as the strain in the quantum well, quantum well thickness, and the internal electric fields have been investigated.

6.2.1.1 Strain State of the AlGaN Layers

The strain state of the quantum well strongly influences the Al concentration, i.e., the wavelength, at which the polarization switching of the emitted light takes place [17, 20, 21]. The strain in the $Al_xGa_{1-x}N$ quantum well layers grown epitaxially on substrates such as SiC, sapphire, GaN, and AlN is dependent on the substrate or the underlying $Al_yGa_{1-y}N$ template ($x<y$).

In strained layers due to the deformation of the crystal, the crystal field splitting differs from that in an unstrained bulk crystal. Chuang et al. [22] derived analytical expressions for the ordering of the valence subbands in strained wurtzite semiconductors using the $k \cdot p$ approach with the cubic approximation. In the case of strained $Al_xGa_{1-x}N$ layers, with isotropic in-plane strain, the energetic position of the Γ_9 band with respect to the Γ_7 band is given by

$$\Gamma_9 - \Gamma_7 = -\frac{\Delta' + \Delta_{SO}}{2} + \sqrt{\left(\frac{\Delta' + \Delta_{SO}}{2}\right)^2 - \frac{2}{3}\Delta'\Delta_{SO}}$$

$$\Delta' = \Delta_{CF} + [D_3 - D_4(C_{33}/C_{13})]\varepsilon_{zz}$$

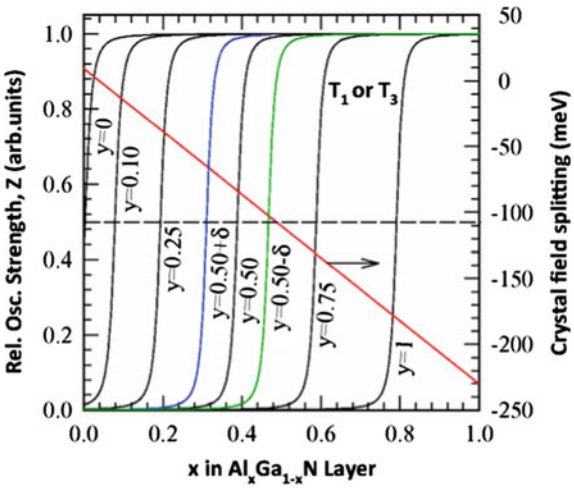


Fig. 6.6 Relative oscillator strength of the lowest excitonic transition, $\Gamma_{7c} \rightarrow \Gamma_{9v}(T_1)$ or $\Gamma_{7c} \rightarrow \Gamma_{7v}(T_3)$, under strain for light polarized along the z-direction plotted as functions of Al compositions of $Al_xGa_{1-x}N$ layers grown on $Al_yGa_{1-y}N$ templates. The *dashed line* defines the critical Al composition at which polarization switching occurs. The residual strain in $Al_{0.50}Ga_{0.50}N$ templates is considered to be $\delta = 0.4$ %. The interpolated values of the crystal field splitting of the $Al_xGa_{1-x}N$ layers are also shown in the same graph (*right axis*). Reprinted figure with permission from [21], Copyright (2011) by the American Physical Society

where Δ_{SO} is the split-off energy, Δ_{CF} is the crystal field splitting energy, D_i are the deformation potentials, C_{ij} are the elastic stiffness constants, and ε_{zz} is the strain tensor element along the c-direction [17, 22].

The polarization switching of the light emitted from $Al_xGa_{1-x}N$ layers occurs at the Al concentration at which $\Delta' = 0$. Hence, the Al concentration at which polarization switching occurs can be shifted to higher or lower values depending on the strain in the layer. Theoretical calculations reveal that for AlGaN layers grown along the c-direction, compressive in-plane strain pushes the $|X \pm iY\rangle$-like bands (Γ_9 and Γ_7) upward and tensile strain along the c-direction pushes the $|Z\rangle$-like band (Γ_7) downward [17, 20, 23]. Hence, compressive in-plane strain moves the Al concentration at which polarization switching occurs to higher values, while tensile in-plane strain moves the Al concentration to lower values. Sharma et al. [21] calculated the relative oscillator strength of the lowest excitonic transition under strain for light polarized along the z direction in $Al_xGa_{1-x}N$ layers grown on $Al_yGa_{1-y}N$ templates ($x < y$) (see Fig. 6.6). The critical Al concentration at which polarization switching occurs was found to increase linearly with the Al content in the $Al_yGa_{1-y}N$ template or substrate. Northrup et al. [20] have shown that the critical Al concentration can be controlled by changing the strain in the quantum well. Using this method, 253 nm LEDs with dominant TE emission have been demonstrated (see Fig. 6.5). Kolbe et al. [24] demonstrated a dependence of the in-plane light polarization of 380 nm LEDs on the in-plane strain of the active

region. The TM-polarized part of the in-plane emitted light was found to become more dominant as compared to the TE-polarized part for MQWs with decreasing tensile in-plane strain of the MQW barriers.

6.2.1.2 Quantum Confinement

Quantum confinement in $Al_xGa_{1-x}N/Al_yGa_{1-y}N$ MQWs affects the ordering of the valence subbands in the quantum well and hence the optical polarization of the emitted light [17, 20, 21, 25]. The quantum well thickness, the barrier composition, and the internal electric fields (due to spontaneous and piezoelectric polarization) influence the quantum confinement of the carriers in the QW. Banal et al. [17] proposed a simple qualitative model to describe the effect of quantum confinement on the ordering of the valence subbands in $Al_xGa_{1-x}N$/AlN single quantum wells. Since the hole effective mass in the top most $|Z\rangle$-like band (Γ_7) is much lighter than that in the $|X \pm iY\rangle$-like bands (Γ_9 and Γ_7), the quantum confinement lowers the energy of the $|Z\rangle$-like band (Γ_7) in the $Al_xGa_{1-x}N$ layer. Under sufficiently strong quantum confinement, cross-over of the Γ_7 and the Γ_9 bands will occur causing a switch in the optical polarization. For thin quantum wells (<3 nm), the well width dominates the quantum confinement effect and the critical Al concentration at which polarization switching of the emitted light takes place is shifted to higher values as the well width decreases (see Fig. 6.7). For thick quantum wells (>3 nm), the critical Al concentration is dependent on the internal electric field and is independent of the well width. Sharma et al. [21] reported that the switching of the valence subbands due to quantum confinement only occurs when the three valence subbands are in close proximity. Al Tahtamouni et al. [26] investigated the optical

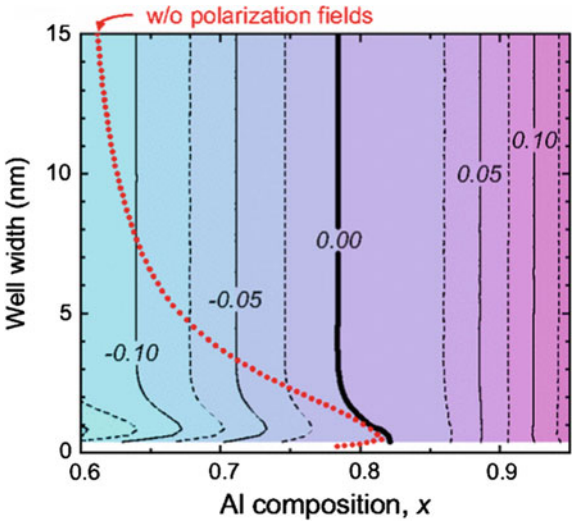


Fig. 6.7 Contour plot of the calculated energy difference of $E(\Gamma_7) - E(\Gamma_9)$ in the unit of electron volts for $Al_xGa_{1-x}N$/AlN single quantum wells grown on unstrained AlN. *Red/gray-dotted thick line* is the $E(\Gamma_7) - E(\Gamma_9) = 0$ line for flat-band QWs without a polarization field, while (*black*) *thick* and *thin lines* are for QWs with polarization fields. The assumed spontaneous polarization was -0.040 C/m^2. Reprinted figure with permission from [17], Copyright (2009) by the American Physical Society

polarization of $Al_{0.65}Ga_{0.35}N$/AlN single quantum wells using photoluminescence spectroscopy. At a well width of 2 nm, the dominant polarization component of the band-edge emission switched from $E||c$ to $E\perp c$. Wierer et al. [27] reported a decrease in the degree of polarization with increasing quantum well thickness for UV LEDs with $Al_xGa_{1-x}N/Al_yGa_{1-y}N$ MQWs.

Northrup et al. [20] investigated the influence of the barrier composition on critical Al concentration for $Al_xGa_{1-x}N/Al_yGa_{1-y}N$ MQWs. Due to the lighter effective mass in the CH band, as compared to the HH band, the hole wavefunction is less localized than that for the HH state. The energy of the CH band is thus more sensitive to the barrier potential as compared to the HH band. For a fixed quantum well thickness of 3 nm, the critical wavelength, at which polarization switching of the emitted light takes place, could be shifted by 15 nm by increasing the Al concentration in the barrier from $y = 0.7$ to $y = 1.0$.

The critical Al concentration, at which polarization switching of the emitted light takes place, decreases gradually with increasing carrier density [27–29]. This can be explained by the fact that at high carrier densities, carriers will occupy higher states above $k = 0$ in the conduction and valence subbands which allows more transitions to the second and third highest valence subbands. The light emission characteristics will thus be affected by transition matrix elements far from $k = 0$. The matrix elements for TM polarization above the band edge are much larger than those for TE polarization. Hence, the light emission for TM polarization becomes larger than that for TE polarization at higher carrier densities.

6.2.2 Optical Polarization Dependence on Substrate Orientation

The optical polarization properties of the spontaneous light emitted from AlGaN quantum wells grown on semipolar and nonpolar substrates have been investigated to improve the performance of UV LEDs [25, 30–32]. Using a 6 × 6 k·p Hamiltonian under the quasi-cubic approximation, Yamaguchi [30] calculated the transition matrix elements for light polarized in the substrate plane and perpendicular to the substrate plane in the case of 1.5-nm-thick $Al_xGa_{1-x}N$/AlN quantum wells grown on AlN substrates with orientation θ with respect to the c-plane (see Fig. 6.8). In the c-plane case due to the sixfold symmetry, there is only a minor interaction between the three valence subbands through the spin–orbit interaction. Hence, an abrupt change from TE to TM polarization is observed at an Al concentration of 76 % (6.8a). Additionally, the in-plane optical properties are isotropic. For substrates with orientation $\theta > 0$, the symmetry in the quantum wells is broken resulting in a mixing of the three valence subbands. Hence, a gradual polarization switching occurs as the Al concentration increases. Furthermore, a large in-plane optical anisotropy appears due to the break-down of the sixfold symmetry and the presence of anisotropic in-plane strain.

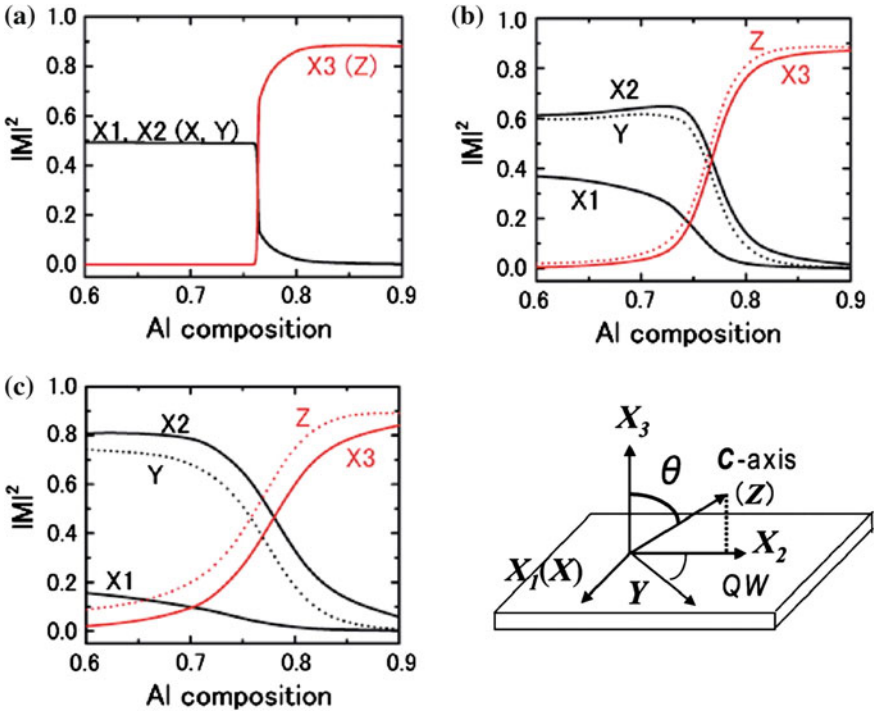


Fig. 6.8 Al composition dependence of the optical matrix elements for a single quantum well layer for *X*1, *X*2, and *X*3 polarization (*solid lines*) and *Y* and *Z* polarization (*broken line*) in 1.5-nm AlGaN quantum wells on **a** exact, **b** 5°-misoriented, and **c** 10°-misoriented *c*-plane AlN substrates. Reprinted with permission from [30], Copyright 2010, AIP Publishing LLC

In the case of $Al_xGa_{1-x}N$ thin films grown on m-plane AlN substrates ($\theta = 90°$), the valence band ordering is affected by the in-plane strain which is compressive and anisotropic [31]. Transition matrix calculations show that the emitted light is mainly polarized in the *z*-direction ($E||c$) which lies in the plane of the substrate, and hence can be easily extracted from the top/bottom surface [31, 32]. LEDs grown on *m*-plane AlN can thus be used for the fabrication of efficient surface-emitting LEDs. Banal et al. [33] showed experimentally that the band-edge photoluminescence from *m*-plane AlGaN quantum wells grown on partially relaxed AlGaN templates has a strong polarization in the direction $E||c$ (see Fig. 6.9). Theoretical investigations reveal that although semipolar AlGaN quantum wells show stronger in-plane polarization of the emitted light as compared to *c*-plane AlGaN quantum wells, they show weaker in-plane polarization as compared to the nonpolar case [30, 32]. Wang et al. [32] reported that $(11\bar{2}2)$-plane AlGaN quantum wells grown on AlN substrates show a weaker in-plane polarization of the emitted light as compared to $(20\bar{2}1)$-plane AlGaN quantum wells.

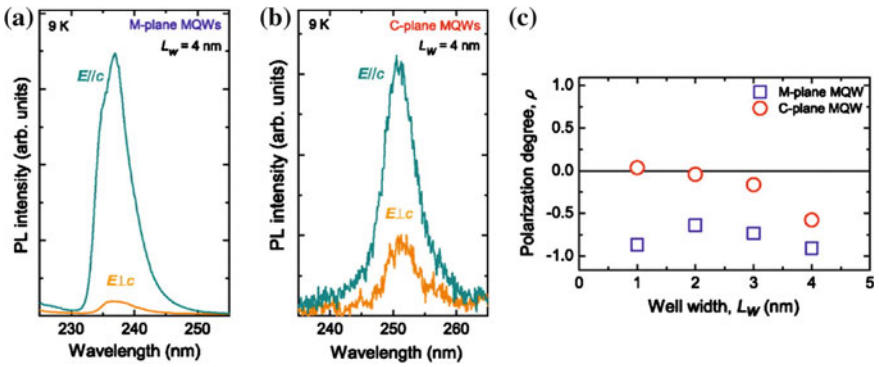


Fig. 6.9 Polarization PL spectra from **a** *m*- and **b** *c*-plane AlGaN MQWs with quantum well width (L_w) = 4 nm. **c** Polarization degree (ρ) of the PL from the *m*- and *c*-plane AlGaN MQWs as a function of L_w. The wavelength of the LEDs varied from 225 to 250 nm. All data were measured at 9 K. Reprinted with permission from [33], Copyright 2014, AIP Publishing LLC

For the InGaN material system, Schade et al. conducted both experimental studies and analytical calculations on polarization properties of InGaN layers and LEDs on polar, semipolar, and nonpolar crystal orientations. It was confirmed that both the inclination angle between the *c*-plane and the plane of growth as well as the indium composition and thus the anisotropic strain state influence the transition point between dominant optical polarization states [34, 35]. While the main difference of the InGaN system in comparison to AlGaN is the negative crystal field splitting Δ_{CF}, the model itself is valid for the entire AlInGaN system.

6.2.3 *Influence of the Optical Polarization on the Light Extraction Efficiency*

The polarization of the emitted light is an important issue for the extraction of light from UV LEDs grown along the *c*-axis since the angular distribution of the light emitted from the active region in the LED is dependent on the degree of polarization. Here, we will use a qualitative approach to estimate the angular emission distribution from a III-nitride semiconductor using a simplified model based on the basis states for a bulk Hamiltonian system according to [34, 36].

In the first approximation, all emitters can be regarded as dipoles. The orientation of the dipole then describes the polarization state and the direction of emission. The electric field vector **E** of the emitted wave lies in the plane defined by the orientation of the dipole and the photon vector **k**. The photon vector **k** is perpendicular to **E**.

In III-nitride semiconductors, the conduction band is an s-orbital which is fully symmetric while the valence subbands are formed by p-orbitals. The three valence subbands in an unstrained system have the dipole distribution according to $|p\rangle$

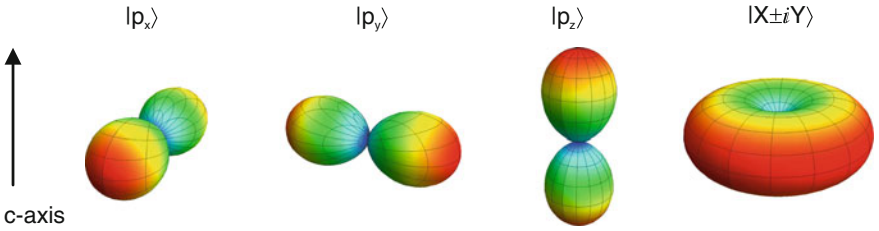


Fig. 6.10 Orientation of the $|p_x\rangle, |p_y\rangle, |p_z\rangle$, and the $|X \pm iY\rangle$ orbitals

orbitals aligned along the x-, y-, and z-axis. The $|p_x\rangle$ and the $|p_y\rangle$ orbital combine and form the HH and LH hole valence bands (wave form $|X \pm iY\rangle$ like), which have a rotational symmetric distribution around the c [0001] axis (see Fig. 6.10). Emission into this subband results in TE-polarized radiation inside the crystal. The $|p_z\rangle$ orbital forms the CH band (wave form $|Z\rangle$ like) which is aligned along the c-axis. Transitions into this band result in the emission of photons that are polarized parallel to **c** and are emitted perpendicular to **c**.

In spherical coordinates, the angular dependence of the wavefunctions of the p-orbitals can be described as follows:

$$\begin{aligned} |p_x\rangle &= \sin\vartheta\cos\phi \\ |p_y\rangle &= \sin\vartheta\sin\phi \\ |p_z\rangle &= \cos\vartheta \end{aligned} \tag{6.7}$$

Since $\mathbf{E} \perp \mathbf{k}$ is required, the intensity distribution for the emitted radiation from a single dipole has a doughnut shape. The intensity I is then given by

$$\begin{aligned} I_x &= I_{x0}\left(\sin^2\vartheta\sin^2\phi + \cos^2\vartheta\right) \\ I_y &= I_{y0}\left(\sin^2\vartheta\cos^2\phi + \cos^2\vartheta\right) \\ I_z &= I_{z0}\sin^2\vartheta \end{aligned} \tag{6.8}$$

In reality, emission from all subbands occurs and therefore the light is not 100 % polarized. The ratio of contributions from each valence band is governed by the separation of the bands and the thermal occupation according to the Fermi–Dirac distribution and expressed in the terms I_{x0}, I_{y0}, and I_{z0}. In the case of emitters on the rotational symmetric (0001) c-plane, $I_{x0} = I_{y0}$.

In Fig. 6.11, the angular distribution of the emitted light with a certain mix of TE–TM polarization is displayed and the overall emission is normalized to $I_{x0} + I_{y0} + I_{z0} = 1$.

In the case of mainly TE-polarized light, most of the light is emitted at small angles with respect to the c-axis, i.e., more light is emitted within the top surface and bottom substrate light escape cones. This results in a high η_{extr} of the device. As the degree of polarization decreases, the light emitted at higher angles increases and

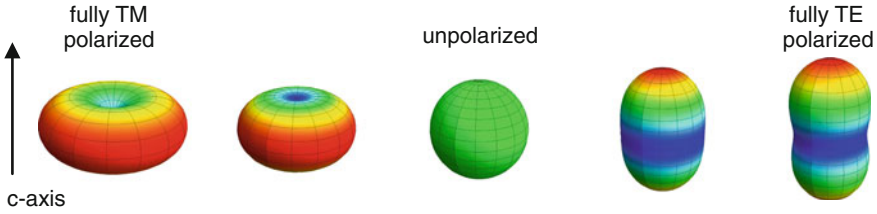


Fig. 6.11 Calculated emission distribution inside the semiconductor of polarized light with different polarization states from fully TM to fully TE polarized

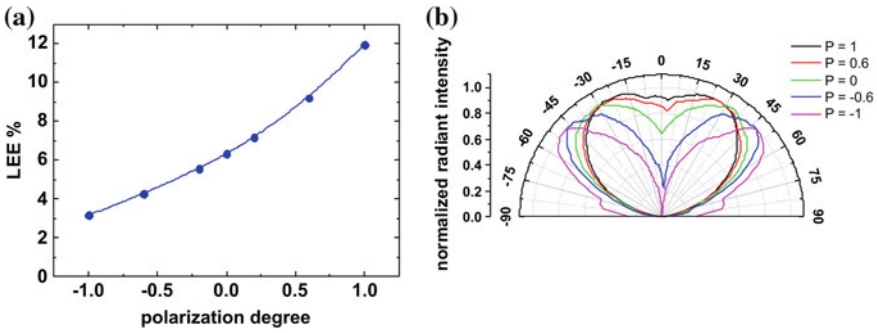


Fig. 6.12 Simulated dependence of the **a** light extraction efficiency from a 320 nm UV LED chip and **b** far-field radiation pattern of a 320 nm UV LED chip on the degree of polarization *P* of the light emitted from the active region

at zero polarization the light emission is isotropic. Further decrease in the degree of polarization results in the emission being mainly TM polarized with most of the light emitted at large angles w.r.t. the *c*-axis. As described in Sect. 6.1, photons emitted at these large angles are trapped and finally absorbed in the LED structure resulting in devices with low η_{extr} values.

In Fig. 6.12, the simulated dependence of the η_{extr} of a 320 nm AlInGaN LED on the polarization degree of the light emitted from the active region is shown. For TE-polarized emission, 12 % of the emitted light is outcoupled from the LED (see Fig. 6.12a). The η_{extr} was found to decrease as the light emission from the active region becomes more TM polarized. For completely TM-polarized emission, only 3 % of the emitted light can be outcoupled. The rest of the light is lost due to absorption in the LED. The degree of polarization of the light emitted from the active region of the LED also impacts the far-field radiation pattern of the device (see Fig. 6.12b). As the polarization switches from predominantly TE polarization to predominantly TM polarization, the emergence of *rabbit ears* is seen due to outcoupling of light from the sidewalls of the sapphire substrate. In applications where the production of directional light is necessary, this dependence of the

far-field radiation pattern of UV LEDs on the polarization degree is an important issue.

Hence, to achieve highly efficient UV LEDs, it is necessary to either shift the wavelength at which switching of the polarization occurs to shorter wavelengths, grow on nonpolar substrates, or to develop novel methods to extract the light emitted at large angles with respect to the *c*-axis.

6.3 Concepts for Improved Light Extraction

The design of an LED is a complex and challenging task since many aspects and boundary conditions need to be considered which often lead to conflicting requirements. The contact metallization for the p-contact needs to be large and homogeneous since it usually defines the emitting area of the diode. On the other hand, the n-contact must not be placed too far from the center of the p-contact since the lateral current transport is limited and hence current crowding effects will play a large role in diminishing the device performance. In order to dissipate the heat generated in the LED, efficient heat sinking needs to be included which might also conflict with the contact design. In the case of bottom emitter LEDs, the metal for the p-contact should ideally be UV-reflective in order to improve the light extraction while it is also required to possess a high work function to achieve low contact resistivities and low operating voltages. The surface, the backside, and the interfaces of the LED can be patterned or modified to allow efficient light extraction, while other parameters must not be deteriorated. In the following sections, various design considerations and requirements for metal contacts, surface patterning, and the subsequent packaging of LEDs are presented and discussed.

6.3.1 Contact Materials and Design

The design of the metal contacts of UV LEDs has a large influence on the light extraction efficiency. As explained in Sect. 6.1, only light that is emitted in a narrow angle with respect to the wafer surface can be extracted. Usually, the transparent substrate, typically sapphire, is used for light extraction. Therefore, light that is emitted in the opposite directions toward the epitaxial layer and p-metal contact is normally lost. By employing UV-reflective metal contacts and UV-transparent p-layer materials, part of the emitted light can be reflected back and the chances for light extraction through the substrate are enhanced. Overall, an increase of the extraction efficiency by a factor of two seems possible. In addition, if the surface of the wafer is not flat but patterned, the escape angle is changed and after (multiple) reflections at interfaces or contacts light rays can be extracted that did not have the correct angle for extraction in the beginning.

In order to increase the light extraction efficiency through reflective contacts, several boundary conditions have to be met: First, the semiconductor layer structure must not absorb the photons. Typically, the top contact layer is made of Mg-doped p-type GaN or p-type AlGaN with a bandgap smaller than the quantum well bandgap, and hence absorption occurs. Also, acceptor-related deep-level transitions, which originate from the high magnesium doping levels in p-type materials, can significantly increase the UV absorption. This problem can be heightened by multiple reflections within the LED that extend the path of the photon inside the absorbing structure. To avoid absorption, the thickness of the p-type layers should be as small as possible without deterioration of the current spreading properties. Using slanted or structured surfaces or edge emission, the extraction efficiency can be increased and the optical path reduced.

Another important aspect is the choice of reflective materials for the metal contacts. When choosing a material or a material system for the p-type contact, not only the reflectivity but also the metal work function and hence the ability to form an ohmic contact needs to be taken into consideration.

6.3.1.1 Ohmic Contacts for UV LEDs

The barrier ϕ_B for carriers at the interface between semiconductor and metal is a function of the bandgap E_g, the metal work function ϕ_m, the semiconductor work function ϕ_s, and the electron affinity χ_s of the semiconductor:

$$\begin{aligned} q\phi_B &= q(\phi_m - \chi_s) && n-\text{semiconductor} \\ &= E_g - q(\phi_m - \chi_s) && p-\text{semiconductor} \end{aligned} \tag{6.9}$$

In order to allow carrier injection into the semiconductor by thermionic transport, the barrier ϕ_B needs to be zero. This is easy for the case of Si-doped n-type GaN, since metals such as titanium (ϕ_m = 4.33 eV) or aluminum (ϕ_m = 4.28 eV) [37] have similar work function as the electron affinity of n-GaN ($\chi_s = 4.1$ eV) [38]. With increasing aluminum content in AlGaN-based structures, χ_s and ϕ_s increase and hence metals with a larger work function ϕ_m are needed. Recently, vanadium-based contacts on ICP-etched UV-B transparent $Al_{0.4}Ga_{0.6}N$ were demonstrated with contact resistivities as low as $\rho_c = 2.3 \times 10^{-6}\,\Omega\,\text{cm}^2$ [39].

For metal contacts to p-type semiconductor materials, the formation of ohmic contacts is much more challenging: Since the bandgap E_g of GaN is large, a metal with a work function of approximately 7.2 eV would ideally be required, which, however, does not exist. Ohmic metal contacts to Mg-doped p-AlGaN would be even more challenging due to the increased values for χ_s, ϕ_s, and E_g. In order to reduce the p-contact resistance in UV LEDs, typically a thin highly Mg-doped p-GaN contact layer is placed on top of the p-AlGaN. Even though p-GaN is still far from ideal considering its high work function, the high Mg-doping levels can facilitate tunnel injection and consequently low resistance ohmic p-contacts. Nevertheless, as discussed above the Mg-doped GaN contact layer should be as thin

as possible to avoid absorption. For example, a 50-nm-thick p-GaN contact layer would absorb more than 81 % of the UV light on a roundtrip from (UV-reflective) metal contacts (assuming an emission peak near 275 nm). By reducing the p-GaN thickness to 5 nm, the absorption loss per roundtrip can be reduced to 16 %.

The formation of p-type contacts to p-GaN is usually achieved by depositing palladium, platinum, nickel, or nickel–gold metal layers and the subsequent annealing in oxygen or nitrogen atmosphere in order to form ohmic contacts. However, the work function of all these metals is considerably smaller than the ideal value according to (6.9), with the highest value for platinum (5.65 eV), followed by palladium (5.12 eV) and nickel–gold (Ni: 5.15 eV), where in the latter case the nickel is oxidized to the p-semiconductor NiO under oxygen ambient [37, 40]. Also, silver has been used ($\phi_m = 4.26\,\text{eV}$) [37].

Despite the fact that the condition for ϕ_B is in general not met for these metals, ohmic contacts have been realized on p-GaN. This is aided by the fact that the experimentally determined Schottky barrier height for the metal contacts on p-GaN was found to be in the range of 0.5 bis 0.65 eV for platinum, nickel, gold, and titanium. This is much lower than the theoretical values according to (6.9) which predicts Schottky barrier heights near 2 eV. Also, ϕ_B was found to only weakly depend on ϕ_m [41, 42]. This deviation can be explained by the presence of surface states and Fermi-level pinning. Furthermore, the metal contacts on highly doped GaN layers often employ tunneling transport instead of thermionic emission [43–47].

While the metals mentioned above are suitable for visible LEDs due to their high reflectivity or the possibility to make them transparent (NiO) and combine them with additional reflective layers, this is not true anymore for deep UV emission. Most metals become highly absorbing at shorter wavelengths, making them unsuitable for reflective contacts. In the following section, the optical properties of various metals will be discussed.

6.3.1.2 Reflectivity of Contact Metals

The optical reflectivity R for light with normal incidence is a function of the complex refractive index $\overline{n} = n - ik$ where n is the real refractive index and k is the extinction coefficient. Both the real and the imaginary parts of $\overline{n}$ are functions of the frequency ω or wavelength λ.

$$R(\bar{h}\omega) = \left|\frac{\overline{n}-1}{\overline{n}+1}\right|^2 = \frac{n^2-2n+k^2+1}{n^2+2n+k^2+1} \tag{6.10}$$

The reflectivity is therefore strongly dependent on the wavelength of the incident light and can become small at shorter wavelength due to transitions in the band structure which lead to strong absorption. Figure 6.13 shows the reflectivity R and the real refractive index n of various metals that are mostly used for semiconductor

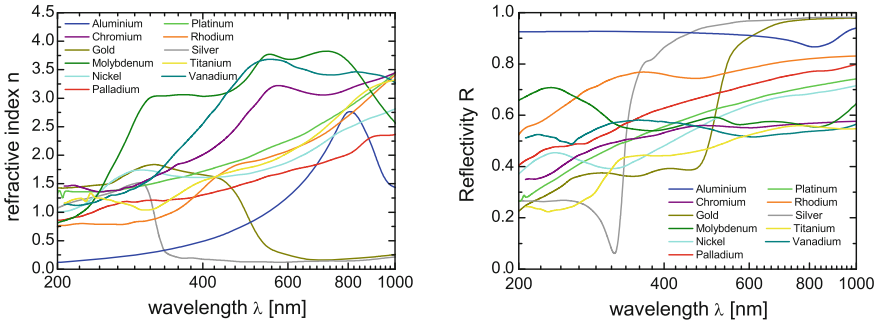


Fig. 6.13 Real part of the refractive index *n* (*left*) and calculated reflectivities *R* of various metals, usually calculated at an interface between the metal and air/vacuum. Based on [1]

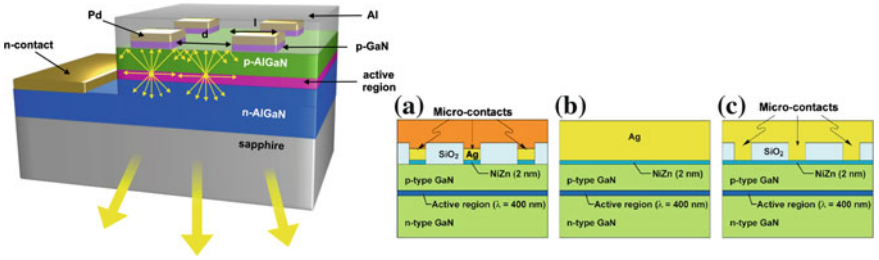


Fig. 6.14 *Left* Schematic of a UV LED with nanopixel p-contacts made of palladium with additional aluminum reflector. *Right* Violet LED with aluminum-based (**a**) or silver-based (**c**) omnidirectional reflector with micro-contacts, **b** silver-based standard reflector. Reprinted with permission from [49], Copyright 2006, AIP Publishing LLC

contacts. While many metals have a sufficiently high reflectivity in the visible range allowing the formation of reflective ohmic contacts, this is not true for the UV spectral range. Silver, palladium, and other metals become highly absorbing, making new concepts for the formation of reflective contacts necessary. Aluminum, which is highly reflective even at wavelength shorter than 200 nm, is known to exhibit Schottky behavior when deposited on p-type GaN or p-AlGaN, leading to high contact resistivities, voltage drops at the metal-semiconductor interface and therefore to heating, lifetime degradation, and ultimately device failure.

A novel concept that combines high work function metals for good ohmic contacts with UV-reflective metals for a high extraction efficiency is based on the so-called nanopixel contact design. The nanopixel LED geometry consists of small (less than one micrometer wide) laterally distributed ohmic metal contacts (e.g., palladium, nickel) and an UV-reflective aluminum layer, which covers most of the semiconductor surface and reflects the light back into the LED. This design has been shown to work best when the contact spacing is smaller or at least in the same range as the current spreading length in order to allow homogeneous current injection [48]. Therefore, the nanopixel contact spacing is typically in the order of

few hundred nm to a few microns. Figure 6.14 shows a schematic illustrating this design. The size of the nanopixel contacts, the spacing, and the thickness of the p-(Al)GaN current spreading layer have to be carefully adjusted in order to achieve a homogeneous lateral current distribution as well as a high coverage of the surface area with UV-reflective aluminum metal compared to low-reflectance ohmic palladium contacts.

A similar concept was applied by Kim et al. for near-UV LEDs with 400 nm wavelength. While most metals still show acceptable reflectivities at this wavelength, an increased extraction efficiency could still be achieved using the so-called aluminum-based omnidirectional reflectors with micro-contacts [49]. For this design, silver contacts (partly with an additional thin NiZn layer) where used in a micro-contact geometry and a SiO_2 insulation layer was deposited between the contacts. A large area aluminum or silver reflecting layer was deposited on top of this structure, increasing the light output by 38 % (Al) and 16 % (Ag), respectively, in comparison to standard large area silver contacts. A distributed Bragg reflector (DBR) consisting of 11 layers of alternating quarter-wave thick Ti_3O_5 and Al_2O_3 layers was used, by Jeong et al. [50], along with a p-ohmic contact ITO interlayer to increase the output power of 385 nm LEDs by 15 % compared to LEDs with a Ag reflector.

6.3.1.3 Thermal Management and Current Crowding

One of the most important challenges for high-power LEDs is efficient heat extraction from the active region of the device. Especially, LEDs with a single large area p-contact will suffer from inhomogeneous heat distribution and temperature-driven droop of the internal and external quantum efficiency. Various groups investigated and applied different concepts for efficient heat extraction such as micro-pixel contact arrays [51, 52] and multi-finger contacts [53, 54]. In all cases, the goal is to spread the heat more evenly over the semiconductor chip and to efficiently extract it from the device. Adivarahan et al. employed a micro-LEDs design where an array of 10 × 10 columns of 26 μm diameter mesas was etched into the semiconductor heterostructure [51]. The n-contact filled the whole area between these columns which reduces current crowding effects and helps to extract the heat from the active region. After planarization, a large area p-contact was deposited. It was shown that the output power can be increased by 50 % due to thermal management and reduced current crowding. A similar design for InGaN visible LEDs was employed by Choi et al. [55]. Here, micro-LEDs with diameters of 8–20 μm were etched into the semiconductor surface and metal interconnects were processed. A smaller size of those pixels led to an increase of the operation voltage of up to 4 V (a factor of two) and an increase by a factor of 1.5–4 in the emitted power per unit active area. This is mostly attributed to an improved thermal management and an improved light extraction efficiency due to scattering of emitted light at the etched side walls as well as a shorter photon flight distance to the side walls, reducing the likelihood of reabsorption.

In a later study, the influence of the geometry and pixel size of micro-LEDs on output power and efficiency was studied in detail by Lobo et al. [56]. Different concepts such as micro-pixels, interdigitated finger contacts, and large area contacts were compared, and the influence of pixel size and their spacing was analyzed. It was shown in this study that micro-pixel LEDs with 10 µm × 10 µm contact size could increase the output power of UV-B LEDs by more than a factor of two as compared to conventional large area contacts. The series resistance and operation voltages also reduced and flip chip mounting was successfully demonstrated.

The concept of interdigitated finger contacts was further studied by Rodriguez et al. showing that devices with smaller finger width and the same p-contact area exhibited higher output power levels, improved external quantum efficiencies, lower operation voltage, and a thermal roll over at higher dc currents [53]. A detailed study of heat distribution, thermal resistance, and output power of blue and ultraviolet LEDs with multi-finger contacts by Chakraborty et al. showed that devices with an effective contact area of 300 µm × 300 µm can be driven at dc currents as high as 3 A without thermal rollover [54].

6.3.2 Surface Preparation

In this section, various concepts are discussed which are employed to improve the light extraction from the semiconductor. The general concept in most cases is the variation of the angle θ between the emitted photon from the active region and the normal to the interface between semiconductor and air or the substrate and air. As explained in Sect. 6.1, only photons emitted within the light extraction cone can escape from the semiconductor. Thus concepts to increase the critical extraction angle are employed.

6.3.2.1 Surface Patterning

In the past, many technological concepts have been developed in order to increase η_{extr} by changing θ. These include encapsulation (see Sect. 6.3.3) as well as roughening of the front side, back side, using slanted side walls, and employing techniques such as photonic crystals and plasmonic.

One of the most promising approaches to vary the angle θ between the photon and the surface normal in UV LEDs is based on shaped semiconductor chips. In the case of visible LEDs, a truncated inverted pyramide (TIP) geometry has been successfully applied [57] to improve the light extraction efficiency. Here, the side walls of the semiconductor chip are slanted in a way that leads to a redirection of the light beams after internal reflection, allowing the beam to leave the LED through the surface (see Fig. 6.15). These concepts work most efficiently if the thickness of the LED chip is close to its lateral dimensions. While this can be easily achieved for LEDs in the visible range, e.g., utilizing thick GaP substrates, this is

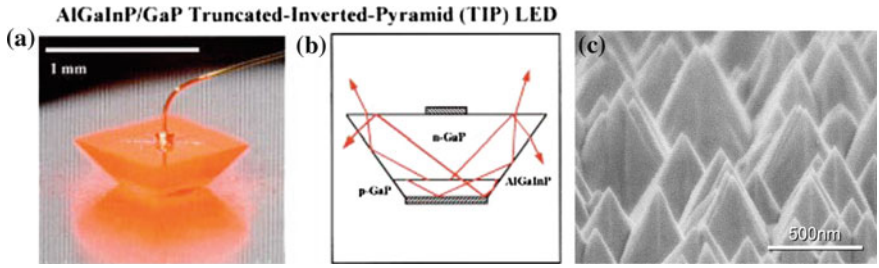


Fig. 6.15 *Left* Trunkated inverted pyramid design in a AlInGaP LED, reprinted with permission from [57], Copyright 1999, AIP Publishing LLC. *Right* N-side of a GaN-based 410 nm LED etched by PEC, reprinted with permission from [59], Copyright 2004, AIP Publishing LLC

not possible for UV LEDs consisting of only a few microns thick Al(Ga)N layer grown on top of a foreign substrates like sapphire or silicon.

Wierer et al. [58] used deep etched angled mesa sidewalls along with an Al reflector to outcouple the UV LED light emitted in-plane, due to TM polarization of the light, through the sapphire substrate. The light extraction efficiency was found to increase as the average distance to the mesa side wall decreased. A fourfold increase in the output power was achieved for ≈270 nm LEDs using such reflecting structures, with sidewall angle of $\approx 70^\circ - 80^\circ$ with respect to the epitaxial plane, as compared to standard LEDs at low polarization degrees.

Another approach to increase the likelihood for photon escape by changing the angle θ is to roughen the surface of the emitting interface. This technique not only increases the one bounce extraction efficiency but also randomizes the angular distribution of the photons in the LED, allowing photons to find the light escape cone after multiple reflections. This can be done by treatment with a rough polishing paste, wet chemical, or dry chemical etching [60, 61] or by other patterning techniques. By removing the substrate using laser lift-off [62] or sacrificial layers [63, 64], thin-film LEDs can be created and patterning of the remaining layer is simplified. Fujii et al. applied a combined method of laser lift-off to remove the sapphire substrate and subsequent photo-electrochemical (PEC) etching of the exposed semiconductor surface using KOH [59]. This lead to a rough backside of the GaN layer with a cone-like surface structure (see Fig. 6.15). Using this approach for 410 nm LEDs, a threefold increase in output power has been achieved. A similar approach has been successfully demonstrated by Zhou et al. [65], showing enhanced light extraction from surface roughened AlGaN-based thin-film deep UV LEDs (see Fig. 6.16). Using a low-temperature metamorphic AlN strain-relief interlayer for the growth on GaN/sapphire templates, the sapphire substrate could be removed by excimer laser lift-off. The roughening of the n-AlGaN layers was achieved through photo-electrochemical etching in KOH yielding an increase in light extraction efficiency by a factor of 4.6 and 2.5 for 280 and 325 nm LEDs, respectively.

For GaAs-based LEDs, another surface patterning technique was used employing randomly distributed polystyrene spheres that act as a mask for the

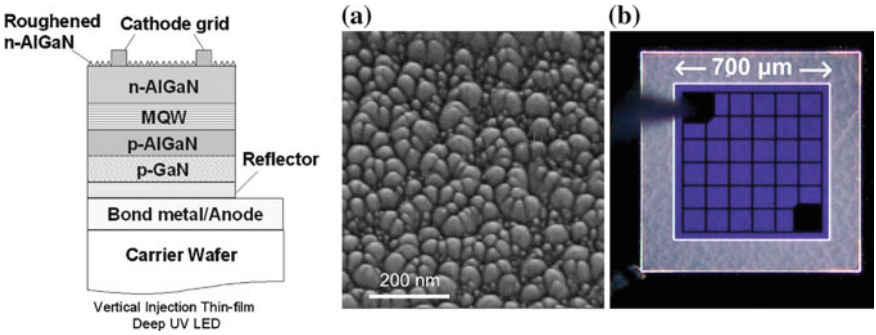


Fig. 6.16 *Left* Layer structure of a UV flip chip LED with roughened AlGaN surface, *Center* SEM image of the N-polar n-AlGaN surface, *Right* Emission pattern of a 325 nm LED under current injection. Reprinted with permission from [65], Copyright 2006, AIP Publishing LLC

subsequent dry etching process [66]. The result is a surface covered with cylindrical pillars that change the angle of the emitted light cone. Using 300-µm-thick spheres, an increase of angular integrated light extraction by a factor of two at a wavelength of 910 nm was shown. It can be expected that for UV LEDs with considerably shorter wavelength a smaller diameter of spheres will be most efficient.

Using these methods of surface patterning does not only increase the light extraction efficiency but in addition leads to a change in the emission profile. This can be beneficial if the light needs to be focused onto a certain spot area or into a fiber. One technique to achieve this goal is to cover the surface of the LED with an array of microlenses. These can be formed by various methods and are usually fabricated by standard lithography techniques and a subsequent plasma dry etching step in order to transfer the pattern into the semiconductor or the sapphire substrate. One method that was shown to be very efficient is the formation of microlenses using a reflow technique to shape the photo resist. In their approach, Khizar et al. patterned a photoresist array on the polished backside of the sapphire substrate of 280 nm LEDs into cylinders [67]. Upon heating, the resist flows into a hemispherical shape which is subsequently transferred into the sapphire by an ICP plasma etching process. Using this approach, an increase in output power of 55 % was achieved with microlenses of 12 µm diameter and 1 µm height.

One of the disadvantages of the reflow method is that the resulting shape of the lenses is relatively sensitive to process parameters, and hence the final result may vary strongly. A more stable method was developed by Lobo et al. where instead of lenses an array of micro-frustrums in a hexagonal array was formed on the polished sapphire substrate. After photolithography, a dry etching process was used to transfer the cylindrical photoresist pattern into the substrate. The dry etching process parameters were optimized in order to modify the slope angle of the etched sidewalls. This led to the formation of frustrums and increase of the light extraction efficiency. The magnitude of this increase depends on the slope angle and was also simulated using ray tracing analysis. Figure 6.17 shows the resulting pattern and the increase in output power. Using this method, an increase of output power by 68 %

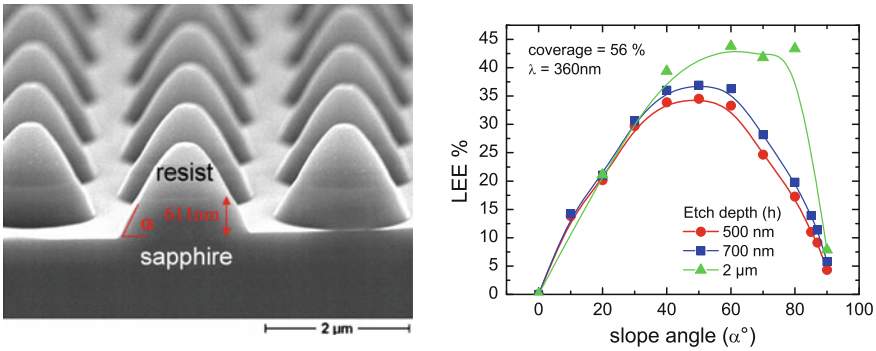


Fig. 6.17 *Left* SEM image of micro-frustrums etched into sapphire with residual photo resist on top. *Right* Calculated increase in extraction efficiency as function of slope angle and etch depth

for an etching angle of around 59° was achieved for 386 nm LEDs grown on GaN substrates and a 27 % increase in the output power was achieved for 323 nm LED grown on sapphire substrates.

A technologically challenging but very promising approach is the application of photonic crystals (PCs) to suppress or enhance the propagation of certain optical modes. Using two-dimensional arrays of holes etched into the semiconductor, photonic band gaps are created that prevent light from traveling in the in-plane direction. The spacing and size of the holes has to be adjusted to the emission wavelength. This makes the realization of PCs very challenging for UV LEDs. Oder et al. presented results of LEDs emitting in the blue (460 nm) and UV-A region (340 nm) [68]. The photonic crystal with diameters of 300 nm and a periodicity of 700 nm was formed by electron beam lithography and subsequent 250 nm deep etching by ICP into the p-side of the LEDs. This leads to an increase of the emitted power by 63 % (visible) and 95 % (UV-A), respectively. By careful adjustment of the PC spacing, size, and etch depth, a further increase seems probable. Wierer et al. reported on 460 nm LEDs with PCs etched into the surface layer [69]. Hole diameters between 200 and 250 nm with lattice constants of 270–340 nm were used in a hexagonal pattern. In their InGaN-based LEDs, a tunnel junction was embedded in order to be able to place the PC close to the QW while keeping the absorbing contacts at a large distance. The emission pattern was significantly altered and an increase of light extraction by ≈50 % was achieved. Shakya et al. [70] developed a design in which the light generation region of the LED was separated from the light extraction region where 2-D PCs were fabricated in the p-GaN layer (see Fig. 6.18). The light output from LEDs is increased by extracting the lateral guided modes of light in the vertical direction with the help of the PCs. A 2.5-fold increase in the output power of 333 nm LEDs was demonstrated with the use of PCs with triangular lattice patterns of circular holes with diameter of 200 nm and lattice constant of 600 nm.

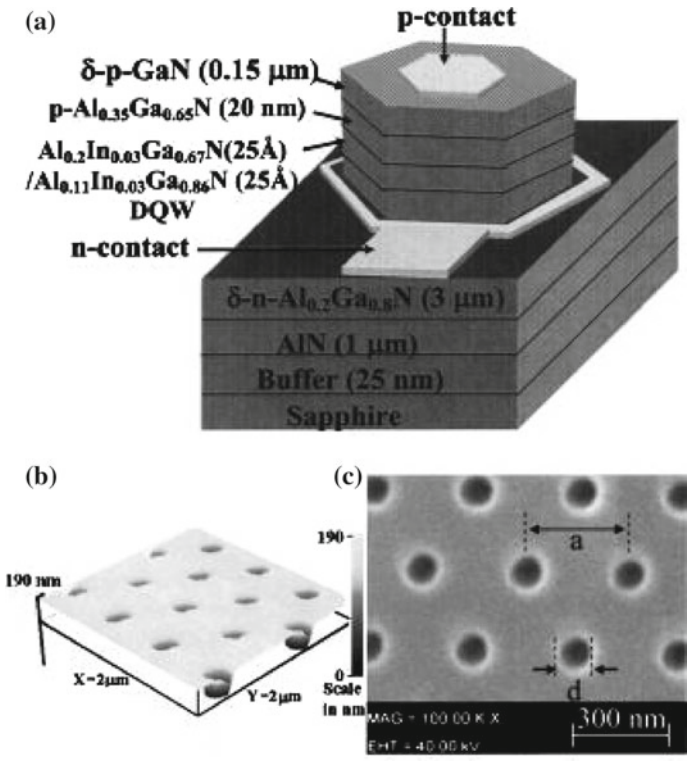


Fig. 6.18 **a** Schematic diagram of a 333 nm UV LED structure, with 2-D PCs etched into the p-GaN layer, showing mesa and contact pads. **b** AFM image of the PCs on a UV LED with lattice constant a =600 nm and hole diameter d =200 nm. The etch depth is $\sim$190 nm. **c** SEM image of the PCs on a UV LED with a = 300 nm d = 100 nm. Reprinted with permission from [70], Copyright 2004, AIP Publishing LLC

6.3.2.2 Patterned Substrates

Since nitride-based light-emitting devices grown epitaxially on foreign substrates such as sapphire, silicon carbide, or silicon suffer from a high density of threading dislocations, various concepts have been developed to reduce the defect density. The most often used among these is the epitaxial lateral overgrowth (ELO) [71–73]. Here, a part of the GaN or sapphire surface is covered by SiO, preventing GaN growth on this area. By applying the correct growth conditions, lateral growth of GaN is encouraged and the SiO-covered area is overgrown. After coalescence of the epitaxial layer, the defect density in the overgrown area is drastically reduced. While this technique works very well for GaN, it is rather difficult for AlN due to the very small lateral to vertical growth rate ratio. Nonetheless, coalescence of AlN layers on sapphire was achieved (see Fig. 6.19a) and UV LEDs grown on this template showed increased output power by more than a factor of two [74].

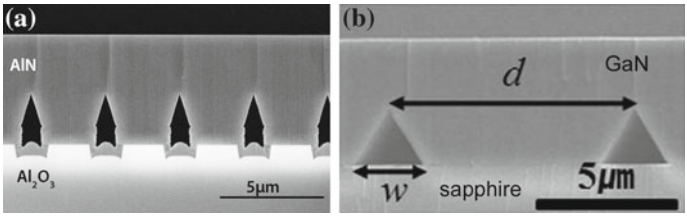


Fig. 6.19 **a** Coalesced ELO stripes of AlN on a patterned sapphire substrate [75]. **b** Etched air voids in GaN formed by ELOG and subsequent KOH etching, reprinted with permission from [76], Copyright 2012, the Optical Society

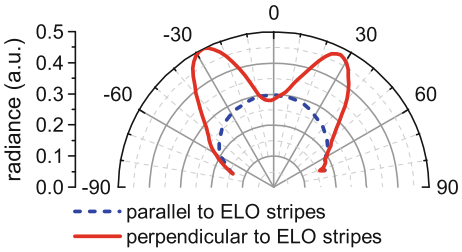


Fig. 6.20 Angular emission pattern from a 235-nm flip chip mounted LED grown on an ELO–sapphire template measured at 20 mA. The air voids in the AlN strongly influence the angular emission

While this improvement is mostly due to the improved internal quantum efficiency resulting from the reduced defect density in the ELO structure, the light extraction efficiency can also be enhanced by the appropriate design of the ELO pattern.

Since a strong change in the refractive index is present at the interfaces of the ELO stripes to the air voids, light scattering and refraction occur, leading to a redirection of the photons and hence to a potential increase in light extraction efficiency.

Figure 6.20 shows the angular-resolved emission pattern from flip chip mounted 235 nm LEDs grown on AlN ELO-patterned substrates. While light emitted along the stripes shows a regular isotropic distribution, the light emitted perpendicular to the stripes is diffracted at the air–AlN interfaces and a rabbit ear pattern is observed with a maximum at $\pm 27^\circ$ emission angle [77].

A study on blue InGaN-based LEDs with ELO structure showed a strong increase in output power in dependence on the size and shape of the air gaps above the SiO stripes [76]. In their study, Kang et al. grew LEDs on a SiO-masked sapphire wafer. After regrowth, the SiO was removed using HF, and diluted KOH was applied to etch triangular air voids with $\{10\bar{1}1\}$ sidewalls into the N-face of the GaN (see Fig. 6.19b). This leads to an increase of light output by up to 117 % as compared to a conventional planar LED. Furthermore, the light output angle and emission profile were altered depending on the stripe spacings.

A study using hexagonal patterned sapphire substrates for blue and near-UV LEDs near 400 nm in combination with a mesh-shaped rhodium-based p-contact showed increased emission power due to light scattering at the interface between the GaN buffer and the honeycomb-shaped sapphire structures [78]. Compared to a non-patterned sapphire substrate, an output power increase of 29 % was observed. The aperture size of the contact mesh also influenced the output power which indicates that absorption in the p-metal played a significant role. Using an aperture ratio of 70 %, an increase of output power by more than 40 % was obtained.

6.3.2.3 Plasmonics

An entirely different approach to increase the output power of light-emitting diodes is the use of metal layers and the utilization of surface plasmonic effects. A plasmon is a quasi-particle describing the collective oscillation of a free electron gas in highly conductive media, in particular metals [79]. At the interface between a dielectric material (i.e., a material where the real part of the dielectric function is positive) and a metal (i.e., a material where the real part of the dielectric function is negative), a surface plasmon (SP) can be excited. SPs are coherent electron oscillations generating an electromagnetic field that fluctuates with the plasma frequency ω_{sp}. The electromagnetic field intensity associated with the SP oscillations decays exponentially within the metal as well as the dielectric material. When the SP couples to the electromagnetic wave of a photon, a so-called surface plasmon polariton (SPP) is created. Due to its unique properties, the SPP can only propagate along the interface and hence will be strongly attenuated after traveling some distance within the metal. In order to induce light extraction, surface modifications such as roughening or patterning need to be applied to allow for scattering processes to occur. The advantage of the use of SPPs in semiconductor light emitters is the much shorter lifetime and therefore the higher recombination rate of SPPs as compared to radiative and nonradiative recombination processes in LEDs. Therefore, higher values of internal quantum efficiency can be achieved, provided that the light is coupled out from the interface. Okamoto et al. studied SPP processes on InGaN–GaN quantum wells using photoluminescence spectroscopy (PL) [80]. They could show an increase in PL intensity by a factor of 14 using a silver layer deposited 10 nm above the quantum well emitting at 470 nm. If aluminum was used, the increase was sevenfold, while gold did not show any improved emission properties. The plasmon frequencies for these materials were given as $\omega_{sp}(\mathrm{Ag}) = 2.84\,\mathrm{eV}$, $\omega_{sp}(\mathrm{Al}) = 5.5\,\mathrm{eV}$, and $\omega_{sp}(\mathrm{Au}) = 2.46\,\mathrm{eV}$, respectively. It appears that aluminum is ideally suited for ultraviolet applications. In the same paper, it was shown that due to the exponential decay of the evanescent SPP field the metal layer has to be situated closely to the quantum well. The enhancement factor for the silver layer reduced from 14 (10 nm distance) to 4 (40 nm) and no enhancement was shown for larger spacings.

This poses large technological challenges for the fabrication of LEDs with plasmonic enhancement since the p-layer normally is much thicker to allow proper current injection. Two main methods have been used to integrate SPP features into LEDs. Yeh et al. used a conventional design with 88 nm spacing between a silver layer and the InGaN quantum well [81]. Due to this large spacing, the coupling efficiency of the SPP was relatively weak, but nonetheless an 25–50 % output power enhancement was achieved for a 440 nm LED. In order to allow efficient coupling, Kwon et al. used a buried silver layer between the n-GaN and the InGaN quantum well which was overgrown and afterward processed into an LED [82]. After thermal annealing in the MOVPE system, the remaining Ag coverage was only about 3 %, most likely due to Ostwald ripening and evaporation, reducing the coupling efficiency. The LEDs had a wavelength of approximately 450 nm and by comparison of LEDs with and without silver nanoparticles a significant change in the effective exciton lifetime was observed. At 300 K, the lifetime was 80 ps for the SPP LED as compared to 140 ps to the conventional LED. This leads to an increased radiative recombination rate, resulting in an output power enhancement by 32 %. Gao et al. [83] demonstrated a 217 % enhancement in peak photoluminescence intensity at 294 nm for AlGaN-based LEDs using the metal aluminum (Al) for SP coupling. Although no enhancement of the internal quantum efficiency was observed due to SP–QW coupling, the extraction efficiency of the LEDs was enhanced by the SP-transverse magnetic wave coupling. This technique of increasing the extraction efficiency becomes increasing useful in the case of deep UV LEDs which mainly have TM-polarized light emission.

Due to the technological challenges, it remains doubtful if the application of surface plasmon polaritons for an increased LED efficiency is the best way to increase the overall device performance.

6.3.3 Packaging

Almost all light-emitting diodes are capped and encapsulated today. This has several reasons: An encapsulant protects the semiconductor chip and especially the fragile bond wires from mechanical damages. Also, oxidation of the contacts or other parts is prevented in a sealed encapsulant. Another important feature of an encapsulant is the increased extraction efficiency due to a wider light extraction cone and the possibility to shape the beam and integrate optical elements directly into the package. While common packages like TO cans provide only mechanical protection, direct integration of transparent-shaped dielectric materials is also adding the advantage of optical improvements. In the visible wavelength range, LEDs are usually placed inside a hemispherical dome of epoxy or silicone with a refractive index close to or similar to the encapsulated semiconductor materials. As described above, the light extraction angle is defined by the refractive index contrast between two media. Therefore, the encapsulating material should have a refractive index as close to the semiconductor as possible. If perfect matching is achieved, all

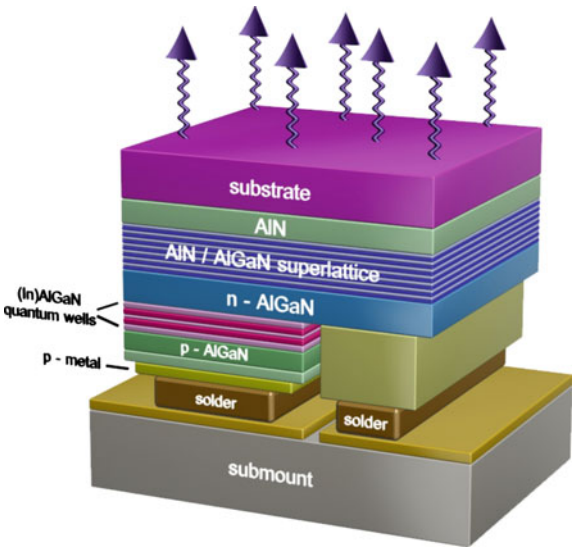


Fig. 6.21 Schematic of a UV LED flip chip mounted on a submount. The light is collected from the transparent substrate [86]

light from the LED is coupled into the encapsulant. If now the capsule is shaped into a sphere with the semiconductor at the center, all light beams meet the interface between air and encapsulant at normal incidence, avoiding total internal reflexion completely. Therefore, encapsulation with epoxy or silicone normally leads to a significant increase in the extraction efficiency.

This ideal case, however, is not easily achieved. Manufacturing demands make it necessary that the material for encapsulating the LED is cheap, can be easily formed by flow, stamping or molding, and it has of course to be transparent for the desired wavelength. Furthermore, bleaching and oxidation of the material have to be avoided since this would degrade the LED output power. The only suitable material that meets most of these requirements is the polymer. They have usually refractive indices between 1.4 and 1.6 and make therefore additional light extraction techniques necessary, as mentioned above. In the visible wavelength range, polymethylmethacrylate (PMMA) is widely used as a cheap and easily usable transparent substance. However, it absorbs strongly in the UV range.

The application of polymers for encapsulation of LEDs is not easily transferable to UV, since many epoxy and silicone materials start to absorb at near-UV wavelength, leading to reduced UV transmission and degradation of the package. Therefore, the search for UV-transparent, long-term stable, and high index encapsulation materials will be critical to enhance the light extraction and output power of UV LEDs.

Recently, polymers based on dimethyl chains have been used more and more for UV applications such as UV lithography, optical interconnects, and LED encapsulants [84]. One of the most promising materials of this group is polydimethylsiloxane (PDMS). The absorption was to be reported to be as low as 0.09 dB/cm at a wavelength of 300 nm [84].

Recent experiments by Lobo et al. have shown that polydimethylsiloxane (PDMS) might be a good candidate as encapsulant for UV LEDs. PDMS is highly transparent in the UV-A, UV-B, and large parts of the UV-C spectral range and is also fairly stable under UV light exposure. Ray tracing analysis of UVC LEDs with a PDMS encapsulant shows that the light extraction efficiency from the LED chip can be increased by a factor of 2–3 using this approach.

Yamada et al. presented results on 265 and 285 nm UVC LEDs encapsulated with polymerized perfluoro(4-vinyloxy-1-butene) [85]. Two versions of this encapsulant with a stable end (called S-type) and with an acid end (A-type) were compared. The S-type material has a transparency level above 90 % down to 200 nm and no visible aging or degradation was found after more than 3,000 h of operation.

Another method to increase the extraction efficiency is the flip chip bonding of an LED [87] in which the LED die is inverted and mounted on a submount with the epitaxial side down (see Fig. 6.21). In the case of flip chip UV LEDs grown on sapphire, the light is extracted from the transparent sapphire substrate avoiding absorption at the ohmic p-contact, bonding pads, and the bonding wires. Furthermore, if the contacts are replaced by highly reflective mirrors, light propagating downward can be redirected up and extracted through the substrate increasing the extraction efficiency. Other advantages of flip chip bonding includes reduced thermal resistance of the device due to efficient transfer of heat through the metal bonding pads and subsequently increased lifetimes, no distortion of the radiation pattern due to the absence of bonding wires, and compatibility with wafer scale packaging.

References

1. E.D. Palik, *Handbook of Optical Constants of Solids* (Academic Press Inc., Orlando, 1985)
2. M. Bass, *Handbook of Optics: Fundamentals, techniques, and design* (McGraw-Hill, 1994)
3. J.-S. Kim, P.K.H. Ho, N.C. Greenham, R.H. Friend, Electroluminescence emission pattern of organic light-emitting diodes: Implications for device efficiency calculations. J. Appl. Phys. **88** (2), 1073–1081 (2000)
4. M. Suzuki, T. Uenoyama, A. Yanase, First-principles calculations of effective-mass parameters of AlN and GaN. Phys. Rev. B **52**, 8132–8139 (1995)
5. J. Hopfdeld, Fine structure in the optical absorption edge of anisotropic crystals. J. Phys. Chem. Solids **15**(12), 97–107 (1960)
6. A.A. Yamaguchi, Y. Mochizuki, H. Sunakawa, A. Usui, Determination of valence band splitting parameters in GaN. J. Appl. Phys. **83**(8), 4542–4544 (1998)
7. N.V. Edwards, S.D. Yoo, M.D. Bremser, T.W. Weeks, O.H. Nam, R.F. Davis, H. Liu, R.A. Stall, M.N. Horton, N.R. Perkins, T.F. Kuech, D.E. Aspnes, Variation of GaN valence bands with biaxial stress and quantification of residual stress. Appl. Phys. Lett. **70**(15), 2001–2003 (1997)
8. I. Vurgaftman, J.R. Meyer, Band parameters for nitrogen-containing semiconductors. J. Appl. Phys. **94**(6), 3675–3696 (2003)
9. A. Sedhain, J.Y. Lin, H.X. Jiang, Valence band structure of AlN probed by photoluminescence. Appl. Phys. Lett. **92**(4), 041114 (2008)

10. G.D. Chen, M. Smith, J.Y. Lin, H.X. Jiang, S. Wei, M. Asif Khan, C.J. Sun, Fundamental optical transitions in GaN. Appl. Phys. Lett. **68**(20), 2784–2786 (1996)
11. K.B. Nam, J. Li, M.L. Nakarmi, J.Y. Lin, H.X. Jiang, Unique optical properties of AlGaN alloys and related ultraviolet emitters. Appl. Phys. Lett. **84**(25), 5264–5266 (2004)
12. R. Goldhahn, C. Buchheim, P. Schley, A.T. Winzer, H. Wenzel, *Optical Constants of Bulk Nitrides* (Wiley-VCH Verlag GmbH & Co. KGaA, 2007)
13. J. Li, K.B. Nam, M.L. Nakarmi, J.Y. Lin, H.X. Jiang, P. Carrier, S.-H. Wei, Band structure and fundamental optical transitions in wurtzite AlN. Appl. Phys. Lett. **83**(25), 5163–5165 (2003)
14. B. Neuschl, J. Helbing, M. Knab, H. Lauer, M. Madel, K. Thonke, T. Meisch, K. Forghani, F. Scholz, M. Feneberg, Composition dependent valence band order in c-oriented wurtzite AlGaN layers. J. Appl. Phys. **116**(11), 113506 (2014)
15. C. Coughlan, S. Schulz, M.A. Caro, E.P. O'Reilly, Band gap bowing and optical polarization switching in $Al_{1-x}Ga_xN$ alloys. Phys. Status Solidi (b) (2015)
16. T. Kolbe, A. Knauer, C. Chua, Z. Yang, S. Einfeldt, P. Vogt, N.M. Johnson, M. Weyers, M. Kneissl, Optical polarization characteristics of ultraviolet (In)(Al)GaN multiple quantum well light emitting diodes. Appl. Phys. Lett. **97**(17), 171105 (2010)
17. R.G. Banal, M. Funato, Y. Kawakami, Optical anisotropy in [0001]-oriented $Al_xGa_{1-x}N$/AlN quantum wells (x>0.69). Phys. Rev. B **79**, 121308 (2009)
18. H. Kawanishi, M. Senuma, T. Nukui, Anisotropic polarization characteristics of lasing and spontaneous surface and edge emissions from deep-ultraviolet (240 nm) AlGaN multiple-quantum-well lasers. Appl. Phys. Lett. **89**(4), 041126 (2006)
19. C. Netzel, A. Knauer, M. Weyers, Impact of light polarization on photoluminescence intensity and quantum efficiency in AlGaN and AlInGaN layers. Appl. Phys. Lett. **101**(24), 242102 (2012)
20. J.E. Northrup, C.L. Chua, Z. Yang, T. Wunderer, M. Kneissl, N.M. Johnson, T. Kolbe, Effect of strain and barrier composition on the polarization of light emission from AlGaN/AlN quantum wells. Appl. Phys. Lett. **100**(2), 021101 (2012)
21. T.K. Sharma, D. Naveh, E. Towe, Strain-driven light-polarization switching in deep ultraviolet nitride emitters. Phys. Rev. B **84**, 035305 (2011)
22. S.L. Chuang, C.S. Chang, k·p method for strained wurtzite semiconductors. Phys. Rev. B **54**, 2491–2504 (1996)
23. D. Fu, R. Zhang, B. Liu, Z.L. Xie, X.Q. Xiu, H. Lu, Y.D. Zheng, G. Edwards, Exploring optimal UV emission windows for AlGaN and AlInN alloys grown on different templates. Phys. Status Solidi (b) **248**(12), 2816–2820 (2011)
24. T. Kolbe, A. Knauer, C. Chua, Z. Yang, V. Kueller, S. Einfeldt, P. Vogt, N.M. Johnson, M. Weyers, M. Kneissl, Effect of temperature and strain on the optical polarization of (In)(Al) GaN ultraviolet light emitting diodes. Appl. Phys. Lett. **99**(26), 261105 (2011)
25. A. Atsushi Yamaguchi, Valence band engineering for remarkable enhancement of surface emission in AlGaN deep-ultraviolet light emitting diodes. Phys. Status Solidi (c) **5**(6), 2364–2366 (2008)
26. T.M. Al tahtamouni, J.Y. Lin, H.X. Jiang, Optical polarization in c-plane Al-rich AlN/$Al_xGa_{1-x}N$ single quantum wells. Appl. Phys. Lett. **101**(4), 042103 (2012)
27. J.J. Wierer, I. Montao, M.H. Crawford, A.A. Allerman, Effect of thickness and carrier density on the optical polarization of $Al_{0.44}Ga_{0.56}N/Al_{0.55}Ga_{0.45}N$ quantum well layers. J. Appl. Phys. **115**(17), 174501 (2014)
28. S.-H. Park, J.-I. Shim, Carrier density dependence of polarization switching characteristics of light emission in deep-ultraviolet AlGaN/AlN quantum well structures. Appl. Phys. Lett. **102**(22), 221109 (2013)
29. S. Wieczorek, W.W. Chow, S.R. Lee, A.J. Fischer, A.A. Allerman, M.H. Crawford, Analysis of optical emission from high-aluminum AlGaN quantum-well structures. Appl. Phys. Lett. **84**(24), 4899–4901 (2004)
30. A.A. Yamaguchi, Theoretical investigation of optical polarization properties in Al-rich AlGaN quantum wells with various substrate orientations. Appl. Phys. Lett. **96**(15), 151911 (2010)

31. J. Bhattacharyya, S. Ghosh, H.T. Grahn, Are AlN and GaN substrates useful for the growth of non-polar nitride films for UV emission? The oscillator strength perspective. Phys. Status Solidi (b) **246**(6), 1184–1187 (2009)
32. C.-P. Wang, Y.-R. Wu, Study of optical anisotropy in nonpolar and semipolar AlGaN quantum well deep ultraviolet light emission diode. J. Appl. Phys. **112**(3), 033104 (2012)
33. R.G. Banal, Y. Taniyasu, H. Yamamoto, Deep-ultraviolet light emission properties of nonpolar M-plane AlGaN quantum wells. Appl. Phys. Lett. **105**(5), 053104 (2014)
34. L. Schade, U.T. Schwarz, T. Wernicke, M. Weyers, M. Kneissl, Impact of band structure and transition matrix elements on polarization properties of the photoluminescence of semipolar and nonpolar InGaN quantum wells. Phys. Status Solidi (b) **248**(3), 638–646 (2011)
35. L. Schade, U.T. Schwarz, T. Wernicke, J. Rass, S. Ploch, M. Weyers, M. Kneissl, On the optical polarization properties of semipolar InGaN quantum wells. Appl. Phys. Lett. **99**(5) (2011)
36. S.L. Chuang, C.S. Chang, k·p method for strained wurtzite semiconductors. Phys. Rev. B **54**, 2491–2504 (1996)
37. H.B. Michaelson, The work function of the elements and its periodicity. J. Appl. Phys. **48**, 4729 (1977)
38. E. Kalinia, N. Kuznetsov, V. Dmitriev, K. Iirvine, C. Carter, Schottky barriers on n-GaN grown on SiC. J. Electron. Mater. **25**, 831 (1996)
39. M. Lapeyrade, A. Muhin, S. Einfeldt, U. Zeimer, A. Mogilatenko, M. Weyers, M. Kneissl, Electrical properties and microstructure of vanadium-based contacts on ICP plasma etched n-type AlGaN: Si and GaN: Si surfaces. Semicond. Sci. Technol. **28**(12), 125015 (2013)
40. J.-K. Ho, C.-S. Jong, C.C. Chiu, C.-N. Huang, K.-K. Shih, L.-C. Chen, F.-R. Chen, J.-J. Kai, Low-resistance ohmic contacts to p-type GaN achieved by the oxidation of Ni/Au films. J. Appl. Phys. **86**, 4491 (1999)
41. T. Mori, T. Kozawa, T. Ohwaki, Y. Taga, S. Nagai, S. Yamasaki, S. Asami, N. Shibata, M. Koike, Schottky barriers and contact resistances on p-type GaN. Appl. Phys. Lett. **69**, 3537 (1996)
42. C.I. Wu, A. Kahn, Investigation of the chemistry and electronic properties of metal/gallium nitride interfaces. J. Vac. Sci. Technol. B **16**, 2218 (1998)
43. C.-S. Lee, Y.-J. Lin, C.-T. Lee, Investigation of oxidation mechanism for ohmic formation in NiOAu contacts to p-type GaN layers. Appl. Phys. Lett. **79**, 3815 (2001)
44. H.W. Jang, S.Y. Kim, J.-L. Lee, Mechanism for ohmic contact formation of oxidized NiOAu on p-type GaN. J. Appl. Phys. **94**, 1748 (2003)
45. D.C. Look, D.C. Reynolds, J.W. Hemsky, J.R. Sizelove, R.L. Jones, R.J. Molnar, Defect donor and acceptor in GaN. Phys. Rev. Lett. **79**, 2273–2276 (1997)
46. K. Saarinen, T. Suski, I. Grzegory, D.C. Look, Thermal stability of isolated and complexed Ga vacancies in GaN bulk crystals. Phys. Rev. B **64**, 233201 (2001)
47. J. Neugebauer, C.G. van de Walle, Gallium vacancies and the yellow luminescence in GaN. Appl. Phys. Lett. **69**, 503 (1996)
48. N. Lobo, H. Rodriguez, A. Knauer, M. Hoppe, S. Einfeldt, P. Vogt, M. Weyers, M. Kneissl, Enhancement of light extraction in ultraviolet light-emitting diodes using nanopixel contact design with Al reflector. Appl. Phys. Lett. **96**(8), 081109 (2010)
49. J.K. Kim, J.-Q. Xi, H. Luo, E. Fred Schubert, J. Cho, C. Sone, Y. Park, Enhanced light-extraction in GaInN near-ultraviolet light-emitting diode with Al-based omnidirectional reflector having NiZn/Ag microcontacts. Appl. Phys. Lett. **89**(14), 141123 (2006)
50. T. Jeong, H.H. Lee, S.-H. Park, J.H. Baek, J.K. Lee, Ingan/algan ultraviolet light-emitting diode with a Ti_3O_5/Al_2O_3 distributed bragg reflector. Jpn. J. Appl. Phys. **47**(12), 8811–8814 (2008)
51. V. Adivarahan, S. Wu, W.H. Sun, V. Mandavilli, M.S. Shatalov, G. Simin, J.W. Yang, H. P. Maruska, M.A. Khan, High-power deep ultraviolet light-emitting diodes based on a micro-pixel design. Appl. Phys. Lett. **85**(10), 1838–1840 (2004)

52. S. Wu, V. Adivarahan, M. Shatalov, A. Chitnis, W.-H. Sun, M.A. Khan, Micro-pixel design milliwatt power 254 nm emission light emitting diodes. Jpn. J. Appl. Phys. **43**(8A), L1035–L1037 (2004)
53. H. Rodríguez, N. Lobo, S. Einfeldt, A. Knauer, M. Weyers, M. Kneissl, GaN-based ultraviolet light-emitting diodes with multifinger contacts. Phys. Status Solidi (a) **207**(11), 2585–2588 (2010)
54. A. Chakraborty, L. Shen, U.K. Mishra, Interdigitated multipixel arrays for the fabrication of high-power light-emitting diodes with very low series resistances, reduced current crowding, and improved heat sinking. IEEE Trans. Electron Dev. **54**(5), 1083–1090 (2007)
55. H. Choi, C. Jeon, M. Dawson, P. Edwards, R. Martin, Fabrication and performance of parallel-addressed InGaN micro-LED arrays. IEEE Photon. Technol. Lett **15**(4), 510–512 (2003)
56. N. Lobo Ploch, H. Rodriguez, C. Stolmacker, M. Hoppe, M. Lapeyrade, J. Stellmach, F. Mehnke, T. Wernicke, A. Knauer, V. Kueller, M. Weyers, S. Einfeldt, M. Kneissl, Effective thermal management in ultraviolet light-emitting diodes with micro-LED arrays. IEEE Trans. Electron Dev. **60**(2), 782–786 (2013)
57. M.R. Krames, M. Ochiai-Holcomb, G.E. Hïfler, C. Carter-Coman, E.I. Chen, I.-H. Tan, P. Grillot, N.F. Gardner, H.C. Chui, J.-W. Huang, S.A. Stockman, F.A. Kish, M.G. Craford, T. S. Tan, C.P. Kocot, M. Hueschen, J. Posselt, B. Loh, G. Sasser, D. Collins, High-power truncated-inverted-pyramid $(Al_xGa_{1-x})_{0.5}$ $In_{0.5}P/GaP$ light-emitting diodes exhibiting > 50 % external quantum efficiency. Appl. Phys. Lett. **75**(16), 2365–2367 (1999)
58. J.J. Wierer, A.A. Allerman, I. Montao, M.W. Moseley, Influence of optical polarization on the improvement of light extraction efficiency from reflective scattering structures in AlGaN ultraviolet light-emitting diodes. Appl. Phys. Lett. **105**(6), 061106 (2014)
59. T. Fujii, Y. Gao, R. Sharma, E.L. Hu, S.P. DenBaars, S. Nakamura, Increase in the extraction efficiency of GaN-based light-emitting diodes via surface roughening. Appl. Phys. Lett. **84**(6), 855–857 (2004)
60. C. Huh, K.-S. Lee, E.-J. Kang, S.-J. Park, Improved light-output and electrical performance of InGaN-based light-emitting diode by microroughening of the p-GaN surface. J. Appl. Phys. **93** (11), 9383–9385 (2003)
61. D.-S. Han, J.-Y. Kim, S.-I. Na, S.-H. Kim, K.-D. Lee, B. Kim, S.-J. Park, Improvement of light extraction efficiency of flip-chip light-emitting diode by texturing the bottom side surface of sapphire substrate. IEEE Photon. Technol. Lett. **18**, 1406–1408 (2006)
62. W.S. Wong, T. Sands, N.W. Cheung, M. Kneissl, D.P. Bour, P. Mei, L.T. Romano, N.M. Johnson, Fabrication of thin-film InGaN light-emitting diode membranes by laser lift-off. Appl. Phys. Lett. **75**(10), 1360–1362 (1999)
63. M. Takeuchi, T. Maegawa, H. Shimizu, S. Ooishi, T. Ohtsuka, Y. Aoyagi, AlN/AlGaN short-period superlattice sacrificial layers in laser lift-off for vertical-type AlGaN-based deep ultraviolet light emitting diodes. Appl. Phys. Lett. **94**(6), 061117 (2009)
64. S.-H. Chuang, C.-T. Pan, K.-C. Shen, S.-L. Ou, D.-S. Wuu, R.-H. Horng, Thin film GaN LEDs using a patterned oxide sacrificial layer by chemical lift-off process. IEEE Photon. Technol. Lett. **25**, 2435–2438 (2013)
65. L. Zhou, J.E. Epler, M.R. Krames, W. Goetz, M. Gherasimova, Z. Ren, J. Han, M. Kneissl, N. M. Johnson, Vertical injection thin-film AlGaN/AlGaN multiple-quantum-well deep ultraviolet light-emitting diodes. Appl. Phys. Lett. **89**(24), 241113 (2006)
66. R. Windisch, C. Rooman, S. Meinlschmidt, P. Kiesel, D. Zipperer, G.H. Dïhler, B. Dutta, M. Kuijk, G. Borghs, P. Heremans, Impact of texture-enhanced transmission on high-efficiency surface-textured light-emitting diodes. Appl. Phys. Lett. **79**(15), 2315–2317 (2001)
67. M. Khizar, Z.Y. Fan, K.H. Kim, J.Y. Lin, H.X. Jiang, Nitride deep-ultraviolet light-emitting diodes with microlens array. Appl. Phys. Lett. **86**(17), 173504 (2005)
68. T.N. Oder, K.H. Kim, J.Y. Lin, H.X. Jiang, III-nitride blue and ultraviolet photonic crystal light emitting diodes. Appl. Phys. Lett. **84**(4), 466–468 (2004)

69. J.J. Wierer, M.R. Krames, J.E. Epler, N.F. Gardner, M.G. Craford, J.R. Wendt, J.A. Simmons, M.M. Sigalas, InGaN/GaN quantum-well heterostructure light-emitting diodes employing photonic crystal structures. Appl. Phys. Lett. **84**(19), 3885–3887 (2004)
70. J. Shakya, K.H. Kim, J.Y. Lin, H.X. Jiang, Enhanced light extraction in III-nitride ultraviolet photonic crystal light-emitting diodes. Appl. Phys. Lett. **85**(1), 142–144 (2004)
71. S. Nakamura, M. Senoh, S. Nagahama, N. Iwasa, T. Yamada, T. Matsushita, H. Kiyoku, Y. Sugimoto, T. Kozaki, H. Umemoto, M. Sano, K. Chocho, High-power, long-lifetime InGaN/GaN/AlGaN-based laser diodes grown on pure GaN substrates. Jpn. J. Appl. Phys. **37**, L309 (1998)
72. A. Sakai, H. Sunakawa, A. Usui, Defect structure in selectively grown GaN films with low threading dislocation density. Appl. Phys. Lett. **71**, 2259 (1997)
73. T.S. Zheleva, O.-H. Nam, M.D. Bremser, R.F. Davis, Dislocation density reduction via lateral epitaxy in selectively grown GaN structures. Appl. Phys. Lett. **71**, 2472 (1997)
74. V. Kueller, A. Knauer, C. Reich, A. Mogilatenko, M. Weyers, J. Stellmach, T. Wernicke, M. Kneissl, Z. Yang, C. Chua, N. Johnson, Modulated epitaxial lateral overgrowth of AlN for efficient UV LEDs. IEEE Photon. Technol. Lett. **24**(18), 1603–1605 (2012)
75. S. Hagedorn, V. Küller et al., private communication, Ferdinand-Braun-Institut, Leibniz-Institut für Höchstfrequenztechnik, Berlin, Germany
76. J.H. Kang, H.G. Kim, S. Chandramohan, H.K. Kim, H.Y. Kim, J.H. Ryu, Y.J. Park, Y.S. Beak, J.-S. Lee, J.S. Park, V.V. Lysak, C.-H. Hong, Improving the optical performance of InGaN light-emitting diodes by altering light reflection and refraction with triangular air prism arrays. Opt. Lett. **37**, 88–90 (2012)
77. M. Guttmann et al., private communication, TU Berlin, Institute of solid state physics
78. M. Yamada, T. Mitani, Y. Narukawa, S. Shioji, I. Niki, S. Sonobe, K. Deguchi, M. Sano, T. Mukai, InGaN-based near-ultraviolet and blue-light-emitting diodes with high external quantum efficiency using a patterned sapphire substrate and a mesh electrode. Jpn. J. Appl. Phys. **41**(Part 2, No. 12B), L1431–L1433 (2002)
79. W.L. Barnes, A. Dereux, T.W. Ebbesen, Surface plasmon subwavelength optics. Nature **424**, 824–830 (2003)
80. K. Okamoto, Y. Kawakami, High-efficiency InGaN/GaN light emitters based on nanophotonics and plasmonics. IEEE J. Sel. Topics Quant. Electron. **15**(4), 1199–1209 (2009)
81. D.-M. Yeh, C.-F. Huang, C.-Y. Chen, Y.-C. Lu, C. Yang, Surface plasmon coupling effect in an InGaN/GaN single-quantum-well light-emitting diode. Appl. Phys. Lett. **91**(17), 171103 (2007)
82. M.-K. Kwon, J.-Y. Kim, B.-H. Kim, I.-K. Park, C.-Y. Cho, C.C. Byeon, S.-J. Park, Surface-plasmon-enhanced light-emitting diodes. Adv. Mater. **20**(7), 1253–1257 (2008)
83. N. Gao, K. Huang, J. Li, S. Li, X. Yang, J. Kang, Surface-plasmon-enhanced deep-UV light emitting diodes based on AlGaN multi-quantum wells. Sci. Rep. **2**, 5 (2012)
84. J.V. DeGroot, Jr., A. Norris, S.O. Glover, T.V. Clapp, Highly transparent silicone materials (2004)
85. K. Yamada, Y. Furusawa, S. Nagai, A. Hirano, M. Ippommatsu, K. Aosaki, N. Morishima, H. Amano, I. Akasaki, Development of underfilling and encapsulation for deep-ultraviolet LEDs. Appl. Phys. Exp. **8**(1), 012101 (2015)
86. R. Kremzow, private communication, TU Berlin, Institute of solid state physics
87. J.J. Wierer, D.A. Steigerwald, M.R. Krames, J.J. OShea, M.J. Ludowise, G. Christenson, Y.-C. Shen, C. Lowery, P.S. Martin, S. Subramanya, W. Götz, N.F. Gardner, R.S. Kern, S.A. Stockman, High-power AlGaInN flip-chip light-emitting diodes. Appl. Phys. Lett. **78**(22), 3379–3381 (2001)

Chapter 7
Fabrication of High Performance UVC LEDs on Aluminum-Nitride Semiconductor Substrates and Their Potential Application in Point-of-Use Water Disinfection Systems

James R. Grandusky, Rajul V. Randive, Therese C. Jordan and Leo J. Schowalter

Abstract Water disinfection has always been a focal point of public discourse due to both the shortage of water and the abundance of water-transmitted diseases. According to the World Health Organization (WHO), there are over 3.4 million reported deaths annually due to water, sanitation, and hygiene-related issues [1]. There are a number of technologies being developed to fight against issues related to waterborne diseases. The use of UV light is gaining popularity over chlorine disinfection due to a lack of aftertaste and harmful by-products after treatment. Specifically, UV radiation in the wavelength range of 250–280 nm (UVC) has been shown to effectively disinfect water. Current UVC technology, which uses low and medium pressure mercury lamps, is hampered by the use of fragile quartz housings, long warm up times, and the toxicity of mercury [2]. There is tremendous development happening in the field of semiconductor-based UVC LED technology. This technology can be efficient, cost-effective, and an environmentally friendlier alternative to traditional UVC technology. Emerging $Al_xGa_{1-x}N$ and AlN-based UVC light-emitting diodes (LEDs) provide many advantages over mercury lamps—including design flexibility, low power consumption, and environmentally friendly construction [3]. Unlike low-pressure mercury lamp technology, which is limited to an emission wavelength near 254 nm, LEDs can be tailored to specific wavelengths throughout the UVC range. UVC LEDs are being developed for disinfection in the 265 nm wavelength range and are showing tremendous progress in power output and device lifetime [4]. This progress has been driven by the relatively recent development of high quality, single-crystal AlN substrates. These AlN substrates allow the growth of pseudomorphic $Al_xGa_{1-x}N$ device layers with very low defect densities.

J.R. Grandusky · R.V. Randive · T.C. Jordan · L.J. Schowalter (✉)
Crystal IS, 70 Cohoes Avenue, Green Island, NY 12183, USA
e-mail: leo@cisuvc.com

R.V. Randive
e-mail: randive@cisuvc.com

© Springer International Publishing Switzerland 2016

M. Kneissl and J. Rass (eds.), *III-Nitride Ultraviolet Emitters*,
Springer Series in Materials Science 227, DOI 10.1007/978-3-319-24100-5_7

These low defect densities have resulted in improvements in efficiency and power as discussed in this chapter. In addition, UVC LEDs emit radiation in a very different pattern than mercury lamps or other UVC sources that they are replacing. For instance, the LEDs can be designed to emit in a "Lambertian" pattern, allowing the LED to be imaged as a near point source. Using UVC LEDs in water disinfection requires substantial rethinking in the arrangement of UVC radiation sources to achieve an efficient system. In this chapter, we will discuss some of the important parameters necessary for successful flow cell design. The chapter will show the design flexibility offered by UVC LEDs, with some examples of potential designs examined through optical modeling. We will also review some of the recent progress in improving UVC LEDs through pseudomorphic growth of $Al_xGa_{1-x}N$ on single crystal AlN substrates.

7.1 Introduction

LEDs have entered mainstream lighting due to their significant benefits. Compared to traditional lighting sources, such as incandescent light bulbs and fluorescent light tubes, LEDs are environmentally friendly, wavelength specific and provide high optical output, long lifetime, low power consumption, and low maintenance costs.

Similarly, UVC LEDs are poised to begin replacing mercury lamps and other sources of UVC radiation. The UVC radiation is used either in combination with traditional chemical treatment with chlorine to disinfect drinking water, or instead of chemical treatment, because of the formation of chemical by-products and some chlorine resistant microorganisms.

7.1.1 Types of UVC Light Sources

In general, UVC light can be produced by the following variety of lamps:

- Low-pressure (LP) mercury vapor lamps
- Medium pressure (MP) mercury vapor lamps
- Metal Halide lamps
- Xenon Lamps (pulsed UV)
- Deuterium Lamps
- UVC LEDs

UVC LEDs, as semiconductor light sources, are an emerging technology and their use in large-scale manufacturing is new. Their benefits, including environmentally friendly construction, low power consumption, low maintenance costs, and wavelength specificity, are driving an increased focus on this new technology [5].

Advantages of using UVC over chlorine disinfection:

- UVC cannot be overdosed
- No by-products or toxins
- No volatile organic compound (VOC) emissions or toxic air emissions
- Does not require storage of hazardous material
- Requires minimal space for equipment and contact chamber
- Does not affect the smell, taste, or minerals in the water

7.1.2 What Is UVC Light?

Ultraviolet (UV) light, the wavelength range of 100–400 nm, is a component of sunlight that falls in the region between visible light and X-rays of the electromagnetic spectrum (Fig. 7.1). The UV light can further be categorized into separate regions as follows [6]:

- Far UV (or "vacuum") 100–220 nm
- UVC 220–280 nm
- UVB 280–315 nm
- UVA 315–400 nm

Of these UV regions, UVC has significant germicidal properties; however it is almost entirely filtered out by the Earth's atmosphere. Therefore, to utilize the germicidal properties of UVC light, it must be artificially generated using manufactured light sources.

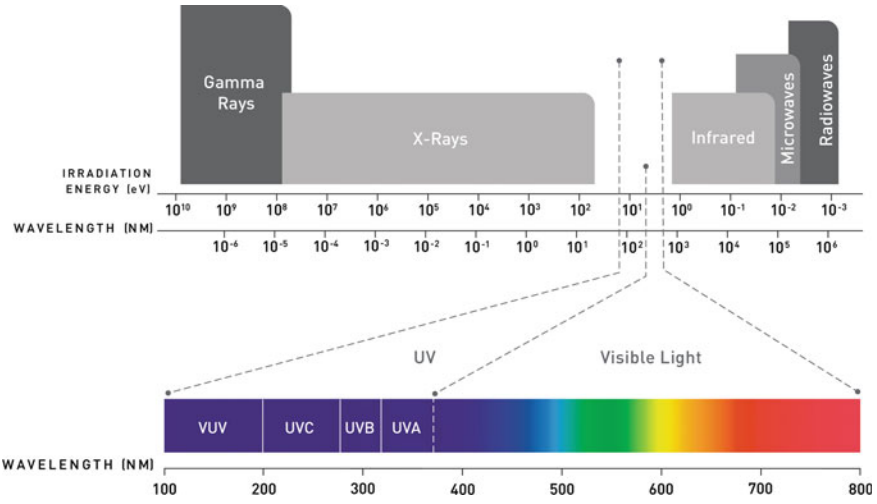


Fig. 7.1 Electromagnetic spectrum

Table 7.1 Comparison of UVC LEDs with other UV technologies

	UVC LED	Deuterium lamp	Xenon flash lamp	Mercury lamp
Spectrum	Single peak	Broad spectrum	Broad spectrum	Broad spectrum
Stability of light output	Excellent	Good	Relatively poor	Relatively poor
Warm up time	Instantaneous	20–30 min	Instantaneous	1–15 min
Forward heat radiation	No	Yes	No	Yes
Overall cost of ownership	Low[a]	High	High	Low
Drive electronics	Simple	Complex	Complex	Complex
Environmentally friendly	Yes	No	No	No
Safety	Low voltage, cold light source with shock resistant construction	Hot bulb surface with high voltage power supply	High voltage supply with ignition and sparking risk	High voltage supply and contains mercury in fragile quartz envelope

[a]Lowered cost of ownership due to cost savings on power supply and housing

Although UVC LED technology is new, it holds many benefits over the existing UVC technologies (Table 7.1).

UVC LEDs have many advantages over other technologies that produce UVC light. UVC LEDs come on instantaneously and are well suited for situations where the radiation can advantageously be switched on and off quickly. Also, the lifetime of the LEDs are not degraded by multiple on and off cycles, unlike mercury lamps where the lifetimes decrease with frequent on/off cycles. Another significant benefit for using LEDs is the simplified drive electronics needed to operate them compared to other UVC sources.

Some applications, such as analysis of heat-sensitive samples, also benefit from the lack of forward heat radiation from LEDs. Backside waste heat from LEDs is removed by thermal conduction, typically from the backside, unlike other UVC light sources where it is radiated forward with the UVC light.

7.1.3 How Does Germicidal UV Work

The UVC wavelength range deactivates bacteria, viruses, and other pathogens by attacking their DNA. UVC light is able to penetrate the cells of microorganisms and disrupt the structure of their DNA molecules (Fig. 7.2) [7]. In doing so, the microorganism is prohibited from surviving and/or reproducing, thereby, rendering it inactive and no longer pathogenic.

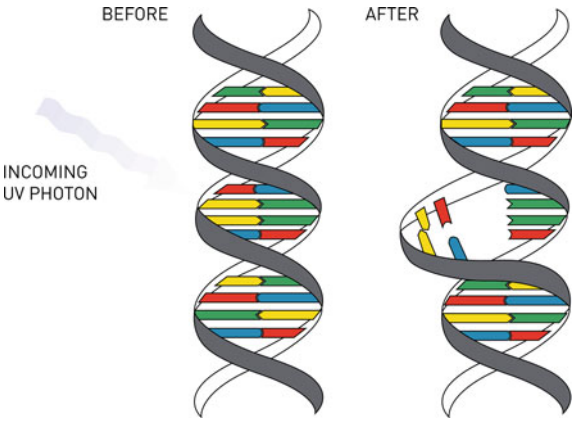


Fig. 7.2 UVC Radiation disrupts DNA (from [7] by David Herring, NASA, open source)

Mercury lamps, both low pressure and medium pressure, are currently widely used for disinfection. However, in point-of-use (POU) water disinfection, UVC LED technology has become more interesting as output powers and wall plug efficiencies have improved over the last few years. Also, UVC LEDs can be tuned to a desired wavelength, allowing them to provide maximum power at 265 nm—the ideal wavelength for disinfection of most pathogens.

Given the potential advantages of UVC LEDs, it is not surprising that there is an international development effort based on the AlN/GaN compound semiconductor system, more commonly referred to as the III-nitride semiconductors. The majority of this work has involved heteroepitaxial growth of alloys of these semiconductors grown on sapphire substrates by either organometallic vapor phase epitaxy (OMVPE) or molecular beam epitaxy (MBE). While sapphire substrates are capable of meeting the temperature and chemical compatibility requirements for heteroepitaxial growth of the III-nitride semiconductors (and is described elsewhere in this book), the large lattice and thermal expansion mismatch results in a high defect density, which lowers the performance of the resulting UVC LEDs. The number of defects in the heteroepitaxial layers can be dramatically reduced through special epitaxial growth techniques (also described elsewhere in this book). However, higher quality layers of high aluminum content III-nitride semiconductors can be grown pseudomorphically on AlN substrates.

7.2 Fabrication of UVC LEDs on AlN Substrates

Pseudomorphic growth of AlGaN structures on AlN substrates has produced LEDs with dislocation densities much lower than achievable with conventional heteroepitaxy on sapphire or SiC [8]. In order to define a pseudomorphic limit, various growths were carried out with different compositions and thicknesses [9]. This included n-type $Al_xGa_{1-x}N$ with x from 0.45 up to 0.75 and thickness values

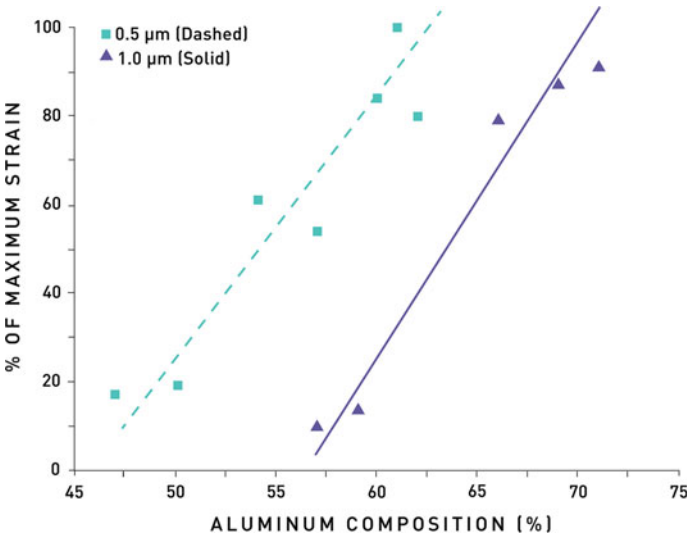


Fig. 7.3 Percent of maximum (pseudomorphic) strain versus Al composition for different thickness layers. The lines are guides to the eye for each thickness (*dashed line* is 0.5 µm and *solid line* is 1.0 µm) [8]

from 0.5 to 1.3 µm thick. In this range, layers found were nearly completely relaxed to completely strained. A plot of the data is shown in Fig. 7.3. As it can be seen, layers of ~60 % Al can be grown fully pseudomorphic up to a thickness of 0.5 µm while layers of ~70 % Al can be grown nearly pseudomorphic up to a thickness of 1 µm. There is a considerable spread in the data, which could be due to the properties of the AlN substrates, such as surface miscut.

The main advantage to the pseudomorphic growth is that, since no misfit dislocations are generated, no new threading dislocations will need to be generated. Additionally, it is possible to grow thick layers with a threading dislocation density (TDD) comparable to the starting substrate. X-ray rocking curves are shown in Fig. 7.4a for a pseudomorphic layer and in Fig. 7.4b for a relaxed layer. These rocking curves are normalized and plotted with the omega axis shifted to allow for overlaying the $Al_xGa_{1-x}N$ peak over the AlN peak. For the pseudomorphic sample, the (0 0 0 2) rocking curve width increases from 64 s for the AlN to 81 s for the $Al_xGa_{1-x}N$ layer while the (10 $\bar{1}$ 2) rocking curve width increases from 89 to 104 s.

This is in sharp contrast to the relaxed sample in which the (0 0 0 2) rocking curve width increases from 49 s for the AlN to 239 s for the $Al_xGa_{1-x}N$ layer while for the (10 $\bar{1}$ 2) rocking curve width increases from 30 to 302 s. From these scans, it can be seen that by appropriately controlling the Al composition and thickness, very few dislocations are generated during the heteroepitaxy. By keeping the Al composition fixed at 70 % and between 0.5 and 1.0 µm thick, layers can routinely be grown with both symmetric and asymmetric rocking curves less than 100 arc sec. In addition to the narrow rocking curves, it is also important for the n-type $Al_xGa_{1-x}N$

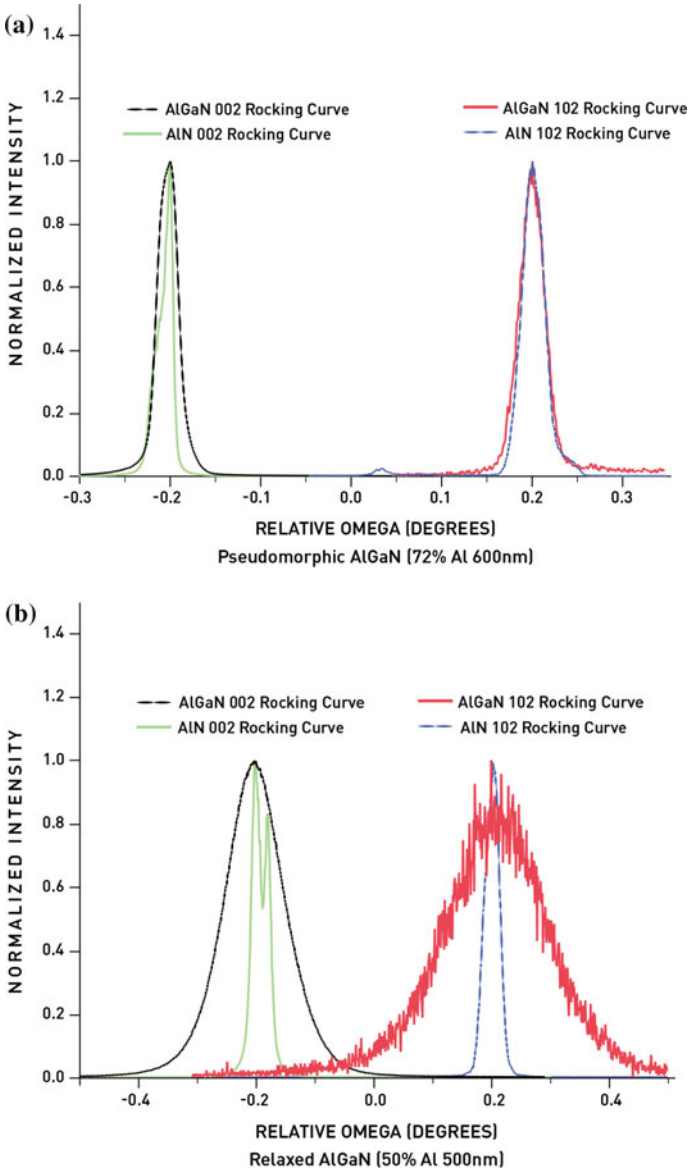


Fig. 7.4 X-ray rocking curves of the AlN substrates and $Al_xGa_{1-x}N$ epitaxial layers for **a** pseudomorphic layer and **b** relaxed layer. The data is normalized and the X-axis is plotted in relative degrees to allow for the overlaying of the symmetric and asymmetric peaks for AlN and $Al_xGa_{1-x}N$ [8]

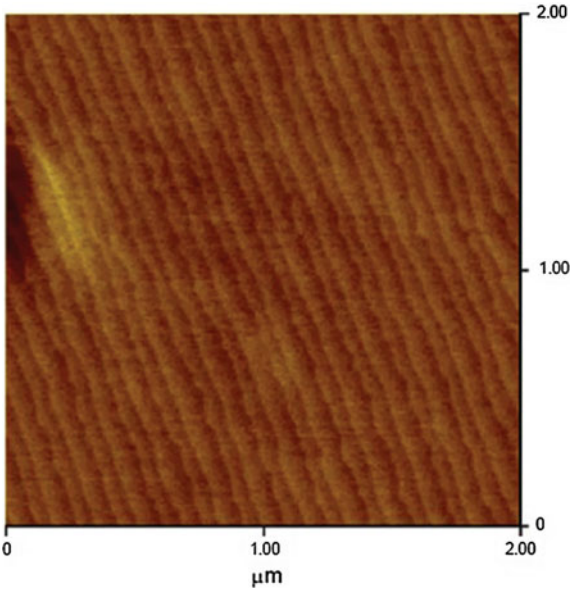


Fig. 7.5 A 2 × 2 µm^2 AFM scan showing the step flow growth of the pseudomorphic n-type $Al_xGa_{1-x}N$ layer with a composition of 70 % Al. The RMS roughness is 0.1 nm and the Z-range is 1.7 nm (for a 20 × 20 µm^2 scan the RMS roughness is 0.4 nm and the Z-range is 2.1 nm) [8]

to have smooth surfaces in order to provide sharp interfaces in the p–n junction and thin active region. It was found that layers begin relaxing by a surface roughening mechanism. Initially, the surface appears to buckle to reduce the compressive strain in the layers. Upon continued growth, very rough surfaces were obtained for the $Al_xGa_{1-x}N$ layers with 60 % Al at 0.5 µm thick. This is similar to what was seen previously in the growth of lower composition $Al_xGa_{1-x}N$ on low dislocation density bulk AlN substrates in which plateaus develop on the surface [10]. However, the $Al_xGa_{1-x}N$ layers with 70 % Al can be grown with very smooth surfaces as seen in Fig. 7.5.

This step flow growth pattern with atomically smooth surfaces is typical over large areas with 20 × 20 µm^2 scans showing similar Z-range and RMS values (not shown). One challenge of incorporating this 70 % Al $Al_xGa_{1-x}N$ layer into an LED structure is the conductivity. As the Al concentration is increased, the conductivity is typically decreased, due mainly to the reduced mobilities [11] and deeper level of the donor in the conduction band [12]. Hall measurements were performed in the Van der Pauw geometry and gave conductivity values suitable for an LED structure, a resistivity of 0.0437 Ω cm with a mobility of 62 cm^2/V s at a carrier concentration of 2.4E18 cm^3. These values were obtained without any optimization of the doping levels or growth conditions and it is expected that improved conductivity can be obtained.

The next step in obtaining a full LED structure is the growth of the Multiple Quantum Wells (MQW) [13]. This was carried out on the smooth 70 % Al $Al_xGa_{1-x}N$ layer. The step flow growth mode and atomically smooth surfaces continued during growth of the MQW and the surface roughness was similar to that of the 70 % Al

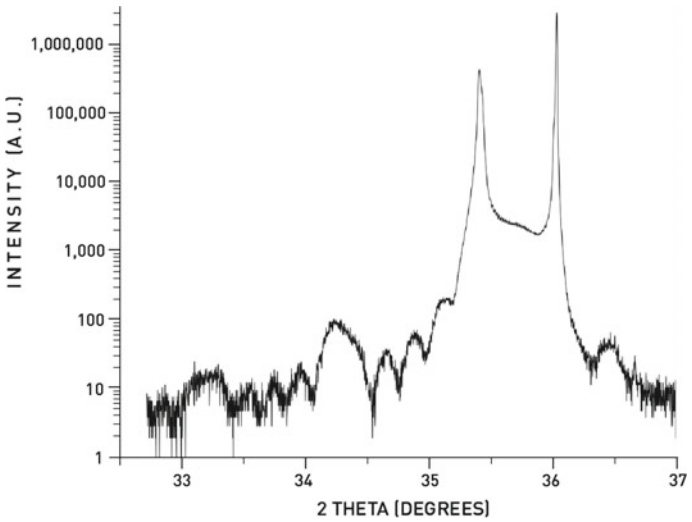


Fig. 7.6 Omega-2 theta scan of the MQW structure showing the sharp AlN and 70 % $Al_xGa_{1-x}N$ layer as well as the interference fringes from the MQW [8]

$Al_xGa_{1-x}N$ layer. XRD was carried out on this structure and is shown in Fig. 7.6. In addition to the sharp peaks coming from the AlN substrate and the 70 % Al $Al_xGa_{1-x}N$ layer, interference fringes are observed from the MQW allowing measurement of the compositions and thickness of the well and barrier layers which matched very well to the desired structure. Finally, a full LED structure was grown consisting of a high Al-content electron blocking layer, a p-type $Al_xGa_{1-x}N$ hole injection layer and a p-type GaN contact layer. The device structure was grown on c-plane AlN substrates using conventional metal organic chemical vapor deposition. It consists of an $Al_{0.7}Ga_{0.3}N$:Si layer, a five period multiple quantum well (MQW) layer consisting of n-$Al_{0.7}Ga_{0.3}N$ barriers and $Al_{0.55}Ga_{0.45}N$ wells, an $Al_{0.8}Ga_{0.2}N$ electron blocking layer (EBL), and a p-GaN contact layer [14]. Again, step flow growth continued as can be seen in Fig. 7.7. XRD (not shown) also showed narrow GaN peaks indicating that the low defect density is carried throughout the entire structure. This improvement in both defect density and surface roughness is expected to lead to dramatic improvements in device structures fabricated into UVC LEDs.

While the epitaxial material quality is improved due to the low dislocation density, one issue with the use of AlN substrates prepared from bulk crystals is absorption of the UV light generated even though the crystal quality is very high. While intrinsically transparent at these wavelengths, point defects in the bulk substrates can result in absorption, many times resulting in opaque substrates. One technique that has been used to achieve substrates with high transparency is HVPE AlN growth on PVT grown AlN substrates. HVPE growth can achieve low impurity incorporation and is able to closely replicate the underlying high quality substrate with low dislocation density. This technique was demonstrated successfully with a

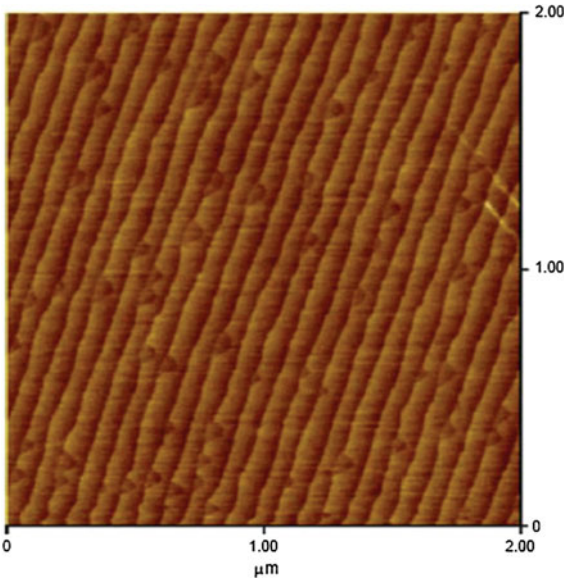


Fig. 7.7 A 2 × 2 μm^2 AFM scan showing the step flow growth of the full LED structure (p-type GaN contact layer). The RMS roughness is 0.2 nm and the Z-range is 1.6 nm (for a 20 × 20 μm^2 scan the RMS roughness is 0.2 nm and the Z-range is 2.0 nm) [8]

28 mW measurement from a 268 nm LED [15] after removing the PVT substrate with an applied current of 300 mA.

Recently, it has been demonstrated that pseudomorphic growth of UVC LEDs gives improved reliability. The LED structures were grown by metal organic chemical-vapor deposition (MOCVD) on free standing AlN substrates as described above [16]. Devices were fabricated via standard lateral LED processing, with a final die size of 820 μm by 820 μm. Interdigitated mesas were used to improve current spreading, and the emitting area was approximately 0.37 μm^2. Following contact metallization, but prior to singulation, the substrate was thinned to 200 μm. After flip-chip bonding, some LEDs were further thinned to approximately 20 μm. One of two packaging options was used depending on the LEDs eventual use, either a lead frame package for high-power measurements or a hermetically sealed TO-39 package with a ball lens to provide a nearly collimated beam for instrumentation applications. Lead frame devices were encapsulated to improve extraction efficiency [17]. All devices were mounted to heat sinks for optimal thermal dissipation.

Figure 7.8 shows recent L-I results for two LEDs with peak wavelengths of 266 and 278 nm, as independently measured by the US Army Research Laboratory (ARL) [18]. The LEDs were driven in both continuous wave and pulsed modes. The two current input methods diverge only slightly beginning above 150 mA as device self-heating begins to limit the output power of the continuously driven LED. In pulsed operation, there is a minimal drop in external quantum efficiency up to current densities of 120 A/cm^2.

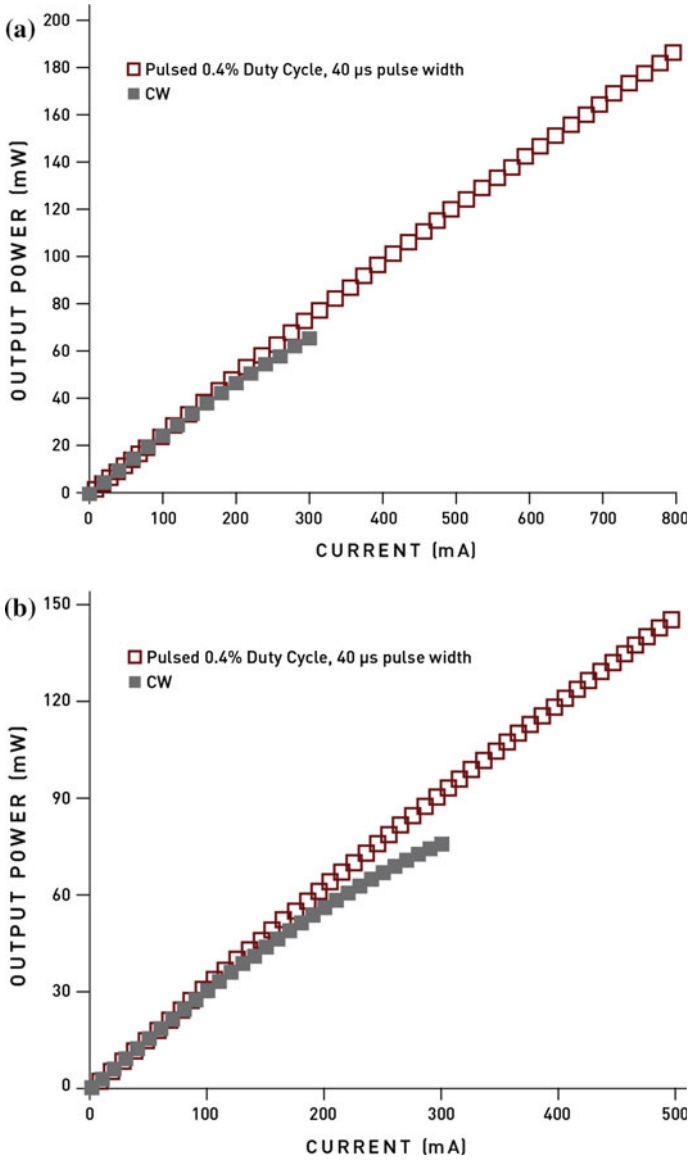


Fig. 7.8 L-I curves for 266 **a** and 278 nm; **b** LEDs under CW and pulsed conditions as measured by the U.S. Army Research Laboratory [18]

Absorption of ultraviolet light in the substrate remains a source of concern. Though the larger band gap of AlN should allow for transmission of UV down to 205 nm, defects and impurities introduced in the bulk crystal growth process can produce significant substrate absorption. We observe an absorption peak centered around 265 nm, with a peak value ranging from 20 to 85 cm^{-1} for the substrates

used in this work. Thinning of the substrate to 200 μm increases the measured output power by roughly 2×, while further thinning to 20 μm increases light extraction by another 2×.

In spectroscopic applications, the ratio of peak wavelength emission to light at longer wavelengths impacts measurement quality. Many biological compounds measured in these applications are excited by UVC wavelengths and produce light in the longer wavelengths. Autofluorescence describes the phenomena of light absorption and reemission by the LED substrate. Stray peaks emitted by the LED at these longer wavelengths can diminish accuracy in absorption and fluorescence spectroscopy. High quality UVC LEDs with a lower absorbing substrate will reduce the magnitude of this auto fluorescence.

The autofluorescence ratio was measured on a sample of UVC LEDs where the substrate had been thinned to 20 μm. For the devices displayed in Fig. 7.8 measured at ARL, the peak-to-325 nm emission ratio was 1,000, and the peak-to-400 nm emission was 2,000 at 10 mA drive current. When measured at Crystal IS, the same devices showed ratios of 3,000 at 100 mA (a difference seen due to signal-to-noise ratios). A sample of 721 diodes with thicker substrates, where the chance of re-emission is increased, showed peak-to-visible emission ratios greater than 100.

Pseudomorphic growth results in improvements to reliability. Figure 7.9 shows a histogram of the relative output power of 170 lead frame packaged LEDs after 1,000 h of CW operation at 100 mA. The median LED emits 97.2 % of its initial output power. Twenty-one devices (12.4 %) emit less than 40 % of their initial output power. The latter devices are primarily clustered around 0, indicating catastrophic failures due to a malfunction of the contact metallization or packaging. Analysis of the failed devices showed corrosion and metal migration, often exacerbated by environmental conditions. A sample of 40 devices in a hermetically sealed TO-39 package showed no failures of this nature.

In conclusion, improvements in device design have produced UVC diodes with more consistent emitting wavelength, reliability, and emission peak fidelity without sacrificing efficiency gains. AlN substrate absorption has a significant effect on

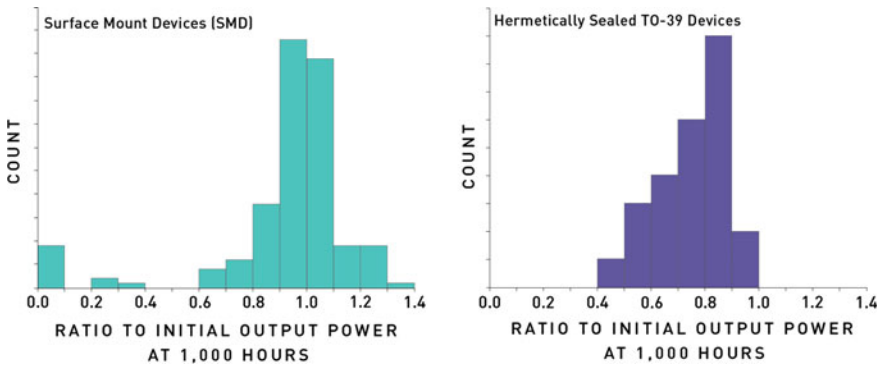


Fig. 7.9 Histogram of relative output power after 1,000 h operation at 100 mA for LEDs in an SMD (*left*) and hermetically sealed TO-39 package (*right*)

on-wafer results, but can be mitigated in the final device with advanced manufacturing techniques. Packaging improvements can also eliminate catastrophic failures in devices and allow for consistent device lifetimes with L_{50} values in excess of 1,000 h.

7.3 Leveraging Performance Gains in UVC LEDs for POU Water Disinfection

The performance gains in recent UVC LEDs have increased the interest in using these light sources for point-of-use (POU) water disinfection systems. In designing these systems, consider the following factors:

(a) Water Quality
(b) Flow cell dimension
(c) Dosage
(d) Material of construction
(e) Pathogen(s) to be inactivated
(f) Thermal management

What follows is a discussion on guiding principles for each of these factors.

(a) *Water Quality*

Water quality is critical in determining the amount of UVC light needed for disinfection. Of all water quality parameters, ultraviolet transmissivity (UVT) is the most important. The UVT of the water determines how well the UVC light will penetrate into the water, ensuring pathogens in the water are exposed to sufficient UVC light to be inactivated. Particles can reduce UVC disinfection capability by shielding microbes and absorbing UVC light. The use of filters will remove these suspended particles prior to UVC treatment.

As a general rule, a UVC unit would be installed in series following a filtration unit. If the reverse were implemented—that is, UVC unit then filter—higher UVC doses would be required to achieve the same level of inactivation, due to higher levels of Natural Organic Matter (NOM) turbidity and particulate matter.

7.3.1 Effect of UVT

UVT describes the amount of UV light passing through water according to the following:

$$\%\text{UVT} = 100 \times 10^{(-\text{A254} * d)}$$

where:

UVT	UV transmittance at a 254 nm and a 1 cm path length
A254	UV absorbance at 254 nm based on a 1 cm path length
d	distance from UV lamp (cm)

Turbidity, particulate matters, and organic matter in the water affect the UVT. As the turbidity increases, UVT decreases and as UVT decreases, UV intensity delivered to the microorganism decreases [19].

(b) *Flow Cell Dimension*

The efficiency of a UVC disinfection system depends on the size of the flow cell. The size is often dictated by the space available in a particular design and the amount of water requiring disinfection. These dimensions determine the amount of optical power required for disinfection.

The tube dimension and flow rate are used to calculate the residence time of the microbe(s) in the flow cell. Typical flow rates for point-of-use application are about 1 gallon per minute and point-of-entry systems can have flow rates between 1 and 8 gallons per minute.

(c) *Dosage*

A key factor in determining how effective UVC light will be in deactivating a given pathogen is the dosage that the pathogen in the water receives. The dosage is defined as the intensity of the UV light times the residence time:

UV Dose = Intensity (I) × Residence time (t)

where Intensity (I) is measured in milliwatts per cm^2 (mW/cm^2) and Exposure time (t) is measured in seconds (s).

The longer the residence or exposure time, the more UVC radiation will penetrate the pathogen's cells, and therefore, the more effective the inactivation process will be. The slower the flow rate of the water through the UVC system, the longer the UVC exposure time, and vice versa. Therefore, considering the maximum necessary and minimum allowable flow rate of the water in a particular system is a determining factor for setting the power requirement for the application.

(d) *Material of Construction*

The material used for the flow cell will impact the system efficacy. For example, materials with highly reflective properties for the UVC light will enhance its effectiveness. A list of materials with varying reflectance of UVC light, specifically around 250 nm, is available from the International Ultraviolet Association (IUVA) [20].

The most common material currently used in mercury lamp-based systems is stainless steel, although it only has 28–33 % reflectance [20]. Considering materials containing e-Polytetraflouroethylene [20], which has over 90 % reflectance in the

UVC range, may create a much more effective system. Polished aluminum also has high UVC reflectance. It is, however, sometimes unacceptable for reactor designs due to leaching of Al ions.

(e) *Pathogen(s) to be inactivated*

Another factor to consider is the type of microorganism that needs to be inactivated. Different pathogens have differing resistance to UV; some are more susceptible than others and so require different amounts of exposure to inactivate them. In order to correctly size and select a UV system, it is generally recommended to establish which pathogen(s) are to be targeted.

It is common for microbe inactivation to be measure on a logarithmic scale. Thus, a "one log," or 1 log, reduction describes pathogen reduction of 90 % from the influent level. A 2 log reduction describes a 99 % reduction, 3 log by 99.9 %, and so on. The dosage required for the inactivation has historically been measured only for low or medium pressure mercury lamps. Achieving the same log reduction using UVC LEDs requires proper testing.

Scientists have calculated the amount of UV exposure required to inactivate a whole range of different pathogens by various log reductions. NSF 55 standard describes requirements for meeting point-of-use and/or point-of-entry water disinfection specifications [21]. Class A requirements, which corresponds to 6 log reduction of bacteria, 4 log for virus and 3 log for *Giardia*, specifies a dosage of 40 mJ/cm^2 based on the spectrum of the standard mercury lamp. Class B, which corresponds to reduction of most all nuisance microbes, specifies a 16 mJ/cm^2.

(f) *Thermal Management*

When voltage or current is applied across the junction of an LED, the input electrical energy is converted into light and the rest into heat. The cooler the LED is kept, the better the performance—as seen in Fig. 7.10 for light output versus temperature. Managing the heat conduction path from the backside of an LED will promote optimal performance in LED-based applications.

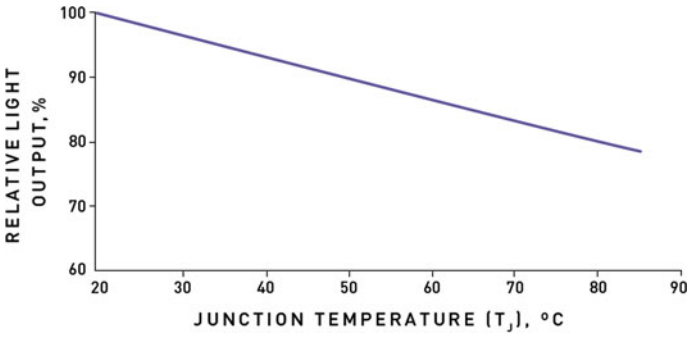


Fig. 7.10 Effect of light output as a function of junction temperature

The amount of electrical energy that is converted to heat (P_D) can be estimated by using the parameters, forward voltage (V_f), applied current (I_f), and the LED wall plug efficiency (WPE), and it is represented in the equation below.

$$\mathrm{PD} = V_f * I_f * (1 - \mathrm{WPE})$$

This means that if the Wall Plug Efficiency is 1 % for UVC LEDs, then 99 % of the input electrical power needs to be removed as heat.

Figure 7.10 shows the impact on optical power output if the junction temperature of the LED is allowed to increase due to heat that is generated from the operation of the LED. The junction temperature can be maintained by having an appropriate heat sink. If operating conditions call for further improvement of the thermal transfer beyond this simple passive heat sink-to-air interface, then fans may be added to the system to force convection and move cooler air between the fins. Other such active cooling techniques include the treated water from the flow cell and heat pipes to enhance thermal transfer [22].

7.3.2 Design Flexibility

Once the key application requirements are known, a system can be considered to achieve a targeted level of UVC disinfection. As extremely compact light sources, a major advantage of LEDs is that they can be incorporated into almost any design, theme, or object. Unlike traditional UVC sources, such as mercury lamps that only offer a single tube format, LEDs are a point source and can be used in applications in a variety of ways. The small size, scalability of arrays, and directional light emission of LEDs can be easily and ideally suited for use in linear, flat, or round area applications. For example, a traditional flow cell system for water disinfection places a mercury lamp in the center of a stainless steel tube with a quartz tube around the bulb as shown in the Fig. 7.11a. In the case of LEDs, there are number of different possibilities for mounting depending on the flow rate. Figure 7.11b–d illustrates varied placements for LEDs in end caps of the tube, on the outside of the flow cell, or as vertical arrays on the inside of the tube.

7.3.3 Modeling Flow Cells

It is generally desirable to maximize the water residence time in a flow cell. Computational fluid dynamics (CFD) is a useful tool to understand the flow constraints of a particular design. Optical modeling may also be used to examine various arrangement and location possibilities for LEDs in a given system. An optical model can be a guide for proper arrangement of diodes to have the flow cell

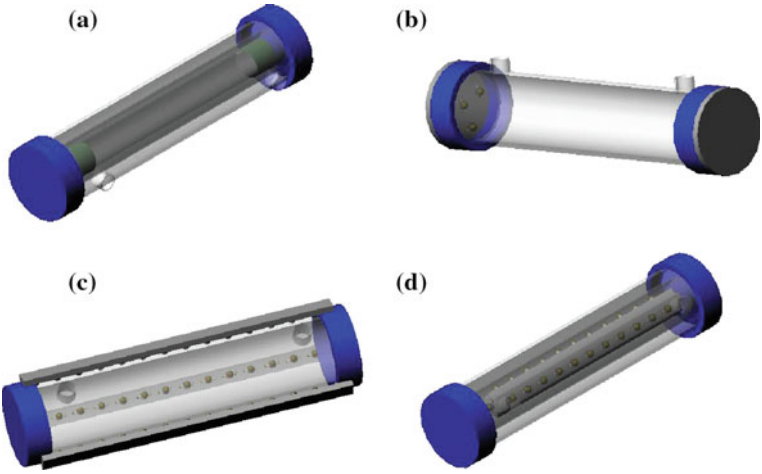


Fig. 7.11 **a** Flow Cell with center-mounted mercury lamp; **b** flow cell with LEDs mounted in end caps; **c** flow cell with LEDs positioned outside UV transparent tube; **d** flow cell with LEDs array mounted inside

completely illuminated with maximum uniformity and determine the minimum and maximum irradiance values experienced.

7.3.4 Example Flow Analysis

The following example outlines a process for developing a flow cell for UVC disinfection using UVC LEDs. The process starts with a flow analysis for the given application.

The calculations for the flow pattern were carried out using open CFD software called OpenFOAM [23]. The flow pattern will help determine the shortest and the mean time it takes for a microbe to pass through the flow cell. This provides the amount of irradiance needed to meet the NSF 55 requirement of 6 log reduction for bacteria, 4 log for Virus, and 3 log for protozoa.

This example evaluates three different flow cells (Fig. 7.12) with the same dimensions, but different internal designs to increase the residence time of the microbe in the flow cell.

These flow cell designs were modeled to determine the shortest and mean flow once the water entered into flow cell to its exit point. This provides the time the typical microbe stays in the flow cell and determines the appropriate amount of UVC light required to inactivate the microbe. The streamlines for possible flow paths can be modeled for each flow cell. The total residence time is calculated based on these streamlines. Figure 7.13a-1, b-1, c-1 show the streamlines for of the three different flow cells from Fig. 7.12. The single streamline shown in Fig. 7.13a-2, b-2, c-2 illustrate the direct path for water to flow from inlet to outlet.

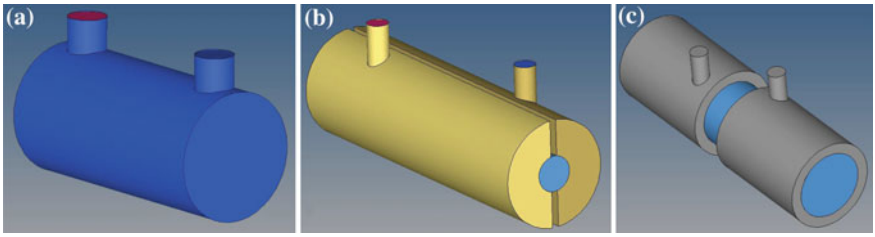


Fig. 7.12 Different flow cell conceptual designs with same volume

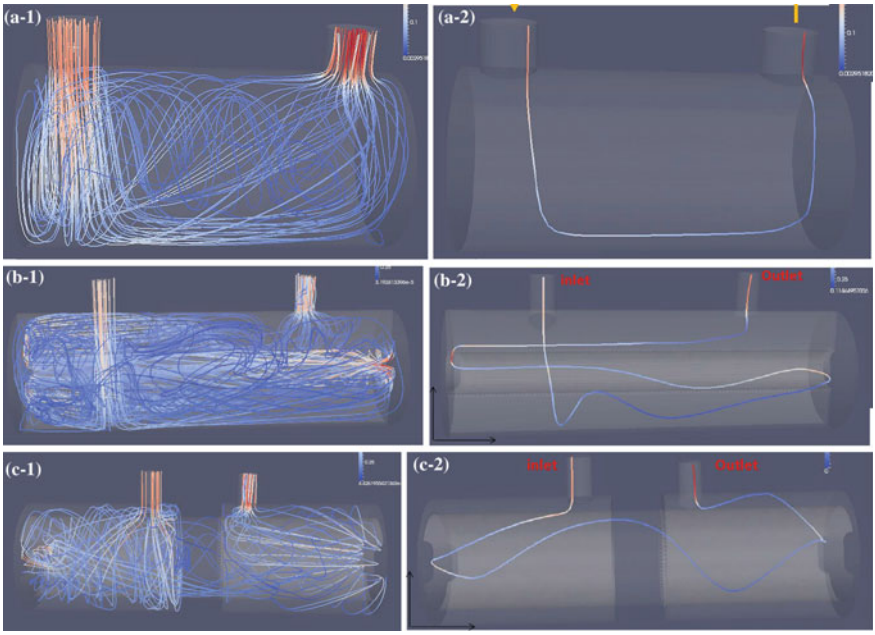


Fig. 7.13 The models show the streamline for water flow using OpenFOAM software for the three different flow cells

The modeling suggests a mean path of a target microbe in different flow cell designs. The table below shows calculations for the minimum and mean hold up times compared to the ideal flow time for the three concepts (Table 7.2).

The minimum hold up time is similar across all three flow cell concept designs. However there is variation in the mean hold up time. In this example, concepts B and C appear more desirable as they maximize the residence time of water in the flow cell.

Further analysis through Zemax® optical modeling helps to predict the pattern of light emission in the flow cell. Figure 7.14 shows the optical model for Fig. 7.11b with the lowest mean holdup time. Using the arrangement of LEDs placed in end caps on the flow cell, the model was used to predict the irradiation pattern on the

Table 7.2 Calculations for the minimum and mean hold up times compared to the ideal flow time for the three flow cell concepts

Model	Minimum holdup (s)	Ratio (to ideal[a] flow)	Mean holdup (s)	Ratio (to ideal[a] flow)
Concept A	1.16	0.39	3.09	1.03
Concept B	1.19	0.40	3.84	1.27
Concept C	1.12	0.37	3.76	1.25

[a]Water flow time in flow cell based on theoretical calculations of 3 s

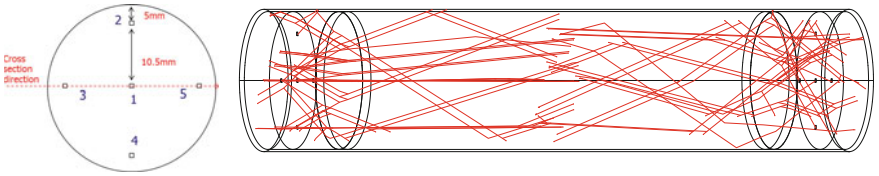


Fig. 7.14 Location of diodes mounted in the end cap and the optical model for light in the flow cell with the lowest mean hold up time

flow cell. Figure 7.15a, b shows the slice view of the optical model—both near the end cap and in the center of the flow cell.

Once the optical modeling was complete, the flow cell and circuitry was manufactured. The circuit boards were mounted to the proper heat sink to maintain the thermal management of the system. Once completely assembled, biological testing was performed based on EPA (Environmental Protection Agency) protocol [24].

Based on the CFD modeling for the water flow pattern and the optical modeling it was decided to manufacture two flow cells, the best case and worst case—Concept A and Concept C. Comparing these extremes shows the importance of residence time. Tests were performed at three flow rates with a UVT of 90 % and a single power input (100 %). Each test used samples taken of the influent and effluent. The influent was seeded with T1 and MS2 coliphage, and the bench test influent and effluent samples were analyzed for each phage surrogate.

The resulting data is represented in Fig. 7.16 for MS2 and T1 bacteriophage.

The data shows that Concept C has higher log reduction for both MS2 and T1. Based on the CFD modeling, it was predicted that Concept C would have a higher mean hold up time compared to Concept A. The optical model showed the amount of light in the flow cell and the optical power was consistent for both flow cells. Thus, the data reveals that the main parameter for increased log reduction was the holdup time—or rather the residence time. If the flow cell with a longer residence time is designed, the disinfection of the water is maximized.

7.3.5 Working with UVC Light

This chapter has discussed some of the design principles to take into account while designing a flow cell for POU water disinfection using LEDs, as well as illustrating

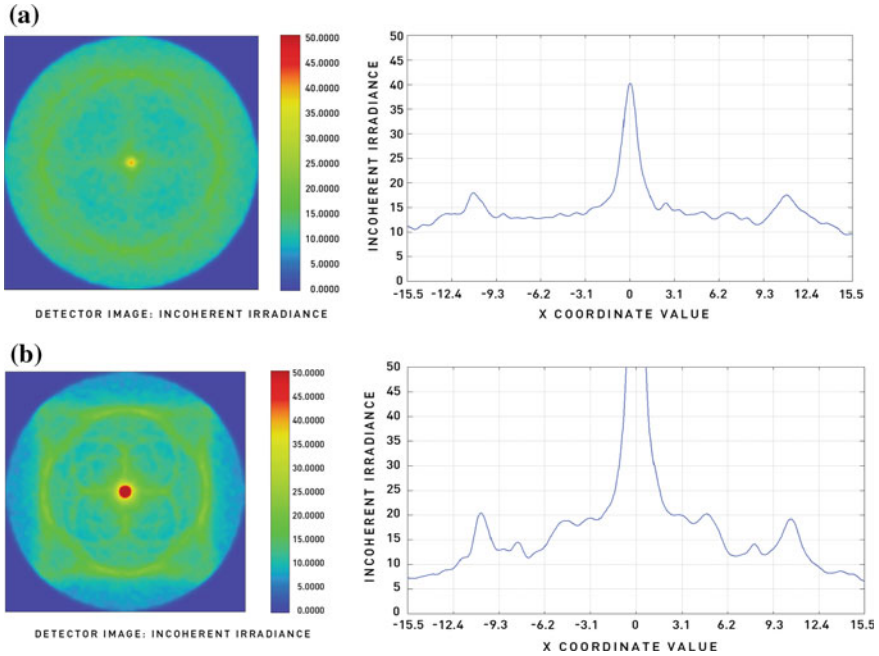


Fig. 7.15 Shows the slice view of the optical model. **a** Near the end cap and **b** in center of the flow cell

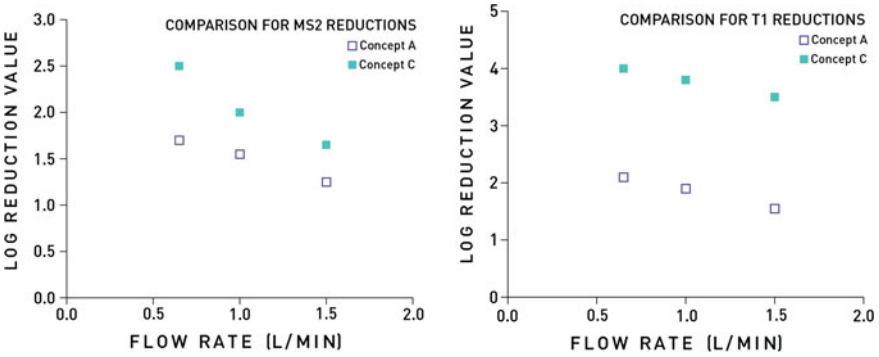


Fig. 7.16 Comparison for concept A and concept C for flow cell for MS2 and T1 reductions

how modeling and testing can be performed to validate these principles. Additionally, there are precautions that need to be taken with an operational unit.

(a) *Fouling of quartz window in front of UVC source*

A quartz window allows the UVC light to reach the water while protecting the LEDs and circuitry from water damage. Fouling of this quartz window, also known

as lamp jacket fouling, could occur due to the hardness of the water and/or presence of iron in the water. If this occurs, the amount of UVC light getting into the system is reduced and would potentially reduce disinfection.

Surface fouling is problematic because it absorbs UVC irradiation, reducing the dose applied to the water treated, and is most significant in waters with high concentrations of dissolved metals. One suspected precursor to lamp jacket fouling is aqueous phosphate [25]. Phosphates are often added to drinking water to aid in sequestering dissolved metals and prevent distribution network corrosion. However, orthophosphate and condensed phosphates have the potential to speed lamp jacket fouling by combining with dissolved metals and precipitating onto lamp jacket surfaces.

(b) *Monitoring UVC light output*

Monitoring UV light ensures that the right dosage for meeting desired disinfection requirements is occurring. A UVC monitor will detect the levels of light output in the system and let the end user know the unit is operating efficiently. The design can incorporate some existing optometer that measures in the UVC range, or create an additional circuit using a silicon-based pin diode.

(c) *Safety*

Depending on the length of exposure, UVC light can have adverse effects on human skin and eyes. UVC light exposure can be easily prevented during development, testing, and operation if proper precautions are put in place. The American Conference of Governmental Industrial Hygienist (ACGIH) [26] provides guidelines on use of proper PPE and permissible limits for exposure for individuals.

Including safety design controls for the equipment in-use is almost always a key aspect of design. Likewise, performing routine maintenance of the equipment and providing the proper training when working with UVC light is advisable.

References

1. http://whqlibdoc.who.int/publications/2008/9789241596435_eng.pdf
2. W. Heering, UV Sources-basics, properties and applications. IUVA News **6**(4) (2004)
3. M.A. Wurtele, T. Kolbe, M. Lipsz, A. Kulberg, M. Weyers, M. Kneissl, M. Jekel, Application of GaN-based ultraviolet-C light emitting diodes UV LEDs for water disinfection. Water Res. 1481–1489 (2011)
4. J.R. Grandusky, J. Chen, S.R. Gibb, M.C. Mendrick, C.G. Moe, L. Rodak, G.A. Garrett, M. Wraback, L.J. Schowalter, Appl. Exp. Lett. **6** (2013)
5. R. Schaefer, M. Grapperhaus, I. Schaefer, K. Linden, Pulsed UV lamp performance and comparison with UV mercury lamps. J. Environ. Eng. Sci. **6**, 303–310 (2007)
6. B.L. Diffey, Sources and measurement of ultraviolet radiation. Methods **28**, 4–13 (2002)
7. http://www.nasa.gov/topics/solarsystem/features/uv-exposure_prt.htm
8. J.R. Grandusky, J.A. Smart, M.C. Mendrick, L.J. Schowalter, K.X. Chen, E.F. Schubert, Pseudomorphic growth of thick n-type $Al_xGa_{1-x}N$ layers on low-defect-density bulk AlN substrates for UV LED applications. J. Cryst. Growth **311**, 2864 (2009)

9. J.Z. Ren, Q. Sun, S.Y. Kwon, J. Han, K. Davitt, Y.K. Song, A.V. Nurmikko, H.-K. Cho, W. Liu, J.A. Smart, L.J. Schowalter, Appl. Phys. Lett. 91, 051116 (2007)
10. A.A. Allerman, M.H. Crawford, A.J. Fischer, K.H.A. Bogart, S.R. Lee, D.M. Follstaedt, P. P. Provencio, D.D. Koleske, J. Cryst. Growth 272, 227 (2004)
11. J.T. Xu, C. Thomidis, I. Friel, T.D. Moustakas, Phys. Status Solidi (c) 2, 2220 (2005)
12. F. Mehnke, T. Wernicke, H. Pingel, C. Kuhn, V. Kueller, A. Knauer, M. Lapeyrade, M. Weyers, M. Kneissl, Highly conductive n-AlxGa1-xN layers with aluminum mole fractions above 80 %. Appl. Phys. Lett. 1103 212109 (2013)
13. J.R. Grandusky, S.R. Gibb, M.C. Mendrick, C.G. Moe, M. Wraback, L.J. Schowalter, Properties of mid-Ultraviolet light emitting diodes fabricated from psuedomorphic layer on bulk aluminum nitride substrates. Appl. Phys. Exp. 3, 072103 (2010)
14. T. Kinoshita, K. Hironaka, T. Obata, T. Nagashima, R. Dalmau, R. Schlesser, B. Moody, J. Xie, S. Inoue, Y. Kumagai, A. Koukitu, Z. Sitar, Deep-ultraviolet light-emitting diodes fabricated on AlN substrates prepared by hydride vapor phase epitaxy. Appl. Phys. Exp. 5, 122101 (2012)
15. J.R. Grandusky, S.R. Gibb, M.C. Mendrick, C.G. Moe, M. Wraback, L.J. Schowalter, High output power from 260 nm pseudomorphic ultraviolet light emitting diodes with improved thermal performance. Appl. Phys. Exp. 4(8), 082101 (2011)
16. J. Chen, J.R. Grandusky, M.C. Mendrick, S.R. Gibb, L.J. Schowalter, Improved photon extraction by substrate thinning and surface roughening in 260 nm pseudomorphic ultraviolet light emitting diodes, in Lester Eastman Conference on High Performance Devices (2012)
17. J.R. Grandusky, J. Chen, S.R. Gibb, M.C. Mendrick, C.G. Moe, L.E. Rodak, G.A. Garrett, M. Wraback, L.J. Schowalter, 270 nm pseudomorphic ultraviolet light-emitting diodes with over 60 mW continuous wave output power. Appl. Phys. Express 6(3), 032101 (2013)
18. C.G. Moe, J.R. Grandusky, J. Chen, K. Kitamura, M.C. Mendrick, M. Jamil, M. Toita, S.R. Gibb, L.J. Schowalter, High-power pseudomorphic mid-ultraviolet light-emitting diodes with improved efficiency and lifetime. SPIE 89861V (2014)
19. M. Templeton, R.C. Andrews, R. Hofmann, Particle characteristics influencing the UV disinfection of drinking water, in *Water Quality Technology Conference, American Water Works Association* (2004)
20. http://iuva.org/sites/default/files/IUVAG01A-2005.pdf, 50 (2005)
21. https://www.water2drink.com/resource-center/how-it-works-nsf-testing-standards.asp
22. https://www.cooliance.com/custom_heatpipes.html
23. https://www.openfoam.com
24. Ultraviolet disinfection guidance manual for the final long term 2 enhanced surface water treatment rule; office of water (4601), EPA 815-R-06-007, November 2006
25. I.W. Wait, C.T. Johnston, E.R. Blatchley III, ASCE 110, 343 (2004)
26. Ultraviolet Radiation, ACGIH (2001)

Chapter 8
AlGaN-Based Ultraviolet Laser Diodes

Thomas Wunderer, John E. Northrup and Noble M. Johnson

Abstract The current status of UV lasers and laser diodes (LDs) based on group III-nitrides is reviewed. The focus is on the design, fabrication, and performance of AlGa(In)N laser heterostructures grown by metal–organic vapor phase epitaxy (MOVPE) on high-quality bulk AlN substrates. The review begins with the fundamentals of laser diode operation and identifies the challenges to realize short-wavelength devices with wide band gap materials. In particular, simultaneously achieving high material quality and good p-type conductivity becomes increasingly challenging with higher aluminum concentrations in the epitaxial films. Using low defect density bulk AlN substrates is a good strategy to realize high internal quantum efficiencies and, ultimately, high gain within the active zone. Polarization-assisted hole generation with a short-period superlattice for the cladding layer is a viable approach to overcome the limitations of thermally activated p-type doping. Topics include LD processing considerations that are relevant for the high band gap materials, issues related to efficient carrier injection at the high current densities required for LD operation, and specific approaches to improve the functionality of the electron blocking layer. Next, results are presented for optically pumped UV lasers, with wavelengths down to λ = 237 nm and low lasing thresholds, and design options are described to manipulate the polarization of the emitted laser light. The review concludes with a discussion of alternative laser designs to realize deep-UV laser emission with nitride semiconductors.

T. Wunderer (✉) · J.E. Northrup · N.M. Johnson
PARC Palo Alto Research Center, Inc., 3333 Coyote Hill Road,
Palo Alto, CA 94304, USA
e-mail: Thomas.Wunderer@parc.com

N.M. Johnson
e-mail: noble.johnson@parc.com

© Springer International Publishing Switzerland 2016

M. Kneissl and J. Rass (eds.), *III-Nitride Ultraviolet Emitters*,
Springer Series in Materials Science 227, DOI 10.1007/978-3-319-24100-5_8

8.1 Introduction

Since the invention of the laser by A.L. Schawlow and C.H. Townes in 1958 [1], the sophisticated devices have continued to revolutionize our lives. They have generated an enormous list of new applications in the fields of telecommunication, data storage, consumer electronics, spectroscopy, materials processing, biophotonics, and life sciences. The unique properties of laser light with its high spatial and temporal coherence are particularly enabling in areas where light has to be focused to tiny spots allowing extremely high power densities or where the spectral quality and/or modulation speed of the emission is important.

Semiconductor lasers are often realized as edge-type emitting laser diodes (Fig. 8.1). The heterostructure is epitaxially grown by using either metal-organic vapor phase epitaxy (MOVPE) or molecular beam epitaxy (MBE). The active zone typically consists of several quantum wells (QWs) and is embedded in waveguide layers that are surrounded by p- and n-type cladding layers that confine the optical mode in transversal direction. For the electrically driven devices, electrons and holes are injected from opposite sides into the active region where they recombine to generate the desired photons. To achieve current densities of several kA/cm^2 and to confine the optical mode in lateral direction, the current is typically imposed through a narrow ridge that is only several microns wide and etched into the semiconductor material. A Fabry–Perot resonator with a typical length of 400 µm to about 2000 µm is formed by cleaved or etched mirror facets and provides feedback of photons through reflections at the semiconductor/air interfaces. Additionally, mirror coatings can be deposited to change the reflectivity properties for high-power or low-threshold devices.

Laser diodes in the group III-nitride material system were first realized by Nakamura and coworkers in 1996 [2] and have since then been commercialized with up to several Watts of output power in the wavelength regime between about 400 and 500 nm [3, 4]. For longer wavelength emitters the laser performance typically degrades significantly, which is commonly referred to as the "green gap"

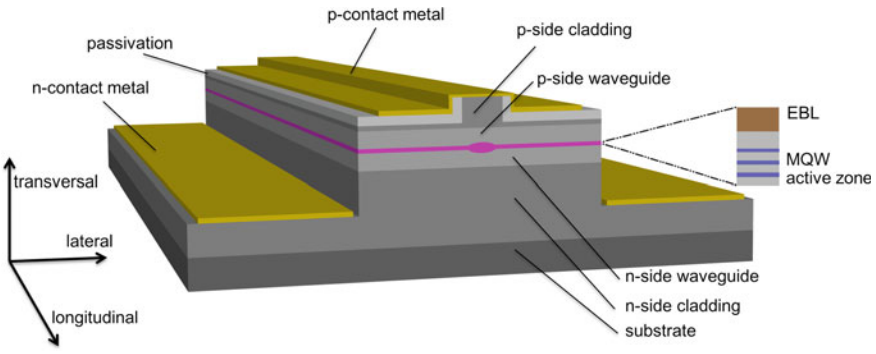


Fig. 8.1 Schematic of a laser diode device layout with lateral current injection

and arises due to difficulties in growing high-quality InGaN layers with high in-concentrations and strong built-in electrical fields within the QWs that lower the radiative recombination probability. With availability of low defect density GaN substrates, low threshold, continuous-wave (cw) laser diodes with lifetimes of several thousand hours have been demonstrated [5].

Whereas GaN substrates are a good choice for lasers emitting at wavelengths longer than about 370 nm, the lattice mismatch between the epitaxial layers and the substrate becomes increasingly large for devices emitting at shorter wavelength. The higher aluminum compositions that are needed for the shorter emission wavelengths induce a significant amount of stress into the crystal. If the critical thickness is exceeded [6], crystal defects in the form of threading dislocations are created. Even worse, AlGaN layers on a GaN substrates are under tensile stress and can be rendered useless by forming extended cracks within the heterostructure. No functional laser device can be fabricated with such material. In addition to the lack of a suitable substrate, the growth of high aluminum-containing layers becomes increasingly difficult due to the low mobility of the Al-species. A more serious issue, however, arises from the fact that as the band gap increases the thermally activated carrier concentration significantly drops [7]. This is particularly challenging for p-type AlGaInN where Mg is used as p-type dopant. High doping concentrations are needed to compensate for the inefficient holes activation process. This typically degrades the material quality, increases the absorption losses, and increases lasing threshold properties. Difficulties in p-type doping are also problematic for efficient injection of carriers into the active zone. A p-doped electron blocking layer (EBL) is typically inserted between the multiple quantum wells (MQWs) and the p-waveguide or p-cladding layer. The EBL is designed to hinder electrons from overshooting into the p-region where they recombine nonradiatively. However, it is not trivial to realize an EBL that simultaneously provides both good hole injection and electron blocking capability for high drive currents in the high band gap materials. Unlike the case for UV-LEDs, where satisfactory performance can be realized with the p-side fully or partly absorptive for the emission wavelength, the p-side of a laser diode must be highly transparent. Waveguiding of the laser mode can only be achieved with the cladding layers having a lower refractive index than the active zone and its surrounding waveguide layers. I.e., high band gap materials are mandatory for the p-side waveguide and cladding layers. Absorption levels of below about 100 cm^{-1} in the p-layers are typically acceptable.

Figure 8.2 shows a collection of measured current-injected laser diode performance metrics [8]. To date, the laser diode with the shortest emission wavelength was demonstrated by Hamamatsu in 2008 [9]. The group used a specifically prepared thick $Al_{0.3}Ga_{0.7}N$ template based on selective area epitaxy to improve the threading dislocation density and the strain situation within the heterostructure. Lasing was achieved at a wavelength of $\lambda = 336$ nm and a threshold current density of 17.6 kA/cm^2 under pulsed current injection (10 ns, 5 kHz). The output power level reached about 3 mW per facet [9].

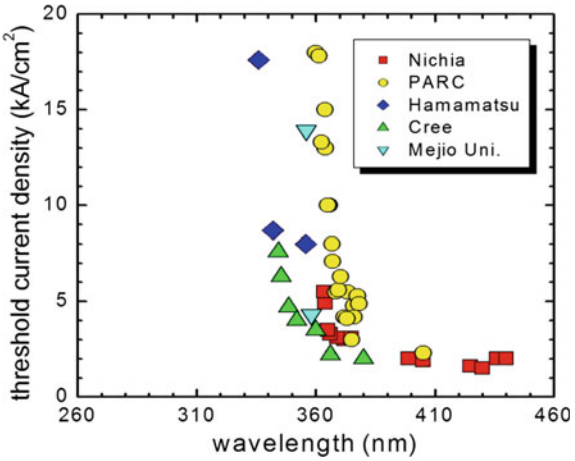


Fig. 8.2 Collection of measured current-injected UV laser diode performance metrics. Reproduced with permission from [8]. Copyright 2011 Optical Society of America

8.2 Growth on Bulk AlN for Highest Material Quality

Due to the above described difficulties of using GaN as the base layer for UV lasers at short emission wavelengths, bulk AlN has been considered as an alternative substrate source. The AlGa(In)N-based epitaxial heterostructures can be grown compressively strained on AlN. But even if the critical thickness is exceeded and the layers start to (partly) relax, with formation of new threading dislocations, functional devices can still be realized because the layers do not necessarily crack, as opposed to the case for relaxed AlGaN films on GaN substrate. The first electrically driven laser diode on a bulk AlN substrate was demonstrated at PARC in 2007 [10]. Although the AlGaN layers were fully relaxed, threshold current densities of 13 kA/cm^2 were achieved for laser emission wavelengths as short as 368 nm. The maximum light output power under pulsed conditions was near 300 mW with a differential quantum efficiency of $\eta_d = 6.7\,\%$. In the intervening years significant progress has been made in AlN boule growth and fabricating high-quality AlN substrates [11–13]. Here, we will discuss the use of AlN substrates for realizing AlGaN laser diode heterostructures for target emission wavelengths shorter than 300 nm.

8.2.1 Bulk AlN Substrate

The single-crystal AlN substrates for this work were fabricated by HexaTech, Inc. The AlN boules were grown by physical vapor transport (PVT). Typical growth conditions include high growth temperatures of T = 2200–2300 °C and N_2 pressures of 600–800 Torr. Further details on the substrate fabrication procedure can be

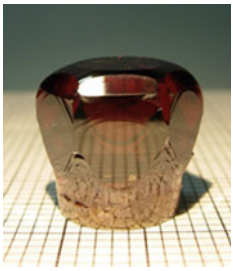


Fig. 8.3 Single crystal AlN boule grown by HexaTech, Inc. using physical vapor transport (PVT) growth technique. Reproduced with permission from [16]. Copyright 2012 Wiley-VCH Verlag GmbH & Co. KGaA

found elsewhere [14]. Figure 8.3 shows a picture of one of HexaTech's single-crystal AlN boules. After slicing, the substrates were chemomechanically polished (CMP) and feature a typical root mean square (rms) surface roughness of about 0.1 nm measured by atomic force microscopy (AFM) [15]. The dislocation density is typically $<10^5$ cm^2 [14]. Prior to the growth of the laser structure, the substrates were chemically cleaned in an etching solution of $H_3PO_4 : H_2SO_4 : H_2O$ (1 : 1 : 1) [15].

8.2.2 *Homoepitaxial AlN*

The epitaxial growth of PARC's laser heterostructures was conducted in metal-organic vapor phase reactors with conventional precursors for group III-nitride growth. These included trimethyl-aluminum (TMA), trimethyl-gallium (TMG), and trimethyl-indium (TMI) as the group III sources, and NH_3 as the group V source. The growth of a laser diode heterostructures typically starts with an AlN homoepitaxial layer before the transition to the AlGa(In)N layers is initiated.

Figure 8.4 shows an AFM image of a homoepitaxially grown AlN film with a thickness of about 500 nm on bulk AlN substrate. The layer is atomically smooth with an rms roughness <0.15 nm. The excellent material quality was also confirmed with X-ray diffraction and low temperature photoluminescence (PL) measurements, respectively. Figure 8.5 shows the PL near-band edge emission recorded at $T = 10$ K when excited by an ArF (193 nm) excimer laser. The measurements were conducted by B. Neuschl et al. at the Institute of Quantum Matter/Semiconductor Physics Group at the University of Ulm, Germany [17]. The exceptionally narrow linewidth of the Si^0X transition of only 500 μeV is a clear indication of the very high material quality of the layer.

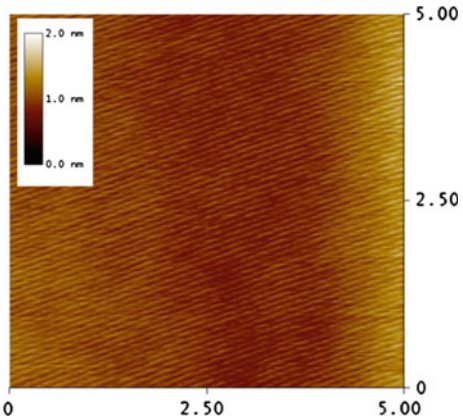


Fig. 8.4 AFM image of homoepitaxially grown AlN film on bulk AlN substrate. The rms surface roughness of a 5 μm × 5 μm scan is <0.15 nm

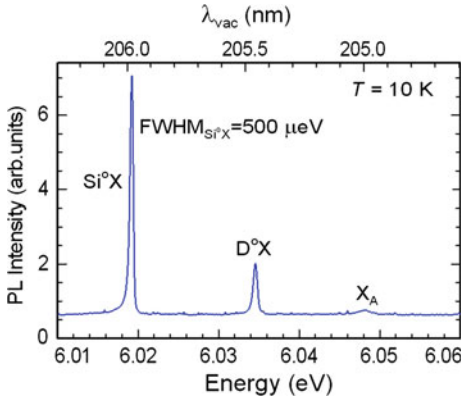


Fig. 8.5 Low-T PL measurement of homoepitaxially grown AlN on bulk AlN substrate. The very narrow linewidth of the Si^0X transition of only 500 μeV is a clear indication of the high material quality of the film. The measurements were performed by B. Neuschl from the University of Ulm, Germany [17]

8.2.3 AlGaN Laser Heterostructure

After growth of the AlN base layer, the heterostructure is continued with the transition to $Al_xGa_{1-x}N$. The laser heterostructure typically consists of n- and p-type AlGaN cladding layers, n- and p-type waveguide layers, and a MQW active zone that is embedded therein. Ideally, to maintain the low defect density material of the initial high-quality substrate the Al-composition should not be too low and the layers not too thick to avoid formation of extended defects in the form of threading dislocations. On the other hand, all the layers fulfill a specific function that

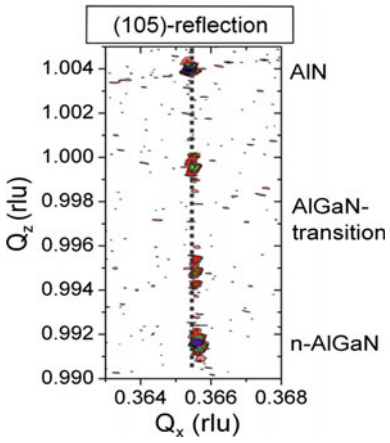


Fig. 8.6 X-ray reciprocal space map of 1 µm thick *n*-$Al_xGa_{1-x}N$ ($x = 74$ %) on AlN substrate with AlGaN transition layers. The layers are fully strained with respect to the substrate

determines specific boundary conditions. For example, both the n- and p-type cladding layers must provide a certain thickness to effectively suppress the electric field extension and allow for proper wave guiding of the lasing mode featuring a good confinement factor. At the same time, the conductivity of the layers has to be sufficiently high to sustain current densities of several tens of kA/cm^2, which typically requires lower Al-compositions. The proper design of the heterostructure is essential to achieve high-performance devices.

Fully strained n-type $Al_xGa_{1-x}N$ ($x = 74$ %) films with a thickness of 1 µm can be grown on bulk AlN substrate as shown in Fig. 8.6 with the X-ray reciprocal space map. In addition, the layer is highly transparent for wavelengths longer than about $\lambda = 250$ nm (transmission curve not shown), and Hall effect measurements of the sample reveal good electrical performance with an n-type carrier concentration of $n = 4 \times 10^{18}$ cm^{-3} and a carrier mobility of $\mu = 32$ cm^2/Vs [18]. These are satisfactory properties for an n-type cladding layer for UV lasers.

8.2.4 *Multiple Quantum Well Active Zone*

The next layer in the laser heterostructure is the multi-quantum wells active zone that is embedded in the waveguide layers. This is shown in Fig. 8.7 with a scanning transmission electron microscopy (STEM) image. Very sharp and abrupt interfaces can be achieved within the active layer, which reflects the high structural material quality of the heterostructure.

The optical properties of the laser heterostructures were evaluated with excitation power variable, time-resolved photoluminescence measurements. The investigations were performed by G. Garrett at the Army Research Laboratory, Adelphi, MD, USA [19]. Figure 8.8 shows the initial effective PL lifetimes as a function of pump fluence at 14 and 295 K. At low temperature, the PL transient exhibits a

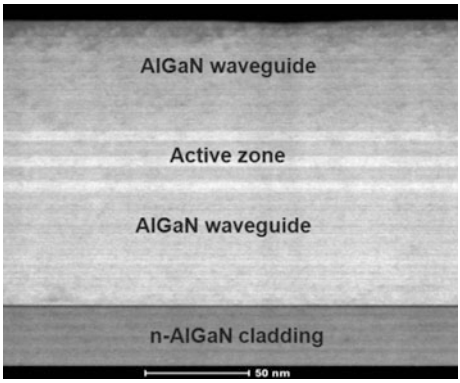


Fig. 8.7 STEM image of the active zone of an AlGaN-based laser heterostructure with emission wavelength at λ = 267 nm

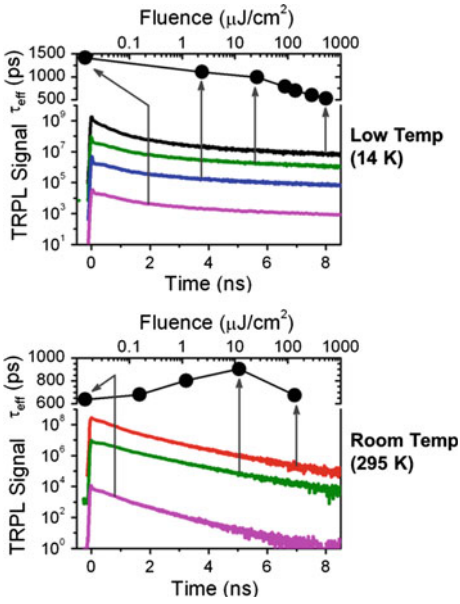


Fig. 8.8 Initial effective PL lifetime as a function of pump fluence at 14 and 295 K along with recorded time-resolved PL traces. Reproduced with permission from [19]. Copyright 2011 The Japan Society of Applied Physics

stretched behavior with an initial effective decay time that becomes progressively shorter with increasing pump fluence, reaching 528 ps at the highest fluence of 525 μJ/cm^2. This is to be expected from QWs within the nitride material system where the band structure is strongly tilted due to high internal electrical fields [20]. Values of the internal field in an AlGaN quantum well depend on the material compositions of the well and surrounding barriers. Typical values of the average field vary from about 0.1 to 0.05 eV/nm depending on the carrier concentration in the well. With nonradiative recombination largely frozen out at the low temperature, the decrease in lifetime with increasing pump fluence can be associated with the modification of the wave function overlap by carrier-density-dependent partial screening of the polarization field in the QWs. At room temperature, we observed

longer lifetimes with increasing fluence, reaching a peak of about 900 ps at 10 μJ/cm^2, before decreasing when the fluence is raised by another order of magnitude. The initial increase in PL lifetime is consistent with saturation of non-radiative centers at higher pump fluence. The subsequent drop in the PL lifetime at the highest fluence may be related to the onset of nonlinear radiative recombination approaching stimulated emission. Later, it will be shown that similar samples display very low lasing threshold power densities when operated as laser devices, which is consistent with the observations from the TR-PL investigation.

8.3 High Current Capability in High Band Gap AlGaN Materials

One of the biggest challenges in realizing UV laser diodes is the fact that the doping efficiency significantly drops with increasing the band gap of the semiconductor. This is especially relevant for p-type III-N materials. Unlike in UV LEDs, it is essential that the p-side layers of the laser diode heterostructure possess low absorption and provide efficient modal confinement at the wavelength of interest. This means that for a conventional LD design, the p-cladding layer should have an Al-composition similar to that of the n-side cladding and a higher composition than used for the waveguide layers. Dependent on the specific wavelength of interest, achieving the desired electrical performance and providing low absorption can be quite challenging. This is in particular true for lasers designed for wavelengths shorter than about 300 nm.

The issue is well illustrated by the work of Nakarmi et al. [21]. They deposited p-type $Al_xGa_{1-x}N$:Mg on an AlN/sapphire template with an Al-composition of x = 70 % and measured the electrical properties. They determined a thermal activation energy for holes of about 400 meV and measured a layer resistivity as high as 10^5 Ω cm [21]. This is five orders of magnitude above what is achievable with p-type GaN:Mg. Such a layer is inadequate as a p-cladding layer in a UV laser diode.

Needed is an AlGaN-based p-type heterostructure that does not rely (only) on thermally activated hole generation. Detailed first principles calculations suggested that a short-period $Al_xGa_{1-x}N/Al_yGa_{1-y}N$ superlattice (SPSL) heterostructure with extremely thin layer pairs could be an alternative for overcoming the limitations of thermally activated hole generation [22]. The strong piezoelectric and spontaneous polarization fields within the nitride materials system together with the band offset at the alternating layer interfaces can be utilized to effectively ionize Mg dopant atoms without additional thermal assistance. The design allows both high vertical and lateral hole transport, provided the layers are sufficiently thin. We have fabricated superlattices in which each AlGaN layer is in the order of 1 nm in thickness. In calculations we have examined $Al_{0.75}Ga_{0.25}N/Al_{0.5}Ga_{0.5}N$ superlattices of various periods. The tunneling rate of holes in the vertical direction is expected to vary

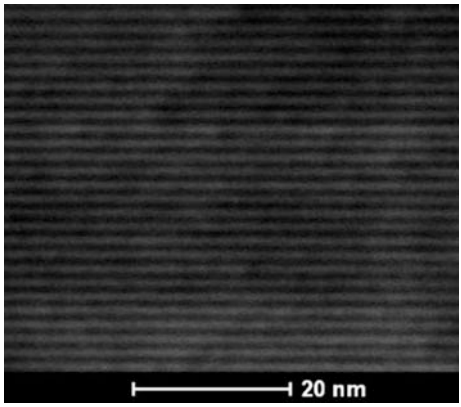


Fig. 8.9 STEM image of p-type AlGaN-based SPSL grown on bulk AlN substrate with average Al-composition of 60 %. Reproduced with permission from [22]. Copyright 2013 AIP Publishing LLC

inversely with the effective mass along the *c*-axis. Our density functional calculations indicate that the effective mass, along the *c*-axis, of the topmost valence band is reduced by a factor of about 5 in going from a 1 nm by 1 nm superlattice to a 0.75 nm by 0.75 nm superlattice. Figure 8.9 shows a STEM image of PARC's p-type AlGaN SPSL with an average Al-composition of about 60 % [22].

High-energy spectroscopic ellipsometry measurements were performed to determine the optical properties of the p-type SPSL [23]. With a sophisticated model, the collected ellipsometry data was analyzed to obtain accurate values for the refractive index n and the extinction coefficient k, as shown in Fig. 8.10. The values are particularly useful as input parameters for laser waveguide simulations.

To evaluate the electrical properties of the p-type SPSL, planar test devices were used to measure the lateral conductivity and full LD test devices for vertical carrier transport. Figure 8.11 shows the temperature-dependent resistivity of the p-type SPSL with an average Al-composition of 60 %. For comparison the resistivity curves of homogeneous GaN and $Al_{0.7}Ga_{0.3}N$ are also shown [21, 24]. At room temperature, the resistivity of the SPSL is only 9.6 Ω cm, which is within about 10× of reported values for p-type GaN and orders of magnitude better than for homogeneous AlGaN with similar Al-composition. The results indicate that a substantial number of holes are activated even at room temperature. The weak temperature dependence provides further evidence for polarization-activated holes that are immune to carrier freeze-out at 100 K. The effective activation energy E_A can be extracted from the measured curve by employing an Arrhenius equation with the approximation that the mobility is comparatively weakly dependent on temperature. Our SPSL shows an effective E_A value of only 17 meV, much lower than the values of 146 and 323 meV for homogeneous p-type GaN and $Al_{0.7}Ga_{0.3}N$, respectively [22].

Vertical carrier transport of the p-type SPSL was evaluated with full LD test devices that were designed for emission at about λ = 295 nm and included the MQW active zone and electron blocking layer (EBL). Figure 8.12 shows the IV characteristic of a fully processed LD test device. Under DC conditions the device sustained up to 11 kA/cm^2, which was the limit of the power supply. Under pulsed

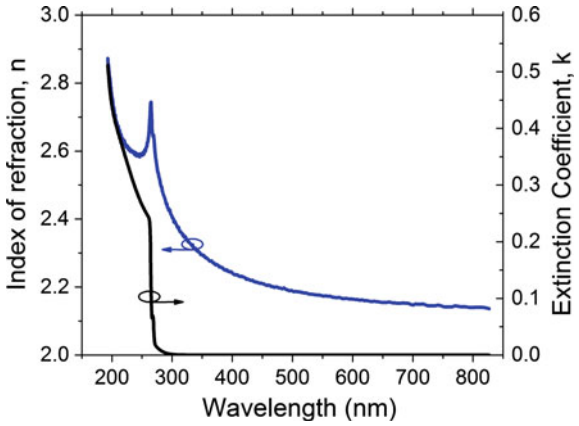


Fig. 8.10 Experimentally determined values for the refractive index and extinction coefficient of p-type AlGaN-based SPSL. The measurements were performed by M. Feneberg and R. Goldhahn, University of Magdeburg, Germany [23]

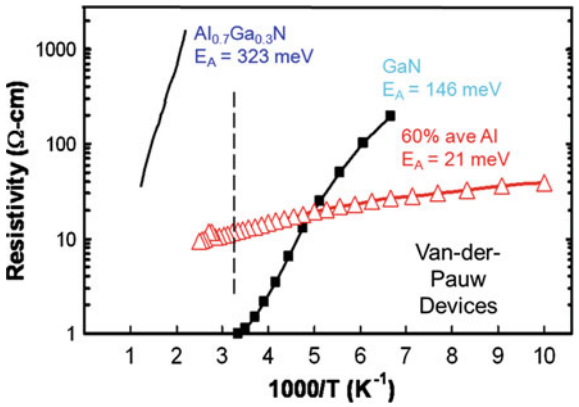


Fig. 8.11 Temperature-dependent resistivity values for p-type SPSL with average Al-composition of about 60 % (*open triangles*). The *solid squares* correspond to a reported resistivity for homogeneous p-type GaN [24]. The *solid line* corresponds to resistivity values reported for p-type $Al_{0.7}Ga_{0.3}N$ [21]

current injection current density levels as high as 21 kA/cm^2 were achieved. The voltage of the full LD was about 25 V at the highest current density of 21 kA/cm^2. As can be seen in Fig. 8.12, this is significantly better than the electrical performance of the LD with the shortest emission wavelength to date from Hamamatsu, in which the Al-composition of their n- and p-claddings was only 30 % [9]. The lower limit of the vertical conductivity of the p-SPSL at high current density was estimated under the approximation that the resistivity of the p-SPSL was the dominant

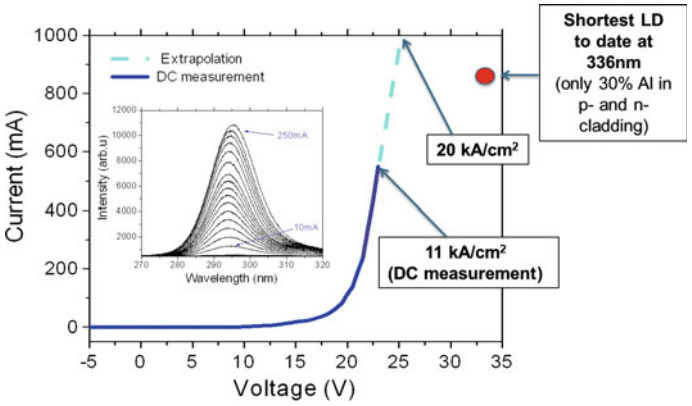


Fig. 8.12 IV characteristic of full LD test device with implemented thick p-type AlGaN SPSL cladding layer (average Al-composition of 60 %). Current densities of 11 kA/cm^2 under DC conditions (power supply limit) and up to 21 kA/cm^2 under pulsed conditions could be achieved. *Inset* Electroluminescence emission spectra of LD test device

component in the diode heterostructure. With this assumption, the differential resistance of the IV curve above turn-on approximates the resistance from the p-SPSL. The vertical conductivity was 7×10^{-5} S/cm for a current density of 20 A/cm^2, increased to about 0.01 S/cm at a current density of 1 kA/cm^2, and reached 0.1 S/cm for the highest current density of 11 kA/cm^2.

The magnitude of the vertical conductivity at high current densities approaches that for the lateral conductivity determined with the Hall effect measurements described above. Carrier transport in the vertical direction relies on tunneling processes via the higher band gap layers in the SL and might vary with changes in the applied voltage and temperature during operation. Monitoring the QW emission wavelength for different currents indicated a temperature change within the device. Specifically, we observed a blue shift of the QW emission for current densities up to 0.5 kA/cm^2. For higher drive current densities, the emission shifted to longer wavelengths. The shift to higher energies can be explained by a reduced influence of the quantum confined Stark effect by screening the internal field with injected carriers, whereas the shift to lower energies is related to an increase in temperature within the active zone. This suggests that the strong increase in vertical conductivity at low current levels might result from band bending effects, whereas, for current densities greater than about 0.5 kA/cm^2, heating might additionally contribute to the increased vertical conductivity at high current levels. The actual vertical conductivity of the p-layer may be even higher than the estimated values because the potential differences across the several contributing resistive components in series were all attributed to only the p-layer for the estimation [22]. The p-type AlGaN SPSL appears to be a viable candidate for p-type cladding layers in UV LDs.

8.4 High Injection Efficiency at High Current Levels

The difficulties in achieving high electrical (p-type) conductivity in high band gap materials have consequences not only for the maximal current levels that can be reached and its contribution to the series resistance of the device. It also strongly influences how efficiently carriers can be injected into the active zone to produce the desired photons. It is well known that within the nitride material system strong internal spontaneous and piezoelectric polarization fields alter the band structure of the laser heterostructure [20]. For example, the strong internal fields tilt the conduction and valence bands of the active zone so that electrons and holes accumulate at opposite regions within the QWs. This significantly reduces the radiative recombination probability and, as a consequence, the internal quantum efficiency. The internal fields in combination with the strong asymmetry between electron and hole mobility and effective carrier concentration lead to a situation where electrons from the n-side can easily reach the p-side of the diode without recombining radiatively within the active zone [25]. This is why a so-called electron blocking layer (EBL) is typically inserted between the active zone and the p-side layers. A conventional EBL is about 10–30 nm thick with a band gap that is noticeable higher than the MQW barrier composition and typically also significantly higher than the p-cladding layer. This reduces the probability that electrons will overshoot into the p-region of the device. However, the higher band gap material of the EBL also hinders holes from the p-side to easily enter the active zone. This is why it is meaningful to p-type dope the EBL. This will reduce the barrier height for holes in the valence band. However, as we have seen above, realizing effective p-type doping in AlGaN with high Al-compositions is quite challenging. As a consequence, we have to deal with an asymmetry of the pn junction, specifically, the disparity between electron and hole concentrations and mobilities. This can lead to carrier leakage out of the active zone despite the use of an EBL [25].

Figure 8.13 shows the LI (left) and the efficiency (normalized external quantum efficiency, right) characteristic of a test device with conventional EBL emitting at $\lambda = 295$ nm. Often the so-called ABC model is used to describe the recombination process $R = An + Bn^2 + Cn^3 + f(n)$ in optical emitters, where n, A, B, and C represent carrier concentration, Shockley–Read–Hall (SRH) recombination, radiative recombination, and Auger recombination coefficient, respectively and $f(n)$ represents carrier leakage out of the active region [25]. As can be seen in Fig. 8.13, even at low injection levels of only a few hundred μA the emission output rises with a slope of 1 in the double-logarithmic plot. This means that radiative recombination is the dominating contribution even at very low injection levels. This is a direct confirmation of the very high material quality of the devices when grown on high-quality bulk AlN substrate. However, the emission output drops from the linear increase at around 1 mA and continues with a slope of 2/3 before thermal effects further reduce the output power. Although there is ongoing discussion about the origin of the so-called droop phenomenon in visible III-nitride

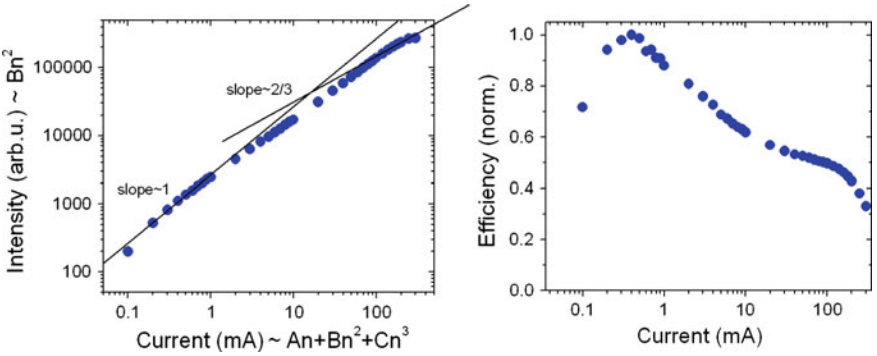


Fig. 8.13 Experimentally determined LI and efficiency characteristic of LD test device with conventional EBL emitting at $\lambda = 295$ nm plotted in double-logarithmic chart. The different slopes (1, 2/3) identify the dominant recombination process from the ABC model at different injection levels

LEDs [26], we believe that in the case of UV LD heterostructures a serious limitation is inefficient carrier injection.

We modeled the injection efficiency of our laser heterostructures using the commercial software package SiLENSe from the STR group. Figure 8.14 shows the calculated injection efficiency of a UV LD with target emission wavelength at $\lambda = 295$ nm for different injection levels. The LD design includes a standard EBL with Al-composition of 85 % and a thickness of 10 nm. Simulation results at 10 kA/cm^2 are also shown for an EBL thickness of 5 and 15 nm. As can be seen, the efficiency drops monotonically from close to 100 % to values of only about 40 % (for the 10 nm thick EBL) at current densities that are relevant for laser operation (>1 kA/cm^2). According to the simulation, both the thinner (5 nm) and thicker (15 nm) EBL would perform even worse. The right side of Fig. 8.14 shows the band diagram and position-dependent electron and hole currents in the vicinity of the active zone. The light green segments highlight the position of the QWs, the dark green section represents the EBL. As can be seen, a significant portion of the total current within the p-region (right side in diagram) can be attributed to current carried by electrons rather than by holes. This means that despite the EBL a significant portion of electrons (here: $\sim$60 %) overshoots over the barrier into the p-region. Or in other words, the limited capability of the EBL to effectively allow holes to penetrate through the EBL into the active zone is responsible for the drop in efficiency at high drive currents.

To improve the issues described above, we evaluated the use of specifically designed EBLs that provide both good electron blocking and good hole injection capability at the same time. As an alternative to solely thermally activated hole generation in high band gap materials Simon et al. developed polarization-induced 3D hole generation with composition-graded AlGaN:Mg [24]. When grown on the nitrogen-face of a GaN crystal, the Al-composition has to be ramped from low to high values to achieve the effect [24]. Following this idea, Zhang et al. later realized

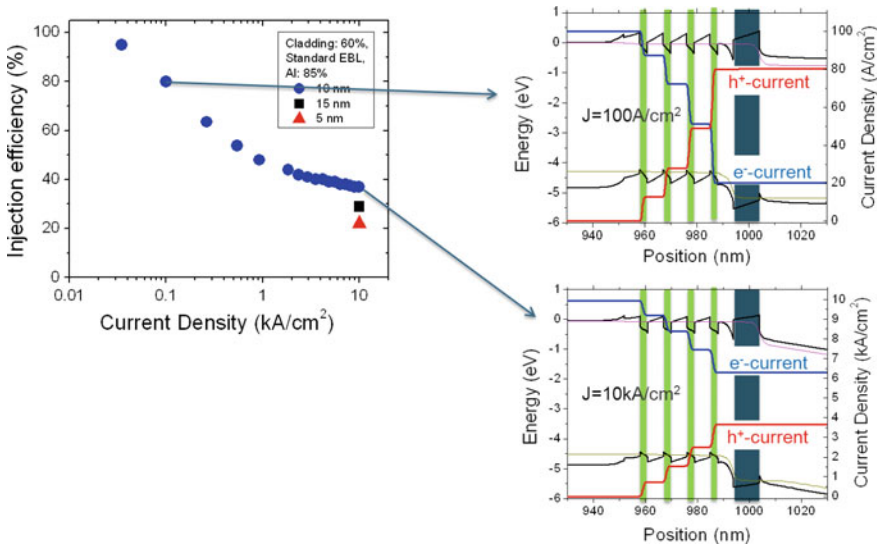


Fig. 8.14 Calculated injection efficiency of UV LD (target emission wavelength λ = 295 nm) with standard EBL and Al-composition of 85 % for 10, 5, and 15 nm for different current injection levels (*left*). Band diagram and position-dependent electron and hole currents in the vicinity of the active zone. The *light green* segments are the QWs, the *dark green* section represents the EBL (*right*)

conductive p-type materials on Al-face AlN where the Al-composition is ramped from high to low [27]. The idea of polarization-induced 3D hole generation via composition-graded AlGaN is quite attractive as EBL element in UV light emitters. We evaluated the concept of a composition-graded AlGaN EBL in UV emitters by simulating the injection efficiency. Our UV LDs are grown on Al-face AlN substrates. This is why the Al-composition of the EBL should be graded from high to low (Fig. 8.15, left). On the right side of Fig. 8.15, we show the band diagram of the modeled device including position-dependent electron and hole concentrations. As can be seen, within the composition-graded EBL a strong enhancement of the hole concentration can be achieved that will facilitate hole injection into the active zone. At the same time, electrons are efficiently blocked due to the fact that the band offset at the EBL/last QW barrier interface preliminary appears in the conduction band. Our simulations show that a significant improvement in injection efficiency can be expected by incorporation of the novel EBL design.

We experimentally implemented the graded-composition EBL designs into full LD test devices and compared them to LDs with conventional EBL designs. As can be seen in Fig. 8.16, a significant improvement in performance could be achieved with the novel design. While further optimization of the heterostructure is required, it is evident that efficient carrier injection is essential for high-performance UV LDs and that the proposed concept is a viable means to meeting this requirement.

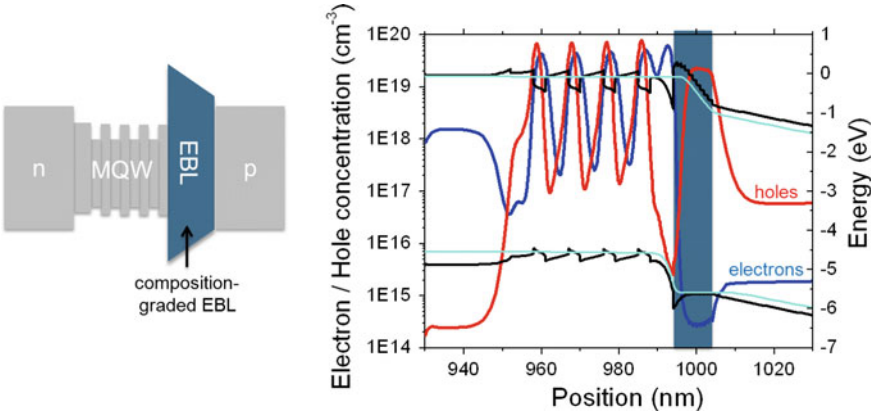


Fig. 8.15 Composition-graded EBL design to improve carrier injection efficiency. The EBL provides good electron blocking (band offset mainly appears in conduction band) and good hole injection capability (polarization-induced 3D hole gas)

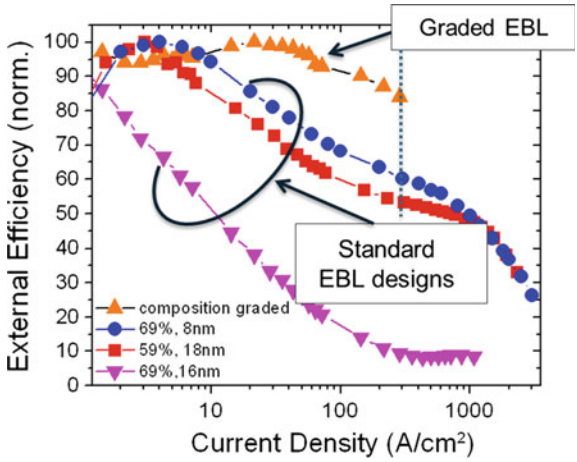


Fig. 8.16 Experimental evaluation of different EBL designs in UV LD test devices. Not fully optimized graded EBL design shows significant improvement in performance in comparison to standard EBLs

8.5 Optically Pumped UV Lasers

In this section we present and discuss experimental results for optically pumped UV lasers grown on bulk AlN substrate. Studying the laser performance via optical excitation is an excellent tool for optimizing the material quality and device heterostructure design including the active zone, waveguide, and cladding layers. These experiments provide very valuable information for the development of full LDs, because the laser heterostructure can be very similar to the electrically injected devices. Our long experience in developing semiconductor lasers gives us a good database and metric of how to relatively compare optically and electrically pumped

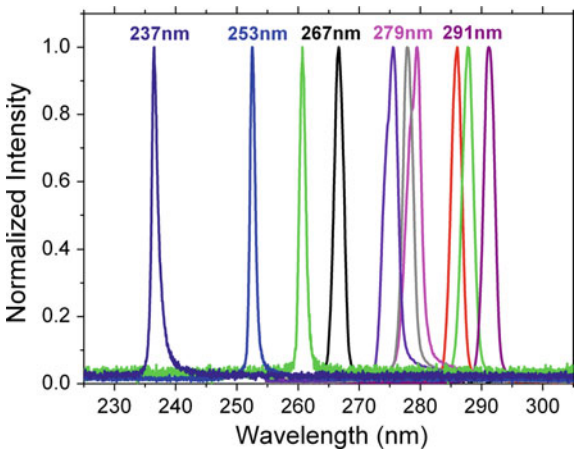


Fig. 8.17 Lasing spectra of PARC's optically pumped sub-300 nm UV AlGaN lasers on bulk AlN substrate. Optical excitation was performed with either a KrF (λ = 248 nm) or ArF (λ = 193 nm) excimer laser

lasers. The laser resonators with a length of about 1 mm were prepared by cleaving the semiconductor crystal to form m-plane mirror facets. No mirror coatings were used. To pump our sub-300 nm UV lasers we used either a KrF (λ = 248 nm) or ArF (λ = 193 nm) excimer laser as excitation source. The stripe width was in the order of about 100 μm. Figure 8.17 shows the laser spectra of selected sub-300 nm UV lasers that were grown on bulk AlN substrate. We successfully demonstrated optically pumped lasers over a range of wavelengths down to the shortest attempted wavelength at λ = 237 nm. To the best of our knowledge, this is the shortest emission wavelength yet demonstrated for a semiconductor laser heterostructure (Fig. 8.17). All of our sub-300 nm lasers showed laser threshold power densities below 200 kW/cm^2 [16, 19]. This is significantly better than what has been achieved on SiC or sapphire substrates [28, 29]. More recently, other groups have also successfully demonstrated optically pumped lasers on bulk AlN [30–32]. Our best device showed a laser threshold power density of only 41 kW/cm^2 at an emission wavelength of λ = 266 nm (Fig. 8.18). This value compares favorably with our very best results for lasers emitting in the blue-violet spectral regime based on GaN with InGaN QWs, for which the IQE values approach 90 %.

An important materials aspect of AlGaN-based devices is the fact that GaN and AlN feature a different sign in the crystal field splitting. Whereas it is negative for AlN (Δcr = −217 meV), it is positive for GaN (Δcr = +10 meV) [33]. As a consequence, the order of the valence bands differs between AlN and GaN (Γ_7 vs. Γ_9). This means that light that is generated within a GaN layer is predominantly TE polarized with the electric field vector E ⊥ c-direction. The light emission is mainly TM polarized when emitted in AlN with E ∥ c. For ternary AlGaN materials as used in UV light emitters we can expect a transition from TE to TM as the Al-concentration increases within the active zone [34]. This physical fact is another reason why the performance of UV LEDs typically degrades as the wavelength decreases. TM polarized light cannot be extracted parallel to the *c*-direction, which is the most commonly used growth direction for III-N materials (Fig. 8.19) [35].

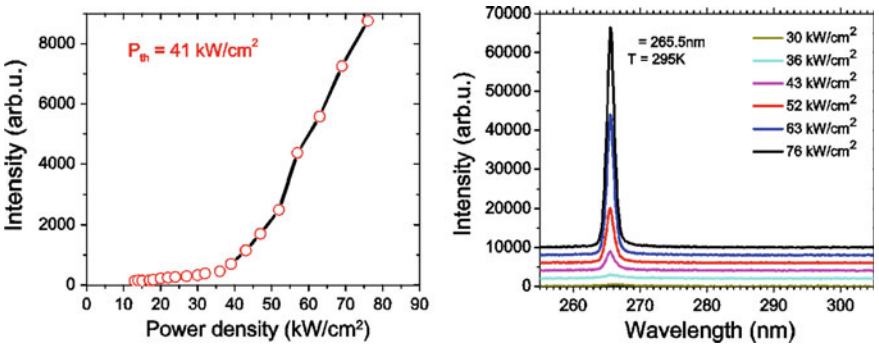


Fig. 8.18 Output power versus pump power density of AlGaN-based optically pumped laser at $\lambda = 266$ nm (*left*). Lasing spectra recorded at different excitation levels at room temperature (*right*)

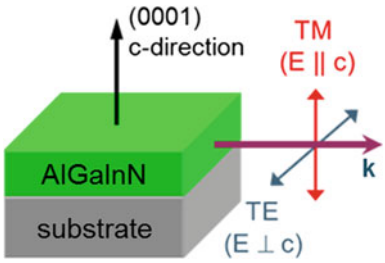


Fig. 8.19 Schematic of light polarization in AlGaN materials grown in the commonly used c-direction of the crystal

For edge-type emitting lasers the polarization is also an important aspect. Although it should be possible to realize lasers independent of the light polarization in this case, TE polarized emission is preferable. For the electrical field distribution of the guided modes in edge-type emitting lasers the TE modes do not expand as deeply into the p-region of the laser heterostructure as TM modes would do. Due to the fact that the heavily doped p-region significantly contributes to intrinsic losses in the device [36], TE polarization should provide lower threshold lasers.

In UV LED and LD heterostructures it is not only the composition of the AlGaN materials, in which the photons are generated, that determines the polarization of the emitted light. Other parameters such as the quantization within the QWs and the strain state of the layers play an important role too. This means that the design of the active zone including QW thickness and barrier composition and the substrate choice are considerable design parameters. Kolbe et al. investigated the degree of polarization for UV LEDs grown on sapphire substrates with the heterostructure being fully relaxed. At a wavelength of about 300 nm the transition from mainly TE polarized light to TM polarized light is observed [34]. However, for heterostructures that are pseudomorphically grown on bulk AlN substrate, where the AlGaN layers are highly compressively strained, the transition can be shifted to much lower wavelengths. For our UV-C lasers on bulk AlN substrates we observed the

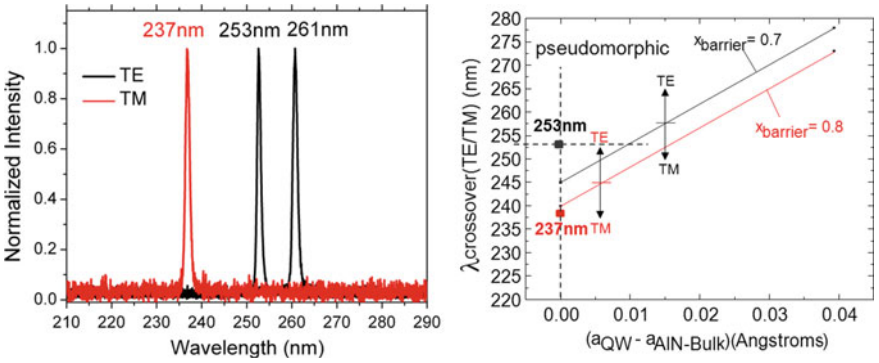


Fig. 8.20 Polarization-resolved laser spectra of optically pumped PARC UV-C lasers (*left*). Calculated crossover wavelength between TE and TM polarization versus relaxation degree for different active zone designs (*right*)

following. For the devices emitting at $\lambda = 253$, 261 nm and at longer wavelength the laser emission is still highly TE polarized, whereas the laser device emitting at $\lambda = 237$ nm is highly TM polarized (Fig. 8.20, left). We performed model calculations for the transition wavelength between TE and TM polarization for different active zone designs using k·p theory to better understand the underlying mechanism. The results are shown in Fig. 8.20 (right), which includes the experimentally determined values for our UV lasers measured at room temperature. The *x*-axis of the diagram in the figure represents the difference of the *a*-lattice constant of the QW a_{QW} in comparison to the one of the AlN substrate a_{AlN}. Or in other words, it represents the strain within the QWs. The *y*-axis shows the crossover wavelength between TE and TM polarization. For this case, calculations were performed for a QW thickness of 3 nm. The black and red lines show the transition wavelengths for an aluminum barrier composition of 70 and 80 %, respectively. For all device parameters that fall above the applicable line the emission is TE polarized, for all that fall below it is TM polarized. Looking at our 253 nm device with an aluminum barrier composition of 70 % and being fully strained to the substrate ($a_{QW} - a_{AlN} = 0$) TE polarization dominates for wavelength longer than about 245 nm. Our 237 nm device had a barrier composition of 80 % and was fully strained to the substrate. Because it falls below the red line, TM polarization is expected. The actual experimental results are in full agreement with the k·p calculations [33].

8.6 Alternative Concepts for Compact Deep-UV III-N Lasers

The previous sections demonstrate that high-quality III-N heterostructures can be grown on low dislocation density bulk AlN substrates and enable high-performance optically pumped UV lasers, with emission wavelengths down to $\lambda = 237$ nm.

However, realizing electrically pumped LDs remains problematic. The shortest wavelength demonstrated to date for a nitride LD is 336 nm. This suggests that at shorter wavelengths the achievable optical gain is not sufficiently high to overcome the intrinsic material and mirror losses. To a large degree this is attributable to the high doping concentration in the p-type layers that is necessary to compensate for the inefficient hole activation process and to optimize carrier injection efficiency into the active zone.

The question naturally arises as to whether there are alternative pump concepts other than carrier injection via a pn-junction that can be utilized to realize compact, high-performance UV lasers. In other words, is it possible to build a compact high-power UV laser source without using p-type materials? Indeed, two potential candidate approaches appear particularly interesting and will be briefly discussed in the following.

8.6.1 Electron-Beam Pumped Laser

The first alternative approach is based on electron-beam pumping of a semiconductor laser heterostructure. Electron–hole pairs can be generated by ballistic energy transfer of high-energy electrons impinging on the material. An electron from the valence band is promoted to the conduction band leaving behind a hole. About 1/3 of the beam energy is typically converted into electron hole pairs. Subsequent radiative recombination can then be used to create the desired photons. This phenomenon is well known and used in applications such as cathode ray tube television where the e-beam excites phosphors that emit visible light as a response to the excitation. The location of carrier generation and their desired radiative recombination cannot be as precisely manipulated through the heterostructure design as it is the case in a pn-diode. It is mainly dominated by the energy of the incident electrons and the materials used within the devices. These parameters determine the energy deposition volume, which approximates the location of electron-hole-pair generation.

Lasing in the group III-nitride material system with an electron-beam as excitation source was first demonstrated by Kozlovsky et al. in 1997 [37]. The device was grown on a sapphire substrate and operated as an edge-type emitter. Lasing was reported at λ = 409 nm and room temperature under short pulse operation (1 ns). The threshold current density was 200–300 A/cm^2 at an electron energy of 150 keV. Lasing of II–VI semiconductor materials was also demonstrated in a vertical cavity configuration [38]. High optical output power of up to 10 W was achieved for a large-area device in scanning e-beam mode. In addition, e-beam excitation was used for spontaneous emission at λ = 240 nm from an AlGaN heterostructure [39]. The optical output power reached 100 mW at a current level of 45 μA and a voltage of 8 keV. This corresponds to a power-to-power conversion efficiency of $\sim$30 % with a peak efficiency of 40 % at lower operation conditions.

This value is orders of magnitude higher than what can be achieved today with a conventional LED at these wavelengths.

To realize a compact UV laser source that is based on electron-beam excitation significant challenges still have to be mastered. These include operation in vacuum, development of laser-grade gain chips at the wavelength of interest, laser mirror implementation, and thermal management. Despite these challenges, avoiding the need of high band gap p-type materials is particularly attractive. Direct laser emission from a semiconductor material at wavelengths in the deep-UV spectral regime is completely feasible by this approach.

8.6.2 InGaN-Based VECSEL + Second Harmonic Generation

Another alternative approach to realizing a compact deep-UV laser source is based on second harmonic generation (SHG) of a laser emitting in the visible spectral range. Efficient SHG with a nonlinear crystal (e.g., BBO) relies on high electric field intensities and requires a narrow fundamental laser emission line width with an excellent beam profile. In our opinion, the best solution for efficient SHG is to place the nonlinear crystal within the cavity of a vertical emitting laser. The so-called Vertical-External-Cavity Surface-Emitting Laser (VECSEL), also known as Optically Pumped Semiconductor Laser (OPSL) or Thin Disk Laser, provides these desirable laser features. High optical output power with a nearly diffraction limited beam profile and narrow emission line width can be simultaneously achieved [40]. High-performance VECSELs, with and without frequency multiplication, have been demonstrated in the group III-arsenide and -phosphide material systems [40] and are commercially available. GaN-based VECSELs are still at an early stage of development [41–44]. However, there are no fundamental limitations that would preclude GaN materials for high-power cw VECSEL operation. With continuing progress in the performance of violet-blue LD, which can be used as pump lasers, and advances in the design and development of gain chip heterostructures, high-performance cw GaN-based VECSELs can be anticipated in the near future. This will allow the realization of cw, compact, high-power UV-C lasers emitting in the range of λ = 200–265 nm with excellent spatial and spectral beam properties. With such laser sources in hand, new applications in the scientific, commercial and military fields will be enabled and applications such as Raman spectroscopy will experience a significant boost in system features and performance.

8.7 Summary and Conclusion

This chapter has reviewed the current status and issues in the development of AlGaInN-based UV laser diodes. Materials challenges and laser design considerations were discussed with strong emphasis on the practical implementation for UV emitters. It was shown that by using low defect density bulk AlN substrates high-performance optically pumped lasers can be fabricated with emission wavelength as short as $\lambda = 237$ nm and threshold power densities that are comparable to the best InGaN-based counterparts ($P_{th} = 41$ kW/cm^2 @ 266 nm). Furthermore, it was demonstrated that the limitation of thermally activated hole generation can be overcome by utilizing p-type AlGaN-based SPSL with the strong built-in polarization fields of the nitride material system. Novel heterostructure device concepts were discussed to improve the carrier injection efficiency. A composition-graded electron blocking layer can enable both good electron blocking and efficient hole injection at the same time. However, despite the significant progress for sub-300 nm laser test devices, the achievable optical gain that can be generated through direct current injection does not yet exceed the intrinsic and mirror losses. Alternative laser concepts were briefly discussed that offer the advantage of not requiring high band gap p-type layers, which are a major hurdle to realizing deep-UV LDs. These included AlGaN-based laser heterostructures that are pumped by a high-energy electron-beam source and InGaN-based vertical emitting lasers combined with frequency doubling. These approaches are particularly attractive for sub-250 nm emission.

Wide band gap semiconductors based on the AlGaInN materials system offer the greatest promise for realizing compact and efficient laser sources in the UV spectral regime. It remains an open question as to which combination of alloy constituents, laser device type, device architecture, and laser system will deliver most fully and expeditiously on the requirements of UV laser applications. Each of the alternative approaches bypasses the most serious difficulties confronting deep-UV nitride laser diodes, but each has its own set of unique materials, device, or system challenges. Interesting developments and breakthroughs are anticipated within the next few years.

Acknowledgment We would like to thank Dr. Chris Chua, Zhihong Yang, Mark Teepe, Clifford Knollenberg, Dr. Bowen Cheng, and Dr. Suk Choi from PARC for their crucial support throughout the project. Special thanks are expressed to Dr. Gregory A. Garrett and Dr. Michael Wraback from the Army Research Laboratory, Adelphi, MD, USA, Dr. Martin Feneberg and Prof. Rüdiger Goldhahn from the OvG University Magdeburg, Germany, and Dr. Benjamin Neuschl and Prof. Klaus Thonke from the University of Ulm, Germany. We are pleased to acknowledge financial support from the Defense Advanced Research Projects Agency (DARPA) and the Defense Threat Reduction Agency (DTRA) under U.S. Army Cooperative Agreement no. W911NF-10-02-0102 and W911NF-10-2-0008.

References

1. A.L. Schawlow, C.H. Townes, Infrared and optical masers. Phys. Rev. **112**, 1940 (1958)
2. S. Nakamura, M. Senoh, S. Nagahama, N. Iwasa, T. Yamada, T. Matsushita, Y. Sugimoto, H. Kiyoku, Room-temperature continuous-wave operation of InGaN multi-quantum-well structure laser diodes. Appl. Phys. Lett. **69**, 4056 (1996)
3. S. Brüninghoff, C. Eichler, S. Tautz, A. Lell, M. Sabathil, S. Lutgen, U. Strauß, 8 W single-emitter InGaN laser in pulsed operation. Phys. Status Solidi A **206**, 1149 (2009)
4. S. Nagahama, Current Status and future prospects of GaN-based LDs, in *IWN 2012 Conference, Sapporo* (2012)
5. K. Yanashima, H. Nakajima, K. Tasai et al., Long-lifetime true green laser diodes with output power over 50 mW above 525 nm grown on semipolar 2021 GaN substrates. Appl. Phys. Exp. **5**, 082103 (2012)
6. S.R. Lee, D.D. Koleske, K.C. Cross, J.A. Floro, K.E. Waldrip, A.T. Wise, S. Mahajan, In situ measurements of the critical thickness for strain relaxation in AlGaN/GaN heterostructures. Appl. Phys. Lett. **85**, 6164 (2004)
7. K.B. Nam, M.L. Nakarmi, J. Li, J.Y. Lin, H.X. Jiang, Mg acceptor level in AlN probed by deep ultraviolet photoluminescence. Appl. Phys. Lett. **83**, 878 (2003)
8. M. Kneissl, T. Kolbe, J. Schlegel, J. Stellmach, C. Chua, Z. Yang, A. Knauer, M. Weyers, N. M. Johnson, *AlGaN-Based Ultraviolet Lasers—Applications and Materials Challenges. OSA Technical Digest (CD)* (Optical Society of America, 2011), JTuB1 (2011)
9. H. Yoshida, Y. Yamashita, M. Kuwabara, H. Kan, Demonstration of an ultraviolet 336 nm AlGaN multiple-quantum-well laser diode. Appl. Phys. Lett. **93**, 241106 (2008)
10. M. Kneissl, Z. Yang, M. Teepe, C. Knollenberg, O. Schmidt, P. Kiesel, N.M. Johnson, S. Schujman, L.J. Schowalter, Ultraviolet semiconductor laser diodes on bulk AlN. J. Appl. Phys. **101**, 123103 (2007)
11. S.B. Schujman, L.J. Schowalter, R.T. Bondokov, K.E. Morgan, W. Liu, J.A. Smart, T. Bettles, Structural and surface characterization of large diameter, crystalline AlN substrates for device fabrication. J. Cryst. Growth **310**, 887 (2008)
12. R. Dalmau, B. Moody, R. Schlesser, S. Mita, J. Xie, M. Feneberg, B. Neuschl, K. Thonke, R. Collazo, A. Rice, J. Tweedie, Z. Sitar, Growth and characterization of AlN and AlGaN epitaxial films on AlN single crystal substrates. J. Electrochem. Soc. **158**, H530 (2011)
13. C. Guguschev, A. Dittmar, E. Moukhina, C. Hartmann, S. Golka, J. Wollweber, M. Bickermann, R. Fornari, Growth of bulk AlN single crystals with low oxygen content taking into account thermal and kinetic effects of oxygen-related gaseous species. J. Cryst. Growth **360**, 185 (2012)
14. P. Lu, R. Collazo, R. Dalmau, G. Durkaya, N. Dietz, B. Raghothamachar, M. Dudley, Z. Sitar, Seeded growth of AlN bulk crystals in m- and c-orientation. J. Cryst. Growth **312**, 58 (2009)
15. A. Rice, R. Collazo, J. Tweedie, R. Dalmau, S. Mita, J. Xie, Z. Sitar, Surface preparation and homoepitaxial deposition of AlN on (0001)-oriented AlN substrates by metalorganic chemical vapor deposition. J. Appl. Phys. **108**, 043510 (2010)
16. T. Wunderer, C.L. Chua, J.E. Northrup, Z. Yang, N.M. Johnson, M. Kneissl, G.A. Garrett, H. Shen, M. Wraback, B. Moody, H.S. Craft, R. Schlesser, R.F. Dalmau, Z. Sitar, Optically pumped UV lasers grown on bulk AlN substrates. Phys. Status Solidi (c) **9**, 822–825 (2012)
17. B. Neuschl, K. Thonke, M. Feneberg, R. Goldhahn, T. Wunderer, Z. Yang, N.M. Johnson, J. Xie, S. Mita, A. Rice, R. Collazo, Z. Sitar, Direct determination of the silicon donor ionization energy in homoepitaxial AlN from photoluminescence two-electron transitions. Appl. Phys. Lett. **103**, 122105 (2013)
18. R. Collazo, S. Mita, J. Xie, A. Rice, J. Tweedie, R. Dalmau, Z. Sitar, Progress on n-type doping of AlGaN alloys on AlN single crystal substrates for UV optoelectronic applications. Phys. Status Solidi (c) **8**, 2031 (2011)

19. T. Wunderer, C.L. Chua, Z. Yang, J.E. Northrup, N.M. Johnson, G.A. Garrett, H. Shen, M. Wraback, Pseudomorphically grown ultraviolet-C photopumped lasers on bulk AlN substrates. Appl. Phys. Exp. **4**, 092101 (2011)
20. F. Bernardini, in *Nitride Semiconductor Devices: Principles and Simulations*, ed. by J. Piprek (Wiley-VCH, Weinheim, 2007), pp. 49–67
21. M.L. Nakarmi, K.H. Kim, M. Khizar, Z.Y. Fan, J.Y. Lin, X. Jianga, Electrical and optical properties of Mg-doped $Al_{0.7}Ga_{0.3}N$ alloys. Appl. Phys. Lett. **86**, 092108 (2005)
22. B. Cheng, S. Choi, J.E. Northrup, Z. Yang, C. Knollenberg, M. Teepe, T. Wunderer, C.L. Chua, N.M. Johnson, Enhanced vertical and lateral hole transport in high aluminum-containing AlGaN for deep ultraviolet light emitters. Appl. Phys. Lett. **102**, 231106 (2013)
23. R. Goldhahn, M. Feneberg, Private communication
24. J. Simon, V. Protasenko, C. Lian, H. Xing, D. Jena, Polarization-induced hole doping in wide–band-gap uniaxial semiconductor heterostructures. Science **327**, 60–64 (2010)
25. J. Cho, E.F. Schubert, J.K. Kim, Efficiency droop in light-emitting diodes: Challenges and countermeasures. Laser Photon. Rev. **7**, 408 (2013)
26. C. Verzellesi, D. Saguatti, M. Meneghini, F. Bertazzi, M. Goano, G. Meneghesso, E. Zanoni, Efficiency droop in InGaN/GaN blue light-emitting diodes: Physical mechanisms and remedies. J. Appl. Phys. **114**, 071101 (2013)
27. L. Zhang, K. Ding, J.C. Yan, J.X. Wang, Y.P. Zeng, T.B. Wei, Y.Y. Li, B.J. Sun, R.F. Duan, J.M. Li, Three-dimensional hole gas induced by polarization in (0001)-oriented metal-face III-nitride structure. Appl. Phys. Lett. **97**, 062103 (2010)
28. T. Takano, Y. Narita, A. Horiuchi, H. Kawanishi, Room-temperature deep-ultraviolet lasing at 241.5 nm of AlGaN multiple-quantum-well laser. Appl. Phys. Lett. **84**, 3567 (2004)
29. M. Martens, F. Mehnke, C. Kuhn, C. Reich, V. Kueller, A. Knauer, C. Netzel, C. Hartmann, J. Wollweber, J. Rass, T. Wernicke, M. Bickermann, M. Weyers, M. Kneissl, Performance characteristics of UV-C AlGaN-based lasers grown on sapphire and bulk AlN substrates. IEEE Photon. Tech. Lett. **26**, 342 (2014)
30. Z. Lochner, T.-T. Kao, Y.-S. Liu, X.-H. Li, M. Satter, S.-C. Shen, P.D. Yoder, J.-H. Ryou, R. D. Dupuis, Y. Wei, H. Xie, A. Fischer, F.A. Ponce, Deep-ultraviolet lasing at 243 nm from photopumped AlGaN/AlN heterostructure on AlN substrate. Appl. Phys. Lett. **102**, 101110 (2013)
31. J. Xie, S. Mita, Z. Bryan, W. Guo, L. Hussey, B. Moody, R. Schlesser, R. Kirste, M. Gerhold, R. Collazo, Z. Sitar, Lasing and longitudinal cavity modes in photo-pumped deep ultraviolet AlGaN heterostructures. Appl. Phys. Lett. **102**, 171102 (2013)
32. M. Martens, F. Mehnke, C. Kuhn, C. Reich, T. Wernicke, J. Rass, V. Küller, A. Knauer, C. Netzel, M. Weyers, M. Bickermann, M. Kneissl, Performance characteristics of UV-C AlGaN-based lasers grown on sapphire and bulk AlN substrates. IEEE Photon. Tech. Lett. **26**, 342 (2014)
33. J.E. Northrup, C.L. Chua, Z. Yang, T. Wunderer, M. Kneissl, N.M. Johnson, T. Kolbe, Effect of strain and barrier composition on the polarization of light emission from AlGaN/AlN quantum wells. Appl. Phys. Lett. **100**, 021101 (2012)
34. T. Kolbe, A. Knauer, C. Chua, Z. Yang, S. Einfeldt, P. Vogt, N.M. Johnson, M. Weyers, M. Kneissl, Optical polarization characteristics of ultraviolet (In)(Al)GaN multiple quantum well light emitting diodes. Appl. Phys. Lett. **97**, 171105 (2010)
35. K.B. Nam, J. Li, M.L. Nakarmi, J.Y. Lin, H.X. Jiang, Unique optical properties of AlGaN alloys and related ultraviolet emitters. Appl. Phys. Lett. **84**, 5264 (2004)
36. D.S. Sizov, R. Bhat, A. Heberle, K. Song, C. Zah, Internal optical waveguide loss and p-type absorption in blue and green InGaN quantum well laser diodes. Appl. Phys. Express **3**, 122104 (2010)
37. V.I. Kozlovsky, A.B. Krysa, Y.K. Skyasyrsky, Y.M. Popov, A. Abare, M.P. Mack, S. Keller, U. K. Mishra, L. Coldren, Steven DenBaars, Michael D. Tiberi, T. George, Electron beam pumped MQW InGaN/GaN laser. MRS Internet J. Nitride Semicond. Res. **2**, 38 (1997)

38. M. Tiberi, V. Kozlovsky, P. Kuznetsov, Electron beam pumped lasers based on II–VI compound nanostructures from the visible to UVA. Phys. Status Solidi (B) **247**, 1547 (2010)
39. T. Oto, R.G. Banal, K Kataoka, M. Funato, 100 mW deep-ultraviolet emission from aluminium-nitride-based quantum wells pumped by an electron beam. Nat. Photon. **4**, 767 (2010)
40. O.G. Okhotnikov, *Semiconductor Disk Laser* (Wiley-VCH Verlag GmbH & Co, KGaA, Weinheim, 2010)
41. S.-H. Park, J. Kim, H. Jeon, T. Sakong, S.-N. Lee, S. Chae, Y. Park, C.-H. Jeong, G.-Y. Yeom, Y.-H. Cho, Room-temperature GaN vertical-cavity surface-emitting laser operation in an extended cavity scheme. Appl. Phys. Lett. **83**, 2121 (2003)
42. R. Debusmann, N. Dhidah, V. Hoffmann, L. Weixelbaum, U. Brauch, T. Graf, M. Weyers, M. Kneissl, InGaN-GaN disk laser for blue-violet emission wavelengths. IEEE Photon. Technol. Lett. **22**, 652 (2010)
43. T. Wunderer, J.E. Northrup, Z. Yang, M. Teepe, A. Strittmatter, N.M. Johnson, P. Rotella, M. Wraback, In-well pumping of InGaN/GaN vertical-external-cavity surface-emitting lasers. Appl. Phys. Lett. **99**, 201109 (2011)
44. X. Zeng, D.L. Boïko, G. Cosendey, M. Glauser, J.-F. Carlin, N. Grandjean, Optically pumped long external cavity InGaN/GaN surface-emitting laser with injection seeding from a planar microcavity. Appl. Phys. Lett. **101**, 141120 (2012)

Chapter 9
Solar- and Visible-Blind AlGaN Photodetectors

Moritz Brendel, Enrico Pertzsch, Vera Abrosimova, Torsten Trenkler and Markus Weyers

Abstract This chapter presents an overview on UV photodetectors based on the $Al_xGa_{1-x}N$ material system. After an introduction into the field of UV photodetection and material-related issues, the main physics, the operation principles, and characteristic parameters of the most popular photodetector device types will be briefly addressed including the photoconductor, the Schottky barrier diode, the metal–semiconductor–metal structure, the p-i-n diode, the avalanche detector as well as the phototube and the photomultiplier tube. Further, scientific results on $Al_xGa_{1-x}N$-based photodetectors are compiled in order to illustrate the potential of the different photodetector device types for a wide range of UV applications. And finally, the state-of-the-art of commercially available photodetectors for UV detection and monitoring is discussed.

9.1 Introduction

The ultraviolet (UV) portion of the electromagnetic spectrum, i.e., electromagnetic radiation in the wavelength range between 400 and 10 nm, is divided into several subranges, e.g., UV-A (380–315 nm), UV-B (315–280 nm), UV-C (280–200 nm),

M. Brendel (✉) · M. Weyers
Ferdinand-Braun-Institut, Leibniz-Institut für Höchstfrequenztechnik, Gustav-Kirchhoff-Str. 4, 12489 Berlin, Germany
e-mail: moritz.brendel@fbh-berlin.de

M. Weyers
e-mail: markus.weyers@fbh-berlin.de

E. Pertzsch · V. Abrosimova · T. Trenkler
JENOPTIK Polymer Systems GmbH, Köpenicker Strasse 325b, 12555 Berlin, Germany
e-mail: enrico.pertzsch@jenoptik.com

V. Abrosimova
e-mail: vera.abrosimova@jenoptik.com

T. Trenkler
e-mail: torsten.trenkler@jenoptik.com

© Springer International Publishing Switzerland 2016

M. Kneissl and J. Rass (eds.), *III-Nitride Ultraviolet Emitters*,
Springer Series in Materials Science 227, DOI 10.1007/978-3-319-24100-5_9

and VUV (200–10 nm),[1] which help to classify optoelectronic devices, i.e., emitters and detectors, by their operational range. A photodetector (PD)[2] sensitive only in the UV range thus can be visible-blind or even solar-blind whenever detection capability is limited to wavelengths below 380 or 280 nm, respectively. Application fields for such devices in industry, military, medicine, and science include UV dosimetry, flame sensing, non-line-of-sight communication and biological as well as chemical sensing. Some specific examples are

- UV lithography (193 nm)
- UV curing of paints, adhesives, compounds, and polyester plastics (e.g., 365 nm)
- Disinfection of water, air, and surfaces (240–290 nm)
- Detection of corona discharges (<280 nm)
- Missile plume detection and combustion engine control
- Chemical and biological threat detection
- UV spectroscopy
- UV astronomy.

As an example, UV-C lamps for water and air disinfection have to be monitored in order to detect failure and to ensure the required UV-C dose. As long as mercury medium pressure lamps are used in such systems,[3] for an accurate measurement of the UV-C dose of the 254 nm line, the parasitic UV-A and UV-B emission has to be excluded. Similar examples are the imaging of corona discharges at broken transmission lines or of missile plume and other launching actions, which are usually against a daylight background within the earth's atmosphere. III–V semiconductor materials bearing the possibility to design the spectral properties of a PD accordingly, without the use of an external spectral filter, that is costly and tends to age under UV radiation, are favorable in such applications.

The ternary $Al_xGa_{1-x}N$ material system spans a range of bandgap energies between those values for the binaries GaN with 3.5 eV and AlN with 6.2 eV [1], covering band edge cut-offs between about 360 and 200 nm, respectively. AlGaN-based PDs are visible-blind and solar blindness can be tuned via the Al mole fraction with $x_{Al} \geq 0.45$, where alternative materials, such as Si, GaAs, GaP, and SiC are not intrinsically blind to visible portions of the spectrum. Radiation hardness and the capability to withstand high-thermal stress due to the wide direct energy gap put the AlGaN system in favor for its usage in a number of UV applications. High values for spontaneous polarization along the c-axis of the wurtzite cell as well as a strain-dependent piezoelectric polarization have to be considered, since both affect the optical and electrical properties of III-nitride devices consisting of heterojunctions [1]. However, with increasing Al content

[1]VUV: vacuum UV.

[2]The abbreviation PD will be used for *photodetector* and *photodiode* throughout the text.

[3]Hg-lamps deliver the required intensities between 10^{-4} to 0.1 W cm^{-2}, where UVC-LEDs with an output of 10^{-4} W cm^{-2} are commercially available but are still too weak for water disinfection.

several difficulties had to be dealt with during the past two decades of UV photodetector development.

- First of all, due to the tensile strain resulting from lattice and thermal mismatch, the heteroepitaxial growth of an $Al_xGa_{1-x}N$ layer of a certain thickness directly on a GaN/sapphire template is limited to AlN mole fractions below about 30 % before cracking of the layers occurs (see e.g., [2] and references therein). Material defects, such as stacking faults, threading dislocations and grain boundaries are usually known to deteriorate the performance of any optoelectronic device. Several approaches to grow high-quality $Al_xGa_{1-x}N$ material have been reported, e.g., the use of low-temperature (LT) AlN buffer layers [3], superlattices of GaN/AlN [4], GaN/AlGaN, and AlN/AlGaN [5] layers and different epitaxial lateral overgrowth techniques [6–8]. Anyway, in terms of back-illuminated PDs, the substrate as well as the buffer layers may limit the short-wavelength performance due to the onset of absorption, hence the material should be chosen reasonably.
- Another major issue is the p-type conductivity of $Al_xGa_{1-x}N$ layers. Doping of GaN with Mg introduces a shallow acceptor level of the substitutional magnesium on a gallium lattice site Mg_{Ga} with an ionization energy of 200 meV [9]. But due to the passivation of incorporated Mg by hydrogen, a post-growth annealing step at temperature above 600 °C is necessary to obtain conductive p-type GaN:Mg [10, 11]. Maximum hole concentration of about 10^{18} cm^3 for Mg concentration of about 3.3×10^{19} cm^3 can be achieved [12], and a further increase of the Mg concentration leads to a subsequent decrease of the free-hole concentration since the Mg_{Ga} acceptor is expected to self-compensate via the nitrogen vacancy V_N^{3+} [13, 14]. With increasing x_{Al}, the ionization energy of the magnesium acceptor level also increases up to 0.51 eV in AlN [15, 16] resulting in a strongly reduced concentration of free holes in AlN:Mg compared to GaN:Mg for the same net acceptor concentration.
- Last but not least, the development of proper ohmic contacts to both n- and p-type $Al_xGa_{1-x}N$ layers as well as the formation of non-leaky Schottky-type metal-$Al_xGa_{1-x}N$ junctions are not straight forward. The main issue concerning ohmic contacts is the absence of a metal with sufficient work function, so that a thermal annealing step after the metallization is necessary to obtain ohmic behavior of the respective metal-$Al_xGa_{1-x}N$ junction. For an n-GaN layer, this can be done using Ti/Al layers annealed at 900 °C for 20–30 s and for a p-GaN layer by annealing Ni/Au for 30 s at 700 °C [17, 18]. These examples illustrate that devices with n-type as well as p-type ohmic contacts need two different process steps for contact formation due to the differences in annealing temperature and time. From the above–mentioned, it seems that Schottky barriers to the $Al_xGa_{1-x}N$ material—with barrier heights between 0.1 eV using Ti and more than 1.1 eV for Pt—would be easily produced by just leaving out the annealing step. But also a proper surface treatment prior to metallization, e.g., removing native oxides by N_2^+ ion sputtering [19] or HCl wet etching [20], has to be ensured for the desired metal-$Al_xGa_{1-x}N$ combination. Dependent on the metal

used the thermal stability of Schottky contacts is limited since above where annealing effects set in the electrical behavior of the contact changes. Thus, it is necessary to arrange the process flow accordingly, i.e., any ohmic formation needs to be done prior to a Schottky metallization and the thermal range of device operation must be chosen reasonably. Since a number of metals have already been used to process the ohmic as well as the Schottky contacts, the interested reader is referred to the comprehensive review article of Pearton et al. [21].

However, during the last two decades, many research groups have developed different strategies to deal with those difficulties. Although a number of review articles on III-Nitride UV photodetectors have already been published (e.g., [22–28]), a summarized view on the development of some device types will be presented and various approaches to achieve high-performance devices will be addressed in this chapter.

9.2 Basics of Photodetectors

In this section, the relevant basics about photodetectors will be introduced. After a part covering physical essentials of photodetection, the structural and operational principles of certain photodetector types are presented. We emphasize here that this collection is based on several contributions from the literature to which the reader is referred for deeper insights into the matter, e.g., [29–35]. A complete coverage is not possible here due to the limited space. Nevertheless, a sufficient backbone should be available after the study of this section, in order to handle the more material and research-related parts that follow in Sect. 9.3.

9.2.1 Characteristic Parameters and Phenomena

The main physical parameters that determine the properties of a photodetector (PD), such as optical properties, quantum efficiency and responsivity, rise and fall times, linearity as well as noise properties, will be introduced.

9.2.1.1 Optical Properties of Semiconductors

The dielectric function of a solid determines its optical constants, i.e., its refractive index n_{ref} and extinction coefficient κ. On the one hand, these quantities define the reflected portion R_{ji} (see Fig. 9.1a) of an optical signal of power $P_j(\lambda)$ incident on a material i with n_i and κ_i within a medium j with n_j and $\kappa_j = 0$ [36]

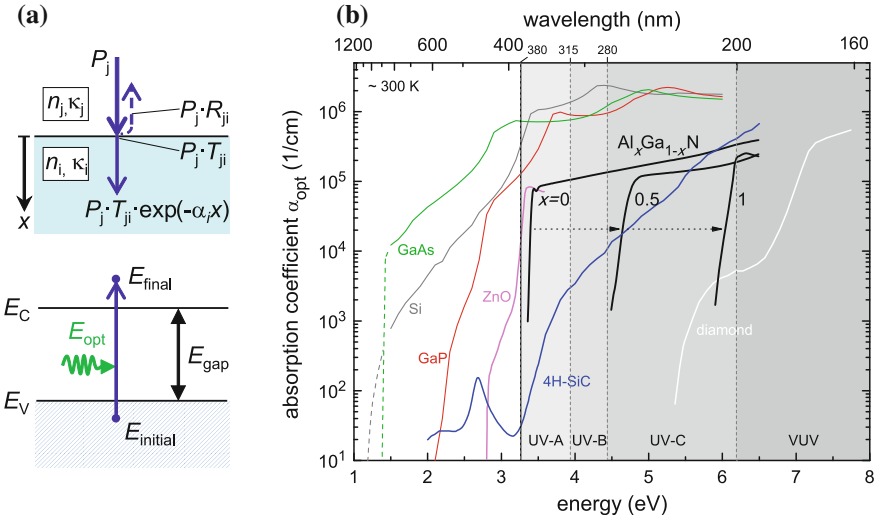


Fig. 9.1 **a** (*Top*) Beam propagates through medium *j*, impinges on surface of material *i* and is attenuated within material *i* due to absorption, (*bottom*) schematic of fundamental band-to-band absorption process. **b** Optical absorption coefficient α_{opt} for various semiconductors (Si: dashed [35] full [37], GaAs: dashed [38] full [37], GaP [37], 4H–SiC [39], ZnO [40], AlGaN [41], diamond [42, 43])—for further explanation see text and footnote 5

$$R_{ji} = \frac{(n_i - n_j)^2 + \kappa_i^2}{(n_i + n_j)^2 + \kappa_i^2}, \tag{9.1}$$

where all quantities depend on the optical wavelength λ of the incident photons.[4] Thus, only the portion $T_{ji} = 1 - R_{ji}$ of P_j is transmitted into the medium *i*. On the other hand, the optical absorption coefficient $\alpha_{opt,i}(\lambda) = 4\pi\kappa_i(\lambda)/\lambda$ determines the number of photogenerated free charges—i.e., electron–hole pairs—and gives a measure of attenuation of the optical power *P* along the distance *x* according to Lambert-Beers law $P(x) \propto \exp(-\alpha x)$. Considering the fundamental band-to-band absorption process, shown in the bottom image of Fig. 9.1a, i.e., intrinsic excitation of electrons from the filled valence band states with energies $E_{initial} \leq E_V$ to the empty conduction band states with $E_{final} \geq E_C$, a threshold wavelength $\lambda_{thr} \leq hc/E_{gap}$ for photoabsorption can be derived, where *h* is Plancks constant, *c* is the vacuum velocity for electromagnetic radiation and $E_{gap} = E_C - E_V$ is the direct or indirect bandgap energy of the material. By further neglecting absorption processes from or to energy levels within the bandgap, λ_{thr} therefore defines the wavelength range of the material suitable for photodetection. Figure 9.1b summarizes spectra of α_{opt} at about room temperature for various indirect (Si, GaP, SiC,

[4]This (λ)-dependence will sometimes be omitted for the sake of clarity.

and diamond) as well as direct (GaAs, ZnO, and AlGaN) semiconductor materials suitable to fabricate photodetectors with λ_{thr} ranging from the near infra-red (NIR) to the UV-C region.[5] Si, GaAs, and GaP show relatively high values of $\alpha_{opt} \geq 10^3$ cm^{-1} for wavelengths above 380 nm, unlike the wide bandgap materials ZnO, SiC, $Al_xGa_{1-x}N$, and diamond, which thus are attractive alternatives for visible-blind or solar-blind photodetection.

9.2.1.2 Quantum Efficiency and Responsivity

The quantum efficiency (QE) of a photodetector, also called the external quantum efficiency (EQE), is an experimentally accessible quantity. It is given by the ratio of electric charge measured in an external circuit and the number of incident photons upon illumination on the active area. Thus, it can directly be determined via measurement of the device photocurrent $I_{photo}(\lambda)$ when the optical power $P_{opt}(\lambda)$ of the incident photons with energy $E_{opt}(\lambda)$ is known [31]

$$\eta_{ext}(\lambda) = \frac{\#\,\text{charge measured}}{\#\,\text{photons incident}} = \frac{I_{photo}(\lambda)/q}{P_{opt}(\lambda)/E_{opt}(\lambda)}, \tag{9.2}$$

where q is the elementary charge. In order to relate η_{ext} to the underlying physical processes in a device, the theoretical approach put forward by Geist in [33] is helpful, where the EQE for normal incidence is given by

$$\eta_{ext}(\lambda) = T_{opt}(\lambda) \cdot Y(\lambda) \cdot CE(\lambda) = T_{opt} \cdot \eta_{int} \tag{9.3}$$

with T_{opt} the fraction of power transmitted into the photodetector, Y the quantum yield, CE the collection efficiency, and η_{int} the internal quantum efficiency (IQE), accounting for the recombination losses only by giving the ratio of electron–hole pairs created and photons absorbed within the device. As long as free-carrier absorption or impact ionization is negligible, the quantum yield is $Y \approx 1$. The collection efficiency CE accounts for structural and electrical properties (carrier sweep-out) as well as for optical properties (optical absorption) of a certain photodetector device and it can be calculated by integration of

$$CE = \int \alpha_{opt} \cdot \exp\left[-\alpha_{opt} \cdot x\right] \cdot P(x)\mathrm{d}x \tag{9.4}$$

over the whole device along x (c.f. Fig. 9.2a). $P(x)$ describes the carrier collection probability and can be approximated by drift-diffusion modeling [33]. As a rule of thumb, $P(x)$ is high ($\rightarrow 1$) where photogenerated carriers are either drifting or are

[5]Data of α_{opt} was either directly extracted from the literature (*tabular*: Si, GaAs, GaP [37] or *plot-digitized*: Si [35], SiC [39], diamond [42], GaAs [38], ZnO [40]) or calculated from the dielectric function (all digitized: diamond [43], AlGaN [41]).

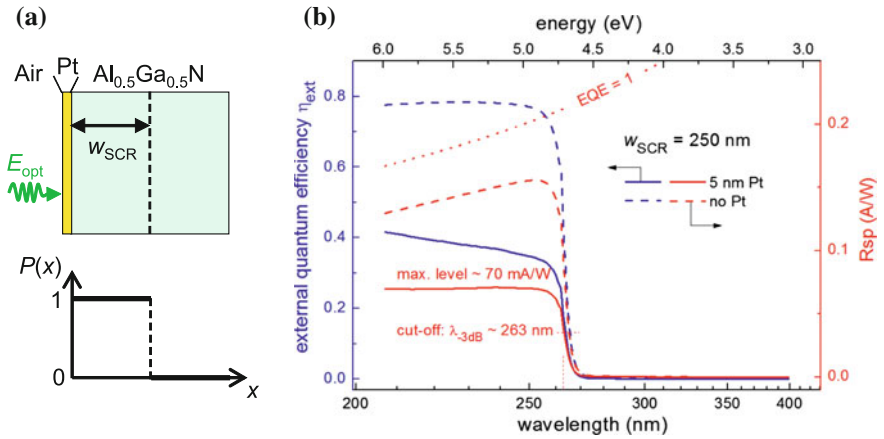


Fig. 9.2 **a** Cross-sectional schematic (*top*) of a Pt/n-$Al_{0.5}Ga_{0.5}N$ Schottky barrier PD as well as a possible collection efficiency probability $P(x)$ (*bottom*) within the device. **b** The calculated EQE (*blue*) and responsivity (*red*) for finite (*full*) and zero (*dashed*) Pt-layer thickness

subject to diffusion into field regions, and it is low ($\rightarrow 0$) where recombination losses become dominant.

Referring to the cross-section of a simplified Pt/n-$Al_{0.5}Ga_{0.5}N$ Schottky barrier photodetector[6] irradiated from the Pt-side, as shown in Fig. 9.2a, the EQE can be estimated utilizing (9.3) and (9.4) as follows:

1. When the optical constants n_{ref} and κ of all materials involved are known,[7] the optical transmission in (9.3) can be estimated by

$$T_{\text{opt}} = (1 - R_{\text{air-Pt}}) \cdot \exp(-\alpha_{\text{Pt}} \cdot t_{\text{Pt}}) \cdot (1 - R_{\text{Pt-AlGaN}}), \tag{9.5}$$

   where the R_{ji} are calculated from (9.1) and the exponential factor accounts for attenuation within the Pt-layer of $t_{\text{Pt}} = 5$ nm thickness. Multiple reflections in any layer are neglected.
2. Assuming, that the photogenerated carriers within the space charge region (SCR) of width $w_{\text{SCR}} = 250$ nm in the n-type $Al_{0.5}Ga_{0.5}N$-layer will all be collected, the carrier collection probability writes

$$P(x) = \begin{cases} 1 & \text{within } w_{\text{SCR}} \\ 0 & \text{elsewhere.} \end{cases} \tag{9.6}$$

   This is illustrated in the bottom image of Fig. 9.2a.

[6] A more detailed description of that type of PD will be given below.

[7] Data for n and κ in this example are taken from [44] for Pt and have been derived from the dielectric function given in [41] for $Al_{0.5}Ga_{0.5}N$.

3. The resulting spectral shape of the EQE for the example PD can be calculated as

$$\eta_{\text{ext}} = T_{\text{opt}} \cdot \left(1 - \exp(-\alpha_{\text{opt}} \cdot w_{\text{SCR}})\right), \tag{9.7}$$

which is plotted in Fig. 9.2b (blue lines, left axis).

The onset of absorption results in an increase in EQE for wavelengths below about 270 nm. The influence of the optical properties of the Pt-layer, especially its reflectance, on the EQE is evident when comparing the strongly reduced EQE (full line) with that for the hypothetical case without the Pt-layer (dashed line), where $R_{\text{air-Pt}}, t_{\text{Pt}} \rightarrow 0$ and $R_{\text{Pt-AlGaN}} \rightarrow R_{\text{air-AlGaN}}$. Further, recombination losses at the surface, in the bulk, and at the contacts may reduce *CE* and thus lower the EQE significantly. Anyway, the main restriction to the validity of (9.2) is a linear relationship between the photocurrent I_{photo} and the optical power P_{opt}

$$I_{\text{photo}} = Rsp \cdot P_{\text{opt}} \quad \Leftrightarrow \quad Rsp(\lambda) = \frac{I_{\text{photo}}(\lambda)}{P_{\text{opt}}(\lambda)} \tag{9.8}$$

with $Rsp(\lambda)$ the responsivity, which is the most fundamental figure-of-merit in practice to describe a detectors capability to convert an optical signal measured in Watt into an electric current signal measured in Ampère. When combining (9.2) and (9.8), the responsivity is related to the EQE via

$$Rsp(\lambda) = \eta_{\text{ext}}(\lambda) \cdot \frac{q}{E_{\text{phot}}(\lambda)}. \tag{9.9}$$

The resulting responsivity of the example PD is also plotted in Fig. 9.2b (red lines, right axis) and the explanations made above for the EQE translate into this responsivity spectrum, accordingly. But concerning the optical properties of the Pt-layer, besides a reduction of the absolute *Rsp*, it can be seen that the presence of the semitransparent Pt-layer alters the spectral shape from rather flat to increasing with wavelength, until the *Rsp* suddenly drops for $\lambda > 255$ nm (the $Rsp(EQE = 1)$ line has been introduced for comparison).

A cut-off wavelength λ_{co} is often defined to serve as a spectral measure indicating the operation wavelength range of a photodetector. This spectral cut-off is defined as the wavelength where the responsivity drops to a certain value, e.g., 50 or 10 %, of its maximum value toward long wavelengths. Just as the threshold wavelength λ_{thr}, it directly corresponds to the onset of absorption and is thus related to the bandgap energy. The 50 % cut-off wavelength in Fig. 9.2 is 263 nm, indicating a solar-blind operation range for this Pt/$Al_{0.5}Ga_{0.5}N$ Schottky barrier PD.

9.2.1.3 Rise and Fall Times

The response time for a certain change in measured electrical signal—current or voltage—upon a change in the incident optical signal intensity is of importance for photodetection applications. Practically, the rise time τ_{rise} from the dark signal to 90 % of maximum signal upon illumination and the fall time τ_{fall} to 10 %, as shown in Fig. 9.3a, are the common parameters used for device specification. These time constants are influenced by several factors which are related to the material properties, the photodetector structure, and the output circuitry. To illustrate these relations, we refer to the p-i-n diode structure shown in Fig. 9.3a.[8] The equivalent circuit parameters of a photodiode are illustrated in Fig. 9.3b. According to (9.2), the static response of a photodiode can be viewed as a photocurrent I_p generated upon illumination due to the optical signal of power P_{opt}. This current source is in parallel with the rectifying diode junction and the reverse bias-dependent diode capacitance C_D of the junction. A series resistance R_S, in the order of a few Ohms, accounts for the resistance due to ohmic contacts and the bulk material. Parasitic inductances in series to R_S, e.g., due to wire lines, and parasitic capacitors in parallel to C_D, e.g., due to bond pads, as well as the parallel shunt resistance of the junction, which is usually $>10^7$, are neglected. From that, a low-pass filter behavior of the photodiode response—current or voltage—upon a modulated incident signal can be expected. Hence, the dependence of the responsivity *Rsp* on the signal modulation frequency f is approximated by [31]

$$Rsp(f) = \frac{Rsp_0}{\sqrt{1 + (f/f_{co})^2}}, \quad \text{where} \quad f_{co} = \frac{1}{2\pi\tau_r} \tag{9.10}$$

with Rsp_0 the static responsivity and f_{co} the cut-off frequency, also referred to as the bandwidth of the photodiode. This behavior is shown in Fig. 9.3c for the case of $f_{co} = 3$ MHz. The cut-off frequency measures the capability of the photodetector to follow a frequency-modulated input signal,[9] and it is determined by the response time τ_r, which depends on different contributions:

- The drift of photo-excited carriers in high-field regions, i.e., the i-layer, of the device. The respective response time τ_{tr} is set by the field-dependent carrier transit time t_{tr} and can be approximated by [31]

$$\tau_{tr} \approx 0.36 \cdot t_{tr}, \quad \text{where} \quad t_{tr} = w_{SCR}/(\mu \cdot F) \tag{9.11}$$

[8] A more detailed description of that type of PD will be given below.

[9] After (9.10) the responsivity drops by a factor of $1/\sqrt{2}$ at the bandwidth f_{co}, which corresponds to a decrease in power level of −3 dB ($\sim -1/2$). Therefore, f_{co} is also called the 3 dB-bandwidth f_{3dB}.

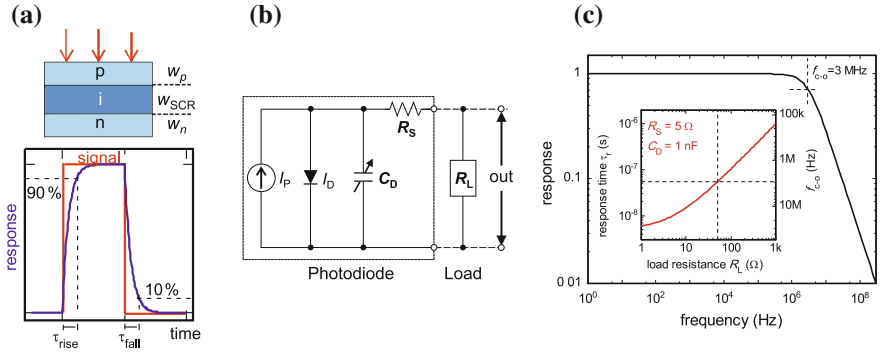


Fig. 9.3 **a** The schematic layer structure (*top*) of a p-i-n diode, rise time τ_{rise} and fall time τ_{fall} (*bottom*) of the system response upon signal change. **b** Equivalent circuit of a photodiode with readout (simplified, see text). **c** Low-pass output characteristics of a photodiode response upon a frequency-modulated input light signal—inset shows dependency of the response time (*left axis*) and thus the cut-off frequency (*right axis*) on the load resistance

with w_{SCR} the width of the space charge region, μ the mobility of the traveling carriers and F the electric field strength. Thus this contribution can be adjusted by the depletion layer width and the applied bias.

- Diffusion of photo-excited minority carriers in field-free regions, i.e., the p- and n-regions: The diffusion time before recombination τ_{diff} is given by the minority carrier lifetime τ_{rec} via [31]

$$\tau_{diff} \approx \frac{w^2}{2D}, \quad \text{where} \quad D = L^2/\tau_{rec} \tag{9.12}$$

with w the length of the field-free region, D the diffusion constant, and L the corresponding diffusion length.[10] This contribution to the response time is reduced when w is as small as possible and D is sufficiently large.

- The combination of the load resistance R_L to read out the detector signal, the diode series resistance R_S, and the junction capacitance C_D leads to a *RC*-time constant τ_{RC} given by

$$\tau_{RC} = (R_S + R_L) \cdot C_D \tag{9.13}$$

that limits the bandwidth. A reduction of R_S and of C_D lowers this contribution. Since $C_D \sim A/w_{SCR}$ with A the junction area, the diode capacitance is lowered for a small junction area and a wide space charge region.

[10] D and L refer to *minority* carrier values, e.g., electrons with D_n and L_n in a p-type region of width w_p.

The total response time τ_r, i.e., rise or fall time, is then estimated as

$$\tau_r = \sqrt{\tau_{tr}^2 + \tau_{diff}^2 + \tau_{RC}^2}, \tag{9.14}$$

where the contributions of τ_{tr} and τ_{diff}, and τ_{RC} can be altered by device geometry and material properties to match the application requirements. In the inset of Fig. 9.3c, the dependence of the response time τ_r on the load resistance R_L is shown for 5 Ω series resistance, 1 nF junction capacitance, and vanishing contributions of τ_{tr} and τ_{diff}. The cut-off $f_{co} = 3$ MHz can be achieved with a load resistance of 50 Ω and a further reduction in τ_r is possible for even smaller R_L.

A closer look on the recombination lifetime τ_{rec} of excess carriers, which contributes to the response time τ_r, is possible by a simple theoretical analysis of temporal changes in the photo-induced free-carrier enhancement $\Delta n(t)$ [29]. Considering mono-molecular recombination processes only, exponential terms of the form $\Delta n(t) \sim \left[1 - \exp(-t/\tau_{growth})\right]$ for signal growth and $\Delta n(t) \sim \exp(-t/\tau_{decay})$ for signal decay result, which are easy to interpret by means of the respective time constants[11] [29, 32]. When regarding trapping processes in such an analysis, more complex terms for $\Delta n(t)$ then can be approximated which may be used to fit experimental data—see e.g., the summarizing table given in Sect. 9.2 in Bube [29]. Generally, deep centers with certain capture cross sections for mobile carriers have been found to cause long lifetimes in transient processes—see also the following paragraph. Additionally, carrier trapping processes are dependent on external or internal electrical fields and on temperature. Therefore, unpredictable instabilities may occur during operation, deteriorating the performance of a photodetector in applications utilizing modulated radiation sources.

9.2.1.4 Persistent Photoconductivity (PPC)

Rise and fall times of an optically excited system in excess of several 1000 s have been reported for many different poly- and single-crystalline semiconductor materials as well as alloys since Kohlrausch examined the residual discharge of a Leyden jar in 1854 [45]. This phenomenon is commonly termed persistent photoconductivity (PPC) and manifests itself in the transient build-up and decay of a photo-induced current, which is often found to be well described by a stretched exponential of the form $I(t) \sim \exp\left[(-t/\tau)^{\beta}\right]$, where τ is a constant with the dimensions of time and $0 < \beta \leq 1$ is the Kohlrausch stretching parameter, which accounts for the microscopic nature of the electronic and atomic relaxation processes underlying the non-exponential change in measured conductivity [46, 47]. However, a large amount of literature dealing with PPC in III-Nitrides has been

[11]The time constants τ_{growth} and τ_{decay} describe the corresponding change in signal as either an increase to $(1 - 1/e) \approx 64\,\%$ or a decrease to $1/e \approx 37\,\%$ of the maximum signal.

published so far, and many different models have been proposed to explain the origin of PPC. An example transient build-up and decay curve of photocurrent in a GaN MSM photodetector sample is shown in Fig. 9.4. It can be seen that the photocurrent steadily increases during illumination at a constant optical power. After removing the light source, several processes are visible during the decay transient. The multi-exponential function (parameters given in the inset table) reproduces this switch-off behavior very well. However, there have been theoretical and experimental investigations considering macroscopic potential barriers at surfaces, interfaces, grain boundaries, and doping or material inhomogeneities that hinder the recombination process, in order to explain the long-decay constants $\tau \sim 10^3$ s in conjunction with the huge photoconductive gains $\sim 10^3$ observed in GaN photoconductors [49]. But most of the research reported refers to processes on the microscopic level, i.e., the trapping of free carriers at localized defects. Park et al. proposed that PPC in p-type GaN:Mg arises from the bi-stability of a nitrogen vacancy V_N accompanied by a change in the charge state [50]. Ursaki et al. reported for n-type GaN:Si that their measurements of photoconductivity reveal a mechanism associated with a broad distribution of electron traps located 2.2 eV below the conduction band [51]. They also concluded that rather the gallium vacancy V_{Ga} or the nitrogen antisite N_{Ga} may be the possible cause of PPC. Katz et al. proposed a model for PPC in n-GaN-based Schottky barrier PDs that considers the electron re-occupation of the filled hole traps at the semiconductor–metal interface after switching off the illumination, which then leads to a gradual recovery of the Schottky barrier [52].

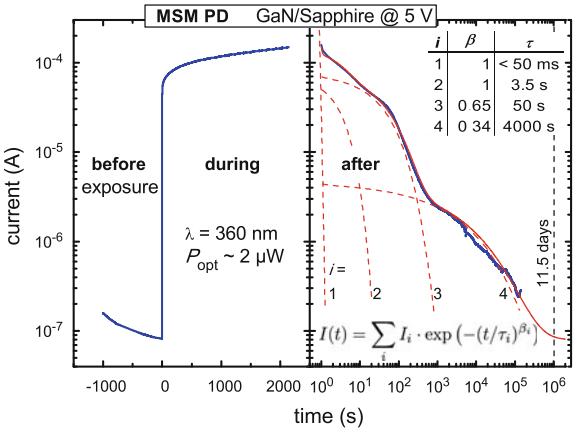


Fig. 9.4 Transient build-up (*left*) and decay curve (*right*) of photocurrent in a GaN MSM PD at 5 V bias upon 360 nm illumination. The decay transient can be modeled with a sum of stretched exponential functions; table lists the relevant parameters used for each contribution (unpublished data [48])

However, although the controversy about the origin of the PPC has not come to an end yet, many AlGaN-based photodetecting devices have been reported that do not show this unwanted effect. A deeper discussion of PPC is beyond the scope of this chapter and the reader is referred to the cited work and references therein.

9.2.1.5 Linearity

The linearity between I_{photo} and P_{opt} of a photoconducting device plays an important role, not only to define a power-independent responsivity *Rsp* as described in (9.8), but also to achieve reliable device operation. As mentioned for the rise and fall times, also the linearity is affected by the carrier recombination kinetics in the absorber material and the equivalent electrical circuit of the photodetector as well as the readout circuit.

Considering trap-free semiconductor material with a dark carrier density n_0 and an enhancement in carrier density Δn upon illumination at an optical generation rate G_{opt} ($\sim P_{\text{opt}}$), the mono-molecular recombination via a single center may be investigated simply by arguing with rate equations for steady-state conditions [29]. For the insulator case ($n_0 \ll \Delta n$), it is found that a square root dependence $\Delta n \sim \sqrt{G_{\text{opt}}}$ holds, whereas for the semiconductor case ($n_0 \gg \Delta n$), a linear dependence $\Delta n \sim G_{\text{opt}}$ is valid. Including trapping centers, the situation becomes more complicated, but it can be summarized to depend on the energetic distribution of trap states. First of all, a uniform distribution of the density of traps, e.g., below the conduction band, can change the root dependence for the insulator into a linear relation. But also an exponential distribution of traps in the insulator case can change the power of G_{opt} from 1/2 to 1, when the incident power allows the light-induced free–carrier density Δn to stay below the density of trapped carriers ΔN_{t}. When for high intensity Δn becomes higher than ΔN_{t}, bimolecular recombination may dominate and thus $\Delta n \sim \sqrt{G_{\text{opt}}}$ will be possible—even with trapping. Any trap-related non-linearities may change certain device properties in an uncontrollable way and thus are to be avoided.

Even if the material itself responds linearly to an incident photon flux, the connection to an external circuit causes limitations in the low and high power regimes. At the low end, the noise-equivalent-power, introduced further below, limits the photocurrent signal of any type of device. The saturation of photocurrent, e.g., in a p-i-n PD, at high power levels sets in above a value of about [53]

$$P_{\text{opt,sat}} = \frac{q\phi_{\text{bi}} - U_{\text{bias}}}{(R_{\text{S}} + R_{\text{L}}) \cdot Rsp(\lambda)}, \tag{9.15}$$

where $q\phi_{\text{bi}}$ is the built-in voltage drop across the p-i-n junction at zero bias and U_{bias} is the applied bias. Hence, this upper limit can be enhanced by applying a higher reverse bias ($U_{\text{bias}} < 0$) or utilizing a smaller load resistance. Note also the dependence on the responsivity.

9.2.1.6 Detection Capability

The minimum detectable optical power of a photodetector is limited by different sources of noise. Noise arises either from certain detector properties and the readout setup, e.g., the noise in an amplifying transistor, or from the statistical fluctuations of the radiation signal and any significant background radiation during the detection process. For detailed description of noise sources, the reader is referred to the literature [31, 32, 54]. A very useful measure to compare the radiation-induced signal to the total noise of a detection system is the signal-to-noise ratio *S/N*. When the noise level in a detection system has been experimentally determined, the minimum detectable power, the noise-equivalent-power (NEP), can be estimated from $S/N = 1$. To compare the performance of different detection systems, the specific detectivity $D^* = \sqrt{AB}/\mathrm{NEP}$, with the detector area A and the bandwidth B, is commonly used. It is clear that the expressions for noise sources and consequently for D^* depend not only on the detector type and its design but also on the readout circuit components used. Thus, when designing the detector and readout for applications relying on high speed and precision, any noise from the electronic circuitry must be reduced below the detector noise level.

9.2.2 Various Types of Semiconductor Photodetectors

In this chapter, the principles of design and operation of the most common types of semiconductor photodetectors will be summarized. This includes the photoconductor, Schottky barrier photodiode (Schottky PD), metal–semiconductor–metal photodetector (MSM PD), p-i-n PD, and the avalanche photodiode (APD). Due to increasing interest in the development of wide bandgap semiconductor cathodes for efficient electron emitters also the phototube (PT) as well as the photomultiplier tube (PMT) and related issues will also be introduced.

9.2.2.1 Photoconductor

A photoconductive detector, also termed photoconductor, usually consists of a pair of ohmic electrodes processed on the semiconductor surface (see Fig. 9.5a). A large detection area can be realized utilizing an inter-digital arrangement of multiple pairs of electrodes. But this planar design also leads to a loss of optical signal due to the shadowing effect of electrodes. The current in the device is driven by the electric field between a pair of electrodes, which is adjusted by an externally applied bias U_{bias}. In the dark, i.e., when no radiation is absorbed, the dark current I_{dark} is given by $I_{\mathrm{dark}} = U_{\mathrm{bias}}/R_{\mathrm{dark}}$ with R_{dark} the resistance given by the dark resistivity of the material (dashed line in Fig. 9.5b). When the biased photoconductor is illuminated with photons having sufficient photon energy to create free carriers, i.e., $E_{\mathrm{opt}} \geq E_{\mathrm{gap}}$, the resistivity

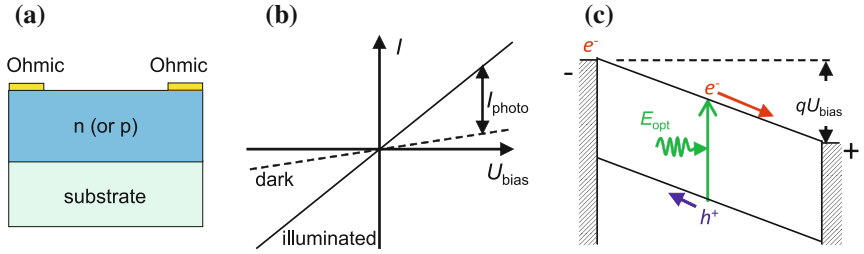


Fig. 9.5 **a** Cross-sectional schematic of a photoconductor. **b** Schematic I–V characteristics of a photoconductor in the dark (*dashed*) and under illumination (*solid*) (after [34]). **c** Schematic band diagram of the photoconductor biased under illumination

decreases to a value $R_{illum} < R_{dark}$. The photocurrent is then $I_{photo} = U_{bias} \cdot (R_{illum}^{-1} - R_{dark}^{-1})$ (full line in Fig. 9.5b). When a photoconductor, working in series on a load resistance R_{load}, is homogeneously illuminated with photons of optical power P_{opt} between its electrodes, at $R_{load} = 0$ the short-circuit photocurrent I_{photo}^{sc} is given by [31]:

$$I_{photo}^{sc} = \frac{qP_{opt}}{E_{opt}} \cdot \eta_{ext} \cdot g \tag{9.16}$$

with the elementary charge q, the external quantum efficiency η_{ext}, and the gain factor g. Since electron and hole mobilities usually are different, e.g., $\mu_e > \mu_h$ in n-type material, the gain factor can be written as:

$$g = \frac{\tau_{rec,h}}{t_{tr,e}}, \tag{9.17}$$

where $\tau_{rec,h}$ is the hole recombination lifetime and $t_{tr,e}$ the electron transit time. Thus, in photoconductors a photoconductive gain mechanism occurs for certain values of $\tau_{rec,h}$ and $t_{tr,e} = d^2/\mu_e U_{bias}$, since the latter depends on the electrode spacing d, the electron mobility μ_e, and on the bias voltage U_{bias}. In a simplified picture, as illustrated in Fig. 9.5c, the photo-excited electron will reach the anode earlier than the hole—indicated by the different arrow lengths—and due to the requirement of charge neutrality an additional electron has to be injected at the cathode. This feedback lasts until a trapped hole captures a free electron. Thus, the number of electron loops increases g. It should be emphasized, that this gain does not refer to multiple carriers being generated by the absorption process of a single photon, but rather to the number of loops the faster sort of carriers can traverse the semiconductor before recombining with the slower (or trapped) carriers.

When scaling a photoconductor for an application, the limitations to the photocurrent due to electric field effects, such as space charge limited current, avalanche and dielectric breakdown come into play. Furthermore, a trade-off between a high gain factor and a fast response has to be found, since the device becomes slow when τ_{rec} is long. The main drawback of a photoconductor is the neccessity of a

non-zero bias operation because the dark current levels give rise to additional noise and thus decrease the detectivity of the device. However, when a metal is available to form electrodes with ohmic behavior on the semiconductor, the fabrication of photoconductor devices is rather simple, compared to devices with several epitaxial layers, e.g., the p-i-n PD or an APD.

9.2.2.2 Schottky Barrier Photodiode

The Schottky barrier photodiode is based on the Schottky-type metal-semiconductor junction with rectifying current–voltage characteristics. As shown in Fig. 9.6a, a metal is deposited onto the optically active semiconductor layer that can be n- or p-type or even undoped. Prior to the moderately doped n-type (or p-type) absorber layer, a highly doped n^+-layer (or p^+-layer) is grown to reduce the contact resistance at the ohmic contact. In the following, a brief description of the n-type Schottky barrier diode and its characteristics will be given. For a deeper study on metal–semiconductor contacts, we refer the reader to the detailed monograph of Rhoderick and Williams [55] as well as to a recently published review on the physics and chemistry of the Schottky barrier by Tung [56]. The left image in Fig. 9.6b illustrates that for a Schottky barrier contact to be formed, the relation between metal work function ϕ_m, which is measured from the Fermi level $E_{F,m}$ to the vacuum level E_{vac}, and the semiconductor electron affinity χ_s, which measured from the conduction band minimum E_C to the vacuum level, is essential. Within the concept of the Schottky-Mott theory, an ideal Schottky barrier of height $\phi_b = \phi_m - \chi_s$ will be present for electrons facing the junction from the metal side if $\chi_s < \phi_m$. Below the metal electrode, a space charge region (SCR) is formed, being depleted of free electrons. This leads to an increasing electric field toward the

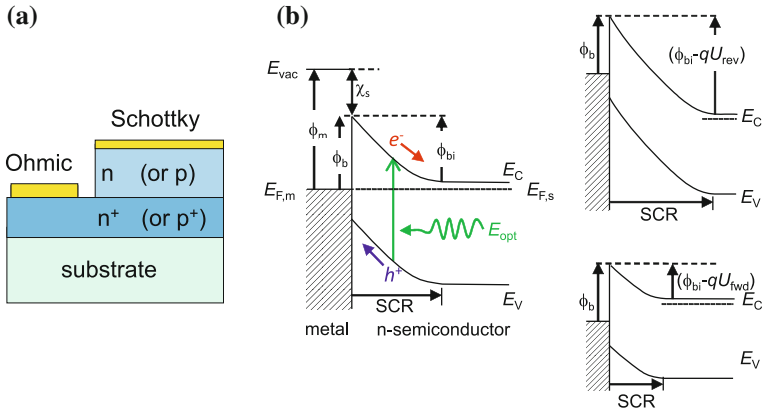


Fig. 9.6 **a** Cross-sectional schematic of a Schottky PD. **b** Band diagram of the metal/n-semiconductor junction under illumination at zero bias (*left*), and in the dark reversely biased $U_{rev} < 0$ V (*right top*) as well as at forward bias $U_{fwd} > 0$ V (*right bottom*)

metal–semiconductor junction due to an approximately constant density of positively charged ionized donors. This electric field causes an upward bending of the energy bands toward the surface, such that free electrons in the semiconductor have to overcome the built-in potential ϕ_{bi} to reach the metal contact. Biasing the Schottky contact negatively, as depicted in the top right image of Fig. 9.6b, enhances the potential barrier according to $\phi_{\mathrm{bi}} - qU_{\mathrm{rev}}$, with q the elementary charge and $U_{\mathrm{rev}} < 0$ V the reverse bias. The resulting net thermionic electron emission from the metal can be expressed as the saturation current density [55]

$$J_0 = A^{**}T^2 \exp\{-(\phi_{\mathrm{b}} - \Delta\phi_{\mathrm{b}})/kT\} \tag{9.18}$$

with Boltzmann's constant k, Richardson's constant A^{**}, the absolute temperature T, and the bias-dependent lowering $\Delta\phi_{\mathrm{b}}(U)$ of the Schottky barrier height due to image forces and dipole interactions at the metal/semiconductor interface. At very high-reverse bias conditions, band-to-band Zener tunneling or avalanche effects enhance the free-carrier density very rapidly resulting in the dielectric breakdown. Contrary, the bottom right image of Fig. 9.6b illustrates a barrier reduction due to forward bias conditions ($U_{\mathrm{fwd}} > 0$ V). This leads to an enhanced injection of electrons into the metal,[12] causing the current to increase exponentially. Thus, the current density of an ideal Schottky diode in the dark obeys a diode characteristics of the form [55]

$$J_{\mathrm{dark}} = J_0\{\exp(qU/kT) - 1\} \tag{9.19}$$

with J_0 given by (9.18). This relationship is further altered due to trap-assisted or phonon-assisted tunneling processes through the Schottky barrier, i.e., thermionic field emission or even field emission, all increasing with electric field strength close to the junction and thus with reverse bias U_{rev}. Further, shallow as well as deep energy levels, which can be induced by defects and impurities, may affect the charge distribution across the SCR and thus lead to a modification of the dark current characteristics discussed so far (see e.g., [57]).

For a Schottky diode operating as a radiation detector, the bias-dependent modulation of the depletion region characteristics, i.e., width and electric field distribution, is essential since photogenerated carriers in the SCR are separated and swept out by the electric field to contribute a drift current. Excess minority carriers in the field-free contact layer contribute a diffusion current, if generated within a diffusion length from the SCR. Thus, on the one hand, the resulting photocurrent signal I_{photo} depends on carrier transport mechanisms, such as the transit time of excess carriers and the minority carrier diffusion length. On the other hand, the incident photon flux, absorption coefficient, and minority carrier lifetime determine photogeneration and recombination processes. The I–V characteristics of a Schottky PD is very similar to that of other photodiode structures and for brevity, we refer to that depicted for the p-i-n PD shown in Fig. 9.8b. Accordingly, an

[12] Electrons are delivered by the ohmic contact.

unbiased Schottky PD already induces a short-circuit current upon illumination. This makes the Schottky PD an attractive alternative to the photoconductor that requires an external voltage.

Considering the design of a Schottky PD for front illumination, semitransparent metal layers have to be deposited for optimal photogeneration within the SCR near the Schottky junction, where the field is the highest. Furthermore, to minimize optical reflection losses, the top metal layer has to be very thin (<10 nm) and additionally an antireflection coating, optimized to a certain wavelength range, can be used.

9.2.2.3 Metal–Semiconductor–Metal Photodetector

A metal–semiconductor–metal (MSM) photodetector consists of two Schottky barrier junctions connected "back-to-back," as depicted in Fig. 9.7a. It means, separated metal electrodes are placed in the planar inter-digital arrangement side-by-side, on the surface of an optically active semiconductor absorber layer. As the device operation relies on the variation of the SCR regions near the metal electrodes, as in a Schottky PD, we distinguish the MSM PD from the photoconductor, which has two ohmic contacts and—ideally—no depletion region to separate photogenerated charges.

Due to the Schottky barrier contacts, the dark current flow is governed by either thermionic emission, thermionic field-emission or field-emission from the metal into the semiconductor and the barrier-lowering effects, as mentioned above for the Schottky PD [55]. But for the MSM device saturation currents for both, electrons at the cathode and holes at the anode, have to be considered [58]. Bias of any polarity reverses one electrode and forwards the other (see Fig. 9.7b) resulting in symmetric *I–V* characteristics in the dark as well as under illumination conditions (see Fig. 9.7c). By utilizing analytic expressions for the photocurrent in a simplified 1D-Structure, Sarto et al. found that recombination of photo-excited carriers almost

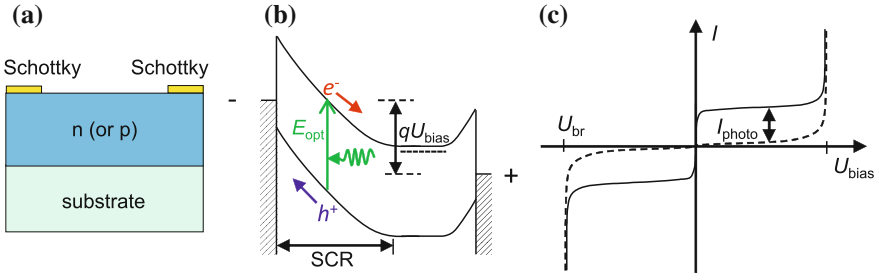


Fig. 9.7 **a** Cross-sectional schematic of an MSM photodetector. **b** Schematic band diagram of the MSM biased under illumination. **c** Schematic *I–V* characterisitcs of an MSM PD in the dark (*dashed*) and under illumination (*solid*)

has no effect on the dc characteristics and pulse response of a fully depleted absorber layer [59].

Due to the lack of a photovoltaic mode for an MSM, additional noise due to the bias applied has to be considered. However, the small contact area reduces the device capacitance leading to short *RC* time constants. Utilizing electrode spacings of several 10 nm enables for high-speed operation even in the THz range [60, 61].

9.2.2.4 p-i-n Photodiode

The p-i-n photodiode consists of an n-type layer, an undoped i-layer (i = intrinsic), and a p-type layer. As shown in Fig. 9.8a, additional p^+ and n^+ layers are used to form proper ohmic contacts with low contact resistances. In contrast to a pn-junction, the depletion region of a p-i-n diode is given by the i-layer and can be chosen to be much wider in order to allow for more efficient absorption as well as offering a lower junction capacitance, which is useful for high-frequency operation. Due to an almost constant electric field within the i-layer, the width of the SCR is nearly independent of the applied bias voltage resulting in a stable operation as well as increased breakdown voltage U_{br}.

Neglecting generation and recombination in the neutral i-region, the dark current of a p-i-n diode shows a diode behavior similar to (9.19), but with the saturation current density J_0 determined by minority carrier diffusion terms [34]

$$J_0 = qn_i^2\left(\frac{D_p}{L_pN_{\mathrm{D}}} + \frac{D_n}{L_nN_{\mathrm{A}}}\right). \tag{9.20}$$

Here D_j with $j = n$ for electrons and $j = p$ for holes are the diffusion constants as well as $L_j = \sqrt{D_j\tau_{\mathrm{rec},j}}$ the diffusion lengths of the respective minority carriers, with the carrier lifetime $\tau_{\mathrm{rec},j}$. Further, n_i is the intrinsic carrier concentration, and N_{D} and N_{A} are the donor and acceptor concentrations, respectively. The dashed line in Fig. 9.8b illustrates the dark current characteristics of a p-i-n diode. At high-forward

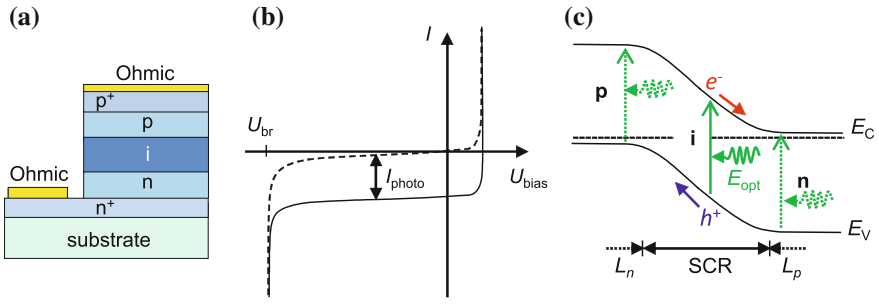


Fig. 9.8 **a** Cross-sectional schematic of a p-i-n PD. **b** Current–voltage characteristics of the p-i-n photodiode. **c** Band diagram of the p-i-n junction under illumination at zero bias

bias, the current will be limited due to the series resistance (not shown in the image) and at large reverse bias the breakdown due to avalanche effects and band-to-band Zener tunneling occurs. As illustrated in Fig. 9.8c, photogenerated excess charge carriers within the i-layer are swept out by the electric field even at zero bias and contribute a drift current, which is slightly enhanced by applying a reverse bias. Minority carriers being photogenerated within their respective diffusion length L_j from the depletion region are also swept across the field region and thus make up a current related to diffusion. The total photocurrent adds to the dark current as depicted by the solid line in Fig. 9.8b. However, depending on the illumination scenario (front or back), special care has to be taken in order to avoid absorption losses of the incident signal in these field-free layers before entering the absorber layer. Such absorption losses may be reduced and the diffusion tail in the temporal current signal can be suppressed, e.g., using very thin p- or n-type layers. Also appropriate heterojunctions can be used to reduce the diffusion tail: when choosing a wider bandgap for the doped entrance layer in comparison to the absorbing i-layer, the radiation within a certain spectral range can reach the i-layer. However, this approach is challenging in terms of fabrication, regarding the issues with doping and ohmic contact formation in the III-Nitrides, as will be discussed further below.

9.2.2.5 Avalanche Photodiode

An avalanche photodiode (APD) can be designed in several ways, since its operation principle is based on a carrier multiplication mechanism by impact ionization processes at high electric fields near breakdown. Regions of high electric field are generally the depletion regions that have different field distribution depending on the device structure and are present below and especially near the edges of a Schottky-type contact (MSM and Schottky PD) and at the p-n junction or within the i-layer of the p-i-n PD at a sufficient reverse bias. When a free-carrier gains sufficient kinetic energy ($> E_{\mathrm{gap}}$), i.e., negligible energy loss due to collisions with the lattice occuring during its travel, the excitation of additional e–h pairs can be initiated—(1), (2), (1′), and (2′) in Fig. 9.9a—and these impact ionization processes consequently lead to carrier multiplication. In general, the probabilities of impact ionization are different for electrons and holes and are described per unit length (cm^{-1}) via the respective ionization coefficients α_n and α_p, which have a dependence on the electric field strength F as [31]:

$$\alpha_i = \alpha_{i,0} \cdot \exp(-F_i/F)^{\gamma}, \tag{9.21}$$

where $i = n, p$ for electrons and holes, and γ, $\alpha_{i,0}$ as well as F_i are the fitting parameters to experimental results or calculations. The inset in Fig. 9.9b shows impact ionization coefficients as a function of the inverse electric field as calculated by Oguzman et al., for electrons (black squares) and holes (red squares) in wurtzite phase GaN [62] and fits to these data with (9.21) for $\gamma = 1$ (full lines). According to these results, the ionization coefficient for holes is larger than for electrons in GaN

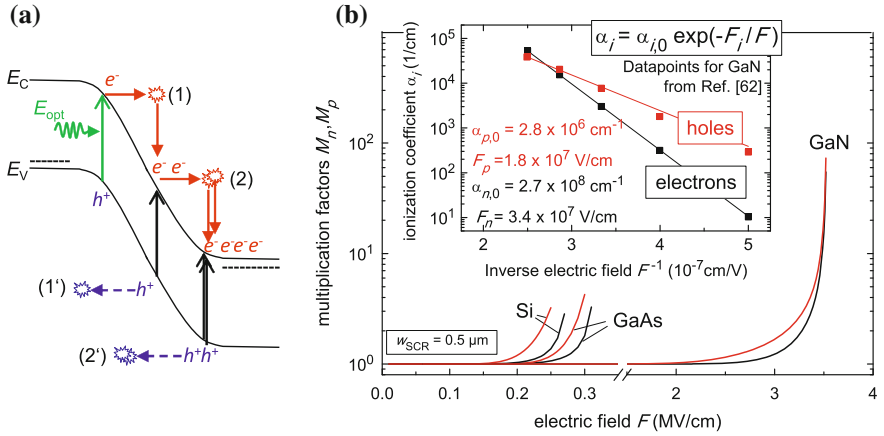


Fig. 9.9 **a** Schematic of carrier multiplication in a highly reverse-biased p-i-n structure: Impact ionization occurs upon electron injection at the p-side. **b** Multiplication factors calculated after (9.22) for pure electron (*black*) or hole (*red*) injection into the multiplication region of a reverse-biased p^+-π-n^+ photodiode based on either Si, GaAs or GaN; the inset shows data (from [62]) for electron and hole ionization coefficients in GaN with a fit of (9.21) (further explanation in text)

for electric fields below 3.7 MV cm^{-1}, indicating hole-initiated avalanche processes to occur at a higher rate. Thus, while the p-i-n *I*–*V* characteristics at low fields are as described above for the other PD types, at high fields the carrier multiplication due to impact ionization increases the current in the device by the multiplication factor M_i. These multiplication factors can be derived for any particular PD type. In a p^+-π-n^+ diode (π = very low p-type) with constant electric field in the π-region of width w the multiplication factors can be written as [31]:

$$M_i = \frac{(1-k_i)\cdot \exp[\alpha_i \cdot w \cdot (1-k_i)]}{1-k_i \cdot \exp[\alpha_i \cdot w \cdot (1-k_i)]} \quad (i = n, p), \tag{9.22}$$

where $k_n := \alpha_p/\alpha_n$ is the ionization ratio, and $k_p = 1/k_n$. Multiplication factors calculated with (9.22) for electron (black) and hole (red) multiplication in Si, GaAs, and GaN are shown in Fig. 9.9b for an i-layer thicknesses of $w_{SCR} = 0.5$, where α_i values for Si and GaAs have been calculated after [31] and those for GaN are shown in the inset of Fig. 9.9b. Thus, for GaN the multiplication of carriers is expected to set in at electric fields an order of magnitude higher, than for Si and GaAs. However, since α_i as well as the k_i are exponential functions of the inverse electric field, small changes in F cause a very steep increase in M_i near the breakdown field for $k_n > 1$. In this case, the stable operation of such a p^+-π-n^+ diode becomes critical, whenever electrons and holes are injected simultaneously in the same high-field region. Due to spatial inhomogeneities in either the doping profile or the width w_{SCR} of the space charge region the electric field strength varies locally, so that, if $\alpha_n < \alpha_p$ holds, a sudden multiplication of electrons can deteriorate the device performance or even cause local breakdown effects.

Thus, it is preferred to separate the absorption region, an i-layer for electron and hole photogeneration, from the multiplication region, another i-layer, where ideally one type of carriers is injected to initiate multiplication. The resulting separate absorption and multiplication (SAM) APD structures are manifold, e.g., the p^+-n-ν-n^+ (ν = very low n-type) or p^+-n^--n-ν-n^+ (lo-hi-lo) structure, and thus, the target spectral range, the temporal behavior as well as the prevailing carrier type for impact ionization have to be considered for their design. Experimentally, the multiplication factor for the photocurrent signal at a fixed bias can be deduced using [31]

$$M_{\text{photo}} = \frac{I_{\text{M,photo}} - I_{\text{M,dark}}}{I_{\text{pr,photo}} - I_{\text{pr,dark}}}, \tag{9.23}$$

where I_{M} and I_{pr} are the multiplied and the primary (unmultiplied) current signals, respectively. For the detection of modulated radiation, the limitations to device performance due to a constant product of multiplication factor M and bandwidth $f_{\text{c-o}}$ as well as the influence of noise, measured by the effective excess noise factor, have to be considered for optimal operation (see e.g., [31, 63]). Finally, it should be noted, that the breakdown voltage due to avalanche processes increases for increasing temperature (positive temperature coefficient), since the lattice vibrations cool down the hot carriers. Zener-tunneling causes opposite behavior (negative temperature coefficient), since the bound carriers gain energy to overcome the tunneling barrier at a smaller voltage. Therefore, these processes can be distinguished by their temperature dependence.

9.2.2.6 Phototube and Photomultiplier Tube

The phototube is a gas filled or vacuum tube containing an element being sensitive to radiation due to the external photoelectric effect. Such a tube consists of two opposite electrodes, cathode and anode, in a sealed glass tube. The cathode, located at an entrance window either in transmissive or reflective mode, is coated with a photo-emissive material sensitive to a desired wavelength range. Photons entering the entrance window hit the photocathode material and excite electrons that may be released from the cathode surface, if the excess kinetic energy delivered by the

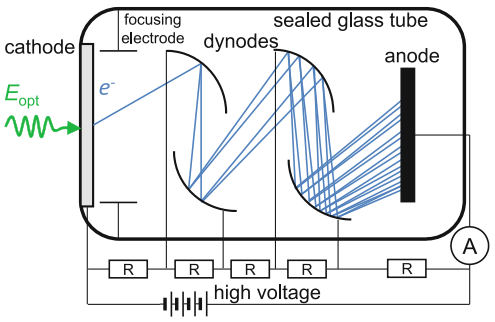


Fig. 9.10 Cross-sectional schematic of a photomultiplier tube (PMT)

photons is sufficiently large, as will be discussed below. The electrons freed at the cathode are then accelerated toward the positively biased anode and cause an electric current of a few microamperes in an external circuit. A photomultiplier tube (PMT) is a modification of the vacuum phototube, where the primary photocurrent emitted from the cathode is multiplied at subsequent electrodes, the dynode stages as shown in Fig. 9.10. When every dynode is held at a more positive potential compared to its prior electrode, electrons in the vacuum gain a corresponding kinetic energy. Depending on the dynode material, the applied voltage has to be chosen accordingly, to create secondary electrons at every stage. Thus, an electron emitted at the cathode hits the first dynode stage and generates secondary electrons that are accelerated toward the second dynode, and so on, until an increased number of electrons reaches the anode and causes a current signal that is proportional to the amount of incident photons. The multiplied current produced by incident radiation can be enhanced by factors of up to 10^7 depending on the number of dynode stages. This enables a PMT for applications where single photons have to be detected.

A PMT can be designed, like the simple phototube, by choosing the suitable photo-emissive cathode material to meet different wavelength ranges in the UV, the visible, and the NIR spectral regions. Due to its high sensitivity, a PMT has to be protected from radiation that may irreversibly harm the dynode coating due to excessive current levels. As for any photodetector type, the transmission of the window material limits the spectral bandwidth and height of the device responsivity. The physical processes occuring in the cathode material upon illumination can be understood utilizing the simple three-step model of photoemission which was developed by Spicer and Berglund for alkali-antimonides [65–67]. As illustrated in Fig. 9.11a, these steps—(1) optical excitation, (2) electron transport in the p-type solid and (3) carrier escape accross the surface—can be treated separately [64]. The electron emission efficiency η_e of a photocathode is approximated by

$$\eta_e = (1 - R_{opt}) \frac{\alpha^\dagger}{\alpha} \left\{ \frac{P_e}{1 + 1/\alpha L_n} \right\} \tag{9.24}$$

with R_{opt} the optical reflection, α the optical absorption coefficient, $\alpha^\dagger$ the absorption coefficient for excitation into states above the vacuum level, P_e the probability of electron escape into the vacuum, and L_n the electron diffusion length in p-type material. Neglecting band bending effects due to Fermi level pinning, which is caused by a high density of defect levels at the surface, from (9.24) it is clear that the spectral shape of η_e is governed by a threshold energy $E_{thr} = E_{gap} + \chi$, where χ is the electron affinity of the material defined as the energy distance between the vacuum level and the bottom of the conduction band right at the surface (c.f. Fig. 9.10a). Since a modification of electronic surface properties by adsorbate-induced surface dipoles and surface states—e.g., due to the formation of a Cs, Cs_2O, Li or NF_3 adlayer with rather n-type properties on the surface of p-GaAs [68, 69]—can result in a band bending at the surface below the conduction band minimum in the bulk material, it is possible to obtain a negative electron

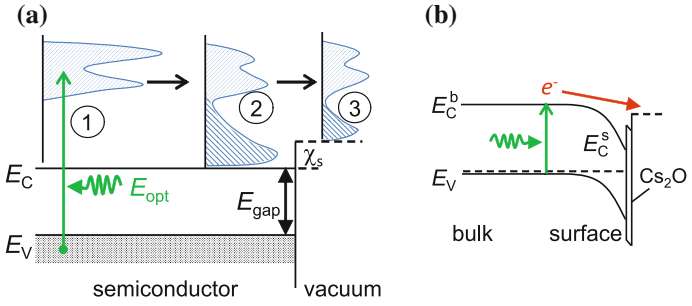


Fig. 9.11 **a** Schematic band diagram of semiconductor/vacuum junction showing three steps of photoemission of electrons: *1* excitation, *2* transport, and *3* escape (after [64]). **b** Schematic band diagram for effective negative electron affinity (NEA) assisted by Cs_2O adlayer on the p-type semiconductors surface

affinity (NEA), as shown in Fig. 9.11b. The semiconductor NEA may be *effective*, corresponding to E_{vac} below the bulk conduction band minimum E_C^b, or *true*, when E_{vac} is below the surface conduction band minimum E_C^s. For effective NEA, the affinity χ is positive but small and the energy bands are bent downward at the surface, as it may occur for a p-type semiconductor. If electrons, excited in the bulk, thermalize to E_C^b and further travel ballistically across the depletion region toward the surface, they have sufficient kinetic energy to escape from the semiconductor. In the case of true NEA, electrons thermalized even at the surface have sufficient energy to escape from the solid. Consequently, in NEA semiconductors the cathode threshold energy for electron emission is reduced and an enhancement of η_e is achievable. This makes such materials attractive for efficient electron emitters for the use in phototubes or PMTs.

9.3 III-Nitrides for Solid-State UV Photodetection

The ability to directly tune the detector cut-off wavelength via the Al mole fraction x_{Al} of the active layer is one of the main advantages of the $Al_xGa_{1-x}N$ material system compared to e.g., SiC, diamond or other elemental materials. This enables the blocking of unwanted signals with wavelengths above 365–200 nm, depending on x_{Al}, and thus the exploration of the UV-A, UV-B, and the UV-C spectral region without the use of additional filters. A comparison of typical responsivity spectra of Schottky (GaP, GaN, AlGaN) as well as p-i-n (SiC) photodiodes is shown in Fig. 9.12 (unpublished data [70]). The GaP photodiode EPD-150 covers a wide range of wavelengths from 150 nm up to the VIS spectral range with EQE levels between about 8 % at 150 nm and 30 % at 410 nm. In combination with an external low-pass filter for a cut-off at 365 nm, the spectrum of the photodiode EPD-365 (GaP + Filter) shows cut-offs in the UV-C at about 260 nm and in the UV-A

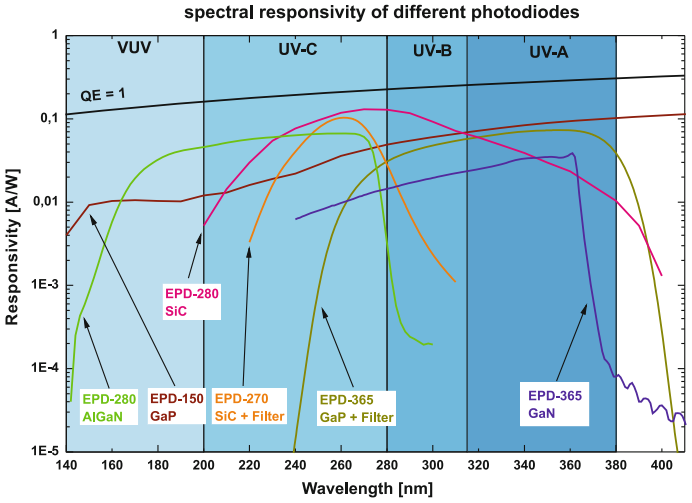


Fig. 9.12 Comparison of responsivity spectra for different types of photodetectors (unpublished data [70])

at about 380 nm. But due to the high-absorption values for GaP for $\lambda \geq 360$ nm (c.f. Fig. 9.1b), the UV-A cut-off results in a rather weak rejection of signals up to 400 nm: The responsivity of 70 mA W^{-1} at 380 nm corresponds to a quite high EQE of about 22 %. A similar situation can be observed for a SiC photodiode. Due to its indirect bandgap, the EPD-280 (SiC) without external filter covers the range from 200 to 400 nm not showing a sharp cut-off but a peak responsivity of about 100 mA W^{-1} at 280 nm. An external filter for UV-C limits the detection range from 220 to 315 nm, as it is shown for the SiC EPD-270 (SiC + Filter). So it is possible to tune a photodetectors spectral range of responsivity using external filters but in conjunction with the optical properties of the semiconductor used, the spectral performance is often limited. However, the main drawbacks to be mentioned are the commercial availability, the price, and the degradation of the filter characteristics. Whenever precise requirements for a specific UV application rely on the filter characteristics, the $Al_xGa_{1-x}N$ material with its tunable intrinsic cut-off promises true visible-blind or solar-blind operation, as it is shown in Fig. 9.12 for the GaN photodiode EPD-365 as well as for the $Al_{0.45}Ga_{0.55}N$ photodiode EPD-280.

Despite the difficulties in AlGaN epitaxy and processing mentioned in the introduction, the first report on photoconductivity measurements in GaN samples was by Pankove and Berkeyheiser in 1974. In this early work, the near-gap photoconductivity edge was attributed to the fundamental absorption edge of GaN:Zn crystals grown by hydride vapor phase epitaxy (HVPE) [71]. The samples were prepared with soldered indium contacts in order to study the photoconductive properties of the material as a function of Zn doping. Where as-grown HVPE GaN films at those times were usually found intrinsically n-type due to very high concentrations of nitrogen vacancies [72], an abrupt transition of the electrical properties from conducting to insulating as well as an enhancement of material quality

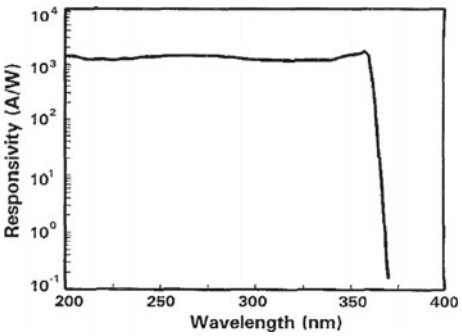


Fig. 9.13 Responsivity spectrum of the first MOCVD grown GaN-based photoconductor device at 5 V bias. Reprinted with permission from [73], Copyright 1992, AIP Publishing LLC

was observed as the Zn concentration was increased. From these findings, it was concluded that Zn atoms would occupy the vacant N sites, and thus reduce the dark conductivity.

About two decades later, in 1992, Khan et al. utilized a low pressure metal organic chemical vapor deposition (MOCVD)-based growth technique, called switched atomic layer epitaxy (SALE), in order to obtain insulating GaN films [3] and shortly after that they also showed characterisation results of the first UV photodetectors fabricated on such GaN layers grown on an AlN/sapphire template [73]. The GaN photoconductors processed had an inter-digital arrangement of Au-electrodes. The *I–V* characteristics of those sensors were linear with dark current level as low as 2 nA at 200 V. At 5 V applied bias, a rather flat responsivity spectrum of 1000 to 2000 A W^{-1} between 200 to 365 nm was obtained with an abrupt drop in signal by three orders of magnitude within 10 nm of the band edge (see Fig. 9.13). Despite the presence of a very high photocurrent gain of 6×10^3 at 365 nm, the response of those devices at 254 nm was found to be linear over five orders of incident optical power and the bandwidth was in excess of 2 kHz. In summary, those first results illustrated a very high potential of GaN material for UV sensing applications.

In the following, many other research groups also succeeded in developing AlGaN-based UV photosensitive devices such as photoconductors, phototransistors, MSM detectors, Schottky barrier photodiodes, MIS diodes as well as p-n and p-i-n diodes. Even the integration of AlGaN-based focal-plane arrays to silicon read-out circuits was achieved and thus the applicability of the III-Nitrides on a rather complex level of technology was demonstrated [74].

9.3.1 AlGaN-Based Photoconductor

First studies on AlGaN-based photoconductors indicated the potential of III-Nitrides, despite some findings that might also hamper device operation in several applications. The high photoconductive gain levels reported led to

long-decay times in the ms range and thus device operation was usually limited to kHz-bandwidths. The gain mechanism was attributed to either the trapping of photogenerated holes and the resulting enhanced effective electron lifetime [75] or the light-induced modulation of the conductive volume [49, 76]. Furthermore, photoconductor devices require biasing, which leads to additional dark current noise. Thus, specific detectivities reported were as low as 10^7–10^9 cm $Hz^{1/2}$ W^{-1} [73, 77]. With increasing Al content in the $Al_xGa_{1-x}N$ layers, the free carrier lifetime was found to decrease as the material becomes more insulating. This result was attributed to an exponential distribution of band-tail states due to the potential fluctuations which arise from an increasing density of defects [78]. Linear photocurrent-power dependencies, even over a wide range of power levels [79] as well as sublinear responses and excitation-dependent response times were observed [80]. Additionally, metastability and persistent photoconductivity (PPC) effects, which can lead to decay times in the order of several 1000 s, were observed in p-type [81] as well as n-type [82] material.

In conclusion, despite the high photocurrents achieved in GaN photoconductors, the gain-related issues, such as device bandwidth and linearity, restrict that type of PD to low frequency applications. In addition to that, the difficulties in processing proper ohmic contacts with increasing x_{Al} impede the development of AlGaN-based photoconductors for the UV-C range.

9.3.2 AlGaN-Based MSM Photodetector

Metal–semiconductor–metal (MSM) photodetectors based on AlGaN offer some advantages over other device types considering their simple fabrication process, since no p- or n-type doping is required and they are easy to integrate in planar process technology. But as well as the photoconductors, metal–semiconductor–metal PDs need an external bias to be driven. This complicates the evaluation of scientific reports, since there is no standard for the bias voltage at which an MSM PD needs is operated.

However, first GaN MSM PDs were demonstrated with an EQE of about 50 % at 6 V, 350 nm cut-off wavelength, a high rejection to visible-light, and low dark current of 800 fA at 10 V [83]. MSM PDs are capable of very high-speed operation, when fully depleted. GaN MSM devices, having 2 μm electrode spacing, with a rise time of 23 ps and a 3 dB cut-off frequency of 16 GHz have been shown [84]. An analysis of the MSM PD performance considering bias and electrode spacing indicates a transit time-limited operation and the modeling of the temporal response reveals the slower holes, compared to electrons in GaN, to be responsible for a slow tail measured experimentally (see Fig. 9.14). However, MSM PDs have been subject to a huge number of publications. In the year 2000, back-illuminated solar-blind $Al_xGa_{1-x}N$ MSM PDs with 260 nm peak wavelength have been presented [85]. As shown in [86], a significant overlap between the depletion region below the biased contacts on the front surface and the photon absorption depth at

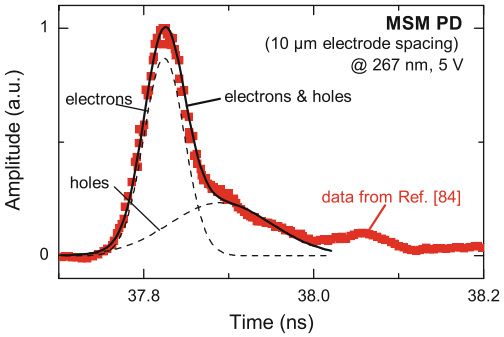


Fig. 9.14 Measured photo-response transients (*scatter*) of a GaN MSM PD with 10 electrode spacing upon pulsed excitation at 267 nm under 25 V. For the modeled data (*lines*) contributions of fast electrons and slow holes have been assumed (data taken from [84])

the backside of the device has to be created either by increasing the bias voltage or decreasing the absorber layer thickness sufficiently. For this reason, the EQE found in [85] increases from about 4.7 % at 4 V to about 48 % at 100 V. The dark current level in this device stayed below the experimental detection limit of 20 fA. Operation of solar-blind MSM PDs under 150 °C temperature has been demonstrated recently [87]. The $Al_{0.4}Ga_{0.6}N$ MSM PD with semitransparent Ni/Au contact electrodes showed a low-dark current in the fA-range at elevated temperature up to 20 V bias and a breakdown voltage higher than 300 V. At 10 V bias, the peak EQE of about 64 % at 275 nm and room temperature and was decreased by only 20–40 % with increasing temperature, possibly due to enhanced carrier recombination losses at elevated temperatures. Pt-AlN MSM detectors with a very low dark current below 100 fA up to 200 V and a very sharp cut-off at 207 nm showed a peak responsivity of 0.4 A W^{-1} at 200 nm for 100 V bias. The reported data (EQE $\sim$ 2.4 at about 200 nm) indicate a bias-dependent gain. Nevertheless, these results demonstrate AlN MSMs as suitable candidates for DUV device applications [88].

$Al_{0.4}Ga_{0.6}N$ layers grown on laterally overgrown AlN on stripe-patterned AlN/sapphire templates turned out to exhibit anisotropic compositional fluctuations throughout the epilayer [89]. At elevated bias, the solar-blind MSM PDs on this material operated linearly with incident optical power but with anisotropic characteristics. Devices with electrodes oriented perpendicular to the underlying stripe pattern showed photoconductive gain (EQE $\sim$ 77 at 30 V) which was absent in devices with parallel electrode orientation. An exponential quenching of this anisotropic EQE with temperature increased from room temperature to about 150 °C was observed and it was suggested that the gain has to be due to a carrier accumulation mechanism at the interfaces between the matrix material with high Al-content and the Ga-rich stripes with a smaller bandgap [90]. This allows not only for highly sensitive devices but also for different detector characteristics integrated on the same wafer.

In summary, a high detection capability achieved by the electrode geometry, the processing of Schottky-type electrodes as well as the epitaxy of non-intentionally doped $Al_xGa_{1-x}N$ layers within the whole composition range make the AlGaN-based MSM PD an easy-to-fabricate device. Moreover, by backside illumination of properly designed MSM PDs, the optical loss due to electrode shading can be circumvented.

9.3.3 AlGaN-Based Schottky Barrier Photodiode

The first AlGaN-based Schottky-type PD was a back-illuminated 1 mm^2 Ti/Au p-type GaN:Mg device with a zero bias EQE of 50 % at 320 nm ($Rsp \sim 0.13\,A.W^{-1}$) and a response time of 1 μs [91]. On n-type GaN material Schottky barrier heights of 0.88, 0.92, 0.99, and 1.08 eV were obtained for Au, Pd, Ni, and Pt, respectively [92]. A front-illuminated device consisting of a semi-transparent Pd layer on n-GaN was fabricated and characterized with $Rsp \sim 0.18$ A.W and a *RC*-limited decay time of 118 ps [93]. Dominant leakage current mechanisms through GaN—as well as AlGaN-Schottky interfaces were recently found to be well described by donor-like surface states which reduce the depletion width and enhance tunneling transport processes [94]. Photoconductive gain mechanisms were attributed to the trapping of minority carriers at the semiconductor/metal interface in conjunction with a subsequent reduction of the Schottky barrier height, such that electron tunneling processes through the barrier are enhanced [52]. UV-B photodetectors with an active $Al_{0.25}Ga_{0.75}N$ layer grown on an $Al_{0.2}Ga_{0.8}N$/GaN superlattice layer (SL) stack showed superior device performance compared to those PDs without SL [95]: Dark current as low as 100pA at −5 V, zero bias responsivity of 97 mA W^{-1} and specific detectivity of 8×10^{13} cm $Hz^{1/2}$ W^{-1} at 290 nm were reported. Solar-blind AlGaN Schottky photodetectors with a diameter of 800 have been fabricated [96]. These devices on AlN/sapphire templates consisted of a semitransparent Ni/Au contact on 200 nm undoped i-$Al_{0.5}Ga_{0.5}N$ deposited on a doped n-AlGaN layer contacted with Ti/Al ohmic contacts. These devices showed responsivity in the range between 100–265 nm under front illumination. High-quality AlN Schottky PDs on an n-type SiC substrate showed a cut-off at 210 nm and a zero bias peak responsivity of 0.12 A W^{-1} at 200 nm corresponding to an EQE of about 74 % (Fig. 9.15). The very low dark current levels of below 1 pA up to 150 V reverse bias as well as the zero bias detectivity of about 10^{15} cm $Hz^{1/2}$ W^{-1}, which is comparable to the detectivity of conventional PMTs, demonstrate the potential of AlN Schottky diodes for DUV optoelectronic device applications [97].

The AlGaN-based Schottky-type photodetectors developed so far show low dark currents due to the blocking Schottky contact, and despite the use of semitransparent metals, high values for the zero bias EQE could be achieved. In comparison

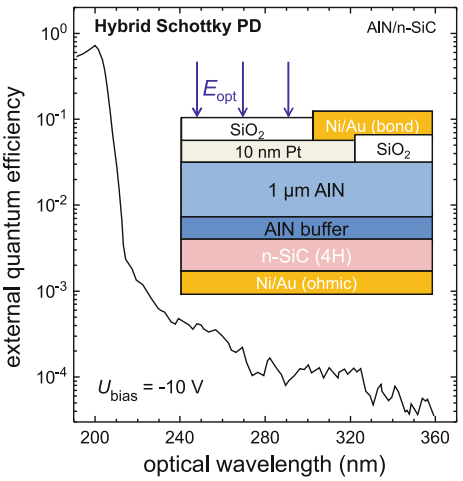


Fig. 9.15 External quantum efficiency of a hybrid Pt-AlN/4H-SiC Schottky PD biased at −10 V; the *inset* shows the device structure with SiO_2 passivation layers (EQE calculated from [97])

to the MSM PD, the difficulties of doping and ohmic contact formation with increasing x_{Al} remain an issue for that type of PD.

9.3.4 AlGaN-Based p-i-n Photodiode

The device structure of a visible-blind GaN based p-i-n photodiode usually consists of an n-type GaN:Si layer with a free-electron concentration of $n \sim 10^{19}$ cm^{-3} followed by an intrinsic GaN region with a background concentration of $n \sim 10^{16}$ cm^{-3} and a top p-type GaN:Mg layer with a hole concentration ranging between 10^{17} to 10^{18} cm^{-3} (see e.g., [98]). Additionally, highly doped n^+- and p^+-type layers are utilized to lower the contact resistance at the device terminals. After mesa-etching down to the n-layer region, proper ohmic contacts with low contact resistances need to be processed on both of the doped layers. An entrance area for the device can now be realized for front- or backside illumination. In both cases, optical losses due to reflection at interfaces as well as due to absorption need to be minimized. For front-illuminated PDs, meshed contacts on the p-layer can be used to reduce electrode shading losses [99]. GaN devices with a semitransparent p-$Al_{0.13}Ga_{0.87}N$ entrance window on top of the photoactive intrinsic GaN region have been reported [100]. An ohmic Ni/Au contact ring on an etched p^+-GaN cap layer defines the entrance window to the absorber layer, which was passivated by a SiO_2 layer. The EQE spectrum at 1 V is flat on a level of about 45 % in the band between 365 to 330 nm and then decreases toward short wavelength due to the onset of absorption in the p-AlGaN layer. For back-illuminated GaN p-i-n devices, an n-$Al_{0.28}Ga_{0.72}N$ layer/i-GaN heterojunction was used and a zero bias EQE of 75 % at 355 nm could be obtained [101]. To achieve solar-blind operation in back-illuminated devices, all layers below the active $Al_xGa_{1-x}N$ layer with

$x_{Al} \geq 0.45$ have to be transparent for the incident radiation. Hence, either substrates opaque to UV-C radiation (Si, SiC) have to be removed or sapphire has to be used. Using this approach, the responsivity of a back-illuminated device is spectrally limited to a narrow wavelength band, which is defined by the different bandgap energies in the layer stack. Besides a sufficient optical transparency, the electronic properties of the n- and the n^+-$Al_xGa_{1-x}N$ layers have to be properly optimized in order to achieve low-series resistance, i.e., high mobility and electron concentration. At x_{Al} of about 60 % an electron mobility of 20 $cm^2\ V^{-1}\ s^{-1}$ and electron concentration of $1 \times 10^{19}\ cm^{-3}$ could be achieved at room temperature, which resulted in a zero bias EQE of 58 % at 274 nm for solar-blind p-i-n PDs [102]. The minimization of any voltage drop across the p- or the n-layers is necessary in order to confine the depletion region to the i-layer and also to enhance the carrier collection efficiency *CE* due to reduced minority carrier losses [103]. Record high zero bias EQE values of about 80 % at 275 nm have been reported recently for the back-illuminated solar-blind diodes (see Fig. 9.16) [104]. The high quality of a Si-In co-doped n^+-type $Al_{0.5}Ga_{0.5}N$ window layer with resistivity, mobility, and carrier concentrations of $1.55 \times 10^{-2}\ \Omega$ cm, 74 $cm^2\ V^{-1}\ s^{-1}$, and $4.41 \times 10^{18}\ cm^{-3}$, respectively, is claimed to significantly contribute to these results.

Since specific detectivities in the range between 10^{13} and 10^{15} cm $Hz^{1/2}\ W^{-1}$ have been reported during the last two decades for p-i-n-type PDs [99, 105–107], it is an attractive alternative device to the PMT whenever low intensity signals have to be detected. Even flame luminescence detection between 250 to 280 nm in the nW cm^{-2} range was demonstrated under fluorescent room light with a front-illuminated n-$Al_{0.44}Ga_{0.56}N$/i-$Al_{0.44}Ga_{0.56}N$/p-GaN/p-mesh heterojunction photodiode [108].

Due to the heterojunctions in a p-i-n sample stack, the effects of piezoelectric polarization (in combination with the spontaneous polarization of the absorber layer) have to be considered. According to modeling results of Kuek et al., dealing

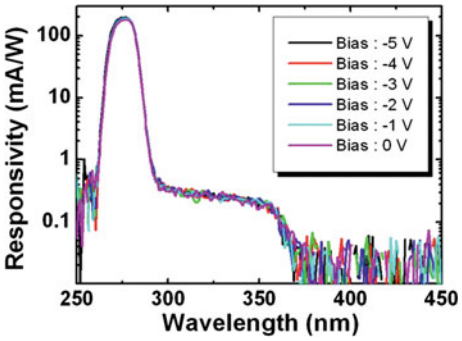


Fig. 9.16 Responsivity spectra of back-illuminated solar-blind p-i-n PDs biased up to −5 V, the maximum peak responsivity at −5 V of about 200 mA/W corresponds to 89 % external quantum efficiency. Reprinted with permission from [104], Copyright 2013, AIP Publishing LLC

with the effect of polarization charges in a UV-B p-GaN/i-$Al_{0.33}Ga_{0.67}N$/n-GaN PD [109], the polarization-induced interface charges increase the barrier to carriers photogenerated within the GaN regions resulting in an enhanced rejection of UV-A radiation.

The development of p-i-n PD profits from the advancing development of AlGaN-based emitting devices, such as LEDs and laser diodes, and vice versa. However, the uniformity of the high electric field and its confinement to the i-layer both play key roles concerning device stability and reliability. A broad range of the UV-region could be covered by the utilization of heterojunction devices as well as the backside illumination approach. The doping and contact formation issues are usually handled by utilizing a sophisticated layer structure including heterojunctions. Therefore, any progress in the fabrication of AlGaN-based p-i-n PDs supports the development of AlGaN-based avalanche photodetectors, discussed in the next paragraph.

9.3.5 AlGaN-Based Avalanche Photodetector

An avalanche photodiode (APD) is usually realized utilizing carrier multiplication in an optimized structure of the p-i-n diode type or the SAM photodiode introduced in Sect. 9.2. However, avalanche multiplication due to soft breakdown characteristics is also found for many of the conventional AlGaN-based devices. These results will be discussed first.

A visible-blind MSM structure with its planar rectifying electrodes is subject to enhanced electric fields within the semiconductor at the metal contact edges. A maximum field strength of 3.5 MV cm^{-1} at a bias of 134 V was estimated by simulating the electrical properties of such a device. These fields are high enough to initiate impact ionization, such that an avalanche gain of more than 1188 at 145 V was measured [110]. For a solar-blind p-i-n structure, a maximum optical gain of 700 at a reverse bias of 60 V was achieved without evidence of abrupt breakdown [111]. The electric field strength at the onset of impact ionization was estimated to be about 1.7 MV cm^{-1}. A solar-blind Schottky PD was reported with 1560 gain at 68 V and a detectivity as high as 1.4×10^{14} cm $Hz^{1/2}$ W^{-1}. For the Pt/AlN Schottky PD on an n-SiC substrate a gain as high as 1200 at 250 V reverse bias was obtained [112]. In all cases mentioned, the bias- and temperature-dependencies have been investigated in order to rule out Zener-tunneling or photoconductive gain as dominant mechanisms for the breakdown process.

Homoepitaxial GaN APDs, illuminated from the top-side, have been reported by Dupuis et al. [113]. As shown in Fig. 9.17, an almost constant and low-leakage current level of 5×10^{-9} A cm^{-2} below 20 V as well as an avalanche gain exceeding 100 have been achieved.

GaN p-i-n APDs fabricated on bulk GaN substrates have been demonstrated with an optical gain of 10^4 at 280 nm under front illumination, dark current densities below 10^{-7} A cm^{-2} up to 45 V, and breakdown voltage of about 92 V, which

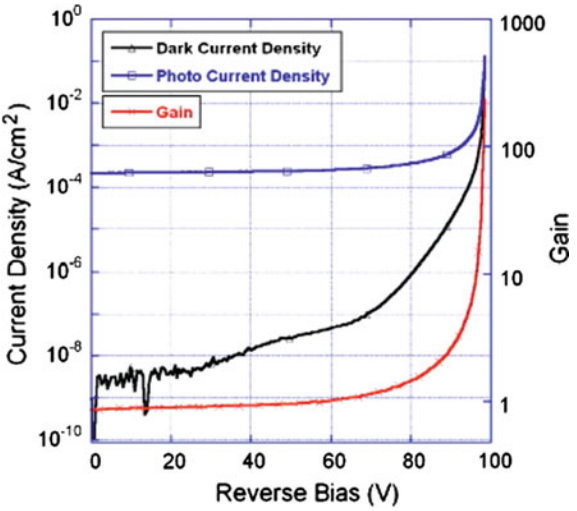


Fig. 9.17 *I–V* characteristics of a front-illuminated homoepitaxial GaN APD (p-i-n) in the dark and under illumination; the multiplication gain is also shown on the *right axis*. Reprinted from [113], Copyright (2008), with permission from Elsevier

corresponds to 2.6 MV cm^{-2} for this structure [111]. For a number of AlGaN APDs, a broadening of the responsivity edge near cut-off was found at elevated reverse bias voltage [112, 114, 115]. This can be attributed to the Franz–Keldysh-Effect, but also an impurity-related absorption band located in the depleted part of the p-GaN at the p-i junction is suggested to be involved in such behavior.

For stable operation of APDs in Geiger-mode—i.e., at a certain over-voltage above breakdown—spatially uniform multiplication regions, free of microplasmas due to defects in the material, are essential. An APD then can be temporarily over-biased with μs-pulses to avoid a large multiplication of the dark current [116]. This enables photon-counting measurements with sufficient gain, where usually PMTs are used. In such experiments, instead of EQE and dark current, the photon detection efficiency (PDE), which is determined by the ratio between recorded and incident pulses, and the dark count rate, i.e., the average number of counts per second, give the significant figures-of-merit. In the year 2000, HVPE grown GaN π-i-n APDs have been demonstrated at 300 K with a PDE of 13 % at 325 nm and a dark count rate of 400 kHz [117]. Also solar-blind AlGaN-based p-i-n APDs have been fabricated and a multiplication gain of 700 at 60 V reverse bias was obtained [118].

Recent results on the performance of back-illuminated separate absorption and multiplication (SAM) AlGaN solar-blind APDs of p-i-n-i-n structure showed a low dark current density of 1.06×10^{-8} A cm^{-2} at 20 V reverse bias and a multiplication gain of about 3000 at 91 V [115]. An even higher gain of 1.2×10^4 at 84 V reverse bias was realized recently by Zhen et al. exploiting the higher ionization coefficient for holes along the (0001) direction of wurtzite GaN mentioned above, in a SAM structure (p-i-n-i-n) in the back-illuminated configuration [119]. Although these and comparable results promise AlGaN-based APDs to be superior to PMTs or Si-based photon-counting units, besides the AlGaN APD also the readout electronics have to

be considered. It means, even if the background noise is low for a wide-bandgap detector, the readout circuit noise may limit the measurement of single photons in a given sampling time. Hence, rather than the NEP, the number of rms noise equivalent electrons with no signal incident is considered as figure-of-merit to properly design a photon-counting sensor [120].

The effects of polarization on the device characteristics of a back-illuminated AlGaN SAM PD have been modeled by Dong et al. [121]. According to their analysis, an increase in Al mole fraction of the p-AlGaN layer results in a significant reduction of avalanche breakdown voltage of the APDs. Moreover, the introduction of a polarization-induced electric field in the multiplication region leads to an increase in multiplication gain. Finally, by utilizing the polarization-doping effect in the p-type AlGaN layer, the simulated maximum gain of the APDs could further be increased.

As pointed out above, the p-i-n PD is the basis of the APD or the SAM PD. In order to meet the conditions of photon-counting applications, due to the structural complexity on the one hand, and the requirement of well-defined as well as homogeneous high-field regions on the other hand, the highest level of device reliability has to be achieved. However, the scientific results presented clearly prove the possibility to obtain outstanding performance utilizing AlGaN-based APDs—even in a wide range of the UV.

9.3.6 AlGaN-Based Photocathode

For clean n- and p-GaN(0001) surfaces Eyckeler et al. experimentally derived work functions of 3.88 and 3.6 eV and revealed the existence of depletion and inversion layers, respectively [122]. An exposure of p-GaN to oxygen followed by Cs deposition was found to lower the vacuum level to about 0.7 eV below the bulk conduction band minimum—i.e., a negative electron affinity (NEA) results [123].

Machuca et al. investigated the oxygen species in Cs/O activated p-type GaN NEA photocathodes utilizing synchrotron radiation photoemission spectroscopy to monitor the oxygen during the activation of NEA as well as during operation of the photocathode under UHV conditions [124]. An ion of molecular oxygen was found to be the dominant chemical species of oxygen in the thin Cs/O adlayer that activates the GaN surface. After about 10 h of UV illumination, a decay of the QE from $\sim$20 % to less than 10 % within further 7.5 h was observed. An analysis of the valence band and core level states revealed a physical alteration of the Cs/O layer causing a change in the electronic structure of the initial di-oxygen from a -2 charge state to the -1 charge state during the QE shift.

Siegmund et al. reported about the stability of their p-GaN (Cs) photocathodes [125]. The QE has not vanished after an atmospheric pressure N_2 exposure and can be recovered to >50 % of the initial QE by a vacuum bakeout at 200 °C. Only the long wavelength QE near cut-off is found to be significantly changed, as assumed from electron surface escape characteristics. A photocathode in a sealed tube was

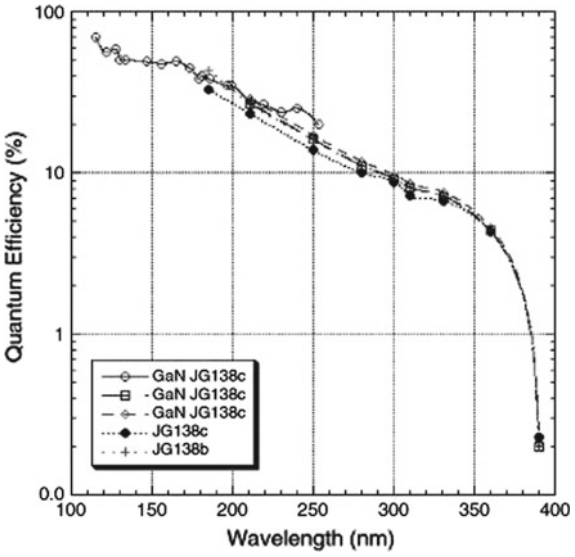


Fig. 9.18 Spectra of external quantum efficiency for a photocathode device taken over a 3 year period, no significant aging is observed. Reprinted from [125], Copyright (2006), with permission from Elsevier

found to be stable over 3 years, as shown in Fig. 9.18, and samples measured in a process tank at 10^{-9} Torr did not degrade over a 6-month period. They also pointed out that this level of stability is better in comparison to that of common cathode materials, e.g., made of CsI or CsTe.

Visible-blind phototubes based on cesiated p-GaN photocathodes have been fabricated [126]. The NEA cathode sample of 0.5 × 0.3 cm^2 area was placed opposed to a 1-mm-thick wire loop anode in a sealed glass tube of 2 cm diameter and 7 cm length. In this configuration, a QE of 30 % at 200 nm wavelength and VIS/UV rejection of up to four orders of magnitude have been measured. The authors also claimed a long-term stability of their cesiated cathodes, since the measured QE changed less than 1 % within a storage duration of two months. In addition, an increase in QE with p-type conductivity of the material was reported. This indicates difficulties for material with high Al content, since the higher acceptor ionization energy then causes the QE to be reduced, accordingly.

The electron affinity of a clean AlN surface was found to be $\chi_{AlN} \approx 1.9$ eV and Cs adsorption then led to a true NEA with $\chi_{Cs/AlN} \approx -0.7$ eV [123, 127, 128], but no data on the performance of AlN photocathodes has been reported so far.

In conclusion, the QE values of p-GaN photocathodes range from about 10 % at the threshold wavelength [125] to about 72 % at 230 nm [129]. For the p-type AlGaN-based photocathode, the doping issues hold, as for the Schottky and p-i-n PD. Finally, the chemical instability of the Cs adlayer remains the main obstacle that needs to be solved in the future, especially in terms of device degradation. However, the integration in an electron-multiplying setup can be done straight forward, based on mature technologies.

9.3.7 III-Nitride-Based Devices of High Integration Level

Since the first report on visible-blind GaN-based 32 × 32 pixel focal-plane-array (FPA) cameras, consisting of GaN/AlGaN p-i-n photodiodes hybridized to silicon readout integrated circuits (ROICs) [130, 131], further GaN or AlGaN FPAs in linear [132, 133] and two-dimensional arrangement have been realized. The main detector types, such as Schottky diodes [132, 134], MSM detectors [132] and p-i-n diodes [74, 135] were fabricated and the standard characterization results, similar to those of the single devices mentioned above, showed that visible-blind as well as solar-blind 2D-imaging with 8 × 8 [136], 128 × 128 [137], 256 × 256 [74] or even 320 × 256 [104, 137–140] pixels is possible (see Fig. 9.19).

However, lattice mismatch and defects are a challenge to such large-area devices. Recently, Cicek et al. reported on an effective approach to reduce the number of cracks in solar-blind p-i-n based FPA imaging strucures by utilizing reduced area epitaxy [141]. With this approach, 97 % of the pixels were obtained crack-free and showed an enhancement of about 10 % in the peak EQE compared to devices on a conventionally grown reference sample. However, the prepatterning procedure of the AlN template prior to device growth led to a reduction of the pixel fill-factor to about 48 % (22 μm × 22 μm total device at 30 μm × 30 μm periodicity) compared to 73 % achievable by conventional mesa-structuring the whole p-i-n device [104].

In the design of such FPA systems, flip-chip mounting is usually utilized to integrate the AlGaN photodetector via In-bump technology with a Si readout integrated circuit (ROIC) chip. As already mentioned, back-illumination of a PD results in the limitation of the response to wavelengths above the respective cut-off from any radiation filtering layers, such as substrates, which is crucial for the detection of VUV radiation below about 140 nm. The removal of a sapphire substrate requires high mechanical stresses and may cause harmful damage of the thin remaining device layers. To overcome these difficulties, Malinowski et al.

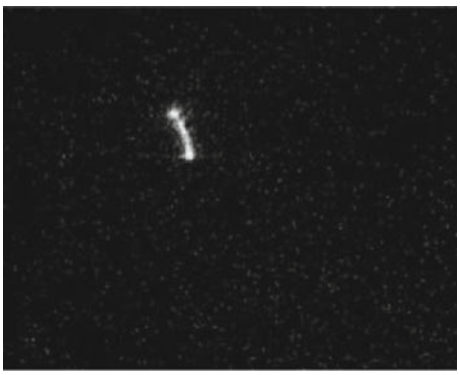


Fig. 9.19 Electric arc recorded with a solar-blind FPA camera with 320 × 256 pixels. Reprinted with permission from [138], Copyright 2005, AIP Publishing LLC

fabricated 400-nm-thick AlGaN membranes by locally etching away the Si(111) substrate after face-down integration to a Si-ROIC [134]. The individual solar-blind Schottky PDs of the 7 × 3 array showed the capability for solar-blind detection with high VIS/UV rejection.

In conclusion, the integration of AlGaN-based photodetectors to ROICs has already been realized at a comparably early stage in III-Nitride photodetector research. Useful processing steps and techniques have been successfully employed in order to enhance the yield of individual PDs making up such large-scale devices.

9.4 Present Status of Wide Bandgap Photodetectors

During the 1980's, there have been developments in GaN and AlGaN growth that led to different patents mainly on the epitaxy of single layers [142–151]. Although, subsequently more patents on complete photodetector structures were released [152–154] and new materials—such as several oxides like TiO_2, SnO_2, ZrO_2, or ZnO—emerged [155, 156], the work on improvement of material quality is a key issue in the field of UV photodetectors up to now [157, 158]. This incomplete listing is meant to give a brief overview of the companies dealing with UV photodiodes.[13] In 1993 APA OPTICS Inc. filed a patent on GaN and AlGaN-based photoconductors [159]. In 2000, there have been patents by SANYO on a Pd-Schottky electrode on an n-SiC substrate [160] and by APA OPTICS Inc. on a 8 × 8 Schottky-type photodetector array based on GaN with a pixel size of 200 μm by 200 μm [161]. The next year, General Electric patented a photodetector based on homoepitaxial GaN having a dislocation density below 10^5 cm^{-2} [162]. In 2002, a Schottky PD based on metal-oxides—TiO_2, ZnO, SnO_2, SiO_2, ZrO_2, PbO, MnO, Fe_2O_3, or In_2O_3—with a Schottky contact made of Pt, Pd, Ni, Au, or Ag was claimed by the company sglux [155]. In 2005, Hamamatsu filed a patent on a back-illuminated photodiode array for computed tomography [163] and OSAKA GAS CO. LTD. filed a patent on a flame sensor based on an AlGaN p-i-n photodiode using a GaN-layer process with ELO [164]. In 2007, Iwate Information System Corp. filed a patent on a UV PD based on ZnO substrate and AlGaN active layer [156]. Also in 2008, Canon filed a patent on a Schottky photodiode with a periodic concavo-convex structured surface for higher efficiency [165] and NEC filed a patent on a back-illuminated Schottky photodiode with a surface plasmon periodic structure to combine sensitivity and speed [166]. In July 2010, Hamamatsu released the first GaN-based transmission photocathode for the UV range [167, 168]. In 2012, Lai et al. released a paper and a patent on a solar-blind Schottky diode based on Au/wurzite MgS/n^+-GaAs (111) substrate [169, 170]. This detector has a cut-off at 240 nm and shows an EQE of 10 % at a peak wavelength of 225 nm.

[13]Companies like: Kyosemi Corporation, Hamamatsu Photonics K.K., SANYO Electric Co. Ltd., General Electric Company, Cree Inc., and others.

Table 9.1 Typical parameters of commercially available photodetectors

Material [Ref.] Type	A_{sens} (mm^2)	$\Delta\lambda$ λ_{peak} (nm)	*Rsp* at λ, U_{rev} (mA W^{-1})	I_{dark} at U_{rev} (pA)	*NEP* at λ ($W/\sqrt{Hz}$)	τ_{rise}/τ_{fall} (ns)	C_t at 0 V (pF)
GaP [172]	1.2	150–550	28	10	1.1×10^{-14}	1/20	300
Schottky		440	254 nm, 5 V	5 V	440 nm		
CsTe [173]	78.5	160–320	1.4×10^{7}	300		2.5/24	2
PMT		240	254 nm, 1 kV	1 kV			
TiO_2 [174]	4.18	215–385	21	30			1000
Schottky		300	300 nm, 3 V	1 V			
ZnO [175]		225–380	2600			10/960	
Photoconductor[a]		370	370 nm, 10 V				
GaN [176]		200–365	1,500,000	5		300/600	
Photoconductor[a]		365	254 nm, 10 V	10 V			
GaN [177]	0.8	290–365	150	1000			
p-i-n		365	350 nm, 0 V	1 V			
GaN [178]	0.09	230–375	80	50			24
Schottky		365	254 nm, 0 V	1 V			
AlGaN [179]	1.0	150–282	66	5	1.33×10^{-14}	40/60	320
Schottky		260	254 nm, 0 V	1 V	254 nm		
AlGaN [180]	1.536	210–280	50	20			
p-i-n		280	254 nm, 0 V	0.1 V			
AlGaN [181]	0.031	240–278	66.3	145			
APD[a]		260	260 nm, 0 V	20 V			
SiC [182]	0.056	230–285	84	0.005	9×10^{-16}		20
p-i-n		270	254 nm, 0 V	1 V	270 nm		
SiC [183]	1	220–275	80	0.001			195
p-i-n		265	254 nm, 0 V	1 V			

Sensitive area A_{sens}, wavelength λ, spectral range $\Delta\lambda$ ($Rsp \geq 1\,\%Rsp_{max}$), peak wavelength λ_{peak}, responsivity *Rsp*, reverse bias voltage U_{rev}, dark current I_{dark}, noise-equivalent-power *NEP*, rise and fall times $\tau_{rise,fall}$ (10–90 %), and the device capacitance C_t

[a]Not commercially available, scientific reports (for comparison only)

In 2013, NEC filed a patent on a waveguide-coupled MSM photodetector based on GaN. The reduced light reflection at the MSM electrode improves the efficiency, so that the bias voltage can be reduced [171].

In Table 9.1 different types of UV photodetectors are listed, which are based on several material systems and have an active area between 0.031 and 78.5 mm^2. Except for the GaP Schottky PD, all PDs operate solely in the UV, showing peak wavelengths between 370 and 240 nm, and thus are suitable for applications requiring visible-blind or even solar-blind detection capabilities. For the PDs based on $Al_xGa_{1-x}N$, that can be operated at zero bias, the responsivities range between 60 to 150 mA W^{-1}, which is competitive to SiC-based p-i-n PDs having about 80 mA W^{-1}. Except the GaN as well as the ZnO photoconductor with their enhanced responsivities at 10 V bias, values below 28 mA W^{-1} are achieved with GaP Schottky PDs, and TiO_2 Schottky PD at a small bias voltage. In comparison to that, the CsTe PMT requires a high voltage of 1 kV in order to operate at a responsivity of 1.4×10^7 mA W^{-1} at 254 nm due to the gain of 5×10^5 at this bias. The dark current level of 300 pA for this PMT has been obtained after storing the device for 30 min in the dark. But the very short rise and fall times as well as the low device capacitance for the PMT are remarkable in comparison to all other devices. However, given values for the *NEP* range between 10^{-16} and 10^{-14} cm $Hz^{1/2}$ W^{-1} for the SiC p-i-n PD, the GaP and the $Al_xGa_{1-x}N$ Schottky PDs promising high performance in detecting low power levels.

We conclude, that in comparison to rather mature technologies in SiC or GaP device fabrication, the $Al_xGa_{1-x}N$-based UV PDs are definitely competitive today, and outstanding performance can be achieved, regardless of the device type.

9.5 Summary and Conclusions

This overview on AlGaN-based UV photodetectors (PDs) covers the simple device types, such as the photoconductor, the metal–semiconductor–metal (MSM) PD and the Schottky PD as well as rather complex p-i-n PDs, avalanche PDs (APDs), separate absorption multiplication PDs (SAM PDs), their integration as 1D- or even 2D-arrays, and AlGaN photocathode material for photomultiplier tubes (PMTs), which were developed within the last two decades. According to the different device structures and designs on the one hand, and the challenges in the epitaxy of $Al_xGa_{1-x}N$ layer structures as well as related processing issues on the other hand, a variety of performance data was reported.

The high photocurrents observed for GaN photoconductors with ohmic contacts usually correlate with photoconductive gain which results in a low frequency bandwidth, whereas the easy-to-fabricate MSM PD with two blocking contacts on an non-intentionally doped AlGaN layer can achieve low dark current levels and also high detection capability by utilizing a suitable electrode geometry. Since these devices rely on an applied bias voltage, the Schottky PD as well as the p-i-n PD constitute very attractive alternatives, because they can be operated in zero bias

mode. In general the p-i-n design offers a potentially higher stability compared to the Schottky PD, since electric fields can be controlled by the properties of the i-layer. But in order to tailor, the whole UV range from the UV-A to the UV-C or even the VUV with the p-i-n design, p- or n-type $Al_xGa_{1-x}N$ material with arbitrary Al mole fraction x_{Al} of high quality is required. However, even today the doping of AlGaN and the processing of ohmic contacts to AlGaN layers are not straight forward, especially with rising x_{Al}. Therefore, only the MSM PD and the Schottky PD could be fabricated on AlN layers with a corresponding cut-off wavelength λ_c of about 200 nm (VUV). Nevertheless, very efficient solar-blind ($\lambda_c = 280$ nm) p-i-n PDs were obtained by utilizing complex heterostructure designs and the concept of backside illumination. For all these device types, typical values for the external quantum efficiency (EQE) range between several 10 % and about 90 % below breakdown without the indication of any gain mechanism. Moreover, AlGaN-based APDs and even SAM PDs were realized enabling photon-counting measurements that prove competitive performance of AlGaN-based APDs to conventional PMTs. Also the successful processing of Schottky PDs and p-i-n PDs on the wafer-level to form 1D or 2D focal-plane arrays integrated into read-out circuits was demonstrated. Although, the p-GaN photocathode material developed may suffer from chemical alterations of the cesiated surface under UV illumination, and a decreasing EQE for higher x_{Al} (supposed to correlate to the increasing acceptor ionization energy), the overall performance of photocathodes obtained shows very promising results.

In conclusion, $Al_xGa_{1-x}N$-based photodetectors have been realized in a variety of device types which for some applications offer advantages over devices made from other materials, such as Si, SiC, and GaP. Although there is still room for improvement concerning material quality and process technology, $Al_xGa_{1-x}N$-based PDs are already commercially available. Especially the large and tunable band gap energies, resulting in high radiation hardness and enabling custom-made cut-off wavelengths, make $Al_xGa_{1-x}N$-based photodetectors promising candidates for solar-blind and visible-blind photodetection in UV applications.

References

1. I. Vurgaftman, J.R. Meyer, L.R. Ram-Mohan, Band parameters for III-V compound semiconductors and their alloys. J. Appl. Phys. **89**(11), 5815–5875 (2001)
2. S. Einfeldt, V. Kirchner, H. Heinke, M. Dießelberg, S. Figge, K. Vogeler, D. Hommel, Strain relaxation in AlGaN under tensile plane stress. J. Appl. Phys. **88**(12), 7029–7036 (2000)
3. M. Asif Khan, R.A. Skogman, J.M. Van Hove, D.T. Olson, J.N. Kuznia, Atomic layer epitaxy of GaN over sapphire using switched metalorganic chemical vapor deposition. Appl. Phys. Lett. **60**(11), 1366–1368 (1992)
4. E. Valcheva, T. Paskova, G. Radnoczi, L. Hultman, B. Monemar, H. Amano, and I. Akasaki, Growth-induced defects in AlN/GaN superlattices with different periods. Phys. B: Condens. Matter **340–342**(0), 1129–1132 (2003). (Proceedings of the 22nd international conference on defects in semiconductors)

5. J.P. Zhang, H.M. Wang, M.E. Gaevski, C.Q. Chen, Q. Fareed, J.W. Yang, G. Simin, M.A. Khan, Crack-free thick AlGaN grown on sapphire using AlN/AlGaN superlattices for strain management. Appl. Phys. Lett. **80**(19), 3542–3544 (2002)
6. K. Nagamatsu, N. Okada, H. Sugimura, H. Tsuzuki, F. Mori, K. Iida, A. Bando, M. Iwaya, S. Kamiyama, H. Amano, I. Akasaki, High-efficiency AlGaN-based UV light-emitting diode on laterally overgrown AlN. J. Cryst. Growth **310**(7–9), 2326–2329 (2008). (The Proceedings of the 15th international conference on crystal growth (ICCG-15) in conjunction with the international conference on vapor growth and epitaxy and the US Biennial workshop on organometallic vapor phase epitaxy)
7. H. Hirayama, S. Fujikawa, J. Norimatsu, T. Takano, K. Tsubaki, N. Kamata, Fabrication of a low threading dislocation density ELO-AlN template for application to deep-UV LEDs. Phys. Status Solidi (C) **6**(S2), S356–S359 (2009)
8. V. Kueller, A. Knauer, C. Reich, A. Mogilatenko, M. Weyers, J. Stellmach, T. Wernicke, M. Kneissl, Z. Yang, C. Chua, N. Johnson, Modulated epitaxial lateral overgrowth of AlN for efficient UV LEDs. IEEE Photonics Technol. Lett. **24**, 1603–1605 (2012)
9. H. Harima, T. Inoue, S. Nakashima, M. Ishida, M. Taneya, Local vibrational modes as a probe of activation process in p-type GaN. Appl. Phys. Lett. **75**(10), 1383–1385 (1999)
10. S. Nakamura, N. Iwasa, M. Senoh, T. Mukai, Hole compensation mechanism of p-type GaN films. Jpn. J. Appl. Phys. **31**(Part 1, No. 5A), 1258–1266 (1992)
11. S. Nakamura, T. Mukai, M. Senoh, N. Iwasa, Thermal annealing effects on p-type mg-doped GaN films. Jpn. J. Appl. Phys. **31**(Part 2, No. 2B), L139–L142 (1992)
12. H. Obloh, K. Bachem, U. Kaufmann, M. Kunzer, M. Maier, A. Ramakrishnan, P. Schlotter, Self-compensation in mg doped p-type GaN grown by MOCVD. J. Cryst. Growth **195**(1–4), 270–273 (1998)
13. U. Kaufmann, M. Kunzer, M. Maier, H. Obloh, A. Ramakrishnan, B. Santic, P. Schlotter, Nature of the 2.8 eV photoluminescence band in mg doped GaN. Appl. Phys. Lett. **72**(11), 1326–1328 (1998)
14. M.L. Nakarmi, N. Nepal, J.Y. Lin, H.X. Jiang, Photoluminescence studies of impurity transitions in Mg-doped AlGaN alloys. Appl. Phys. Lett. **94**(9) (2009)
15. K.B. Nam, M.L. Nakarmi, J. Li, J.Y. Lin, H.X. Jiang, Mg acceptor level in AlN probed by deep ultraviolet photoluminescence. Appl. Phys. Lett. **83**(5), 878–880 (2003)
16. M.L. Nakarmi, N. Nepal, C. Ugolini, T.M. Altahtamouni, J.Y. Lin, H.X. Jiang, Correlation between optical and electrical properties of mg-doped AlN epilayers. Appl. Phys. Lett. **89** (15) (2006)
17. Q. Liu, S. Lau, A review of the metal-GaN contact technology. Solid-State Electron. **42**(5), 677–691 (1998)
18. S. Pal, T. Sugino, Fabrication and characterization of metal/GaN contacts. Appl. Surf. Sci. **161**(1–2), 263–267 (2000)
19. V.M. Bermudez, Study of oxygen chemisorption on the GaN(0001)-(1×1) surface. J. Appl. Phys. **80**(2), 1190–1200 (1996)
20. Q.Z. Liu, S.S. Lau, N.R. Perkins, T.F. Kuech, Room temperature epitaxy of Pd films on GaN under conventional vacuum conditions. Appl. Phys. Lett. **69**(12), 1722–1724 (1996)
21. S.J. Pearton, J.C. Zolper, R.J. Shul, F. Ren, GaN: Processing, defects, and devices. J. Appl. Phys. **86**(1), 1–78 (1999)
22. M. Razeghi, A. Rogalski, Semiconductor ultraviolet detectors. J. Appl. Phys. **79**(10), 7433–7473 (1996)
23. E. Muñoz, E. Monroy, J.L. Pau, F. Calle, F. Omnès, P. Gibart, III nitrides and UV detection. J. Phys.: Condens. Matter **13**(32), 7115 (2001)
24. M. Razeghi, Short-wavelength solar-blind detectors-status, prospects, and markets. Proc. IEEE **90**, 1006–1014 (2002)
25. M.A. Khan, M. Shatalov, H.P. Maruska, H.M. Wang, E. Kuokstis, III-nitride UV devices. Jpn. J. Appl. Phys. **44**(10R), 7191 (2005)
26. E. Muñoz, (Al,In,Ga)N-based photodetectors. some materials issues. Phys. Status Solidi (b) **244**(8), 2859–2877 (2007)

27. Wide bandgap UV photodetectors: a short review of devices and applications **6473** (2007)
28. L. Sang, M. Liao, M. Sumiya, A comprehensive review of semiconductor ultraviolet photodetectors: From thin film to one-dimensional nanostructures. Sensors **13**(8), 10482–10518 (2013)
29. R. Bube, *Photoconductivity of solids* (Wiley, 1960)
30. H. Tholl, *Bauelemente der Halbleiterelektronik: Teil 2 Feldeffekt-Transistoren, Thyristoren und Optoelektronik (Leitfaden der Elektrotechnik) (German Edition)*, (Vieweg+Teubner Verlag, 1978)
31. G. Winstel, C. Weyrich, *Optoelektronik II: Photodioden* (Phototransistoren, Photoleiter und Bildsensoren (Halbleiter-Elektronik) (German Edition), Springer, 1986)
32. P. Dennis, *Photodetectors: an introduction to current technology* (Springer, 1986)
33. J. Geist, Planar silicon photosensors. In: *Sensor Technology and Devices (Optoelectronics Library)*, ed. by L. Ristic (Artech House Publishers, 1994)
34. K.K. Ng, *Complete Guide to Semiconductor Devices* (McGraw-Hill Education (ISE Editions), 1995)
35. S.M. Sze, K.K. Ng, *Physics of Semiconductor Devices* (Wiley-Interscience, 2006)
36. J.I. Pankove, H.P. Maruska, J.E. Berkeyheiser, Optical absoption of GaN. Appl. Phys. Lett. **17**(5), 197–199 (1970)
37. D.E. Aspnes, A.A. Studna, Dielectric functions and optical parameters of Si, Ge, GaP, GaAs, GaSb, InP, InAs, and InSb from 1.5 to 6.0 eV. Phys. Rev. B **27**, 985–1009 (1983)
38. M.D. Sturge, Optical absorption of gallium arsenide between 0.6 and 2.75 eV. Phys. Rev. **127**, 768–773 (1962)
39. S. Zollner, J.G. Chen, E. Duda, T. Wetteroth, S.R. Wilson, J.N. Hilfiker, Dielectric functions of bulk 4 h and 6 h SiC and spectroscopic ellipsometry studies of thin SiC films on Si. J. Appl. Phys. **85**(12), 8353–8361 (1999)
40. V. Srikant, D.R. Clarke, Optical absorption edge of ZnO thin films: the effect of substrate. J. Appl. Phys. **81**(9), 6357–6364 (1997)
41. M. Röppischer, *Optische Eigenschaften von Aluminium-Galliumnitrid-Halbleitern* (Südwestdeutscher Verlag für Hochschulschriften, Saarbrücken, 2011)
42. H.R. Phillip, E.A. Taft, Kramers-Kronig analysis of reflectance data for diamond. Phys. Rev. **136**, A1445–A1448 (1964)
43. A.D. Papadopoulos, E. Anastassakis, Optical properties of diamond. Phys. Rev. B **43**, 5090–5097 (1991)
44. E. Palik, *Handbook of Optical Constants of Solids, Volumes I, II, and III: Subject Index and Contributor Index.* Academic Press Handbook Series (Elsevier Science & Technology, 1985)
45. R. Kohlrausch, Theorie des elektrischen Rückstandes in der Leidener Flasche. Ann. Phys. **167**(1), 56–82 (1854)
46. J. Phillips, Kohlrausch relaxation and glass transitions in experiment and in molecular dynamics simulations. J. Non-Cryst. Solids **182**(1–2), 155–161 (1995)
47. M. Cardona, R. Chamberlin, W. Marx, The history of the stretched exponential function. Ann. Phys. **16**(12), 842–845 (2007)
48. M. Brendel, *Build-up and decay transient of a GaN MSM photodetector showing persistent photoconductivity (PPC)*. Unpublished data from Ferdinand-Braun-Institut, Leibniz-Intitut für Höchstfrequenztechnik (FBH)
49. J.A. Garrido, E. Monroy, I. Izpura, E.M. Noz, Photoconductive gain modelling of GaN photodetectors. Semicond. Sci. Technol. **13**(6), 563 (1998)
50. C.H. Park, D.J. Chadi, Stability of deep donor and acceptor centers in GaN, AlN, and BN. Phys. Rev. B **55**, 12995–13001 (1997)
51. V.V. Ursaki, I.M. Tiginyanu, P.C. Ricci, A. Anedda, S. Hubbard, D. Pavlidis, Persistent photoconductivity and optical quenching of photocurrent in GaN layers under dual excitation. J. Appl. Phys. **94**(6), 3875–3882 (2003)
52. O. Katz, V. Garber, B. Meyler, G. Bahir, J. Salzman, Gain mechanism in GaN schottky ultraviolet detectors. Appl. Phys. Lett. **79**(10), 1417–1419 (2001)
53. K.K. Hamamatsu Photonics, Si photodiodes

54. R. Müller, *Rauschen: Zweite, überarbeitete und erweiterte Auflage (Halbleiter-Elektronik) (Volume 15) (German Edition)* (Springer, 1989)
55. E. Rhoderick, R. Williams, *Metal-semiconductor contacts*, Monographs in electrical and electronic engineering (Clarendon Press, 1988)
56. R.T. Tung, The physics and chemistry of the schottky barrier height. Appl. Phys. Rev. **1**(1) (2014)
57. K. Böer, *Introduction to space charge effects in semiconductors.* Springer Series in Solid-State Sciences (Springer, 2009)
58. S.M. Sze, D.J. Jr Coleman, A. Loya, Current transport in metal-semiconductor-metal (MSM) structures. Solid-State Electron. **14**(12), 1209–1218 (1971)
59. A. Sarto, B. Van Zeghbroeck, Photocurrents in a metal-semiconductor-metal photodetector. IEEE J. Quantum Electron. **33**, 2188–2194 (1997)
60. S. Chou, M.Y. Liu, Nanoscale tera-hertz metal-semiconductor-metal photodetectors. IEEE J. Quantum Electron. **28**, 2358–2368 (1992)
61. Z. Marks, B. Van Zeghbroeck, High-speed nanoscale metal-semiconductor-metal photodetectors with terahertz bandwidth. In: 2010 10th International Conference on Numerical Simulation of Optoelectronic Devices (NUSOD) (2010), pp. 11–12
62. I.H. Oguzman, E. Bellotti, K.F. Brennan, J. Kolnk, R. Wang, P.P. Ruden, Theory of hole initiated impact ionization in bulk zincblende and wurtzite GaN. J. Appl. Phys. **81**(12), 7827–7834 (1997)
63. B.E.A. Saleh, M.C. Teich, *Fundamentals of Photonics* (Wiley, 2007)
64. W.E. Spicer, The use of photoemission to determine the electronic structure of solids. J. Phys. Colloques **34**, C6–19–C6–33 (1973)
65. W.E. Spicer, Photoemissive, photoconductive, and optical absorption studies of alkali-antimony compounds. Phys. Rev. **112**, 114–122 (1958)
66. W.E. Spicer, Photoemission and related properties of the alkali-antimonides. J. Appl. Phys. **31**(12), 2077–2084 (1960)
67. C.N. Berglund, W.E. Spicer, Photoemission studies of copper and silver: Theory. Phys. Rev. **136**, A1030–A1044 (1964)
68. J. Scheer, J. van Laar, GaAs-Cs: A new type of photoemitter. Solid State Commun. **3**(8), 189–193 (1965)
69. Y. Sun, R.E. Kirby, T. Maruyama, G.A. Mulhollan, J.C. Bierman, P. Pianetta, The surface activation layer of GaAs negative electron affinity photocathode activated by Cs, Li, and NF3. Appl. Phys. Lett. **95**(17) (2009)
70. E. Pertzsch, Responsivity spectra: Comparison between several AlGaN-based photodetectors and SiC as well as GaP photodetectors. Unpublished data from JENOPTIK Polymer Systems GmbH (JOPS)
71. J.I. Pankove, J.E. Berkeyheiser, Properties of Zn-doped GaN. II. Photoconductivity. J. Appl. Phys. **45**(9), 3892–3895 (1974)
72. H.P. Maruska, J.J. Tietjen, The preparation and properties of vapor-deposited single-crystalline GaN. Appl. Phys. Lett. **15**(10), 327–329 (1969)
73. M.A. Khan, J.N. Kuznia, D.T. Olson, J.M. Van Hove, M. Blasingame, L.F. Reitz, High-responsivity photoconductive ultraviolet sensors based on insulating single-crystal GaN epilayers. Appl. Phys. Lett. **60**(23), 2917–2919 (1992)
74. P. Lamarre, A. Hairston, S. Tobin, K. Wong, A. Sood, M. Reine, M. Pophristic, R. Birkham, I. Ferguson, R. Singh, C. Eddy, U. Chowdhury, M. Wong, R. Dupuis, P. Kozodoy, E. Tarsa, AlGaN UV focal plane arrays. Phys. Status Solidi (A) **188**(1), 289–292 (2001)
75. F. Binet, J.Y. Duboz, E. Rosencher, F. Scholz, V. Haerle, Mechanisms of recombination in GaN photodetectors. Appl. Phys. Lett. **69**(9), 1202–1204 (1996)
76. E. Monroy, F. Calle, J.A. Garrido, P. Youinou, E. Muñoz, F. Omnès, B. Beaumont, P. Gibart, Si-doped $Al_xGa_{1-x}N$ photoconductive detectors. Semicond. Sci. Technol. **14**(8), 685 (1999)

77. D. Walker, X. Zhang, A. Saxler, P. Kung, J. Xu, M. Razeghi, $Al_xGa_{1-x}N$ ($0 \leq x \leq 1$) ultraviolet photodetectors grown on sapphire by metal-organic chemical-vapor deposition. Appl. Phys. Lett. **70**(8), 949–951 (1997)
78. T.D. Moustakas, M. Misra, Origin of the high photoconductive gain in AlGaN films. Proc. SPIE **6766** (2007)
79. K.S. Stevens, M. Kinniburgh, R. Beresford, Photoconductive ultraviolet sensor using Mg-doped GaN on Si(111). Appl. Phys. Lett. **66**(25), 3518–3520 (1995)
80. P. Kung, X. Zhang, D. Walker, A. Saxler, J. Piotrowski, A. Rogalski, M. Razeghi, Kinetics of photoconductivity in n-type GaN photodetector. Appl. Phys. Lett. **67**(25), 3792–3794 (1995)
81. C. Johnson, J.Y. Lin, H.X. Jiang, M.A. Khan, C.J. Sun, Metastability and persistent photoconductivity in Mg-doped p-type GaN. Appl. Phys. Lett. **68**(13), 1808–1810 (1996)
82. H.M. Chen, Y.F. Chen, M.C. Lee, M.S. Feng, Persistent photoconductivity in n-type GaN. J. Appl. Phys. **82**(2), 899–901 (1997)
83. J. Carrano, T. Li, P. Grudowski, C. Eiting, R. Dupuis, J. Campbell, High quantum efficiency metal-semiconductor-metal ultraviolet photodetectors fabricated on single-crystal GaN epitaxial layers. Electron. Lett. **33**, 1980–1981 (1997)
84. J.C. Carrano, T. Li, D.L. Brown, P.A. Grudowski, C.J. Eiting, R.D. Dupuis, J.C. Campbell, Very high-speed metal-semiconductor-metal ultraviolet photodetectors fabricated on GaN. Appl. Phys. Lett. **73**(17), 2405–2407 (1998)
85. B. Yang, D.J.H. Lambert, T. Li, C. Collins, M. Wong, U. Chowdhury, R. Dupuis, J. Campbell, High-performance back-illuminated solar-blind AlGaN metal-semiconductor-metal photodetectors. Electron. Lett. **36**, 1866–1867 (2000)
86. M. Brendel, M. Helbling, A. Knauer, S. Einfeldt, A. Knigge, M. Weyers, Top- and bottom-illumination of solar-blind AlGaN metal-semiconductor-metal photodetectors. Phys. Status Solidi (A) (2015)
87. F. Xie, H. Lu, D. Chen, X. Ji, F. Yan, R. Zhang, Y. Zheng, L. Li, J. Zhou, Ultra-low dark current AlGaN-based solar-blind metal-semiconductor-metal photodetectors for high-temperature applications. IEEE Sens. J. **12**, 2086–2090 (2012)
88. J. Li, Z.Y. Fan, R. Dahal, M.L. Nakarmi, J.Y. Lin, H.X. Jiang, 200 nm deep ultraviolet photodetectors based on AlN. Appl. Phys. Lett. **89**(21) (2006)
89. A. Knigge, M. Brendel, F. Brunner, S. Einfeldt, A. Knauer, V. Kueller, M. Weyers, AlGaN photodetectors for the UV-C spectral region on planar and epitaxial laterally overgrown AlN/sapphire templates. Phys. Status Solidi (C) **10**(3), 294–297 (2013)
90. M. Brendel, A. Knigge, F. Brunner, S. Einfeldt, A. Knauer, V. Kueller, U. Zeimer, M. Weyers, Anisotropic responsivity of AlGaN metalsemiconductormetal photodetectors on epitaxial laterally overgrown AlN/sapphire templates. J. Electron. Mater. **43**(4), 833–837 (2014)
91. M. Asif Khan, J.N. Kuznia, D.T. Olson, M. Blasingame, A.R. Bhattarai, Schottky barrier photodetector based on Mg-doped p-type GaN films. Appl. Phys. Lett. **63**(18), 2455–2456 (1993)
92. A.C. Schmitz, A.T. Ping, M.A. Khan, Q. Chen, J.W. Yang, I. Adesida, Schottky barrier properties of various metals on n-type GaN. Semicond. Sci. Technol. **11**(10), 1464 (1996)
93. Q. Chen, J.W. Yang, A. Osinsky, S. Gangopadhyay, B. Lim, M.Z. Anwar, M. Asif Khan, D. Kuksenkov, H. Temkin, Schottky barrier detectors on GaN for visible-blind ultraviolet detection. Appl. Phys. Lett. **70**(17), 2277–2279 (1997)
94. T. Hashizume, J. Kotani, H. Hasegawa, Leakage mechanism in GaN and AlGaN schottky interfaces. Appl. Phys. Lett. **84**(24), 4884–4886 (2004)
95. K.Y. Park, B.J. Kwon, Y.-H. Cho, S.A. Lee, J.H. Son, Growth and characteristics of Ni-based schottky-type $Al_xGa_{1-x}N$ ultraviolet photodetectors with AlGaN/GaN superlattices. J. Appl. Phys. **98**(12) (2005)
96. H. Miyake, H. Yasukawa, Y. Kida, K. Ohta, Y. Shibata, A. Motogaito, K. Hiramatsu, Y. Ohuchi, K. Tadatomo, Y. Hamamura, K. Fukui, High performance schottky UV detectors (265–100 nm) using n-$Al_{0.5}Ga_{0.5}N$ on AlN epitaxial layer. Phys. Status Solidi (A) **200**(1), 151–154 (2003)

97. R. Dahal, T.M. Al Tahtamouni, Z.Y. Fan, J.Y. Lin, H.X. Jiang, Hybrid AlN/SiC deep ultraviolet schottky barrier photodetectors. Appl. Phys. Lett. **90**(26) (2007)
98. C.J. Collins, T. Li, A.L. Beck, R.D. Dupuis, J.C. Campbell, J.C. Carrano, M.J. Schurman, I. A. Ferguson, Improved device performance using a semi-transparent p-contact AlGaN/GaN heterojunction positive-intrinsic-negative photodiode. Appl. Phys. Lett. **75**(14), 2138–2140 (1999)
99. C. Pernot, A. Hirano, M. Iwaya, T. Detchprohm, H. Amano, I. Akasaki, Solar-blind UV photodetectors based on GaN/AlGaN p-i-n photodiodes. Jpn. J. Appl. Phys. **39**(5A), L387 (2000)
100. T. Li, A.L. Beck, C. Collins, R.D. Dupuis, J.C. Campbell, J.C. Carrano, M.J. Schurman, I.A. Ferguson, Improved ultraviolet quantum efficiency using a semitransparent recessed window AlGaN/GaN heterojunction p-i-n photodiode. Appl. Phys. Lett. **75**(16), 2421–2423 (1999)
101. W. Yang, T. Nohova, S. Krishnankutty, R. Torreano, S. McPherson, H. Marsh, Back-illuminated GaN/AlGaN heterojunction photodiodes with high quantum efficiency and low noise. Appl. Phys. Lett. **73**(8), 1086–1088 (1998)
102. U. Chowdhury, M.M. Wong, C.J. Collins, B. Yang, J.C. Denyszyn, J.C. Campbell, R.D. Dupuis, High-performance solar-blind photodetector using an $Al_{0.6}Ga_{0.4}N$ n-type window layer. J. Cryst. Growth **248**(0), 552–555 (2003). (Proceedings of the eleventh international conference on Metalorga nic Vapor Phase Epitaxy)
103. D.J.H. Lambert, M.M. Wong, U. Chowdhury, C. Collins, T. Li, H.K. Kwon, B.S. Shelton, T. G. Zhu, J.C. Campbell, R.D. Dupuis, Back illuminated AlGaN solar-blind photodetectors. Appl. Phys. Lett. **77**(12), 1900–1902 (2000)
104. E. Cicek, R. McClintock, C.Y. Cho, B. Rahnema, M. Razeghi, $Al_xGa_{1-x}N$-based back-illuminated solar-blind photodetectors with external quantum efficiency of 89 %. Appl. Phys. Lett. **103**(19) (2013)
105. C.J. Collins, U. Chowdhury, M.M. Wong, B. Yang, A.L. Beck, R.D. Dupuis, J.C. Campbell, Improved solar-blind detectivity using an $Al_xGa_{1-x}N$ heterojunction p-i-n photodiode. Appl. Phys. Lett. **80**(20), 3754–3756 (2002)
106. N. Biyikli, I. Kimukin, O. Aytur, E. Ozbay, Solar-blind AlGaN-based p-i-n photodiodes with low dark current and high detectivity. IEEE Photonics Technol. Lett. **16**, 1718–1720 (2004)
107. H. Jiang, T. Egawa, Low-dark-current high-performance AlGaN solar-blind pin photodiodes. Jpn. J. Appl. Phys. **47**(3R), 1541 (2008)
108. A. Hirano, C. Pernot, M. Iwaya, T. Detchprohm, H. Amano, I. Akasaki, Demonstration of flame detection in room light background by solar-blind AlGaN pin photodiode. Phys. Status Solidi (A) **188**(1), 293–296 (2001)
109. J. Kuek, D. Pulfrey, B. Nener, J. Dell, G. Parish, U. Mishra, Effects of polarisation on solar-blind AlGaN UV photodiodes. In Proceedings conference on optoelectronic and microelectronic materials and devices, 2000. COMMAD 2000 (2000), pp. 459–462
110. F. Xie, H. Lu, D. Chen, X. Xiu, H. Zhao, R. Zhang, Y. Zheng, Metal-semiconductor-metal ultraviolet avalanche photodiodes fabricated on bulk GaN substrate. IEEE Electron Device Lett. **32**, 1260–1262 (2011)
111. S.-C. Shen, Y. Zhang, D. Yoo, J.-B. Limb, J.-H. Ryou, P. Yoder, R.D. Dupuis, Performance of deep ultraviolet GaN avalanche photodiodes grown by mocvd. IEEE Photonics Technol. Lett. **19**, 1744–1746 (2007)
112. T. Tut, M. Gokkavas, A. Inal, E. Ozbay, $Al_xGa_{1-x}N$-based avalanche photodiodes with high reproducible avalanche gain. Appl. Phys. Lett. **90**(16) (2007)
113. R.D. Dupuis, J.-H. Ryou, S.-C. Shen, P.D. Yoder, Y. Zhang, H.J. Kim, S. Choi, Z. Lochner, Growth and fabrication of high-performance GaN-based ultraviolet avalanche photodiodes. J. Cryst. Growth **310**(23), 5217–5222 (2008). (The Fourteenth International conference on Metalorganic Vapor Phase Epitax The 14th International conference on Metalorganic Vapor Phase Epitaxy)
114. J.L. Pau, C. Bayram, R. McClintock, M. Razeghi, D. Silversmith, Back-illuminated separate absorption and multiplication GaN avalanche photodiodes. Appl. Phys. Lett. **92**(10) (2008)

115. Y. Huang, D.J. Chen, H. Lu, K.X. Dong, R. Zhang, Y.D. Zheng, L. Li, Z.H. Li, Back-illuminated separate absorption and multiplication AlGaN solar-blind avalanche photodiodes. Appl. Phys. Lett. **101**(25) (2012)
116. R. Mcintyre, On the avalanche initiation probability of avalanche diodes above the breakdown voltage. IEEE Trans. Electron Devices **20**, 637–641 (1973)
117. K.A. McIntosh, R.J. Molnar, L.J. Mahoney, K.M. Molvar, N. Efremow, S. Verghese, Ultraviolet photon counting with GaN avalanche photodiodes. Appl. Phys. Lett. **76**(26), 3938–3940 (2000)
118. R. McClintock, A. Yasan, K. Minder, P. Kung, M. Razeghi, Avalanche multiplication in AlGaN based solar-blind photodetectors. Appl. Phys. Lett. **87**(24) (2005)
119. Z.G. Shao, D.J. Chen, H. Lu, R. Zhang, D.P. Cao, W.J. Luo, Y.D. Zheng, L. Li, Z.H. Li, High-gain AlGaN solar-blind avalanche photodiodes. IEEE Electron Device Lett. **35**, 372–374 (2014)
120. S. Verghese, K.A. McIntosh, R. Molnar, L.J. Mahoney, R. Aggarwal, M. Geis, K. Molvar, E. Duerr, I. Melngailis, GaN avalanche photodiodes operating in linear-gain mode and geiger mode. IEEE Trans. Electron Devices **48**, 502–511 (2001)
121. K.X. Dong, D.J. Chen, H. Lu, B. Liu, P. Han, R. Zhang, Y.D. Zheng, Exploitation of polarization in back-illuminated AlGaN avalanche photodiodes. IEEE Photonics Technol. Lett. **25**, 1510–1513 (2013)
122. M. Eyckeler, W. Mönch, T.U. Kampen, R. Dimitrov, O. Ambacher, M. Stutzmann, Negative electron affinity of cesiated p-GaN(0001) surfaces. J. Vac. Sci. Technol., B **16**(4), 2224–2228 (1998)
123. C.I. Wu, A. Kahn, Electronic states and effective negative electron affinity at cesiated p-GaN surfaces. J. Appl. Phys. **86**(6), 3209–3212 (1999)
124. F. Machuca, Z. Liu, Y. Sun, P. Pianetta, W.E. Spicer, R.F.W. Pease, Oxygen species in Cs/O activated gallium nitride (GaN) negative electron affinity photocathodes. J. Vac. Sci. Technol., B **21**(4), 1863–1869 (2003)
125. O. Siegmund, J. Vallerga, J. McPhate, J. Malloy, A. Tremsin, A. Martin, M. Ulmer, B. Wessels, Development of GaN photocathodes for UV detectors. Nucl. Instrum. Methods Phys. Res. Sect. A: Accelerators, Spectrometers, Detectors Associated Equipment **567**(1), 89–92 (2006). (Proceedings of the 4th international conference on new developments in photodetection BEAUNE 2005 fourth international conference on new developments in photodetection)
126. F. Shahedipour, M. Ulmer, B. Wessels, C. Joseph, T. Nihashi, Efficient GaN photocathodes for low-level ultraviolet signal detection. IEEE J. Quant. Electron. **38**, 333–335 (2002)
127. M.C. Benjamin, C. Wang, R.F. Davis, R.J. Nemanich, Observation of a negative electron affinity for heteroepitaxial AlN on α(6 h)-SiC(0001). Appl. Phys. Lett. **64**(24), 3288–3290 (1994)
128. C. Wu, A. Kahn, Negative electron affinity and electron emission at cesiated GaN and AlN surfaces. Appl. Surf. Sci. **162–163**, 250–255 (2000)
129. S. Uchiyama, Y. Takagi, M. Niigaki, H. Kan, H. Kondoh, GaN-based photocathodes with extremely high quantum efficiency. Appl. Phys. Lett. **86**(10) (2005)
130. J. Brown, J. Matthews, S. Harney, J. Boney, J. Schetzina, J. Benson, K. Dang, T. Nohava, W. Yang, S. Krishnankutty, High-sensitivity visible-blind AlGaN photodiodes and photodiode arrays. MRS Proc. **595**, 1 (1999)
131. J. Brown, J. Matthews, S. Harney, J. Boney, J. Schetzina, J. Benson, K. Dang, T. Nohava, W. Yang, S. Krishnankutty, Visible-blind UV digital camera based on a 32x32 array of GaN/AlGaN p-i-n photodiodes. MRS Internet J. Nitride Semicond. **4** (1999)
132. Status of AlGaN based focal plane arrays for UV solar blind detection **5964** (2005)
133. G. Mazzeo, J.-L. Reverchon, J. Duboz, A. Dussaigne, AlGaN-based linear array for UV solar-blind imaging from 240 to 280 nm. IEEE Sens. J. **6**, 957–963 (2006)
134. P.E. Malinowski, J.-Y. Duboz, P. De Moor, J. John, K. Minoglou, P. Srivastava, H. Abdul, M. Patel, H. Osman, F. Semond, E. Frayssinet, J.-F. Hochedez, B. Giordanengo, C. Van

Hoof, R. Mertens, Backside illuminated AlGaN-on-Si UV detectors integrated by high density flip-chip bonding. Physica Status Solidi (C) **8**(7–8), 2476–2478 (2011)
135. E. Cicek, R. McClintock, C. Cho, B. Rahnema, M. Razeghi, $Al_xGa_{1-x}N$-based solar-blind ultraviolet photodetector based on lateral epitaxial overgrowth of AlN on Si substrate. Appl. Phys. Lett. **103**(18), 181113 (2013)
136. K.C. Kim, Y.M. Sung, I.H. Lee, C.R. Lee, M.D. Kim, Y. Park, T.G. Kim, Visible-blind ultraviolet imagers consisting of 8 × 8 AlGaN p-i-n photodiode arrays. J. Vac. Sci. Technol., A **24**(3), 641–644 (2006)
137. J. Long, S. Varadaraajan, J. Matthews, J. Schetzina, UV detectors and focal plane array imagers based on AlGaN p-i-n photodiodes. Opto-Electron. Rev. **10**(4), 251–260 (2002)
138. R. McClintock, K. Mayes, A. Yasan, D. Shiell, P. Kung, M. Razeghi, 320x256 solar-blind focal plane arrays based on $Al_xGa_{1-x}N$. Appl. Phys. Lett. **86**(1) (2005)
139. First demonstration and performance of AlGaN based focal plane array for deep-UV imaging **7474** (2009)
140. E. Cicek, Z. Vashaei, E.K.-W. Huang, R. McClintock, M. Razeghi, $Al_xGa_{1-x}N$-based deep-ultraviolet 320 × 256 focal plane array. Opt. Lett. **37**(5), 896–898 (2012)
141. E. Cicek, R. McClintock, Z. Vashaei, Y. Zhang, S. Gautier, C.Y. Cho, M. Razeghi, Crack-free AlGaN for solar-blind focal plane arrays through reduced area epitaxy. Appl. Phys. Lett. **102**(5) (2013)
142. E. Michael, N. C. J, III-V direct-bandgap semiconductor optical filter. 11 (1981)
143. H.M. Manasevit, Epitaxial composite and method of making. 1 (1983)
144. K.M. ASIF, S.R.G, and S.R.A, UV detector and method for fabricating it. 4 (1986)
145. K.M. Asif [US], S.R.G [US], S.R.A [US], Tunable cut-off UV detector based on the aluminum gallium nitride material system. 9 (1986)
146. K.M. Asif [US], S.R. G [US], UV photocathode using negative electron affinity effect in $Al_xGa_{1-x}N$. 10 (1986)
147. S.W.H [US], Interference filter design using flip-flop optimization. 5 (1987)
148. H. Kai-Feng [CN], J.J.L [US], M.J.S. L [US], T. Kuochou [US], Quantum well vertical cavity laser. 3 (1991)
149. I. Toshihide [JP], O. Yasuo [JP], H. Ako [JP], Semiconductor light-emitting diode and method of manufacturing the same. 4 (1991)
150. L. Sergey [US], X. Ya-Hong [US], Vertical cavity semiconductor laser with lattice-mismatched mirror stack. 4 (1991)
151. K.P. C [AU], Current injection laser. 9 (1991)
152. S.J. Hwan, Semiconductor element for detecting ultraviolet rays at constant reliability and manufacturing method thereof. 12 (2004)
153. N. Katsuhiko, T. Toshiyuki, Ultraviolet ray detector. 5 (2006)
154. S. Charles [HK], Ultraviolet detector. 12 (2006)
155. W. Tilman [DE], T. Christoph [DE], L. Stefan [DE], H. Oliver [DE], K. H. Georg [DE], S. Sebastian [DE], S. Stephan [DE], Semiconductor component, electronic component, sensor system and method for producing a semiconductor component. 8 (2002)
156. S. Mayo [JP], T. Kohsuke [JP], G. Shunsuke [JP], K. Yasube [JP], E. Haruyuki [JP], H. Tatsuo [JP], I. Fukunori [JP], O. Eriko [JP], Photovoltaic ultraviolet sensor. 6 (2007)
157. K. Satoshi [JP], A. Hiroshi [JP], Nitride semiconductor substrate production method thereof and semiconductor optical device using the same. 2 (2005)
158. S.R. P [US], S.S. T [US], P.J. W [US], Dielectric passivation for semiconductor devices. 11 (2005)
159. J.M. Van Hove, J.N. Kuznia, D.T. Olson, M.A. Khan, M.C. Blasingame, High responsivity ultraviolet gallium nitride detector. 12 (1993)
160. T. Tadao, Semiconductor optical sensor. 6 (2000)
161. C. Qisheng [US], Schottky barrier detectors for visible-blind ultraviolet detection. 8 (2000)
162. D.M. Philip [US], E.N. Andrea [US], C. Kanin [US], Homoepitaxial gallium nitride based photodetector and method of producing. 2 (2005)

163. S. Katsumi [JP], I. Masayuki [JP], Y. Takafumi [JP], Backside-illuminated photodiode array, method for manufacturing same, and semiconductor device. 8 (2005)
164. H. Hikari, K. Satoshi, A. Hiroshi, A. Isamu, GaN-based compound semiconductor light receiving element. 9 (2005)
165. O. Ryota, D. Toru, Photoelectric conversion element, and its manufacturing method. 3 (2008)
166. F. Junichi [JP], O. Daisuke [JP], M. Kikuo [JP], N. Kenichi [JP], O. Keishi [JP], Photodiode, optical communication device, and optical interconnection module. 6 (2008)
167. K.K. Hamamatsu Photonics, Hamamatsu develops a new, highly sensitive GaN photocathode for UV detection (2010)
168. K.K. Hamamatsu Photonics, Photocathode technology (2014)
169. Y.-H. Lai, W.-Y. Cheung, S.-K. Lok, G. K. L. Wong, S.-K. Ho, K.-W. Tam, I.-K. Sou, Rocksalt mgs solar blind ultra-violet detectors. AIP Adv. **2**(1) (2012)
170. S.I. Keong [CN], L.Y. Hoi [CN], L.S. Kin [CN], C.W. Yip [CN], W.G.K. Lun [CN], T.K. Weng [CN], H.S. Kam [CN], Mgs solar-blind UV radiation detector. 12 (2012)
171. F. Junichi [JP], N. Takahiro [JP]
172. Jenoptik Polymer Systems GmbH, Data sheet epd-440-0-1.4 (2014)
173. K.K. Hamamatsu Photonics, Data sheet r759 (2014)
174. sglux GmbH, Data sheet tw30sx (2014)
175. J. Sun, F.-J. Liu, H.-Q. Huang, J.-W. Zhao, Z.-F. Hu, X.-Q. Zhang, Y.-S. Wang, Fast response ultraviolet photoconductive detectors based on Ga-doped ZnO films grown by radio-frequency magnetron sputtering. Appl. Surf. Sci. **257**(3), 921–924 (2010)
176. D.K. Wickenden, Z. Huang, D.B. Mott, P.K. Shu, Development of gallium nitride photoconductive detectors. Johns Hopkins APL Technical Digist **18**(2) (1997)
177. ITME - Institute of Electronic Materials Technology Poland, Catalog of 2010 (2010)
178. IL-Metronic Sensortechnik GmbH, Data sheet UVD 370 (2014)
179. Jenoptik Polymer Systems GmbH, Prototype data sheet epd-260-1.0 (2014)
180. Genicom, Data sheet GUVC-T10GD-L (2014)
181. L. Jian-Fei, H. Ze-Qiang, Z. Wen-Le, J. Hao, Large active area AlGaN solar-blind schottky avalanche photodiodes with high multiplication gain. Chin. Phys. Lett. **30**(3), 037803 (2013)
182. Jenoptik Polymer Systems GmbH, Data sheet epd-270-0-0.3-1 (2014)
183. IFW Optronics, Data sheet jec 1c (2014)

Chapter 10
Ultraviolet Light-Emitting Diodes for Water Disinfection

Martina A. Lange, Tim Kolbe and Martin Jekel

Abstract This chapter presents basic principles of water disinfection using UV light. It provides a comparison of conventional UV light sources and UV LEDs. Additionally, based on a detailed case study, the potential of UV LEDs for water disinfection systems is discussed. This study presents results of static and flow-through tests conducted with UV LEDs of different emission wavelengths.

10.1 Introduction

In the modern world, more than ever, potable water quality is an issue of global concern, particularly with regard to health care and health protection. This is reflected above all in the fact that 2.2 million people die every year from diarrhea associated with pathogens transmitted by drinking water [52].

As a measure to reduce the risk of infections associated with high levels of microorganisms, water disinfection methods have been developed using physical or chemical disinfection techniques [23].

A proven physical disinfection method in drinking water purification is the use of ultraviolet (UV) light with wavelengths between approximately 200–300 nm to inactivate microorganisms [5, 17]. The wavelength of the applied UV light depends on the implemented UV emitter. Conventionally low- and medium-pressure mercury

M.A. Lange · M. Jekel
Technische Universität Berlin, Fachgebiet Wasserreinhaltung,
Sekr. KF4, Straße des 17 Juni 135, 10623 Berlin, Germany
e-mail: marlange@posteo.de

M. Jekel
e-mail: martin.jekel@tu-berlin.de

T. Kolbe (✉)
Ferdinand-Braun-Institut, Leibniz-Institut für Höchstfrequenztechnik,
Gustav-Kirchhoff-Straße 4, 12489 Berlin, Germany
e-mail: tim.kolbe@fbh-berlin.de

© Springer International Publishing Switzerland 2016

M. Kneissl and J. Rass (eds.), *III-Nitride Ultraviolet Emitters*,
Springer Series in Materials Science 227, DOI 10.1007/978-3-319-24100-5_10

lamps are used; their application for water disinfection of stationary water systems is well investigated (e.g., [3, 27, 32]). More recently, UV light-emitting diodes (LEDs)—for which the emitted wavelength can be adjusted to the target wavelength—are of great interest for water disinfection.

Compared to other techniques, UV disinfection is relatively inexpensive with low capital and operating costs. A UV reactor has a low weight, small footprint and is easy to operate [5]. Owing to these properties, UV disinfection is a promising technique to ensure safe potable water quality. However, UV disinfection is highly dependent on electrical power, since no UV light is produced during power supply interruptions. Moreover, some microorganisms are able to reactivate after UV exposure (cp., e.g., review of [22]). Finally, UV light has no residual disinfection capacity and regrowth may deteriorate water quality after UV disinfection [5].

In water purification applications, particularly in discontinuously operated, decentralized, and mobile water systems, UV LEDs have some advantages compared to conventional UV emitters: LEDs do not contain mercury and the overall system architecture does not need counteractive measures for the breakage of a mercury UV lamp during operation which may contaminate the water, nor is a disposal problem given. LEDs have a compact and robust design without glass or filaments and are therefore more durable in transit and during handling. LEDs have low electrical power requirements and need lower voltages than conventional mercury lamps therefore offering the option to be operated with solar cells or rechargeable batteries. They are more suitable for just-in-time applications because no warm-up time is needed and high frequencies of activation and deactivation are possible without reducing their efficiency [10, 48]. However, at this state of development, UV LEDs suffer from high costs, low output powers, and high initial degradation [32, 53].

10.2 Basic Principles of UV Disinfection

Based on the ability of UV light—produced from conventional or innovative light sources—to function as a broad-spectrum antimicrobial agent with short contact times and minimal disinfection by-product formation, it is a viable alternative to chemical disinfectants. UV light at the proper *wavelength* and *fluence* inactivates microorganisms [20] by disrupting their DNA or RNA, rendering them unable to reproduce.

Wavelength In water purification, wavelengths below 230 nm are absorbed by water molecules. Therefore only UV wavelengths between 230 and 300 nm are available for disinfection. Within this wavelength range, DNA and RNA are the components of microorganisms, which mostly absorb UV light. Proteins, which also absorb UV light, need high fluences at wavelengths below 230 nm (not applied in water disinfection) to be destroyed. Therefore disinfection is mainly achieved by DNA/RNA disruption (e.g., [3, 17, 21, 27]).

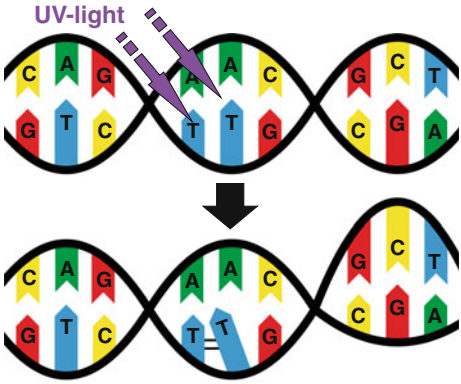


Fig. 10.1 Disruption of DNA structure caused by UV-light-induced thymine dimer formation (*A* adenine, *G* guanine, *T* thymine, *C* cytosine)

DNA and RNA are built up by nucleotides forming polynucleotides. These nucleotides are composed of a backbone made of alternating sugars and phosphate groups; and nucleobases—guanine (G), adenine (A), thymine (T) or uracil in RNA, and cytosine (C)—attached to the sugars. The specific sequence of the DNA/RNA is determined by the order of the nucleobases [31].

UV light is absorbed by all nucleobases. However, UV light may induce dimerization of adjacent thymine/uracil bases causing a chemical bond between these bases (cp. Fig. 10.1). These dimers disrupt the structure of the DNA/RNA and above a critical number of dimers impede the DNA/RNA replication. The microorganism may still be metabolically active, but infections are prevented since reproduction is hindered [5].

Maximum UV light absorption through DNA is typically reached at a wavelength of around 260 nm, but the peak wavelength distribution depends on the target organism [5, 11, 15]. For example *Bacillus subtilis* spores—which are often applied as surrogate organism for protozoan oocysts [22] and in UV reactor certification [17, 38, 47]—have two absorption maxima: one below 240 nm and one around 270 nm [7, 11, 33]. Chen et al. [11] also demonstrated that *B. subtilis* spores have similar fluence–inactivation response curves for 254 and 279 nm wavelengths (cp. Fig. 10.2).[1]

Fluence The term fluence is used in UV disinfection to describe the applied UV "dose". Dose is a term that relates to the total absorbed energy. Since microorganisms only absorb a few percent of the UV light, while the rest of the light passes through the organism, the term *fluence* is more appropriate for UV disinfection than the term dose. Fluence relates to the incident UV energy, rather than the absorbed UV energy [5].

Fluence (J/m^2) is defined as the total amount of radiant energy from all directions passing through an infinitesimally small sphere of cross-sectional area (dA) divided

[1]The same fluence is needed at both wavelengths to obtain a comparable inactivation result.

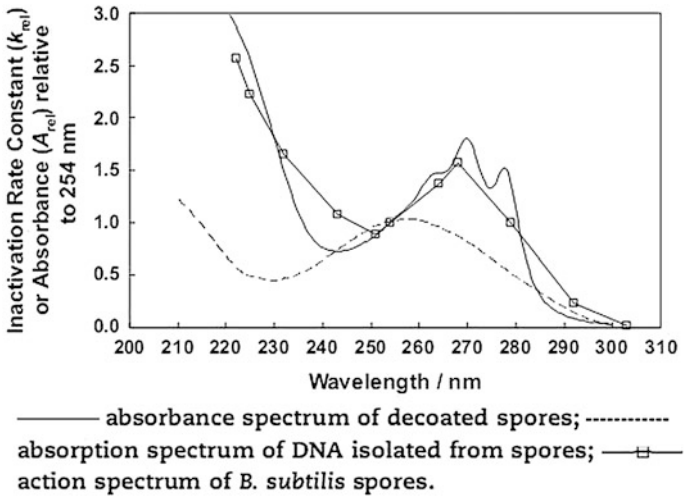


Fig. 10.2 Inactivation rate constant (k) (cp. Sect. 10.3.2.2) of decoated *B. subtilis* spores, DNA isolated from *B. subtilis* spores, and *B. subtilis* spores at different wavelengths [11]

by dA. It is calculated as the product of incident irradiance (or fluence rate) (W/m^2) and exposure time (s) (10.1) [6]:

$$H_0 = E_0 \cdot t \tag{10.1}$$

H_0 fluence (J/m^2)
E_0 incident irradiance (W/m^2)
t exposure time (s).

Irradiance is the appropriate term when a surface is irradiated by UV light coming from all directions above the surface. In a well-designed bench-scale setup—as e.g., a "collimated beam device" (CBD) which delivers a highly uniform beam of UV light to a water sample in a Petri dish—the fluence rate and the irradiance are nearly the same. Fluence rate, instead of irradiance or intensity, is the appropriate term for UV disinfection in a UV reactor, since UV light can penetrate the microorganism from any direction [4]. The fluence rate then is the radiant power passing from all directions through an infinitesimally small sphere of cross-sectional area dA divided by dA (SI unit: W/m^2) [6].

To achieve an optimum disinfection, it is crucial to accurately determine the fluence. Since various factors have been found to have an impact on the applied fluence in UV reactors, it is important to understand these factors (cp. Sect. 10.2.1) and use appropriate modeling and validation tools for UV reactor performance (cp. Sect. 10.2.2), taking these influencing factors into account.

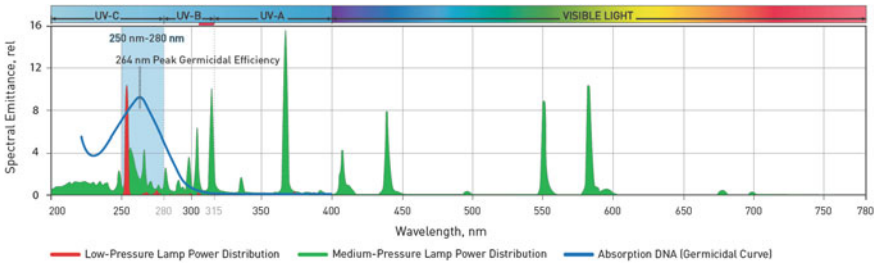


Fig. 10.3 Emission spectra of a typical low-pressure and a medium-pressure UV lamp (Copyrighted work of Pentair Aquatic Eco-Systems, Inc. Used by permission of owner. All rights reserved.)

10.2.1 Factors Influencing UV Fluence

A great deal of research has been undertaken to investigate the factors impacting on UV fluence. Researchers have found that factors like lamp performance, water quality, and exposure time influence the delivered fluence (cp., e.g. [8, 9, 46]).

Lamp Performance Various wavelengths are emitted, depending on the UV light source (cp. Fig. 10.3). Conventionally, UV light is generated from mercury-vapor lamps. Low-pressure (LP) and low-pressure high output (LPHO) lamps emit nearly monochromatic UV light at a wavelength of 254 nm, whereas medium-pressure lamps emit a polychromatic spectrum with various wavelengths [5].

Low-pressure mercury lamps have a higher germicidal efficiency, but lower output powers. They are therefore more suitable for smaller applications. The optimum operation temperature of their lamp bulbs is commonly 40 °C. With increasing or decreasing temperatures, the lamp performance is reduced [5].

Medium-pressure lamps have a lower germicidal efficiency, however, they are installed in applications with high flow rates because they have higher output powers and a smaller number of lamps are needed, thus reducing maintenance costs. They operate at temperatures between 600 to 900 °C and are therefore less sensitive to temperature changes [5].

A relatively new method to generate UV light is by means of LEDs [48]. UV LEDs offer the possibility to apply the optimal disinfection wavelength of targeted microorganisms by manipulating the base materials/composition of the alloy (aluminum gallium nitride, AlGaN), instead of using the 254 nm wavelength emitted by low-pressure mercury lamps [48].

However, at this state of development UV LEDs suffer from low output powers and high initial degradation. Even the best UV LEDs exhibit external quantum efficiencies[2] of around 10 % [42].[3] The reasons for the initial degradation are not

[2]External quantum efficiencies: number of photons emitted into free space per second divided by the number of electrons injected into LED per second.

[3]Typical external quantum efficiencies of LEDs used for lightning applications are in the range of 60–70 % [34].

completely understood but most likely related to high defect densities[4] in the AlGaN materials [26]. Several researchers predict a high physical improvement potential for UV LEDs with regard to the reduction of defect densities and the increase of the output efficiency by increasing the heat extraction [1, 24, 25]. For example, Adivarahan et al. [1] presented an output power of 42 mW for a 4 × 4 LED array lamp (approximately 2.6 mW/LED)[5] emitting at 280 nm.

Since the performance of the UV light source changes over its life time, lamp performance is monitored using a UV sensor. This sensor measures the irradiance at a specific position in the UV reactor. The result of the measurement depends on the UV lamp output, the transmittance of the sensor window, the transmittance of the quartz sleeve, and the transmittance of the water. Besides having a direct impact on the transmittance of UV light, the water quality may also influence the transmittance of the sensor window and quartz sleeve by scaling (or inorganic fouling). Temperature induced scaling is more relevant for conventional mercury lamp UV emitters (due to their higher surface temperatures) than for UV LEDs. However, temperature-independent scaling processes may also affect UV LEDs. The water quality therefore has a significant impact on the disinfection result [6].

Physicochemical Water Quality The presence of dissolved and fine-dispersed water constituents absorbing UV light—measured using the spectral absorption coefficient (a) of the filtered and unfiltered water at the target wavelength (conventionally 254 nm)—reduces the UV light available for microorganism inactivation. It is therefore an important design criterion for UV disinfection. The UV transmittance[6] (UVT) can be calculated from the spectral absorption coefficient [5]:

$$\mathrm{UVT_{cm}} = 100 \times 10^{-a \cdot 0.01\,\mathrm{m}} \tag{10.2}$$

Suspended particles causing turbidity may affect UV disinfection by scattering or absorbing UV light or by shielding microorganisms from UV irradiation. Scattering only redirects UV light and the impact on UV disinfection is minimal, whereas absorption and shielding reduces the UV disinfection efficiency [8, 9, 46].

Scaling deposits on the UV light source reduce the irradiation passing through the scaling layer, reducing the UV light available for microorganism inactivation. Especially iron and manganese and also calcium may scale the quartz sleeve [29, 43, 49]. To restore the transmittance of the sleeve, regular, manual cleaning or cleaning using automatic devices is necessary. It was reported that mechanical cleaning devices were effective in removing scaling deposits [37]. However, it was also reported that mechanical cleaning devices may scratch the surface of the quartz

[4]Defect density: number of local faults originating from the production of semiconductors per surface unit.

[5]For comparison: the 282 nm LEDs applied during this study had an output power of 0.65 mW at 20 mA.

[6]$\mathrm{UVT_{cm}}$ (%): percent transmittance in the medium when the path length is 1 cm and the wavelength is 254 nm; a (1/m): spectral absorption coefficient at a specific wavelength; relates to a 1 m path length.

sleeve, promoting irreversible scaling [39]. Balancing the need for restoring UV transmittance by cleaning and the impact of irreversible scaling may limit the frequency of mechanical cleaning [50]. Since there are no methods available to predict the scaling potential of water [49], pilot testing using the target water was recommended [47, 50].

Exposure Time In contrast to collimated beam devices (CBDs) or chemical disinfection systems, the exposure time of a microorganism in a flow-through UV reactor does not equal the time in which the sample is irradiated. Exposure time has to be derived from the flow rate and hydrodynamics in the UV reactor and can therefore not be monitored directly. Flow rate and hydrodynamics determine the specific path of an organism through the reactor and the time during which the organism is irradiated [3, 15]. On their way through the UV reactor some microorganisms receive more, some less than the average fluence, whereby the microorganisms receiving the lower fluence will determine the performance of the UV reactor [5].

Since the fluence applied on a microorganism in a UV reactor depends on these various factors, fluence calculation has to be carried out with care. The methodology implemented for modeling and validation of the UV reactor performance is described in the following section.

10.2.2 Modeling and Validation of UV Reactor Performance

The complex interplay of factors discussed above, which influence the UV disinfection performance in flow-through reactors, led to the development of a method to calibrate the expected performance of full-scale reactors using collimated beam devices (CBDs). This experimental method called biodosimetry was originally proposed by Qualls and Johnson [40]. It includes the following protocol:

In a first step the test suspension including the test organism is sequentially irradiated in a Petri dish. After every irradiation step, a sample is taken and the number of colony forming units (cfu) of the test organism is determined. By comparison of the number of cfu at the different irradiation steps, an inactivation–response curve is derived. In the second step, the inactivation of the applied test organism is determined in the full-scale UV reactor, varying water quality and flow rate. The determined inactivation rate is assigned according to the fluence obtained on bench-scale. This fluence is called the reduction equivalent fluence (REF). A detailed description of the procedure can be found in [6, 28, 45].

In addition to these extensive biodosimetric tests of UV disinfection reactors the REF can be determined using mathematical models[7] [41]. To calculate the REF with a mathematical model, it is necessary to know the path that a microorganism takes through the reactor and the distribution of the radiation in the UV reactor.

[7]The REF may also be determined using dyed microsphere actinometry cp. e.g., [3].

When the residence time of the organism and the fluence rate is known for every infinitesimally small element of the UV reactor, the fluence can be determined by integration along the path of the microorganism. The path of the microorganism is determined by modeling the momentum and mass transfer in the turbulent current. For the determination of the radiation distribution in the UV reactor varying models are used, which differ in their assumptions and restrictions. An often used calculation approach for UV reactors is the Point Source Summation (PSS) model. More details about turbulence and radiation distribution models are presented by [30].

To investigate UV disinfection on bench-scale for conventional mercury lamps, researchers have made considerable headway in standardizing experimental protocols. There are, for example, standards in Europe and the US that specify protocols for performing microorganism inactivation versus fluence for mercury-lamp-based measurements using, e.g., *B. subtilis* spores [18, 47]. However, a standardized protocol to test UV LEDs has not yet been proposed. An adaptation of the protocol for UV LEDs is needed because of the conventional design, whereby the water sample irradiated from the top down is not applicable to UV LEDs: Top-down methods need high power output sources to compensate for losses (e.g., absorption or scattering) between the UV light source and the water sample which cannot be provided by LEDs. According to Bolton and Linden [6], it is not necessary to completely standardize a bench-scale apparatus, but basic guidelines should be considered when designing a modified apparatus for a specific application. Among other aspects, the design has to ensure that the beam irradiating the water sample is reasonably uniform and the divergence is small enough to ensure accurate sensor readings. The fluence for all microorganisms in the suspension has to be kept equal by carefully controlled stirring without vortex [6].

10.3 Case Study

Over the past few years, various researchers have tested UV LEDs for water disinfection applications (cp., e.g. [2, 12, 14, 35, 36, 48, 51, 53]). These studies investigated LEDs with emission wavelengths between 255 and 405 nm. The experiments were mainly conducted in top-down irradiation geometry irradiating water sample volumes between 190 µl and 100 ml.

Most studies applied UV-sensitive microorganisms as *E. coli* as test organism due to the low output power and high costs of LEDs at this stage of development. In the following case study an experimental setup is presented that allows testing of less sensitive organisms as *B. subtilis* spores which are often used as organism in UV unit certification. Batch and flow-through tests are discussed for two different emission wavelengths of the LED array.

10.3.1 Proposal for an Experimental Setup to Test UV LEDs

Two UV LED disinfection modules were designed by the Institute of Solid State Physics in cooperation with the Chair of Water Quality Control of TU Berlin and constructed by the Ferdinand-Braun-Institut in order to perform biodosimetry trials with AlGaN-based UV LEDs emitting at 269 and 282 nm. LEDs were placed on the base of two different test modules to conduct static and flow-through tests. Module I was designed for static tests only. Module II was designed for static and flow-through tests. Schematic diagrams of the experimental setups are shown in Fig. 10.4 (a) static and (b) flow-through.

For static tests (Fig. 10.4a) a Petri dish with a diameter of 6 cm and a 2 mm thick Suprasil® base was placed on top of the UV LED array. The Suprasil® base allows over 90 % of the deep UV light to be transmitted. Homogeneous irradiation of the entire water volume was furthermore ensured by an electrically driven stirrer, installed at the top of the Petri dish. The output power of the LEDs was measured with a UV-sensitive silicon photodiode, ensuring constant irradiation during all microbiological tests.

For conducting flow-through tests (Fig. 10.4b) the Petri dish was replaced by a flow-through reactor. The flow-through reactor body was made of aluminum to increase UV reflection. 6 mm wide and 5 mm deep water channels were milled into the aluminum and the reactor body was then covered with a 2 mm thick Suprasil® window to enable UV exposure of the water channels. The test water flowed from the feed reservoir through the flow-through reactor and was collected in the catchment tank.

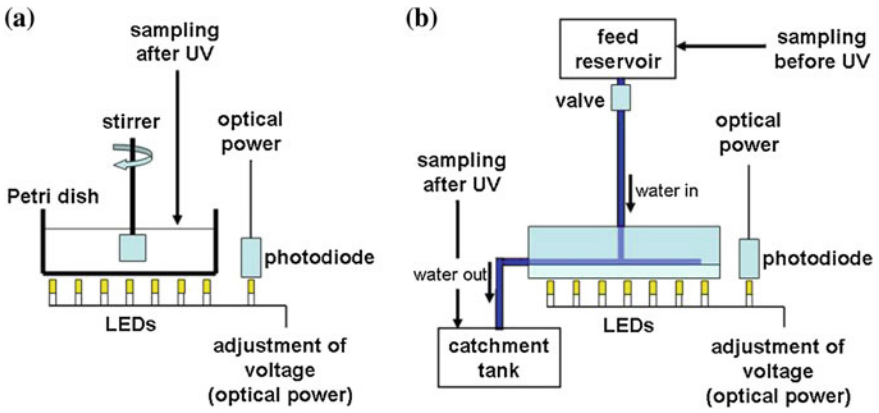


Fig. 10.4 Schematic diagram of the experimental setup for **a** static tests and **b** flow-through tests (according to [53])

The incident irradiance was calculated from (10.3) [6] (UV absorption by the Suprasil® window was neglected):

$$E_0 = \frac{P_{\mathrm{LED}}}{A_{\mathrm{petri}}} \cdot \#_{\mathrm{LED}} \tag{10.3}$$

E_0 incident irradiance (W/m^2)
P_{LED} power output of one LED (W)
A_{petri} area of irradiated Petri dish (m^2)
$\#_{\mathrm{LED}}$ number of active LEDs (–).

Test module I was only designed for static disinfection tests and equipped with 269 nm LEDs. Therefore 33 LEDs were arranged in a hexagonal grid of one LED/cm^2. Owing to the LED array design, only 28.5 of the LEDs were overlapping with the footprint of the Petri dish.

In test module II 35 LEDs with an emission wavelength of 282 nm were positioned in three concentric circles with diameters of 1.8, 3.5, and 5.2 cm. The LEDs were placed on the base of the water disinfection module at a distance of 1 cm in order to obtain a sufficiently high power density and a nearly homogeneous UV light distribution. This test unit was used in the static configuration (Fig. 10.5a) and with the flow-through reactor (Fig. 10.5b) with a maximum flow rate of ~12 ml/min.

A series of the applied UV LEDs was characterized in order to investigate the optimum operating conditions for the water disinfection modules. The module characteristics are summarized in Table 10.1.

LEDs were characterized with respect to their emission spectra, current–voltage and power–current properties, and their development of emission power over time, to select LEDs with similar characteristics.

Spectra were measured under continuous wave (cw) conditions at 20 mA with an optical fiber spectrometer. No variation in the peak wavelength was observed for the different 269 nm LEDs. UV LEDs emitting at 282 nm showed a difference less

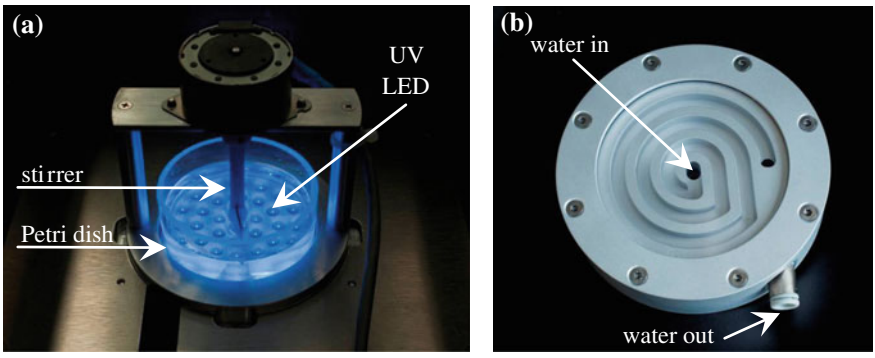


Fig. 10.5 Test module II; **a** LED array with stirrer unit; **b** flow-through reactor (according to [53])

Table 10.1 LED parameters (mean values) during stationary tests of the disinfection modules

Module	LED wavelength (nm)	LED output power (mW)	Number of LEDs	Number of active LEDs	LED configuration	Module output power (mW)
I	269	0.16	33	28.5	1/cm^2 (hexagonal grid)	4.56
II	282	0.19	35	35	3 circles	6.65

Module II was constructed to also perform flow-through tests (according to [53])

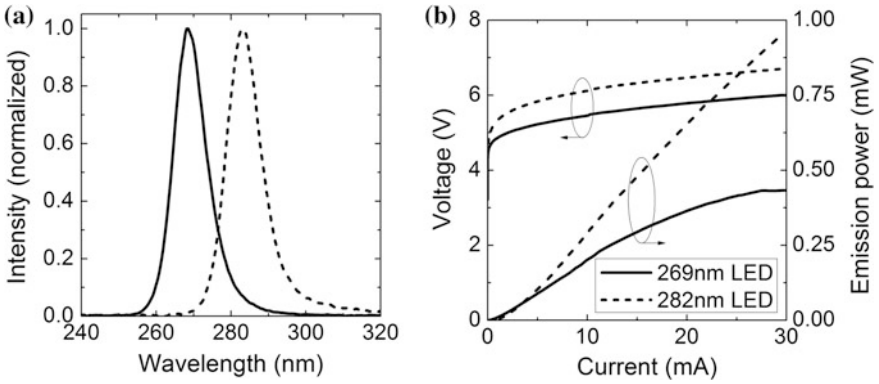


Fig. 10.6 Typical electrical and optical characteristics of 269 and 282 nm LEDs. **a** Emission spectra, **b** current–voltage and current–emission power characteristic

than 1 nm between different LEDs. A typical emission spectrum for both wavelengths is shown in Fig. 10.6a.

The current–voltage characteristics of the UV LEDs were measured at 20 mA under continuous wave (cw) conditions. All LEDs had very similar current–voltage characteristics with typical operating voltages around 5.8 V (269 nm LEDs) and 6.3 V (282 nm LEDs). All LEDs exhibited similar power–current characteristics. The emission power was measured using a calibrated silicon photodiode having a detector area of 100 mm^2. At a current of 20 mA an emission power of 0.33 mW was observed for the 269 nm LEDs and an emission power of 0.65 mW was observed for the 282 nm LEDs (cp. Fig. 10.6b).

The development of emission power over time was monitored for 269 and 282 nm LEDs. In both cases the emission power decreased by around 30–40 % after 100 h of operation at a constant current of 20 mA. The measurement of the current voltage characteristic showed only insignificant differences before and after 100 h of operation time for the 269 and 282 nm LEDs. Additionally, no changes in the emission spectra were observed over time. After the initial drop the emission power nearly stabilized at operating times longer than 100 h. Since maintaining a constant output power is crucial for a water disinfection module, the strong

degradation of the emission power requires active monitoring of the light output during testing and adjustment of the drive current in order to maintain a constant optical power density and fluence.

10.3.2 Test Conditions

10.3.2.1 Disinfection Tests Conducted with UV LEDs

A UV fluence–inactivation response curve of *B. subtilis* ATCC 6633 spores was generated with a laboratory apparatus especially designed for UV LEDs. The test organism was obtained from the Institute of Hygiene and Public Health (University of Bonn, Germany), where it was cultivated and characterized according to the German standard DVGW [18] with monochromatic low-pressure UV lamps [18].

For the exposure tests the applied test organism was suspended in the test water according to DVGW [18] to obtain a concentration of 10^6–10^7 cfu/ml. Tests were conducted at room temperature (23 ± 2 °C). They were performed with stationary samples of 30 ml, and exposed to decreasing fluences.

The fluence was corrected for UV absorbance considering the water factor as presented in (10.4),

$$H_0 = E_0 \cdot \mathrm{WF} \cdot t \tag{10.4}$$

H_0 fluence (J/m^2)
E_0 incident irradiance (W/m^2)
WF water factor (–)
t exposure time (s).

The water factor was derived from integrating the Beer–Lambert Law (10.6) over the sample depth of a completely mixed sample according to [6] as presented in (10.5):

$$\mathrm{WF} = \frac{1 - 10^{-a \cdot d}}{a \cdot d \cdot \ln(10)} \tag{10.5}$$

WF water factor (–)
a spectral absorption coefficient (1/m)
d depths of the suspension (m)
t exposure time (s).

Beer–Lambert Law is

$$a = \log \frac{E_0}{E_t} \tag{10.6}$$

a spectral absorption coefficient (1/m)
E_0 incident irradiance (W/m^2)
E_t transmitted irradiance (W/m^2).

To avoid contamination due to microorganism carryover, disinfection tests were conducted starting with the highest fluence.

During static tests with the 269 nm LEDs, samples of 1.5 ml were taken after 372, 248, 155, 62, and 0 s. Samples of the tests conducted with the 282 nm LEDs were taken after 255, 170, 106, 43, and 0 s to achieve comparable fluences (approx. 600, 400, 250, 100, 0 J/m^2).

Flow-through tests were performed with the 282 nm LEDs in a single pass operation mode. Different fluences were obtained by varying the flow rate and optical output power of the LEDs. Flow rates were chosen based on limitations of the module design and the available light output power from the UV LEDs resulting in laminar conditions. Table 10.2 summarizes the test conditions of the flow-through tests.

The experiments were performed based on DVGW [18] starting with the highest fluence. The following test protocol was applied:

1. initializing the system (adjustment of flow rate and UV power)
2. sampling in reservoir, before UV exposure
3. turning on UV light
4. starting flow, discarding five test cell volumes
5. sampling after UV exposure (after 1, 2, 3, and 4 min)
6. repeated sampling in feed reservoir, before UV exposure.

The concentration of *B. subtilis* spores determined before UV disinfection was calculated by averaging the test results of the samples taken from the reservoir prior to UV exposure.

Table 10.2 Test conditions applied during flow-through tests with 282 nm UV LEDs

Flow rate (ml/min)	Residence time (s)	LED power (mW)
10.8 ± 0.4	45.8	0.50; 0.70
7.8 ± 0.4	63.5	0.35; 0.49

10.3.2.2 Microbial Data Analysis

The inactivation of *B. subtilis* spores, presented as the decimal reduction factor (RF), was calculated based on (10.7)

$$\mathrm{RF} = \log \frac{N_0}{N} \tag{10.7}$$

RF decimal reduction factor
N_0 cfu concentration determined before UV
N cfu concentration determined after UV.

The RF was plotted against fluence to derive a fluence–inactivation relation. The fluence–inactivation response curve of *B. subtilis* spores can be described by three phases [22]: a shoulder phase, a log-linear phase, and a tailing phase. When low fluences are applied the RF changes only slightly with increasing fluence. Researchers attributed this phase to DNA repair or the requirement of several DNA damage sites [33, 44]. After an offset fluence, inactivation starts in a log-linear relationship, followed by an occasionally existing tailing phase, in which the RF again changes slowly with fluence. Causes for the tailing phase are still under discussion; possible causes could be microorganism clumping or association with particles, experimental bias or hydraulic effects [13]. This curve progression, not considering the tailing phase, was described by a shoulder model [22]:

$$\mathrm{RF} = k \cdot \mathrm{Fluence} - b \tag{10.8}$$

RF decimal reduction factor
k inactivation rate constant (m^2/J)
b offset value (crosses the fluence axis at the fluence, where log-linear relation ship starts).

The sensitivity of *B. subtilis* spores was determined from linear regression of the RF between fluences presenting a log-linear relationship. The goodness of fit of the linear regression was analyzed with the coefficient of determination (r^2) and the standard error (StE; the StE measures the error in predicting $f(x) = y$ for an individual x in the regression).

The error of the mean value was calculated according to the following equation [19]:

$$\sigma_{\bar{\mu}} = \pm \frac{\sqrt{\bar{\mu}}}{\sqrt{n}} \tag{10.9}$$

$\sigma_{\bar{\mu}}$ error of the mean value
$\bar{\mu}$ standard deviation
n number of measurements.

Table 10.3 Water quality parameters (mean values) of the applied test waters

	Parameter	Unit	DI	TW	SW	SE
Test waters for tests conducted with 269 nm LEDs						
Unfiltered	a (254)	(1/m)	1.1	–	–	–
	UVT (254)	(%)	97.5	–	–	–
Filtered	a (254)	(1/m)	0.8	–	–	–
	UVT (254)	(%)	98.2	–	–	–
Test waters for tests conducted with 282 nm LEDs						
Unfiltered	a (254)	(1/m)	2.7	10.8	18.4	28.7
	UVT (254)	(%)	94.1	78.0	65.5	51.7
	a (282)	(1/m)	2.3	8.2	13.4	22.1
	UVT (282)	(%)	94.8	82.8	73.5	60.1
Filtered	a (254)	(1/m)	0.7	7.9	15.9	23.6
	UVT (254)	(%)	98.4	83.4	69.3	58.1
	a (282)	(1/m)	0.4	5.4	11.0	17.6
	UVT (282)	(%)	99.0	88.3	77.6	66.7

DI deionized water, *TW* tap water, *SW* surface water, *SE* secondary effluent

10.3.2.3 Physicochemical Water Quality

Tests were performed with different water qualities: deionized water (DI), tap water (TW), surface water (SW), and secondary effluent (SE). Water samples were taken in Berlin, Germany. Tap water was obtained from the local water supply of the city of Berlin. Surface water samples were taken at the Landwehrkanal and secondary effluent was provided by the waste water treatment plant Ruhleben.[8]

Table 10.3 summarizes the measured and calculated water absorption parameters for wavelength of a conventional low-pressure mercury lamp (254 nm) and a UV LED with an emission of 282 nm. The UV absorption (a) was measured with a two beam spectrometer in a 5 cm quartz cuvette. Afterwards the UV transmittance (UVT) was calculated from (10.2).

The high turbidity of the *B. subtilis* suspension reduced UVT (254) of the unfiltered deionized water samples. Higher absorption of the test waters used in experiments with the 282 nm LEDs was caused by a higher initial spore concentration. The tap water of the city of Berlin contains a high amount of UV active dissolved organic matter, resulting in a high UV absorbance of the tap water test samples.

[8]The waste water treatment plant Ruhleben treats combined municipal waste water with parts of rainwater by mechanical separation, activated sludge process with nitrification, post-denitrification, and biological phosphorus removal.

10.3.3 Results of Tests Conducted with UV LEDs

The potential of UV LEDs for mobile water disinfection was investigated in three steps: First, a UV LED module was constructed, tested with various water qualities, and the results were compared to results obtained with a conventional standardized mercury lamp system (cp. Sect. 10.3.3.1). Then, the influence of two different LED wavelengths on the disinfection of *B. subtilis* spores was compared based on their disinfection capacity and power consumption (cp. Sect. 10.3.3.2). Finally, real water disinfection applications were simulated with a bench-scale flow-through reactor (cp. Sect. 10.3.3.3).

10.3.3.1 Module Development and Validation

The test modules were developed based on the low output power of the UV LEDs causing long irradiation times and low flow rates. The design consisted of a LED array, irradiating the water sample from the bottom up, in contrast to the conventional collimated beam device (CBD), in which the mercury lamp is located on top of the water sample. The inhomogeneous light emission was addressed by constant stirring during static tests. Validation tests were performed with arrays of UV LEDs emitting at 282 nm. *B. subtilis* spores were used as test organism and exposed successively to UV light.

In the first step of the validation process, the reproducibility of test results obtained with the designed module was evaluated by the error of mean value of repeated tests and by applying various water qualities. In the second step of the validation, test results were compared to disinfection tests conducted on a standardized mercury lamp CBD.

The inactivation results to evaluate the reproducibility of the test module with different water qualities are presented in Fig. 10.7. Increasing UVT was considered in fluence calculation causing lower applied fluences at the same exposure time for waters containing higher amounts of UV absorbing compounds (cp. Equation 10.4).

Linear regression was performed for all data points between 97 and 581 J/m^2 with a high goodness of fit (StE = 0.44; r^2 = 0.94). Data points beneath 97 J/m^2 were not included for data analysis due to a non-log-linear relationship (shoulder effect; cp. Sect. 10.3.2.2).

The maximum error of mean value of the RF in DI water tests was the same as the maximum error of mean value of the triplicate analysis (both 1.5; n = 3). This comparison indicates that the test setup generates reproducible results which are in the range of the triplicate analysis. Reproducibility of the tests conducted with the UV LED test module was also underlined by a highest error of mean value of 0.9 (n = 9) between all conducted experiments.

In a second validation step, *B. subtilis* spores were used under different experimental conditions: in the 282 nm LED module and in a 254 nm mercury lamp

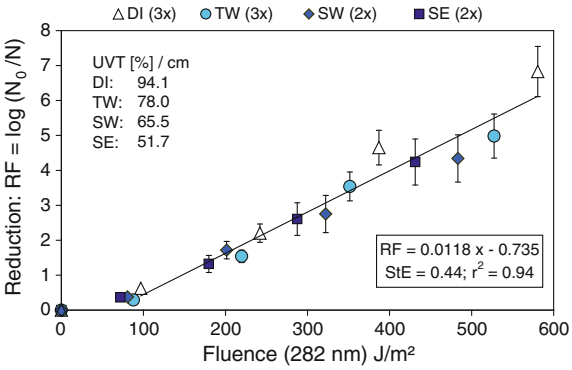


Fig. 10.7 Fluence–inactivation response and curve derived by linear regression of *B. subtilis* spores in different waters (*DI* deionized water, *TW* tap water, *SW* surface water, *SE* secondary effluent) with different qualities (UVT_{254} as representative parameter) for 282 nm LEDs; in parentheses are the numbers of test batches. Presented data are geometric mean values ± error of mean value of three test rows. Test rows were cultivated in triplicates

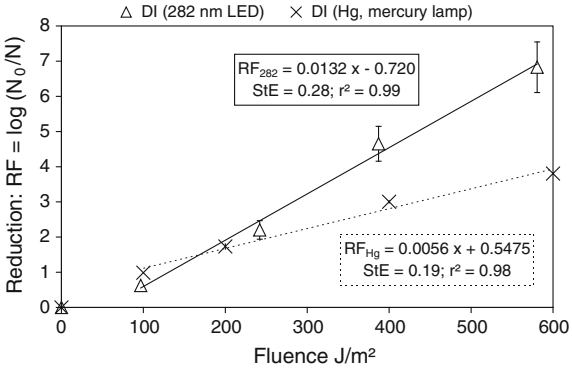


Fig. 10.8 Fluence–inactivation response and curves derived by linear regression of *B. subtilis* spores irradiated with UV light in deionized water for 282 nm LEDs and a mercury lamp. Presented data are geometric mean values ± error of mean value of three test rows. Test rows were cultivated in triplicates

CBD.[9] According to literature data, the fluence–inactivation response curve of *B. subtilis* spores should be comparable at wavelengths of 254 and 279 nm (Fig. 10.2, [11]), and therefore the sensitivity of the surrogate spores should be comparable in both experimental setups.

[9]These CBD tests conducted with a mercury lamp was performed by an external laboratory (Institute of Hygiene and Public Health, University of Bonn).

The UV sensitivity of a microorganism is described by the inactivation rate constant k (m^2/J) and the offset value—b (cp. Sect. 10.3.2.2) derived from linear regression of the reduction factor (RF) over fluence plot. Spore inactivation results in DI water obtained with 282 nm LEDs and a conventional mercury lamp are presented in Fig. 10.8.

Linear regression was performed for fluences above 100 J/m^2, due to a missing log-linear relation ship (offset value). For the 282 nm LEDs a shoulder effect at low fluences was observed (negative offset value). Tailing was neither observed for the 282 nm LEDs nor for the mercury lamp at the investigated fluences. A linear fluence–inactivation relationship was observed in both experimental setups between 100 and 600 J/m^2. Regression analysis led to low StE and r^2 values for the 282 nm LEDs (StE = 0.28, r^2 = 0.99) and the mercury lamp (StE 0.19, r^2 = 0.98).

A comparison of the inactivation rate constants k of the 282 nm LEDs (0.0132 J/m^2) and the mercury lamp (0.0056 J/m^2) indicated a two times higher sensitivity of the *B. subtilis* spores in the LED module. The difference of spore reduction between the 282 nm LEDs and the mercury lamp therefore increased with higher fluences. Based on the assumption that the different wavelengths should result in the same sensitivity (according to [11]), the difference of the disinfection kinetics may have to be attributed to the different experimental setups. Various factors, such as the condition of the test suspension, the fluence calculation, and/or the different constructions of the LED apparatus and the CBD, might have influenced the test results. At this stage, a clear explanation for this higher disinfection capacity at higher fluences compared to the conventional UV source needs further investigation.

However, as the LED system generated reproducible results, the inactivation results obtained for different wavelengths on the same experimental setup are comparable. The influence of different UV LED wavelengths on the disinfection of *B. subtilis* spores is discussed in the following section.

10.3.3.2 Comparison of LEDs Emitting at 282 nm and 269 nm

The disinfection capacity of 269 and 282 nm emitting LEDs was investigated by running disinfection tests with deionized water. According to previous research, the 269 nm wavelength corresponds to the absorption maximum of the *B. subtilis* spores [7, 11, 33] and should therefore show a greater inactivation than the 282 nm LEDs. On the other hand, the 282 nm LEDs have a higher optical power output. The consequences are discussed in the following. Figure 10.9 presents the inactivation curves derived from the results obtained with different UV LED wavelengths in the static apparatus configuration.

Deduced from linear regression, *B. subtilis* was equally sensitive to both wavelengths above 100 J/m^2 (k_{282} = 0.0132; k_{269} = 0.0133). The offset value for the 282 nm LEDs was negative, indicating a shoulder effect, as discussed above. The offset value for the 269 nm LEDs was positive and therefore no shoulder effect existed. As the 269 nm LEDs showed no shoulder effect, the absolute difference of

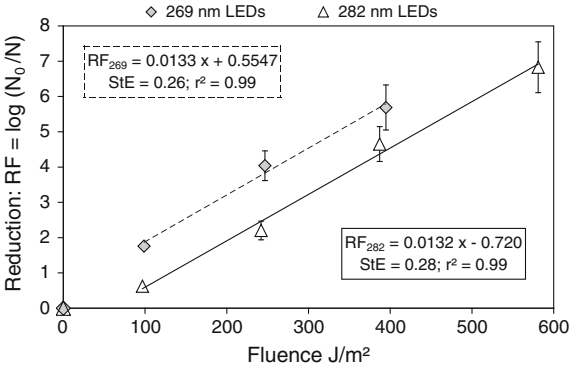


Fig. 10.9 Comparison of fluence–inactivation response and curves derived by linear regression for *B. subtilis* spores in deionized water, obtained with UV LEDs of 269 and 282 nm in the static apparatus. Presented data are geometric mean values ± error of mean value

more than one log in the investigated fluence range demonstrated a higher absolute disinfection using 269 nm LEDs. This enhanced disinfection capacity could be attributed to the higher germicidal efficiency at a wavelength of 269 nm.

In a next step, the 269 and 282 nm LEDs were compared, based on a model calculation considering the same input power and time, which resulted in different fluence. A model calculation was conducted, based on a nominal drive current of 20 mA, at which the 269 nm LEDs have an optical power output of 0.33 mW, whereas the 282 nm LEDs have an optical power output of 0.65 mW. Various resulting fluences were calculated according to (10.3). The resulting inactivation was calculated from the inactivation curves derived in Fig. 10.9. The results of the model calculation are summarized in Table 10.4.

Although the 269 nm LEDs exhibit a higher germicidal efficiency, the spore inactivation caused by the 282 nm LEDs is higher than for the 269 nm LEDs during the same time span and at the same input power. Irradiation for a period of 300 s,

Table 10.4 Summary of model calculation for the comparison of power consumption and inactivation performance of the 269 and 282 nm LEDs; boundary conditions: input current of 20 mA and a total of five LEDs

	269 nm Output: 0.33 mW		282 nm Output: 0.65 mW		Difference
Time (s)	Fluence (J/m^2)	RF_{269} (log N_0/N)	Fluence (J/m^2)	RF_{282} (log N_0/N)	$RF_{282} - RF_{269}$ (log N_0/N)
200	117	1.9	230	2.4	0.5
250	146	2.3	287	3.0	0.7
300	175	2.7	345	3.7	1.0
350	204	3.1	402	4.4	1.3
400	233	3.6	460	5.1	1.5

Reduction factor: $RF_{269} = 0.01133\ x + 0.5547$; $RF_{282} = 0.0132\ x - 0.720$

for example, led to an applied fluence of 175 J/m^2 for the 269 nm LEDs and an applied fluence of 345 J/m^2 for the 282 nm LEDs. At this fluence value the reduction factor for the 269 nm LEDs is 1.0 log lower than for the 282 nm LEDs. This is due to the higher output power (at the same current) of the 282 nm LEDs. The higher disinfection capacity of the 269 nm LEDs, which is due to an output wavelength close to the absorption maximum (around 270 nm) of the *B. subtilis* spores, is compensated by a higher output power of the 282 nm LEDs. As a consequence, the use of 282 nm LEDs is preferable for the overall performance of the UV purification module, as long as the performance of the LEDs at the shorter wavelength is not improved. In the future, with increasing output power of the LEDs available for both wavelengths, the trend may be different. The optimum wavelength will have to be chosen based on a comparison between the UV output power and the reduction factor applying the same fluence.

10.3.3.3 Flow-Through Tests

During this study flow-through tests were conducted with the higher output power 282 nm LEDs. Flow-through tests were performed with a flow-through reactor to obtain first results for the applicability of UV LEDs under real conditions. Differing fluences were obtained by varying the flow rate and optical power output of the 282 nm LEDs (cp. Sect. 10.3.2). The flow rate was adjusted to (10.8 ± 0.4) ml/min and (7.8 ± 0.4) ml/min, resulting in laminar conditions. The results are presented in Fig. 10.10.

Linear regression was performed, including all data obtained with a flow rate of (10.8 ± 0.4) ml/min and (7.8 ± 0.4) ml/min, to investigate whether the flow rates have an influence on the spore inactivation. The low StE of 0.20 and a goodness of

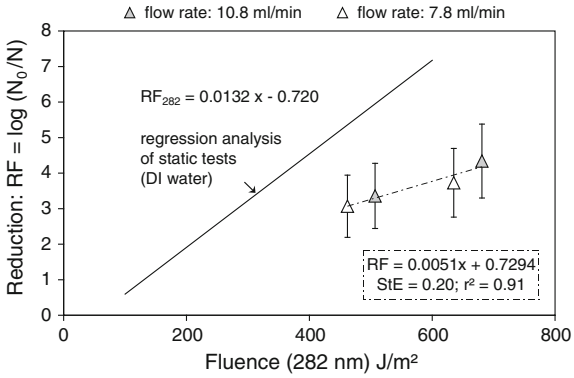


Fig. 10.10 Fluence–inactivation response and the curves derived by linear regression of *B. subtilis* spores in deionized (DI) water, obtained with the apparatus designed for 282 nm UV LEDs in static tests (regression analysis of static tests in DI water) compared to results obtained during flow-through tests. Presented data are geometric mean values ± error of mean value

fit of $r^2 = 0.91$ indicated that—applying laminar conditions—the flow rate has no significant influence on the spore reduction. Therefore, the fluence–inactivation response curve—including data of differing flow rates—was used for further evaluation. With regard to this curve, the sensitivity (inactivation rate constant k) of the *B. subtilis* spores was more than halved in flow-through tests compared to static test results (represented in Fig. 10.10 as regression analysis of static tests). Although nominally the same fluence was applied, the inactivation of *B. subtilis* in the flow-through test reactor was reduced compared to static tests. This is a common phenomenon when scaling up UV reactors and constructing flow-through reactors instead of static reactors. These results indicate that the flow conditions lead to areas of lower UV irradiation by incomplete illumination and short-circuiting by shadowing effects within the flow-through test reactor, reducing the overall disinfection efficiency. Nevertheless, an increase in the applied fluence leads to a higher inactivation, indicating a promising design of the UV LED configuration in the flow-through reactor.

In the German procedure of UV reactor certification for potable water production, a target fluence of 400 J/m^2 is set [16]. Based on the sensitivity of the applied test organism in CBD tests, 400 J/m^2 are achieved when the spores are reduced by three log (cp. Sect. 10.3.2). However, even with a lower sensitivity of the applied test spores in flow-through tests a 3-log reduction in *B. subtilis* spore count was demonstrated, applying only a minimally higher fluence of approx. 450 J/m^2 than needed in CBD tests.

10.4 Potential of UV LEDs for Water Disinfection

The objective of this chapter was to evaluate the suitability of AlGaN-based UV LEDs for water disinfection. Therefore published investigations using UV LEDs were reviewed and results of a case study were summarized.

The case study included the evaluation of the performance characteristics of UV LEDs at different operating conditions as well as the design and development of a UV LED module in view of the requirements for water treatment applications. Bioanalytical testing was conducted using *B. subtilis* spores as test organism and UV LEDs with emission wavelengths of 269 and 282 nm.

Test results indicated an effective inactivation of *B. subtilis* spores through UV LEDs at emitting wavelengths of 269 and 282 nm and therefore a basic applicability of UV LEDs for water disinfection. The higher disinfection efficiency of the 269 nm LEDs than the 282 nm LEDs was compensated by the higher optical output power of the 282 nm LEDs.

In general, the optical output power of the UV LEDs is still very low and needs further improvement in order to make them suitable for real-world applications. Water purification applications where water has to be disinfected within a few seconds are still limited by long exposure times when using UV LEDs. As a consequence, the reactor design would have to be reduced to small diameters.

UV LEDs might therefore only be applicable at the tap outlet, where water flows are lower. On the one hand, this UV disinfection system design would reduce the impact of microbial regrowth in the piping system on the extracted water and increase water quality at the point of use. On the other hand, the installation of various UV light point sources requires the development of a completely new monitoring system. Special attention would have to be paid to UV light emission monitoring for each single UV LED to avoid unperceived UV LED failure and loss of disinfection efficiency.

However, due to the big advantages of UV LEDs—like the tunable emission wavelength, the low voltages, the immediate availability of UV radiation, their robust and compact design, and predicted longer life times—UV LEDs will be promising candidates to realize new disinfection applications in the area of mobile disinfection systems. Additionally, they will be also good candidates for replacing conventional UV disinfection systems especially for applications where only low flow rates are needed. This process will be supported in the future by the continuously increasing development in the UV LED area and the expected reduction of the LED costs through production scale-up due to the increasing demand for such devices.

Acknowledgments The authors thank Boris Lesjean and Eric Hoa from the Berlin Centre of Competence for Water and Florencio Martin from Veolia Water, Anjou Recherche, for their helpful expertise, Katharina Kutz for her laboratory work and the Berliner Wasserbetriebe for providing the samples of secondary effluents. This work was partially supported by the Berlin Centre of Competence for Water in the frame of the FP6 project TECHNEAU, and financed by the European Commission and Veolia Water.

References

1. V. Adivarahan, A. Heidari, B. Zhang, Q. Fareed, S. Hwang, M. Islam, A. Khan, 280 nm deep ultraviolet light emitting diode lamp with an AlGaN multiple quantum well active region. Appl. Phys. Exp. **2**(102101) (2009)
2. J. Bak, S.D. Ladefoged, M. Tvede, T. begovic, A. Gregersen, Disinfection of Pseudomonas aeruginosa biofilm contaminated tube lumens with ultraviolet C light emitting diodes. Biofouling **26**(1), 31–38 (2010)
3. E.R. Blatchley, C. Shen, O.K. Scheible, J.P. Robinson, K. Ragheb, D.E. Bergstrom, D. Rokjer, Validation of large-scale, monochromatic UV disinfection systems for drinking water using dyed microspheres. Water Res. **42**(3), 677–688 (2008)
4. J.R. Bolton, Calculation of ultraviolet fluence rate distributions in an annular reactor: Significance of refraction and reflection. Water Res. **34**(13), 3315–3324 (2000)
5. J.R. Bolton, C.A. Cotton, *The Ultraviolet Disinfection Handbook* (American Water Works Association, Denver, 2008)
6. J.R. Bolton, K.G. Linden, Standardization of methods for fluence (UV dose) determination in bench-scale UV experiments. J. Environ. Eng. ASCE **129**(3), 209–215 (2003)
7. A. Cabaj, R. Sommer, W. Pribil, T. Haider, The spectral UV sensitivity of microorganisms used in biodosimetry. Water Suppl. IWA Publ. **2**(3), 175–181 (2002)

8. R.E. Cantwell, R. Hofmann, Inactivation of indigenous coliform bacteria in unfiltered surface water by ultraviolet light. Water Res. **42**(10–11), 2729–2735 (2008)
9. E. Caron, G. Chevrefils, B. Barbeau, P. Payment, M. Prévost, Impact of microparticles on UV disinfection of indigenous aerobic spores. Water Res. **41**, 4546–4556 (2007)
10. C. Chatterley, K. Linden, Demonstration and evaluation of germicidal UV-LEDs for point-of-use water disinfection. J. Water Health IWA Publ. **8**(3), 479–486 (2010)
11. R.Z. Chen, S.A. Craik, J.R. Bolton, Comparison of the action spectra and relative DNA absorbance spectra of microorganisms: Information important for the determination of germicidal fluence (UV dose) in an ultraviolet disinfection of water. Water Res. **43**(20), 5087–5096 (2009)
12. A.C. Chevremont, A.M. Farnet, M. Sergent, B. Coulomb, J.L. Boudenne, Multivariate optimization of fecal bioindicator inactivation by coupling UV-A and UV-C LEDs. Desalination **285**, 219–225 (2012)
13. S.A. Craik, G.R. Finch, J.R. Bolton, M. Belosevic, Inactivation of Giardia muris cysts using medium-pressure ultraviolet radiation in filtered drinking water. Water Res. **34**(18), 4325–4332 (2000)
14. M.H. Crawford, M.A. Banas, M.P. Ross, D.S. Ruby, J.S. Nelson, R. Boucher, A.A. Allerman, *Final LDRD Report: Ultraviolet Water Purification Systems for Rural Environments and Mobile Applications* (Sandria National Laboratories, Albuquerque, New Mexico, 2005), pp. 1–37
15. J.C. Crittenden, R.R. Trussell, D.W. Hand, K.J. Howe, G. Tchobanoglous, Disinfection with ultraviolet light, in *Water Treatment: Principles and Design*, Chapter 13.8 (Wiley, Hoboken, 2005)
16. DVGW, *Arbeitsblatt W 290: Trinkwasserdesinfektion - Einsatz und Anforderungskriterien* (Deutsche Vereinigung des Gas- und Wasserfaches, Bonn, 2005)
17. DVGW, *Arbeitsblatt W 294-1: UV-Geräte zur Desinfektion in der Wasserversorgung Teil 1: Anforderungen an Beschaffenheit, Funktion und Betrieb* (Deutsche Vereinigung des Gas- und Wasserfaches, Bonn, 2006a)
18. DVGW, *Arbeitsblatt W 294-2: UV-Geräte zur Desinfektion in der Wasserversorgung Teil 2: Prüfung von Beschaffenheit, Funktion und Desinfektionswirkung* (Deutsche Vereinigung des Gas- und Wasserfaches, Bonn, 2006b)
19. F. Embacher, *Mathematische Grundlagen für das Lehramtsstudium Physik* (Vieweg + Teubner | GWV Fachverlage GmbH, Wiesbaden, 2011)
20. F.L. Gates, A study of the bactericidal action of ultraviolet light: III. The absorption of ultraviolet light by bacteria. J. Gen. Physiol. **14**(1), 31–42 (1930)
21. W. Harm, *Biological Effects of Ultraviolet Radiation* (Cambridge University Press, New York, 1980)
22. W.A.M. Hijnen, E.F. Beerendonk, G.J. Medema, Inactivation credit of UV radiation for viruses, bacteria and protozoan (oo)cysts in water: A review. Water Res. **40**(1), 3–22 (2006)
23. K. Höll, *Wasser. Nutzung im Kreislauf. Hygiene, Analyse und Bewertung.* (Walter de Gruyter, Berlin, 2002)
24. A. Khan, K. Balakrishnan, T. Katona, Ultraviolet light-emitting diodes based on group three nitrides. Nat. Photon. **2**, 77–84 (2008)
25. M. Kneissl, Ultraviolet light-emitting diodes promise new solutions for water purification. World Water & Environmental Engineering **31**(3), 35 (2008)
26. T. Kolbe, *Einfluss des Heterostrukturdesigns auf die Effzienz und die optische Polarisation von (In)AlGaN-basierten Leuchtdioden im ultravioletten Spektralbereich*. Ph.D. Thesis, Fakultät II - Mathematik und Naturwissenschaften; Technische Universität Berlin, Berlin, 2012
27. A. Kolch, UV-Disinfection of drinking water—the new DVGW work sheet 94 Part 1–3. IUVA News **9**, 17–20 (2007)

28. J. Kuo, C.L. Chen, M. Nellor, Standardized collimated beam testing protocol for water/wastewater ultraviolet disinfection. J. Environ. Eng. ASCE **129**(8), 774–779 (2003)
29. L.-S. Lin, C.T. Johnston, E.R. Blatchley III, Inorganic fouling at quartz: Water interfaces in ultraviolet photoreactors: II. Temporal and spatial distributions. Water Res. **33**(15), 3330–3338 (1999)
30. D. Liu, *Numerical Simulation of UV Disinfection Reactors: Impact of Fluence Rate Distribution and Turbulence Modeling*. Dissertation, North Carolina State University, 2004
31. M.T. Madigan, J.M. Martinko, J. Parker, *Makromoleküle*. In: *Brock Mikrobiologie*, Chapter 24 (W. Goebel. Spektrum Akademischer Verlag GmbH, Heidelberg, 2001)
32. J.P. Malley, UV in water treatment issues for the next decade. IUVA News **12**(1), 18–25 (2010)
33. H. Mamane-Gravetz, K.G. Linden, A. Cabaj, R. Sommer, Spectral sensitivity of Bacillus subtilis spores and MS2 Coliphage for validation testing of ultraviolet reactors for water disinfection. Environ. Sci. Technol. **39**(20), 7845–7852 (2005)
34. T. Miyoshi, T. Yanamoto, T. Kozaki, S.-I. Nagahama, Y. Narukawa, M. Sano, T. Yamada, T. Mukai, *Recent status of white LEDs and nitride LDs* (2008)
35. K.Y. Nelson, D.W. McMartin, C.K. Yost, K.J. Runtz, T. Ono, Point-of-use water disinfection using UV light-emitting diodes to reduce bacterial contamination. Environ. Sci. Pollut. Res. **20**(8), 5441–5448 (2013)
36. K. Oguma, R. Kita, H. Sakai, M. Murakami, S. Takizawa, Application of UV light emitting diodes to batch and flow-through water disinfection systems. Desalination **328**, 24–30 (2013)
37. M. Oliver, UV cleaning system performance validation. IUVA News **5**(1)
38. ÖNORM, *Plants for Disinfection of Water Using Ultraviolet Radiation: Requirements and Testing, Part 1: Low Pressure Mercury Lamp Plants* (Austrian Standards Institute, Vienna, 2001), www.on-norm.at
39. J. Peng, Y. Qiu, R. Gehr, Characterization of permanent fouling on the surfaces of UV lamps used for wastewater disinfection. Water Environ. Res. **77**(4), 309–322 (2005)
40. R.G. Qualls, J.D. Johnson, Bioassay and dose measurement in UV disinfection. Appl. Environ. Microbiol. **45**(3), 872–877 (1983)
41. C. Reichl, C. Buchner, G. Hirschmann, R. Sommer, A. Cabaj, *Development of a Simulation Method to Predict UV Disinfection Reactor Performance and Comparison to Biodosimetric Measurements*. *Conference on Modelling Fluid Flow*, Budapest (2006)
42. M. Shatalov, W. Sun, A. Lunev, X. Hu, A. Dobrinsky, Y. Bilenko, J. Yang, M. Shur, R. Gaska, C. Moe, G. Garrett, M. Wraback, AlGaN deep-ultraviolet light-emitting diodes with external quantum efficiency above 10 %. Appl. Phys. Exp. **5**(8), 082101 1–3 (2012)
43. M. Sheriff, R. Gehr, Laboratory investigation of inorganic fouling of low pressure UV disinfection lamps. Water Qual. Res. J. Can. **36**(1), 71–92 (2001)
44. R. Sommer, A. Cabaj, T. Sandu, M. Lhotsky, Measurement of UV radiation using suspensions of microorganisms. J. Photochem. Photobiol. B **53**(1–3), 1–6 (1999)
45. R. Sommer, A. Cabaj, D. Schoenen, J. Gebel, A. Kolch, A.H. Havelaar, F.M. Schets, Comparison of three laboratory devices for UV-inactivation of microorganisms. Water Sci. Technol. **31**(5–6), 147–156 (1995)
46. M.R. Templeton, R.C. Andrews, R. Hofmann, Inactivation of particle-associated viral surrogates by ultraviolet light. Water Res. **39**, 3487–3500 (2005)
47. USEPA, *Ultraviolet Disinfection Guidance Manual for the Final Long Term 2 Enhanced Surface Water Treatment Rule. 815-R-06-007,* Washington DC (2006)
48. S. Vilhunen, H. Särkkä, M. Sillanpää, Ultraviolet light-emitting diodes in water disinfection. Environ. Sci. Pollut. Res. **16**(4), 439–442 (2009)
49. I.W. Wait, C.T. Johnston, E.R. Blatchley III, The influence of oxidation reduction potential and water treatment processes on quartz lamp sleeve fouling in ultraviolet disinfection reactors. Water Res. **41**(11), 2427–2436 (2007)

50. I.W. Wait, M. Yonkin, E.R. Blatchley III, *Quartz lamp sleeve fouling and cleaning system evaluation at the Albany, New York Loudonville UV treatment facility*. IUVA News **8**(4), 11–14 (2006)
51. S. Wengraitis, P. McCubbin, M.M. Wade, T.D. Biggs, S. Hall, L.I. Williams, A.W. Zulich, *Pulsed UV-C disinfection of Escherichia coli with light-emitting diodes, emitted at various repetition rates and duty cycles*. Photochem. Photobiol. **89**, 127–131 (2013)
52. WHO, *Water for Health—WHO Guidelines for Drinking-water Quality* (WHO Press, 2010)
53. M.A. Würtele, T. Kolbe, M. Lipsz, A. Külberg, M. Weyers, M. Kneissl, M. Jekel, Application of GaN-based ultraviolet-C light emitting diodes—UV LEDs—for water disinfection. Water Res. **45**(3), 1481–1489 (2011)

Chapter 11
Application of UV Emitters in Dermatological Phototherapy

Uwe Wollina, Bernd Seme, Armin Scheibe and Emmanuel Gutmann

Abstract UV phototherapy is a highly effective therapy option for the treatment of skin diseases. In this chapter light sources for and variants of dermatological phototherapy are introduced together with their indications and mechanisms of action. Moreover, the outcomes of clinical studies using novel UV emitters including UV-LEDs are discussed.

11.1 Introduction

The skin is the largest organ of the human body and represents a biological barrier between ourselves and the environment. Impairments of the skin functions are very common. They are usually associated with distress for the patient and can result in acute or chronic diseases which sometimes even require inpatient treatment. The objective of phototherapy is to use light to cure or ease skin diseases while minimizing adverse effects on non-affected skin.

Phototherapy has a long history in medicine going back to ancient Egypt. In 1903 Niels Ryberg Finsen won a Nobel Prize for the use of phototherapy to treat lupus vulgaris. This can be regarded as the birthplace of modern phototherapy which is based on artificial light sources. In 1926 William Goeckerman at Mayo Clinic invented the combined crude tar phototherapy, later named after him as Goeckerman regimen. PUVA therapy, that is Psoralen plus UVA (320–400 nm)

U. Wollina (✉)
Department of Dermatology and Allergology, Hospital Dresden-Friedrichstadt,
Academic Teaching Hospital of the Technical University of Dresden,
Friedrichstrasse 41, 01067 Dresden, Germany
e-mail: Wollina-Uw@khdf.de

B. Seme · A. Scheibe · E. Gutmann
Department Photonics and Sensorics, Gesellschaft zur Förderung von Medizin-,
Bio- und Umwelttechnologien e.V. (GMBU), Felsbachstrasse 7, 07745 Jena, Germany
e-mail: gutmann@gmbu-jena.de

© Springer International Publishing Switzerland 2016

M. Kneissl and J. Rass (eds.), *III-Nitride Ultraviolet Emitters*,
Springer Series in Materials Science 227, DOI 10.1007/978-3-319-24100-5_11

radiation, was initiated in the early 1970s and in 1984 Phillips TL-01 lamps allowed narrowband UVB (280–320 nm) phototherapy with a wavelength of 311 nm ± 2 nm. Starting from here, in the last decades another type of light sources emitting at around 308 nm, namely excimer lamps and lasers, have been developed and successfully applied in phototherapy [1]. Finally, devices utilizing solid state UV light emitting diodes (UV-LEDs) begin to find their way into the clinical practice. The different light sources used in UV phototherapy are introduced in Sect. 11.2.

Nowadays both the UVB and the UVA spectrum are used therapeutically. The irradiation can be applied as a single or monotherapy, but quite often it is used in combination with drugs like in PUVA therapy [2]. Due to optical characteristics of human skin, UVB penetrates only to the epidermis and the most superficial parts of rete ridges, whereas UVA goes deeper reaching the vascular bed. This of course has some consequences on the applicability of different variants of phototherapy, which is issued in Sect. 11.3.

There are several photobiological mechanisms of action on which phototherapy is based on. In Sect. 11.4 these are specified for the majority of indications. A short introduction to mechanisms having adverse effects on the organism is given as well. Subsequently, recent studies applying phototherapeutic demonstrator devices with newly developed electrodeless excimer lamps or UV-LEDs as light sources are reviewed and an outlook on future directions in phototherapy is given.

11.2 Sources for UV Phototherapy

UV sources for dermatological phototherapy can be divided into two main groups: luminescence and incandescence emitters. Incandescence emitters are thermal radiation sources that emit a continuous spectrum according to Planck's law. Niels Ryberg Finsen, the father of modern phototherapy, applied a carbon arc incandescence lamp to mimic natural sunlight and to cure lupus vulgaris [2, 3]. The problem with incandescence sources is that they are inefficient UV sources because a lot of unwanted radiation is produced in the infrared (IR) and visible (VIS) spectral range. Thus, the only incandescence emitter used for UV phototherapeutic purposes today is the sun. Artificial therapeutic UV emitters in current dermatology are solely luminescence emitters. These are nonthermal sources that generate UV photons by de-excitation of energy states in atoms, molecules, or solids. The associated transitions result in a discontinuous line spectrum. Depending on the type of source used, the line spectrum may be broadened or superimposed by a continuum due to different physical processes like Doppler effect, Bremsstrahlung, recombination radiation, or thermal emission. Gas discharge lamps and excimer lasers are well-established UV luminescence emitters in the modern dermatological practice [4]. UV-LEDs represent solid state luminescence emitters. In the future, they may more and more become dermatological standard tools because LEDs are easy to handle, cost-effective, compact, safe, and mercury free.

11.2.1 Natural Sunlight

The sun is an incandescence emitter with a surface temperature of about 5,800 K. Its radiation has already been used by ancient healers about 3,500 years ago to treat skin diseases [2]. Radiation from the sun reaches us through its gas atmosphere and through the atmosphere of the earth. Consequently, the spectral distribution of sunlight measured at the surface of the earth deviates from the spectrum of a blackbody radiator. The UVC radiation (200–280 nm) is mostly blocked by the earth's atmosphere and the atmosphere of the sun results in Fraunhofer absorption lines, Fig. 11.1. Only about 5 % of the sunlight reaching the earth's ground level is UV radiation and more than 90 % of that is UVA radiation. The total natural UV irradiance in summer in central Germany is about 30 W/m^2. Of course this value fluctuates strongly with time, season, clouds, etc. Therefore it is difficult to apply exact and repeatable doses of natural UV light. Moreover, the spectral distribution of the UV radiation is always broad and a narrowband exposure would require additional filtering. However, in certain areas like, for example, the dead sea region [5], where the UV radiation from the sun is predictable and spectrally beneficial due to the geographical position below sea level and the climate, natural sunlight is used successfully for phototherapy.

As sufficient sunlight is not available at all times at all locations artificial UV sources that mimic the curative effect of the sun have been introduced. These sources can be optimized for the desired therapeutic effect. They also enable an exclusive irradiation of affected skin areas and a protection of surrounding, healthy skin (targeted therapy).

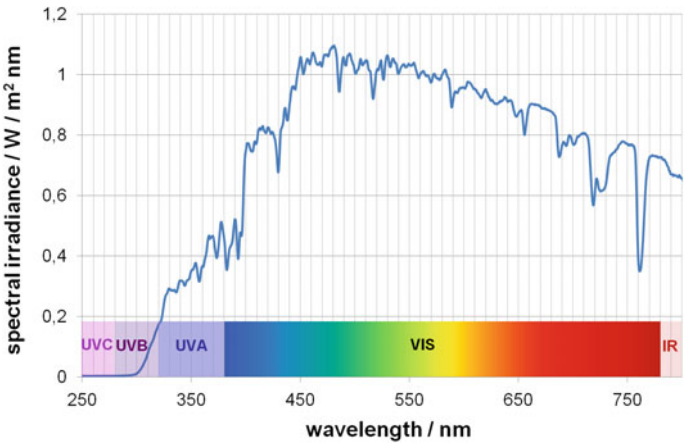


Fig. 11.1 Spectral distribution of natural sunlight in summer in central Germany at ground level

11.2.2 Gas Discharge Lamps

In gas discharge lamps an electric current is passed through a gas, a vapor or a mixture of both. That is, free charge carriers are accelerated in an electric field that penetrates a gaseous medium which is enclosed in a glass vessel. By collisions with free charge carriers the gas atoms receive energy or they are ionized. The absorbed energy is emitted again by the gas atoms in form of radiation. Thereby the wavelengths and widths of the emitted spectral lines are determined by the type of gas and the gas pressure. This is an essential difference compared to incandescent lamps, whose continuous emission spectrum is determined by the temperature of the hot material only. Because the gas pressure affects the spectral distribution of the emitted radiation significantly, gas discharge lamps are subdivided into low-, medium-, and high-pressure lamps.

11.2.2.1 Mercury Discharge Lamps

Low-Pressure Mercury Discharge Fluorescent Lamps

In low-pressure discharge lamps a pressure of up to 10 mbar is applied. Thereby the most important filling medium used in dermatology is mercury vapor. At the pressures quoted it gives rise to a dominant UVC spectral line at a wavelength of 254 nm. To transform the shortwave output into the UVB or UVA range the inside of the lamp's glass vessel is coated with special fluorophores, typically phosphores. The exact composition of the fluorophores determines the emission spectrum of the lamp which then is basically a fluorescent lamp. Lamps with broadband UVA and UVA-1 (340–400 nm), broadband UVB and narrowband UVB emission around 311 nm are available [6], Fig. 11.2. Low-pressure fluorescent lamps are the most commonly used sources for UV phototherapy [3]. They allow the irradiation of large areas by using long discharge tubes (>1 m) with an UV output in the range of 10 W/m, but they are also offered as compact folded fluorescent tubes [6]. These lamps are very cost-effective and have a durability of about 1,000 h [7].

Medium- and High-Pressure Mercury Discharge Lamps

When mercury vapor discharge lamps are operated at medium (10 $mbar^{-1}$ bar), high (1–20 bar), or even maximum (>20 bar) pressures, additional UV emission at 297, 302, 313, 334, and 365 nm is significant [3]. Furthermore, the spectral lines become broadened and are more and more superimposed by a continuum. High and maximum pressure discharges in mercury result in short, punctual arcs, compact lamps, and high radiances [8, 9]. Therefore they are ideally suited for irradiation devices that require a fiber coupling. For direct phototherapeutic applications metal halide lamps are more common. These lamps are medium or high-pressure mercury

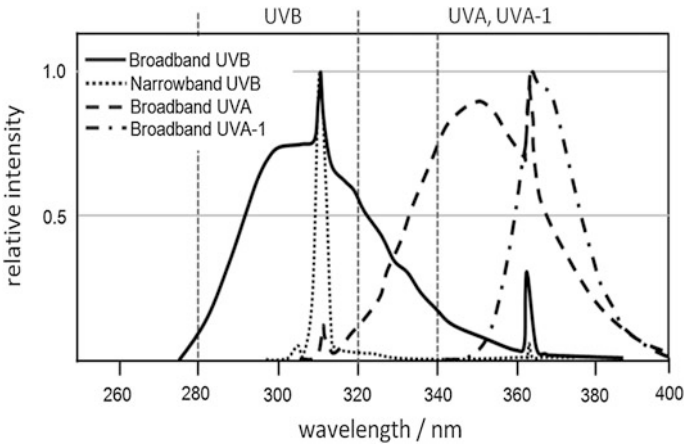


Fig. 11.2 Schematic representation of UV fluorescent lamp spectra

discharge sources with metal halide additives, e.g., iron or cobalt halides. Hereby the spectral gaps between the mercury emission lines are partly filled and a quasicontinuum is generated [6]. Almost any UVA or UVB spectral intensity distribution can be generated by choosing different metal halides and by combining the lamp with spectral filters. Metal halide lamps are more difficult to operate and more expensive than low-pressure mercury fluorescent lamps, but allow for higher UV powers and thus for shorter treatment times [3, 4]. Metal halide lamps have lengths in the range of 50–200 mm [9]. Thus a uniform whole body irradiation is difficult, but can be achieved by using multiple lamps in combination with reflectors [4].

11.2.2.2 Dielectric Barrier Discharge Lamps

Dielectric barrier discharge (DBD) UV lamps are special forms of high- or medium-pressure discharge sources that avoid the use of toxic mercury. They manage to extract narrowband (full width at half maximum less than 5 nm) UV radiation from a discharge in rare gas halide mixtures at elevated pressures by inserting at least one insulating layer (the dielectric) between metal electrodes [10]. The electrodes are supplied with an alternating high voltage. Launched discharges extinguish themselves continuously within about 10 ns because accumulated charges in the dielectric built up an electrical field that countervails and weakens the outer one. That is, the dielectric prevents the lamp from arcing and as a result it spreads the discharge over the entire electrode area in the form of multiple microdischarges. Due to the short discharge times only little gas heating appears, the plasma remains nonthermal [11] and an efficient energy transfer from energetic electrons to gas atoms can be achieved. Dermatological DBD lamps work with a mixture of xenon and chlorine gases in a glass vessel. Excited xenon–chlorine

molecule complexes (exciplexes) are generated in the microdischarges of the DBD and the subsequent decomposition of the exciplexes is associated with a narrowband UVB emission around 308 nm. Due to the generation of exciplexes these sources are also referred to as exciplex lamps or excimer lamps. Excimer lamps are non-laser sources and they may not be confused with excimer lasers. Compared to fluorescent tubes excimer lamps are more eco-friendly because they avoid the use of toxic mercury. Devices for the irradiation of surfaces up to 500 cm^2 with a narrowband UVB power of about 50 mW/cm^2 are on the market. In dermatology excimer lamps are currently mostly applied for targeted therapies. The disadvantage of dermatological DBD lamps is their limited lifetime of about 1,000 h [12, 13] and the application of high voltages, which may be a safety issue.

11.2.2.3 Electrodeless Excimer Lamps

Electrodeless excimer lamps achieve the formation of xenon–chlorine exciplexes in a low-pressure gas discharge without the use of a dielectric. This is of interest because in this case no high voltages are required to drive the discharge and to generate narrowband UVB radiation around 308 nm by the decomposition of exciplexes. Moreover, energy is coupled inductively into the low-pressure gas discharge by using a radio frequency (RF) in the MHz range. Therefore this kind of lamp is completely electrodeless. Due to the absence of both, a dielectric and electrodes, the wear of the lamp is minimized and its durability is estimated to be in the range of about 50,000 h. Up to now, electrodeless dermatological excimer lamps have only been studied in research projects [14] and they are not commercially available for phototherapeutic use. The reasons for this are the lack of adequate compact, low-cost electronics, the comparatively low narrowband UVB power of only about 20 mW/cm^2 achieved so far, and the small size of the irradiatable area of up to now only of some square centimeters.

11.2.3 Lasers

Lasers (=**l**ight **a**mplification by **s**timulated **e**mission of **r**adiation) are luminescence emitters that are characterized by the fact that they generate radiation via a process called stimulated emission. That is, if atoms in excited states encounter photons with energy that exactly matches the energy difference between the excited state and a lower energy level, the atoms can be stimulated by these photons to change over to the lower level [8]. Hereby the atoms emit photons that are an identical copy of the stimulating ones. If the number of atoms in the excited state is higher than the number of atoms in the lower energy state, radiation of a certain wavelength can be amplified in the energetic medium by photon multiplication. In a laser device radiation passes several times through an energetically activated medium by the use of mirrors. In so doing lasers are able to generate monochromatic radiation of very

high intensities. This requires that energy is permanently pumped into the laser medium to keep it in the activated state of population inversion.

For UV phototherapeutic purposes in dermatology xenon–chlorine excimer lasers that emit monochromatic UVB at a wavelength of 308 nm are applied [15, 16]. Just like excimer lamps excimer lasers use the decay of exciplexes to generate narrowband UVB radiation. However, due to the above-mentioned amplification principle dermatological excimer lasers deliver UVB intensities that are about 10 times higher than that of excimer lamps [16]. Besides, laser radiation has a narrower bandwidth than radiation of excimer lamps. The required population inversion between the bounded XeCl* exciplex state and the free xenon plus chlorine state is built up via a pulsed high-pressure gas discharge [17]. Consequently, the laser emission is discontinuous with a typical pulse width of some 10 ns and a frequency of up to 200 Hz [15, 16]. Excimer lasers deliver small spot sizes of only some square centimeters and are therefore solely suited for targeted therapies. Furthermore, dermatological lasers are expensive and bulky devices. Nevertheless, they offer an effective and economic treatment option for selected patients with recalcitrant lesions [18].

11.2.4 UV-LEDs

LEDs are solid state luminescence emitters that consist of a junction of n- and p-doped semiconductors. They generate UV radiation by the transition of electrons between energy bands in the semiconductor material [19]. Similar to the case of gas discharge lamps, a current flow through the LED is necessary to run the UV source. To achieve this, an external low voltage has to be applied in forward direction of the diode. Photons are generated, when electrons in the conduction band recombine with positive charge carriers (“holes”) in the energetically lower valence band of the semiconductor. Although LEDs are available for more than 50 years, UV-LEDs have evolved only over the past decade [20] and just a few dermatological LED devices that work in the UVA and even in the UVB spectral range are on the market today, Table 11.6. In the UVA range around 370 nm devices that generate irradiances of up to about 250 mW/cm^2 within an area of 15 cm^2 are state of the art. Current commercial dermatological UVB-LED devices are far less powerful. In each case, the spectral bandwidth of these sources is narrow and in the range of 10 nm.

Compared to gas discharge sources, LEDs have several significant advantages. LEDs are very compact and do not require high voltages. They are mercury free, long lasting, and do not need costly electronics to operate. Currently, from an economic point of view, they are not the right tool for large area or even whole body irradiations but they are very interesting for targeted therapies. Because LEDs are semiconductor devices, it is expected that prizes will decrease and powers will increase in the future. Thus, UV-LEDs will become more and more interesting for dermatologists.

11.3 Variants of Dermatological UV Phototherapy

In clinical practice several technologies for phototherapy have been developed and are used today. The major field of application is dermatology, but not exclusively. Oncology, transplantation medicine, pediatrics, vascular medicine, dentistry, and rheumatology—just to name a few—also use phototherapy.

Dermatological phototherapy is generally contraindicated in patients with a history of skin cancer or photosensitive diseases that may aggravate during treatment, patients with defective DNA repair mechanisms (like xeroderma pigmentosum), patients taking photosensitizing drugs and during pregnancy. The indication for phototherapy is more critical for children and adolescents. All treatments need proper equipment, clinical investigations of patients, dosimetry, documentation, and follow-up.

11.3.1 Psoralen Plus UVA (PUVA) Therapy

PUVA is an acronym for psoralen plus ultraviolet A radiation. The treatment consists of drug therapy in combination with UVA irradiation. The most commonly used drug is 8-methoxypsoralen (8-MOP). A less commonly used drug is 5-methoxypsoralen (5-MOP). Trimethylpsoralen (Trioxsalen) is used in Scandinavia for bath PUVA. Psoralen has to be applied about half an hour before irradiation and then works as a photosensitizer. Psoralen may be given orally, topically (ointment) or as PUVA-bath therapy. The initial UVA dosage for oral PUVA is 75 % of the minimal phototoxic dosage (MPD). In case of bath or cream PUVA treatment is started with 20–30 % of MPD. Oral 8-MOP is given at a dosage of 0.6 mg/kg body weight (bw), oral 5-MOP at 1.2 mg/kg bw. For bath PUVA 0.5–1.0 mg/L 8-MOP is used, the concentration for topical use in ointments varies between 0.0006 and 0.005 %. PUVA therapy is performed two to four times a week [21]. It is used successfully for a number of skin disorders, Table 11.1. Compared to narrowband UVB (NB-UVB) PUVA needs fewer sessions and provides a longer lasting clearance in psoriasis [27].

Potential risks and limitations of PUVA therapy are dependent on the way of application of psoralen. With oral treatment, nausea and vomiting are not uncommon. Therefore bath or cream PUVA are preferred today to avoid gastrointestinal adverse effects. Indeed, bath PUVA may achieve systemic psoralen concentrations comparable to oral application but with shorter half-life [28]. Generally, ocular protection is recommended to avoid lens opacities and cataracts [29]. There is a variation of PUVA called PUVAsol, which is used frequently in sun-rich countries like India. Here, psoralens are combined with natural sunlight. It is very popular for vitiligo therapy [30].

Table 11.1 Possible indications for PUVA therapy

Disorder	Remarks
Psoriasis, moderate to severe [21]	PASI[a] 75–100 after 6 weeks of treatment
Pustular psoriasis [22]	Best use in combination with oral retinoids
Cutaneous T-cell lymphomas	In particular for large plaque-type and Sezary Syndrome [23]
Disseminated granuloma annulare	In combination with fumaric acid esters [24]
Systemic sclerosis, morphoea	Improvement of skin sclerosis [25]
Graft-versus-host disease	Some improvement in lichenoid type [25]
Atopic dermatitis	Uncommonly used in severe forms [26]

[a]PASI, Psoriasis area and severity index. PASI 75 means a reduction of psoriasis area and severity by 75 %



Fig. 11.3 Bullous PUVA burn during treatment of plantar psoriasis

Acute adverse effects of PUVA therapy are pruritus and burns (Fig. 11.3). These patients may develop persistent post-inflammatory hyperpigmentation [31]. The induction of lentigines is not uncommon [32]. High PUVA exposure with oral 8-MOP bears an increased risk for the development of squamous cell carcinoma of skin (SCC) as shown by the American PUVA prospective trial [33]. In contrast to this, no increased cancer risk was documented in a European PUVA follow-up study [34]. The pharmacokinetic profile of psoralens applied topically suggests a lower skin cancer risk per se [35]. A large Scandinavian trial with trioxsalen bath PUVA did not find an increased risk for nonmelanoma skin cancer at all [36]. Nevertheless, genital skin should be protected and patients with a history of drug therapies or with an increased skin cancer risk should be excluded from PUVA. Accidental burns are a possible adverse effect in vitiligo. If patients also suffer from atopic dermatitis, prurigo nodularis may result [37].

11.3.2 Broadband UVB (BB-UVB) Therapy

BB-UVB covers the range of wavelengths from 280 to 320 nm. At least in Europe bulbs emitting a spectrum of 300–320 nm have been used for therapy. BB-UVB was a standard phototherapy for mild-to-moderate psoriasis for many decades [38]. The initial dose should be about 70 % of the minimal erythema dose (MED). Dose increase is monitored by clinical assessment of erythema. When treating plaque-type psoriasis 50–75 % of patient will reach a PASI 75 (see footnote Table 11.1) at week six [21]. Spa saltwater baths taken before BB-UVB increase the short-term clinical response [39]. On the other hand, it is ineffective in pustular psoriasis [21]. Other possible indications are patch-type mycosis fungoides [23] and vitiligo [40]. Possible adverse effects include sunburn and keratitis. Protective goggles are mandatory.

Compared to narrowband UVB (NB-UVB), broadband UVB (BB-UVB) has several disadvantages. Studies suggest that BB-UVB is less effective in the treatment of psoriasis and the risk of erythema and sunburn of non-affected skin is higher [21]. Contrary, a study including 12 psoriasis patients compared the erythema dose–response on unaffected skin using either BB-UVB or NB-UVB and found no significant differences [41]. Moreover, several long-term follow-up studies of psoriasis patients treated with BB-UVA did not observe an increased risk for nonmelanoma skin cancer [42] and in a single randomized controlled trial in patients with vitiligo, BB-UVB was more effective than NB-UVB [43] in contrast to a recent meta-analysis [44] and a retrospective trial [40].

11.3.3 Narrowband UVB (NB-UVB) Therapy

NB-UVB therapy is performed with lamps that have an emission peak around 311 nm. Initial dose and dose increase are similar to the values used in BB-UVB therapy. The 311 nm peak emission of the lamps is close to the 313 nm clearance maximum for psoriasis [45]. After 20 weeks a PASI 75 can be achieved in 40–100 % of cases depending on the severity of psoriasis and the weekly frequency of phototherapy [21]. The anti-psoriatic efficacy is increased by saltwater bathing before irradiation. A randomized controlled trial reported a PASI 75 in 68.1 % of psoriasis patients with combined modality versus 16.7 % with NB-UVB alone three times a week [46]. Synergistic effects have also been described for NB-UVB and tumor necrosis alpha inhibitors [47]. A meta-analysis for vitiligo suggested that NB-UVB is the most effective treatment with the least adverse effects [44]. Possible indications for NB-UVB are summarized in Table 11.2.

The rate of acute adverse effects is low. In a multicenter study 8,784 phototherapy treatments were evaluated. NB-UVB showed acute adverse effects in only 0.6 % of the treatments compared to 1.3 % for both oral and bath PUVA [49]. The most common adverse effect is erythema. Whereas the cancer risk is increased with

Table 11.2 Possible indications for NB-UVB

Disorders	Remarks
Psoriasis, plaque-type	PASI 75 in 40–100 % after 20 weeks [21]
Atopic dermatitis	For chronic and severe types [48]
Vitiligo	Ca. 44 % improvement after 16 weeks [43]
Cutaneous T-cell lymphoma	Patch type [23]
Polymorphic light eruption	Performed before sun season for UV hardening [48]

PUVA, there are no data suggesting an increased cancer risk for UVB phototherapies. Nevertheless, for safety reasons guidelines of the French Society of Photodermatology set a maximum number of 250 treatment sessions [50].

In several countries like Spain, USA and the Netherlands, home-based phototherapy is performed. Home-based NB-UVB therapy in the Netherlands was evaluated safe and as effective as in outpatient settings for psoriasis [51, 52]. NB-UVB was evaluated cost-effective and more efficient than biological drugs [53]. It is important to note that ocular protection is necessary to prevent cataract.

11.3.4 UVA-1 Therapy

UVA-1 phototherapy emerged as a specific phototherapeutic modality using the 340–400 nm wavelength range. Due to the deep penetration into the skin, UVA-1 affects T lymphocytes and activates endothelial cells, thereby promoting neovascularization [54]. Furthermore, UVA-1 can induce rapid apoptosis by induction of the Fas-FAAD (Fas-associating protein with death domain)-caspase 8 death complex [55].

UVA-1 is used in a variety of chronic inflammatory skin diseases. It is considered the first-line treatment in sclerotic skin diseases like morphoea, granuloma annulare, and sarcoidosis [56]. In contrast to PUVA and UVB phototherapy large trials are completely missing, but patients with darker skin types seem to benefit more than skin types I and II [57]. A selection of possible indications is summarized in Table 11.3. Acute adverse effects are rare and minimal [21]. Long-term risks such as skin cancer are unknown [57]. Currently, the major limitation for UVA-1 treatment is the expensive and large equipment [62].

11.3.5 Targeted UV Phototherapy

Targeted phototherapy describes the irradiation of small areas of lesional skin, often in psoriasis or vitiligo [63]. The concept is to protect uninvolved skin while using the highest tolerable doses for the target lesions to obtain a reliably and rapid response. There are several types of targeted phototherapy available:

Table 11.3 Possible indications for UVA-1 phototherapy

Disorders	Remarks
Morphoea	Improves skin sclerosis [58]
Atopic dermatitis	Severe cases [26]
Subacute cutaneous lupus erythematosus	For skin lesions only [59]
Systemic lupus erythematosus	Adjuvant for milder cases [60]
Subacute prurigo	Mixed response [58]
Cutaneous T-cell lymphoma	Plaque and patch types [23]
Graft-versus-host disease	[58]
Sarcoidosis	[61]

- Targeted UVB phototherapy
- Monochromatic light targeted therapy (308 nm excimer laser or excimer light)
- Targeted PUVA therapy
- Targeted photodynamic therapy

Targeted UVB phototherapy is also known as localized or focused or microphototherapy. The targeted NB-UVB device Biopsorin™ demonstrated a 75 % improvement of psoriasis lesions in 64 % of patients after 12 sessions [64]. Comparing different modalities in vitiligo, targeted NB-UVB and topical bethamethasone ointment were the most effective [65].

The 308 nm excimer laser is used in several skin conditions. A meta-analysis of excimer laser therapy in psoriasis comes to the conclusion that the laser is not more effective than NB-UVB, although it spares unaffected skin [66]. On the other hand, at difficult to treat areas like scalp or palms and soles 308 nm excimer laser seems to work safe and fast [67]. In an intraindividual comparison 307 nm excimer light was as effective as topical dithranol but less irritating [68, 69]. In vitiligo excimer laser and noncoherent excimer lamp seem to be of comparable efficacy [70, 71]. In a head-to-head comparison 308 nm excimer laser was less effective as targeted NB-UVB [72]. A list of possible indications is provided in Table 11.4.

11.3.6 Extracorporeal Photochemotherapy (ECP)

Extracorporeal photochemotherapy (ECP) is an apheresis-based immunomodulatory treatment targeting primarily circulating blood cells. Autologous peripheral mononuclear cells harvested by leukapheresis are exposed to the photosensitizer 8-MOP in a soluble form (Uvadex®). These cells are irradiated by UVA light of an approximate exposure of 1.5 J/cm^2. The photoactive blood cells are eventually reinfused into the patient. The technical equipment developed by Therakos, Inc. (Westchester, PA, USA) is now available in its third generation called Cellex. The standard treatment schedule consists of ECP on two consecutive days every 2–4 weeks [78].

Table 11.4 Possible indications for targeted phototherapy

Disorders	Targeted therapy
Psoriasis	Targeted NB-UVB [64]
	308 nm excimer laser [66]
	Excimer light [68, 69]
Vitiligo	Targeted NB-UVB [65]
	308 nm excimer laser [71]
	Excimer light [71]
Alopecia areata	Targeted UVA [73]
Mycosis fungoides	308 nm excimer laser [74]
Chemical leukoderma	308 nm excimer laser [75]
Pityriasis alba	308 nm excimer laser [76]
Lichen planopilaris	308 nm excimer laser [77]



Fig. 11.4 A patient with pre-erythrodermic cutaneous T-cell lymphoma. *Left* before treatment. *Right* with complete remission after a 6 months course with ECP as monotherapy

ECP was approved by the Food and Drug Administration (FDA) in the late eighties for cutaneous T-cell lymphoma. It can be used as monotherapy or in combination with interferon or oral systemic retinoids (Fig. 11.4) [23]. Patients who are responders show a long-term survival [79]. A number of other indications that have been investigated are summarized in Table 11.5.

Table 11.5 Possible indications for ECP

Disorders	Remarks
Cutaneous T-cell lymphoma	More effective when combined with interferon alfa or retinoids [80]
Graft-versus-host disease	More data are available for chronic than acute graft-versus-host disease [81]
Systemic sclerosis	Effects on skin sclerosis [82]
Crohn's disease	50 % response rate [83] and reduction of steroids [84]
Atopic dermatitis	In severe type 73 % response rate [85]
Pemphigus and pemphigoid	Steroid-refractory cases [86]
Solid organ transplant rejection	Significant reduction of rejection in heart and lung transplantation [87]

11.4 Mechanisms of Action for Major Dermatological Indications

UV irradiation in general induces a cellular and cytokine response of tissue. UVB can induce single cell death (apoptosis) of keratinocytes, generally known as sunburn cells. Furthermore epidermal uric acid becomes isomerized. Proinflammatory cytokines like interleukin-1, which is responsible for fever reaction after severe sunburn, are released. In addition, UVB has an impact on the sensory skin function by interacting with transient receptor potential ion channels of epidermal keratinocytes—a mechanism that is involved in sunburn pain [88].

UVA can aggravate skin aging (extrinsic aging) and potentiate negative effects on smoking, another extrinsic pro-aging factor. UVA affects in particular the skin-associated lymphocytic tissue (SALT) and causes molecular injuries of dermal elastic fibers leading to elastosis. When used in combination with psoralens as in PUVA therapy, oxygen-dependent and oxygen-independent photoreactions occur. The latter type of reaction leads to DNA crosslinks and cyclobutane rings. The oxygen-dependent pathway produces reactive oxygen species that result in membrane damage, protein and lipid oxidation, and mitochondrial disturbances. Keratinocytes seem to be less sensitive compared to inflammatory cells [89–92].

The major dermatological indications for phototherapy are chronic inflammatory disorders like psoriasis, autoimmune diseases of skin such as lichen ruber or vitiligo and selected cutaneous malignancies in particular cutaneous T-cell lymphoma. In the following section the corresponding photobiological mechanisms of action are discussed.

11.4.1 Psoriasis

Psoriasis is a chronic or chronic relapsing disease of unknown origin. T lymphocytes and dendritic cells seem to play a major role in psoriasis pathogenesis. Psoriasis affects about 2–3 % of the world population. It can occur in every age but is most frequently in adults of younger and middle age. Psoriasis has a broad variety of cutaneous lesions and severity. Phototherapy is normally applied together with topical therapy and/or systemic therapies. The goal of the treatment is complete remission, i.e., PASI 100. The mode of action seems to be the inhibition of leukocyte and T-lymphocyte proinflammatory activity and apoptosis of inflammatory cells. For pustular psoriasis phototherapy is combined with oral retinoids, i.e., Re-PUVA. Phototherapy has no significant effects on extracutaneous manifestations of psoriasis, e.g., arthritis, dactylitis, enthesitis, and iridocyclitis [93].

11.4.2 Atopic Dermatitis

Atopic dermatitis is a common inflammatory disease that belongs to a group of atopic disorders together with pollinosis and allergic asthma. Its incidence is increasing and up to 20 % of western population is affected. About two-third of patients have their first manifestation of atopic dermatitis in preschool age. The disease is associated with dry and sensitive skin. It can run a limited or a generalized severe course, Fig. 11.5.

For atopic dermatitis UVB, UVA, UVB/UVA mixed spectrum, high intensity UVA-1, and ECP all have been used as an adjuvant treatment during maintenance. All UV-based therapies improve the major symptom—pruritus. There is a decrease of epidermal Langerhans cells, apoptosis of inflammatory cells, reduction of proinflammatory cytokines, and reduction of bacterial colonization. Another possible effect is the improvement of vitamin D levels. Phototherapy alone is not effective in atopic dermatitis. The basis of treatment is skin care with moisturizer to repair the epidermal barrier function and topical anti-inflammatory drug therapy.

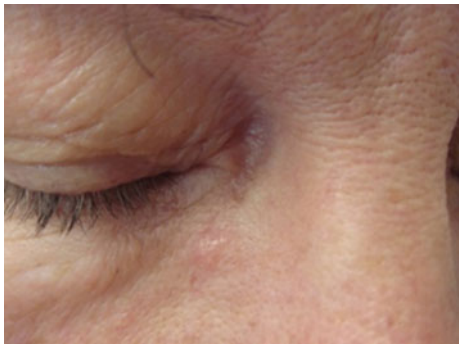


Fig. 11.5 Subacute atopic eczema of the eyelids. Lid edema is obvious

The average broad-spectrum UV/UVB/UVA/PUVA treatment consists of a course of 2–3 weeks with at least three treatments per week [94, 95].

11.4.3 Vitiligo

Vitiligo is a disorder of pigmentation, known as white spot disease. Although the disease is not life-threatening, it has a great social and psychological negative impact. About 2 % of the world population is affected by this disease. There are a number of hypotheses including autoimmune pathogenesis, but the disease is not completely understood. There is a loss of pigmentation and a loss of melanocytes in lesional skin. This leads to an imbalance of reactive oxygen production and oxygen radical scavengers during UV irradiation. Phototherapy of vitiligo is widely accepted, but needs many months up to 2 years for a stable response. The response is often only partial. The mode of action is at least twofold. (a) Resting melanocytes become stimulated again to produce melanin by UV irradiation. (b) The cellular inflammatory infiltrate in young lesions is suppressed. A 75 % re-pigmentation is considered a good outcome. Acral vitiligo of hands and feet is almost unresponsive to phototherapy. Generalized vitiligo is no indication for phototherapy at all. Due to the higher risk of sunburn in vitiligo skin, dose increase should be slow and carefully monitored.

11.4.4 Cutaneous T-Cell Lymphomas

Cutaneous T-cell lymphomas are rare disorders. The most common types are mycosis fungoides and Sezary syndrome. The patch and plaque type of mycosis fungoides can be treated by phototherapy. Patches are responsive to UVB, plaques need PUVA. The efficacy of PUVA can be further increased by combining it with oral retinoids. This is also known as Re-PUVA. The treatment is focussing on intraepidermal malignant T lymphocytes and aims to induce apoptosis.

When cutaneous T-cell lymphomas are treated by ECP, the goal is to produce a higher number of dendritic cells from circulating macrophages acting against malignant T lymphocytes. The assumed mode of action is immunostimulatory to target neoplastic T lymphocytes in cutaneous T-cell lymphomas. Apoptotic lymphocytes stimulate the differentiation of monocytes into dendritic cells releasing tumor necrosis factor-alpha and interleukin-6. These cells also produce cytokines with an immunosuppressive effect like interleukin-10 and interleukin-1Ra [96].

The treatment aims to get a complete remission or at least a partial remission to control the disease [23].

11.4.5 Lichen Planus and Alopecia Areata

In lichen planus and alopecia areata, an autoimmune T-cell response against either basal keratinocytes or hair follicle epithelium is responsible for the clinical symptoms. Both disorders are not uncommon. They may affect patients of any age. Phototherapy is used to interrupt the T-cell reaction and serves as an induction therapy rather than a maintenance therapy. PUVA seems to work better than UVB due to the location of the inflammatory infiltrate within the dermis [58].

11.4.6 Systemic Sclerosis and Morphoea

Systemic sclerosis and morphoea are autoimmune connective tissue diseases. Morphoea usually runs a milder and often self-limiting course, whereas systemic sclerosis is a multiorgan disease with significant mortality. A major player in skin fibrosis is tumor necrosis factor-beta. Phototherapy including ECP leads to a reduction of this cytokine and a partial remission of skin fibrosis. It has no significant effects on internal organs. Therefore phototherapy is used as an adjuvant therapy [58, 82].

11.4.7 Graft-Versus-Host Disease

Graft-versus-host disease (GVHD) is the consequence of infusion of mature donor T lymphocytes in allogeneic hematopoietic cellular transplantation. Clinically, GVHD can be separated into an acute and chronic type. The incidence of acute GVHD varies from 20 to 70 % depending on genetic differences between donor and patients. The donor T lymphocytes attack skin, gastrointestinal system, and liver. Patients not responsive to corticosteroids may be candidates for ECP since mortality rates are up to 70 %. Chronic GVHD affects about 50–70 % of patients after allogeneic transplantation. Here the skin is the most affected organ but virtually every organ may be affected. Acute GVHD shows three separate phases. It starts with liberation of cytokines during the cytotoxic conditioning treatment. During transplantation allogeneic T lymphocytes are transferred and in the last phase they expand into cytotoxic T lymphocytes attacking disparate antigens in multiple tissues. The chronic GVHD is less understood. But here the donor T lymphocytes attack also common antigens of donor and recipient [81].

The mode of action of ECP is apoptosis of inflammatory cells, induction of dendritic cells of the recipient and development of peripheral tolerance to self [96]. Most data are available from ECP treatment of chronic GVHD [97].

11.4.8 Polymorphic Light Eruption

Polymorphic light eruption (PLE) is a photosensitive pruritic skin disease. It has a prevalence of up to 20 % in Central and Northern Europe and the USA. An impairment of neutrophil responsiveness to leucotriene B4 and formyl-methionyl-leucyl-phenylalanin has been detected in PLE patients. Diagnosis is made on clinical presentation of pruritic papules and plaques in sun-exposed areas during early summertime confirmed by photoprovocation with UVA and UVB light. In PLE phototherapy is a preventive measure not suitable after clinical manifestation. It is used before the sunny season to adapt the skin to higher dosages of light. The therapeutic principle is known as skin hardening. Skin hardening aims to stimulate the cutaneous protective measures before the skin becomes exposed to higher intensity sunlight. Such effects include increase of epidermal thickness and increased pigmentation by melanin. Furthermore, skin hardening restores the neutrophil responsiveness to leucotriens [98]. Skin hardening is effective with UVA and/or UVB devices depending on the responsible wavelength. A home-based UVB device (SunshowerMedical™) was as effective and safe as an office-based broadband UVB irradiation in a smaller trial from the Netherlands [99].

11.5 Clinical Studies with Novel UV Emitters

The efficacy of dermatological phototherapy has been demonstrated in numerous clinical studies and NB-UVB is recommended for the treatment of psoriasis in national guidelines all over the world [21, 50, 100]. One of the major technological trends that can be identified within this field is represented by the application of mercury-free UV sources for targeted NB-UVB phototherapy. Examples for this approach are excimer lamps and UV-LEDs. In this chapter two recent clinical studies on psoriasis using an electrodeless excimer lamp and UVB-LEDs will be discussed in detail to illustrate the clinical methodology and to show that an UVB-LED based phototherapy is a promising and feasible concept, especially for home therapy purposes.

11.5.1 Study with an Electrodeless Excimer Lamp

The efficacy of UVB excimer lamps for psoriasis phototherapy has been described in a variety of publications [101–103]. By the authors of this chapter, a clinical study on psoriasis has been carried out using the unique electrodeless excimer lamp demonstrator setup described in Sect. 11.2 [14, 68, 69]. The proband collective consisted of 21 hospitalized patients. 15 patients were male and six female subjects. The age of the patients was in the range of 26–84 years. During the study two

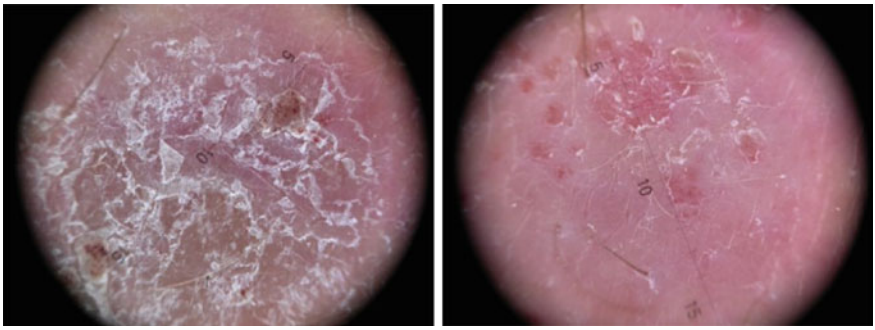


Fig. 11.6 Photo documentation of a psoriatic lesion. *Left* initial state. *Right* end state of the irradiated lesion (scale in mm)

dropouts appeared that were not related to the UVB treatment. For this research, patients with small localized lesions of a size that roughly matches the maximum irradiatable area of 3 cm^2 were selected. All patients were suffering from psoriasis for many years with a recent acute episode that necessitated a stationary treatment. 15 patients had psoriasis vulgaris, three patients plaque psoriasis and three patients psoriasis vulgaris of plaque-type. For each patient one selected lesion was irradiated with UVB and all other lesions, including a comparison lesion, were treated twice daily with dithranol, a strong anti-psoriatic drug applied topically. Before each UVB application clinical inspections as well as an objective spectroscopic measurement of the lesions were performed. For almost all patients the UVB application has been carried out three times at intervals of approximately a week. The applied dose was adjusted by means of the irradiation time and dependent on the skin type of the proband and the type of disease. However, the starting doses were the minimal erythema dose of the patients in each case. The irradiation periods for single sessions have been in the range of 10–30 s with an average value of 20 s and an irradiance of about 20 mW/cm^2.

For the clinical diagnosis of the patients the local Psoriasis Severity Index (PSI) was used. The PSI is a modified PASI index for selected plaques [104]. It describes erythema, scaling and infiltration as features of local psoriasis intensity. Based on the PSI score, a successful NB-UVB treatment could be demonstrated, Fig. 11.6. The total averaged PSI improvement was 3.0 points. This corresponds to a 40 % enhancement. Moreover, the results demonstrated that NB-UVB irradiation is equipotent to topical dithranol when the PSI score is considered. But, in total, the UVB treatment consumes less time and it is not associated with skin staining as in the case of dithranol. The most common adverse effects of excimer light treatment were mild-to-moderate erythema and temporary blistering.

11.5.2 Study with UV-LEDs

Devices for targeted phototherapy using UV-LEDs are still rare. Currently, no more than three units that have been developed for commercialization could be identified on the market, Table 11.6. It is expected that the number of dermatological LED-based irradiation devices will increase with the emergence of more efficient UV-LEDs. Due to the small number of commercially available irradiation devices only very few clinical studies that applied UV-LEDs for dermatological phototherapy exist. One of them is a study of Kemény et al. [105, 106] which used an array of 72 UVB-LEDs for psoriasis treatment with particular reference to a home-based therapy. The applied LED device was exclusively manufactured for this research by Allux Medical Inc. and is not yet commercially available. It emits 1 mW/cm^2 at a central wavelength of 310 nm with 15 nm bandwidth and a maximum irradiatable area of about 100 cm^2. Although the delivered irradiance is comparatively low, the study demonstrates that this device is capable of treating psoriasis lesions successfully. Twenty subjects with chronic plaque-type psoriasis were participating in the study. Three of the subjects were female and 17 male. The age was ranging from 29 to 71 years (average 51.7 years). The dimensions of the used LED irradiation device were very compact and amounted to only 128 mm × 90 mm × 38 mm so that the unit could be attached to the patient for treatment, Fig. 11.7. To protect surrounding healthy skin during delivery of the UVB irradiation an UV-blocking polymer foil was used.

Table 11.6 Devices for UV phototherapy using UV-LEDs

Device	Manufacturer	Spectral range
LEDA HP 370	Alma Laser GmbH	UVA
Psoria-Light	Psoria-Shield Inc.	UVA and UVB
Resolve UVB Phototherapy system	Allux Medical Inc.	UVB

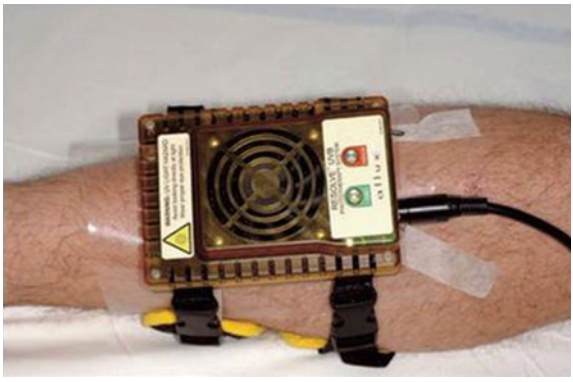


Fig. 11.7 UVB-LED irradiation device attached to a patient. Reprinted with permission from [106], Copyright 2010, John Wiley & Sons

For purpose of assessment of the treatment success symmetrical psoriasis lesions located on extremities or trunk were chosen. One of the lesions was treated with the LED device, whereas the other one served as an untreated control. Just like described in Sect. 11.5.1, the PSI was used to evaluate clinical improvements numerically. UV treatments were performed four times weekly for up to 8 weeks or until complete clearance has been achieved. Two different irradiation regimens were used in the study, one with a fast dose increase from session to session according to the doses typically used for outpatient treatment and one with a slow increase in dose, similar to regimens used for home-based treatments. In each case, ten subjects have been treated. The starting dose in the first regime was one MED. The dose was increased every visit by 20–50 % up to a final maximum dose of five MED. This maximal dose corresponded to 1.75 J/cm^2. In the second regimen (low dose home therapy range) the starting dose has been only 0.7 MED and the dose was increased by only 0.1 MED per session up to a maximum value of 3.8 MED.

Patients in both groups responded very well to the UVB therapy. Overall improvement of PSI at the end of the therapy was 93 and 84 % for the high and the low dose regimen, respectively. Thus, one important outcome of the study is that comparable results were achieved in the high and the low dose group. But, in contrast to the high dose group, in the low dose regime no side effects were reported. That is, it has been demonstrated that UVB-LEDs are well suited for a psoriasis home therapy. The safety profile of such a therapy is considered excellent and the therapy may also be useful for other UV responsive diseases [106].

11.6 Summary and Outlook

UV phototherapy is well established in the treatment of a wide range of photoresponsive skin diseases. Historically several variants, benefiting also from technological innovations in the field of UV light sources, have evolved and now are routinely applied in the clinical practice. The introduction of UV-LEDs undoubtedly is the most recent step in the development of new light sources for phototherapeutic purpose. The combination of these safe and economic light sources with additional device integrated safety features holds the potential to bring phototherapy out of the clinic and into the patient's home environment in a larger extend. Home phototherapy devices have first become available in the 1980s and since then home phototherapy has been growing steadily, especially for the treatment of psoriasis [107]. In the future also smart textiles equipped with flexible organic light emitting diodes may be used for home phototherapy [108]. Nevertheless, an adequate therapy management under guidance by professional dermatologists will stay mandatory in order to ensure the proper application of phototherapy.

References

1. E.A. Sosnin, T. Oppenländer, V.F. Tarasenko, Applications of capacitive and barrier discharge excilamps in photoscience. J. Photochem. Photobiol. **7**, 145–163 (2006)
2. H. Hönigsmann, History of phototherapy in dermatology. Photochem. Photobiol. Sci. **12**, 16–21 (2013)
3. H. Lui, R. Rox Anderson, Radiation sources and interaction with skin, in *Photodermatology,* ed. by H.W. Lim, H. Hönigsmann, J.L.M. Hawk (Informa Healthcare, New York, 2007)
4. AWMF online, Empfehlungen der deutschen dermatologischen Gesellschaft, Empfehlungen zur UV-Phototherapie und Photochemotherapie, http://www.awmf.org/leitlinien/detail/ll/013-029.html. Accessed 17 Jan 2014
5. The dead sea research center 2006, http://www.deadsea-health.org/new_html/general_main.html. Accessed 17 Jan 2014
6. Philips brochures: Philips lamps for phototherapy treatment. And: Light sources for phototherapy. Philips Electronics N.V., http://www.lighting.philips.com/pwc_li/main/subsites/special_lighting/phototherapy/assets/Phototherapy_range_brochure_2012.pdf. Accessed 17 Jan 2014. http://www.lighting.philips.com/pwc_li/main/application_areas/assets/phototheraphy/phototherapy_treatment.pdf. Accessed 10 Feb 2014
7. S. Lautenschlager, Phototherapie (UVB/Schmalspektrum UVB/UVA), in *Physikalische Therapiemaßnahmen der Dermatologie*, 2nd edn. (Steinkopf Verlag, Darmstadt, 2006)
8. D. Kühlke, *Optik* (Verlag Harri Deutsch, Frankfurt a.M, 2007)
9. L. Endres, R. Breit, UV radiation, irradiation and dosimetry, in *Dermatological Phototherapy and Photodiagnostic Methods,* ed. by J. Krutmann, H. Hönigsmann, C.A. Elmets, 2nd edn. (Springer, Berlin, 2009)
10. U. Kogelschatz, Dielectric barrier discharge: Their history, discharge physics and industrial applications. Plasma Chem. Plasma Process. **23**, 1–46 (2003)
11. A. Chirokov, A. Gutsol, A. Fridman, Atmospheric pressure plasma of dielectric barrier discharges. Pure Appl. Chem. **77**, 487–495 (2005)
12. Cin Laser, Corporacion internaciolal del laser, http://www.cinlaser.com/pdf/308Excimer_es.pdf. Accessed 22 Jan 2014
13. V.F. Tarasenko, Excilamps as efficient UV-VUV light sources. Pure Appl. Chem. **74**, 465–469 (2002)
14. B. Seme, A. Meyer, S. Marke, I. Streit, Light for treating skin diseases. Optik und Photonik. (4), 44–46 (2010)
15. T. Passeron, J.-P. Ortonne, Use of the 308-nm excimer laser for psoriasis and vitiligo. Clin. Dermatol. **24**, 33–42 (2006)
16. S.R. Feldman, B.G. Mellen, T.S. Housman, R.E. Fitzpatrick, R.G. Geronemus, P.M. Friedman, D.B. Vasily, W.L. Morison, Efficacy of the 308-nm excimer laser for treatment of psoriasis: Results of a multicenter study. J. Am. Acad. Dermatol. **46**, 900–906 (2002)
17. H.V. Bergmann, U. Rebhan, U. Stamm, Design and technology of excimer lasers, in *Excimer Laser Technology,* ed. by D. Basting, G. Marowsky (Springer, Berlin, 2005)
18. A. Marchetti, S.R. Feldman, A. Boer Kimball, R. Rox Anderson, L.H. Miller, J. Martin, P. An, Treatments for mild-to-moderate recalcitrant plaque psoriasis: Expected clinical and economic outcomes for first-line and second-line care. Dermatol. Online J., **11**, 1 (2005)
19. L. Halonen, E. Tetri, P. Bhusal (eds.), Lighting technologies, in *Guidebook on Energy Efficient Electric Lighting for Buildings* (Aalto University School of Science and Technology, Department of Electronics, Lighting Unit, Aalto, Finland, 2010)
20. C. Edwards, A.V. Anstey, Therapeutic ultraviolet light-emitting diode sources: A new phase in the evolution of phototherapy. Br. J. Dermatol. **163**, 3–4 (2010)
21. A. Nast, W.H. Boehncke, U. Mrowietz, H.M. Ockenfels, S. Philipp, K. Reich, T. Rosenbach, A. Sammain, M. Schlaeger, M. Sebastian, W. Sterry, V. Streit, M. Augustin, R. Erdmann, J. Klaus, J. Koza, S. Müller, H.D. Orzechowski, S. Rosumeck, G. Schmid-Ott, T. Weberschock, B. Rzany, Deutsche Dermatologische Gesellschaft (DDG);

Berufsverband Deutscher Dermatologen (BVDD): S3—Guidelines on the treatment of psoriasis vulgaris (English version) Update. J. Dtsch. Dermatol. Ges. **10**(Suppl 2), S1–S95 (2012)
22. X. Chen, M. Yang, Y. Cheng, G.J. Liu, M. Zhang, Narrow-band ultraviolet B phototherapy versus broad-band ultraviolet B or psoralen-ultraviolet A photochemotherapy for psoriasis. Cochrane Database Syst. Rev. **10**, CD009481 (2013)
23. U. Wollina, Cutaneous T-cell lymphoma: Update on treatment. Int. J. Dermatol. **51**, 1019–1036 (2012)
24. U. Wollina, D. Langner, Treatment of disseminated granuloma annulare recalcitrant to topical therapy: A retrospective 10-year analysis with comparison of photochemotherapy alone versus photochemotherapy plus oral fumaric acid esters. J. Eur. Acad. Dermatol. Venereol. **26**, 1319–1321 (2012)
25. F. Breuckmann, T. Gambichler, P. Altmeyer, A. Kreuter, UVA/UVA I phototherapy and PUVA photochemotherapy in connective tissue diseases and related disorders: A research based review. BMC Dermatol. **4**, 11 (2004)
26. F.M. Garritsen, M.W. Brouwer, J. Limpens, P.I. Spuls, Photo(chemo)therapy in the management of atopic dermatitis: an updated systematic review with the use of GRADE and implications for practice and research. Br. J. Dermatol. (in press)
27. E. Archier, S. Devaux, E. Castela, A. Gallini, F. Aubin, M. Le Maître, S. Aractingi, H. Bachelez, B. Cribier, P. Joly, D. Jullien, L. Misery, C. Paul, J.P. Ortonne, M.A. Richard, Efficacy of psoralen UV-A therapy vs. narrowband UV-B therapy in chronic plaque psoriasis: a systematic literature review. J. Eur. Acad. Dermatol. Venereol. **26**(Suppl. 3), 11–21 (2012)
28. U.P. Kappes, U. Barta, U. Merkel, A. Balogh, P. Elsner, High plasma levels of 8-methoxypsoralen following bath water delivery in dermatological patients. Skin Pharmacol. Appl. Skin Physiol. **16**, 305–312 (2003)
29. A.N. Abdullah, K. Kevczkes, Cutaneous and ocular side-effects of PUVA photochemotherapy—a 10-year follow-up study. Clin. Exp. Dermatol. **14**, 421–424 (1989)
30. R. Rai, C.R. Srinvinas, Phototherapy: An Indian perspective. Indian J. Dermatol. **52**, 169–175 (2007)
31. H. Herr, H.J. Cho, S. Yu, Burns caused by accidental overdose of photochemotherapy (PUVA). Burns. **33**, 372–375 (2007)
32. M.B. Abdel-Naser, U. Wollina, M. El Okby, S. El Shiemy, Psoralen plus ultraviolet A irradiation-induced lentigines arising in vitiligo: involvement of vitiliginous and normal appearing skin. Clin. Exp. Dermatol. **29**, 380–382 (2004)
33. R.S. Stern, E.J. Liebman, L. Vakeva, Oral psoralen and ultraviolet-A light (PUVA) treatment of psoriasis and persistent risk of nonmelanoma skin cancer, PUVA Follow-up Study. J. Natl. Cancer Inst. **90**, 1278–1284 (1998)
34. T. Henseler, E. Christophers, H. Hönigsmann, K. Wolff, Skin tumors in the European PUVA Study. Eight-year follow-up of 1,643 patients treated with PUVA for psoriasis. J. Am. Acad. Dermatol. **16**, 108–116 (1984)
35. S.E. Shephard, R.G. Panizzon, Carcinogenic risk of bath PUVA in comparison to oral PUVA therapy. Dermatology **199**, 106–112 (1999)
36. A. Hannuksela-Svahn, B. Sigurgeirsson, E. Pukkala, B. Lindelöf, B. Berne, M. Hannuksela, K. Poikolainen, J. Karvonen, Trioxsalen bath PUVA did not increase the risk of squamous cell skin carcinoma and cutaneous malignant melanoma in a joint analysis of 944 Swedish and Finnish patients with psoriasis. Br. J. Dermatol. **141**, 497–501 (1999)
37. S.B. Verma, U. Wollina, Accidental PUVA burns, vitiligo and atopic diathesis resulting in prurigo nodularis: a logical but undocumented rarity. An. Bras. Dermatol. **87**, 891–893 (2012)
38. J.A. Parrish, Phototherapy and photochemotherapy of skin diseases. J. Invest. Dermatol. **77**, 167–171 (1981)
39. W. Lapolla, B.A. Yentzer, J. Bagel, C.R. Halvorson, S.R. Feldman, A review of phototherapy protocols for psoriasis treatment. J. Am. Acad. Dermatol. **64**, 936–949 (2011)

40. A. Akar, M. Tunca, E. Koc, Z. Kurumlu, Broadband targeted UVB phototherapy for localized vitiligo: A retrospective study. Photodermatol. Photoimmunol. Photomed. **25**, 161–163 (2009)
41. S. Das, J.J. Lloyd, P.M. Far, Similar dose-response and persistence of erythema with broad-band and narrow-band ultraviolet B lamps. J. Invest. Dermatol. **117**, 1318–1321 (2001)
42. Medical Advisory Secretariat, Ultraviolet phototherapy management of moderate-to-severe plaque psoriasis: An evidence-based analysis. Ont. Health Technol. Asssess. Ser. **9**, 1–66 (2009)
43. M. El-Mofty, W. Mostafa, R. Youssef, M. El-Fangary, A. El-Ramly, D. Mahgoub, M. Fawzy, M. El-Hawary, BB-UVA vs. NB-UVB in the treatment of vitiligo: a randomized controlled clinical study (single blinded). Photodermatol. Photoimmunol. Photomed. **29**, 239–246 (2013)
44. R.M. Bacigalupi, A. Postolova, R.S. Davis, Evidence-based, non-surgical treatments for vitiligo: A review. Am. J. Clin. Dermatol. **13**, 217–237 (2012)
45. J.A. Parrish, K.F. Jaenicke, Action spectrum for phototherapy of psoriasis. J. Invest. Dermatol. **76**, 359–362 (1981)
46. J.H. Eysteinsdóttir, J.H. Olafsson, B.A. Agnarsson, B.R. Lùðviksson, B. Sigurgeirsson, Psoriasis treatment: faster and long-standing results after bathing in geothermal seawater. A randomized trial of three UVB phototherapy regimens. Photodermatol. Photoimmunol. Photomed. **30**, 25–34 (2014)
47. P.G. Calzavara-Pinton, R. Sala, M. Arisi, M.T. Rossi, M. Venturini, B. Ortel, Synergism between narrowband ultraviolet B phototherapy and etanercept for the treatment of plaque-type psoriasis. Br. J. Dermatol. **169**, 130–136 (2013)
48. T. Gambichler, F. Breuckmann, S. Boms, P. Altmeyer, A. Kreuter, Narrowband UVB phototherapy in skin conditions beyond psoriasis. J. Am. Acad. Dermatol. **52**, 660–670 (2005)
49. J.A. Martin, S. Laube, C. Edwards, B. Gambles, A.V. Anstey, Rate of acute adverse events for narrow-band UVB and Psoralen-UVA phototherapy. Photodermatol. Photoimmunol. Photomed. **23**, 68–72 (2007)
50. J.C. Beani, M. Jeanmougin, Narrow-band UVB therapy in psoriasis vulgaris: Good practice guideline and recommendations of the French Society of Photodermatology. Ann. Dermatol. Venereol. **137**, 21–31 (2010)
51. M.B. Koek, E. Buskens, H. van Weelden, P.H. Steegmans, C.A. Bruijnzeel-Koomen, V. Sigurdsson, Home versus outpatient ultraviolet B phototherapy for mild to severe psoriasis: Pragmatic multicentre randomised controlled non-inferiority trial (PLUTO study). BMJ **338**, b1542 (2009)
52. A.N. Rajpara, J.L. O'Neill, B.V. Nolan, B.A. Yentzer, S.R. Feldman, Review of home phototherapy. Dermatol. Online J. **16**, 2 (2010)
53. S. Vañó-Galván, M.T. Gárate, B. Fleta-Asín, A. Hidalgo, M. Fernández-Guarino, T. Bermejo, P. Jaén, Analysis of the cost effectiveness of home-based phototherapy with narrow-band UV-B radiation compared with biological drugs for the treatment of moderate to severe psoriasis. Actas. Dermosifiliogr. **103**, 127–137 (2012)
54. N.R. York, H.T. Jacobe, UVA1 phototherapy: A review of mechanisms and therapeutic applications. Int. J. Dermatol. **49**, 623–630 (2010)
55. S. Zhuang, I.E. Kochevar, Ultraviolet A radiation induces rapid apoptosis of human leukemia cells by FAS ligand-independent activation of the Fas death pathways. Photochem. Photobiol. **78**, 61–67 (2003)
56. S. Rombold, K. Lobisch, K. Katzer, T.C. Grazziotin, J. Ring, B. Eberlein, Efficacy of UVA1 phototherapy in 230 patients with various skin diseases. Photodermatol. Photoimmunol. Photomed. **24**, 19–23 (2008)
57. H.T. Jacobe, R. Cayce, J. Nguyen, UVA1 phototherapy is effective in darker skin: A review of 101 patients of Fitzpatrick skin types I-V. Br. J. Dermatol. **159**, 691–696 (2008)

58. T. Gambichler, S. Terras, A. Kreuter, Treatment regimens, protocols, dosages, and indications for UVA1 phototherapy: Facts and controversies. Clin. Dermatol. **31**, 438–454 (2013)
59. N. Sönnichsen, H. Meffert, V. Kunzelmann, H. Audring, UV-A-1 therapy of subacute cutaneous lupus erythematosus. Hautarzt **44**, 723–725 (1993)
60. M.C. Polderman, S. le Cessie, T.W. Huizinga, S. Pavel, Efficacy of UVA-1 cold light as an adjuvant therapy for systemic lupus erythematosus. Rheumatology (Oxford) **43**, 1402–1404 (2004)
61. T. Graefe, H. Konrad, U. Barta, U. Wollina, P. Elsner, Successful ultraviolet al treatment of cutaneous Sarcoidosis. Br. J. Dermatol. **145**, 354–355 (2001)
62. A.C. Kerr, J. Ferguson, S.K. Attili, P.E. Battie, A.J. Coleman, R.S. Dawe, B. Eberlein, V. Goulden, S.H. Ibbotson, P. Menage Hdu, H. Moosley, L. Novakovic, S.L. Walker, J.A. Woods, A.R. Young, R.P. Sarkany, Ultraviolet A1 phototherapy: A British photodermatology group workshop report. Clin. Exp. Dermatol. **37**, 219–226 (2012)
63. T. Lotti, R. Rossi, P. Campolmi, Targeted UV-B phototherapy: when and why to start. Arch. Dermatol. **142**, 933–934 (2006)
64. T. Lotti, L. Tripo, M. Grazzini, A. Krysenka, G. Buggiani, V. De Giorgi, Focused UV-B narrowband microphototherapy (Biopsorin). A new treatment for plaque psoriasis. Dermatol. Ther. **22**, 383–385 (2009)
65. T. Lotti, G. Buggiani, M. Troiano, G.B. Assad, J. Delescluse, V. De Giorgi, J. Hercogova, Targeted and combination treatments for vitiligo. Comparative evaluation of different current modalities in 458 subjects. Dermatol. Ther. **21**(Suppl. 1), S20–S26 (2008)
66. T. Mudigonda, T.S. Dabade, C.E. West, S.R. Feldman, Therapeutic modalities for localized psoriasis: 308-nm UVB excimer laser versus nontargeted phototherapy. Cutis **90**, 149–154 (2012)
67. N. Al-Mutairi, A. Al-Haddad, Targeted phototherapy using 308 nm Xecl monochromatic excimer laser for psoriasis at difficult to treat sites. Lasers Med. Sci. **28**, 1119–1124 (2013)
68. U. Wollina, A. Koch, A. Scheibe, B. Seme, I. Streit, W.D. Schmidt, W. D.: Targeted 307 nm UVB-phototherapy in psoriasis. A pilot study comparing a 307 nm excimer light with topical dithranol. Skin Res. Technol. **18**, 212–218 (2012)
69. U. Wollina, A. Koch, A. Scheibe, B. Seme, I. Streit, W.D. Schmidt, Targeted 307 nm UVB-excimer light vs. topical dithranol in psoriasis. J. Eur. Acad. Dermatol. Venereol. **26**, 122–123 (2012)
70. K.K. Park, W. Liao, J.E. Murase, A review of monochromatic excimer light in vitiligo. Br. J. Dermatol. **167**, 468–478 (2012)
71. Q. Shi, K. Li, J. Fu, Y. Wang, C. Ma, Q. Li, C. Li, T. Gao, Comparison of the 308-nm excimer laser with the 308-nm excimer lamp in the treatment of vitiligo–a randomized bilateral comparison study. Photodermatol. Photoimmunol. Photomed. **29**, 27–33 (2013)
72. E. Verhaeghe, E. Lodewick, N. van Geel, J. Lambert, Intrapatient comparison of 308-nm monochromatic excimer light and localized narrow-band UVB phototherapy in the treatment of vitiligo: a randomized controlled trial. Dermatology **223**, 343–348 (2011)
73. G. Açikgöz, H. Yeşil, E. Calışkan, M. Tunca, A. Akar, Targeted photochemotherapy in alopecia areata. Photodermatol. Photoimmunol. Photomed. (in press)
74. J. Huang, S. Cowper, J. Moss, M. Girardi, Case experience of 308-nm excimer laser therapy compatibility with PUVA and oral bexarotene for the treatment of cutaneous lesions in mycosis fungoides. J. Drugs Dermatol. **12**, 487–489 (2013)
75. E. Ghazi, J. Ragi, S. Milgraum, Treatment of chemical leukoderma using a 308-nm excimer laser. Dermatol. Surg. **38**, 1407–1409 (2012)
76. N. Al-Mutairi, A.A. Hadad, Efficacy of 308-nm xenon chloride excimer laser in pityriasis alba. Dermatol. Surg. **38**, 604–609 (2012)
77. A.A. Navarini, A.G. Kolios, B.M. Prinz-Vavricka, S. Haug, R.M. Trüeb, Low-dose excimer 308-nm laser for treatment of lichen planopilaris. Arch. Dermatol. **147**, 1325–1326 (2011)
78. R. Knobler, G. Berlin, P. Calzavara-Pinton, H. Greinix, P. Jaksch, L. Laroche, J. Ludvigsson, P. Quaglino, W. Reinisch, J. Scarisbrick, T. Schwarz, P. Wolf, P. Arenberger, C. Assaf, M.

Bagot, M. Barr, A. Bohbot, L. Bruckner-Tuderman, B. Dreno, A. Enk, L. French, R. Gniadecki, H. Gollnick, M. Hertl, C. Jantschitsch, A. Jung, U. Just, C.D. Klemke, U. Lippert, T. Luger, E. Papadavid, H. Pehamberger, A. Ranki, R. Stadler, W. Sterry, I.H. Wolf, M. Worm, J. Zic, C.C. Zouboulis, U. Hillen, Guidelines on the use of extracorporeal photopheresis. J. Eur. Acad. Dermatol. Venereol. **28**(Suppl 1), 1–37 (2014)
79. U. Wollina, K. Liebold, M. Kaatz, A. Looks, A. Stuhlert, D. Lange, Survival of patients with cutaneous T cell lymphoma after treatment with extracorporeal photochemotherapy. Oncol. Rep. **7**, 1197–1201 (2000)
80. U. Wollina, M. Kaatz, Extracorporeal photochemotherapy in cutaneous T-cell lymphoma. An overview of current status. Int. J. Immunopathol. Pharmacol. (Section Dermatol). **13**, 479–488 (2000)
81. J.W. Hart, L.H. Shiue, E.J. Shpall, A.M. Alousi, Extracorporeal photopheresis in the treatment of graft-versus-host disease: Evidence and opinion. Ther. Adv. Hematol. **4**, 320–334 (2013)
82. R.M. Knobler, L.E. French, Y. Kim, E. Bisaccia, W. Graninger, H. Nahavandi, F.J. Strobl, E. Keystone, M. Mehlmauer, A.H. Rook, I. Braverman, Systemic sclerosis study group: A randomized, double-blind, placebo-controlled trial of photopheresis in systemic sclerosis. J. Am. Acad. Dermatol. **54**, 793–799 (2006)
83. M.T. Abreu, C. von Tirpitz, R. Hardi, M. Kaatz, G. Van Assche, P. Rutgeerts, E. Bisaccia, S. Goerdt, S. Hanauer, R. Knobler, P. Mannon, L. Mayer, T. Ochsenkuhn, W.J. Sandborn, D. Parenti, K. Lee, W. Reinisch, Crohn's disease photopheresis study group: Extracorporeal photopheresis for the treatment of refractory Crohn's disease: Results of an open-label pilot study. Inflamm. Bowel Dis. **15**, 829–836 (2009)
84. W. Reinisch, R. Knobler, P.J. Rutgeerts, T. Ochsenkühn, F. Anderson, C. von Tirpitz, M. Kaatz, C. Janneke van der Woude, D. Parenti, P.J. Mannon, Extracorporeal photopheresis (ECP) in patients with steroid-dependent Crohn's disease: An open-label, multicenter, prospective trial. Inflamm. Bowel Dis. **19**, 293–300 (2013)
85. M. Radenhausen, S. Michelsen, G. Plewig, F.G. Bechara, P. Altmeyer, K. Hoffmann, Bicentre experience in the treatment of severe generalised atopic dermatitis with extracorporeal photochemotherapy. J. Dermatol. **31**, 961–970 (2004)
86. U. Wollina, D. Lange, A. Looks, Short-time extracorporeal photochemotherapy in the treatment of drug-resistant autoimmune bullous diseases. Dermatology **198**, 140–144 (1999)
87. M.B. Marques, J. Schwartz, Update on extracorporeal photopheresis in heart and lung transplantation. J. Clin. Apher. **26**, 146–151 (2011)
88. C. Moore, F. Cevikbas, H.A. Pasolli, Y. Chen, W. Kong, C. Kempkes, P. Parekh, S.H. Lee, N.A. Kontchou, I. Yeh, N.M. Jokerst, E. Fuchs, M. Steinhoff, W.B. Liedtke, UVB radiation generates sunburn pain and affects skin by activating epidermal TRPV4 ion channels and triggering endothelin-1 signaling. Proc. Natl. Acad. Sci. U.S.A. **110**, E3225–E3234 (2013)
89. H. Chang, W. Oehrl, P. Elsner, J.J. Thiele, The role of H_2O_2 as a mediator of UVB-induced apoptosis in keratinocytes. Free Radic. Res. **37**, 655–663 (2003)
90. K.A. Hwang, B.R. Yi, K.C. Choi, Molecular mechanisms and in vivo mouse models of skin aging associated with dermal matrix alterations. Lab. Anim. Res. **27**, 1–8 (2011)
91. C.-H. Lee, S.-B. Wu, C.-H. Hong, H.-S. Yu, Y.-H. Wei, Molecular mechanisms of UV-induced apoptosis and its effect on skin residential cells: implication in UV-based phototherapy. Int. J. Mol. Sci. **14**, 6414–6435 (2013)
92. M. Egbert, M. Ruetze, M. Sattler, H. Wenck, S. Gallinat, R. Lucius, J.M. Weise, The matricellular protein periostin contributes to proper collagen function and is downregulated during skin aging. J. Dermatol. Sci. **73**, 40–48 (2014)
93. U. Wollina, L. Unger, B. Heinig, T. Kittner, Psoroatic arthritis. Dermatol. Ther. **23**, 123–136 (2010)
94. J. Ring, A. Alomar, T. Bieber, M. Deleuran, A. Fink-Wagner, C. Gelmetti, U. Gieler, J. Lipozencic, T. Luger, A.P. Oranje, T. Schäfer, T. Schwennesen, S. Seidenari, D. Simon, S. Ständer, G. Stingl, S. Szalai, J.C. Szepietowski, A. Taïeb, T. Werfel, A. Wollenberg, U. Darsow, European Dermatology Forum; European Academy of Dermatology and

Venereology; European Task Force on Atopic Dermatitis; European Federation of Allergy; European Society of Pediatric Dermatology; Global Allergy and Asthma European Network: Guidelines for treatment of atopic eczema (atopic dermatitis) Part I. J. Eur. Acad. Dermatol. Venereol. **26**, 1045–1060 (2012)

95. J. Ring, A. Alomar, T. Bieber, M. Deleuran, A. Fink-Wagner, C. Gelmetti, U. Gieler, J. Lipozencic, T. Luger, A.P. Oranje, T. Schäfer, T. Schwennesen, S. Seidenari, D. Simon, S. Ständer, G. Stingl, S. Szalai, J.C. Szepietowski, A. Taïeb, T. Werfel, A. Wollenberg, U. Darsow, European Dermatology Forum; European Academy of Dermatology and Venereology; European Task Force on Atopic Dermatitis; European Federation of Allergy; European Society of Pediatric Dermatology; Global Allergy and Asthma European Network: Guidelines for treatment of atopic eczema (atopic dermatitis) Part II. J. Eur. Acad. Dermatol. Venereol. **26**, 1176–1193 (2012)
96. R.L. Edelson, Mechanistic insights into extracorporeal photochemotherapy: Efficient induction of monocyte-to-dendritic cell maturation. Transfus. Apher. Sci. pii: S1473-0502 (13)00258-9 (2013)
97. P. Perseghin, M. Marchetti, C. Messina, A. Mazzoni, P. Carlier, C. Perotti, L. Salvaneschi, M Risso, R. Fanin, A. Olivieri, P. Accorsi, F. Locatelli, A. Bacigalupo, L. Pierelli, A. Bosi, Società Italiana di Emaferesi e Manipolazione Cellulare; Gruppo Italiano Trapianto di Midollo Osseo: Best practice recommendations in: (1) Peripheral blood stem cell mobilization and collection and (2) acute and chronic GvHD treatment using extracorporeal photopheresis. A joint effort from SIdEM (Società Italiana di Emaferesi e Manipolazione Cellulare) and GITMO (Gruppo Italiano Trapianto di Midollo Osseo). Transfus. Apher. Sci. **48**, 195–196 (2013)
98. P. Wolf, A. Gruber-Wackernagel, B. Rinner, A. Griesbacher, K. Eberhard, A. Groselj-Strele, G. Mayer, R.E. Stauber, S.N. Byrne, Phototherapeutic hardening modulates systemic cytokine levels in patients with polymorphic light eruption. Photochem. Photobiol. Sci. **12**, 166–173 (2013)
99. S.M. Franken, R.E. Genders, F.R. de Gruijl, T. Rustemeyer, S. Pavel, Skin hardening effect in patients with polymorphic light eruption: comparison of UVB hardening in hospital with a novel home UV-hardening device. J. Eur. Acad. Dermatol. Venereol. **27**, 67–72 (2013)
100. S.H. Ibbotson, D. Bilsland, N.H. Cox, R.S. Dawe, B. Diffey, C. Edwards, P.M. Farr, J. Ferguson, G. Hart, J. Hawk, J. Lloyd, C. Martin, H. Moseley, K. McKenna, L.E. Rhodes, D.K. Taylor, British association of dermatologists: An update and guidance on narrowband ultraviolet B phototherapy: A British photodermatology group workshop report. Br. J. Dermatol. **151**(2), 283–297 (2004)
101. Y. Niwa, T. Hasegawa, S. Ko, Y. Okuyama, A. Ohtsuki, A. Takagi, S. Ikeda, Efficacy of 308-nm excimer light for Japanese patients with psoriasis. J. Dermatol. **36**, 579–582 (2009)
102. L. Mavilia, M. Mori, R. Rossi, P. Campolmi, A. Puglisi, Guerra, T. Lotti: 308 nm monochromatic excimer light in dermatology: Personal experience and review of the literature. G. Ital. Dermatol. Venereol. **143**, 329–337 (2009)
103. S.P. Nistico, R. Saraceno, C. Schipani, A. Costanzo, S. Chimenti, Different applications of monochromatic excimer light in skin diseases. Photomed. Laser Surg. **27**(4), 647–654 (2009)
104. S.M. Taibjee, S.T. Cheung, S. Laube, S.W. Lanigan, Controlled study of excimer and pulsed dye lasers in the treatment of psoriasis. Br. J. Dermatol. **153**, 960–966 (2005)
105. L. Kemény, A. Koreck, Z. Csoma, Ultraviolet B treatment of plaque-type psoriasis using light-emitting diodes: A new phototherapeutic approach. J. Am. Acad. Dermatol. **60**, AB8 (2009)
106. L. Kemény, Z. Csoma, E. Bagdi, A.H. Banham, L. Krenacs, A. Koreck, Targeted phototherapy of plaque-type psoriasis using ultraviolet B-light-emitting diodes. Br. J. Dermatol. **163**, 167–173 (2010)
107. A.N. Rajpara, J.L. O´Neill, B.V. Nolan, B.A. Yentzer, S.R. Feldman, A review of home phototherapy for psoriasis. Dermatol. Online J. **16**, 12 (2010)
108. K. van Os, K. Cherenack, Wearable textile-based phototherapy systems. Stud. Health Technol. Inform. **189**, 91–95 (2013)

Chapter 12
UV Emitters in Gas Sensing Applications

Martin Degner and Hartmut Ewald

Abstract The *LED-based spectroscope* is described. Example measurements using the gases O_3, SO_2, and NO_2 are given. The unique properties of UV-LEDs are utilized in combination with standard broadband photodiodes (PD). These low-cost components can be arranged in a simple design which produces cost-effective but high-resolution sensors compared with current state-of-the-art measurement systems. Broad UV absorption lines/bands are well suited for UV emitter-based sensing.

12.1 Introduction

Optical spectroscopy has been widely used for substance analysis and concentration measurements such as gas-sensing application for a long time. When light is propagated through a medium the molecules and atoms in that medium interact with the photons in a manner which is dependent on their energy, and hence wavelength. Photon energy can be transferred to the matter. Specific sections of the spectrum of the incident light are absorbed in a manner which is characteristic for each substance. This selective light attenuation is utilized in absorption spectroscopy.

The light interaction is based on the spatial distribution of charges in a molecule that leads to vibrational and rotational excitation as well as valence electron excitation of molecules and atoms by higher energy photons.

The infrared region (IR) typically is the domain for identification and concentration determination of substances. The interaction between the light and molecules create unique and highly resolved signatures for nearly each molecule or

M. Degner · H. Ewald (✉)
Institute of General Electrical Engineering, University of Rostock,
Albert-Einstein-Str. 2, D-18059 Rostock, Germany
e-mail: hartmut.ewald@uni-rostock.de

M. Degner
e-mail: martin.degner@uni-rostock.de

© Springer International Publishing Switzerland 2016

M. Kneissl and J. Rass (eds.), *III-Nitride Ultraviolet Emitters*,
Springer Series in Materials Science 227, DOI 10.1007/978-3-319-24100-5_12

molecule group in this wavelength range. In particular, the mid-infrared (MIR) region is the so-called fingerprint region. Overtones of the MIR absorptions appear in the near infrared (NIR) range and often are used for measurements, because of the good technical access to this range (optics, optoelectronics). A considerable number of light sources and detectors have been available in the infrared for a long time. Thus there are a lot of systems on the market based on thermal light sources such as glow bars or on infrared lasers that already enable very high precision measurements.

The visible wavelength range is mainly characterized by an absence of strong absorptions, especially in our ambient surroundings (air, water). Therefore in nature, this optical window is predominately used for general observation and the spectral responsiveness of eyes is well known. In the visible range (VIS) only weak overtones of the infrared molecular light interaction appear. However, electron excitations of mainly complex linked molecules absorb light in the visible region.

The ultraviolet range is dominated by electron excitation, molecules such as NH_3, NO, O_3, SO_2, NO_2, and some hydrocarbons show strong absorptions here [1]. The absence of absorptions of high concentrated substances in the environment such as water vapor or CO_2 above 200 nm is a big advantage for sensor application compared with the infrared wavelength range. These substances, as well as oxygen or nitrogen, absorb mainly in the far UV (100–200 nm). Therefore, the wavelength region shorter than 200 nm is the so-called vacuum ultraviolet (VUV) range because the absorption in normal atmospheres is too strong for measurements.

Typically, the ultraviolet was not used for sensing application because of the lack of easy to use and robust light sources in this wavelength range. Predominately mechanically fragile short lifetime and costly gas discharge lamps such as the deuterium lamp had to be used. The development of semiconductor light sources changed this (see Chap. 1).

The first **L**ight **E**mitted **D**iodes (LED) were developed in the red and infrared region, followed by further visible LEDs. However, because of their low optical power emissions these LEDs were mainly used as indicator light sources. With the development of efficient shorter wavelength blue LEDs [2] a range of lighting application became feasible. In parallel, LEDs for the near and mid-infrared range have been developed that can also be utilized for spectroscopic application [3]. More important, in the last few years LEDs in the ultraviolet became available. Pioneering work in AlGaN-based LEDs for the UV wavelength range was done by companies such as *Nichia*,[1] *SETi*[2] as well as the *RIKEN*[3]-research institute [4, 5]. SETi is currently a major commercial supplier of deep ultraviolet LEDs with peak emissions from 240 to 355 nm [6]. UV-LEDs show a characteristically narrow emission bandwidth compared to longer wavelength LEDs. In contrast to the line-structure molecule absorption and the broadband LED emissions in the

[1] *Nichia—Nichia Chemical Industries, Ltd.*, Japan.

[2] *SETi—Sensor Electronic Technology, Inc.*, USA.

[3] *RIKEN—Independent Administrative Institution*, Japan.

infrared, the emission bandwidth of the UV-LEDs can be smaller than the bandwidth of broad absorption bands in the UV-VIS. Therewith, LEDs are predestinated to be utilized as wavelength-selective light sources for spectroscopic measurements [7, 8].

The possibility to generate light by forward biasing a semiconductor p–n junction creates a new electroluminescent light source. This 'cold' light source has unique properties that can be used for many applications. The 'color' or the wavelength range of the emitted light results from the superposition of the emitted photons with wavelength λ_{Photon}

$$\lambda_{\text{Photon}} = \frac{hc}{\Delta E} \tag{12.1}$$

c *speed of light*
h *Planck constant*

that are determined by the band gap energies $\Delta E = E_2 - E_1$ from the recombination of conduction band electrons with holes in the valence band. The band gap energy with the highest transition probability in consideration of the number of possible transitions and the occupation probability defines the peak emission wavelength of the LED. The relation between the band gap energy (eV) and the wavelength (μm) of the emitted photons is shown in Fig. 12.1 [9]. The band gap energies of the different semiconductor materials have a direct influence on the forward voltages of the LED. The band gap can be controlled and adjusted by the choice of semiconductor material and its material composition. Therefore, today LEDs can be created for nearly each wavelength over a very wide spectral range

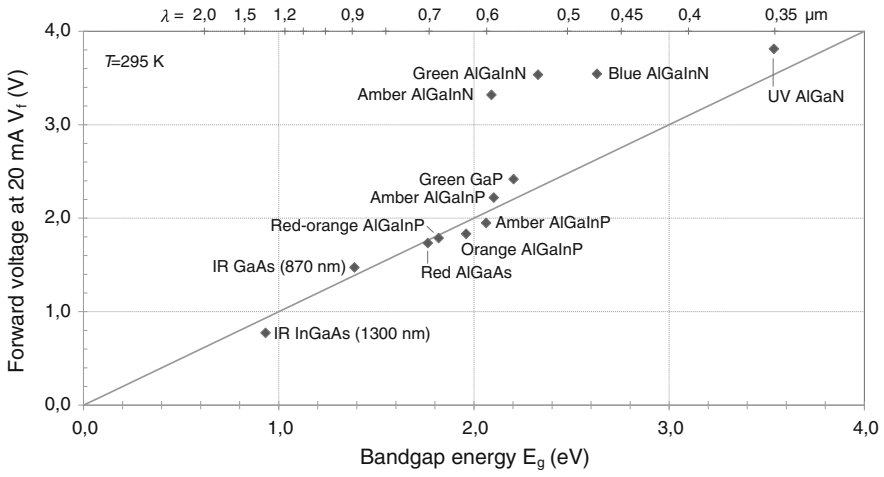


Fig. 12.1 Emission wavelength and forward voltages versus the band gap energies of the different semiconductor materials [9]

from the deep UV until the mid-infrared. This enables a huge number of applications for the so-called LED spectroscopy.

The newly developed UV-LEDs are essential for the LED spectroscopy in the ultraviolet using the strong absorptions of important gases in this wavelength range. The LED spectroscopy is especially well suited for concentration measurements with low-cost sensor designs and it enables robust and high resolved concentration measurements. In a basic measurement principle, unfiltered LEDs are directly used as wavelength-selective sources.

Due to the limited spectral resolution and the superposition of absorptions of various substances in the electron excitation range (UV-VIS) this method is not well suited for selective substance analyses but it can be used very successfully in applications where the participant substances are well known, such as process control application. This method will be described in following section. Moreover, UV-LEDs also can be used as UV light sources in combination with dedicated spectral selective detector units and optics in spectral highly resolved analyzing devices to replace commonly used UV light sources.

12.2 Light Absorption Spectroscopy

Light absorptions spectroscopy is based on the wavelength-selective interaction of light with matter. In opposite to the vibrational or rotational molecule excitation in the infrared region or the atomic interaction of high-energy radiation such as in the Röntgen range the dominating absorption mechanism in the UV-VIS range is the valence electron transition.

The lifetime of electron transitions is several magnitudes shorter than the transitions of vibrations in the infrared. Therefore, the resulting natural absorption linewidth is wider in the UV than in the sharp absorption lines in the infrared. Due to the electron excitation also vibrational and rotational modes are excited. They appear in the ultraviolet as an additional fine structure next to the electron absorption lines. The more complex a molecule is, respectively, the more conjugated double bonds are present, the more electron energy levels appear also with smaller gaps. This results in a higher number of possible transitions or absorption lines and in a red shift of the whole spectrum. The high density and number of absorption lines in addition with the fine structure and additional line broadening effects yields to overlapping of the absorption lines. In the UV-VIS range this superposition often results in broadband absorption spectra, with a high number of absorption lines overlaid. Figure 12.2 shows typical broadband absorption spectra of the example gases NO_2, SO_2, and O_3. Molecules with a less complex bonds show clearly separated absorption bands, such as NO and NH_3.

While the magnitude and shape of the absorption lines, and thus the differential structure of the UV absorption, is affected by ambient parameters such as pressure and temperature, the overall absorption band is hardly affected [10]. Therefore, the low spectral resolution of the unfiltered LED measurement is quite robust with

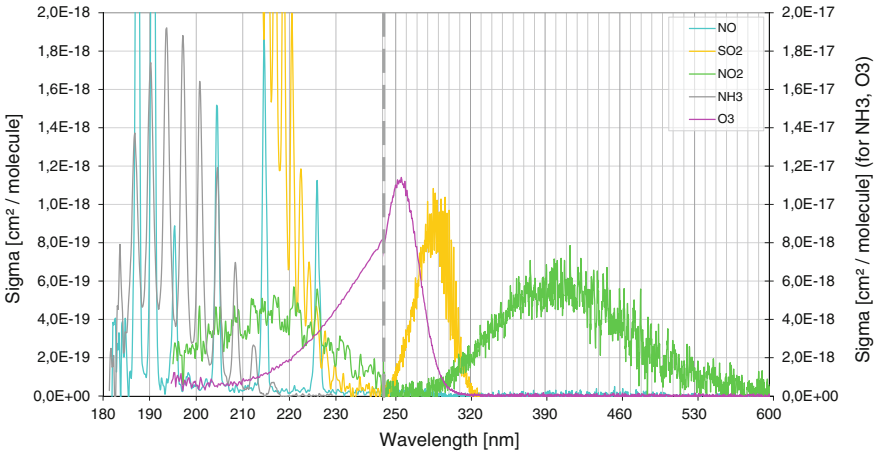


Fig. 12.2 UV-VIS absorption spectra of gases NO_2, SO_2, O_3, NO, and NH_3

respect to the ambient influence parameters. Nevertheless, temperature and pressure have an influence on the gas density and also on a real sensor design, thus it has to be measured for sensor signal compensation.

In a basic form the light absorption can functionally be described by the Bouguer–Lambert–Beer's law: The attenuation of the light intensity (I) passing a sample cell is wavelength-specific $I(\lambda)$. The change of intensity $\mathrm{d}I(\lambda)$ of a light beam that is passing a media over a path length $\mathrm{d}x$ is proportional to the local light intensity $I(\lambda)$, the path length $\mathrm{d}x$, and the absorbers concentration c (ppm) and its absorption coefficient $\alpha(\lambda)$ (cm^{-1}):

$$\mathrm{d}I(\lambda) = -\alpha(\lambda)cI(\lambda)\mathrm{d}x \tag{12.2}$$

By integration of (12.2) over the optical path length x (cm) of a sample cell the relationship between the measured intensity $I(\lambda)$ past the cell in relation to the incident light $I_0(\lambda)$ results with the exponential relation to the concentration c, the path length x, and the absorption coefficient $\alpha(\lambda)$ is obtained:

$$I(\lambda) = I_0(\lambda)e^{-\alpha(\lambda)cx} \tag{12.3}$$

This wavelength-specific absorption is illustrated in Fig. 12.3 at the example of one absorption line of NO_2. This basic absorption law assumes a homogenous absorber distribution and the absence of scattering and geometrical losses. Further nonlinearities regarding this law appear for instance at high concentrations.

By measuring the transmission of light of the absorption cell the concentration can be easily determined taking into account (12.3) and the known absorption length x as well as the absorption coefficient $\alpha(\lambda)$:

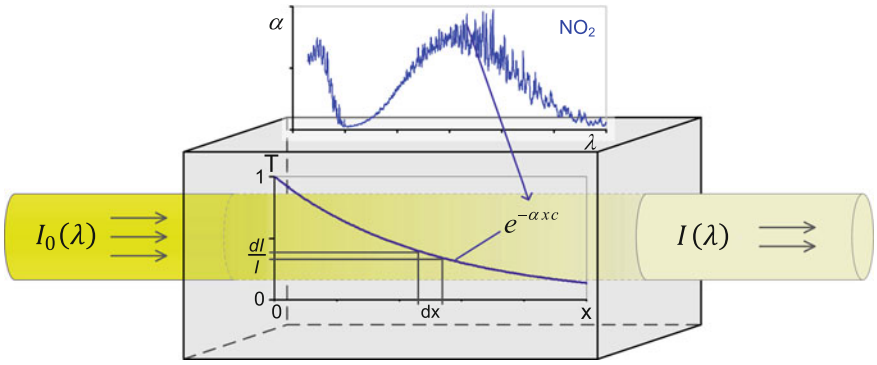


Fig. 12.3 Principle of wavelength-specific light absorption: the decay of intensity of the incident light $I_0(\lambda)$ for one absorption line of the absorption spectra of NO_2

$$c = \frac{\ln(T(\lambda))}{-\alpha(\lambda)x}; \quad \left(T(\lambda) = \frac{I(\lambda)}{I_0(\lambda)}\right) \tag{12.4}$$

Instead of using a length-depending attenuation coefficient the more comparable absorption cross section $\sigma(\lambda)$ per molecule is often used. The volume density of the molecules can be used to convert between the absorption coefficients. Equation (12.5) shows the calculation for a gas under standard conditions, using the Avogadro constant (N_A = 6.022136 × 10^{23} mol^{-1}) and molar volume (V_m = 22,414 cm^3/mol):

$$\sigma(\lambda) \cdot \frac{N_A}{10^6 \cdot V_m} = \alpha(\lambda) \tag{12.5}$$

In practical applications the spectral resolution of a sensor system has to be considered as well, when the gas absorption within the sensor, respectively, sensor measurement effect needs to be calculated. In the case of LED spectroscopy of gases with broad absorptions, typically no additional filters are used. All emitted wavelength from the LED interact specifically regarding the gas absorption characteristic. Thus the resulting absorption will be smaller than the maximum possible in this range. It is useful to calculate the effective absorption coefficient $\bar{\alpha}$ for the arrangement to estimate the sensor effect and enable further calculations for sensor resolution. $I_0(\lambda)$ is the spectral distribution of the emitted LED light intensity as it is detected by the sensor system so it includes the light transmission and (relative) responsivity of the system. Typically the wavelength dependency of the optical transmission and the responsivity is nearly constant over the few nanometers of the LED emission, thus these characteristics can be neglected and the LED emission can be used as $I_0(\lambda)$.

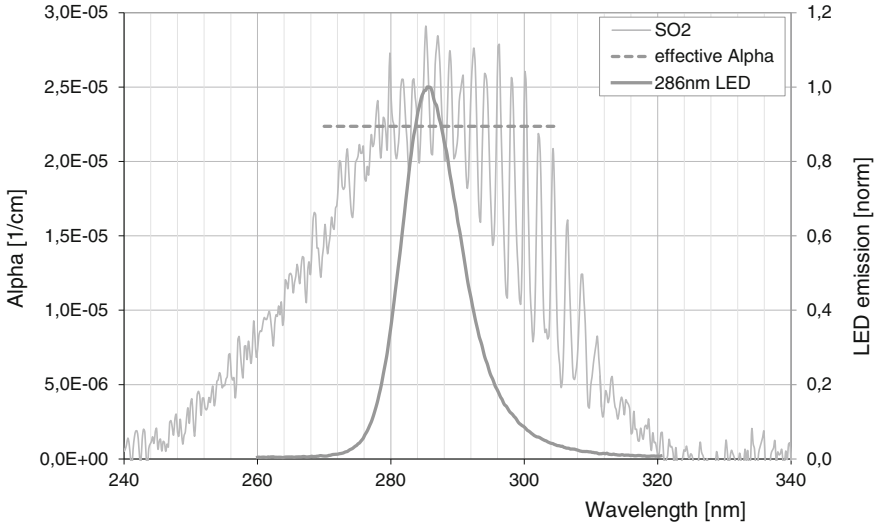


Fig. 12.4 Absorption characteristic of SO_2 superimposed with the normalized emission characteristic of a 286 nm LED, the effective absorption coefficient $\bar{\alpha}$ for LED–gas combination

$$T_{\text{ges}} = \frac{I_{\text{ges}}}{I_{0\text{ges}}} = e^{-\bar{\alpha}xc} = \frac{\int I_0(\lambda)T(\lambda)\mathrm{d}\lambda}{\int I_0(\lambda)\mathrm{d}\lambda}$$
$$\rightarrow \bar{\alpha} = \ln\frac{\int I_0(\lambda)T(\lambda)\mathrm{d}\lambda}{\int I_0(\lambda)\mathrm{d}\lambda} / -xc \tag{12.6}$$

In Fig. 12.4 an example calculation for an LED-based SO_2 measurement is shown.

In sensor applications the electronic resolution (signal to noise ratio) of an optical transmission system can be estimated from the expected optical power at the receiver. In combination with the effective absorption coefficient the resulting concentration resolution of the measurement system can be calculated at a given path length. The relationship between the electronic sensor resolution, the absorption path length, and the resulting concentration resolution is plotted in Fig. 12.5. Therefore, the design of a sensor system can be optimized with respect to the required resolution as well as for the maximum concentration dynamic that is limited by strong absorptions that lead to nonlinearities and saturation effects. It has to be considered that the optical path length and its optical design (e.g., reflection cell, multipath cell) can affect the detectable optical power significantly.

Concentration measurements in practical applications require a high level of robustness. A high robustness versus wavelength-independent attenuations within the optical path can be realized by implementing at least a second LED light source with a different wavelength as a reference. It is explained formally by (12.7), k is a wavelength-independent disturbance, which influences the transmission

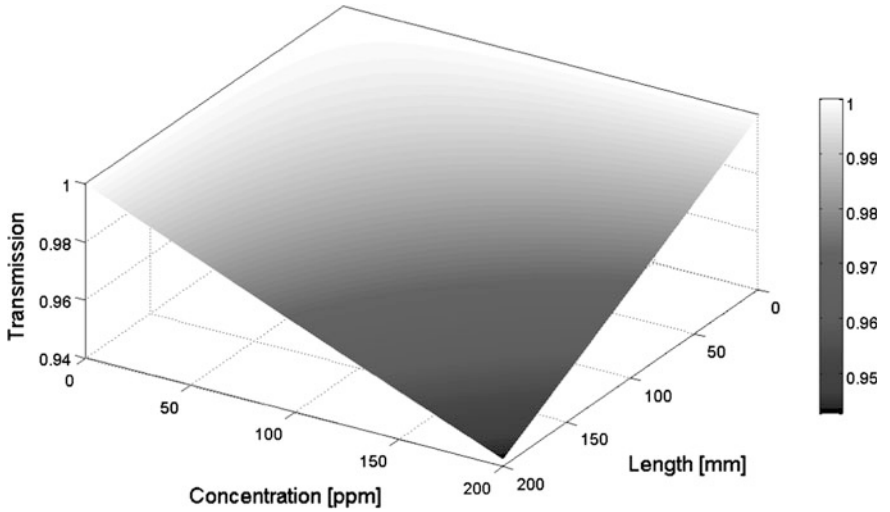


Fig. 12.5 NO_2 gas absorption sensing: relationship between gas concentration (resolution), absorption path length (related to sensor cell dimensions), and the optical transmission (relates to the electronic resolution)

measurement at a gas absorption wavelength $T_{\lambda\text{gas}}$ and at the reference wavelength $T_{\lambda\text{ref}}$. The resulting transmission T_{res} is compensated regarding wavelength-independent interferences and can be used for concentration calculation:

$$T_{\text{res}} = \frac{T_{\text{interf}\lambda\text{gas}}}{T_{\text{interf}\lambda\text{ref}}} = \frac{kT_{\lambda\text{gas}}}{kT_{\lambda\text{ref}}} = e^{-xc\left(\alpha_{\lambda\text{gas}} - \alpha_{\lambda\text{ref}}\right)} \tag{12.7}$$

Smooth wavelength-dependent interferences such as temperature caused changes of dispersion in the optical setup and can be compensated by a further reference wavelength.

In addition to the interference compensation, (12.7) demonstrates that the reference wavelength should be placed apart from the gas absorption, otherwise the resulting absorption coefficient is reduced. TDLAS (tunable diode laser absorption spectroscopy) systems applied to broadband electron absorption bands such as NO_2 are faced with this problem [11]. Because of the small wavelength shift of the laser only a small absorption change of a 'needle' from the absorption structure is used for the measurement although the integral absorption at the measurement point can be quite strong.

Spectral highly resolved measurement systems for instance based on spectrometer detectors or TDLAS systems use a higher number of spectral reference points, therefore the absorption shape can be identified and also wavelength-dependent interferences such as cross-interfering gases can be suppressed effectively.

In a system with low spectral resolution such as in LED spectroscopy, a cross-interfering substance can be actively compensated by an additional measurement of this substance with a further LED measurement channel. Sometimes a passive compensation can be realized by placing the reference wavelength ($\alpha_{\lambda ref}$) at a point where the interfering substance shows the same absorption as at the position of ($\alpha_{\lambda gas}$).

12.3 Absorption Spectroscopic Systems

Optical spectroscopy is used in an extremely wide range of application, it is implemented in harsh industrial application as well as in clean laboratory environment; it is also used for long-distance remote sensing as well as in miniature such as in biological cell analysis. Therefore, a huge number of different spectroscopic methods and systems exist.

In general spectroscopic methods can be distinguished in direct and indirect measurement principles. Direct measurement principles such as photoacoustic or fluorescence spectroscopy generate a measurement signal when the investigated substance is present. This is an advantage compared to the indirect methods. Absorption spectroscopy is an indirect method. The specific attenuation of a measurement signal is analyzed and correlated with the signature of the investigated substance to estimate for instance its concentration. A schematic overview of the general functional principle of absorptions measurement systems is shown in Fig. 12.6.

Absorption measurement systems require a light source that emits the necessary wavelength (also systems with a passive optical light source utilizing for instance the back ground radiation are available). Further optoelectronic detectors and adequate signal-processing are essential. Either the light source (A) or/and the detector (E) is optically filtered to utilize the spectral characteristic of the investigated substance for a selective and efficient measurement. Different possibilities for optical filtering are used such as dichroitic or tuneable filters, diffractive and

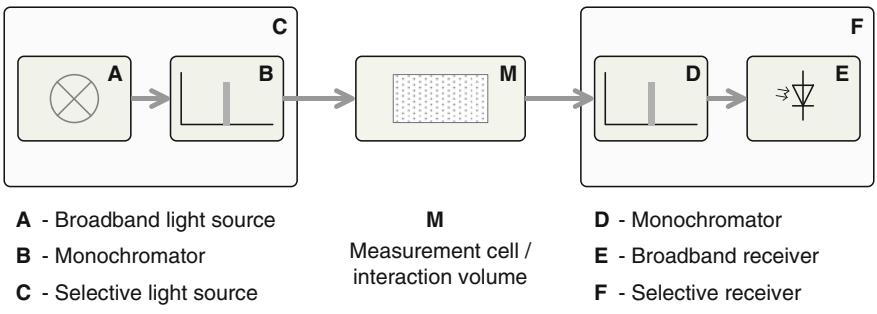


Fig. 12.6 Block diagram/principal of an optical absorption measurement system [12]

refractive filtering methods (e.g., monochromators, or spectrometers). Instead of a filtered broadband light source, also lasers are used as a selective light source (C). The utilized emission wavelength of the laser is shifted (e.g., in TDLAS) to detect the absorption shape and strength to realize selective concentration measurements of the investigated substance.

Within the measurement cell (M) or the interaction volume the light absorption by the substance under investigation takes place. A huge number of different designs and principles are used here depending on the application requirements and also on the optical properties of the light source. For instance, free path absorption cells, reflection or multipath cells, evanescent field or free atmospheric interaction (e.g., LIDAR—light detection and ranging spectroscopy) zones are used.

Two basic methods in LED-based spectroscopy can be used depending on the absorption characteristic of the investigated substance:

1. In the case of discrete and narrow linewidth absorption characteristics (e.g., NH_3 see Fig. 12.2) the LED emission appears to be broadband. Here it is beneficial to use optical filters such as dichroitic filters to increase the effective absorption coefficient and therewith realize high resolved concentration measurements. The LED is used here as a conventional broadband light source but the limited emission range leads to much lower requirements to the optical filters compared to typical broadband sources. Instead of application of optical filters also gas correlation filter technics can be used with LEDs. The limited LED emission range is advantageous here as well [13].
2. In a second type of application, the absorption characteristic is dominated by broad absorption bands as they are typical for the ultraviolet (e.g., O_3, SO_2 see Fig. 12.7). The LED emission is narrow band compared to the substance

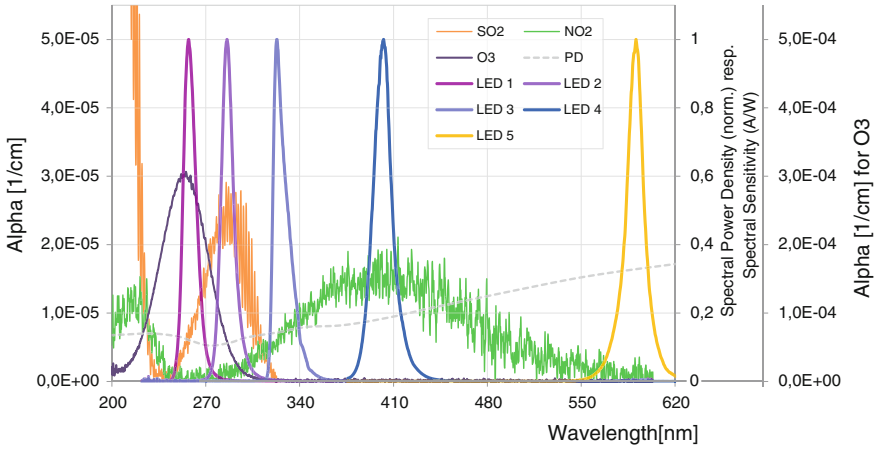


Fig. 12.7 Spectral absorption characteristics of SO_2, NO_2, and O_3 qualitatively superimposed with the normalized spectral power density of the utilized LEDs and the spectral power sensitivity of photodiode detector (PD)

absorption. LEDs with different emission spectra are used as selective light sources to sample the absorption characteristic of the substance and enable a spectral referenced measurement (see Fig. 12.7) [14, 15].

The following explanations are related to the second type of application because the properties of LEDs are most beneficial here.

The absorption measurement concept explained in Fig. 12.6 is considerably simplified in case of LED spectroscopy and therefore very low cost systems can be realized. The light of LEDs with different emission wavelength is optically coupled into a measurement cell and detected by a standard photodiode receiver with a broadband responsivity. To distinguish between the different LEDs, respectively, different wavelengths the LEDs are modulated electronically and the detector signal is demodulated. No mechanically moved parts such as optomechanical switches or shutters are required. Different options for electronically modulation such as time or frequency multiplex can be used. Which type of electronic modulation is best to use depends on the measurement time requirements and the needs of the detector amplifier unit for specific applications.

In opposite to TDLAS or classical broadband light source spectroscopy in this LED-based arrangement there is no fixed link between the emission power of the gas and reference wavelengths. Thus this link cannot be utilized to calculate the optical transmission without knowing the incident light intensity that is principally essential for the calculation of concentration by the transmission measurement [see, e.g., (12.4)]. The following equation represents the transmission estimation for light sources with a fixed ratio (k) between the emission wavelengths:

$$\begin{aligned} I_{0\,\lambda\,\mathrm{ref}} &= kI_{0\,\lambda\,\mathrm{gas}} \\ T_{\mathrm{res}} &= \frac{T_{\lambda\,\mathrm{gas}}}{T_{\lambda\,\mathrm{ref}}} = \frac{\frac{I_{\lambda\,\mathrm{gas}}}{I_{0\,\lambda\,\mathrm{gas}}}}{\frac{I_{\lambda\,\mathrm{ref}}}{I_{0\,\lambda\,\mathrm{ref}}}} = k\frac{I_{\lambda\,\mathrm{gas}}}{I_{\lambda\,\mathrm{ref}}} = ke^{-xc\left(\alpha\left(\lambda_{\mathrm{gas}}\right)-\alpha\left(\lambda_{\mathrm{ref}}\right)\right)} \end{aligned} \tag{12.8}$$

In LED spectroscopy, an optical reference detector is used to determine a signal that is proportional to the incident optical intensity $I_0(\lambda)$. This enables the calculation of the transmission of each LED channel and finally the determination of the substance concentration.

Spectral fluctuation within the emission spectrum of broadband light sources as well as changing wavelength shift conditions in a TDLAS application often also requires additional reference measurements for the correction of the intensity ratio (k) (12.8), respectively, the direct determination of incident light intensity $I_0(\lambda)$ via additional optics to enable high concentration resolutions. In laser application the monitor diode is well suited for this task.

A time sequence of typical LED spectroscopy signals of one ‘LED channel’ signal (received signal of the photodiode $I_1(\lambda)$ in absent of the measured gases) is shown in Fig. 12.8. The raw data of the measurement and reference signals correspond to the optical light intensities $I_{\lambda\,\mathrm{gas}}$ and $I_{0\,\lambda\,\mathrm{gas}}$. Based on these raw signals the transmission $T_{\lambda\,\mathrm{gas}}$ is calculated. There is no gas absorption present. The

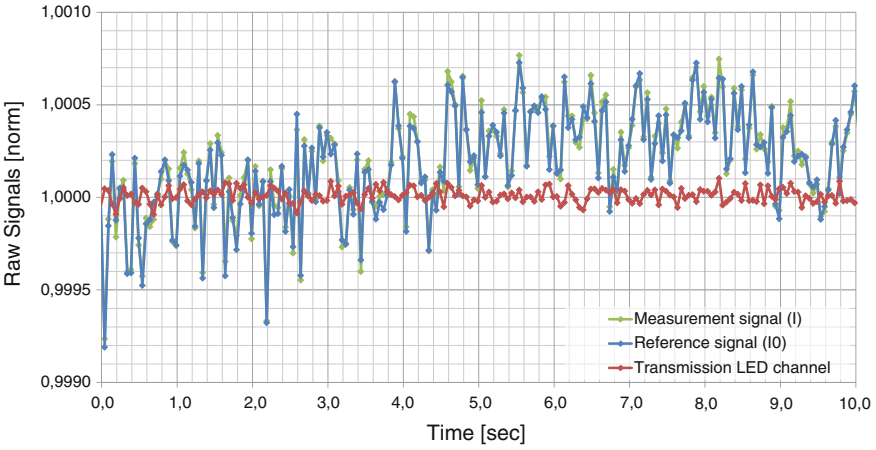


Fig. 12.8 LED spectroscopy: measurement and reference raw signals for one LED channel and the herewith calculated transmission signal as an example of signal disturbance reduction and drift compensation using a reference signal

reduction of fluctuations and the compensation of drift effects are obvious. The reduction in disturbance noise and drift of the electronic detection unit is important since it can increase the sensor resolution and the accuracy. Alternatively, the sensor dimensions (length of absorption cell) can be reduced (see Fig. 12.5).

The LED spectroscopy measurement principle based on UV-LEDs shows advantages compared to other spectroscopic state-of-the-art methods: The broadband absorptions in the UV can be used efficiently for the sensor effect and changes in the shape of the single lines due to surrounding parameters affecting the integral measurement only minimally. The absence of strong interfering absorbers such as water vapor enables much less effort for sensing gas preparation as it is commonly done in infrared analyzers. Even in situ measurements in harsh environment are possible in a number of applications such as exhaust gas sensing [12, 14, 15]. In addition to the strong absorption bands photodetectors in the UV show a much lower thermal noise than IR detectors. Therefore, high concentration resolutions can be achieved also with small absorption cells. Further the LED spectroscopy enables the measurement of more than one gas within one sensor cell. For each additional substance at least one additional LED channel has to be installed. Dichroitic filters can realize the optical linkage but since this requires a number of specific adapted filters the system costs will rise. Therefore, geometric optics can be used to combine the light output of different LEDs. Hence the light attenuation of each LED channel increases significantly with each additional LED. Therefore, the number of LEDs in a sensor system should be as low as possible. Another disadvantage of the UV-LED spectroscopy is caused by the overlapping of absorption bands of a number of different substances and the lack in spectral resolution to discriminate between these absorbers (see Fig. 12.2). Therefore, the sensor design, especially the spectral ranges of the LEDs, has to be adapted to the application.

12.4 Light Sources for UV Spectroscopy

In general, light sources can be distinguished in thermal and cold light sources. Thermal light sources emit a wide continuous radiation spectrum that is dependent only on the temperature of the emitter and can be described by the PLANCK's law. The higher the temperature the more the spectrum is shifted from the IR to the VIS (see Fig. 12.9). The materials limit the maximum temperature of the emitters and even at high temperatures, the light emission in the ultraviolet range is quite low. Therefore thermal light sources are unsuitable for UV sensing. The so-called "cold" light sources are based on luminescence effects, photons are generated by the transition from an excited energy state to a lower state. A number of different types of excitations of luminescence are known. Gas discharge lamps are cold light sources and still they are the dominant light source for ultraviolet sensing. Regarding the progress in the last year in development of ultraviolet semiconductor light sources this will change in near future.

The emission spectrum of gas discharge lamps can be varied by the gas composition, its pressure and by adding fluorescence materials. Typically, gas discharge lamps utilize a mercury base gas mixture but also xenon and deuterium are widely used.

In Fig. 12.10 the emission spectra of different low-pressure gas discharge lamps are shown. Narrow emission lines typically dominate the spectrum. The broadband fluorescence emissions are obvious also in that their different wavelength ranges

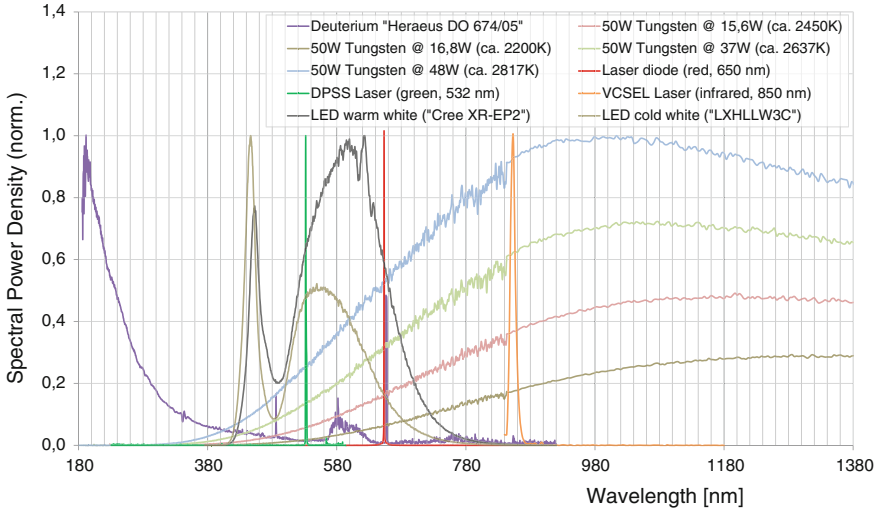


Fig. 12.9 Spectral emission characteristics of different types of light sources: continuous spectra of a deuterium lamp, incandescent lamp at different emission temperatures, white light fluorescence LEDs and laser

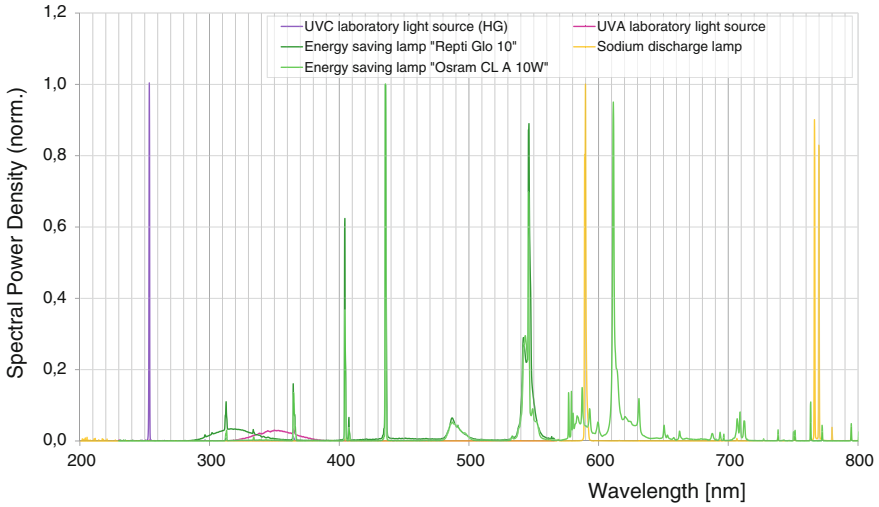


Fig. 12.10 Spectral emission characteristics of different low-pressure gas discharge lamps

have been chosen with regard to the fluorescence material and to the requirements of the application.

The emission lines of high-pressure gas discharge lamps are strongly broadened and result in a continuous emission spectrum that is overlaid with a huge number of emission lines. Xenon lamps are a typical example, depending on its design they can show strong emissions in the UV range. The spectral stability often is not suitable for spectroscopic application.

The deuterium lamp is a clear exception within the ultraviolet gas discharge lamps. The emission characteristic is very continuous and strong in the deep UV, only a few emission lines overlap. Due to these properties, the deuterium lamp is the light source predominantly used in ultraviolet spectroscopy. The emission spectrum of a deuterium lamp is shown in Fig. 12.9.

The main drawbacks of UV discharge lamps such as xenon or deuterium lamps are that they require complex control electronics, have a quite limited lifetime, are mechanically sensitive, often bulky and cost intensive. At certain wavelength lasers are also available in the ultraviolet range. These are at least frequency-doubled systems with a complex design and not suited for low-cost sensor application. In relation with the development of AlGaN-based LEDs [16] in the recent years research on UV-diode laser has also been undertaken. Especially because of the limited availability of various wavelengths gas sensing application are often restricted.

About 10 years ago, first AlGaN-based LEDs emitting in the ultraviolet range below 370 nm became commercially available by Sensor Electronic Technology, Inc. Currently, these LEDs are used for disinfection applications and curing of paints, epoxy resins, and polymers. Today UV-LEDs are commercial available at

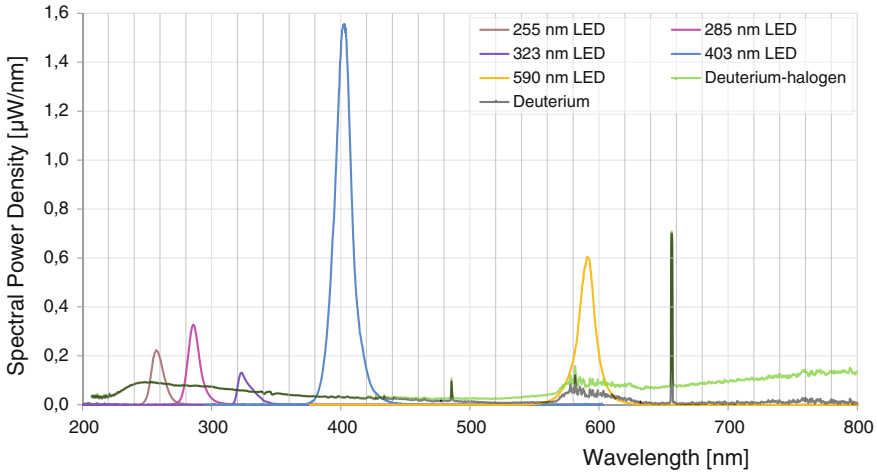


Fig. 12.11 Spectral power density of light source: comparison of different UV-LEDs versus deuterium discharge lamp and halogen lamp [13]

almost any wavelength between 400 and 240 nm [6, 17]. With respect to optical spectroscopy and sensor application UV-LEDs provide several advantages:

The full width at half maximum of the UV-LED emission spectrum (FWHM) is quite limited and thus well suited as a wavelength-selective light source. Typically, the FWHM of UV-LED emission spectra is between 10 and 20 nm. Although the total emission power of UV-LEDs is quite moderate, their spectral power density is quite high due to their narrow emission band. Compared to gas discharge lamps the point like emission area of the LEDs enables an efficient coupling within an optical system. For instance, fiber optics can be used for combining the light of different LEDs.

Figure 12.11 shows the spectral power density of five LEDs that are coupled into one 200 µm step index fiber in comparison to the fiber optical output spectrum of a commercial deuterium/halogen tungsten lamp (AvaLight-DH-S-DUV, [18]) coupled into the same type of optical fiber.

Although the efficiency of deep UV-LEDs is actually not that high the spectral power density of the fiber-coupled LEDs is higher than that of the deuterium light source. The total electrical power consumption of all LEDs in this test is about 750 mW, the overall electrical power consumption of the broadband light source is about 78 W. Fiber optical coupling enables a dedicated combination of several LEDs without the use of complex free path optics. Moreover, sensor applications in harsh environments (e.g., high temperature, strong electromagnetic fields) become feasible (see Sect. 12.5).

Compared to other light sources the optical output of LEDs can be controlled electronically very well. For instance the optical power can easily be controlled from minimum to maximum emission also with high modulation frequencies up to the MHz range. These are advantages not only compared to discharge lamps but

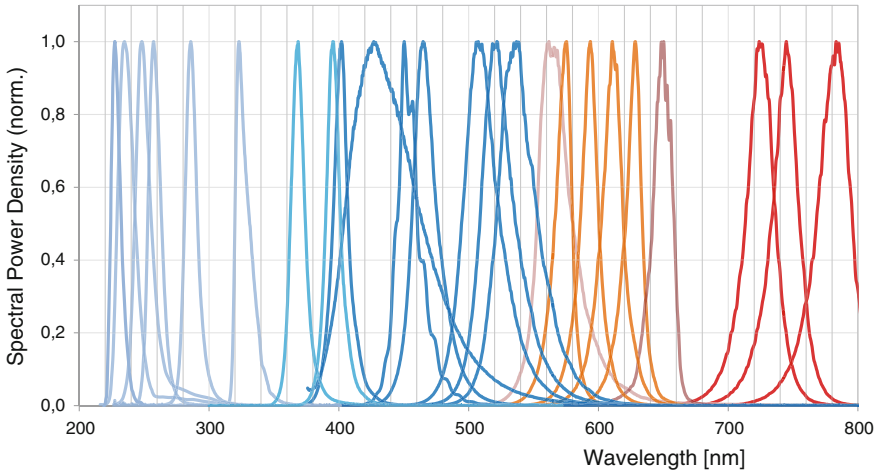


Fig. 12.12 Normalized spectral emission of LEDs from Deep UV to VIS range, (revised from [12, 19])

also to diode lasers. A good modulation is important in spectroscopic measurements to combine different sources and realize proper signal detection without interferences. In LED spectroscopy no mechanically moved parts are required. In addition LEDs, compared to other light sources, are shock- and vibration proof. In combination with their small size, very robust and compact sensors can be designed. In some application it is also important that in case of damage no danger by hazardous substances rises from the component. This can be guaranteed by LEDs as opposed to the commonly used discharge lamps. The historical development of light emitting diodes, for instance at blue wavelengths, showed LEDs can be produced in high quantities for low costs per unit. Today nearly each peak emission wavelength from the deep UV to the VIS (and also to the IR) range can be realized, see example emission spectra in Fig. 12.12.

The lifetime of LEDs is strongly dependent on the operation mode in relation to its efficiency. For instance, due to high efficiency and thus low thermal charge at high optical output power blue LEDs can have very high lifetime of 100,000 h and more. Currently, UV-LEDs especially deep ultraviolet emitters have still lower lifetimes.

However, a lifetime of 10,000 h for a 310 nm LED has been demonstrated [20] and further improvements can be expected.

The main drawbacks of LEDs are the temperature dependency of emission power and its spectral characteristic. Especially, for industrial application the limited upper operation temperature is a restriction. These properties have to be included and compensated by the sensor design. For high-resolution measurements, the limited stability of LED light emission has also to be considered.

Under the aspect of spectroscopic applications, a qualitative comparison of the properties of the above-mentioned light sources is given in Table 12.1 in an

Table 12.1 Comparison of properties of light sources for spectroscopy application

	Thermal light source	Gas discharge lamp		Laser	LED
		Low pressure	High pressure		
Spectral characteristic					
Availability	−	o	o	−	+
Selectivity	−−	++	−	++	o
Power density	−	+	+	++	o
Directional characteristic	−	−−	o	++	+
Modulation capability	o	−−	−−	+	++
Stability	+	−−	−	+	−
Robustness	o	−	−	+	+
Structural shape	+	−	−	−	++
Life time	−	+	−	+	+
High quantity costs	+	o	o	−	++

−− very negative, − negative, o neutral, + positive, ++ very positive

abstracted form. Important properties for spectroscopic application are listed and benchmarked.

In compare to commonly used light sources for spectroscopic application (in the ultraviolet), the properties of LEDs are unique. These devices enable totally new possibilities in sensing application such as LED spectroscopy. However, the restrictions especially of low efficient deep UV-LEDs has to be considered.

12.5 Optical and Electrical Properties of the LEDs for Spectroscopy Application

The light generation within the UV-LED is dominated by spontaneous emission of photons and therefore the light emission is isotropic in all directions and incoherent. The efficiency of generating photons within a semiconductor LED is characterized by the internal quantum efficiency (IQE). Because of photon reabsorption within the semiconductor heterostructure and reflection of photons at the semiconductor/air interfaces only a small percentage of photons is able to escape the semiconductor chip. Therefore, the external quantum efficiency (EQE) is typically much lower than the IQE.

In Fig. 12.13 an overview about the available wavelength range of the UV-LEDs is given [20]. Moreover the maximum external quantum efficiency is marked. The high EQE of LEDs around 400 nm is remarkable but for sensor design it has to be considered that currently the LEDs at shorter wavelength have an external quantum efficiency that is a few decades lower. In low effective materials in addition to the

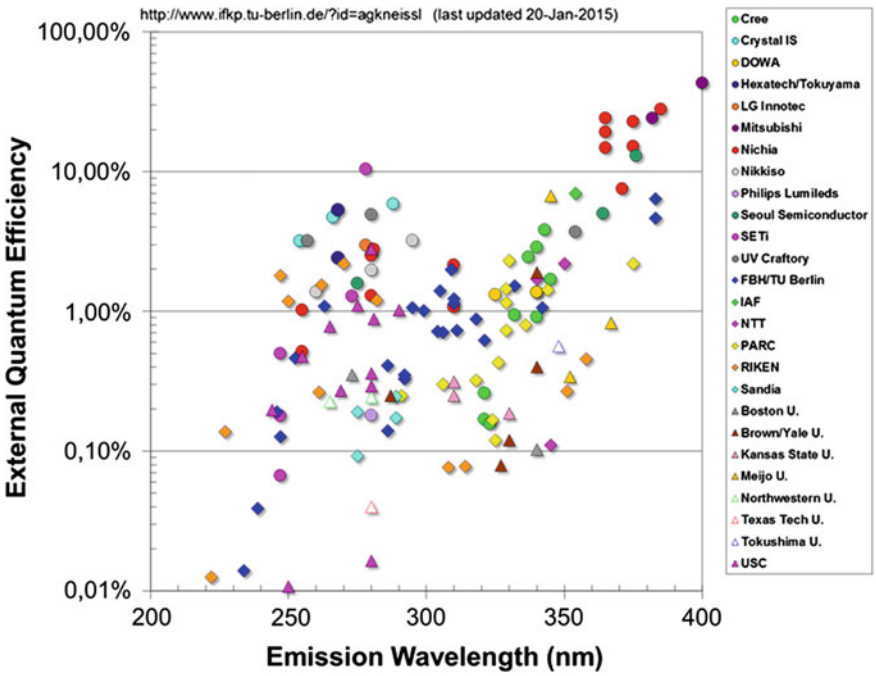


Fig. 12.13 Overview about the UV-LED: reached EQE versus wavelengths from [20]

band to band luminescence also the deep level luminescence can be significant. The deep level luminescence is an additional light emission at higher wavelength that can affect the LED absorption measurement strongly. A reduced effective absorption coefficient as well as additional cross sensitivities can result.

Thereby currently it is quite difficult to measure gases in the deep UV region with high concentration resolution.

The schematic shown in Fig. 12.14 visualizes the linkage between electrical parameter as well as the chip temperature and the optical output parameter such as optical emission power P_{opt}, peak wavelength λ and the emission bandwidth $\Delta\lambda$ respectively the emission shape. Along each of the dark lines specific curves can be determined for characterization and optimal LED control. Depending on the material and design each type of LED will have a different electro-optical behavior that can be represented by the specific characterization curves. For example the emission power is strongly depending on the temperature and also the emission peak wavelength can vary by temperature significantly. It is important to notice, that the differences between various LED types can be significant (see Fig. 12.16). Further it has to be considered that during the lifetime of an LED these curves will change for instance by degradation processes. For example, during degradation the nonradiative defect densities can rise and the IQE of the LED becomes smaller. Thus the available light for sensor measurement is decreasing and therewith the

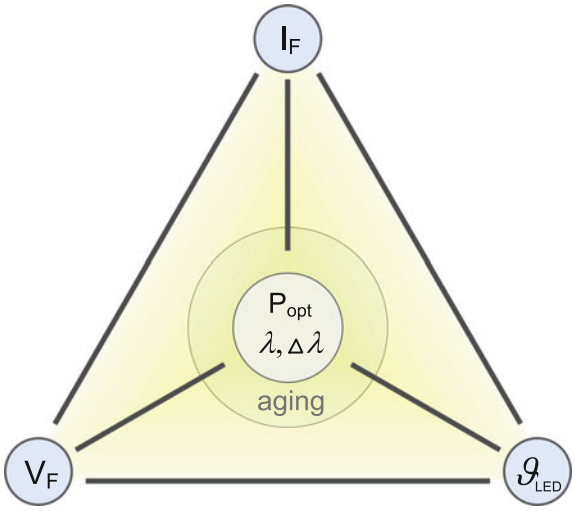


Fig. 12.14 LED light source: relationship between the electrical and optical parameter: forward current (*IF*), forward voltage (*VF*), LED temperature (ϑ_{LED}), optical output power (P_{opt}), peak wavelength (λ) and FWHM wavelength ($\Delta\lambda$)

sensor resolution. Furthermore the amount of dissipated heat rises and assuming a constant thermal resistance also the temperature within the LED will increase. As temperatures rise the efficiency of LEDs is reduced and degradation processes increase [21, 22, 23].

By controlling the characteristic curves only of the electrical parameters at certain operating points it is possible to monitor the aging of the semiconductor emitter. This enables a control of the sensor function that is very important especially for industrial application with high demands to sensor reliability.

Changes of the electro-optical parameters of different LEDs that are installed in absorption sensors can result in concentration measurement errors. For instance, a change of LED chip temperature causes respectively a slight change of the emission shape and position that can result in a change of the effective absorption coefficient and therewith in an attenuation error that influences the concentration determination. The influence of chip temperature and the different behavior of different LED types on the emitted optical spectrum are shown in Fig. 12.15a, b.

For applications that require high accuracies, the typical behavior of the LEDs should be considered during the system design and at accuracy estimations. Linearized temperature dependencies for different LEDs are shown in Fig. 12.16 normalized for the optical output power at 20 °C and change of peak wavelength (at 10 mA cw).

The spatial and angular light emission of an LED is not constant over the time. Fluctuations appear because of changes in the local current distribution and the distribution of radiative and nonradiative transition areas. That demands considerations in the design of the (optical) setup for an LED spectroscopy application [12].

All LEDs are working in forward direction of the p–n junction. The equivalent electric circuit of an LED at DC or low frequencies can be described in forward

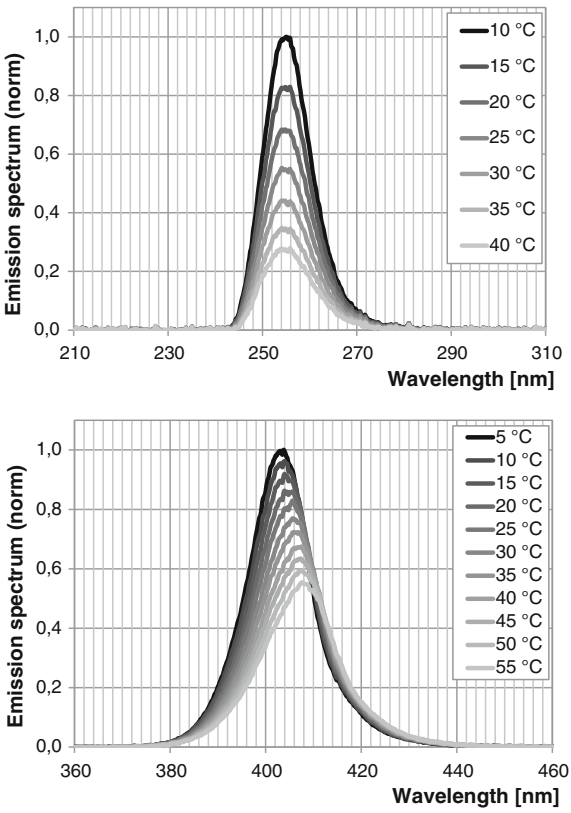


Fig. 12.15 Spectral temperature dependency of two different types of LEDs: (*top*) 255 nm DUV-LED (normalized to 10 °C); (*bottom*) 405 nm LED (normalized to 5 °C)

direction by a serious resistor and a parallel resistor to an ideal rectifier diode, but all parameter are temperature dependent. The high frequency equivalent circuit includes capacitances from contacts and the semiconductor structure in forward regime (distribution of charge) and the series inductance from the connecting lead [24].

The relationship between the forward current and optical output (radiation) is just approximately linear for low current operation and is not different between DC mode and pulsed working regime in millisecond range. With short pulse regimes in µs-range the peak output power can be increased several times by increasing the current amplitude. The pulse peak power in relation to the efficiency and the duty cycle determine the average electrical power losses which heat up the LED.

The chip temperature influences the electrical voltage current characteristic curve. The forward characteristics of LEDs with different emissions wavelengths are shown in Fig. 12.17. The relation between the emission wavelength and the forward voltage (see Fig. 12.1) is obvious. Further the temperature dependency of the forward voltage is plotted as an example for the 405 nm LED.

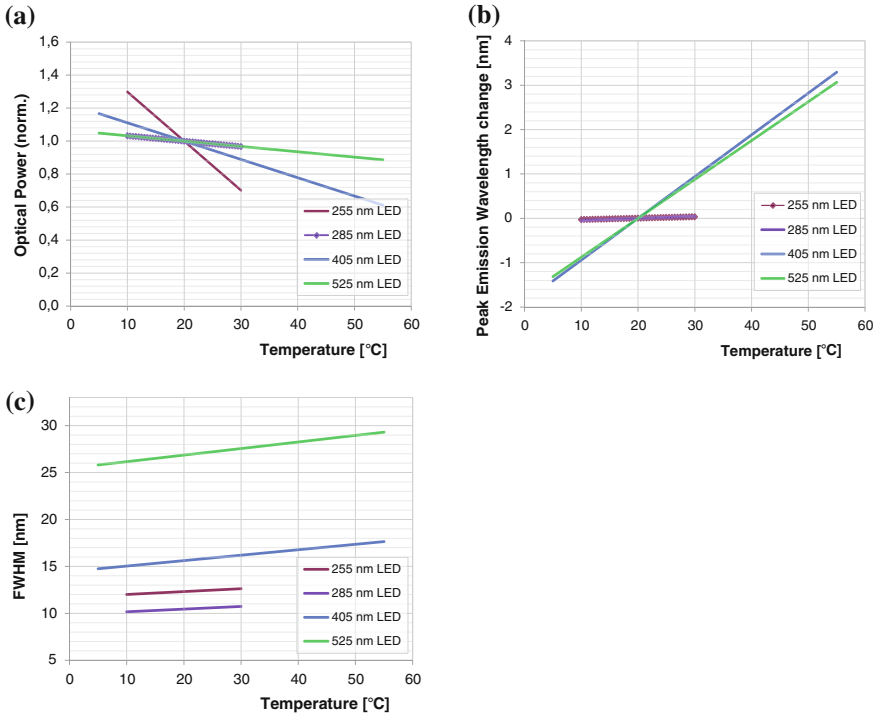


Fig. 12.16 Influence of LED chip temperature onto its optical output power (**a**), wavelength shift (**b**), linewidth (FWHM) (**c**) (remarks: linearized and normalized plots) [12]

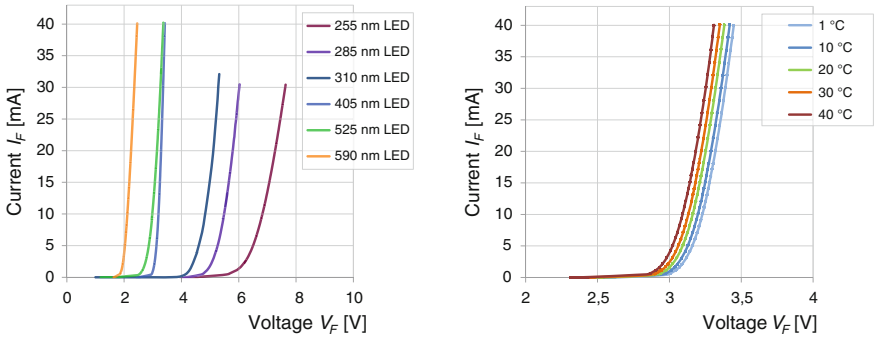


Fig. 12.17 Forward characteristics of different UV-VIS LEDs and its influence of temperature (405 nm LED) [12]

The electronic current, voltage and temperature control of the LED is besides the optical referencing a key element of any LED-based spectroscopic system. Aging of the LED (degradation processes) is mainly determined by operation temperature, forward current and environmental conditions of the LED as well.

12.6 Application of UV-LED Absorption Spectroscopy

LED light sources are well suited for applications in absorption spectroscopy as discussed before. The first LED-based absorption spectroscopic systems were proposed in early 1980s for ozone measurements using their absorption band in the VIS around 600 nm utilizing a yellow-orange LED [7, 8]. The availability of LEDs in further wavelength ranges enabled the detection of additional gases. The implementation of blue, green, yellow and red LEDs in an analytical device has been proposed already [8] to detect different gases such as O_3, Br_2 and NO_2 and experimental results are shown.

An optical fiber-coupled LED-based sensor for in situ detection of hazardous exhaust gases in the harsh environment of a tailpipe system is proposed in [14]. Also a pure fiber optical internal reference without mechanically moved components is demonstrated to enable a high sensor resolution and stability [13].

Two examples of the application of LED spectroscopy based on ultraviolet emitters are presented: a fiber-coupled optical sensor for ppb range Ozone detection and sensor for detection of harmful gases SO_2 and NO_2 using UV-LED spectroscopy.

12.6.1 Ozone Sensor

Ozone is very oxidizing and is a toxic gas. Even concentrations above approx. 100 ppb can lead to irritations at the human body. In nature O_3 is generated mainly by cracking of air oxygen induced by ultraviolet radiation of the sun. Its concentration can affect the human life especially in mountain regions (high natural UV radiation) and in summer smog situations where the presence of specific pollutants supports the O_3 generation [15]. In industrial applications ozone is utilized in manifold ways, in chemistry as oxidation partner as well as for bleaching and disinfection. The unplanned O_3 generated by electrical discharges in air can be utilized as a malfunction or aging indicator in mechanical power electronic switches.

12.6.2 Ozone Sensor Design

The realized sensor design is based on an optical free path reflection sensor cell. The measurement cell is completely optical fiber coupled. Therefore the sensitive electronics are spatially separated from the harsh environment at the measurement position, this is important for instance in application with strong electromagnetic interferences as it is caused for instance by the electric arc in power electronic switches. A UV-LED around 255 nm is utilized to measure the ozone at a wavelength close to its absorption maximum and an additional LED at higher wavelength aside the O_3 absorption is used as spectral reference. The O_3 absorption characteristic as well as the spectral LED emission characteristic is shown in Fig. 12.18. Two measurement cells with different absorption lengths are realized.

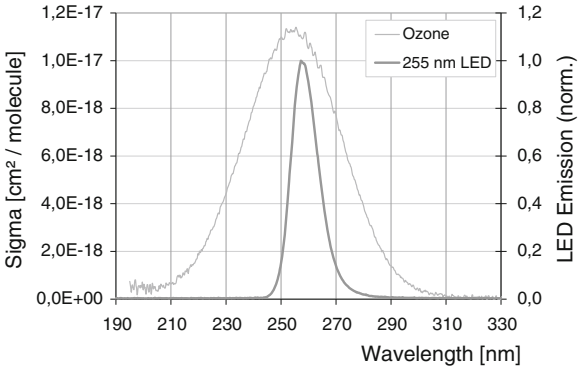


Fig. 12.18 Spectral characteristics of UV-LED emission (chosen wavelength 255 nm) and O_3 absorption

A digital signal processor (DSP) is used to control the LED modulation, acquire the detector raw signals and additional sensor signals (e.g., cell temperature). Further a demodulation, a signal processing and the calculation of gas concentration is done by the DSP.

12.6.3 Measurement Arrangement

Laboratory tests with a xenon flash lamp based ozone generator and a commercial electrochemical reference device have been undertaken.

12.6.4 Results

With a 4 cm optical reflection cell an ozone resolution of about 30 ppb results at a measurement time of 700 ms, the maximum tested O_3 concentration was about 100 ppm. A measurement result of the 40 cm reflection cell is shown in Fig. 12.19.

The dark-marked time-shifted signal corresponds to the electrochemical reference detector. At a measurement time of 1.4 s the concentration resolution of the sensor is about 3 ppb and the maximum ozone concentration is approximately 10 ppm. Thus a high concentration dynamic of several decades is shown.

12.6.5 SO_2 and NO_2 Sensor

LED-based sensor for detection of harmful gases SO_2 and NO_2 is designed for a high temporal resolution. The high-resolution online detection of harmful exhaust gases such as SO_2 and NO_2 is a very important issue with combustion processes such as in

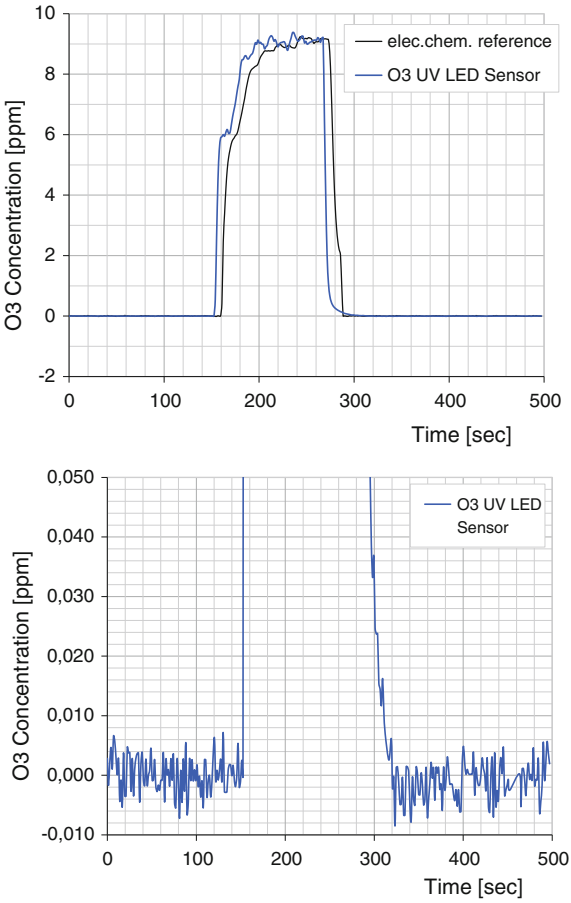


Fig. 12.19 Results of a UV-LED-based ozone measurement (zoomed view at low concentration, below) obtained for a 40 cm reflection cell and 1.4 s measurement time [15]

stationary, ship, lorry, and car engines or at power plants. The measurement results can be used for emission control. Since the emission of harmful gases can be controlled by combustion engine and exhaust after treatment parameters the sensor data can enable a closed loop engine control regarding low emissions.

12.6.6 Sensor Design for SO_2/NO_2 Exhaust Gas Sensor

The realized sensor is based on three different LED light sources (see Fig. 12.20) that are optically fiber coupled to a free path measurement cell with an optical length of 15 cm. The emission wavelength ranges of two LEDs are adjusted to the

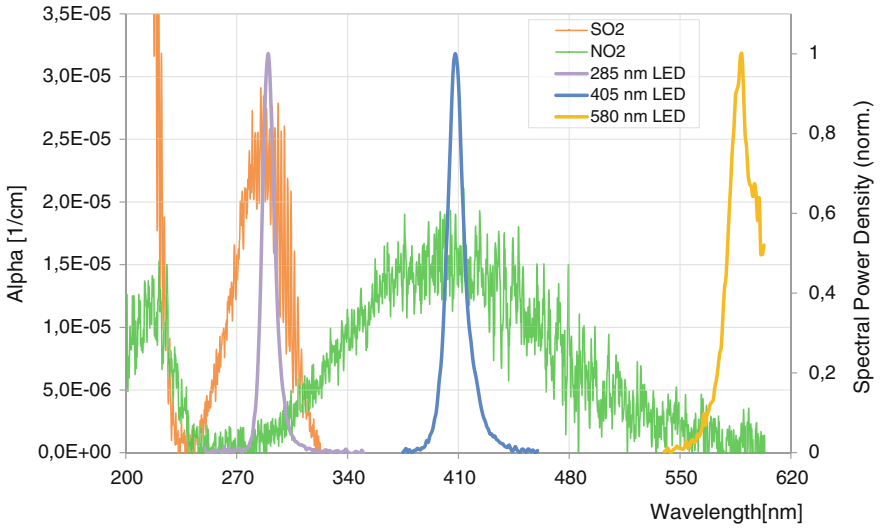


Fig. 12.20 SO_2/NO_2 exhaust gas sensor with the chosen LEDs for SO_2, NO_2 sensing and the reference LED (580 nm)

maximum absorptions of SO_2 and NO_2 around 286 and 405 nm in order to match the absorption peaks of SO_2 and NO_2, respectively. A longer wavelength emission near 590 nm is chosen for the third LED, which is used as the reference as shown in Fig. 12.20.

For exhaust gas applications also fully fiber-coupled reflection cells can be used to enable in situ exhaust gas measurements. Robust materials can be utilized to realize a pure optical sensor cell that can withstand harsh tailpipe conditions such as high temperatures (i.e., several hundred degree Celsius), vibrations and chemical aggressive media [13]. Because of smaller cross interferences on the gas concentration measurements in this sensor design a bypass absorption cell is designed. The measurement time can be varied by the system to adapt it to different application requirements. Very high sensor resolutions can be achieved by a long measurement time whereas fast measurements lead to a reduced concentration resolution.

12.6.7 Measurement Setup

Laboratory test measurements are undertaken using precision calibration gases to evaluate the sensor. The typical result of a calibration gas test with a measurement repetition time of 50 ms is visualized in Fig. 12.21.

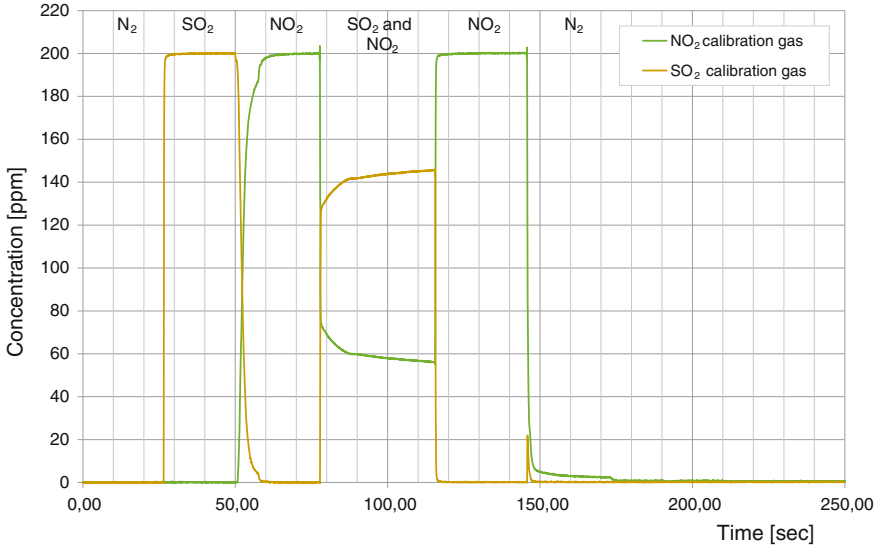


Fig. 12.21 Calibration gas test with UV-LED SO_2/NO_2 exhaust gas sensor, 200 ppm steps

First the sensor cell was filled with N_2, then it was filled with 200 ppm of SO_2 that was flushed out by 200 ppm of NO_2, a mixture of both gases was applied and before the cell was filled with N_2, again 200 ppm NO_2 was applied. The rapid signal changes reflect the high temporal resolution of the sensor.

The magnified plot for the zero concentration visualizes the high concentration resolution of the sensor: For SO_2 as well as for NO_2 the standard deviation for the concentration resolution is about 0.2 ppm (path length 15 cm) as shown in Fig. 12.22. The cross interference free detection of NO_2 and SO_2 can be seen in the magnified plot too. After the cell is finally flushed with N_2 a slow decay of a small amount of NO_2 can be observed. This is caused by a typical behavior of NO_2, it tends to stick to contact surfaces and thus it takes a while until it is flushed out completely. A typical design of a fiber-based UV-LED SO_2/NO_2 car exhaust gas sensor is shown in Fig. 12.23. The reflection cell is constructed for plug-in mounting on the combustion engine exhaust pipe and has a working temperature range up to 600 °C depending on outside conditions (air cooling etc.). The realized effective absorption length x in this sensor is about 10 cm (2 × 5 cm).

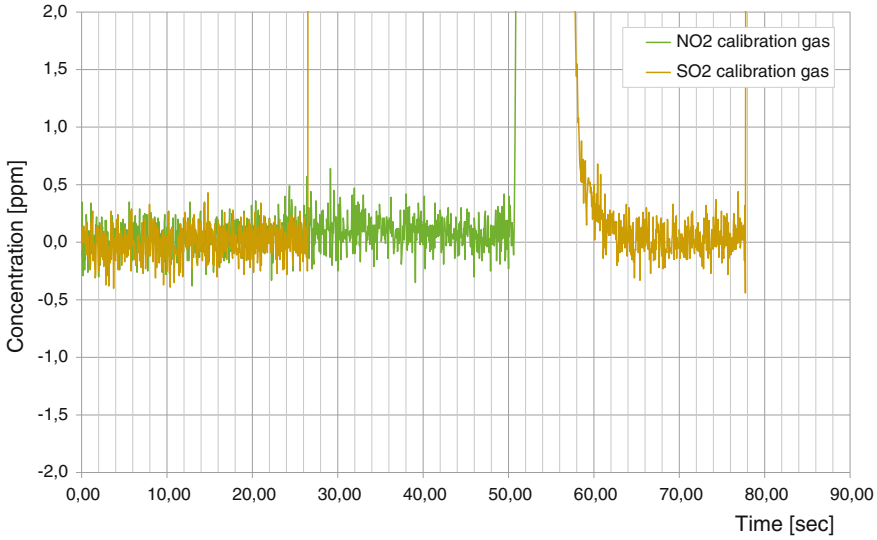


Fig. 12.22 UV-LED SO_2/NO_2 exhaust gas sensor: dynamic behavior by zero concentration (noise)



Fig. 12.23 Typical design of a Fiber-based UV-LED SO_2/NO_2 combustion engine exhaust gas sensor: reflection cell for plug-in mounting with 10 cm (2 × 5 cm) absorption length

12.7 Conclusion and Outlook

For over 30 years, LEDs have been used as spectrally well-defined radiation sources in gas absorption sensing application. Initially, LEDs in the visible and near infrared region were dominant due to their availability or the lack of LEDs at different wavelengths. Today, LEDs ranging from deep UV up to the infrared are available nearly at any wavelengths.

UV-LEDs expand the feasibility of LED-based application especially for gas sensing. In the deep UV range a large number of substances such as the gases SO_2, NO_2 and ozone can be measured with a high accuracy with ppm (or lower) resolution. This is because of the existence of the strong absorption bands in the UV range which additionally do not interfere with other high concentrated environmental gases such as water vapor. Novel deep UV-LEDs will enable cost-effective spectroscopic sensors and instruments for important industrial and environment application such as the selective NO/NO_2 sensing. The high power densities of the ultraviolet semiconductor emitter enable a large number of applications in life science for instance in the field of fluorescence spectroscopy, high performance liquid chromatography systems as well as in wearable electronics for medical diagnostics and in therapeutic systems.

References

1. U. Platt, J. Stutz, in *Differential Optical Absorption Spectroscopy. Physics of Earth and Space Environments* (Springer, New York, 2008), ISSN: 1610-1677
2. S. Nakamura et al. (Nichia Chemical Industries, Ltd.), High-brightness InGaN blue, green and yellow light-emitting diodes with quantum well structures. Jpn. J. Appl. Phys. **34,** L797–L799 (1995)
3. *Ultra Low Power Carbon Dioxide Sensor COZIR™. Datasheet description of CO_2-COZIR Sensor* (Gas Sensing Solutions Ltd, Glasgow, UK, 2014)
4. M.S. Shur, R. Gaska (Sensor Electronic Technology, Inc.), Deep-ultraviolet light-emitting diodes. IEEE Trans. Electron Dev. **57**(1) 12–25 (2010)
5. H. Hirayama, (RIKEN), Quaternary InAlGaN-based high-efficiency ultraviolet light-emitting diodes. J. Appl. Phys. **97–99**, 091101–091101–19 (2005)
6. Sensor Electronic Technology, Inc., UVTOP Deep UV LED Technical Catalogue (2011), http://www.s-et.com/uvtop-catalogue.pdf. Accessed 07 Oct 2014
7. M. Fowles, R.P. Wayne, Ozone monitor using an LED source. J. Phys. E: Sci. Instrum. **14**(10) 1143 (1981)
8. G. Wiegleb, *Einsatz* von *LED-Strahlungsquellen* in Analysengeräten. Laser und Optoelektronik **3**, 308–3110 (1985)
9. E.F. Schubert, *Light-Emitting Diodes*, 2nd edn. (Cambridge University Press, Cambridge, 2006), ISBN: 978-0521865388
10. J. Mellquist, A. Rosen, DOAS for flue gas monitoring-I. Temperature effects in the U.V./visible absorption spectra of NO, NO_2, SO_2 and NH_3. J. Quant. Spectrosc. Radiat. Transf. **56**(2), 187–208 (1996)
11. R.M. Mihalcea, D.S. Baer, R.K. Hanson, Tuneable diode-laser absorption measurements of NO_2 near 670 and 395 nm. Appl. Opt. **35**(21), 4059–4064 (1996)

12. M. Degner, *LED-Spektroskopie for Sensoranwendungen; am Beispiel der in-situ Abgasdetektion für Verbrennungsmaschinen* (Mensch & Buch Verlag, Berlin, 2012), ISBN: 978-3863871413
13. M. Degner, H. Ewald, E. Lewis, LED based spectroscopy—a low cost solution for high resolution concentration measurements e.g. for gas monitoring applications, in *Proceedings of the 5th International Conference on Sensing Technology* (ICST 11) (2011), ISBN 978-1457701665, pp. 145–150
14. M. Degner et al., Online detection of NO, NO_2 and SO_2 in UV-VIS region for exhaust of diesel combustion engines. IOP 2005. J. Phys. Conf. Ser. **15**(2005), 322–328, ISSN: 1742-6588
15. M. Degner et al., UV LED-based fiber coupled optical sensor for detection of ozone in the ppm and ppb range, *in Proceedings of 8th IEEE Conference on Sensors*, ISBN: 978-1424453351, pp. 95–99 (2009)
16. M. Kneissl et al., Ultraviolet InAlGaN light emitting diodes grown on hydride vapor phase epitaxy AlGaN/sapphire templates. Jpn. J. Appl. Phys. **45**(5A), 3905–3908 (2006)
17. Nichia Corporation, Specifications for UV LED, NVSU233A(T), 2014, http://www.nichia.co.jp/specification/products/led/NVSU233A-E.pdf. Accessed 13 June 2015
18. AvaLight-DH-S Deuterium-Halogen Ligth Source, Datasheet description of the *Avantes AvaLight-DH-S Deuterium-Halogen Ligth Source* (Avantes BV, Apeldoorn, NL, 2014)
19. H. Hirayama et al., 226–273 nm AlGaN deep-ultraviolet light-emitting diodes fabricated on multilayer AlN buffers on sapphire. Phys. Status Solid C **5**(9), 150–152, 2969–2971 (2008)
20. J. Rass et al., High power UV-B LEDs with long lifetime. Proc. of SPIE **9363**, 93631K (2015), doi:10.1117/12.2077426
21. Z. Gong et al., Optical power degradation mechanisms in AlGaN-based 280 nm deep ultraviolet light-emitting diodes on sapphire. Appl. Phys. Lett. **88**, 121106–121106–3 (2006)
22. S. Sawyer, S.L. Rumyantsev, M.S. Shur, Degradation of AlGaN-based ultraviolet light emitting diodes. Solid-State Electron. **52**, 968–972 (2008)
23. M. Meneghini et al., Thermal degradation of InGaN/GaN LEDs ohmic contacts. Phys. Status Solid C **5**(6), 2250–2253 (2008)
24. R.-L. Lin, Y.-F. Chen, Equivalent circuit model of light-emitting-diode for system analyses of lighting drivers, in *Industry Applications Society Annual Meeting, 2009. IAS 2009.* IEEE 10.1109/IAS.2009.5324876

Chapter 13
UV Fluorescence Detection and Spectroscopy in Chemistry and Life Sciences

Emmanuel Gutmann, Florian Erfurth, Anke Drewitz, Armin Scheibe and Martina C. Meinke

Abstract Fluorescence techniques are nondestructive analytical methods used in a wide range of applications. Since many fluorophores of interest can be excited with UV light and nowadays compact solid-state UV emitters are available, UV fluorescence methods are emerging. The chapter will give a survey of both fundamentals and applications of fluorescence in chemistry and life sciences emphasizing actual and potential applications of solid-state UV emitters. Particular attention is drawn to the use of autofluorescence spectroscopy for the detection of microorganisms and as diagnostic method for skin diseases.

13.1 Introduction

Fluorescence techniques, spanning fluorescence spectroscopy, fluorescence sensing, imaging, and microscopy are nondestructive optical, analytical methods. They are nowadays increasingly used in numerous scientific disciplines such as molecular biology, biophysics and chemistry, clinical diagnosis, and analytical and environmental chemistry. Besides their widespread use in fundamental and applied research, substantially efforts have been made in commercializing new fluorescence-based analytical devices. In the field of genomics, proteomics and

E. Gutmann (✉) · F. Erfurth · A. Drewitz · A. Scheibe
Department Photonics and Sensorics, Gesellschaft zur Förderung von Medizin-, Bio- und Umwelttechnologien e.V. (GMBU), Felsbachstrasse 7, 07745 Jena, Germany
e-mail: gutmann@gmbu.de

M.C. Meinke
Center of Experimental and Applied Cutaneous Physiology (CCP), Department of Dermatology, Venerology and Allergology, Charité – Universitätsmedizin Berlin, Charitéplatz 1, 10117 Berlin, Germany

© Springer International Publishing Switzerland 2016

M. Kneissl and J. Rass (eds.), *III-Nitride Ultraviolet Emitters*,
Springer Series in Materials Science 227, DOI 10.1007/978-3-319-24100-5_13

drug discovery fluorescence detection systems are indispensable tools enabling high-throughput screenings.

The increased use of fluorescence techniques is greatly enhanced by the commercial availability and further improvement of instrumentation such as compact (laser) light sources, highly sensitive detector arrays, or increasingly efficient sensor and imaging electronics.

Due to the strong influence of the surrounding medium on the fluorescence emission, fluorescent molecules are intensely used as probes for analyte recognition or investigation of chemical and biological systems. Many new fluorescent probes and reporters with selectivity for specific microenvironmental properties have been designed and developed, leading to an enhanced employment of fluorescence techniques in clinical diagnostics and environmental monitoring. Probing inside living cells is another broad field of application in the life sciences benefiting from the availability of novel and highly specialized fluorescent probes.

Besides the development and application of synthetic fluorescent probes specifically labeling (bio-)molecules or biological structures, label-free autofluorescence spectroscopy, making use of intrinsic fluorescent molecular species, is gaining more and more importance in biological cell imaging, tissue diagnostics, microorganism detection, and proteomics. Many of these intrinsic fluorophores, such as aminoacids, pyridine nucleotides, or collagen can be excited by UV light, making this a promising field for application of solid-state UV emitters.

Numerous monographs, handbooks, and reviews are available in the field of fluorescence reflecting its high relevance for a broad field of application (see e.g., [1–8]). Fluorescence detection and spectroscopy of natural and artificial fluorophores in general cover the UV, VIS, and IR spectral range. Due to the broad availability of powerful and compact (laser) light sources in the VIS and NIR, established fluorescence techniques and probes are still focusing on this spectral range. Especially in the context of bioimaging and genomics, fluorescence instrumentations and probes are designed to circumvent short-wavelength light-induced autofluorescence emission potentially disturbing the fluorescence signal of the specific probe (usually emitting in the VIS or NIR spectral range). Nevertheless, many natural and synthetic fluorophores can be excited with UV light. Thus, the scope and merit of this chapter is a survey of the extremely broad field of fluorescence emphasizing actual and potential applications of solid-state UV emitters. It starts with a short compendium of the basic phenomena and instrumental aspects of fluorescence techniques as well as an overview of UV excitable fluorophores (Sect. 13.2). The following Sect. 13.3 covers applications of fluorescence spectroscopy as analytical technique in lab-based organic, analytical and environmental chemistry, and biochemistry. In Sect. 13.4, fluorescent chemical sensing for analyte recognition and monitoring, imaging and detection of biological molecules, structures and cell functions as well as genomic and proteomic studies is introduced. The detection of living microorganisms as special biological analytes of increasing concern is issued separately in Sect. 13.5. Finally, in Sect. 13.6 fluorescence diagnosis of skin and tissue diseases is discussed with special emphasis on multiple wavelengths autofluorescence spectroscopy for skin cancer diagnosis.

13.2 Fundamentals and Apparative Aspects of Fluorescence Detection and Spectroscopy

Luminescence in general is the deactivation of electronically excited states by emission of light. Photoluminescence as an absorption-induced luminescence is subdivided into fluorescence and phosphorescence taking into account the spin multiplicity of the molecule. A molecule that shows fluorescence is called a fluorophore. A common tool to visualize the different processes and energy levels involved in the absorption and emission of light is the Jablonski diagram given in Fig. 13.1 which was first proposed by Professor Alexander Jablonski in 1935 [9]. It illustrates spectra and kinetics of fluorescence, phosphorescence, and delayed fluorescence.

In 1852, Sir George Gabriel Stokes coined the term fluorescence for the effect of UV-induced colored light emission of certain substances and formulated the so-called Stoke's law [10]. It says that the wavelength of a fluorescent light is always greater than the wavelength of the exciting light. This is usually observed for molecules in solution with one photon absorption. The distance between absorption and emission maximum is called the Stokes shift and is commonly expressed in wavenumbers (Fig. 13.2). In general, the Stokes shift is caused by thermalization of vibrational energy of the excited and the ground state but it is also influenced by solvent polarity, complex formation, excited-state reactions, and/or energy transfer. Luminescence whose radiation is located in a spectral region of shorter wavelengths than that of the exciting radiation is called anti-Stokes luminescence. In Raman spectroscopy, the appearance of (inelastically scattered) anti-Stokes radiation is common. In contrast, anti-Stokes luminescence is a less common effect and can only be observed as a result of sophisticated processes like multiphoton absorption [11], phonon-assisted photoluminescence upconversion (e.g., in semiconductor nanostructures) [12], or plasmon enhancement [13].

An important parameter of a photophysical or photochemical process is its quantum yield or quantum efficiency which is equal to the number of photons undergoing the process in relation to the total number of photons absorbed. The

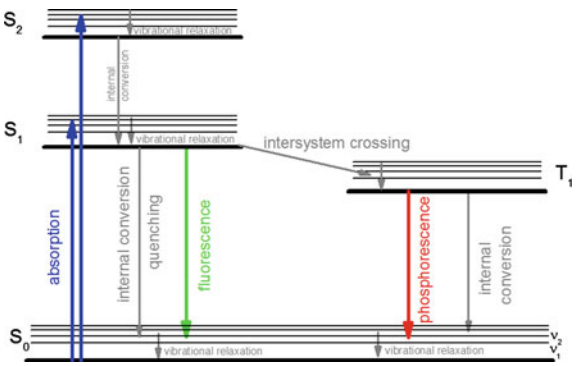


Fig. 13.1 Jablonski diagram

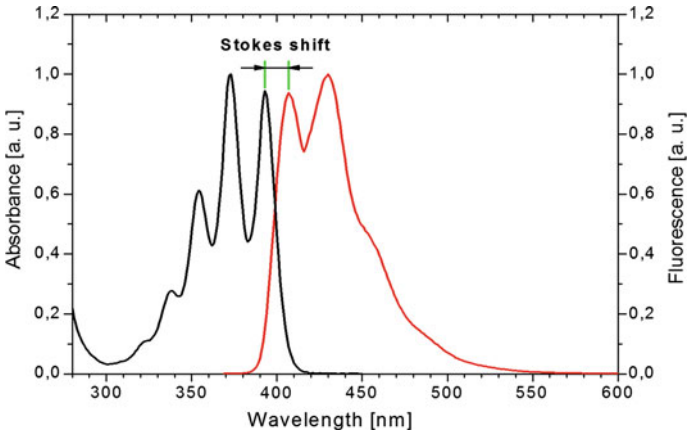


Fig. 13.2 Absorption (*black*) and emission (*red*) spectra of 9, 10-Diphenylanthracene in Cyclohexane (color online)

sum of quantum yields of all possible processes is equal 1. The fluorescence quantum yield Φ_F is the ratio between the number of fluorescence photons emitted and the number of photons absorbed. It provides information of competing non-radiative processes leading to depletion of the excited singlet state S_1 (see Fig. 13.1), like internal conversion (IC), intersystem crossing (ISC), intramolecular charge transfer, conformational changes, and interaction in the excited state with other molecules (electron and proton transfer, energy transfer, excimer, or exciplex formation). Φ_F can be determined experimentally by absolute measurements or relative to a fluorescent standard with a known Φ_F. In [14], different experimental procedures and techniques for the determination of Φ_F are described and compared. Both Φ_F and shape of the emission spectrum are independent of the excitation wavelength. The natural or intrinsic fluorescence lifetime (τ_0) denotes the mean time a molecule spends in the excited state if fluorescence is the only deactivation process. It is a theoretical value that cannot be determined experimentally due to competing processes like IC, ISC, or chemical reactions decreasing the experimentally accessible fluorescence lifetime, the latter referred to as excited-state fluorescence lifetime (τ_{ex}).

The interactions of a fluorescent molecule with its local environment (e.g., solvent, solid surface, organized media) are usually reflected in the spectral appearance and shape of the absorption and emission bands, the fluorescence quantum yield as well as the lifetimes of the excited-state molecules. The solvent-dependence of the position of emission bands is commonly included in the term solvatochromism [15] covering physical, chemical, temperature, and surface effects [16]. Physical effects are caused by dipole–dipole interactions of solute and solvent. In more polar environments, polar fluorophores will relax to a lower vibrational energy state before emission, resulting in emission at lower energies, i.e., longer wavelengths. Chemical effects are intermolecular hydrogen bonding,

proton or electron transfer (e.g., pH), external heavy-atom effects, and complex formation. The temperature of the environment can affect the luminescence behavior directly through temperature dependence of competing nonradiative processes and indirectly through temperature-dependent chemical phenomena like ground state complex formation, hydrogen bonding, or diffusion-controlled reactions (quenching). Further, if two electronically excited states of the solute are of very similar energy, a thermal promotion of the molecule to the upper state can occur. Metallic surfaces may induce an increase or decrease of radiative decay and resonance energy transfer rates of adsorbed fluorophores [1]. In metal or surface-enhanced fluorescence, near-field coupling between the fluorophore and surface modes of the metal plays a crucial role [17].

Reactions of a fluorescent molecule from the excited state S_1 such as proton or electron transfer, energy transfer, complex formation, or collisions with other molecules may lead to a depletion of the excited state by radiationless processes and thus to a decrease in fluorescence intensity and fluorescence lifetime referred to as quenching. The formation of nonfluorescent ground state complexes is called static quenching. For dynamic or collisional quenching, a key requirement is that the quencher must diffuse to the fluorophore during the lifetime of the excited state in order to cause a decrease in fluorescence intensity. It does not require spectral overlap and occurs only when the fluorophore and quencher are in molecular contact (within $\sim$5 Å) [1]. The decrease in fluorescence intensity due to quenching can be expressed by

$$F_0/F = 1 + K_{SV}[Q]$$

where F is the fluorescence intensity in the presence of quencher, F_0 is the intensity in the absence of quencher, $[Q]$ is the quencher concentration, and K_{SV} is the Stern–Volmer quenching constant. K_{SV} is a general term that may refer to either dynamic or static quenching processes. For static and dynamic quenching, the effect of quencher concentration on fluorescence lifetime is different. For static quenching, τ_0/τ is equal to 1 and for dynamic quenching $\tau_0/\tau = F_0/F$. Some examples of typical quenchers are molecular oxygen (quenching almost all fluorophores), aromatic and aliphatic amines (quenching unsubstituted hydrocarbons), and bromide and iodide (quenching through spin–orbit interaction).

Resonance energy transfer (RET, also FRET for Förster or fluorescence resonance energy transfer) is a through space transfer of excitation energy from a donor fluorophore to an acceptor molecule within a distance of 10–100 Å. The donor and acceptor must be spectrally related (donor emission is absorbed by the acceptor) and the donor and acceptor transition dipole orientations must be approximately parallel. By RET to an acceptor (which does not necessarily be fluorescent itself), the detectable emission of light by the donor fluorophore is quenched. This phenomenon is intensively used in biosensing and bioimaging (see Sect. 13.4). The distance at which 50 % of excited donors are deactivated by RET is defined as the Förster radius R_0 with its magnitude depending on the spectral properties of the donor and acceptor dyes.

The extent to which a fluorophore rotates during the excited-state lifetime τ_{ex} determines its polarization or anisotropy. These are both expressions for the same phenomenon. Fluorescence anisotropy (r) and polarization (P) are defined by

$$r = (I_v - I_h)/(I_v + 2I_h) \quad \text{and} \quad P = (I_v - I_h)/(I_v + I_h)$$

where I_v and I_h are the fluorescence intensities of the vertically (v) and horizontally (h) polarized emission, when the sample is excited with vertically polarized light [1]. Anisotropy measurements are widely used in biochemical applications (size and shape of proteins, local viscosity, or rigidity of various molecular environments).

Luminophores (fluorophores and phosphors) can be found in all kinds of compounds (inorganic, organic, and organometallic). The class of inorganic luminophores [4] includes

- transition metal and rare earth cations,
- uranyl ion,
- metal doped glasses,
- crystals and nanocrystals (Quantum dots) of semiconductor materials,
- metal ion doped crystals (e.g., ruby, beryl),
- trapped electron–hole pairs and oxygen-related lattice imperfections in crystals (e.g., silicates), and
- gases (e.g., SO_2, NO).

Organic luminophores are usually divided into natural (intrinsic) and synthetic fluorophores [18, 19]. Natural fluorophores absorbing in the UV are as follows:

- amino acids (tryptophane, tyrosine, phenylalanine);
- pyridine nucleotides (NADH and NADPH), flavins, and vitamins;
- cellulose, chitin, lignin, sporopollenin, collagen, and elastin;
- suberin and cutin;
- chlorophyll and phaeopigments, flavonoids, and alkaloids; and
- DNA/RNA and humic-like substances.

An overview of natural fluorophores relevant for characterization of human tissue can be found in Table 13.1 of Sect. 13.6. Synthetic organic luminophores absorbing in the UV spectral range are as follows:

- aromatic and polycyclic aromatic hydrocarbons (pyrene, anthracene, phenanthrene, benzene, benzo[a]anthracene, chrysene),
- naphthalene derivatives (dansyl chloride, EDANS), pyrene derivatives (Cascade Blue, Alexa Fluor 405 Dye, 1-Pyrenesulfonyl Chloride, HPTS),
- coumarines (Alexa Fluor 350 Dye, AMCA-X, DMACA, Marina Blue),
- quinolines (quinine sulfate),
- indoles, imidizoles (DAPI, Hoechst 33342), and
- other small heterocyclic molecules (Bimane, Lumazine, Carbazole, dyes with diaryloxazole structures).

Table 13.1 Fluorophores in human tissue [141, 142]

Fluorophore	Excitation (nm)	Fluorescence (nm)
Amino acids		
Phenylalanine	260	280
Tyrosine	275	300
Tryptophan	275	350
	280	350
Structural proteins		
Collagen	340–360	395–450
	320–350	400–440
Elastin	360	410
	290–325	340, 400
Collagen cross links	380–420	440–500
Elastin cross links	320–360, 400	480–520
Keratin	450–470	500–530
Enzymes and co-enzymes		
NADH	350	460
	290, 350–370	440–460
NADPH	340	460
FAD, flavins	450	520
	450	500–540
Vitamins		
Vitamin A	327	510
Vitamin D	390	480
Vitamin K	335	480
Vitamin B_6	320–340	400–425
Lipids		
Lipofuscin	340–390	430–460, 540
Ceroid	340–395	430–460, 540
Porphyrins		
	405	630
	400–450, 630	635–690, 704

Further, another class of fluorophores is the organometallic compounds covering complexes of ruthenium, rhenium, platinum, rare earth metals, or lanthanide ions, with most of them absorbing in the UV.

In principle, several parameters of fluorescence can be recorded. These are the intensity at given excitation and emission wavelengths, in dependence of the emission (fluorescence emission spectrum) or excitation wavelength (fluorescence excitation spectrum) or in a scanning mode with constant differences between excitation and emission wavelength (synchronous spectrum). The fluorescence intensity can also be recorded at vertical and horizontal polarizations from which emission anisotropy or polarization can be calculated. The fluorescence intensity

depends on the absorption coefficient of the system at the excitation wavelength as well as from the excitation intensity (until saturation). A further parameter is the fluorescence lifetime. Combining several emission spectra at a range of excitation wavelength gives a so-called excitation-emission matrix (EEM), fluorescent landscape, or total luminescence. An EEM is often used for the characterization of complex multicomponent fluorescent systems like intact food systems or dissolved organic matter in natural water (see Sect. 13.3) and may serve as a unique fingerprint for the characterized sample. In most cases, the complex data are analyzed by multivariate and multiway methods (chemometrics) [20]. Spatial resolution like in fluorescence imaging microscopy, (microarray) scanners, or multiplate readers adds another dimension to fluorescence measurements (see Sect. 13.4).

Instrumentation for fluorescence measurement usually requires the selection of excitation and emission wavelength by monochromators or filters. Usually, the radiation source is positioned at a 90° angle from the emission detector. In some cases (highly concentrated, opaque, or solid samples), the excitation light is focused to the front surface of the sample and then fluorescence emission is collected from the same region under a 22.5° angle (sometimes also 30° or 60°) to minimize reflected and scattered light (front face technique). Commonly used radiation sources in steady-state spectrofluorometers are high-pressure Xenon arc lamps. For special cases, Mercury lamps, Quartz–Tungsten Halogen lamps, LEDs, Lasers, or Laser Diodes are also used. A detailed description and evaluation of light sources and other fluorometer components is given by Lakowicz [1]. Almost all modern spectrofluorometers use photomultiplier tubes (PMTs) as detectors. Nevertheless, for spectral ranges where photomultipliers are unavailable or too expensive analogous detectors like InGaAs, InAs, or InSb photodiodes are applied. Charge-coupled devices (CCDs) enable a more compact design of spectrometers.

Information about the dynamics of excited states is essential in understanding photophysical, photochemical, and photobiological processes. For time-resolved fluorescence measurements, two complementary techniques are used, the time-domain method and the frequency-domain or phase-modulation method. In time-domain fluorescence, emission is recorded as a function of time after exciting the sample by a short pulse of light. In frequency-domain method, the sample is excited by a modulated source of light. The fluorescence emitted by the sample has a similar waveform, but is modulated and phase-shifted from the excitation curve. Both modulation (M) and phase shift (φ) are determined by the lifetime of the sample emission which reversely can be calculated from the observed M and φ [1, 4, 20]. While for frequency domain continuous or pulsed sources are suitable, time domain requires pulsed sources. Lasers and laser diodes are frequently used but also the application of UV LEDs is reported [21–23]. Possible ways to record time-domain data are streak cameras or boxcar integrators, but most instruments are based on the time-correlated single photon counting (TCSPC) method with a PMT or an Avalanche photodiode (APD) as detector [24, 25]. Since its first application for the measurement of luminescence decay curves of molecules in solution TCSPC today is used in very sophisticated areas like time-resolved laser scanning microscopy (fluorescence lifetime imaging microscopy FLIM, FLIM in combination with

FRET…), diffuse optical tomography, autofluorescence of tissue, fluorescence correlation spectroscopy, or time-resolved single-molecule spectroscopy, recent applications are described in detail by Becker [26].

13.3 Fluorescence in Lab-Based Instrumental Analysis

Since about 10 % of all existing molecules are fluorescent itself and many more can be modified by association with fluorescent probes, fluorescence spectroscopy, and fluorescence detection in general, they have found widespread application in organic, analytical, and environmental chemistry as well as biochemistry [27]. Especially in organic chemistry and related fields, steady-state and time-resolved fluorescence methods are extensively used to investigate structure–property relationships, effects of the chemical environment (e.g., solvent viscosity or pH) on structure, and properties of a molecule of interest as well as its electronic structure and excited-state or charge-transfer dynamics. At this point, it is also noteworthy that the latter application is not only limited to organic matter. In solid-state physics, photoluminescence spectroscopy (PL) is increasingly used to study the electronic structure and dynamics of inorganic (especially semiconducting nano-) materials, and contributes to a fundamental understanding of the electronic processes governing the catalytic activity or (opto-) electronic property of a material [28, 29].

In combination with separation methods such as high-performance liquid chromatography (HPLC), capillary electrophoresis (CE), or size exclusion chromatography (SEC), fluorescence spectroscopy is a powerful method in instrumental analysis, where it is routinely used to identify organochemical, biochemical, and pharmaceutical substances with very low thresholds of concentration [27, 30, 31]. Hereby, usually a conventional or laser-induced fluorescence (LIF) flow cell is installed at the outlet of the column of the separation system. The feasibility of UV LED-induced fluorescence detection has also been demonstrated [32–34]. Typically, for strong UV absorbing materials the fluorescence sensitivity is 10–1000 times higher than that of UV absorption, making fluorescence the most sensitive among the existing modern HPLC detection methods. Using modern microfluidic devices and advanced instrumentation, it is even possible to detect the presence of a single analyte molecule in sample volumes down to a few nanoliters [30]. Besides sensitivity, another advantage of fluorescence detection is its high selectivity especially in combination with specific fluorescent indicators linked to analytes in the sample (see Sect. 13.4).

One common application of fluorescence in environmental chemistry is the measurement of carcinogenic polycyclic aromatic hydrocarbons (PAH, e.g., anthracene and perylene) in natural or drinking water by HPLC [27]. In food analysis, HPLC combined with fluorescence helps to study toxins such as aflatoxins (a carcinogenic contaminant present in certain batches of grain cereals), pathogenic microbes, fat oxidation, vitamins, amino acids, and also enzyme activity [35]. In the EEM mode, fluorescence spectroscopy alone can be used for the analysis of

complex multicomponent fluorescent food systems [36] (e.g., natural olive oils [37]) and human or animal blood serum [38, 39].

Fluorescence coupled with separation methods is also routinely used in forensics for the detection of drugs and poison (see Sect. 13.7).

Besides its extensive use in fundamental research and analytical chemistry, fluorescence spectroscopy has also gained importance in some industrial fields of applications from which one is the analysis of fluorescent and phosphorescent dyes and pigments, covering inorganic phosphors for lightning application or optical brighteners on textiles and papers. The latter are also known as blancophores, which are stilbene or triazine derivates absorbing in the UV and emitting in the blue spectral range, resulting in a color impression of "whiter than white" [40]. Another industrial application is the detection of PAHs in crude oil exploration [41]. Fluorescence is also used in authentication and counterfeit detection, whereby bank notes, passports, credit cards, or goods are equipped with special marks made of fluorescent inks that become visible under UV light excitation. Several counterfeit detection systems utilizing UV LEDs emitting in the UVA spectral range are patented and already commercialized (e.g., [42]).

Also, the identification of fluorescence signatures as evidence of organic material possibly present in soil or rocks on the mars surface has been considered [43]. For this purpose, the utility of including a 365 nm LED or a 375 nm laser diode in the panoramic camera system of the ExoMars rover to be launched by the European Space Agency in 2018 has been examined, which would allow to monitor rover drill cuttings optically for aromatic hydrocarbons.

Another emerging field of application is the characterization of organic matter in aerosols or natural and drinking water using fluorescence detection directly without HPLC fractionation [44–48]. In the EEM of a water sample, different fractions of dissolved organic matter, like protein-related amino acids, humic or fulvic acids, and pigments from algae or bacteria, always fluoresce in the same sector and thus can be separated solely by means of data analysis (Fig. 13.3).

Besides natural organic matter, anthropogenic water pollutants such as dyestuffs from textile or paper industry can be identified by means of fluorescence. One approach for water quality monitoring is to measure the complete EEM of a water sample and to subsequently analyze the 2D spectra in a standardized manner using multivariate data analysis [49]. For a rapid surveillance of water quality at the point of care, an economic fluorimetric detection system is conceivable which utilizes several LEDs and photodiodes with band-pass filters (both in the UV–VIS spectral range) that are properly selected according to the excitation and emission maxima of the various fractions of interest [50].

Many techniques in analytical and environmental chemistry as well as biochemistry are based on fluorometric detection systems, usually with both single excitation and emission wavelengths, to qualitatively or quantitatively determine the presence of a target analyte that is either intrinsically fluorescent or made fluorescent by fluorescence derivatization. In the latter case, a fluorescent probe is bound to the analyte by chemical reaction, akin to the procedure employed in colorimetry. For the determination of metal cations for example, chelates are

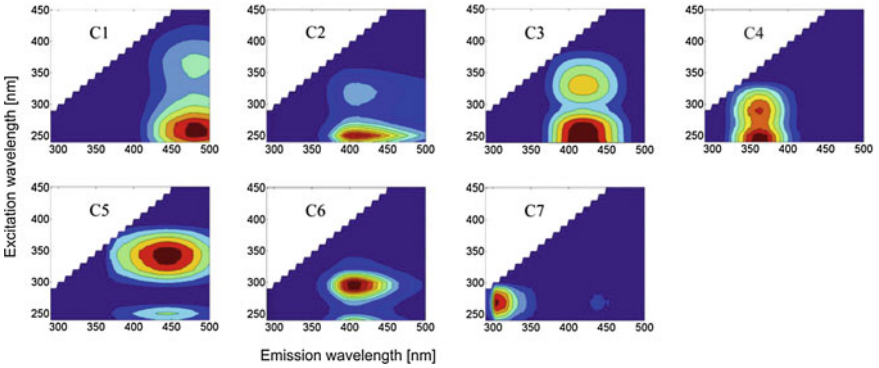


Fig. 13.3 Typical regions in the EEMs of natural water samples (*C1* terrestrial humic substances, *C2* terrestrial/anthropogenic humic substances, *C3* marine and terrestrial humic substances, *C4* amino acids (free or protein bound), *C5* terrestrial humic substances, *C6* marine and terrestrial humic substances, *C7* amino acids (free or protein bound). Reprinted with permission from [48], Copyright 2011, Elsevier

created with oxine (8-hydroxyquinoline), alizarine or benzoin, and afterward extracted by organic solvents [27]. Another example is the quantification of proteins in biological samples making use of the intrinsic protein fluorescence [51].

In the last decades, large efforts have been made to bring fluorometric detection systems out of the lab to the point of interest, where they can be routinely used—ideally by non-specialized personnel—as chemical sensors for a variety of applications. This will be issued in the following section.

13.4 Fluorescence Chemical Sensing for Environmental Monitoring and Bioanalytics

In the last four decades, the field of fluorescent chemical sensing has emerged substantially, due to the need of identification and monitoring potentially harmful substances and pollutants in the environment, including the concern about chemical and biological terrorism. Other important fields of application of fluorescent chemical sensing are bioanalytics, drug development, clinical diagnostics, and food quality surveillance. The field of fluorescent chemical sensing and biosensing is an active area of research and there are already numerous monographs and comprehensive reviews covering many aspects from fundamentals to special issues concerning new classes of fluorescent probes or immobilization [1, 3, 6, 52–55]. This section will be focused on fluorescent chemical sensing for recognition, monitoring, and imaging of (bio-) chemical analytes as well as genomic and proteomic studies, whereas the autofluorescence-based detection of living microorganisms and characterization of skin will be specially issued in two following sections.

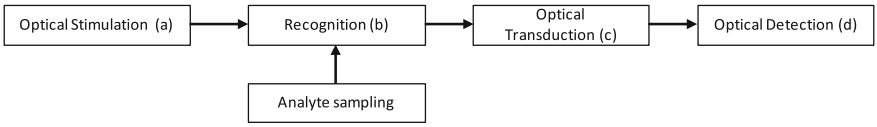


Fig. 13.4 General scheme of a fluorescence chemical sensor

A fluorescence chemical sensor consists of four main components which are a light source (a) to optically stimulate a recognition element (b) specifically interacting with an analyte, an optical transduction element (c) converting the physical or chemical response of the recognition element to a fluorescence optical output signal, and an optical detection system (d) (see Fig. 13.4).

Recognition elements in use are as manifold as analytes to detect ranging from cation, anion, or functional group-specific chemical receptors over enzymes, antibodies, proteins (lectins or avidins), neuroreceptors to DNA, or even living microorganisms.

In special cases, the recognition and transduction element is one chemical species and analyte binding to it results in generation of or change in fluorescence. Examples are dehydrogenase enzyme-catalyzed substrate reactions producing NADH, which can be followed by monitoring the NADH fluorescence with excitation and emission at around 350 nm and 450 nm, respectively [6, 56, 57]:

$$\text{Substrate} + \text{NAD}^+\,(\text{non-fluorescent}) \rightarrow \text{Product} + \text{NADH}\;(\text{fluorescent})$$

Such enzyme-based biosensors are used for the detection of chemical and biochemical analytes, for example, Ethanol or L-Leucine [56, 57].

Functional fluorescent dyes are one main class of transduction elements for fluorescence chemical sensor systems. The toolbox of fluorophores for this application is spanning small organic dyes, metal ligand complexes like metalloporphyrins, transition metal and lanthanide complexes, inorganic quantum dots (QDs) with size-dependent optical properties, carbon, silicon, and luminescent metal nanoparticles as well as inorganic upconversion phosphors. Especially, the use of functional inorganic nanomaterials as a new generation of fluorescent reporters is one of the fastest growing research fields [51].

Another broad class of transduction elements are genetically encoded fluorescent proteins, from which the green fluorescent protein (GFP) is the most prominent. The excitation maxima of the (unmodified) GFP fluorophore lie at 395 nm and 475 nm, whereas the emission maximum is at 509 nm [58]. GFP and alike can be expressed artificially by many cells and organisms. They can be fused specifically to other proteins or host genes, which makes same a valuable tool for investigations of individual cells and biological samples in general [58–60].

In recent decades, the development and application of bioassay systems based on genetically engineered whole cells has been addressed by many researchers [61]. Starting from this, also biosensor systems with whole-cell reporters have been developed and tested as alternative analytical tools. Especially, whole-cell bacterial

biosensors have been considered for testing various effects of water contaminants, such as genotoxicity, cytotoxicity or the potential of membrane, oxidative, or protein damage [61]. In fluorescent biosensors, the reporter bacteria are genetically engineered by fusing of the *gfp* gene reporters to an inducible gene promoter. Due to its stability, sensitivity, and convenient fluorescence detectability GFP, encoded by *gfp* gene, is one of the most popular tools for biosensing [62]. The fluorescence output signal intensity serves as measure for GFP production as a result of analyte-induced gene expression [63]. A disadvantage of GFP as biological transduction element in whole-cell biosensors is the delay between its production and fluorescence emission, which makes it impractical for real-time monitoring applications [63]. Whole-cell-based fluorescent biosensors have been developed and field-tested to measure the relative bioavailability of petroleum product-related aromatic compounds, such as benzene, toluene, ethylbenzene, and xylenes (BTEX) in contaminated water and soil samples [64, 65] or arsenic and other trace amounts in drinking water [66].

In principle, any phenomenon inducing a change in intensity, wavelength, anisotropy, or lifetime of a fluorophore can be used for chemical sensing. The most direct method of chemical sensing is a change in fluorescence intensity of the transducer in response to an analyte. This happens due to a process called collisional quenching in which the analyte influences the optical output intensity (or lifetime) of the fluorophore when it comes into proximity. Examples of fluorescence chemical sensors based on collisional quenching are sensors for oxygen (based on long lifetime metal ligand complexes like $[Ru(Ph_2phen)_3]^{2+}$ absorbing at 450 nm) [67, 68], chloride (based on quinolines absorbing in the UV spectral range of 318–366 nm) [69], sulfur dioxide, or chlorinated hydrocarbons [70, 71].

Fluorescence resonance energy transfer (FRET) is another and perhaps the most valuable mechanism for fluorescence chemical sensing. Although UV excitable fluorophores have been used, most strategies for pH, pCO_2, glucose, or ion sensing based on FRET are focussing on fluorescence excitation in the visible wavelength region in order to circumvent photobleaching or unwanted autofluorescence [72].

For pH and ion sensing, especially for Ca^{2+}, Mg^{2+}, Na^+, and K^+ sensing inside living cells or in body fluid samples, also special wavelength ratiometric fluorescent indicators have been developed (e.g., [73, 74]). The key characteristic of these indicators is a wavelength shift in the fluorescence spectrum occurring upon binding with the ion. The shift may occur in either the excitation or the emission spectrum. Measurement is achieved using two excitation wavelengths (in case of dual excitation indicators) or two detection ranges (dual emission indicators). For the indicator Fura-2, e.g., in the absence of Ca^{2+}, the excitation maximum is at 372 nm shifting to 340 nm when bound to Ca^{2+} [75]. Another ionic species of interest in chemical sensing, especially for applications in imaging cellular systems, are metal ions, such as Zn^{2+} for which also UV excitable fluorescent probes, e.g., based on naphthalimide or quinoline derivates as fluorophores, have been developed [76, 77].

The simplest way to set up a fluorescent chemical sensing system is to mix the target analyte with appropriate amounts of the recognition and transduction

molecular or cellular species in the liquid phase in vitro. The reaction vessel or assay is placed in a fluorescence optical detection system with light source and fluorescence detection channel adjusted to the excitation and emission wavelength of the transducer. This is routinely done in bioanalytics where multiplex analysis based on microplates in 96-, 384-well (or even more) format, according liquid handling systems and plate readers are the state-of-the-art [6].

Especially for field-testing applications as well as high-throughput analysis, liquid handling is sometimes impractical and solid-phase sensors and arrays have to be utilized. In this context, a critical aspect is the immobilization of the recognition and transduction element in order to homogenize and increase its local concentration in the sensor or array. Accessibility by external reagents and in the case of living microorganisms as sensing elements also biocompatibility are further issues of concern. Thus many research activities are focused on immobilization, and as a result various physical and chemical strategies, such as adsorption, crosslinking, covalent binding entrapment, Langmuir–Blodgett deposition, or sol–gel entrapment, have been developed and successfully applied [78–81].

During the past 30 years, fluorescence detection methods have extensively been applied in bioanalytical assays for analyte recognition, DNA sequencing, detection of DNA hybridization, of polymerase chain reaction products and for protein profiling, and determination of protein function [6, 82]. Since fluorescence is a highly sensitive and less restricting method than detection by radioactive labeling in this field, many sophisticated assays, e.g., in association with electrophoretic separation techniques (gel blotting, 2D gel electrophoresis), multiwell plates, or microarrays, as well as adapted and automated fluorescence readout systems have been developed.

With enzyme-linked immunosorbent assays (ELISA) proteins (e.g., antigenes), viruses, hormones, toxines, or pesticides can be detected in a liquid sample. In ELISA, an enzyme-linked antibody binds specifically to the analyte (antigene) and the occurence of an enzyme-catalyzed reaction serves as a measure for the analyte, whereby the enzyme reaction rate can be quantified by means of a fluorescent substrate, which is consumed in the reaction [1].

Since its commercial availability in 1996, DNA microarrays, also commonly known as biochips, are nowadays routinely used in genomics for monitoring the expression of more than thousand of genes using just a single microscopic slide. Microarray technology can be regarded as an extension of biosensing techniques since it utilizes a slide-spotted, micropatterned array of biosensors allowing rapid and simultaneous probing of a large number of bioassemblies [6]. It is of considerable value to high-throughput analysis, e.g., for sequencing of the human genom, where huge numbers of genes and their products need to be characterized [83].

Since the intrinsic DNA fluorescence is almost neglectable (nucleic acid), staining is mandatory [84]. Typical fluorescent nucleic acid probes used in microarray technology are excited in the visible spectral range but if beneficial for some reasons also UV excitable probes like Hoechst 33342 or DAPI can be applied. State-of-the-art microarray readers are based on laser excitation and emission filter. By means of image analysis, signal intensities for each dye at each microarray spot

are determined and the data is analyzed by cluster analysis [6]. Especially for the analysis of multicolor microarrays as well as for a better background discrimination, hyperspectral microarray scanner technology, where the spectrally resolved fluorescence emission of each spot is analyzed, is beneficial [85].

In recent times, the focus of biology has shifted from genomics to proteomics where proteins are cataloged and analyzed aiming at a detailed understanding of biological complexity and functions [6]. Besides pharmacoproteomics, dealing with the mechanistic basis of drug action and toxicity proteins can also serve as new biomarkers for medical diagnosis. In two general areas of proteomics, high-throughput techniques are mandatory, which are protein profiling and determination of protein function. Although protein chip technology is not as well developed as gene chip technology, their improvement is inevitable [6]. Analogous to DNA microarray in a protein microarray, a glass slide is spotted with thousands of protein probes. Subsequently, a biological sample is spread over the slide and binding at any spot is detected. Fluorescence detection is the widely used method [86]. Since labeling sample proteins with a fluorescent reporter (such as fluorescent proteins or BODIPY dyes) bears the risk that the fluorophore binding may alter the ability of the protein to interact with the immobilized capture agent, protein UV absorbance and intrinsic autofluorescence excited in the UV are promising methods of detection in the field [87–90].

Fluorescence microscopy is a well-established technique in the life sciences enabling optical (bio-) imaging. Numerous monographs, handbooks, and reviews are available covering this field (e.g., [1, 6, 91–94]). One advantage of fluorescence as optical contrast method in microscopy is its very high signal-to-noise ratio that allows to distinguish spatial distributions of molecular species of low concentration. Both exogeneous fluorescence, where species of interest in the specimen (cell, tissue or gel) are labeled with a fluorophore, and endogenous fluorescence (autofluorescence), allowing for label-free bioimaging, are used in fluorescence microscopy [6]. Especially, the availability of numerous, specifically engineered fluorescent reporters for labeling different parts and structures of cells or probing different cell functions, in combination with fluorescence microscopic imaging has had a major impact in biology and medicine [6, 91, 95]. Usually, these fluorescent reporters are designed to absorb and emit at wavelengths in the VIS or NIR in order to suppress cell or tissue autofluorescence background (mainly excited in the UV or blue spectral range) potentially disturbing the fluorescence emission signal of the reporter. Nevertheless, UV autofluorescence as contrast method enabling label-free imaging of intrinsic biomarkers such as aminoacids, (co-)enzymes, lipids, or structure proteins is gaining more and more importance in the field [96].

Conventional or wide field fluorescence microscopes widely used today are mainly epifluorescence microscopes, where excitation light illumination of the object or specimen is realized through the same objective lens collecting the fluorescence emission signal for imaging [93]. A dichroic beam splitter, transmitting or reflecting light depending on its wavelength, is implemented to separate the excitation from the fluorescence light.

Historically, the most prevalent fluorescence excitation sources have been Mercury-vapor high-pressure arc lamps (commonly referred to as HBO lamps) but also Metal Halide lamps have been employed [93]. A new development in conventional fluorescence microscopy is the application of LEDs as excitation light sources [92]. LED modules for microscopy now are commercially available from several companies allowing LED illumination at wavelengths in the UV (starting at 255 nm) and VIS spectral range, characterized by compact size, low power consumption, fast switching and adjusting properties (instantly illumination at full intensity), and other advantages inherent to state-of-the-art LED technology [92].

Besides conventional microscopy, LEDs are also promising light sources for prism-based total internal reflection fluorescence microscopy (TIRFM) [92]. In TIRFM, a prism is placed on (and optically coupled to) a cover slip, acting as (total internal reflection based) optical waveguide when collimated (LED-) light is directed onto the prism under a proper incidence angle (Fig. 13.5a). If the object below is intentionally kept in watery low refractive index medium and not optically coupled to the cover slip, an exponentially decaying evanescent wave extends into the specimen perpendicular to the glass/water interface. By this, the fluorescence emission of a thin optical slice of the specimen can be imaged with very low background noise. Inspired by TIRFM and first demonstrated by Ely Silk in 2002 [97], a simple illumination scheme in conventional fluorescence microscopy is to place a prism laterally onto the glass slide support and to immerse the specimen in a mounting medium optically coupled to the glass slide, whereby the excitation light passes through the whole specimen exciting the fluorophores homogeneously (Fig. 13.5b). As a possible application of a cheap and compact LED-based fluorescence microscope, screening of patient`s septum for tuberculosis in developing countries has been officially recommended by the WHO [98].

Since with LEDs the excitation energy can be controlled without noticeable changes of the spectral emission characteristics and furthermore fast switching even in the nanosecond range is possible, they are also beneficial as illumination light

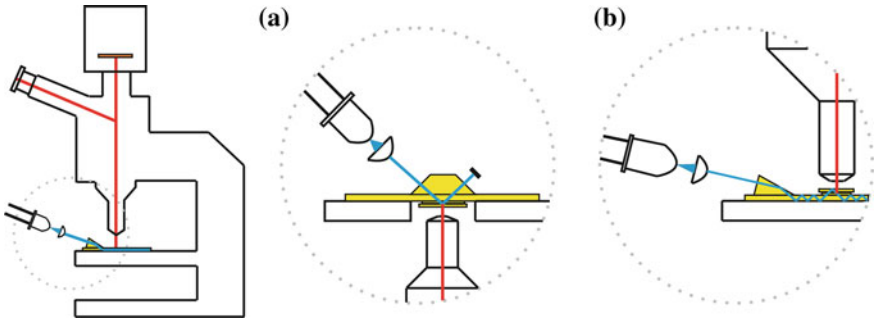


Fig. 13.5 Bright-field fluorescence microscopy setup with LED illumination either based on **a** a TIRFM setup with a prism placed over the observation area onto the microscopic slide (shown here for an inverted microscope setup) or **b** coupled into the side of the microscopic slide via a coupling prism (according to [92])

sources for two specialized variants of fluorescence microscopy, namely fluorescence resonance energy transfer microscopy (FRETM) and fluorescence lifetime imaging microscopy (FLIM). For a qualitative and relative tracking of the FRET process and when only a single FRET polypeptide construct is examined, acquisition of both the donor and acceptor emission at a single excitation wavelength is sufficient. In this case, the spectral contamination, i.e., the contribution to the FRET signal due to donor emission into the acceptor channel and the excitation of acceptor molecules by the donor excitation wavelength (spectral overlap), is constant. However, for quantitative assays or when the spectral contamination varies due to uncertain conditions of the surrounding media (e.g., fluorophore attachment to proteins with local concentration variations throughout a cell), multiple acquisitions are necessary. Here, LEDs are (low cost) alternatives to laser excitation light sources, enabling fast multiple acquisitions, especially when rapid FRET changes are expected in a cellular assay [92]. Another parameter, especially useful for quantitative FRET analysis but also for label-free imaging of intrinsic fluorophores is the fluorescence lifetime [99]. In FLIM, the fluorescence lifetime of a fluorophore is determined with spatial resolution. Lifetimes of most fluorophores typically used in cell biology are in the order of nanoseconds, implying acquisition accuracy in the picosecond range. As already discussed in Sect. 13.2, two principles, time-domain techniques, namely TCSPC and time-gating fluorometry and frequency-domain fluorometry can be applied for assessing fluorescence lifetime, based on either pulsing or modulating the LED emission. Some solutions, also covering the UV spectral range down to 255 nm, are already commercially available [92].

The development of confocal microscopy has further expanded the application of fluorescence microscopy in bioimaging [100]. It is based on an optical system, where a front and a back side focus are conjugated allowing only light from a selected plane of a (moveable) sample to reach the detector. Laser scanning microscopy (LSM) is a variant of confocal microscopy, where the light beam is scanned over the sample by means of movable mirrors, allowing fast optical sectioning of biological specimen even in vivo. Another technique based on confocal microscopy is fluorescence correlation spectroscopy (FCS). It is a powerful method for analyzing dynamics, local concentration, and photophysics of single molecules both in vitro and in vivo [8]. In FCS fluctuations of the fluorescence signal intensity, the mean values are measured and analyzed in a small (confocal) detection volume of the sample.

Both TIRFM and confocal microscopy (also in combination with FCS) can be applied for single molecule detection (SMD) where the size of the detection volume is reduced to less than one femtoliter [8]. Currently, in confocal microscopy and especially in FCS, only lasers are used as excitation light sources [1].

A well-established application of conventional fluorescence microscopy is fluorescence in situ hybridization (FISH), where the distribution of nucleic acids in tissue, cells, or chromosomes is analyzed in situ. It relies on DNA or RNA

specifically labeled with fluorescent probes and their computerized microscopic imaging with sensitive CCD detection [101]. Also, approaches based on probes bearing a mixture of fluorophores have been developed (termed as multicolor FISH and spectral karyotyping), which allow the identification of all 24 chromosomes within one sample [102, 103].

Flow cytometry is an optical method routinely used in both bioanalytics and medical diagnosis whereby cells are suspended in a stream of fluid and passed by a detection apparatus. It is employed in cell counting, cell sorting (fluorescence-activated cell sorting (FACS), which includes the ability of the instrument to sort cells according to specific measurement criteria), and biomarker detection since it allows simultaneous multiparametric analysis of physical and chemical characteristics of up to thousands of cells per second. Both flow cytometry and optical microscopy perform similar functions with the difference that in (confocal) microscopy, the (laser) light beam moves to analyze cells, whereas in flow cytometry the cells are moving (flowing). Typical flow cytometers are based on one or more laser sources for fluorescence excitation [6]. A wide variety of fluorochromes are employed in flow cytometry and the number is still growing driven by specific demands of new applications of flow cytometry [6]. Typical fluorochromes excited in the UV spectral range are coumarins and Cascade Blue for application in immunophenotyping, Hoechst 33342 and DAPI for DNA analysis and chromosome staining, and Indo1 for calcium flux measurements.

As main clinical application of flow cytometry, immunophenotyping basically deals with classification of white blood cells according to their surface antigen characteristics, which can then be used as a profile for a specific disease or malignancy. Measurement of the DNA count is another major application of flow cytometry and is applied to identify cell abnormality which involves genetic changes.

Monolithic integration of both optical and electronic components in general offers the possibility to miniaturize flow cytometers. As in fluorescence microscopy, flow cytometry platform design and versatility is benefiting from the availability of new, compact, and inexpensive (laser) diode emitters replacing bulky and inefficient gas lasers [6]. A particular configuration based on UV LED excited, time-gated fluorescence has already been proposed (Fig. 13.6) [104]. Significant progress has also been made in the area of microfluidics [105, 106]. Put together these two developments provide a good basis to produce flow cytometer-on-a-chip, expanding their versatility and application [6].

Imaging flow cytometry in general combines the statistical power and sensitivity of flow cytometry with spatial resolution and quantitative morphology of digital microscopy. The combination may be beneficial for various clinical applications since cells can be imaged and analyzed directly in bodily fluids. In this context, a compact cell-phone-enabled optofluidic imaging flow cytometer has already been introduced [107].

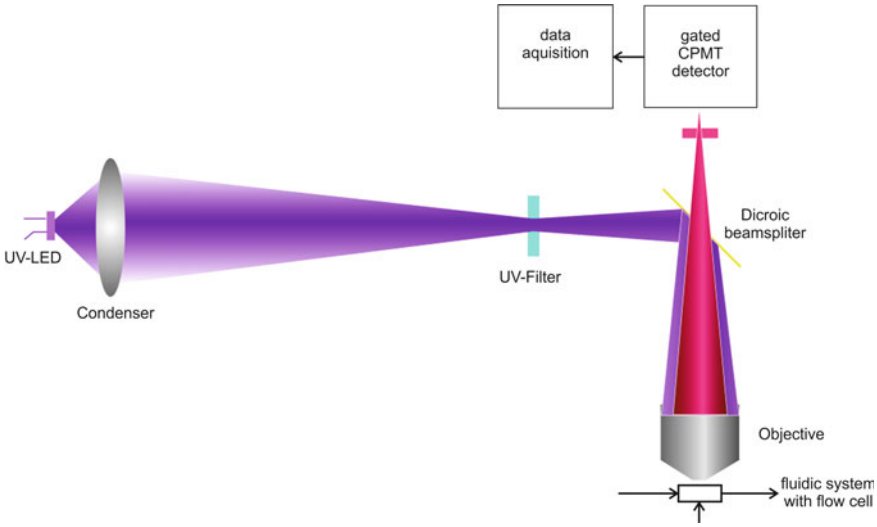


Fig. 13.6 Setup of a UV LED-based time-gated luminescence flow cytometer; *CPMT* channel photomultiplier tube (according to [104])

13.5 Detection of Microorganisms Using Autofluorescence

Microorganisms can be found everywhere: deep inside rocks, below the seafloor, and even in the most hostile environments like poles and deserts. Types that can cause diseases in a host are known as pathogens and their detection is of vital importance for health and safety reasons. Main areas of interest in the health care sector are the food industry, clinical diagnosis, and water or environment quality control [108].

Microorganisms can be divided into prokaryotes, namely bacteria and archaea, and eukaryotes, like fungi and algae. The classification of viruses as microorganisms is under debate, depending on their definition as living or nonliving. Some examples of bacterial pathogens of concern in food industry are *Salmonella*, *Listeria*, *Escherichia coli,* and *Campylobacter* [109]. Healthcare-associated pathogens, like Methicillin-resistant *Staphylococcus aureus* (MRSA) and *Clostridium difficile,* can be responsible for patients acquiring an infection in hospitals.

Various methods for the detection and analysis of microorganisms are in use. They comprise classical as well as modern, biosensor-based techniques. It is dependent on the application whether it is sufficient to just verify the presence of a minimal amount of biomass in an abiotic environment or to know the exact quantity of a specific pathogen on a given biological surface. All detection methods operate somewhere within this range.

Culture methods, which are based on the multiplication of the target organism on a growing medium, followed by visual colony counting, provide a reference. The

main disadvantage of these methods is the time that is needed for incubation which can be several days [108]. Commercially available so-called rapid detection methods such as ELISA, lateral-flow dipstick (LFD), and polymerase chain reaction (PCR) have significantly reduced the time and effort of the analysis of food products, but they still rely on a time-demanding enrichment step [109]. Other drawbacks are the costs for equipment and reagents especially for molecular biological methods.

A comparably new approach for microbial detection is biosensors, incorporating a target microorganism, a bio-specific recognition system, and a physicochemical transducer. Transduction methods in use also include fluorescence optical detection (see also Sect. 13.4). Biosensors can be miniaturized and automated, having the potential to both shorten the time of analysis and to provide selectivity and sensitivity comparable to established methods at a fraction of the cost [109].

Fluorescence methods are also suitable for directly monitoring the fluorescence of cellular components of microorganisms, and their metabolic states (live, dead, spores) [110]. Both extrinsic and intrinsic fluorescence can be applied for sensing purpose. Usually, the emission of exogenous synthetic fluorescent reporters, specifically labeling a target analyte characteristic for a microorganism to detect, is relatively strong and mainly excited in the visible spectral region.

Fluorescence detection methods that do not apply fluorescent reporters to microorganisms make use of the intrinsic or autofluorescence, sometimes also referred to as reagent-free identification. It is caused by fluorophores which exist as a natural component or product of a microorganism under examination. Using intrinsic fluorescence for detection and identification of microorganisms allows for real-time measurements in a noninvasive, contact-free manner rendering sample preparation unnecessary [111]. Only a few methods like flow cytometry are able to detect and differentiate viable but nonculturable (VBNC) bacteria. Using intrinsic fluorescence spectroscopy, it has been shown that this is possible without incubation even in the presence of culturable bacteria [112]. Furthermore, cellular fluorescence may also be used to determine the metabolic state of living cells. It allows their classification into three groups corresponding to the three main phases of the growth profile, i.e., lag phase, exponential phase, and stationary phase [112].

Many fluorescent biomolecules in microorganisms can be excited in the UV spectral range between 220 nm and 360 nm (Fig. 13.7). Proteins, which are an integral part of all organisms, obtain their fluorescent characteristics from aromatic amino acids (AAA) like tryptophan. Other important sources of fluorescence are the pyridine nucleotides NADH and NADPH in their reduced form, which are enzymatic cofactors appearing in all organisms. This is also true for flavines, such as flavin adenine dinucleotide (FAD) and flavin mononucleotide (FMN) fluorescing in their oxidized form and some vitamin B6 compounds. Cell wall components like chitin (fungi, algae) are also a source of strong intrinsic fluorescence as well as dipicolinic acid (DPA) in the presence of calcium ions (spores). A comprehensive overview of relevant fluorophores and their optical parameters is provided by Pöhlker et al. [18].

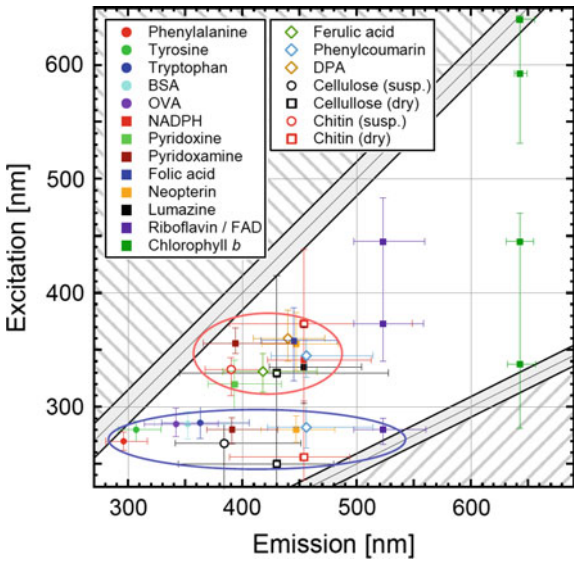


Fig. 13.7 Conceptual EEM displaying excitation and emission ranges of various biological fluorophores (*BSA* bovine serum albumin; *OVA* ovalbumin; *NADPH* nicotinamide adenine dinucleotide phosphate; *FAD* flavin adenine dinucleotide; *DPA* dipicolinic acid). The *red* and *blue* ovals depict "emission hotspots" where the modes of many fluorophores cluster. Reprinted with permission from [18], Copyright 2012, Copernicus Publications

For detection of the intrinsic fluorescence signal of relevant fluorophores, it is often beneficial to acquire with spectral resolution, because several biological fluorophores present very close emission spectra that become difficult to discriminate [96]. The main challenge in using intrinsic fluorescence for microbial detection is that the spectral characteristics of a fluorophore are highly sensitive to its local environment, such as binding of ligands, protein–protein association, pH, hydrophilicity, or lipophilicity. Therefore, the detailed knowledge of how these factors influence the fluorescence signal is essential [96].

As described above, fast and noninvasive methods for the detection of microorganisms would be particularly useful in decontamination tasks, medical assays, or forensic investigations. Depending on the location of the microbial load detection methods for surfaces, fluids, and air can be distinguished.

Surface fluorescence detection of microorganisms can be of different complexities at distinct substrate materials like glass, metal, plastics, cloth, foods, or even living tissue. Several variants of a real-time in situ detection system have been build up using filtered LEDs for the visible (455–635 nm) and the UV (365 nm, 1 mW each) spectral range as excitation sources (see Fig. 13.8) [111, 113, 114]. The UV diodes were used mainly to excite NADH and DPA fluorescence within an area of 1 cm^2. Nearly, hemispherical collection has been applied using parabolic-type reflectors to gather 90 % of the fluorescence [114]. An aspheric lens is another

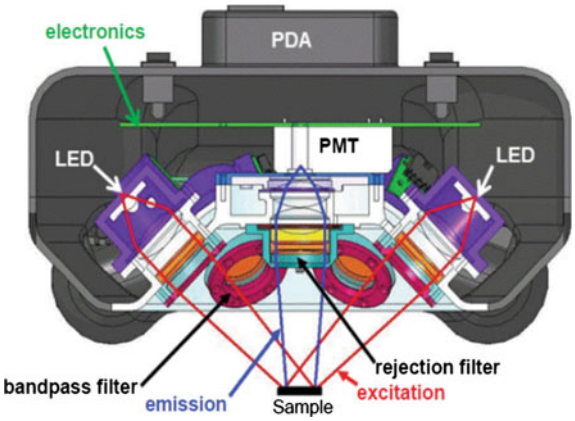


Fig. 13.8 Schematic diagram of a hand-held instrument for detection and quantification of microorganisms based on the intrinsic fluorescence, excitation by visible and UV LEDs, detection of the filtered fluorescence emission by photomultiplier tube (*PDA* personal digital assistant). Reprinted with permission from [111], Copyright 2012, Elsevier

effective way to collect emission from the spot using standard components [113]. With these systems, detection limits as low as 10 microbial cells per cm^2 could be provided on abiotic surfaces. Because of their sensitivity, photomultiplier tubes (PMTs) are often used for the detection of the band-pass filtered emission. Elimination of the excitation signal is done by rejection filters in front of the detector. Using amplitude-modulated light sources further improves the sensitivity and allowed for detecting microbial concentrations that vary by up to nine orders of magnitude [111]. A hemispheric detection geometry has also been accomplished using optical fibers while exciting a biofilm under seawater with a 280 nm LED source (600 μW, area 0.55 cm^2) [115]. Here, bacterial proteins were detected by their tryptophan fluorescence signal to a detection limit of 4×10^3 cells per cm^2 for an artificial biofilm. Fluorescence of surface contamination by clinically relevant bacteria has been investigated using excitation wavelengths of 280–800 nm with a commercial fluorescence spectrometer [116]. Measurements of the spatial distribution of microorganisms on surfaces have also been done using fluorescence imaging methods. A deep UV scanning microscope equipped with hollow-cathode lasers of 224 nm (HeAg) and 249 nm (NeCu) has been used for imaging bacterial fluorescence on opaque mineral and metal surfaces with a spatial resolution of 300 nm providing single cell sensitivity [117]. Another device uses an imaging spectrograph and line scanning to acquire images. Excitation of bacteria relevant in the food industry is done by a UVA lamp at 365 nm [118].

LEDs for the visible and the UV (365 nm) have been used to excite the intrinsic fluorescence of bacteria, fungi, and other microorganisms for monitoring of drinking water. With an instrument specifically designed for this purpose, a detection limit of 50 bacterial cells per liter was achieved [110]. A similar excitation source has been used by a related device, which could detect 10 microbial cells per

mL [111]. Both acquire band-pass filtered fluorescence with a PMT. A UV LED-based multi-wavelength fluorimeter system is described in [119] covering the wavelength range from 250 nm to 375 nm to excite autofluorescence of several microorganisms. The system has a turn-on time of 2–3 ns, internal modulation up to 300 MHz, and can operate in a continuous wave or pulsed mode [119]. Further studies based on non-LED UV light sources are also reported. To excite cultured cells and tissues over a wide range of 180–600 nm, monochromatized synchrotron radiation has been used [96]. Most widespread for investigation of microbial fluorescence is the use of commercial fluorescence spectrometers together with quartz cuvettes for sampling. They have been used to detect and differentiate bacteria like *Escherichia coli*, *Salmonella,* and *Campylobacter*, which are relevant for the food industry. Here, concentrations down to 10^3 cells per mL could be measured at an excitation of 200–400 nm and using principal component analysis (PCA) for data analysis [120]. Excitations of 250 nm for AAA and nucleic acids (NA), 316 nm for NADH and 380 nm for FAD allowed a discrimination of lactic acid bacteria at the genus, species, and subspecies levels [121]. An excitation of 250–340 nm was used to detect the fluorescence of tryptophan and NADH in bacterial cells and their comparison through PCA and factorial discriminant analysis (FDA) [122]. The fluorescence signals of tryptophan at an excitation of 280 nm and of NADH at 350 nm have been used to investigate the metabolism and the growth of cells while chemically restraining them [123]. A method for rapid identification of the clinically significant species *Escherichia coli*, *Enterococcus faecalis,* and *Staphylococcus aureus* has been shown using excitation wavelengths of 330–510 nm. The PCA technique applied to the fluorescence spectra showed that bacterial species could be identified with sensitivity and specificity higher than 90 % and in less than 10 min [124]. There is a certain overlap between the described cuvette-based methods and flow cytometry (see Sect. 13.4). The latter is a common tool in cell biology for rapid analysis of large populations of cells where fluorescence detection is well established. Here also intrinsic fluorescence of cellular molecules can be used beside extrinsic fluorescent stains or antibody probes [116].

The detection of intrinsic fluorescence is also applied to atmospheric aerosol particles, which include small pieces of biological materials and microorganisms (see Fig. 13.9) [18, 125]. Linear arrays of UV LEDs exciting at 290 nm for tryptophan and 340 nm for NADH have been applied to identify bacterial spores even during their time-of-flight [126]. The detection was provided by a UV transmission grating to spectrally disperse the light onto a 32-anode PMT achieving a detection limit of 350 µM of NADH. Using the excitation range of 210–419 nm of an optical parametric oscillator AAA could be identified as dominant features of the aerosols investigated [127]. The fluorescence detection of flavines, NAD(P)H, and tryptophan was accomplished with a parabolic collection mirror, a spectrograph, and an image-intensified CCD camera.

Altogether, the application of UV LED and LD sources is not yet widespread in fluorescence-based detection of microorganisms. However, as soon as emitters with

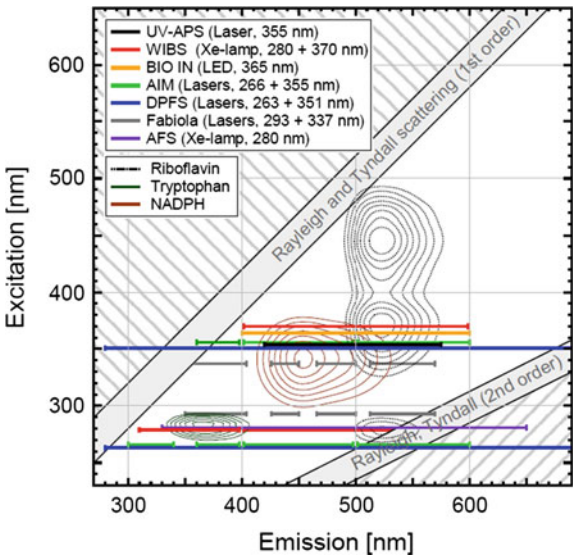


Fig. 13.9 Conceptual EEM displaying contour lines for the fluorophores tryptophan, NADPH, and riboflavin and operational ranges of selected bioaerosol detectors, represented by *horizontal colored lines*. Length of individual *lines* indicates measured emission band for a certain excitation wavelength shown as sharp line for purpose of clarity. Single-wavelength detectors are represented by *one line*, dual-wavelength detectors by *two lines*. Reprinted with permission from [18], Copyright 2012, Copernicus Publications

adequate performance are available at low cost it is very likely that they enable further improvement and development of effective and compact tools in this field.

13.6 Fluorescence in Medical Diagnosis of Skin Diseases

Fluorescence detection as a tissue diagnostic procedure is applied in a wide range of medical fields such as dermatology, dentistry, ophthalmology, laryngology, gastroenterology, neurology, or oncology to name a few [128–134]. This section will focus on fluorescence diagnosis in the field of dermatology, especially on skin cancer diagnosis based on UV autofluorescence excitation and spectroscopy.

In fluorescence diagnosis, it is to be distinguished between autofluorescence and exogenous fluorescence. For exogenous fluorescence, a fluorescent substance such as δ-aminolevulinic acid (ALA) or methylester aminolevulinate (MAL) is applied either topically in the form of a cream or systemically in the form of a drug given prior to the measurement. ALA attaches itself to healthy tissue and to pathological changes, in most cases cancer-affected tissue. In healthy tissue, ALA decomposes into nonfluorescent substances, whereas in damaged tissue, protoporphyrin IX (PpIX) is formed which can be excited to fluorescence by UV irradiation in the

UVA spectral range [135]. In the case of autofluorescence, endogenous fluorophores, such as NAD(P)H or tryptophan, are excited by UV irradiation circumventing the administration of auxiliary substances.

One of the first UV radiation sources for fluorescence excitation was the Woods lamp that had been invented by Robert W. Wood in 1903. Its first use in dermatology was reported in 1925 when it had been applied to detect fungal infections of the scalp [136]. UV radiation in the range of 340–400 nm is generated by a high-pressure mercury arc that passes an optical filter, the so-called Woods filter. It is nowadays primarily used for nonspectrally resolved fluorescence imaging, in order to visualize the borders of carcinogenic lesions. As the radiation intensity of the Woods lamp is low, dark rooms and extended observation periods including eye adaptations are required [137]. With the availability of UV LEDs, this imaging method can be improved by arranging UV LED-based ring lights around a camera objective enabling a more compact design and its adaptation to digital imaging systems [135].

For the noninvasive detection of skin cancer image processing systems based on RGB cameras are state-of-the-art. In part, this applies also to multispectral cameras which often cover also the NIR spectral range [138, 139]. Although image processing systems are very reliable, precancerosis lesions are often difficult to detect and to discriminate with this technology.

Autofluorescence spectroscopy based on excitation of intrinsic dermal fluorophores holds the potential to overcome the limitations of image processing for skin cancer diagnosis [140]. Typical dermal fluorophores and their excitation and emission wavelengths are listed in Table 13.1. The amino acids are generally excited in the shortwave UV range (260–295 nm) and exhibit their fluorescence still in the UVA range. In this context, tryptophan has been attributed an essential role in diagnostics. Structural proteins such as elastin and collagen are important fluorophores of the dermis. A prominent representative of the enzymes and co-enzymes is the NADH/NAD+ system contributing to autofluorescence only in its oxidized form. Some vitamins and lipids as well as porphyrins (emitting in the red spectral range) also show autofluorescence [141].

Before addressing the differentiation of benign from malignant tissue in dermatology, some studies investigating the influence of aging, proliferation, and photoaging on the autofluorescence emission will be discussed. One important finding was that with increasing aging tryptophan decreases and could be absent at high age [143]. Collagen decreases as well, whereas the autofluorescence of elastin increases. This is in agreement with the changes in the collagen/elastin index SAAID which is measured by multiphoton microscopy to evaluate the age of the skin [144]. Proliferation as observed after tape stripping increases the tryptophan autofluorescence that thus can be used as a marker for proliferation [145]. This also explains the increase in the tryptophan autofluorescence in psoriatics [146]. The porphyrin fluorescence is increased in these patients, too [142, 147]. Tryptophan autofluorescence also increases at extended UV exposure which may be due to an intensified epithelial growth. However, the collagen fluorescence is decaying at chronic UV exposure [148] and can, therefore, be used as a marker for photoaging.

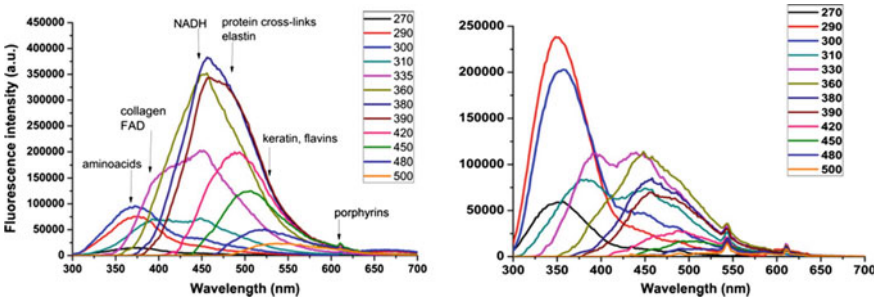


Fig. 13.10 Normal skin (*left*) and BCC (*right*) autofluorescence spectra at different excitation wavelengths (from 270 nm to 500 nm) and identification of the major endogenous fluorescence compounds observed. Spectra of BCC are recorded from an excised lesion. Reprinted with permission from [140], Copyright 2014, IEEE Photonics Society

Furthermore, DeAraujo et al. used laser-excited autofluorescence for discriminating between various types of human pathogenic fungi inducing several skin infections [149].

Dermatological tumor diagnostics by fluorescence spectroscopy has been applied in numerous studies for many years [140]. Nonmelanoma skin cancer (NMSC) lesions are suitable targets for fluorescence spectroscopy-aided diagnosis. NMSC usually covers basal cell carcinoma (BCC) and squamous cell carcinoma (SCC) tumors. These lesions are among the most common cancers affecting Caucasians. BCC occasionally grows aggressively causing tissue destruction and it is often recurring after initial treatment. SCC, the second most widely spread cutaneous tumor, is associated with a risk of metastasis and is usually more aggressive and difficult to treat compared to BCC lesions [150]. The problem in diagnosis of skin cancer is the large variety of malignant forms of skin tumors. There are several subtypes, for example, BCC and SCC and a variety of benign and dysplastic forms with differences in optical and autofluorescence properties.

The autofluorescence spectra of normal tissue are shown in Fig. 13.10 left, at different excitation wavelengths. Borisova et al. [140] measured pure samples of collagen type I, porphyrin, and keratin and evaluated the other compounds in the spectra using the knowledge about excitation and emission maxima cited in the literature and Table 13.1. The amino acid fluorescence appears in the UV, collagen, and FAD at around 400 nm. NADH is the strongest fluorophore with emission at around 450 nm followed by elastin and keratin with green fluorescence. The autofluorescence of porphyrin shows a low-intensity signal at wavelengths above 600 nm. On the right side of Fig. 13.10, the autofluorescence spectra for early BCC tumor are shown at different excitation wavelengths. The most pronounced difference are the overall intensities of the fluorescence spectra which are lower for BCC compared to normal skin. This observation has frequently been reported in the literature [142, 151]. A crucial parameter for the diagnosis is the spectral shift of the autofluorescence. While the intensity doubles in the 320–360 nm range, it drops by a factor of 3 in the 390–460 nm range. This could be due to the changes in the

optical parameters within the tumor and to the increasing thickness of the tissue. The autofluorescence of the porphyrins is also carefully observed as it increases in higher-graded tumors. Autofluorescence diagnostics of malignant melanoma (MM) is hampered by the high absorption and reabsorption of the radiation. Moreover, it is limited to the skin surface due to the low penetration depth. Nevertheless, MM leads to a decay of the NADH fluorescence [152].

Existing studies had been focused on intensity changes in the autofluorescence, also in comparison to normal skin [151, 153–157]. Some researchers linked autofluorescence measurements with diffuse reflectance spectroscopy [158–161]. Wollina et al. could demonstrate that the diffuse reflectance-corrected autofluorescence of NADH, excited by a UV LED, permits BCC to be distinguished from actinic keratosis (AK) [162]. Other researchers complemented their autofluorescence experiments by time-resolved measurements [151].

Borisova et al. performed autofluorescence investigations on 536 patients affected by BCC (137 lesions), SCC (29), MM (41), benign skin lesions (194), keratoacanthoma (11), and dysplastic naevi (124) [140]. In addition to the autofluorescence, the diffuse reflectance of the skin was measured. The spectra were interpreted according to Savelieva et al. [163]. For clinical diagnostics, the spectral shape must be included into the analysis, and thus the autofluorescence analysis was made using excitation wavelengths of 365 nm and 405 nm, extracting 23 spectral parameters, intensity levels, specific minima and maxima, intensity ratios, slopes of the spectra in given ranges, etc. The obtained results permitted the development of a multispectral discrimination algorithm. In most of the BCC lesions (80 %), strong decreases in autofluorescence were observed compared to normal tissue. In case of SCC higher autofluorescence intensities occured. Also, the stage of the tumor changes the behavior of the spectra. In early stages of BCC, the intensity is reduced without changing the spectral form. In their advanced stage, BCC exhibits pronounced fluorescence maxima in the green-red spectral range, related to endogenous porphyrins [140, 164]. For a better specification, the type and melanin content of the skin has to be taken into account, too. It strongly affects the spectra and is an important part of the algorithm. Multispectral analysis provides high sensitivity >99.1 %, specificity >90.5 %, and diagnostic accuracy >93.3 % d for NMSC versus benign, MM versus benign, and MM versus NMSC [140].

Besides direct excitation in the UV spectral range, also two photon techniques are available making use of a femtosecond laser that is tunable from 690 nm to 1000 nm. They are based on two NIR photons exciting the fluorescence of the endogenous fluorophores at one single spot in the tissue [165]. The excitation at only one spot yields a high spatial resolution permitting cellular structures in the skin to be imaged up to approximately 200 µm in depth at high resolution. While NADH is the most important fluorophore, FAD, elastin, and collagen contribute also to the image acquisition. As the multiphoton technique is also capable of determining the fluorescence lifetime, the fluorophores can be differentiated even further. Taking into account that most fluorophores, for instance NADH, are metabolically active substances, possible changes in these substances can be utilized for wound healing or tumor diagnostics [166, 167].

13.7 Summary and Outlook

Many natural and synthetic fluorophores can be excited with UV light, and therefore numerous applications of UV fluorescence detection and spectroscopy are already existent. Since for sensing purpose low or medium power LED modules are usually sufficient, almost all of these applications are benefiting from the availability of solid-state UV emitters replacing bulky and inefficient lamps or lasers. Their compact size, adjustable wavelength, low power consumption, fast switching, and adjusting properties (just to name a few of the advantages inherent to state-of-the-art LED technology) not only enables miniaturization and thus point-of-care testing and analysis but also leads to methodologically new and promising approaches in clinical diagnosis and (environmental) chemical sensing. Especially when the autofluorescence of a multicomponent target is analyzed, UV LED technology is almost without alternative since it easily provides multiple wavelengths for fluorescence excitation of the ensemble of fluorophores that is either characteristically changing due to a malignancy or characteristic for the target to detect.

References

1. J.R. Lakowicz, *Principles of Fluorescence Spectroscopy*, 3rd edn. (Springer Science +Business Media, New York, 2006)
2. J.R. Lakowicz, C.D. Geddes (eds.), *Topics in Fluorescence Spectroscopy* (Springer, Berlin, 1991)
3. O.S. Wolfbeis, M. Hof (eds.), *Springer Series on Fluorescence, Methods and Applications*, vol. 1–13 (Springer, Berlin, 2001–2013)
4. B. Valeur, *Molecular Fluorescence—Principles and Applications* (Wiley, Weinheim, 2006)
5. G.G. Guilbault (ed.), *Practical Fluorescence*, 2nd edn. (Marcel Dekker, New York, 1990)
6. P.N. Prasad, *Introduction to biophotonics* (Wiley, Hoboken, 2003)
7. J. Popp, V.V. Tuchin, A. Chiou, S.H. Heinemann (Eds.), *Handbook of Biophotonics*, Vol. 1–3 (Wiley-VCH, New York, 2011)
8. S. Das, A.M. Powe, G.A. Baker, B. Valle, B. El-Zahab, H.O. Sintim, M. Lowry, S.O. Fakayode, M.E. McCarroll, G. Patonay, M. Li, R.M. Strongin, M.L. Geng, I.M. Warner, Molecular fluorescence, phosphorescence, and chemiluminescence spectrometry. Anal. Chem. **84**(2), 597–625 (2012)
9. A. Jablonski, Über den Mechanismus der Photolumineszenz von Farbstoffphosphoren. Z. Phys. **94**(1–2), 38–46 (1935)
10. G.G. Stokes, On the Change of Refrangibility of Light. Philos. Trans. R. Soc. Lond. **142**, 463–562 (1852)
11. W. Denk, J.H. Strickler, W.W. Webb, Two-photon laser scanning fluorescence microscopy. Science **248**(4951), 73–76 (1990)
12. S. Eshlaghi, W. Worthoff, A. Wieck, D. Suter, Luminescence upconversion in GaAs quantum wells. Phys. Rev. B **77**, 245317 (2008)
13. Y. Wang, F. Nan, X. Liu, L. Zhou, X. Peng, Z. Zhou, Y. Yu, Z. Hao, Y. Wu, W. Zhang, Q. Wang, Z. Zhang, Plasmon-enhanced light harvesting of chlorophylls on near-percolating silver films via one-photon anti-stokes upconversion. Sci. Rep. **3**, 1861 (2013)

14. K. Rurack, Fluorescence quantum yields: methods of determination and standards. in *Standardization and Quality Assurance in Fluorescence Measurements I*, ed. by U. Resch-Genger (Springer, Berlin, 2008), pp. 101–145
15. C. Reichardt, *Solvents and Solvent Effects in Organic Chemistry*, 3rd edn. (Wiley-VCH, Weinheim, 2003)
16. E.L. Wehry, Effects of molecular environment on fluorescence and phosphorescence, in *Practical Fluorescence*, 2nd edn., ed. by G.G. Guilbault (Marcel Dekker Inc, New York, 1990)
17. E. Fort, S. Gresillon, Surface enhanced fluorescence. J. Phys. D Appl. Phys. **41**, 013001 (2008)
18. C. Pöhlker, J.A. Huffman, U. Pöschl, Autofluorescence of atmospheric bioaerosols—fluorescent biomolecules and potential interferences. Atmos. Meas. Tech. **5**, 37–71 (2012)
19. L.D. Lavis, R.T. Raines, Bright ideas for chemical biology. ACS Chem. Biol. **3**, 142–155 (2008)
20. C.A. Stedmon, R. Bro, Characterizing dissolved organic matter fluorescence with parallel factor analysis: a tutorial. Limnol. Oceanogr. Methods **6**, 572–579 (2008)
21. H. Peng, E. Makarona, Y. He, Y.-K. Song, A.V. Nurmikko, J. Su, Z. Ren, M. Gherasimova, S.-R. Jeon, G. Cui, J. Han, Ultraviolet light-emitting diodes operating in the 340 nm wavelength range and application to time-resolved fluorescence spectroscopy. Appl. Phys. Lett. **85**, 1436–1438 (2004)
22. C.D. McGuinness, K. Sagoo, D. McLoskey, D.J.S. Birch, Selective excitation of tryptophan fluorescence decay in proteins using a subnanosecond 295 nm light-emitting diode and time-correlated single-photon counting. Appl. Phys. Lett. **86**, 261911 (2005)
23. C.D. McGuinness, A.M. Macmillan, K. Sagoo, D. McLoskey, D.J.S. Birch, Excitation of fluorescence decay using a 265 nm pulsed light-emitting diode: Evidence for aqueous phenylalanine rotamers. Appl. Phys. Lett. **89**, 063901 (2006)
24. D.V. O'Connor, D. Phillips, *Time-Correlated Single Photon Counting* (Academic Press, London, 1984)
25. W. Becker, *Advanced time-correlated single-photon counting techniques* (Springer, Berlin, 2005)
26. W. Becker, *The bh TCSPC Handbook*, 5th edn. (Becker & Hickl GmbH, Berlin, 2008), http://www.becker-hickl.de/
27. F. Rouessac, A. Rouessac, Fluorimetry and chemiluminescence (Chap.11). in *Chemical Analysis: Modern Instrumentation Methods and Techniques*, 2nd edn. (John Wiley & Sons Ltd, Chichester, 2007)
28. M. Matsuoka, M. Saito, M. Anpo, Photoluminescence Spectroscopy, in *Characterization of Solid Materials and Heterogeneous Catalysts: From Structure to Surface Reactivity*, ed. by M. Che, J.C. Vedrine (Wiley-VCH, Weinheim, 2012)
29. L. Bergman, J.L. McHale (Eds.), *Handbook of Luminescent Semiconductor Materials* (CRC Press, Boca Raton, 2011)
30. S. Das, A.M. Powe, G.A. Baker, B. Valle, B. El-Zahab, H.O. Sintim, M. Lowry, S.O. Fakayode, M.E. McCarroll, G. Patonay, M. Li, R.M. Strongin, M.L. Geng, I.M. Warner, Molecular fluorescence, phosphorescence, and chemiluminescence spectrometry. Anal. Chem. **84**, 597–625 (2011)
31. N. Her, G. Amy, D. McKnight, J. Sohn, Y. Yoon, Characterization of DOM as a function of MW by fluorescence EEM and HPLC-SEC using UVA, DOC and fluorescence detection. Water Res. **37**, 42954303 (2003)
32. Y.-S. Chang, C.-M. Shih, C.-H. Lin, UV light-emitting diode-induced fluorescence detection combined with online sample concentration techniques for capillary electrophoresis. Anal. Sci. **22**, 235–240 (2006)
33. A. Rodat-Boutonnet, P. Naccache, A. Morin, J. Fabre, B. Feurer, F. Couderc, A comparative study of LED-induced fluorescence and laser-induced fluorescence in SDS-CGE: application to the analysis of antibodies. Electrophoresis **33**, 1709–1714 (2012)

34. C. Sluszny, Y. He, E.S. Yeung, Light-emitting diode-induced fluorescence detection of native proteins in capillary electrophoresis. Electrophoresis **26**, 4197–4203 (2005)
35. J.R. Albani, Fluorescence spectroscopy in food analysis. In *Encyclopedia of Analytical Chemistry* (Wiley Online Libary, 2012)
36. J. Christensen, L. Norgaard, R. Bro, S.B. Engelsen, Multivariate autofluorescence of intact food systems. Chem. Rev. **106**(6), 1979–1994 (2006)
37. E. Sikorska, I. Khmelinskii, M. Sikorski, Analysis of olive oils by fluorescence spectroscopy: methods and applications. in *Olive Oil—Constituents, Quality, Health Properties and Bioconversions,* ed. by B. Dimitrios (InTech, Rijeka, 2012)
38. O.S. Wolfbeis, M. Leiner, Mapping of the total fluorescence of human blood serum as a new method for its characterization. Anal. Chim. Acta **167**, 203–215 (1985)
39. L. Bu-hong, Z. Zhen-xi, X. Shu-sen, C. Rong, Fluorescence spectral characteristics of human blood and its endogenous fluorophores. Spectrosc. Spectr. Anal. **26**, 1310–1313 (2006)
40. A.E. Siegrist, C. Eckhardt, J. Kaschig, E. Schmidt, *Optical Brighteners. Ullmann's Encyclopedia of Industrial Chemistry* (Wiley-VCH, New York, 2003)
41. P.A. Pantoja, J. López-Gej, G.A.C. Le Roux, F.H. Quina, C.A.O. Nascimento, Prediction of crude oil properties and chemical composition by means of steady-state and time-resolved fluorescence. Energy Fuels **25**(8), 3598–3604 (2011)
42. M. Dobbs, J. Kelsoe, D. Haas, UV counterfeit currency detector, US 7715613 B2 (2006)
43. M.C. Storrie-Lombardi, J.P. Muller, M.R. Fisk, C. Cousins, B. Sattler, A.D. Griffiths, A. J. Coates, Laser-Induced Fluorescence Emission (L.I.F.E.): searching for Mars organics with a UV-enhanced PanCam. Astrobiology **9**(10), 953–964 (2009)
44. G. Zheng, K. He, F. Duan, Y. Cheng, Y. Ma, Measurement of humic-like substances in aerosols: a review. Environ. Pollut. **181**, 301–314 (2013)
45. S.K.L. Ishii, T.H. Boyer, Behavior of reoccurring PARAFAC components in fluorescent dissolved organic matter in natural and engineered systems: a critical review. Environ. Sci. Technol. **46**, 2006–2017 (2012)
46. J. Bridgeman, M. Bieroza, A. Baker, The application of fluorescence spectroscopy to organic matter characterisation in drinking water treatment. Rev. Environ. Sci. Biotechnol. **10**, 277–290 (2011)
47. A. Andrade-Eiroa, M. Canle, V. Cerdá, Environmental applications of excitation-emission spectrofluorimetry: an in-depth review I. Appl. Spectroscopy Rev. **48**, 1–49 (2013)
48. S.A. Baghoth, S.K. Sharma, G.L. Amy, Tracking natural organic matter (NOM) in a drinking water treatment plant using fluorescence excitation-emission matrices and PARAFAC. Water Res. **45**, 797–809 (2011)
49. C. Goletz, M. Wagner, A. Grübel, W. Schmidt, N. Korf, P. Werner, Standardization of fluorescence excitation-emission-matrices in aquatic milieu. Talanta **85**, 650–656 (2011)
50. S.J. Hart, R.D. JiJi, Light emitting diode excitation emission matrix fluorescence spectroscopy. Analyst **127**, 1693–1699 (2002)
51. P. Desjardins, J.B. Hansen, M. Allen, Microvolume spectrophotometric and fluorometric determination of protein concentration. Curr. Protoc. Protein Sci. Unit 3.10 (2009). doi:10.1002/0471140864.ps0310s55
52. U. Resch-Genger, M. Grabolle, S. Cavaliere-Jaricot, R. Nitschke, T. Nann, Quantum dots versus organic dyes as fluorescent labels. Nat. Methods **5**, 763–775 (2008)
53. Q.A. Zhao, F.Y. Li, C.H. Huang, Phosphorescent chemosensors based on heavy metal complexes. Chem. Soc. Rev. **39**, 3007–3030 (2010)
54. H.N. Kim, Z. Guo, W. Zhu, J. Yoon, H. Tian, Recent progress on polymer-based fluorescent and colorimetric chemosensors. Chem. Soc. Rev. **40**, 79–93 (2011)
55. A.P. de Silva, H.Q.N. Gunaratne, T. Gunnlaugsson, A.J.M. Huxley, C.P. McCoy, J.T. Rademacher, T.E. Rice, Signaling recognition events with fluorescent sensors and switches. Chem. Rev. **97**, 1515–1566 (1997)
56. T. Koshida, T. Arakawa, T. Gessei, D. Takahashi, H. Kudo, H. Saito, K. Yano, K. Mitsubayashi, Fluorescence biosensing system with a UV-LED excitation for l-leucine detection. Sens. Actuators B **146**, 177–182 (2010)

57. H. Kudo, M. Sawai, X. Wang, To Gessei, T. Koshida, K. Miyajima, H. Saito, K. Mitsubayashi, A NADH-dependent fiber-optic biosensor for ethanol determination with a UV-LED excitation system. Sens. Actuators **141**, 20–25 (2009)
58. R.Y. Tsien, The green fluorescent protein. Annu. Rev. Biochem. **67**, 509–544 (1998)
59. N.C. Shaner, P.A. Steinbach, R.Y. Tsien, A guide to choosing fluorescent proteins. Nat. Methods **2**, 905–909 (2005)
60. M. Chalfie, S.R. Kain (Eds.), Green fluorescent protein: properties, applications and protocols. in *Methods of Biochemical Analysis*, vol. 47, 2nd edn. (John Wiley and Sons, Hoboken, 2006)
61. E. Eltzov, R.S. Marks, Whole-cell aquatic biosensors. Anal. Bioanal. Chem. **400**, 895–913 (2011)
62. J.C. Pickup, F. Hussain, N.D. Evans, O.J. Rolinski, D.J.S. Birch, Fluorescence-based glucose sensors. Biosens. Bioelectron. **20**, 2555–2565 (2005)
63. Y. Lei, W. Chen, A. Mulchandani, Microbial biosensors. Anal. Chim. Acta **568**, 200–210 (2006)
64. Y.-F. Li, F.-Y. Li, C.-L. Ho, V.H.-C. Liao, Construction and comparison of fluorescence and bioluminescence bacterial biosensors for the detection of bioavailable toluene and related compounds. Environ. Pollut. **152**, 123–129 (2008)
65. L. Stiner, L.J. Halverson, Development and characterization of a green fluorescent protein-based bacterial biosensor for bioavailable toluene and related compounds. Appl. Environ. Microbiol. **68**, 1962–1971 (2002)
66. J. Theytaz, T. Braschler, H. van Lintel, P. Renaud, E. Diesel, D. Merulla, J. van der Meer, Biochip with E. coli bacteria for detection of arsenic in drinking water. Procedia Chem. **1**(1), 1003–1006 (2009)
67. R.M. Bukowski, R. Ciriminna, M. Pagliaro, F.V. Bright, High-performance quenchometric oxygen sensors based on fluorinated xerogels doped with $[Ru(dpp)_3]^{2+}$. Anal. Chem. **77**, 2670–2672 (2005)
68. S.M. Grist, L. Chrostowski, K.C. Cheung, Optical oxygen sensors for applications in microfluidic cell culture. Sensors **10**, 9286–9316 (2010)
69. J. Biwersi, B. Tulk, A.S. Verkman, Long-wavelength chloride-sensitive fluorescent indicators. Anal. Biochem. **219**, 139–143 (1994)
70. O.S. Wolfbeis, A. Sharma, Fibre-optic fluorosensor for sulphur dioxide. Anal. Chim. Acta **208**, 53–58 (1988)
71. G.M. Omann, J.R. Lakowicz, Interactions of chlorinated hydrocarbon insecticides with membranes. Biochem. Biophys. Acta **648**, 83–95 (1982)
72. G.N.M. van der Krogt, J. Ogink, B. Ponsioen, K. Jalink, A comparison of donor-acceptor pairs for genetically encoded FRET sensors: application to the Epac cAMP sensor as an example. PLoS one **3** (2008). doi:10.1371/journal.pone.0001916
73. P. Buet, B. Gersch, E. Grell, Spectral properties, cation selectivity and dynamic efficiency of fluorescent alkali ion indicators in aqueous solution around neutral pH. J. Fluoresc. **11**, 79–87 (2001)
74. T. Thestrup, J. Litzlbauer, I. Bartholomäus, M. Mues, L. Russo, H. Dana, Y. Kovalchuk, Y. Liang, G. Kalamakis, Y. Laukat, S. Becker, G. Witte, A. Geiger, T. Allen, L.C. Rome, T.-W. Chen, D.S. Kim, O. Garaschuk, C. Griesinger, O. Griesbeck, Optimized ratiometric calcium sensors for functional in vivo imaging of neurons and T lymphocytes. Nat. Methods **11**, 175–182 (2014)
75. I.D. Johnson, M.T.Z. Spence (eds.), in *The Molecular Probes Handbook. A Guide to Fluorescent Probes and Labeling Technologies*, 11th edn. (Life Technologies Corporation, 2010)
76. K.P. Carter, A.M. Young, A.E. Palmer, Fluorescent sensors for measuring metal ions in living systems. Chem. Rev. **114**(8), 4564–4601 (2014)
77. Z. Xu, J. Yoon, D.R. Spring, Fluorescent chemosensors for Zn^{2+}. Chem. Soc. Rev. **39**, 1996–2006 (2010)

78. E. Eltzov, R.S. Marks, Fiber-optic based cell sensors. in *Whole Cell Sensing Systems I*, ed. by S. Belkin, M.B. Gu (Springer, Berlin, 2010), pp. 131–154
79. A.F. Collings, F. Caruso, Biosensors: recent advances. Rep. Prog. Phys. **60**(11), 1397 (1997)
80. M. Pagliaro, *Silica-Based Materials for Advanced Chemical Applications, Chapter 6* (RSC Publishing, Cambridge, 2009)
81. A. Pannier, U. Soltmann, Potential applications of sol-gel immobilized microorganisms for bioremediation systems and biosensors. in *Advances in Materials Science Research*, vol. 12. Ed. by M.C. Wythers (Nova Science Publishers, New York, 2012)
82. B. Rudolph, K. Weber, R. Möller, Biochips as novel bioassays. in *Handbook of Biophotonics,* vol. 2, ed. by J. Popp, V.V. Tuchin, A. Chiou, S.H. Heinemann (Wiley-VCH, New York, 2012)
83. J.C. Venter, M.D. Adams, E.W. Myers, P.W. Li, R.J. Mural, G.G. Sutton, H.O. Smith, M. Yandell, C.A. Evans, R.A. Holt, The sequence of the human genome. Science **291**, 1304–1351 (2001)
84. T. Gustavsson, R. Improta, D. Markovitsi, DNA: building blocks of life under UV irradiation. J. Phys. Chem. Lett. **1**, 2025–2030 (2010)
85. F. Erfurth, A. Tretyakov, B. Nyuyki, G. Mrotzek, W.-D. Schmidt, D. Fassler, H.P. Saluz, Two-laser, large-field hyperspectral microarray scanner for the analysis of multicolor microarrays. Anal. Chem. **80**, 7706–7713 (2008)
86. M.A. Coleman, V.H. Lao, B.W. Segelke, P.T. Beernink, High-throughput, fluorescence-based screening for soluble protein expression. J. Proteome Res. **3**, 1024–1032 (2004)
87. S. Kreusch, S. Schwedler, B. Tautkus, G.A. Cumme, A. Horn, UV measurements in microplates suitable for high-throughput protein determination. Anal. Biochem. **313**, 208–215 (2003)
88. J. Hallbauer, S. Kreusch, A. Klemm, G. Wolf, H. Rhode, Long-term serum proteomes are quite similar under high-and low-flux hemodialysis treatment. Proteomics Clin. Appl. **4**, 953–961 (2010)
89. P. Schulze, M. Ludwig, F. Kohler, D. Belder, Deep UV laser-induced fluorescence detection of unlabeled drugs and proteins in microchip electrophoresis. Anal. Chem. **77**(5), 1325–1329 (2005)
90. H. Szmacinski, K. Ray, J.R. Lakowicz, Metal-enhanced fluorescence of tryptophan residues in proteins: application toward label-free bioassays. Anal. Biochem. **385**(2), 358–364 (2009)
91. M. Schäferling, The art of fluorescence imaging with chemical sensors. Angew. Chem. Int. Ed. **51**, 3532–3554 (2012)
92. J.T. Wessels, U. Pliquett, F.S. Wouters, Light-emitting diodes in modern microscopy—From David to Goliath? Cytometry Part A **81**, 188–197 (2012)
93. B. Hermann, *Fluorescence Microscopy*, 2nd edn. (Bios Scientific Publishers, Oxford, 1998)
94. H.R. Petty, Fluorescence microscopy: established and emerging methods, experimental strategies and applications in immunology. Microsc. Res. Tech. **70**, 687–709 (2007)
95. H. Kobayashi, M. Ogawa, R. Alford, P.L. Choyke, Y. Urano, New strategies for fluorescent probe design in medical diagnostic imaging. Chem. Rev. **110**, 2620–2640 (2009)
96. F. Jamme, S. Kascakova, S. Villette, F. Allouche, S. Pallu, V. Rouam, M. Réfrégiers, Deep UV autofluorescence microscopy for cell biology and tissue histology. Biol. Cell **105**, 277–288 (2013)
97. E. Silk, LED fluorescence microscopy in theory and practice. The Microscope **50**(2/3), 101–118 (2002)
98. L.W. Reza, S. Satyanarayna, D.A. Enarson, A.W.V. Kumar, K. Sagili, S. Kumar, L.A. Prabhakar, N.M. Devendrappa, A. Pandey, N. Wilson, S. Chadha, B. Thapa, K.S. Sachdeva, M.P. Kohli, LED-fluorescence microscopy for diagnosis of pulmonary tuberculosis under programmatic conditions in India. PLoS ONE **8**(10), e75566 (2013). doi:10.1371/journal.pone.0075566

99. M. Schüttpelz, C. Müller, H. Neuweiler, M. Sauer, UV fluorescence lifetime imaging microscopy: a label-free method for detection and quantification of protein interactions. Anal. Chem. **78**, 663–669 (2006)
100. M. Minsky, Microscopy Apparatus US 3013467 A (1957)
101. J.M. Levsky, R.H. Singer, Fluorescence in situ hybridization: past, present and future. J. Cell Sci. **116**, 2833–2838 (2003)
102. J. Bayani, J.A. Squire, Advances in the detection of chromosomal aberrations using spectral karyotyping. Clin. Genet. **59**, 65–73 (2001)
103. T. Liehr, A. Weise, A.B. Hamid, X. Fan, E. Klein, N. Aust, M.A.K. Othman, K. Mrasek, N. Kosyakova, Multicolor FISH methods in current clinical diagnostics. Expert Rev. Mol. Diagn. **13**, 251–255 (2013)
104. D. Jin, R. Connally, J. Piper, Practical time-gated luminescence flow cytometry II: experimental evaluation using UV LED excitation. Cytometry Part A **71**, 797–808 (2007)
105. A.A. Bhagat, S.S. Kuntaegowdanahalli, N. Kaval, C.J. Seliskar, I. Papautsky, Inertial microfluidics for sheath-less high-throughput flow cytometry. Biomed. Microdevices **12**, 187–195 (2010)
106. S. Köhler, S. Nagl, S. Fritzsche, D. Belder, Label-free real-time imaging in microchip free-flow electrophoresis applying high speed deep UV fluorescence scanning. Lab Chip **12** (3), 458–463 (2012)
107. H. Zhu, S. Mavandadi, A.F. Coskun, O. Yaglidere, A. Ozcan, Optofluidic fluorescent imaging cytometry on a cell phone. Anal. Chem. **83**(17), 6641–6647 (2011)
108. O. Lazcka, F. Campo, F.X. Munoz, Pathogen detection: a perspective of traditional methods and biosensors. Biosens. Bioelectron. **22**, 1205–1217 (2007)
109. V. Jasson, L. Jacxsens, P. Luning, A. Rajkovic, M. Uyttendaele, Alternative microbial methods: an overview and selection criteria. Food Microbiol. **27**, 710–730 (2010)
110. A.P. Kilungo, N. Carlton-Carew, L.S. Powers, Continuous real-time detection of microbial contamination in water using intrinsic fluorescence. J. Biosens. Bioelectron. **12**, 3 (2013)
111. L.S. Powers, W.R. Ellis, C.R. Lloyd, Real-time In-situ detection of microbes. J. Biosens. Bioelectron. Spec. Iss. S11 (2012)
112. M.S. Ammor, Recent advances in the use of intrinsic fluorescence for bacterial identification and characterization. J. Fluoresc. **17**, 455–459 (2007)
113. H.D. Smith, A.G. Duncan, P.L. Neary, C.R. Lloyd, A.J. Anderson, R.C. Sims, C.P. McKay, In situ microbial detection in mojave desert soil using native fluorescence. Astrobiology **12**, 247–257 (2012)
114. H.-Y. Kim, C.R. Estes, A.G. Duncan, B.D. Wade, F.C. Cleary, C.R. Lloyd, W.R. Ellis Jr, L. S. Powers, Real-time detection of microbial contamination. Eng. Med. Biol. Mag. IEEE **23**, 122–129 (2004)
115. M. Fischer, M. Wahl, G. Friedrichs, Design and field application of a UV-LED based optical fiber biofilm sensor. Biosens. Bioelectron. **33**, 172–178 (2012)
116. L.R. Dartnell, T.A. Roberts, G. Moore, J.M. Ward, J-Pr Muller, Fluorescence characterization of clinically-important bacteria. PLoS ONE **8**, e75270 (2013)
117. R. Bhartia, E.C. Salas, W.F. Hug, R.D. Reid, A.L. Lane, K.J. Edwards, K.H. Nealson, Label-free bacterial imaging with deep-UV-laser-induced native fluorescence. Appl. Environ. Microbiol. **76**, 7231–7237 (2010)
118. W. Jun, M.S. Kim, B.-K. Cho, P.D. Millner, K. Chao, D.E. Chan, Microbial biofilm detection on food contact surfaces by macro-scale fluorescence imaging. J. Food Eng. **99**, 314–322 (2010)
119. M.S. Shur, R. Gaska, Deep-ultraviolet light-emitting diodes. IEEE Trans. Electron Devices **57**, 12–25 (2010)
120. M. Sohn, D.S. Himmelsbach, F.E. Barton, P.J. Fedorka-Cray, Fluorescence spectroscopy for rapid detection and classification of bacterial pathogens. Appl. Spectrosc. **63**, 1251–1255 (2009)

121. S. Ammor, K. Yaakoubi, I. Chevallier, E. Dufour, Identification by fluorescence spectroscopy of lactic acid bacteria isolated from a small-scale facility producing traditional dry sausages. J. Microbiol. Methods **59**, 271–281 (2004)
122. B. Tourkya, T. Boubellouta, E. Dufour, F. Leriche, Fluorescence spectroscopy as a promising tool for a polyphasic approach to pseudomonad taxonomy. Curr. Microbiol. **58**, 39–46 (2009)
123. H. Wang, J. Wang, J. Xu, R.-X. Cai, Study on the influence of potassium iodate on the metabolism of Escherichia coli by intrinsic fluorescence. Spectrochim. Acta Part A Mol. Biomol. Spectrosc. **64**, 316–320 (2006)
124. H.E. Giana, L. Silveira Jr, R.A. Zângaro, M.T.T. Pacheco, Rapid identification of bacterial species by fluorescence spectroscopy and classification through principal components analysis. J. of Fluoresc. **13**, 489–493 (2003)
125. V.R. Després, J.A. Huffman, S.M. Burrows, C. Hoose, A.S. Safatov, G. Buryak, J. Fröhlich-Nowoisky, W. Elbert, M.O. Andreae, U. Pöschl, R. Jaenicke, Primary biological aerosol particles in the atmosphere: a review. Tellus B **64** (2012)
126. K.M. Davitt, Ultraviolet Light Emitting Diodes and Bio-aerosol Sensing, PhD thesis, Brown University (2006)
127. A. Manninen, M. Putkiranta, J. Saarela, A. Rostedt, T. Sorvajärvi, J. Toivonen, M. Marjamäki, J. Keskinen, R. Hernberg, Fluorescence cross sections of bioaerosols and suspended biological agents. Appl. Opt. **48**, 4320–4328 (2009)
128. J. Popp, V.V. Tuchin, A. Chiou, S.H. Heinemann (eds.), *Handbook of Biophotonics*, Vol. 2, 1st edn. (Wiley-VCH, New York, 2012)
129. D.C.G. De Veld, M.J.H. Witjes, H.J.C.M. Sterenborg, J.L.N. Roodenburg, The status of in vivo autofluorescence spectroscopy and imaging for oral oncology. Oral Oncol. **41**, 117–131 (2005)
130. C. Arens, D. Reussner, H. Neubacher, J. Woenckhaus, H. Glanz, Spectrometric measurement in laryngeal cancer. Eur. Arch. Otorhinolaryngol. **263**, 1001–1007 (2006)
131. V.R. Jacobs, S. Paepke, H. Schaaf, B.-C. Weber, M. Kiechle-Bahat, Autofluorescence ductoscopy: a new imaging technique for intraductal breast endoscopy. Clin. Breast Cancer **7**, 619–623 (2007)
132. B. Mayinger, P. Horner, M. Jordan, C. Gerlach, T. Horbach, W. Hohenberger, E.G. Hahn, Endoscopic fluorescence spectroscopy in the upper GI tract for the detection of GI cancer: initial experience. Am. J. Gastroenterol. **96**, 2616–2621 (2001)
133. B. Mayinger, M. Jordan, P. Horner, C. Gerlach, S. Muehldorfer, B.R. Bittorf, K.E. Matzel, W. Hohenberger, E.G. Hahn, K. Guenther, Endoscopic light-induced autofluorescence spectroscopy for the diagnosis of colorectal cancer and adenoma. J. Photochem. Photobiol. B, Biol. **70**, 13–20 (2003)
134. N.M. Broer, T. Liesenhoff, H.-H. Horch, Laser induced fluorescence spectroscopy for real-time tissue differentiation. Med. Laser Appl. **19**, 45–53 (2004)
135. J. Hegyi, V. Hegyi, T. Ruzicka, P. Arenberger, C. Berking, New developments in fluorescence diagnostics. J. Dtsch. Dermatol. Ges. **9**, 368–372 (2011)
136. J. Margarot, P. Devèze, Aspect de quelques dermatoses en lumière ultraparaviolette. Note prèliminaire. Bull. Soc. Sci. Med. Biol. Montpellier **6**, 375–378 (1925)
137. P. Asawanonda, C.R. Taylor, Wood's light in dermatology. Int. J. Dermatol. **38**, 801–807 (1999)
138. M. Burroni, R. Corona, G. Dell'Eva, F. Sera, R. Bono, P. Puddu, R. Perotti, F. Nobile, L. Andreassi, P. Rubegni, Melanoma computer-aided diagnosis: reliability and feasibility study. Clin. Cancer Res. **10**, 1881–1886 (2004)
139. M. Burroni, U. Wollina, R. Torricelli, S. Gilardi, G. Dell'Eva, C. Helm, W. Bardey, N. Nami, F. Nobile, M. Ceccarini, A. Pomponi, B. Alessandro, P. Rubegni, Impact of digital dermoscopy analysis on the decision to follow up or to excise a pigmented skin lesion: a multicentre study. Skin Res. Technol. **17**, 451–460 (2011)
140. E.G. Borisova, L.P. Angelova, E.P. Pavlova, Endogenous and exogenous fluorescence skin cancer diagnostics for clinical applications. IEEE J. Sel. Top. Quantum Electron. **20** (2014)

141. E. Borisova, P. Pavlova, E. Pavlova, P. Troyanova, L. Avramov, Optical biopsy of human skin—a tool for cutaneous tumours' diagnosis. Int. J. Bioautomation **16**, 53–72 (2012)
142. R. Na, Skin Autofluorescence in Demarcation of Basal Cell Carcinoma. Ph.D Thesis, Department of Dermatology, Copenhagen University (2001)
143. N. Kollias, G.N. Stamatas, Optical non-invasive approaches to diagnosis of skin diseases. J. Invest. Dermatol. Symp. Proc. **7**, 64–75 (2002)
144. M.J. Koehler, K. König, P. Elsner, R. Bückle, M. Kaatz, In vivo assessment of human skin aging by multiphoton laser scanning tomography. Opt. Lett. **31**, 2879–2881 (2006)
145. J.C. Zhang, H.E. Savage, P.G. Sacks, T. Delohery, R.R. Alfano, A. Katz, S.P. Schantz, Innate cellular fluorescence reflects alterations in cellular proliferation. Lasers Surg. Med. **20**, 319–331 (1997)
146. N. Kollias, R. Gillies, R. Anderson, Fluorescence spectra of human skin-preliminary-report. J. Invest. Dermatol. **100**, 530 (1993)
147. R. Bissonnette, H. Zeng, D.I. McLean, W.E. Schreiber, D.L. Roscoe, H. Lui, Psoriatic plaques exhibit red autofluorescence that is due to protoporphyrin IX. J. Invest. Dermatol. **111**, 586–591 (1998)
148. N. Kollias, R. Gillies, M. Moran, I.E. Kochevar, R.R. Anderson, Endogenous skin fluorescence includes bands that may serve as quantitative markers of aging and photoaging. J. Invest. Dermatol. **111**, 776–780 (1998)
149. R.E. de Araujo, D.J. Rativa, M.A. Rodrigues, A. Marsden, L.G. Souza Filho, Optical spectroscopy on fungal diagnosis. in *New Developments in Biomedical Engineering*, ed. by D. Campolo (InTech, Rijeka, 2010)
150. E. Drakaki, T. Vergou, C. Dessinioti, A.J. Stratigos, C. Salavastru, C. Antoniou, Spectroscopic methods for the photodiagnosis of nonmelanoma skin cancer. J. Biomed. Opt. **18**, 061221 (2013)
151. H. Zeng, D.I. McLean, C.E. MacAulay, B. Palcic, H. Lui, Autofluorescence of basal cell carcinoma. Proc. SPIE **3245**, 314–317 (1998)
152. W. Lohmann, E. Paul, In situ detection of melanomas by fluorescence measurements. Naturwissenschaften **75**, 201–202 (1988)
153. R. Na, I.-M. Stender, H.C. Wulf, Can autofluorescence demarcate basal cell carcinoma from normal skin? A comparison with protoporphyrin IX fluorescence. Acta Derm. Venereol. **81**, 246–249 (2001)
154. M. Panjehpour, C.E. Julius, M.N. Phan, T. Vo-Dinh, S. Overholt, Laser-induced fluorescence spectroscopy for in vivo diagnosis of non-melanoma skin cancers. Lasers Surg. Med. **31**, 367–373 (2002)
155. I. Georgakoudi, B.C. Jacobson, M.G. Müller, E.E. Sheets, K. Badizadegan, D.L. Carr-Locke, C.P. Crum, C.W. Boone, R.R. Dasari, J. Van Dam, M.S. Feld, NAD(P)H and collagen as in vivo quantitative fluorescent biomarkers of epithelial precancerous changes. Cancer Res. **62**, 682–687 (2002)
156. L. Brancaleon, A.J. Durkin, J.H. Tu, G. Menaker, J.D. Fallon, N. Kollias, In vivo fluorescence spectroscopy of nonmelanoma skin cancer. Photochem. Photobiol. **73**, 178–183 (2001)
157. J. de Leeuw, N. van der Beek, W.D. Neugebauer, P. Bjerring, H.A. Neumann, Fluorescence detection and diagnosis of non-melanoma skin cancer at an early stage. Lasers Surg. Med. **41**, 96–103 (2009)
158. H. Zeng, H. Lui, D.I. McLean, C.E. MacAulay, B. Palcic, Update on fluorescence spectroscopy studies of diseased skin. Proc. SPIE **2671**(1996), 196–198 (1996)
159. K.M. Katika, L. Pilon, Steady-state directional diffuse reflectance and fluorescence of human skin. Appl. Opt. **45**, 4174–4183 (2006)
160. E. Drakaki, E. Kaselouris, M. Makropoulou, A.A. Serafetinides, A. Tsenga, A.J. Stratigos, A. D. Katsambas, C. Antoniou, Laser-induced fluorescence and reflectance spectroscopy for the discrimination of basal cell carcinoma from the surrounding normal skin tissue. Skin Pharmacol Physiol **22**, 158–165 (2009)

161. E. Borisova, P. Troyanova, P. Pavlova, L. Avramov, Diagnostics of pigmented skin tumors based on laser-induced autofluorescence and diffuse reflectance spectroscopy. Quantum Electron. **38**, 597 (2008)
162. U. Wollina, C. Nelskamp, A. Scheibe, D. Faßler, W.-D. Schmidt, Fluorescence-remission sensoring of skin tumours: preliminary results. Skin Res. Technol. **13**, 463–471 (2007)
163. T. Savelieva, A. Ryabova, I. Andreeva, N. Kalyagina, V. Konov, V. Loschenov, Combined spectroscopic method for determining the fluorophore concentration in highly scattered media. Bull. Lebedev Phys. Inst. **38**, 334–338 (2011)
164. E. Carstea, L. Chervase, G. Pavelescu, D. Savastru, A. Forsea, E. Borisova, Combined optical techniques for skin lesion diagnosis: short communication. Optoelectron. Adv. Mater. RapidCommun. **4**, 1960–1963 (2010)
165. L.H. Laiho, S. Pelet, T.M. Hancewicz, P.D. Kaplan, P.T. So, Two-photon 3-D mapping of ex vivo human skin endogenous fluorescence species based on fluorescence emission spectra. J. Biomed. Opt. **10**, 024016
166. G. Deka, W.W. Wu, F.J. Kao, In vivo wound healing diagnosis with second harmonic and fluorescence lifetime imaging. J. Biomed. Opt. **18**, 061222 (2013)
167. M.C. Skala, K.M. Riching, D.K. Bird, A. Gendron-Fitzpatrick, J. Eickhoff, K.W. Eliceiri, P. J. Keely, N. Ramanujam, In vivo multiphoton fluorescence lifetime imaging of protein-bound and free nicotinamide adenine dinucleotide in normal and precancerous epithelia. J. Biomed. Opt. **12**, 024014 (2007)

Chapter 14
UV-B Elicitation of Secondary Plant Metabolites

Monika Schreiner, Inga Mewis, Susanne Neugart, Rita Zrenner, Johannes Glaab, Melanie Wiesner and Marcel A.K. Jansen

Abstract Epidemiological studies have revealed an inverse association between a high consumption of vegetables and a lower risk of both cancer and cardiovascular diseases. This protective effect is mostly due to secondary plant metabolites present in plant tissues. In this context, it has become increasingly clear during the last decade that UV-B radiation is an important regulator of plant secondary metabolism. Recent studies have highlighted the regulatory properties of low, ecologically relevant UV-B levels contrary to previous studies in which UV-B radiation was exclusively regarded as a stress factor. Low-dosage UV-B applications trigger distinct changes in the plant's secondary metabolism resulting in an accumulation of phenolic compounds such as flavonoids and glucosinolates.

Plants are sessile organisms, and consequently cannot avoid exposure to more or less unfavorable environmental conditions [1]. In this context secondary plant metabolites perform fundamental, protective functions within the plant–environment interaction. In addition to the ecophysiological relevance of these compounds, evidence was found that certain secondary plant metabolites possess human health-promoting effects when consumed regularly in fruits and vegetables [2].

M. Schreiner (✉) · I. Mewis · S. Neugart · R. Zrenner · M. Wiesner
Department Plant Quality, Leibniz-Institute of Vegetable and Ornamental Crops Großbeeren and Erfurt e. V., Theodor-Echtermeyer-Weg 1, 14979 Großbeeren, Germany
e-mail: schreiner@igzev.de

J. Glaab
Ferdinand-Braun-Institut, Leibniz-Institut für Höchstfrequenztechnik, Gustav-Kirchhoff-Straße 4, 12489 Berlin, Germany

M.A.K. Jansen
School of Biological, Environmental and Earth Sciences, University College Cork, Distillery Field, Cork, Ireland

© Springer International Publishing Switzerland 2016

M. Kneissl and J. Rass (eds.), *III-Nitride Ultraviolet Emitters*,
Springer Series in Materials Science 227, DOI 10.1007/978-3-319-24100-5_14

14.1 Nature and Occurrence of Secondary Plant Metabolites

Secondary plant metabolites are grouped according to their chemical structure and physiological function in carotenoids, phenolic compounds, glucosinolates, saponins, sulfides, phytosterols, phytoestrogens, monoterpenes, and protease inhibitors [3].

Secondary plant metabolites, such as polyphenols and carotenoids, are present in a wide range of fruit and vegetable crops, while other secondary plant metabolites are distributed only among few taxonomic groups. For example, glucosinolates are only found in species in the order Brassicales, and the occurrence of sulfides is restricted to the family Liliaceae. Also with each class of secondary plant metabolites, each fruit and vegetable species has a distinct profile of specific secondary plant metabolites. Most of the secondary plant metabolites are present in every plant organ; however, the concentration and composition of the secondary plant metabolites can vary greatly [4, 5].

Secondary plant metabolites mediate the interaction of plants with their environment functioning as feeding deterrents, pollination attractants, and protective compounds against pathogens or various abiotic stresses, antioxidants, or signaling molecules. A fundamental component of this plant–environment interaction is the formation of UV absorbing and photoprotective secondary plant metabolites such as phenolic compounds and carotenoids in response to UV-B radiation exposure [6–8]. In contrast to previous studies in which UV-B radiation was exclusively seen as a stress factor, recent studies have highlighted the regulatory properties of low, ecologically relevant UV-B levels that trigger distinct changes in the plant's secondary metabolism. This results in the accumulation of a broad range of secondary plant metabolites, including antioxidants such as ascorbate, glutathione and tocopherol, isoprenoids, including indole alkaloids and indole amines, as well as complex secondary plant metabolite mixtures such as essential oils, but also phenolic compounds, carotenoids, and glucosinolates [1, 8–13].

Munné-Bosch [14] has referred to a broad, integrated network of interdependent and interplaying compounds, thus predicting that flavonoid accumulation will affect accumulation of further secondary metabolites. Kusano et al. [15] reported comprehensive reprogramming of primary and secondary metabolism in UV-B exposed *Arabidopsis*. Alternatively, biosynthesis pathways may be competing for resources, including shared precursors. Notwithstanding such uncertainties, some trends start to emerge. Polyamines and tocopherols levels are quickly (< 24 h) upregulated in response to UV-B, and it has been hypothesized that these compounds constitute the plants "rapid response" to conditions of eustress [16]. Kusano et al. [15] similarly hypothesized a rapid response role for ascorbate and tocopherol. In contrast, many flavonoids accumulate at a much slower pace, steady state levels typically are reached after several days [15–17]. Glucosinolates also accumulate relatively late during the acclimation process [15]. Previously, it was argued that the metabolite profile of stress exposed plants first displays a transient acclimation phase, followed by a new steady state [18]. Kusano et al. [15] showed an initial (24 h) UV-B

mediated change in primary metabolites, followed by more complex reprogramming of secondary metabolite profiles measured after 96 h. It was argued that during the early stages of UV-B exposure, plants are "primed" by partitioning of carbon toward aromatic amino acid precursors of the phenylpropanoid pathway [15]. Thus, UV-B exposure triggers substantial reprogramming of primary metabolism, accumulation of "rapid response" metabolites, later followed by extensive accumulation of secondary plant metabolites. Clearly, UV-B acclimation is a dynamic process, resulting in a continuum of eustress acclimation states, each with its own specific pattern of secondary metabolites. The question then arises whether the aim is to create foods high in "rapid response" metabolites (ascorbate, polyamines, tocopherols), high in flavonoids, or both. All named secondary plant metabolites are important dietary components of human nutrition, but these compounds may not necessarily occur simultaneously in high concentrations in the plant. For example, polyamines accumulate transiently in UV-B exposed plants [16], and levels have returned to pre-UV-B exposure contents at the time that flavonoids have accumulated in appreciable amounts. More information is needed about the kinetics of UV-B mediated changes in plant secondary metabolite profile, and potential cross talk between biosynthetic routes.

Of course, the UV-B induced accumulation of certain secondary plant metabolites is strongly influenced by the duration of UV-B exposure and UV-B doses [1, 19]. But it also depends on the physiological age of the plant [20] and the morphological structure of the plant organ [12]. In addition, genotypic variations between species, origins, and cultivars occur [1, 19]. Moreover, all these plant-based variables are interacting—beside UV-B radiation—also with other environmental factors such as water and nutrient supply, atmospheric CO_2 concentration, temperature, and solar radiation [21–25]. Thus, the application of UV-B radiation to improve the concentrations and composition of secondary plant metabolites requires precise manipulation. Ultimately, the knowledge of how to do this may form the basis of "recipes" that will enable the grower to precisely manipulate crops in order to maximize the content of nutritionally desirable secondary plant metabolites.

14.2 Nutritional Physiology of Secondary Plant Metabolites

The major classes of secondary plant metabolites with disease-preventing functions are antioxidants, blood pressure, or blood sugar influencing substances, or agents with anticarcinogenic, immunity-supporting, antibacterial, antifungal, antiviral, cholesterol-lowering, antithrombotic, or anti-inflammatory effects [26]. Each class of these functional compounds consists of a wide range of chemicals with differing potency. For example, secondary plant metabolites with antioxidant characteristics are carotenoids, phenolic compounds, protease inhibitors, sulfides, and phytoestrogens [27–29]. Some of these secondary plant metabolites are characterized by a broad

spectrum of health-promoting functions, e.g., phenolic compounds and sulfides [30, 31], whereas other secondary plant metabolites are marked by specific functionality such as the breakdown products of particular glucosinolates with pronounced anticarcinogenic properties due to the induction of phase II detoxification enzymes and antitumorigenic attributes. The latter causes cell cycle arrest and apoptosis of cancer cells [32, 33]. But, a certain balance between distinct secondary metabolites in the plant seems to be necessary. So, a partial enhancement of only one single secondary plant metabolite could lead to protective or adverse effects on the consumer's health. As example, an enrichment of 4-methylsulfinylbutyl glucosinolate in broccoli caused a reduction of blood pressure and influenced the positive cholesterol level in humans [34]. In contrast, the hydrolyzed product of the same glucosinolate (sulforaphane) can inhibit dose- and time-dependent early stage of nucleotide excision repair, one of the most important DNA repair pathways [35]. Another example is that the enrichment of 1-methoxyindol-3-ylmethylglucosinolate in pak choi (*Brassica rapa* ssp. *chinensis*) have shown mutagenic effects in wild-type and human sulfotransferase expressing *S. typhimurium* strains [36].

14.3 Association Between Fruit and Vegetable Consumption and Chronic Diseases

Fresh vegetables and fruits are naturally rich in secondary plant metabolites. Numerous epidemiological studies have already documented an inverse association between fruit and vegetable consumption and lower incidence and mortality rate of various chronic diseases [37]. Ingestion of a range of berry fruits [38] and in particular of cranberry juice [39] is known for cardioprotective effects and cholesterol-lowering influence, respectively.

Verkerk et al. [40] reviewed the *Brassica* vegetables containing glucosinolates with regard to their health benefits, especially anticarcinogenic properties. Data of current meta-analyses by Wu et al. [41–43] revealed *Brassica* mediated reduction in lung, gastric, and colorectal cancer. Furthermore, it is assumed that a diet rich in brassicaceous vegetables effectively retunes the human metabolism by rebalancing anaplerosis and cataplerosis and restoring metabolic homeostasis [44], and therefore, is able to attenuate chronic diseases connected with oxidative stress, hypertension, and inflammation in the cardiovascular system [45].

Epidemiological studies also revealed distinct associations between cancer risk and other vegetable families or categories. For example, a high consumption of tomatoes or tomato-based products—rich in carotenoids, especially lycopene and ß-carotene—is consistently associated with a lower risk of different cancer types, e.g., prostate cancer, as shown by a meta-analysis [46]. Furthermore, legumes seem to play a key role in human diet in preventing cardiovascular disease. Legume consumption was significantly and inversely associated with cardiovascular disease

and lowered the relative risk by about 11 % [47]. In addition, the Mediterranean diet, a dietary pattern that encourages among others the daily consumption of fruits and vegetables, already has shown a reduced risk of metabolic syndrome [48] as well as cardio and cancer protective effects [49, 50]. In contrast, supplementation with synthetic secondary metabolites could lead to different results. One striking example: ingestion of ß-carotene supplements by heavy smokers has been associated with increased lung cancer incidence as demonstrated in the α-Tocopherol, ß-Carotene (ATBC) cancer prevention study [51], and in the ß-Carotene Retinol Efficiency Trial (CARET) [52].

14.4 Secondary Plant Metabolites Within the Plant–Environment Interaction

14.4.1 UV-B Perception and Signaling in the Plant

Plants are able to specifically perceive and react to UV-B radiation (Fig. 14.1). This plant response can be measured on various levels, e.g., as characteristic alterations of gene expression pattern [53, 54], specific changes in morphology and physiology [55, 56], or particularly, the accumulation of certain plant secondary metabolites

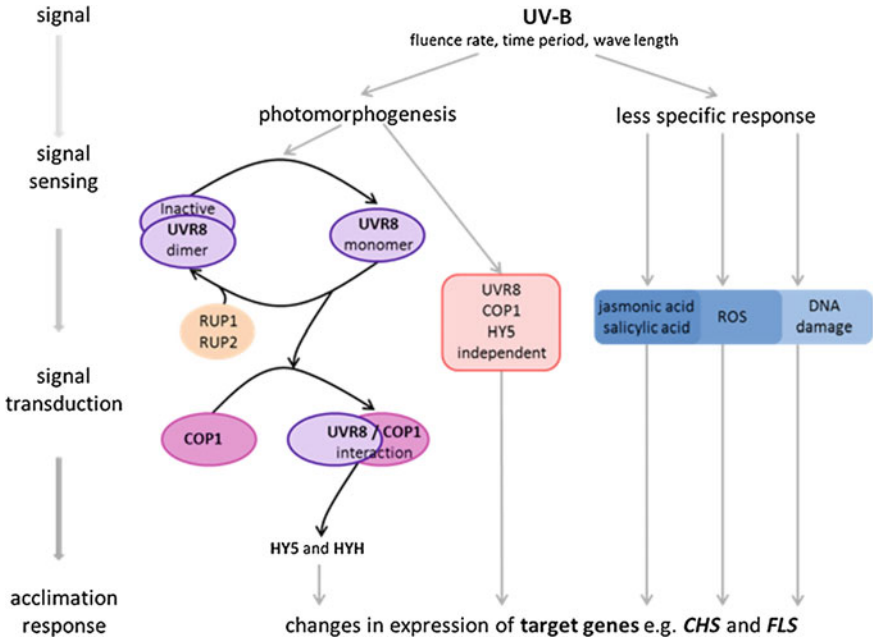


Fig. 14.1 Scheme of UV-B perception and signaling in *Arabidopsis* plants

[1, 8, 11, 12, 19]. The existence of a specific photoreceptor for detection of UV-B radiation was already proposed several decades ago [57]. However, in the last few years substantial progress has been made with identification of the UV-B-specific photoreceptor UV RESPONSE LOCUS 8 (UVR8) [58, 59] and various components involved in the downstream signaling pathway [60, 61]. The UVR8 photoreceptor exists as a homodimer in the cytosol that rapidly monomerizes upon UV-B absorption mediated by conserved tryptophan residues which act as UV-B chromophores [62, 63]. The UV-B-induced monomer of the receptor UVR8 then directly interacts with the multifunctional E3 ubiquitin ligase CONSTITUTIVELY PHOTOMORPHOGENIC 1 (COP1) [64] thus initiating the molecular signaling pathway that transduces gene expression changes. In order to accomplish this, rapid translocation from the cytosol into the nucleus is needed, which is already induced at low levels of UV-B [61, 65]. In the nucleus, UVR8 together with COP1 associates with the chromatin regions of several UV-B activated genes [66]. Presence of the E3 ubiquitin ligase COP1 alone represses photomorphogenesis by promoting degradation of HY5 (ELONGATED HYPOCOTYL 5) and other promotive transcription factors. However, under UV-B radiation and subsequent interaction of UVR8 monomers with COP1, the bZIP transcription factor HY5 is prevented from COP1-mediated degradation and stabilized [64]. In turn, HY5 and HYH (HY5 HOMOLOG) control expression of a range of key elements involved in the UV-B acclimation response and important for UV protection, including genes encoding enzymes of the phenylpropanoid pathway like CHS (CHALCONE SYNTHASE) and FLS (FLAVONOL SYNTHASE) [67, 68]. In addition, also the RUP1 and RUP2 proteins (REPRESSOR OF UV-B PHOTOMORPHOGENESIS 1 and 2) are induced. These WD40-repeat proteins constitute negative feedback on UVR8 activity involving direct protein–protein interaction, thus enabling inactivation and reversion to the ground state of UVR8 by redimerization [69, 70].

While UVR8 responds specifically to exposure with UV-B radiation, HY5, HYH, and COP1 are involved in multiple photomorphogenic signaling cascades and integrate the responses to UV-B with responses to red light exposure, or light–dark transitions. Currently, the UVR8-COP1-HY5 pathway is the most extensively analyzed UV-signaling pathway. In addition, the existence of a further UVR8 independent pathway has been proposed [61, 71]. Similar to the UVR8-COP1-HY5 pathway, this UVR8 independent pathway is thought to operate under low UV-B fluence rates, and exerts additional control on expression of genes involved in flavonoid biosynthesis [61].

At high UV-B fluence rates, UV-B specific signaling pathways are accompanied by less specific damage repair response pathways. High UV-B levels have been extensively demonstrated to cause damage to macromolecules, like DNA and proteins, resulting in impaired DNA replication, compromised transcriptional processes, and impaired photosynthesis [72, 73]. These detrimental reactions are, at least partially, mediated by reactive oxygen species (ROS) [74] which as such are also important signaling molecules. The cellular damage triggers transcriptional responses involving signaling molecules such as ROS and wound or defense-related factors including jasmonic acid, salicylic acid, and ethylene, which are all known to

control expression of specific genes [61, 75, 76]. These responses to high UV-B fluence rates are less stressor-specific [77], and control expression of a particularly broad set of genes associated with defense, wound response, or general stress related genes.

The existence of at least two UV-B specific signaling pathways, each contributing to the control of secondary plant metabolism such as carotenoid, flavonoid, or glucosinolate biosynthesis [6, 8, 53] together with nonspecific UV-B stress responses, is likely to result in a response network that displays a highly specific dose response and wavelength dependence. This emerges from gene expression studies where the dependency of specific expression profiles on the fluence rate [75] and on specific UV-B wavelength [54] has been demonstrated. Thus, the UV-B perception and signaling system might be responsive to even small changes in the solar spectrum [61], and this is an important consideration when investigating UV-B-induced changes in plant metabolite profiles.

14.4.2 UV-B as Stressor and Plant Regulator

Plants exposed to stress display stressor-specific changes in gene expression and protein production. Some of these changes in the transcriptome and proteome will be amplified at the level of the metabolome, making changes in metabolite accumulation amongst the most pronounced responses of plants to stress [78, 79]. Yet, our knowledge and understanding of metabolic changes in stress exposed plants remain fragmented [18], with many studies investigating the response of just one class of metabolites under one particular stress condition. New powerful developments in experimental design, sampling, extraction, metabolite fingerprinting and profiling, and identification are, however, increasingly generating a more comprehensive overview of stress-induced changes in small, secondary metabolites [78]. Generated data sets do not just contribute to the understanding of plant stress responses, but also highlight opportunities to improve the content of nutritionally and pharmaceutically important metabolites in plants.

The dose is critical, and for most stressors a distinction should be made between mild eustress conditions, under which metabolism is reversibly adjusted and the plant is acclimated to its new environment, and more severe distress, which is associated with irreversible macroscopic damage [80–82]. Eustress-associated changes in metabolite accumulation are often interpreted in the context of a physiological benefit for the plant, i.e., a functional role in acclimation to the new environmental conditions. Examples include the accumulation of compatible solutes, antioxidants, and antifreeze compounds [18]. However, it should be recognized that such changes in the plant metabolome may potentially also impact on the wider ecosystem, for example, on trophic interactions [53]. In fact, there is substantial interest in environmentally induced compositional changes in the plant metabolome with a view to increase the nutritional quality and/or pharmaceutical value of plant produce for human consumers [1, 19].

Theoretically, a very broad range of environmental parameters, some of which are stressors, can be exploited to increase the content of nutritionally beneficial plant metabolites. However, in practice only a few stressors are suitable for use in a commercial horticultural setting, where the aim is to raise produce with increased levels of specific secondary plant metabolites. A prime consideration is the ease of application, and especially the control of the dose. The accurate control of the dose is vital, in order to induce eustress conditions, but not distress. Distress, potentially leading to reduced biomass yields and/or blemished produce would lead to a loss of value. Another consideration is that no residue of the stressor is left behind, which would impinge on suitability of the produce for human consumption. UV-B is a strong candidate stressor that can be (and is) used in commercial, horticultural settings. There are two distinct approaches to manipulate UV-B radiation. In essence, in UV-B exclusion studies, solar UV radiation is attenuated using wavelength-specific filters (e.g., cladding material in case of protected cropping), whereas in UV-B supplementation studies, plants are exposed to supplementary, artificial UV-B irradiation generated by UV-B lamps [83]. In the case of supplemental UV-B, the UV-B dose can be easily and accurately controlled by wiring the UV tubes via a timer or appropriate dimmer, and treatments can be stopped whenever required and without leaving a residue. Indeed, another advantage of UV-B applications is that any "treatment" can be instantaneously terminated (i.e., compare with lasting impact chemical plant growth regulators once taken up by the plant). Current advances in the development of UV-transmitting cladding materials, but also UV-emitting LEDs are rapidly advancing opportunities for precision manipulation of UV spectra.

Low doses of UV-B have been demonstrated to cause altered gene expression [64, 68], and altered accumulation of secondary plant metabolites [1, 13, 19, 84], in the absence of distress. Macroscopic damage, accumulation of damaged DNA, and inactivation of the photosynthetic machinery indicate distress, but these are typically associated with high levels of UV-B and/or low levels of accompanying photosynthetically active radiation (PAR) [81]. A review of UV-B effects by the United Nations Environment Programme (2011) reported minimal effects of ambient UV-B on biomass accumulation [85]. Thus, UV-B is more a regulatory environmental parameter, than a stressor [86].

14.5 Structure-Differentiated Response to UV-B

Low levels of UV-B can cause distinct changes in the plant's secondary metabolism resulting in the accumulation of a broad range of secondary plant metabolites [1, 12, 13, 84]. Best documented is the UV-B mediated accumulation of flavonoids which have, *in planta*, both ROS scavenging and UV-screening activities [84]. UV-B radiation has frequently been observed to disproportionally increase accumulation of the more hydroxylated flavonoids, i.e., quercetin to kaempferol ratios increase [16, 84]. Flavonoids with multiple hydroxyl groups have particularly good

ROS scavenging activity [87], and for this reason quercetin and luteolin are considered better ROS scavengers than kaempferol and apigenin [84].

Another group of metabolites that has been studied extensively in the context of UV-B acclimation is the glucosinolates [19, 53]. These sulfur- and nitrogen-containing compounds have been found to be induced by UV-B exposure under both pre- and postharvest conditions in a range of plant species. Specific aliphatic or aromatic glucosinolates accumulate, depending on species, UV-B dose, and developmental stage, and accumulation is either constitutive or transient [19].

14.5.1 Flavonoids and Other Phenolics

Flavonoids of plants are divers and naturally occur as flavonoid glycosides. Based on aglycones they can be divided into six groups (flavanols, flavanones, flavones, flavonols, anthocyanidines, and isoflavonoids); more than 6,500 structures are known due to hydroxylation, glycosylation, acylation, or methoxylation [87–92]. Key flavonoid biosynthesis genes are regulated by UV-B [59] and flavonoids accumulate in a range of cellular compartments, including cell walls, vacuoles, chloroplasts, nucleus, and in trichomes [84]. Intracellular accumulation at sites of ROS production (e.g., chloroplast) highlights the important antioxidant properties of this class of metabolites [93]. Flavonoid compounds have received considerable attention because of the potential health-promoting properties of these compounds for human consumers. Nevertheless, it should be considered that some phenolic compounds also have undesirable properties such as, for example, methyl eugenol in sweet basil (*Ocimum basilicum*) which has both carcinogenic and teratogenic properties [94–97]. The message is that, notwithstanding our general knowledge about UV-mediated upregulation of flavonoid biosynthesis, there is a need to learn much more about the upregulation of specific flavonoid compounds. Indeed, not all flavonoid compounds are similarly induced. The effect of UV-B is modified by UV-B dose, the structure of the flavonoids and other phenolics, and further environmental factors such as PAR and temperature.

Response of flavonoids and other phenolics dependent on UV-B dose

Ambient and increased UV-B radiation, up to 24 kJ m^{-2} d^{-1}, is able to modify the flavonoid profile of different plant species. The biosynthesis of flavonoids and phenolics seems to be dependent on a threshold [98]. Strawberries (*Fragaria* × *ananassa*) grown under higher UV-B levels have higher concentrations of total phenolics, anthocyanins, and phenolic acids [99]. In Lollo Rosso lettuce (*Lactuca sativa* var. *crispa*) a strong negative correlation between UV-A and UV-B doses and the concentration of total phenolics and anthocyanins was demonstrated [100]. Increased concentrations of flavonoids and a higher antioxidant activity were found in Lollo Rosso lettuce grown under UV-transmitting polytunnels compared to greenhouse plants [101]. Often quercetin and *ortho*-dihydroxylated flavonoids are enhanced, while kaempferol and *ortho*-monohydroxylated flavonoids remain unaffected by UV-B or higher intensities of solar radiation [84, 102–105]. In the majority of studies

ambient doses of UV-B radiation lead to an enhanced quercetin to kaempferol ratio [103, 105–109] in *Arabidopsis thaliana*, annual vegetables and ornamentals. A dose-dependent reaction of C-flavonoids (such as vitexin or orientin) was shown in callus cultures of passion flower (*Passiflora quadrangularis*), where additional UV-B application with the lowest and the highest radiations led to a smaller increase than exposure to an intermediate dose of 25.3 kJ m^{-2} d^{-1} [110]. In contrast, in several studies the quercetin and kaempferol glycosides as well as naringenin glycosides were not enhanced by additional UV-B radiation in the mountain plants arnica (*Arnica montana*) and mountain birch (*Betula pubescens* ssp. *czerepanovii*) [21, 111], but the polyhydroxylated myricitin glycosides were increased in mountain birch [111]. Quercetin and its glycosides and kaempferol and most kaempferol glycosides were shown to be enhanced after additional UV-B radiation in broccoli (*Brassica oleracea* var. *italica*) and canola (*Brassica napus*) [112, 113]. Flavonols were shown to increase faster and to higher concentrations than the related anthocyanins in apples, and the antioxidant activity of the apple fruit was highly correlated to this increase [114, 115].

Phenolic acids are less affected by UV-B radiation. Neither Morales et al. [107] nor Antilla et al. [111] found an effect of less than ambient UV-B radiation on caffeoylquinic acid in silver birch (*Betula pendula*) and mountain birch. However, Tegelberg et al. [116] demonstrated an increase in caffeoylquinic acid in silver birch exposed to slightly above-ambient UV-B radiation. No influence of UV-B was found for other hydroxycinnamic acids when investigating effects of ambient or additional UV-B [103, 111, 116]. For example, in pak choi, malates of hydroxycinnamic acid were not enhanced by supplemental UV-B radiation at higher temperatures (22 °C) [117].

Moderate UV-B radiation, less than 5 kJ m^{-2} d^{-1} [118], is known to upregulate genes encoding enzymes of the phenylpropanoid pathway [61, 71]. The impact of moderate UV-B during cultivation is less investigated [19]. Only a few publications describe targeted low or moderate UV-B radiation treatments to increase the level of flavonoids in preharvest [107, 111, 119] and postharvest [12, 120] produce. Flavonols, anthocyanidines, and hydroxybenzoic acids increased in blackcurrant fruits (*Ribes nigrum*) exposed to three moderate, short-term UV-B doses, whereas the hydroxycinnamic acids increased only with the highest dose applied [120]. Furthermore, moderate UV-B as postharvest treatment increased the total phenolic concentration in inflorescences and seeds of nasturtium (*Tropaeolum majus*), but not in the leaves [12]. In kale exposed to single doses of moderate of UV-B radiation (less than 1 kJ m^{-2} d^{-1} UV-B_{BE} (biological effective UV-B_{BE} calculated with the generalized plant weighting function), investigated quercetin glycosides decreased under UV-B. In the case of kaempferol glycosides the amount of sugar moieties and the flavonol glycoside hydroxycinnamic acid residue influenced the response to UV-B [8]. For example, the monoacylated kaempferol tetraglucosides decreased with additional UV-B, whereas the monoacylated kaempferol diglucosides increased strongly with doses of 0.88 kJ m^{-2} d^{-1} UV-B_{BE}. Furthermore, the hydroxycinnamic acid glycosides disinapoyl-gentiobiose and sinapoyl-feruloyl-gentiobiose were enhanced in a dose-dependent manner under UV-B. In a second experiment

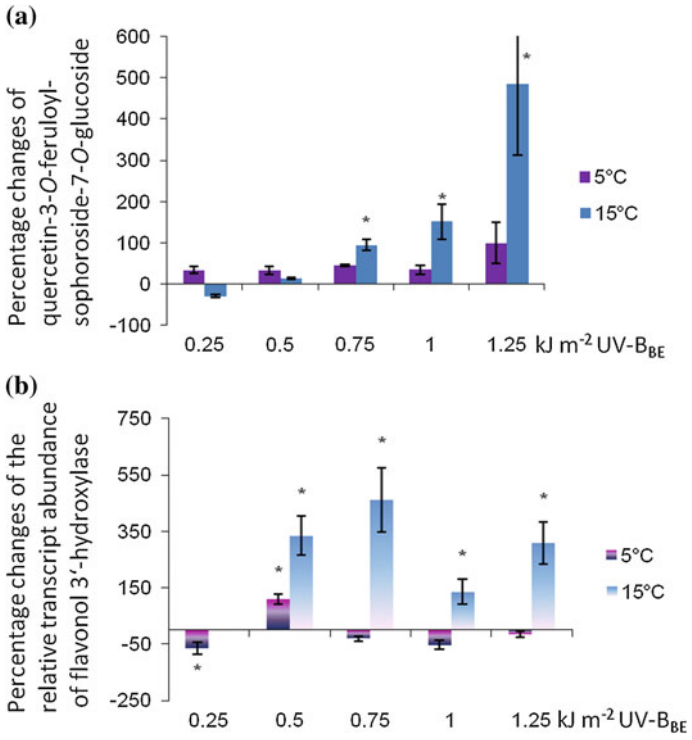


Fig. 14.2 Percentage changes of a representative quercetin glycoside in kale in plants treated with subsequent doses of moderate UV-B compared to the nontreated control plants (**a**); Percentage changes of the relative transcript abundance of *Brassica oleracea*-F3′H in plants treated with subsequent doses of moderate UV-B compared to the nontreated control plants (**b**) [25]; * represents significant differences ($p \leq 0.05$ by Tukey's HSD test) between treated and nontreated plants at each dose

investigating the interaction of moderate UV-B radiation and temperature on structurally different phenolic compounds in kale, levels of monoacylated quercetin glycosides were increased by higher UV-B and temperature [121]. Concomitantly, enhanced mRNA expression of *flavonol 3′- hydroxylase* was found under the same conditions (Fig. 14.2). The response of acylated kaempferol glycosides was more diverse and dependent on the hydroxycinnamic acid residue and the number of glucose moieties in the 7-O position. The hydroxycinnamic acid derivatives itself were hardly affected by UV-B radiation or temperature. However, moderate UV-B can enhance caffeoylquinic acid in apples (*Malus domestica*) [119].

*Response of flavonoids and other phenolics dependent on the chemical structure*3 Recent studies underline the structure-dependent response of flavonoids and other phenolics to UV-B radiation. For flavonoid glycosides there are structural

characteristics regarding the aglycone, the glycosylated sugars, and the acylated phenolic and organic acids.

Quercetin glycosides have a higher antioxidative activity than their corresponding kaempferol glycosides [122]. Consistently, quercetin glycosides were increased stronger in response to UV-B in various species, e.g., silver birch, willow (*Salix myrsinifolia*), or *Arabidopsis thaliana* [1, 106, 107, 123, 124]. In canola the quercetin glycosides were enhanced when exposed to higher UV-B levels while the kaempferol glycoside displayed additional changes dependent on their acylation pattern [113]. In peppermint (*Mentha* × *piperita*) the concentration of narirutin was decreased by UV-B whereas the related compounds eriocitrin and hesperidin were increased [125]. In contrast, naringenin chalcone increased in the peel of tomato (*Solanum lycopersicum*) fruits exposed to UV-B [126]. In the two mountain species, arnica and mountain birch, that are adapted to higher UV-B levels neither quercetin nor kaempferol glycosides were affected by higher UV-B levels [21, 111].

The particular sugar moiety bound to the aglycone does not lead to different reactions of flavonoid glycosides to UV-B in silver birch seedlings. Levels of the flavonol glycosides quercetin-3-galactoside, quercetin-3-rhamnoside, and kaempferol-3-rhamnoside increased with higher UV-B radiation, whereas the myricetin glycosides did not respond, independently of the sugar moiety glycosylated [116]. However, glycosylation of flavones with a glucose molecule in different clones of willow increased under higher UV-B levels whereas luteolin and apigenin glucuronides were not affected by UV-B [127]. Recent studies have also started to reveal UV-B specific effects on flavonoid glycosylation patterns. The flavonoid glycosylation pattern is markedly influenced by exposure to low doses of UV-B as shown for kaempferol glycosides in kale [8]. While monoacylated kaempferol tetraglucosides decreased following exposure to a single dose of up to 0.88 kJ m^{-2} d^{-1} UV-B_{BE}, the monoacylated kaempferol diglucosides increased strongly under the same dose. For example, in *Arabidopsis* exposed to low doses of UV, di- and triglycosides accumulate, with a preponderance of 7-rhamnosylated flavonols [16]. The accumulation of specific flavonoid glycosides appears to be an intrinsic part of the UV-B response, with expression of several UDP-glucosyltransferases being directly controlled by UV-B [68]. Rather paradoxically, glycosylation decreases the antioxidant activity of flavonoids as well as affecting accumulation, stability, and solubility of flavonoids [128, 129].

The response of flavonoid glycosides is dependent on the type of phenolic acid that is acylated to the flavonol glycoside (mainly hydroxycinnamic acids). In pak choi, total flavonoid levels increased with exposure to additional UV-B but kaempferol glycosides acylated with ferulic, hydroxyferulic, or sinapic acid did not respond to UV exposure at 22 °C [117]. In kale it was shown that the structural characteristics of the hydroxycinnamic acids themselves have an impact on response to UV-B [121]. While the levels of caffeic acid and hydroxyferulic acid monoacylated kaempferol triglycosides (containing a catechol structure) were increased with exposure to higher UV-B radiation, the ferulic and sinapic acid

monoacylated kaempferol triglycosides (no catechol structure) were not affected. In canola, the nonacylated kaempferol-3-*O*-sophoroside-7-*O*-D-glucoside increased with the additional UV-B, while the sinapic acid monoacylated kaempferol glycoside did not respond [113]. The nonacylated and the acetic acid monoacylated apigenin glycosides of chamomile flowers (*Matricaria chamomilla*) were increased at higher altitudes (corresponding with higher UV-B levels) while the acetic acid diacylated apigenin glycosides were hardly changed [130].

Also phenolic acids respond to higher levels of UV-B radiation in a structure-dependent manner. Harbaum-Piayda et al. [117] described that caffeoylmalate, hydroxyferuloylmalate, coumaroylmalate, feruloylmalate, and sinapoylmalate in pak choi were not affected by higher UV-B radiation at higher temperatures (22 °C). In silver birch, different hydroxycinnamic acids including most caffeoylquinic acid derivatives and salicylic acid derivatives were also not affected by additional UV-B radiation [111, 116]. Tegelberg et al. [116] showed an increased concentration of 5-caffeoylquinic acid in silver birch, while the concentration of 3-caffoeylquinic acid was not affected. However, investigations of blackcurrant fruit by Huyskens-Keil et al. [120] revealed an increase in hydroxycinnamic acids with a single dose of moderate UV-B radiation (up to 5 kJ m^{-2} d^{-1}). The hydroxycinnamic acid derivatives of kale (caffeoylquinic acid disinapoyl-gentiobiose and sinapoyl-feruloyl-gentiobiose) were hardly affected by subsequent doses of UV-B radiation [121], but a single moderate UV-B dose led to a slight decrease of caffeoylquinic acid but an increase of disinapoyl-gentiobiose and sinapoyl-feruloyl-gentiobiose [8]. Hydroxycinnamic acids were previously shown to act as scavengers to ROS induced by UV-B radiation [89]. In tomato fruit, caffeic acid, ferulic acid, and *p*-coumaric acid were higher in plants exposed to UV-B compared to plants without UV-B exposure [126, 131].

14.5.2 Glucosinolates

Glucosinolates, the characteristic defense compounds in the order Brassicales, are sulfonated thioglycosides sharing a common glycone moiety with a variable aglycone side chain [53, 132]. Based on the side chain structure, glucosinolates are divided into three classes: aliphatic, indolyl, and aromatic glucosinolates. Different chemical glucosinolate structures have been proposed to exhibit different biological activities. As outlined previously, the production of flavonoids and related phenolic compounds as a response to UV-B in several plant species has been well documented [8, 23]; however, less is known about the response of other nonvolatile compounds such as glucosinolates to UV-B. Most studies in the past used a fairly high UV-B irradiation levels (>15 kJ m^{-2} day^{-1}) as stress factor resulting in plant damage and jasmonic acid-related ROS response, that are likely to be unusual in the nature [133]. However, recent studies have also highlighted that ecologically

relevant low UV-B levels can trigger the induction of phenolic compounds and the accumulation of glucosinolates in Brassicaceae as demonstrated for broccoli and nasturtium [12, 53]. While in particular high UV-B fluence rates induce jasmonic acid defense and wound signaling, below ambient UV-B levels have been shown to induce salicylic acid pathway signaling response and expression of genes encoding for pathogenesis-related proteins such as PR-1, PR-2, PR-4, and PR-5 along with PDF1.2 (PLANT DEFENSIN 1.2) [53, 76, 134]. Low ecologically relevant UV-B levels have been shown to confer regulatory properties [61] and may trigger distinct changes in the plant defense metabolism [19] and may prime plant defense responses [53]. Already a moderate ecologically relevant dose of about 1 kJ m^{-2} d^{-1} UV-B for 5 days increased aliphatic glucosinolate levels in broccoli sprouts and subsequently led to decreased host plant suitability for the aphid *Myzus persicae* (Sulzer) and the Lepidoptera *Pieris brassicae* L. [48]. Low to ambient UV-B doses elicited an increase of aliphatic glucosinolates in *Arabidopsis thaliana* and broccoli sprouts and an aromatic glucosinolate in *T. majus* (Table 14.1). Accordingly, the plant suitability to aboveground insect herbivores was changed in broccoli and *A. thaliana* [53, 135]. In particular the related hydrolysis products of glucosinolates—released by the enzyme myrosinase—are known to have functions in plant resistance against insects and pathogens [136–138]. Using different UV-B exclusion films it has been shown that the glucosinolates and myrosinases response depends on leaf age in a species-specific manner [103]. The authors concluded that compared to old leaves, young leaves (rich in nitrogen and soluble protein) were efficiently protected from UV light due to high flavonoid and glucosinolate amounts in *Sinapis alba*, or enhanced flavonoid levels and myrosinase activities in *Nasturtium officinale*.

Glucosinolates are not directly involved in UV protection, but UV-B-mediated effects on glucosinolates are conceivable, since these compounds are involved in the common plant defense response regulated by the two major signaling pathways [19, 53, 139]. Indeed, low to moderate ambient UV-B doses induced specifically the accumulation of 4-methylsulfinylbutyl glucosinolate and 4-methoxyindol-3-ylmethyl glucosinolate in broccoli and *A. thaliana* (Table 14.1), which was distinct from the glucosinolate response elicited by chewing insects involving the jasmonic acid-induced accumulation of 1-methoxyindol-3-ylmethyl glucosinolate [137]. Since studies on supplemental UV-B effects on accumulation on individual glucosinolate in Brassicaceae are rare, a comparison to other studies is a difficult task. However, Nadeau et al. [140] showed that 4-methoxyindol-3-ylmethyl glucosinolate, 4-hydroxyindol-3-ylmethyl glucosinolate, and 4-methylsulfinylbutyl glucosinolate accumulated in broccoli florets in response to exposure to a hormetic dose of UV-C.

Table 14.1 Glucosinolate content in leaves of *B. oleracea* var. *italica* (sprout stage), *A. thaliana* (mature plant), and *T. majus* (mature plant) for 1–2 days postexposure to different UV-B doses

Class		Glucosinolate content (μmol g^{-1} dry weight)										
	Plant species	B. oleracea				A. thaliana				T. majus		
	UV-B dose (kJ d^{-1})	0	0.6	0	0.9	0	0.6	0	1.1	0	0.6	1.2
Aliphatic GS	3-Methylsulfinylpropyl-	23.77	34.27*	2.58	5.84*	0.70	0.90*	2.05	2.29	–	–	–
	(R)-2-Hydroxy-3-butenyl-	0.95	1.48*	0.79	2.35*	–	–	–	–	–	–	–
	4-Methylsulfinylbutyl-	47.69	70.95*	10.34	15.77*	3.58	4.15*	14.38	17.46*	–	–	–
	5-Methylsulfinylpentyl-	0.21	0.34	0.08	0.12*	0.10	0.11	0.45	0.62*	–	–	–
	7-Methylsulfinylheptyl-	–	–	–	–	0.20	0.26	0.38	0.51	–	–	–
	8-Methylsulfinyloctyl-	–	–	–	–	0.12	0.11	1.08	1.63*	–	–	–
	4-Methylthiobutyl-	9.90	13.40*	1.79	1.76	0.58	0.58	0.51	0.42	–	–	–
Indole GS	4-Hydroxy-indol-3ylmethyl-	4.09	4.21	0.88	1.42*	0.06	0.06	0.06	0.03	–	–	–
	Indol-3ylmethyl-	2.92	3.10	0.99	1.58*	2.56	2.49	3.96	5.61*	–	–	–
	4-Methoxy-indol-3ylmethyl-	1.08	1.79*	1.31	1.61*	0.28	0.81*	0.88	2.11*	–	–	–
	1-Methoxy-indol-3ylmethyl-	0.53	0.33*	0.53	0.50	0.09	0.12	2.45	3.05	–	–	–
Arom. GS	Benzyl-	–	–	–	–	–	–	–	–	14.21a	26.46ab	40.33b
	Total	91.23	129.98*	19.28	30.95*	8.27	9.59*	18.85	22.93*	14.21a	26.46ab	40.33b

*Indicates significant differences among treatments ANOVA: $p > 0.05$; different small letters indicate significant differences among treatments Tukey's test: $p \leq 0.05$; gray shadow indicates a different experiment using the same plant species, including varying experimental condition; arom. = aromatic; GS = glucosinolate; data partly adjusted from Schreiner et al. [12] and Mewis et al. [53]

14.6 Tailor-Made UV-B Induction of Secondary Plant Metabolites by UV-B LEDs

The use of LEDs for plant growth lighting or targeted triggering of certain plant properties is a new approach in the horticulture research and the related industry which attracted much interest in the last years [141]. Besides the large-scale vegetable production in greenhouses or other facilities, where an optimized lighting spectrum from LEDs can accelerate the growth and harvest rhythm, other more research oriented applications, like the presented work in this chapter are under development.

14.6.1 Current State of Research: UV-B Light-Emitting Diodes for Plant Lightning

Until the publication date of this book there have been published just prelimary research studies on the influence of narrow-band UV-B radiation from light-emitting diodes on secondary plant metabolites or other plant properties [142]. The plant response to the emission of conventional UV-B sources is already under investigation and selected articles are discussed earlier in this chapter. However, there is only little knowledge about the plant response to UV radiation from LEDs beyond the UV-B range. For example, Li and Kubota [143] have shown that white light complemented by near-UV radiation with a peak at 373 nm can enhance anthocyanin accumulation in baby leaf lettuce during growth.

14.6.2 Advantages of UV-B LEDs for Targeted Triggering of Plant Properties

Most UV radiation-triggered photobiological processes are limited by a lack of UV-B and UV-C radiation within the earth atmosphere, i.e., corresponding radiation stresses the plant. The efficiency of many of these UV-triggered processes has a spectral dependence with single or multiple absorption maxima in the UV spectral range. To selectively trigger a certain photobiological process and efficiently use the radiation of a UV source a narrow emission spectrum with a peak wavelength perfectly fitting to the efficiency maximum is needed.

The efficiency for triggering the production of the discussed secondary plant metabolites, particularly flavonoids and glucosinolates, by UV light is supposed to have local maxima in the UV-B spectral region [12]. Until now, researchers have used conventional UV-B radiation sources with a broad emission peak in the UV-B spectral region, such as low-pressure mercury gas-discharge fluorescent lamps with a phosphor coating to convert UV-C radiation into a broadband UV-B radiation

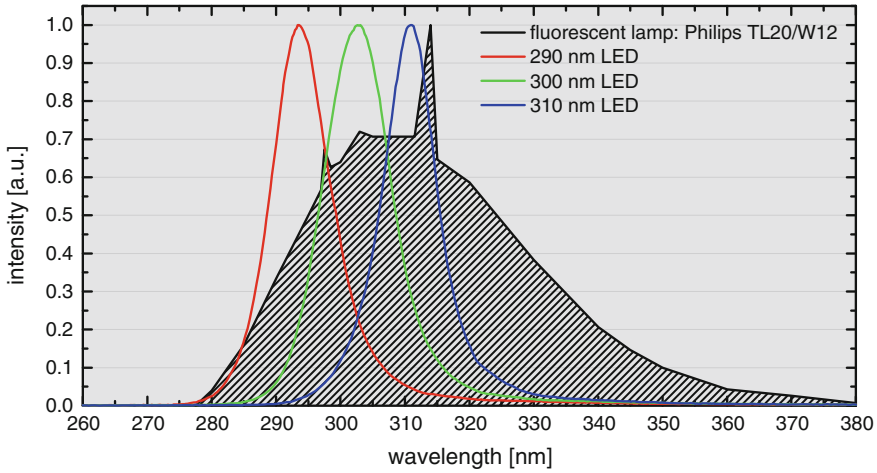


Fig. 14.3 Emission spectra of a conventional UV-B radiation source used in studies for triggering secondary plant metabolites and UV-B LEDs with peak wavelengths between 290 and 310 nm

between 280 and 360 nm (Fig. 14.3—fluorescent lamp). Because of the broad emission spectrum it is not possible to obtain a differentiated plant response to UV radiation of a certain wavelength. Furthermore, an unwanted cross talk or even harmful stress from UV radiation of different wavelengths on certain secondary plant metabolites or other plant properties is possible [19, 86].

One option to study spectral dependencies is the use of an optical band-pass filter whose transmission is limited to a particular wavelength range. However, the performance of commercially available filters is limited in terms of damping ratio and position of the center wavelength. Moreover, the development of a specific filter with tailored transmission is quite expensive, especially when considering large-scale adoption to greenhouses or even larger plant growth facilities.

Figure 14.3 shows the emission spectra of different UV-B LEDs and of a low-pressure mercury gas-discharge lamp with phosphor coating. The UV-B LEDs have a narrow emission spectrum (full width at half maximum $\sim$ 10 nm) without any side peaks. The peak wavelength of the shown spectra is 290, 300, and 310 nm, respectively. However, by adjusting the (InAlGaN-) material composition in the active region of the LED every wavelength within the UV-B spectral region can be reached. Besides the advantages for the photobiological processes, a narrow and perfectly fitting emission spectrum is more efficient in terms of energy conversion.

As many photobiological processes in plants are very sensitive to UV-B radiation, a high fluence rate can harm the plant significantly. The stress on the plant can be reduced by lowering the exposure time and/or decreasing the optical power to an adequate level. However, the output power of conventional UV-B radiation sources is relatively high and can only be varied within a small range without using optical filters. In contrast, the optical power of LEDs is adjustable over a wide range by simply changing the operation current. Another superior property of UV LEDs is

their compact size. With chip sizes of less than 0.4 mm^3 or fully packaged of about 100 mm^3 they allow compact and space-saving module constructions for new ways in plant lighting.

Conventional as well as diode-based UV sources produce large amounts of heat during their operation, due to low conversion efficiency. The problem with conventional sources like gas-discharge lamps is that there is no technological relevant solution to dissipate the heat from the lamp. Thus the heat is radiated toward the plant, which eventually can have negative impacts on its properties. In contrast, using a clever thermal management, for example, by implementing a heat sink or active air/water cooling, the heat from the LEDs can be dissipated efficiently.

In the next section, a novel approach of UV-B LED implementation to an experimental plant growth setup will be discussed.

14.6.3 Experimental Setup for Targeted Triggering of Plant Properties by UV-B LEDs

A lighting module consisting of twelve 310 nm LEDs was developed for first experimental studies on the effect of UV-B radiation from AlGaN-based LEDs on the production of secondary plant metabolites in *Arabidopsis* leaves and broccoli sprouts. The LEDs are so-called research-grade samples manufactured by Sensor Electronic Technology, Inc. with an average optical output power of 1.01 mW ± 0.13 mW at a drive current of 50 mA. Due to the lambertian radiation characteristic of the used LEDs, which is marked by significant optical powers even at large angles, UV reflectors were implemented to focus the entire emission power to the target area. The 12 LEDs including reflectors are positioned on an aluminum heat sink in a way to homogenously illuminate a target area of 20 cm × 30 cm. Using this module construction a homogenous irradiance of ≥0.1 W m^{-2} (equal to ≥ 0.36 kJ m^{-2} at 1 h of exposure) was obtained at a working distance of 30 cm. Figure 14.4 shows the UV-B LED module, which was placed in a growth chamber to keep the plants under highly controlled growth conditions that are optimized for photosynthesis and growth.

Preliminary tests already showed that there is an influence on the production of secondary plant metabolites in *Arabidopsis* leaves and broccoli sprouts. Additionally, the UV radiation-induced stress was minimized by adjusting the intensity. For example, 5 h UV-B exposure increased the total glucosinolate content from 3.0 mg g^{-1} dry matter of untreated *Arabidopsis* control plants up to 5.2 mg g^{-1} dry matter in leaves of treated plants, 24 h after UV-B application.

Besides this small-scale research-oriented design, other configurations of UV LED modules are imaginable, particularly when considering the worldwide implementation of LED-based solid-state lighting in horticulture industry. Many greenhouses and plant-fabrication facilities, where the plants are never exposed to sunlight, started to change their artificial illumination from conventional

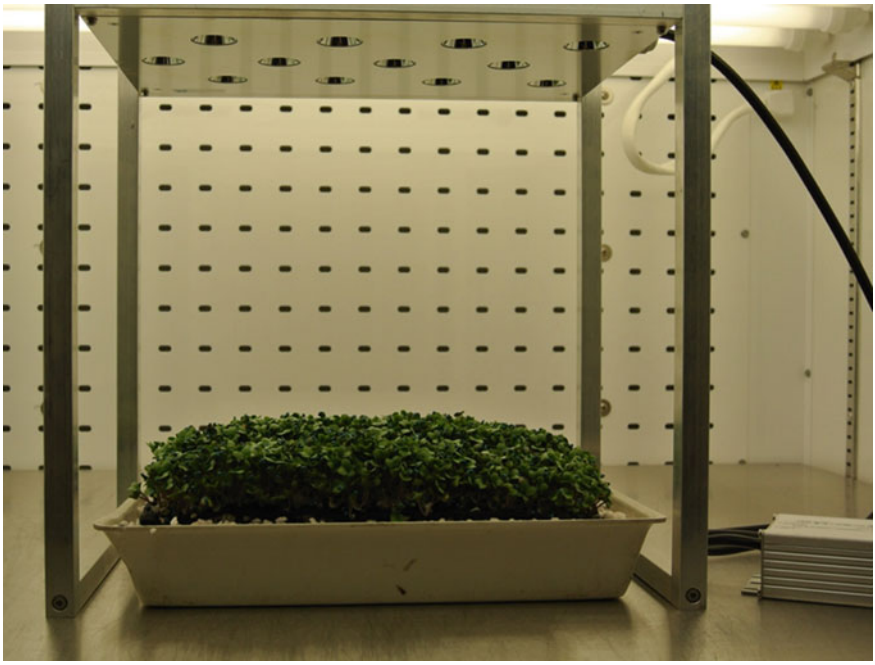


Fig. 14.4 UV-B LED module with homogenous radiation pattern, peak wavelength = 310 nm, and irradiance ≥ 0.1 W m^{-2}, for plant response experiments (here with broccoli sprouts)

gas-discharge lamps to LEDs. Especially, the vertical layering of growth chambers is a new trend to use a given limited space as efficiently as possible and compact LED modules are the perfect lighting source for such an application.

14.7 Outlook

This chapter examined the feasibility of low-dose, but ecological relevant UV-B application as emerging technology for enhancing health-promoting secondary plant metabolites in freshly consumed plant products demonstrated by various fruits, vegetables, herbs, and ornamentals as well as perennial species. Optimizing concentrations and profiles of secondary plant metabolites by targeted and also novel, tailor-made narrow-band UV-B applications will add health value and subsequently generate new opportunities for growers and processors by achieving the health-oriented food market.

Implementing plants in biomanufacturing systems for producing and extracting single or multiple functional secondary plant metabolites as bioactive additives in functional foods and nutraceuticals can be promoted by UV-B elicitation treatments. However, this targeted induction of individual secondary plant metabolites

requires detailed knowledge of key regulatory steps within the biosynthetic pathway of each secondary plant metabolite in order to optimize specifically the desired secondary plant metabolite.

References

1. M.A.K. Jansen, K. Hectors, N.M. O'Brien, Y. Guisez, G. Potters, Plant stress and human health: Do human consumers benefit from UV-B acclimated crops? Plant Sci. **175**, 449–458 (2008)
2. H.C. Hung, K.J. Joshipura, R. Jiang, F.B. Hu, D. Hunter, S.A. Smith-Warner, G.A. Colditz, B. Rosner, D. Spiegelman, W.C. Willett, Fruit and vegetable intake and risk of major chronic disease. J. Natl. Cancer Inst. **96**, 1577–1584 (2004)
3. B. Watzl, C. Leitzmann, *Bioaktive Substanzen in Lebensmitteln* (Hippokrates Verlag, Stuttgart, 2005)
4. E.C. Montilla, M.R. Arzaba, S. Hillebrand, P. Winterhalter, Anthocyanin composition of black carrot (*Daucus carota* ssp. *sativus* var. *atrorubens* Alef.) cultivars antonina, beta sweet, deep purple, and purple haze. J. Agric. Food Chem. **59**, 3385–3390 (2011)
5. M. Wiesner, R. Zrenner, A. Krumbein, H. Glatt, M. Schreiner, Genotypic variation of the glucosinolate profile in Pak Choi (*Brassica rapa* ssp *chinensis*). J. Agric. Food Chem. **61**, 1943–1953 (2013)
6. E. Becatti, K. Petroni, D. Giuntini, A. Castagna, V. Calvenzani, G. Serra, A. Mensuali-Sodi, C. Tonelli, A. Ranieri, Solar UV-B radiation Influences carotenoid accumulation of tomato fruit through both ethylene-dependent and -independent mechanisms. J. Agric. Food Chem. **57**, 10979–10989 (2009)
7. P. Majer, E. Hideg, Existing antioxidant levels are more important in acclimation to supplemental UV-B irradiation than inducible ones: studies with high light pretreated tobacco leaves, in *UV4Growth COST-Action FA09006-2nd Annual Network Meeting*, Book of Abstracts: 22 (2013)
8. S. Neugart, M. Zietz, M. Schreiner, S. Rohn, L.W. Kroh, A. Krumbein, Structurally different flavonol glycosides and hydroxycinnamic acid derivatives respond differently to moderate UV-B radiation exposure. Physiol. Plantarum **145**, 582–593 (2012)
9. L. Cisneros-Zevallos, The use of controlled postharvest abiotic stresses as a tool for enhancing the nutraceutical content and adding-value of fresh fruits and vegetables. J. Food Sci. **68**, 1560–1565 (2003)
10. Z. Katerova, D. Todorova, K. Tasheva, I. Sergiev, Influence of ultraviolet radiation on plant secondary metabolite production. Genet. Plant Physiol. **2**, 113–144 (2012)
11. C.P. Perez, M. Schreiner, A. Krumbein, D. Schwarz, H.P. Kläring, C. Ulrichs, S. Huyskens-Keil, Composition of carotenoids in tomato fruits as affected by moderate UV-B radiation before harvest. Acta Hort. **821**, 217–221 (2009)
12. M. Schreiner, A. Krumbein, I. Mewis, C. Ulrichs, S. Huyskens-Keil, Short-term and moderate UV-B radiation effects on secondary plant metabolism in different organs of nasturtium (*Tropaeolum majus* L.). Innov. Food Sci. Emerg. **10**, 93–96 (2009)
13. W.J. Zhang, L.O. Björn, The effect of ultraviolet radiation on the accumulation of medicinal compounds in plants. Fitoterapia **80**, 207–218 (2009)
14. S. Munné-Bosch, The role of alpha-tocopherol in plant stress tolerance. J. Plant Physiol. **162**, 743–748 (2005)
15. M. Kusano, T. Tohge, A. Fukushima, M. Kobayashi, N. Hayashi, H. Otsuki, Y. Kondou, H. Goto, M. Kawashima, F. Matsuda, R. Niida, M. Matsui, K. Saito, A.R. Fernie, Metabolomics reveals comprehensive reprogramming involving two independent metabolic responses of Arabidopsis to UV-B light. Plant J. **67**, 354–369 (2011)

16. K. Hectors, S. van Oevelen, Y. Guisez, M.A.K. Jansen, E. Prinsen, Dynamic changes in plant secondary metabolites during UV acclimation in *Arabidopsis thaliana*. Physiol. Plantarum (2014)
17. J.P. Schnitzler, T.P. Jungblut, C. Feicht, M. Kofferlein, C. Langebartels, W. Heller, H. Sandermann, UV-B induction of flavonoid biosynthesis in Scots pine (*Pinus sylvestris* L) seedlings. Trees-Struct. Funct. **11**, 162–168 (1997)
18. T. Obata, A.R. Fernie, The use of metabolomics to dissect plant responses to abiotic stresses. Cell. Mol. Life Sci. **69**, 3225–3243 (2012)
19. M. Schreiner, I. Mewis, S. Huyskens-Keil, M.A.K. Jansen, R. Zrenner, J.B. Winkler, N. O'Brien, A. Krumbein, UV-B-induced secondary plant metabolites—potential benefits for plant and human health. Crit. Rev. Plant Sci. **31**, 229–240 (2012)
20. P.D. Brown, J.G. Tokuhisa, M. Reichelt, J. Gershenzon, Variation of glucosinolate accumulation among different organs and developmental stages of *Arabidopsis thaliana*. Phytochemistry **62**, 471–481 (2003)
21. A. Albert, V. Sareedenchai, W. Heller, H.K. Seidlitz, C. Zidorn, Temperature is the key to altitudinal variation of phenolics in *Arnica montana* L. cv. ARBO. Oecologia **160**, 1–8 (2009)
22. H. Behn, A. Albert, F. Marx, G. Noga, A. Ulbrich, Ultraviolet-B and photosynthetically active radiation interactively affect yield and pattern of monoterpenes in leaves of peppermint (*Mentha* x *piperita* L.). J. Agric. Food Chem. **58**, 7361–7367 (2010)
23. M.M. Caldwell, J.F. Bornman, C.L. Ballare, S.D. Flint, G. Kulandaivelu, Terrestrial ecosystems, increased solar ultraviolet radiation, and interactions with other climate change factors. Photochem. Photobiol. Sci. **6**, 252–266 (2007)
24. M. Götz, A. Albert, S. Stich, W. Heller, H. Scherb, A. Krins, C. Langebartels, H.K. Seidlitz, D. Ernst, PAR modulation of the UV-dependent levels of flavonoid metabolites in *Arabidopsis thaliana* (L.) Heynh. leaf rosettes: cumulative effects after a whole vegetative growth period. Protoplasma **243**, 95–103 (2010)
25. S. Neugart, M. Fiol, M. Schreiner, S. Rohn, R. Zrenner, L.W. Kroh, A. Krumbein, Interaction of moderate UV-B exposure and temperature on the formation of structurally different flavonol glycosides and hydroxycinnamic acid derivatives in kale (*Brassica oleracea* var. *sabellica*). J. Agric. Food Chem. (2014)
26. H. Erbersdobler, A. Meyer, in *Praxishandbuch Functional Food* (B. Behr´s Verlag GmbH & Co, Hamburg, 2003)
27. M. Fiol, S. Adermann, S. Neugart, S. Rohn, C. Muegge, M. Schreiner, A. Krumbein, L.W. Kroh, Highly glycosylated and acylated flavonols isolated from kale (*Brassica oleracea* var. *sabellica*)—Structure-antioxidant activity relationship. Food Res. Int. **47**, 80–89 (2012)
28. F.J. Schweigert, Carotinoide, in *Praxishandbuch Functional Food* (B. Behr´s Verlag GmbH & Co., Hamburg, 2003), pp. 1–18
29. R.M. Wang, J.Y. Tu, Q.G. Zhang, X. Zhang, Y. Zhu, W.D. Ma, C. Cheng, D.W. Brann, F. Yang, Genistein attenuates ischemic oxidative damage and behavioral deficits via eNOS/Nrf2/HO-1 signaling. Hippocampus **23**, 634–647 (2013)
30. P. Knekt, J. Kumpulainen, R. Jarvinen, H. Rissanen, M. Heliovaara, A. Reunanen, T. Hakulinen, A. Aromaa, Flavonoid intake and risk of chronic diseases. Am. J. Clin. Nutr. **76**, 560–568 (2002)
31. B. Watzl, Sulfide. Ernährungsumschau **49**, 493–496 (2002)
32. E.H. Jeffery, M. Araya, Physiological effects of broccoli consumption. Phytochem. Rev. **8**, 283–298 (2009)
33. M. Traka, R. Mithen, Glucosinolates, isothiocyanates and human health. Phytochem. Rev. **8**, 269–282 (2009)
34. R. Mithen, High glucoraphanin broccoli—the development of Beneforte™ broccoli and evidence of health benefits, in *International Symposium on Brassica and 18th Crucifer Genetic Workshop. Catania (Sicily) Italy*, 6th edn., pp. 274, ed. by F. Branca

35. A.L. Piberger, B. Köberle, A. Hartwig, The broccoli-born isothiocyanate sulforaphane impairs nucleotide excision repair: XPA as one potential target. Archives of toxicology (2013)
36. M. Wiesner, M. Schreiner, H. Glatt, High mutagenic activity of juice from pak choi (*Brassica rapa* ssp. *chinensis*) sprouts due to its content of 1-methoxy-3-indolylmethyl glucosinolate, and its enhancement by elicitation with methyl jasmonate. Food Chem. Toxicol. (2014)
37. S.R. Boreddy, S.K. Srivastava, Pancreatic cancer chemoprevention by phytochemicals. Cancer Lett. **334**, 86–94 (2013)
38. A. Basu, M. Rhone, T.J. Lyons, Berries: Emerging impact on cardiovascular health. Nutr. Rev. **68**, 168–177 (2010)
39. G. Ruel, S. Pomerleau, P. Couture, S. Lemieux, B. Lamarche, C. Couillard, Favourable impact of low-calorie cranberry juice consumption on plasma HDL-cholesterol concentrations in men. Br. J. Nutr. **96**, 357–364 (2006)
40. R. Verkerk, M. Schreiner, A. Krumbein, E. Ciska, B. Holst, I. Rowland, R. De Schrijver, M. Hansen, C. Gerhauser, R. Mithen, M. Dekker, Glucosinolates in *Brassica* vegetables: The influence of the food supply chain on intake, bioavailability and human health. Mol. Nutr. Food Res. **53**, S219–S265 (2009)
41. Q.J. Wu, L. Xie, W. Zheng, E. Vogtmann, H.L. Li, G. Yang, B.T. Ji, Y.T. Gao, X.O. Shu, Y.B. Xiang, Cruciferous vegetables consumption and the risk of female lung cancer: A prospective study and a meta-analysis. Ann. Oncol. **24**, 1918–1924 (2013)
42. Q.J. Wu, Y. Yang, E. Vogtmann, J. Wang, L.H. Han, H.L. Li, Y.B. Xiang, Cruciferous vegetables intake and the risk of colorectal cancer: A meta-analysis of observational studies. Ann. Oncol. **24**, 1079–1087 (2013)
43. Q.J. Wu, Y. Yang, J. Wang, L.H. Han, Y.B. Xiang, Cruciferous vegetable consumption and gastric cancer risk: A meta-analysis of epidemiological studies. Cancer Sci. **104**, 1067–1073 (2013)
44. C.N. Armah, M.H. Traka, J.R. Dainty, M. Defernez, A. Janssens, W. Leung, J.F. Doleman, J.F. Potter, R.F. Mithen, A diet rich in high-glucoraphanin broccoli interacts with genotype to reduce discordance in plasma metabolite profiles by modulating mitochondrial function. Am. J. Clin. Nutr. **98**, 712–722 (2013)
45. L.Y. Wu, M.H.N. Ashraf, M. Facci, R. Wang, P.G. Paterson, A. Ferrie, B.H.J. Juurlink, Dietary approach to attenuate oxidative stress, hypertension, and inflammation in the cardiovascular system. Proc. Natl. Acad. Sci. U. S. A. **101**, 7094–7099 (2004)
46. J.M. Chan, P.H. Gann, E.L. Giovannucci, Role of diet in prostate cancer development and progression. J. Clin. Oncol. **23**, 8152–8160 (2005)
47. L.A. Bazzano, J. He, L.G. Ogden, C. Loria, S. Vupputuri, L. Myers, P.K. Whelton, Legume consumption and risk of coronary heart disease in US men and women. Arch. Intern. Med. **161**, 2573–2578 (2001)
48. C.M. Kastorini, H.J. Milionis, K. Esposito, D. Giugliano, J.A. Goudevenos, D.B. Panagiotakos, The effect of mediterranean diet on metabolic syndrome and its components a meta-analysis of 50 studies and 534,906 individuals. J. Am. Coll. Cardiol. **57**, 1299–1313 (2011)
49. G. Buckland, N. Travier, V. Cottet, C.A. Gonzalez, L. Lujan-Barroso, A. Agudo, A. Trichopoulou, P. Lagiou, D. Trichopoulos, P.H. Peeters, A. May, H.B. Bueno-de-Mesquita, F.J.B. Duijnhoven, T.J. Key, N. Allen, K.T. Khaw, N. Wareham, I. Romieu, V. McCormack, M. Boutron-Ruault, F. Clavel-Chapelon, S. Panico, C. Agnoli, D. Palli, R. Tumino, P. Vineis, P. Amiano, A. Barricarte, L. Rodriguez, M.J. Sanchez, M.D. Chirlaque, R. Kaaks, B. Teucher, H. Boeing, M.M. Bergmann, K. Overvad, C.C. Dahm, A. Tjonneland, A. Olsen, J. Manjer, E. Wirfalt, G. Hallmans, I. Johansson, E. Lund, A. Hjartaker, G. Skeie, A.C. Vergnaud, T. Norat, D. Romaguera, E. Riboli, Adherence to the mediterranean diet and risk of breast cancer in the European prospective investigation into cancer and nutrition cohort study. Int. J. Cancer **132**, 2918–2927 (2013)
50. R. Estruch, E. Ros, J. Salas-Salvado, M.I. Covas, D. Corella, F. Aros, E. Gomez-Gracia, V. Ruiz-Gutierrez, M. Fiol, J. Lapetra, R.M. Lamuela-Raventos, L. Serra-Majem, X. Pinto,

J. Basora, M.A. Munoz, J.V. Sorli, J.A. Martinez, M.A. Martinez-Gonzalez, P.S. Investigators, Primary prevention of cardiovascular disease with a mediterranean diet. N. Engl. J. Med. **368**, 1279–1290 (2013)
51. The Alpha-Tocopherol BCCPSG, The effect of vitamin E and beta carotene on the incidence of lung cancer and other cancers in male smokers. New Engl. J. Med. **330**, 1029–1035 (1994)
52. G.S. Omenn, G.E. Goodman, M.D. Thornquist, J. Balmes, M.R. Cullen, A. Glass, J.P. Keogh, F.L. Meyskens, B. Valanis, J.H. Williams, S. Barnhart, M.G. Cherniack, C.A. Brodkin, S. Hammar, Risk factors for lung cancer and for intervention effects in CARET, the beta-carotene and retinol efficacy trial. J. Natl. Cancer Inst. **88**, 1550–1559 (1996)
53. I. Mewis, M. Schreiner, N. Chau Nhi, A. Krumbein, C. Ulrichs, M. Lohse, R. Zrenner, UV-B irradiation changes specifically the secondary metabolite Profile in Broccoli sprouts: Induced signaling overlaps with defense response to biotic stressors. Plant Cell Physiol. **53**, 1546–1560 (2012)
54. R. Ulm, A. Baumann, A. Oravecz, Z. Mate, E. Adam, E.J. Oakeley, E. Schafer, F. Nagy, Genome-wide analysis of gene expression reveals function of the bZIP transcription factor HY5 in the UV-B response of Arabidopsis. Proc. Natl. Acad. Sci. U. S. A. **101**, 1397–1402 (2004)
55. K. Hectors, E. Prinsen, W. De Coen, M.A.K. Jansen, Y. Guisez, *Arabidopsis thaliana* plants acclimated to low dose rates of ultraviolet B radiation show specific changes in morphology and gene expression in the absence of stress symptoms. New Phytol. **175**, 255–270 (2007)
56. J.A. Lake, K.J. Field, M.P. Davey, D.J. Beerling, B.H. Lomax, Metabolomic and physiological responses reveal multi-phasic acclimation of *Arabidopsis thaliana* to chronic UV radiation. Plant, Cell Environ. **32**, 1377–1389 (2009)
57. E. Wellmann, UV radiation in photomorphogenesis, in *Photomorphogenesis, Encyclopedia of Plant Physiology*, ed. by W.J. Shropshire, H. Mohr (Springer, Berlin, 1983), pp. 745–756
58. L. Rizzini, J.J. Favory, C. Cloix, D. Faggionato, A. O'Hara, E. Kaiserli, R. Baumeister, E. Schafer, F. Nagy, G.I. Jenkins, R. Ulm, Perception of UV-B by the Arabidopsis UVR8 protein. Science **332**, 103–106 (2011)
59. K. Tilbrook, A.B. Arongaus, M. Binkert, M. Heijde, R. Yin, R. Ulm, The UVR8 UV-B photoreceptor: Perception, signaling and response. Arabidopsis book/Am. Soc. Plant Biol. **11**, e0164 (2013)
60. M. Heijde, R. Ulm, UV-B photoreceptor-mediated signalling in plants. Trends Plant Sci. **17**, 230–237 (2012)
61. G.I. Jenkins, Signal transduction in responses to UV-B radiation. Ann. Rev. Plant Biol. **60**, 407–431 (2009)
62. J.M. Christie, A.S. Arvai, K.J. Baxter, M. Heilmann, A.J. Pratt, A. O'Hara, S.M. Kelly, M. Hothorn, B.O. Smith, K. Hitomi, G.I. Jenkins, E.D. Getzoff, Plant UVR8 photoreceptor senses UV-B by tryptophan-mediated disruption of cross-dimer salt bridges. Science **335**, 1492–1496 (2012)
63. D. Wu, Q. Hu, Z. Yan, W. Chen, C.Y. Yan, X. Huang, J. Zhang, P.Y. Yang, H.T. Deng, J.W. Wang, X.W. Deng, Y.G. Shi, Structural basis of ultraviolet-B perception by UVR8. Nature **484**, U214–U296 (2012)
64. J.J. Favory, A. Stec, H. Gruber, L. Rizzini, A. Oravecz, M. Funk, A. Albert, C. Cloix, G.I. Jenkins, E.J. Oakeley, H.K. Seidlitz, F. Nagy, R. Ulm, Interaction of COP1 and UVR8 regulates UV-B-induced photomorphogenesis and stress acclimation in Arabidopsis. EMBO J. **28**, 591–601 (2009)
65. E. Kaiserli, G.I. Jenkins, UV-B promotes rapid nuclear translocation of the Arabidopsis UV-B-specific signaling component UVR8 and activates its function in the nucleus. Plant Cell **19**, 2662–2673 (2007)
66. C. Cloix, G.I. Jenkins, Interaction of the Arabidopsis UV-B-specific signaling component UVR8 with chromatin. Mol. Plant **1**, 118–128 (2008)
67. B.A. Brown, C. Cloix, G.H. Jiang, E. Kaiserli, P. Herzyk, D.J. Kliebenstein, G.I. Jenkins, A UV-B-specific signaling component orchestrates plant UV protection. Proc. Natl. Acad. Sci. U.S.A. **102**, 18225–18230 (2005)

68. B.A. Brown, G.I. Jenkins, UV-B signaling pathways with different fluence-rate response profiles are distinguished in mature Arabidopsis leaf tissue by requirement for UVR8, HY5, and HYH. Plant Physiol. **146**, 576–588 (2008)
69. M. Heijde, R. Ulm, Reversion of the Arabidopsis UV-B photoreceptor UVR8 to the homodimeric ground state. Proc. Natl. Acad. Sci. U. S. A. **110**, 1113–1118 (2013)
70. M. Heilmann, G.I. Jenkins, Rapid reversion from monomer to dimer regenerates the ultraviolet-B photoreceptor UV RESISTANCE LOCUS8 in intact Arabidopsis plants. Plant Physiol. **161**, 547–555 (2013)
71. C. Lang-Mladek, L. Xie, N. Nigam, N. Chumak, M. Binkert, S. Neubert, M.-T. Hauser, UV-B signaling pathways and fluence rate dependent transcriptional regulation of ARIADNE12. Physiol. Plantarum **145**, 527–539 (2012)
72. M.A.K. Jansen, V. Gaba, B.M. Greenberg, Higher plants and UV-B radiation: Balancing damage, repair and acclimation. Trends Plant Sci. **3**, 131–135 (1998)
73. B.A. Kunz, D.M. Cahill, P.G. Mohr, M.J. Osmond, E.J. Vonarx, Plant responses to UV radiation and links to pathogen resistance, in *International Review of Cytology—A Survey of Cell Biology*, vol. 255, ed. by K.W. Jeon (Elsevier Academic Press Inc., San Diego, 2006), pp. 1–40
74. E. Hideg, T. Nagy, A. Oberschall, D. Dudits, I. Vass, Detoxification function of aldose/aldehyde reductase during drought and ultraviolet-B (280-320 nm) stresses. Plant, Cell Environ. **26**, 513–522 (2003)
75. M. Brosché, A. Strid, Molecular events following perception of ultraviolet-B radiation by plants. Physiol. Plantarum **117**, 1–10 (2003)
76. S.A.H. Mackerness, S.L. Surplus, P. Blake, C.F. John, V. Buchanan-Wollaston, B.R. Jordan, B. Thomas, Ultraviolet-B-induced stress and changes in gene expression in *Arabidopsis thaliana*: role of signalling pathways controlled by jasmonic acid, ethylene and reactive oxygen species. Plant Cell Environ. **22**, 1413–1423 (1999)
77. J. Kilian, D. Whitehead, J. Horak, D. Wanke, S. Weinl, O. Batistic, C. D'Angelo, E. Bornberg-Bauer, J. Kudla, K. Harter, The AtGenExpress global stress expression data set: protocols, evaluation and model data analysis of UV-B light, drought and cold stress responses. Plant J. **50**, 347–363 (2007)
78. C. Brunetti, R.M. George, M. Tattini, K. Field, M.P. Davey, Metabolomics in plant environmental physiology. J. Exp. Bot. **64**, 4011–4020 (2013)
79. B.P. Lankadurai, E.G. Nagato, M.J. Simpson, Environmental metabolomics: An emerging approach to study organism responses to environmental stressors. Environ. Rev. **21**, 180–205 (2013)
80. T. Gaspar, T. Franck, B. Bisbis, C. Kevers, L. Jouve, J.F. Hausman, J. Dommes, Concepts in plant stress physiology. Application to plant tissue cultures. Plant Growth Regul. **37**, 263–285 (2002)
81. E. Hideg, M.A.K. Jansen, A. Strid, UV-B exposure, ROS, and stress: inseparable companions or loosely linked associates? Trends Plant Sci. **18**, 107–115 (2013)
82. I. Kranner, F.V. Minibayeva, R.P. Beckett, C.E. Seal, What is stress? Concepts, definitions and applications in seed science. New Phytol. **188**, 655–673 (2010)
83. P.J. Aphalo, A. Albert, A. McLeod, A. Heikkilä, I. Gómez, F.L. Figueroa, T.M. Robson, A. Strid, Manipulating UV radiation, in *Beyond the Visible: A Handbook of Best Practice in Plant UV Photobiology,* ed. by P.J. Aphalo, A. Albert, L.O. Björn, A. McLeod, T.M. Robson, E. Rosenqvist (University of Helsinki, Department of Biosciences, Division of Plant Biology, 2012), p. 206
84. G. Agati, M. Tattini, Multiple functional roles of flavonoids in photoprotection. New Phytol. **186**, 786–793 (2010)
85. C.L. Ballare, M.M. Caldwell, S.D. Flint, A. Robinson, J.F. Bornman, Effects of solar ultraviolet radiation on terrestrial ecosystems. Patterns, mechanisms, and interactions with climate change. Photochem. Photobiol. Sci. **10**, 226–241 (2011)
86. M.A.K. Jansen, J.F. Bornman, UV-B radiation: from generic stressor to specific regulator. Physiol. Plantarum **145**, 501–504 (2012)

87. K.E. Heim, A.R. Tagliaferro, D.J. Bobilya, Flavonoid antioxidants: chemistry, metabolism and structure-activity relationships. J. Nutr. Biochem. **13**, 572–584 (2002)
88. J.M. Calderon-Montano, E. Burgos-Moron, C. Perez-Guerrero, M. Lopez-Lazaro, A review on the dietary flavonoid kaempferol. Mini-Rev. Med. Chem. **11**, 298–344 (2011)
89. A. Edreva, The importance of non-photosynthetic pigments and cinnamic acid derivatives in photoprotection. Agric. Ecosyst. Environ. **106**, 135–146 (2005)
90. F. Ferreres, C. Sousa, D.M. Pereira, P. Valentao, M. Taveira, A. Martins, J.A. Pereira, R.M. Seabra, P.B. Andrade, Screening of antioxidant phenolic compounds produced by *in vitro* shoots of *Brassica oleracea* L. var. *costata* DC. Comb. Chem. High T. Scr. **12**, 230–240 (2009)
91. T.S. Huang, D. Anzellotti, F. Dedaldechamp, R.K. Ibrahim, Partial purification, kinetic analysis, and amino acid sequence information of a flavonol 3-*O*-methyltransferase from *Serratula tinctoria*. Plant Physiol. **134**, 1366–1376 (2004)
92. A. Scalbert, G. Williamson, Dietary intake and bioavailability of polyphenols. J. Nutr. **130**, 2073S–2085S (2000)
93. I. Hernandez, L. Alegre, F. Van Breusegem, S. Munne-Bosch, How relevant are flavonoids as antioxidants in plants? Trends Plant Sci. **14**, 125–132 (2009)
94. J.L. Burkey, J.-M. Sauer, C.A. McQueen, I. Glenn Sipes, Cytotoxicity and genotoxicity of methyleugenol and related congeners—a mechanism of activation for methyleugenol. Mutat. Res./Fundam. Mol. Mech. Mutagen. **453**, 25–33 (2000)
95. K. Herrmann, F. Schumacher, W. Engst, K.E. Appel, K. Klein, U.M. Zanger, H. Glatt, Abundance of DNA adducts of methyleugenol, a rodent hepatocarcinogen, in human liver samples. Carcinogenesis **34**, 1025–1030 (2013)
96. N.T. Programm, Toxicology and carcinogenesis studies of methyleugenol. In: Natl. Toxicol. Program Tech. Report Series. pp. 1–420 (2000)
97. G.M. Williams, M.J. Iatropoulos, A.M. Jeffrey, J.D. Duan, Methyleugenol hepatocellular cancer initiating effects in rat liver. Food Chem. Toxicol. **53**, 187–196 (2013)
98. D. Comont, J. Martinez Abaigar, A. Albert, P. Aphalo, D.R. Causton, F. Lopez Figueroa, A. Gaberscik, L. Llorens, M.-T. Hauser, M.A.K. Jansen, M. Kardefelt, Luque P. de la Coba, S. Neubert, E. Nunez-Olivera, J. Olsen, M. Robson, M. Schreiner, R. Sommaruga, A. Strid, S. Torre, M. Turunen, S. Veljovic-Jovanovic, D. Verdaguer, M. Vidovic, J. Wagner, J.B. Winkler, G. Zipoli, D. Gwynn-Jones, UV responses of *Lolium perenne* raised along a latitudinal gradient across Europe: A filtration study. Physiol. Plantarum **145**, 604–618 (2012)
99. M. Ordidge, P. Garcia-Macias, N.H. Battey, M.H. Gordon, P. Hadley, P. John, J.A. Lovegrove, E. Vysini, A. Wagstaffe, Phenolic contents of lettuce, strawberry, raspberry, and blueberry crops cultivated under plastic films varying in ultraviolet transparency. Food Chem. **119**, 1224–1227 (2010)
100. E. Tsormpatsidis, R.G.C. Henbest, F.J. Davis, N.H. Battey, P. Hadley, A. Wagstaffe, UV irradiance as a major influence on growth, development and secondary products of commercial importance in Lollo Rosso lettuce 'Revolution' grown under polyethylene films. Environ. Exp. Bot. **63**, 232–239 (2008)
101. P. Garcia-Macias, M. Ordidge, E. Vysini, S. Waroonphan, N.H. Battey, M.H. Gordon, P. Hadley, P. John, J.A. Lovegrove, A. Wagstaffe, Changes in the flavonoid and phenolic acid contents and antioxidant activity of red leaf lettuce (Lollo Rosso) due to cultivation under plastic films varying in ultraviolet transparency. J. Agric. Food Chem. **55**, 10168–10172 (2007)
102. K.R. Markham, K.G. Ryan, S.J. Bloor, K.A. Mitchell, An increase in the luteolin: apigenin ratio in *Marchantia polymorpha* on UV-B enhancement. Phytochemistry **48**, 791–794 (1998)
103. K. Reifenrath, C. Müller, Species-specific and leaf-age dependent effects of ultraviolet radiation on two Brassicaceae. Phytochemistry **68**, 875–885 (2007)
104. M. Tattini, L. Guidi, L. Morassi-Bonzi, P. Pinelli, D. Remorini, E. Degl'Innocenti, C. Giordano, R. Massai, G. Agati, On the role of flavonoids in the integrated mechanisms of response of *Ligustrum vulgare* and *Phillyrea latifolia* to high solar radiation. New Phytol. **167**, 457–470 (2005)

105. T.R. Winter, M. Rostas, Ambient ultraviolet radiation induces protective responses in soybean but does not attenuate indirect defense. Environ. Pollut. **155**, 290–297 (2008)
106. M. Goetz, A. Albert, S. Stich, W. Heller, H. Scherb, A. Krins, C. Langebartels, H.K. Seidlitz, D. Ernst, PAR modulation of the UV-dependent levels of flavonoid metabolites in Arabidopsis thaliana (L.) Heynh. leaf rosettes: cumulative effects after a whole vegetative growth period. Protoplasma **243**, 95–103 (2010)
107. L.O. Morales, R. Tegelberg, M. Brosche, M. Keinanen, A. Lindfors, P.J. Aphalo, Effects of solar UV-A and UV-B radiation on gene expression and phenolic accumulation in *Betula pendula* leaves. Tree Physiol. **30**, 923–934 (2010)
108. K.G. Ryan, K.R. Markham, S.J. Bloor, J.M. Bradley, K.A. Mitchell, B.R. Jordan, UVB radiation induced increase in quercetin: Kaempferol ratio in wild-type and transgenic lines of Petunia. Photochem. Photobiol. **68**, 323–330 (1998)
109. J.M. Zhang, M.B. Satterfield, J.S. Brodbelt, S.J. Britz, B. Clevidence, J.A. Novotny, Structural characterization and detection of kale flavonoids by electrospray ionization mass spectrometry. Anal. Chem. **75**, 6401–6407 (2003)
110. F. Antognoni, S. Zheng, C. Pagnucco, R. Baraldi, F. Poli, S. Biondi, Induction of flavonoid production by UV-B radiation in *Passiflora quadrangularis* callus cultures. Fitoterapia **78**, 345–352 (2007)
111. U. Anttila, R. Julkunen-Tiitto, M. Rousi, S. Yang, M.J. Rantala, T. Ruuhola, Effects of elevated ultraviolet-B radiation on a plant-herbivore interaction. Oecologia **164**, 163–175 (2010)
112. F. Kuhlmann, C. Mueller, Development-dependent effects of UV radiation exposure on broccoli plants and interactions with herbivorous insects. Environ. Exp. Bot. **66**, 61–68 (2009)
113. L.C. Olsson, M. Veit, G. Weissenbock, J.F. Bornman, Differential flavonoid response to enhanced UV-B radiation in *Brassica napus*. Phytochemistry **49**, 1021–1028 (1998)
114. Y. Ban, C. Honda, Y. Hatsuyama, M. Igarashi, H. Bessho, T. Moriguchi, Isolation and functional analysis of a MYB transcription factor gene that is a key regulator for the development of red coloration in apple skin. Plant Cell Physiol. **48**, 958–970 (2007)
115. S.F. Hagen, G.I.A. Borge, G.B. Bengtsson, W. Bilger, A. Berge, K. Haffner, K.A. Solhaug, Phenolic contents and other health and sensory related properties of apple fruit (*Malus domestica* Borkh., cv. Aroma): Effect of postharvest UV-B irradiation. Postharvest Biol. Tec. **45**, 1–10 (2007)
116. R. Tegelberg, R.J. Julkunen-Tiitto, P.J. Aphalo, Red: far-red light ratio and UV-B radiation: Their effects on leaf phenolics and growth of silver birch seedlings. Plant Cell Environ. **27**, 1005–1013 (2004)
117. B. Harbaum-Piayda, B. Walter, G.B. Bengtsson, E.M. Hubbermann, W. Bilger, K. Schwarz, Influence of pre-harvest UV-B irradiation and normal or controlled atmosphere storage on flavonoid and hydroxycinnamic acid contents of pak choi (*Brassica campestris* L. ssp *chinensis* var. *communis*). Postharvest Biol. Tec. **56**, 202–208 (2010)
118. M.H. Sangtarash, M.M. Qaderi, C.C. Chinnappa, D.M. Reid, Differential sensitivity of canola (*Brassica napus*) seedlings to ultraviolet-B radiation, water stress and abscisic acid. Environ. Exp. Bot. **66**, 212–219 (2009)
119. J.E. Lancaster, P.F. Reay, J. Norris, R.C. Butler, Induction of flavonoids and phenolic acids in apple by UV-B and temperature. J. Hort. Sci. Biotech. **75**, 142–148 (2000)
120. S. Huyskens-Keil, I. Eichholz, L.W. Kroh, S. Rohn, UV-B induced changes of phenol composition and antioxidant activity in black currant fruit (*Ribes nigrum* L.). J. Appl. Bot. Food Qual. **81**, 140–144 (2007)
121. S. Neugart, M. Fiol, M. Schreiner, S. Rohn, R. Zrenner, L.W. Kroh, A. Krumbein, Interaction of moderate UV-B exposure and temperature on the formation of structurally different flavonol glycosides and hydroxycinnamic acid derivatives in kale (Brassica oleracea var. sabellica). J. Agricu. Food Chem. (2015)

122. M. Zietz, A. Weckmüller, S. Schmidt, S. Rohn, M. Schreiner, A. Krumbein, L.W. Kroh, Genotypic and climatic influence on the antioxidant activity of flavonoids in Kale (*Brassica oleracea* var. *sabellica*). J. Agric. Food Chem. **58**, 2123–2130 (2010)
123. K. Hectors, S. van Oevelen, Y. Guisez, E. Prinsen, M.A.K. Jansen, The phytohormone auxin is a component of the regulatory system that controls UV-mediated accumulation of flavonoids and UV-induced morphogenesis. Physiol. Plantarum **145**, 594–603 (2012)
124. L. Nybakken, R. Horkka, R. Julkunen-Tiitto, Combined enhancements of temperature and UVB influence growth and phenolics in clones of the sexually dimorphic *Salix myrsinifolia*. Physiol. Plantarum **145**, 551–564 (2012)
125. Y. Dolzhenko, C.M. Bertea, A. Occhipinti, S. Bossi, M.E. Maffei, UV-B modulates the interplay between terpenoids and flavonoids in peppermint (*Mentha* × *piperita* L.). J. Photoch. Photobio. B **100**, 67–75 (2010)
126. D. Giuntini, V. Lazzeri, V. Calvenzani, C. Dall'Asta, G. Galaverna, C. Tonelli, K. Petroni, A. Ranieri, Flavonoid profiling and biosynthetic gene expression in flesh and peel of two tomato genotypes grown under UV-B-depleted conditions during ripening. J. Agric. Food Chem. **56**, 5905–5915 (2008)
127. R. Tegelberg, R. Julkunen-Tiitto, Quantitative changes in secondary metabolites of dark-leaved willow (*Salix myrsinifolia*) exposed to enhanced ultraviolet-B radiation. Physiol. Plantarum **113**, 541–547 (2001)
128. D. Bowles, E.K. Lim, B. Poppenberger, F.E. Vaistij, Glycosyltransferases of lipophilic small molecules. Ann. Rev. Plant Biol. **57**, 567–597 (2006)
129. C.M.M. Gachon, M. Langlois-Meurinne, P. Saindrenan, Plant secondary metabolism glycosyltransferases: The emerging functional analysis. Trends Plant Sci. **10**, 542–549 (2005)
130. M. Ganzera, M. Guggenberger, H. Stuppner, C. Zidorn, Altitudinal variation of secondary metabolite profiles in flowering heads of *Matricaria chamomilla* cv. BONA. Planta Med. **74**, 453–457 (2008)
131. D.L. Luthria, S. Mukhopadhyay, D.T. Krizek, Content of total phenolics and phenolic acids in tomato (*Lycopersicon esculentum* Mill.) fruits as influenced by cultivar and solar UV radiation. J. Food Compos. Anal. **19**, 771–777 (2006)
132. F. Rohr, C. Ulrichs, M. Schreiner, R. Zrenner, I. Mewis, Responses of *Arabidopsis thaliana* plant lines differing in hydroxylation of aliphatic glucosinolate side chains to feeding of a generalist and specialist caterpillar. Plant Physiol. Biochem. **55**, 52–59 (2012)
133. V.G. Kakani, K.R. Reddy, D. Zhao, A.R. Mohammed, Effects of ultraviolet-B radiation on cotton (*Gossypium hirsutum* L.) morphology and anatomy. Ann. Bot. **91**, 817–826 (2003)
134. G.I. Jenkins, B.A. Brown, UV-B perception and signal transduction, in *Light and plant development*, ed. by G.C. Whitlelam, K.J. Halliday (Blackwell Publishing, Oxford, 2007), pp. 155–182
135. I. Mewis, E. Glawischnig, M. Schreiner, C. Ulrichs, R. Zrenner, Eco-physiological consequences of UV-B on Brassicaceae—Impact on the co-evolutionary arms race between plants and their enemies in *International Chemical Ecology Conference* 19–23 Aug 2013, Melbourne, Australia, p. 116 (2013)
136. N.K. Clay, A.M. Adio, C. Denoux, G. Jander, F.M. Ausubel, Glucosinolate metabolites required for an Arabidopsis innate immune response. Science **323**, 95–101 (2009)
137. I. Mewis, H.M. Appel, A. Hom, R. Raina, J.C. Schultz, Major signaling pathways modulate Arabidopsis glucosinolate accumulation and response to both phloem-feeding and chewing insects. Plant Physiol. **138**, 1149–1162 (2005)
138. I. Mewis, J.G. Tokuhisa, J.C. Schultz, H.M. Appel, C. Ulrichs, J. Gershenzon, Gene expression and glucosinolate accumulation in *Arabidopsis thaliana* in response to generalist and specialist herbivores of different feeding guilds and the role of defense signaling pathways. Phytochemistry **67**, 2450–2462 (2006)
139. S. Textor, J. Gershenzon, Herbivore induction of the glucosinolate-myrosinase defense system: major trends, biochemical bases and ecological significance. Phytochem. Rev. **8**, 149–170 (2009)

140. F. Nadeau, A. Gaudreau, P. Angers, J. Arul, Changes in the level of glucosinolates in broccoli florets (*Brassica oleracea* var. *italic*) during storage following postharvest treatment with UV-C. Acta Hort. 145–148 (2012)
141. M. Olle, A. Virsilé, The effects of light-emitting diode lighting on greenhouse plant growth and quality. Agric. Food Sci. **22**, 223–234 (2013)
142. M. Schreiner, J. Martínez-Abaigar, J. Glaab, M.A.K. Jansen, UV-B Induced secondary plant metabolites-potential benefits for plant and human health. Optik & Photonik, **9**(2), 34–37 (2014)
143. Q. Li, C. Kubota, Effects of supplemental light quality on growth and phytochemicals of baby leaf lettuce. Environ. Exp. Bot. **67**, 59–64 (2009)

Chapter 15
Application of LEDs for UV-Curing

Christian Dreyer and Franziska Mildner

Abstract Curing resins by ultraviolet radiation from LEDs is an emerging field in a wide range of applications and offers many advantages compared to thermal polymerization, such as high reaction velocity, solvent-free formulations, low energy consumption, and the operation at ambient temperature. Due to additional benefits like the use of discrete wavelengths, lower heat emission, smaller dimensions, more flexible geometries and the comparatively very low power consumption, UV-LEDs were already proved as good alternatives for commonly used photocuring units based on established mercury-vapor bulbs. By individually adapting the interaction of chemicals, photoinitiators, formulation, and light source many distinct tailor-made polymer formulations are developed for coatings, inks, adhesives, composites, and stereolithography.

15.1 Introduction

Over the last decades UV radiation curing technology has become an evolving field in several applications especially in the coating industry [1]. Depending on the product, e.g., printing plates, optical disks, fiber coatings, and inks as well as adhesives and composites the required photocurable polymers should possess different features. Basically, during a curing reaction a liquid resin is transformed into a highly crosslinked polymer. Therefore, typically four basic components are necessary: (1) A photoinitiator (PI) being cleaved into a reactive species (radical or cation) by the absorption of ultraviolet light, (2) a functionalized oligomer which provides the backbone of the resulting polymer (3) a multifunctional component

C. Dreyer (✉) · F. Mildner
Fraunhofer-Einrichtung für Polymermaterialien und Composite PYCO, Kantstrasse 55, 14513 Teltow, Germany
e-mail: christian.dreyer@pyco.fraunhofer.de

F. Mildner
e-mail: franziska.mildner@pyco.fraunhofer.de

© Springer International Publishing Switzerland 2016

M. Kneissl and J. Rass (eds.), *III-Nitride Ultraviolet Emitters*,
Springer Series in Materials Science 227, DOI 10.1007/978-3-319-24100-5_15

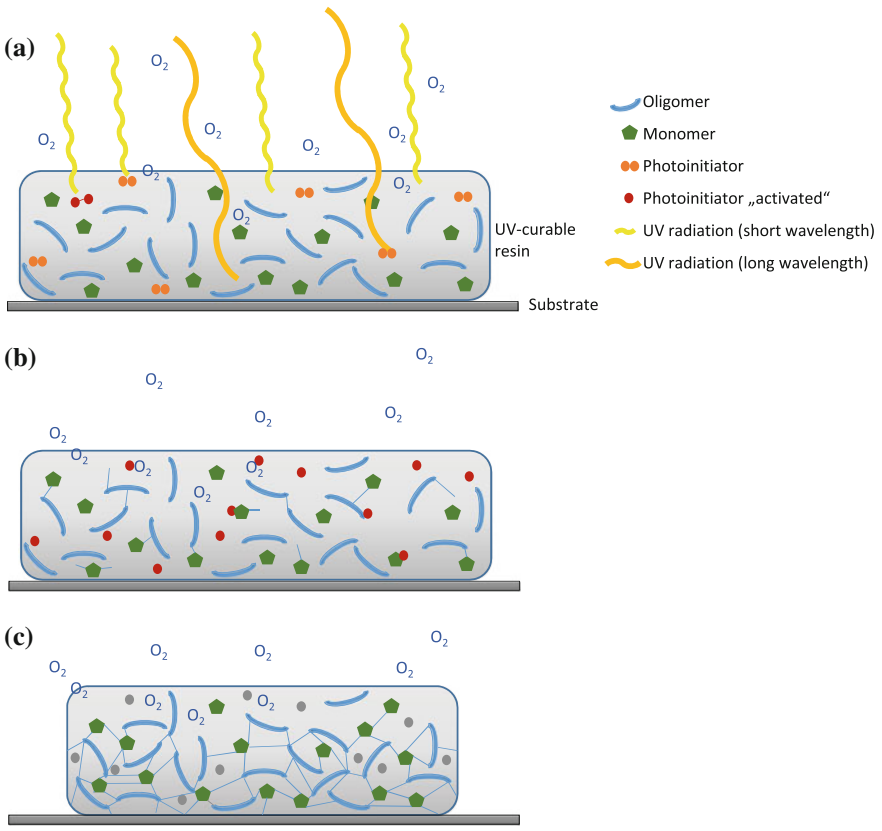


Fig. 15.1 Principle of radical UV-curing reactions. **a** Photoinitiator molecules are excited by the absorption of UV radiation leading to the formation of free radicals. The depth of light penetration depends on its wavelength: longer wavelengths are able to deeply penetrate the material. **b** Monomer and Oligomer molecules are attacked by the photoinitiator radicals and a polymerization is initiated. At the surface the process is inhibited by the presence of oxygen acting as a radical scavenger. **c** After the chemical reaction between the components is completed a cured resin is left. Owing to the formation of new bonds the polymer shrinks during the process. The quenching of initiator radicals by oxygen can result in an uncured "tacky" surface (*Source* Fraunhofer PYCO)

acting as a crosslinker to increase the network density and (4) a mono- or multi-functional monomer acting as a diluent during the reaction to control the viscosity of the mixture and being incorporated into the network afterwards (Fig. 15.1) [2].

Light-induced polymerization offers distinct advantages compared to thermal curing such as the high speed of the reaction, a solvent-free formulation, low energy consumption, and polymerization at ambient temperature. UV-curable formulations often show significantly longer shelf-lifes than thermally curable systems, as far as those are kept away from UV-light, which can be easily achieved by storing the resins in non UV-transparent containments. Despite these advantages a number of

aspects have to be considered when developing a new formulation for a distinct application and how they can affect the chemical and mechanical properties of the resulting material. In the following, some basics and applications of UV-curing in general and UV-LEDs in particular should give an insight into the technology of curing polymers by UV radiation.

15.2 Light Source

Apart from the chemical properties of the resin, the diluent monomer and potential additives, the light source and the corresponding photoinitiator (PI) play a key role providing the initial step of the polymerization process. Conventional light sources for UV-curing like pressure vapor lamps containing mercury or noble gases are emitting a broad multiple line spectrum. These types of lamps operate at very high temperatures and the major part of energy is wasted as heat (and visible light) which also reduces the lifespan of the bulb due to degradation. For an effective activation of the PI a huge overlap of its absorption spectrum with the emission spectrum of the light source is advantageous. Hence, a large amount of radiation is useless, if there is no absorption of the PI in this distinct wavelength range [3].

Moreover, the produced heat can have undesirable effects on the polymerization, up to thermal degradation of the polymer to be cured. However, the use of LEDs can overcome these disadvantages. The light emitted by these has a relatively narrow wavelength range which can be tailored for a distinct PI resulting in a maximum absorption. No overheating can occur because the absence of infrared radiation emission. This results in a long lifetime of the diode (adequate thermal management of the LED and the corresponding electronics assumed) and a low power consumption enabling the use of a battery power supply and the development of small mobile devices. For achieving a successful curing of photopolymers three main issues regarding the light source have to be taken into consideration: The wavelength of the light to reach an effective absorption by the PI, the irradiance, i.e., the power density of the radiation and the duration of light exposure on the specimen. For this reason, often not single LEDs are used for curing polymer resins but modules consisting of several of these light sources, as shown in Fig. 15.2.

The first generation of UV-LEDs showed only low irradiances leading to inadequate polymerization or required considerably longer exposure times [4–6] but recent developments are very promising. The group of Vandewalle et al. compared five LEDs with a halogen lamp for the curing of hybrid and microfilled composite resins at distances between 1 and 5 mm and irradiances between 598 and 1390 mW/cm^2 (at 1 mm). Although the LEDs differ among each other they generally provided similar or even better curing results than the halogen curing unit at a distance of 5 mm. Moreover, the divergence angle of the light was correlated to the degree of polymerization as indirectly proportional at longer distances (5 mm) [7]. All these studies were carried out with LEDs emitting light that is suitable for camphorquinone, a typical PI for the curing of dental materials with its maximum

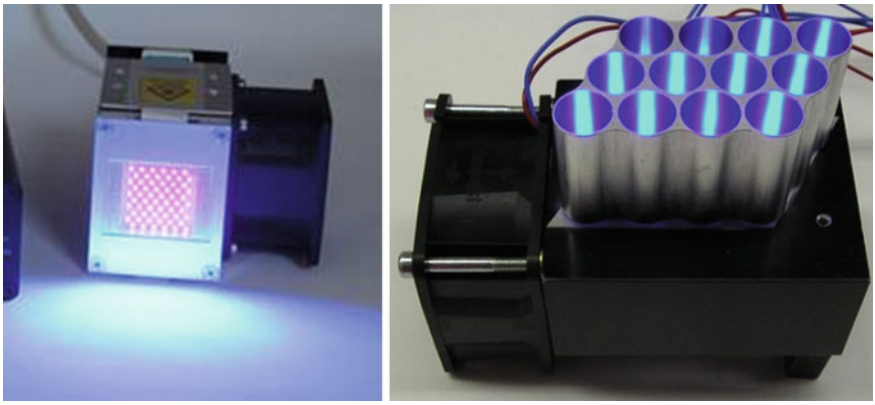


Fig. 15.2 Different UV-LED modules (pictures by courtesy of OSA Opto Light GmbH)

absorption band at about 470 nm, and hence already in the visible (blue) wavelength region.

The curing of acrylate formulations by commercial UV-LEDs in comparison to conventional light sources was examined by Neckers et al [8]. They tested the coating (film thickness: 100 μm) of wood, poly(carbonate), and a corrosion resistant metal paint (film thickness: 150 μm) cured by an H-bulb (emitting from 240 to 320 nm), a Xe-lamp as well as a 395 nm UV-LED module and a single 5-mm 395 nm UV-LED, having a lower output power. The fastest curing in all cases was achieved by the common H-bulb but the same degree of double bond conversion by the other light sources was reached at the latest after 20 s, even though with both the Xe-lamp and the UV-LED already 90 % of the maximum conversion was reached after 2 s. As expected the 5-mm LED underperformed in comparison to the others due to its lower irradiance output but converted nearly the same amount of double bonds as the H-bulb after 30 s. These results suggest the comparability of the UV-LED and the Xe-source which could also be seen in the material properties of the cured coatings: Both light sources resulted in a slightly tacky surface in the case of wood and poly(carbonate) coating but not for the pigmented anticorrosive metal paint. This tackiness results from an incomplete curing and has of course an effect on some material features associated with the degree of curing like the surface hardness. However, other properties like cross-hatch adhesion, solvent resistance, gloss, and abrasion resistance were the same depending on the type of substrate coated but not on the type of light source.

In summary, UV-LEDs are suggested as an acceptable alternative to conventional UV-light emitting sources [8, 9]. Another important factor in the choice of the light source is the thickness of the coating. Curing by radiation is only applicable to relatively thin layers. The curing process is initiated on the surface where the first reactive species are generated and in the following the polymerization starts which changes the viscosity of the mixture due to the increase of the molecular weight distribution of the oligomers, forming an unsoluble network when reaching

the gelation point. This inhibits the curing process and light of a longer wavelength is necessary that is able to penetrate the surface and leads to a complete curing. In principle, UV-LEDs are suitable for curing processes that are until now performed with common broad spectrum light sources but at least two wavelengths, one in the far UV for the initiation of the curing (and the surface curing) and one in the near UV for the deep curing, have to be emitted [10]. Furthermore the curing is influenced by the optical properties of the resin influencing the light absorption, e.g., shade, translucency, the type, and/or constitution of PI, filler particle types and sizes, pigments, and any kind of additive and their distribution, having influence on absorption, refractive index etc.

15.3 Chemistry and Mechanisms

Basically, a UV-curing reaction represents a chain polymerization consisting of three steps: initiation, propagation and termination. In the first step, a PI absorbs light and either a radical or a cation is formed depending on the type of polymerization. These species are able to attack reactive moieties of a monomer or an oligomer being transformed into reactive centers themselves. Repeating this propagation step leads to the formation of a polymer chain whose growth is terminated by any recombination of the present radicals as shown in Fig. 15.3.

To achieve a fast and effective curing, the choice of PI is important because of its responsibility for the initial step and the depth cure by its absorbance characteristics. These molecules should have ideally a large absorbance and a short lifetime to prevent quenching by oxygen or the diluent monomer especially for radical polymerization. The initiation rate (r) is a function of the absorbance (A) of the PI, the quantum yield of initiating species formation (θ), and the light intensity (I_0): $r = \theta I_0\left[1 - \exp^{(-A)}\right]$.

As can be seen by this formula the initiation rate can be increased by a higher light intensity or a higher absorbance. According to the Lambert-Beer law, the absorbance is directly proportional to the sample thickness, the initiator concentration, and its absorption coefficient [11]. For the curing of an acrylate system models do predict both, the existence and the location of the optimal photoinitiator concentration; the corresponding cure depth displayed good correlation with the experiment [12].

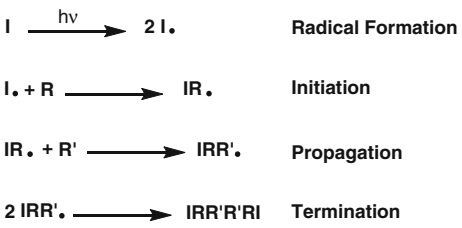


Fig. 15.3 Steps of a radical reaction (I initiator; R, R' organic side chain)

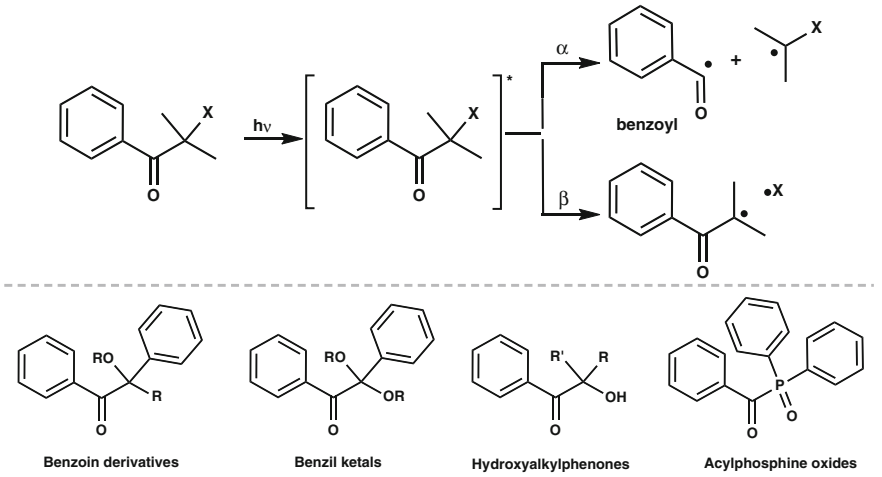


Fig. 15.4 Photocleavage of Type I initiators and examples [11, 15]

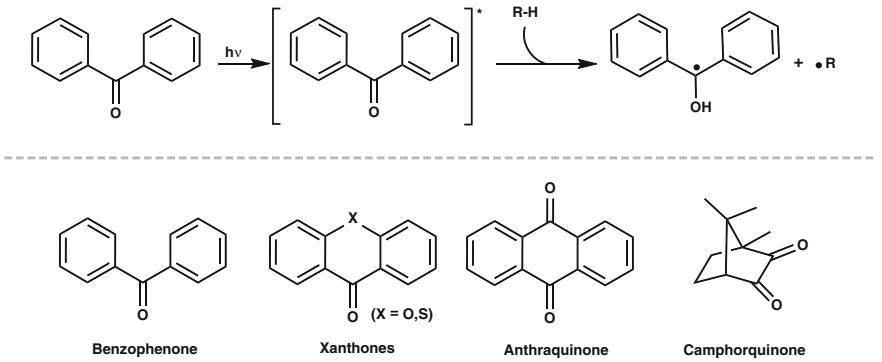


Fig. 15.5 Radical generation by hydrogen abstraction and examples for Type II initiators [11, 15]

The most common photoinitiators can be divided into three classes: The first type of PI forms radicals by simple photocleavage, i.e., aromatic keto compounds undergo a C–C bond cleavage when relaxing from the excited state and two radicals are formed. The fragmentation can occur in the α- or β-position as well. Most of them are based on the acetophenone (benzoyl) fragment (Fig. 15.4).

Radicals of the Type II originate indirectly from the PI. When the PI, e.g., a benzophenone derivative, is excited by light it splits hydrogen from a co-initiator and the latter becomes the actual initiator itself afterwards. As chromophores benzophenones, xanthones, benzils, etc. are utilized (Fig. 15.5). In many applications tertiary amines have become important co-synergists because of their great reactivity and ability to trap oxygen. However, the use of amines could also have adverse effects like yellowing of the polymer or reducing its hardness and gloss.

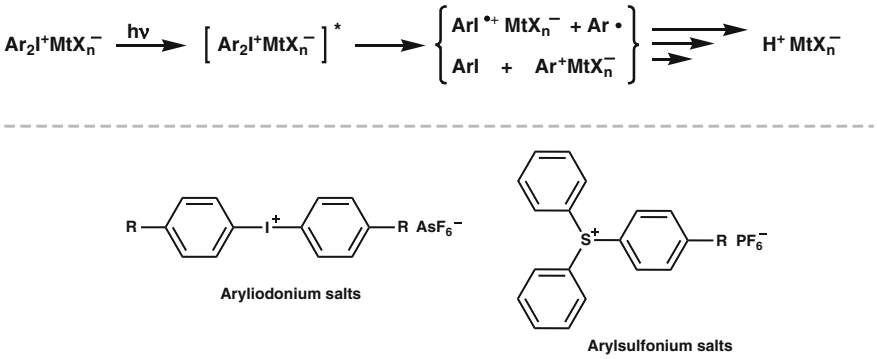


Fig. 15.6 Scheme for diaryliodonium salt decomposition and examples for cationic photoinitiators [14, 15]

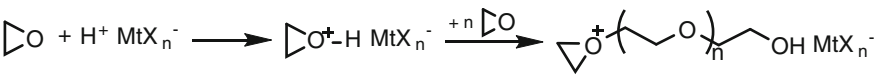


Fig. 15.7 Mechanism of the cationic polymerization of an epoxide monomer [14]

The third class contains initiators for cationic polymerizations represented by onium salts consisting of an organic cation, like diaryliodonium or triarylsulfonium, and an inorganic anion. In the presence of a hydrogen-donor protonic acids are generated in succession of their photolysis. Subsequently, these protons attack the functional groups of the monomers to induce a polymerization (Fig. 15.6).

While the cation is the photosensitive part and controls the absorptivity and the quantum yield, the anion determines the strength of the corresponding acid formed and therefore the reactivity of the propagation step. The initiator can be tuned, since the absorption band of the cation is variable by chemical modifications [13] and the acidity of the corresponding proton-donor is related to its size [14]. The monomer or oligomer is attacked by these protons to generate a cation able to attack another molecule (Fig. 15.7).

Radical photopolymerization is generally applied to multifunctional acrylates and light-induced cationic polymerization occur with monomers that are insensitive toward radicals like multifunctional epoxides and vinyl ethers, unsaturated polyesters, styrene, cyclic ethers, cyclic acetals, and lactones.

Radical reactions run very rapidly and guarantee a fast curing, while cationic curing is much slower. Nevertheless, cationic polymerization reactions have two distinct advantages: No inhibition of the polymerization process by oxygen and the curing continues even in the absence of light because cations do not recombine (so-called “dark reaction”) [15]. A brief overview of common types of monomers is given in Fig. 15.8.

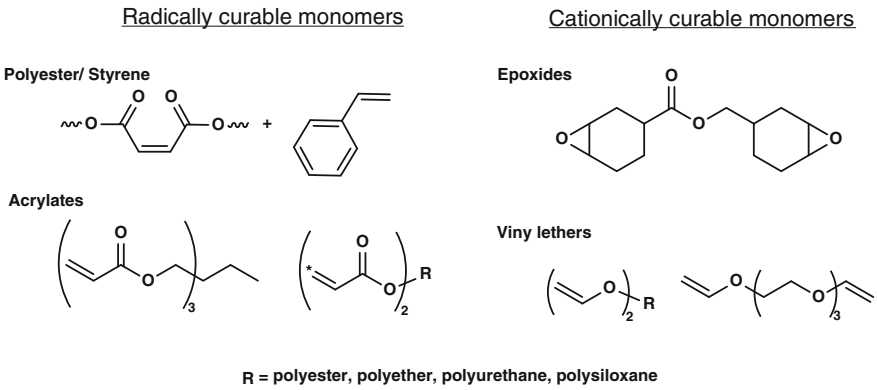


Fig. 15.8 Examples for different types of UV-curable monomers [11]

There are several approaches to overcome radical quenching by oxygen. The most common methods are the use of Type II PIs as mentioned above, other oxygen scavengers like triphenylphosphine [16] or to work under inert atmosphere, which is expensive. Recently, Studer and colleagues investigated a more cost-effective alternative for curing acrylates under carbon dioxide atmosphere showing the best conversion improvements for thin films [17, 18]. Physical methods are the addition of waxes [19] or covering the sample with transparent foils. The simplest way to overcome the inhibiting influence of oxygen is to increase the radiation-intensity. In this way, more radicals are formed which consume the oxygen molecules. After this induction period, the degree of curing rises and the surface is hardened building a sealant against further oxygen diffusion into the material. Additionally, the materials change in viscosity lowers the mobility of the oxygen being trapped in the sample.

Both polymerization processes can also be combined for the development of hybrid polymers, which can be realized by designing monomers having acrylate as well as vinyl-ether functions [20–22].

15.4 Kinetics

An important information, especially for industrial applications, is the rapidity of polymerization that can be estimated by kinetic measurements. With this data photocurable systems can be evaluated and compared to each other. Analytical methods are either based on the observation of the chemical conversion leading to a change in their spectroscopic properties (IR- or NMR-spectroscopy) or the monitoring of the samples physical properties like the heat evolved or the change in

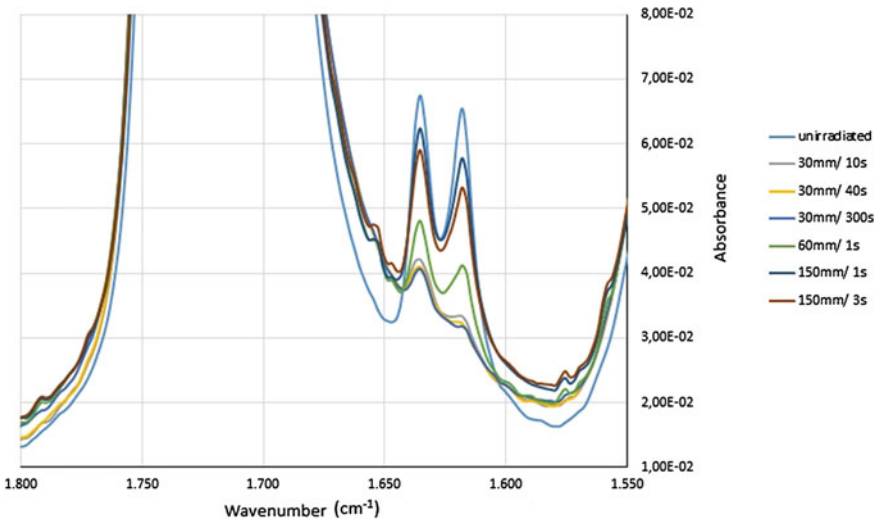


Fig. 15.9 Section of infrared spectra recorded of a pigmented resin cured by an UV-LED at 365 nm. The decrease of the double bond absorbance (absorption band 1600–1650 cm^{-1}) is shown at different distances of the light source (in millimeters) and after variable exposure times (in seconds)

viscosity or refractive index. Especially for ultrafast curing reactions of acrylates real-time infrared spectroscopy (RT-IR) is an appropriate method to follow the chemical reaction while getting qualitative and quantitative information as well. The progress of the curing is proportional to the disappearance of the functional group absorption band of double bonds (Fig. 15.9).

The amount of unreacted photoinitiator can be estimated by recording an UV-spectrum. Not only the optical properties of the PI are decisive for the reaction, but its amount as well. The more PI is added, the more radicals are formed which leads to a high speed of curing. In contrast, an excessive amount of initiator can have an adverse effect: In presence of many radicals the probability of a recombination rises resulting only in a short kinetic chain length (KCL). Due to high crosslinking more effective curing develops with long chains and the mechanical properties are influenced. Furthermore, unreacted PI can have a negative effect on the optical features of the polymer and its migration to the surface poses a risk due to toxicity [23]. The speed of the reaction naturally also depends on the resins formulation. It is composed in view to the specific application. A general overview of a coating composition and its functional parts is given in Table 15.1 [24].

Table 15.1 General composition of coatings for UV-curing [24]

Component	Amount (wt%)	Function
Oligomers	25–90	Basic film properties, film forming
Monomers (reactive diluents)	0–60	Viscosity adjustment, film forming
Photoinitiator	1–10	Initiation of curing process
Pigments, fillers	0–60	Improved mechanical properties, coloration, refractive index tuning, hardness improvement, scratch/abrasion resistance enhancement, improvement of flame retardancy, cost reduction
Additives	0–3	Processing behavior and film appearance

15.5 Medical Applications

The use of UV-LED technique as a substituent for common light curing units for dental applications is well established and a research field of high interest [5–7]. As mentioned before, the irradiance of the LED units has significantly improved over the last decade, leading to effective curing results and good mechanical properties [25]. As an initiator for dental resins most often camphorquinone (CQ) is used with an amine (A) as co-initiating agent [26]. To achieve an effective adhesion between enamel and dentin a self-etching primer is required differing in the absorption maximum. In this case, LEDs with two emission wavelengths are needed otherwise underperforming of a LED against halogen curing units is caused. This was shown by the effects on the shear bond strength of several cured dentin bond agents [27]. Apart from the light source the initiating system has also several disadvantages: The oxidation of amine impurities appearing as yellowing, the lowering of amine-reactivity due to protonation in the acidic aqueous medium in presence of a primer and the interaction of both partners is strongly affected by the viscosity of the system. Therefore, alternatives were investigated but only bisacylphosphine oxides (BAPOs) are applied until now [28]. Recently, benzoylalkylgermanes were suggested as PIs in dental composites. They were prepared in a simple two-step synthesis in good yields and showed very high extinction coefficients up to 7240 dm^2 mol^{-1} (CQ: 380 dm^2 mol^{-1}) at 468 nm wavelength. The polymers of a dimethacrylate composite containing several inorganic fillers were only slightly water soluble and low cytotoxic and showed a shelf time of about 4 years at room temperature. In particular, one of these germanium initiators containing alkyl and methoxy moieties shows the potential to increase the curing depth and decrease the curing time of the composites [29]. Dental fillings require the curing of thick layers up to several millimeters. For this purpose an initiator is beneficial that undergoes photodecomposition, the so-called “photobleaching”, leading to photolysis products showing a variant absorption behavior. If these products are more transparent than the initial PI, the light intensity in the underlying layers is higher which should lead

to an enhanced curing, especially for the use of LEDs as light curing unit emitting nearly monochromatic radiation. The photobleaching of a CQ/amine initiator for the curing of 3 mm thick specimens of an acrylate mixture containing Bisphenol A diglycidyl ether dimethacrylate and triethylene glycol dimethacrylate by a 470 nm LED (intensity: 30, 75, and 140 mW) was investigated. Since the photobleaching rate was much slower than the fast network formation of the dimethacrylates only a fifth of the initiator amount was consumed until the polymerization was nearly terminated. The rate constant for the initiators decay was proportional to the irradiation intensity but the decomposition was spatially extremely inhomogeneous [30]. From a chemical point of view, polymerization is equivalent to the formation of many covalent bonds, i.e., the previously loose monomers get into close proximity. Therefore, a free volume is generated and the material shrinks during the reaction which negatively effects the abrasive stability, causes internal stress (up to 7 MPa) [31] and can lead to secondary caries or breakage of the restorative material. New chemically modified monomers based on multifunctional methacrylates, thiol–enes, or hybrid composites were developed to reduce shrinkage [24, 32, 33]. The simplest way to reduce shrinkage is to enlarge the amount of (inorganic) filler added to dental composites in order to adjust its optical and mechanical properties, i.e., the improvement of abrasion, esthetics, and radiopacity. Usually inorganic particles like silica are used for this purpose having the positive side effect of increasing the curing rate by light scattering. A high compatibility between the filler and the resin is necessary for ideal mechanical properties of the composite that should mimic the dental material. Most commonly used examples are materials that provide a cavity for the resin monomers in order to get an extensive interpenetrating polymer network. Apart from macro- and micro-scale fillers, especially in the last decade, nanoscaled fillers got in the focus of research, bearing a characteristic high specific surface. They range from isolated discrete particles from 5 to 100 nm to fused aggregates with clusters exceeding 100 nm. For the formulation of a composite clusters seem to be favorable since the content of discrete nano-particles is limited by its effect on increasing the viscosity to a higher extent [24, 34]. Silanized nanosilica and porous silanized diatomite added as co-fillers (ratio: 40/60 % wt/wt) enhanced the mechanical strength, elastic modulus, and microhardness of a common methacrylate mixture cured by a LED light source. Moreover, TiO_2-particles in the range of 300–400 nm (0.5 wt%) tuned the visual appearance of the samples by a clear discoloration and additional mechanical strength [35]. Furthermore, the addition of distinct fillers results in medical benefits by promoting remineralization or inhibiting bacterial growth [33]. Inorganic antibacterial agents have proved to be superior to organic ones due to the higher heat resistance, lower surface migration tendency, and lower toxicity. To overcome their poor dispersion and unsatisfying color stability, Ag nanocrystals functionalized with oleic acid were introduced into an acrylate matrix. Thus, a good dispersion of the nanoparticles in organics resulted and consequently smaller amounts of silver were necessary which has a positive effect on the restoration shade. Up to 50 ppm weight the mechanical properties were improved and decreased at higher amounts like the shade as well. In contrast, the antibacterial performance rises with the amount of silver nanocrystals. Hence, a

balance between the mechanical, optical, and antibacterial features has to be found [36].

New light curable resins for medical applications have to be nonhazardous to the patient with regard to the chemicals used [37–39] as well as the curing process itself, in particular the light source. To ensure an adequate depth of cure a powerful light source is needed that can result in an undesired heating of the tooth and the pulp. Therefore, LEDs with a lower temperature increase can minimize the potential harm in comparison to halogen-light curing units [40]. Cells exposed to different dentin-bonding agents either cured by a quartz tungsten halogen lamp or a LED showed a higher survival rate for the latter. Although the experiments were performed ex vivo they clearly correlate light source and cytotoxicity [41].

An emerging field of research is the development of tissue adhesives promoting wound healing and reducing the risk of an infection. Until now there are two main classes of adhesives for biomedical applications. The first one is represented by synthetic formulations like cyanoacrylate reacting very fast but causes inflammation in direct contact to the cell. The second is based on biological substances, such as fibrin, gelatin, collagen, polysaccharides, or biomimetics, all showing a better biocompatibility but a faster degradation as well as a lower adhesion than the artificial ones. It has to be found a compromise between adhesion strength and biocompatibility. Dextran, a glucose polymer that is already applied as plasma volume expander or wound cleansing and healing agent, was investigated as an alternative to common bioadhesives. It has already been intensively studied in tissue engineering because of its low cell-adhesive nature, its ability to form hydrogels via crosslinking and excellent biocompatibility and degradability. In order to overcome its insufficient mechanical properties and the long gelation times, several chemically modified dextrans were tested as potential bioadhesives. The partial functionalization of its abundant hydroxyl moieties with 2-isocyanatoethyl methacrylate in different amounts led to a polyurethane derivative with polymerizable double bonds. In all cases the specimen were irradiated with 30 mW/cm^2 to balance a rapid polymerization and low cell damage. After 5 min of irraditation a double-bond conversion of about 80 % was achieved. The UV-photo crosslinked polymer exhibited an enhanced adhesion strength in comparison to commercially available fibrin adhesives but still lower than cyanoacrylate [42]. In a further step, a hybrid network with the inexpensive gelatin was formed leading to an improved adhesive strength and cytotoxic results [43]. 2 Hydroxyethyl methacrylate (HEMA) turned out to be a monomer less harmful than any other reagent. The urethane methacrylated dextran was polymerized with this monomer which promoted the properties of the initial dextran derivative significantly. The adhesion strength could be raised up to 4.33 MPa, which is 86 times higher than a commercially available fibrin adhesive. Interestingly, the double bond conversion rate of gels containing dextrans was nearly 100 % after 5 min, which was greater than neat HEMA gels, but it decreased with increase of acrylate-concentration. This may be attributed to the higher gel-viscosity of the samples containing dextran, hindering a fast radical recombination. Unfortunately, the swelling-ratio of all dextran hydrogel derivatives studied is still excessively high and has to be improved [44].

15.6 Coatings, Inks, and Printing

Especially in the coating and printing industry UV-curing prevailed because of its striking advantages, i.e., saving time and money. The usage of UV-LEDs increases the efficiency of this method especially in industrial applications like in inkjet-printing applications (see Fig. 15.10). First of all UV-LEDs have a long lifetime and lack a warm-up period and the waste of electrical energy for a standby mode. The narrow emission band and the low amount of waste heat allows printing also on heat sensitive materials widening the range of applications. In terms of safety the low heat emission is important and for UV-A or UV-B LEDs no ozone is formed as a side product.

Despite the large number of beneficial aspects of UV-LEDs, there are still limitations to their use that have to be overcome. The UV ink and coating formulation respectively has to be chemically adjusted to the relatively narrow peaks to achieve the same curing rates. Usually inks and coatings are based on the fast curing acrylates applied in thin layers. In this case, oxygen inhibition has an even stronger influence on the polymerization due to the large surface-to-volume ratio. For this purpose, radical scavengers have to be added or short wavelength radiation has to be used to achieve a fast and effective curing of the surface acting as a shielding against oxygen afterwards. The most expensive possibility is an inert atmosphere that mostly requires a more complicated process setup [45]. Recently, the influence of oxygen during the thermal post-curing reaction (in the absence of light) was investigated. Hexanedioldiacrylate (HDDA) was inkjet-printed on a silicon wafer and cured by an array of 18 LEDs emitting at 365 nm. Atmospheric oxygen had a distinctive effect on the photocuring and the crosslinking occurring with or without the exposure to light. The amount of oxygen that is absorbed during the printing process was already sufficient to have obvious negative effects on the curing rate, even when the reaction itself was performed under inert gas [46].

As an alternative cationic polymerization can be considered. Its high degree of conversion, low tendency to migration, lower volume shrinkage, and good adhesion

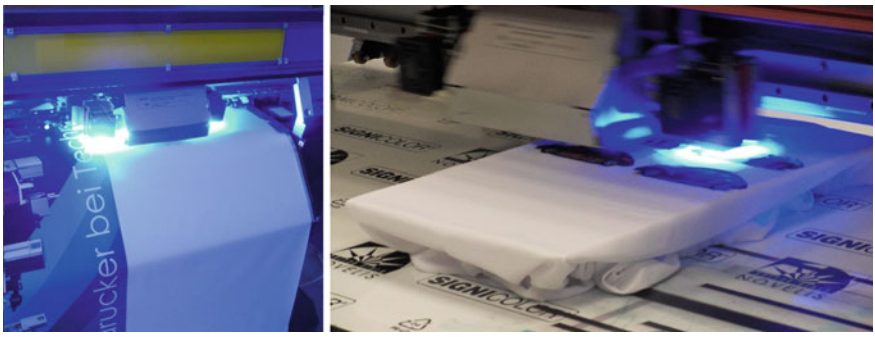


Fig. 15.10 Digital-printer with UV-LED printhead applicable for various materials, e.g., for plastic-films, fabrics, and bulk plastic sheets (pictures by courtesy of TECHNOPLOT CAD Vertriebs GmbH)

properties provide excellent conditions for the application in ink-jet printing. Although cationic polymerization is regarded as slow, strong progress has been made by the modification of the monomers or the formulation in general [14]. The design of low viscosity epoxy resins lead to formulations for solder resists of printed circuit boards (PCB) fabricated by ink-jet printing. Via a nozzle drops of a polymer solution are deposited on a surface followed by a photocuring process. The resolution limit of the method is determined by the droplets' size (approx. 10 μm) [47] which is important due to the miniaturization in electronics. For a good result this technology requires a low viscosity (<60 mPa s) and short curing times (<1 min). The universal epoxy resin E51, based on Bisphenol A, was modified with polyethylene glycols (PEG) of different molecular weight to diminish the viscosity. The mixture with 10 % of PI was applied to either polyimide or polyethylene terephthalate and irradiated by an UV source at 350 nm (1 W cm^{-2}). A ratio of epoxy groups to hydroxyl groups of 2:1 resulted in decrease of viscosity value to 568 mPa s with PEG200. A further increase in hydroxyl moieties is not advantageous since it can lead to a chain entanglement of the flexible aliphatic chains and an increase in viscosity except from the incomplete curing. It turned out, that the addition of active diluent ethylene glycol diglycidyl ether (EDGE) in an amount of 30 % resulted in a viscosity of 60 mPa s needed for the application. Owing to the chemical structure of EDGE with a short main chain, the crosslinking is enhanced which is associated with a brittle, inflexible product. After 40 s the curing rate of the ideal formulation was already beyond 90 % and after 50 s it was completely cured, exhibiting excellent mechanical properties [48]. Inkjet-printing is nowadays an established technique in the production of plastic electronics as polymer transistor circuits and organic LEDs [47].

Apart from this direct writing method UV nanoimprint lithography (UV-NIL) is commonly used for patterning surfaces. For this printing technique a mould is pressed against a resin that is cured by irradiation afterwards and takes the negative form of it [49, 50]. Thereby structures with horizontal resolutions of 5 nm and below can be realized to fabricate substrates for cell or bacterial growth or nonlinear optics, electronic, microfluidic, or semiconductor devices. The most widespread application in polymer patterning is represented by photolithography. In this very cost- effective method, a photoresist is irradiated trough a mask that determines the cured spots. Afterwards, excess uncured resin can be removed. The resolution of this technique ranges from micrometers to sub-100 nm but can be improved by advanced material formulations or lithographic optical practices and short wavelengths of irradiation. Examples of using these patterns are the semiconductor industry, LED production, liquid crystal displays (LCDs), photonic crystals, data storage devices, or microarrays for biological purposes. Introducing hydrogels like polymerized poly(ethylene glycol) diacrylate (PEGDA) for photolithography is useful to provide cavities for cells to localize and manipulate them in a microenvironment and to mimicry in vivo conditions to study the interaction of cells or cells and a certain substrate [47] as well as manufacturing scaffolds for tissue engineering [51]. To further simplify the patterning of polymer surfaces the technique of self-wrinkling can be applied. Until now, there are top-down as well as bottom-up

methods known for micro-folding resulting in a matte surface coating. In the top-down method a photocurable resin is irradiated by high energy photons leading only to a top cured polymer film swimming on the uncured material. After the wrinkling process the patterned polymer is fixed by a second post-curing step initiated by radiation of a longer wavelength [52, 53]. The inverse bottom-up approach starts with the curing of the resins' bottom layer by low energy photons. The oxygen present prevents a thin layer on the top from curing and the residual uncured monomers induce swelling of the underlying crosslinked polymer when diffusing into underlying layers. Due to this in-plane stress wrinkles are formed in only one step leading to well-defined patterns whose wrinkle wavelength and amplitude can be easily modified by tuning the photoinitiator as well as the oxygen concentration [54].

The greatest strength of thermoset polymers in general is their potential to be adjustable to many applications since there are a lot of factors that can be influenced during the process to get a "tailor-made" product. Formulations for printing or coating often contain a significant amount of pigments and/or additives for optical and mechanical modifications. Highly resistant polymer nanocomposites containing small amounts (3 wt%) of organophilic tuned clay particles, were developed. Previous studies have already proved, that the clay dispersion is important for the rate of curing [55] so nanoparticles should ensure this. Both, the curing of an acrylate composite by free radical polymerization and an epoxide composite polymerized by a cationic initiator were not affected by the presence of the inorganic filler. Layers of a few millimeters could be cured within seconds by UV-light that, in contrast to thermal curing, does not lead to thermal degradation of organic salts contained, necessary for the compatibility of the nanoparticles. The nanocomposites made the epoxide more flexible and impact-resistant but the acrylates' viscoelastic properties were not influenced. In both cases, a mattening effect occurred being desirable for some coatings and the layers were resistant against solvents, moisture, weathering, and scratching, making them especially suitable for outdoor applications [56].

The curing of thick samples is an important topic for pipe systems. Composite pipes have become important substituents for metal pipes due to their light weight and their resistance against environmental influences [57]. In this field the rehabilitation of sewers is of great economic importance since large amounts of water are lost because of damaged pipes. In the last two decades, the usage of UV-light for curing composite sewage pipe lining systems has become very important since it allows an enormous acceleration of the process in contrast to thermal curing, as well as a trenchless rehabilitation. Especially, in small diameter pipes UV-LED radiation would be advantageous, since they have smaller geometries and there is no damage of the material due to a hot light source [58].

15.7 Stereolithography

UV-curing is also applied in stereolithography. It is a solid freeform fabrication (SFF) technique which allows the rapid prototyping (RP) of three-dimensional structures. On the basis of the Cartesian coordinates the object is sliced into layers and builds up by the stepwise layer-by-layer deposition of resin cured by UV radiation, followed by a post-curing process to fully polymerize the finished workpiece. In each step, the depth of cure should be slightly larger than the platform height of the (new) resin layer to ensure a good chemical and mechanical adhesion of the new layer to the previous. Usually, the slices range from 25 to 100 μm and are used to manufacture objects from micron-size up to several cubic centimeters with corresponding resolutions from submicron to several micrometers [59]. If nonlinear optics is used for curing like two-photon polymerization the resolution can be increased to sub-100 nm [60, 61]. Most commonly acrylates and/or epoxies of low molecular weight are used for stereolithography giving rigid and glassy products because they are highly crosslinked but also elastomeric-based structures were already presented. In contrast to other SFF techniques just as 3D printing or plotting, stereo-lithography is limited to the use of one resin. Although the use of different resins is in principle possible in stereolithography it requires an advanced setup and elongates the process because of additional rinsing steps etc. In general, this technique allows a bottom-up and a top-down process. In the bottom-up process, the uncured layer is applied and irradiated from above growing upwards. In contrast, in the top-down process the structure part already cured is dipped in a vessel containing the resin. The bottom of the vessel is formed by a transparent plate allowing the radiation to penetrate the sample from below. This method has some advantages in comparison to the bottom-up system such as lower amounts of resin are needed, the surface is always smooth and protected against oxygen and no recoating is necessary. By introducing dynamic mask projectors like a digital mirror device (DMD) or LC displays a complete layer can be cured at once (Fig. 15.11) [62].

Stereolithography is ideal for the rapid manufacturing of small quantities or tailor-made solutions like prototypes in the automotive industry, jewellery, surgical tools, or implants. In the latter case, data from magnetic resonance imaging (MRI) or tomography data of a patient is sufficient to produce a hearing-aid or bone-implant perfectly fitting. In tissue-engineering scaffolds for cell-adhesion and -growth made by stereolithography have gained attention [59] and it is also an emerging field in forensic sciences [63]. Although UV-LED light sources have already been proven as feasible for stereolithographic systems having higher part fabrication efficiency and accuracy, there are still some challenges in their technical implementation. On the one hand the vibration of the focusing lens caused by an increase of scan-speed leads to obvious effects on the accuracy [64, 65]. On the other hand errors occur if a mechanical scanning workbench is used. Due to its kinematic behavior the scanning speed is not constant but changes if the scanner accelerates or decelerates during a line curing. Therefore, the light exposure differs in the distinct areas leading to a so-called bone-shape error, i.e., the beginning and

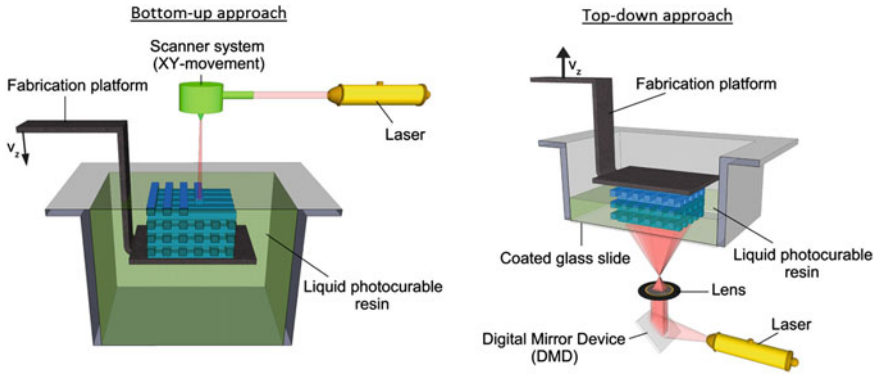


Fig. 15.11 Different setups for stereolithography. *Left* Bottom-up approach with scanning laser for the *x-y* movement of the curing light beam. *Right* Top-down system with a digital mirror device (DMD) as light projector [62]

the end of the cured line are larger than the middle part. Studies revealed that light-switching or power-matching methods for scanning are suitable to improve the accuracy of the final polymer. In the first case, the distance to the scanner is varied and in the latter case the scanning speed is adjusted fitting the beam power [66].

15.8 Conclusion and Outlook

The curing process of various resins by UV radiation is already a well-established technique not least because of its rapid implementation and lower power consumption in comparison to other curing techniques, e.g., thermal curing. This effectiveness can be further improved by using UV-LEDs which require significantly less power and show longer lifetimes than common bulbs. Moreover, their smaller and more compact geometries as well as their low heat emission open up completely new applications. Until now the potential of UV-LEDs was already proven inter alia in the field of dentistry, medicine, coating, printing, and lithography. But there are still challenges that have to be overcome. Further research activities have to focus on the development of LEDs with short wavelengths and high power output. From the chemical point of view the formulation as well as the photoinitiators have to be tailored to the narrow wavelength emitters and the specific application. Especially, the curing of thick layers by LED light is difficult because two wavelengths are needed: A shorter one for the surface curing and radiation of a longer wavelength being able to deeply penetrate the material. However, the application of UV-LEDs for curing will be an emerging field of interest in the future due to their numerous advantages and special features.

References

1. B. Strehmel, Photopolymere in der Industrie. Nachr. Chem. **64**, 128–133 (2014)
2. A. Endruweit, M.S. Johnson, Curing of composite components by ultraviolet radiation: A review. Polym. Compos. **27**,119–128 (2006)
3. J. Kindernay, A. Blažková, J. Rudá et al., Effect of UV light source intensity and spectral distribution on the photopolymerisation reactions of a multifunctional acrylated monomer. J. Photochem. Photobiol. A **151**, 229–236 (2002)
4. A. Uhl, R.W. Mills, R.W. Vowles et al., Knoop hardness depth profiles and compressive strength of selected dental composites polymerized with halogen and LED light curing technologies. J. Biomed. Mater. Res. **63**, 729–738 (2002)
5. D.L. Leonard, D.G. Charlton, H.W. Roberts et al., Polymerization efficiency of LED curing lights. J. Esthet. Restor. Dent. **14**, 286–295 (2002)
6. C. Kurachi, A.M. Tuboy, D.V. Magalhães et al., Hardness evaluation of a dental composite polymerized with experimental LED-based devices. Dent. Mater. **17**, 309–317 (2001)
7. K.S. Vandewalle, H.W. Roberts, J.L. Nadrus et al., Effect of light dispersion of LED curing lights on resin composite polymerization. J. Esthet. Restor. Dent. **17**, 244–255 (2005)
8. D.C. Neckers, A.V. Fedorov, K.C. Anayaogu et al., Performance of the light emitting diodes versus conventional light sources in the UV light cured formulations. J. Appl. Polym. Sci. **105**, 803–808 (2007)
9. S.L. McDermott, J.E. Walsh, R.G. Howard, A comparison of the emission characteristics of UV-LEDs and fluorescent lamps for polymerization applications. Opt. Laser Technol. **40**, 487–493 (2007)
10. Strehmel B (2013) Akzente durch Licht und Polymere- Photopolymere als ökologische und rationelle Produktionsverfahren für zahlreiche industrielle Anwendungen. CHEManager 6/2013
11. C. Decker, Photoinitiated curing of multifunctional monomers. Acta Polym. **45**, 333–347 (1994)
12. J.H. Lee, R.K. Prud'homme, I.A. Aksay, Cure depth in photopolymerization: Experiments and theory. J. Mater. Res. **16**, 3536–3544 (2001)
13. J. Ortyl, R. Popielarz, New photoinitiators for cationic polymerization. Polimery **57**, 510–517 (2012)
14. J.V. Crivello, M. Sangermano, N. Razza Cationic UV-curing: Technology and applications. Macromol. Mater. Eng. (2014), doi:10.1002/mame.201300349
15. N.S. Allen, Photoinitiators for UV and visible curing of coatings: Mechanisms and properties. J. Photochem. Photobiol. A **100**, 101–107 (1996)
16. C. Belon, X. Allonas, C. Croutxé-Barghorn et al., Overcoming the oxygen inhibition in the photopolymerization of acrylates: A study of the beneficial effects of triphenylphosphine. J. Polym. Sci. Part A: Polym. Chem. **48**, 2462–2469 (2010)
17. K. Studer, C. Decker, E. Beck et al., Overcoming oxygen inhibition in UV-curing of acrylate coatings by carbon dioxide inerting, Part I. Prog. Org. Coat. **48**, 92–100 (2003)
18. K. Studer, C. Decker, E. Beck et al., Overcoming oxygen inhibition in UV-curing of acrylate coatings by carbon dioxide inerting, Part II. Prog. Org. Coat. **48**, 101–111 (2003)
19. D.A. Bolon, K.K. Webb, Barrier coats versus inert atmospheres. The elimination of oxygen inhibition in free-radical polymerizations. J. Appl. Polym. Sci. **22**, 2543–2551 (1978)
20. C. Decker, The use of UV irradiation in polymerization. Polym. Int. **45**, 133–141 (1998)
21. C. Decker, T. Nguyen Thi Viet, D. Decker et al., UV-radiation curing of acrylate/epoxide systems. Polymer **42**, 5531–5541 (2001)
22. J.R. Nowers, J.A. Constanzo, B. Narasimhan, Structure-property relationships in acrylate/epoxy interpenetrating polymer networks: Effects of the reaction sequence and composition. J. Appl. Polym. Sci. **104**, 891–901 (2007)
23. C. Decker, Kinetic study and new applications of UV radiation curing. Macromol. Rapid Commun. **23**, 1067–1093 (2002)

24. X. Allonas, C. Croutxé-Barghorn, K.W. Bögl, N. Helle et al., *Radiation Chemistry. Ullmann's Encyclopedia of Industrial Chemistry* (2012), doi:10.1002/14356007.a22_471.pub2
25. F. Stahl, A.A. Ashworth, K.D. Jandt et al., Light-emitting diode (LED) polymerisation of dental composites: flexural properties and polymerization potential. Biomaterials **21**, 1379–1385 (2000)
26. J.W. Stansbury, Curing dental resins and composites by photopolymerization. J. Esthet. Dent. **12**, 300–308 (2000)
27. S.Y. Kim, I.B. Lee, B.H. Cho et al., Curing effectiveness of a light emitting diode on dentin bonding agents. J. Biomed. Mater. Res. **77B**, 164–170 (2006)
28. G. Ullrich, B. Ganster, U. Salz et al., Photoinitiators with functional groups. IX. Hydrophilic bisacylphosphine oxides for acidic aqueous formulations. J. Polym. Sci. A Polym. Chem. **44**, 1686–1700 (2006)
29. N. Moszner, F. Zeuner, I. Lamparth et al., Benzoylgermanium derivatives as novel visible-light photoinitiators for dental composites. Macromol. Mat. Eng. **294**, 877–886 (2009)
30. C. Vallo, S. Asmussen, G. Arenas et al., Photoinitiation rate profiles during polymerization of a dimethacrylate-based resin photoinitiated with camphorquinone/amine. Influence of an initiator photobleaching rate. Eur. Polym. J. **45**, 515–522 (2009)
31. K. Karthick, K. Sivakumar, P. Geetha et al., Polymerization shrinkage of composites—A review. J. Indian Acad. Dent. Spec. **2**, 32–36 (2011)
32. C.M. Chung, J.G. Kim, M.S. Kim et al., Development of a new photocurable composite resin with reduced curing shrinkage. Dent. Mater. **18**, 174–178 (2002)
33. J.G. Kim, C.M. Chung, Trifunctional methacrylate monomers and their photocured composites with reduced curing shrinkage, water sorption, and water solubility. Biomaterials **24**, 3845–3851 (2003)
34. C.N. Bowman, N.B. Cramer, J.W. Stansbury, Recent advances and developments in composite dental restorative materials. J. Dent. Res. **90**, 402–416 (2011)
35. H. Wang, X. Miao, M. Zhu et al., Synthesis of dental resins using diatomite and nano-sized SiO_2 and TiO_2. Prog. Nat. Sci. **22**, 94–99 (2012)
36. M. Zhu, F. Liu, R. Wang et al., Novel Ag nanocrystals based dental resin composites with enhanced mechanical and antibacterial properties. Prog. Nat. Sci. **23**, 573–578 (2013)
37. H. Schweikl, Die biologische Wirkung von Monomeren zahnärztlicher Komposite: Charakterisierung induzierter Genmutationen in vitro und molekulare Analyse HPRT-defizienter V79-Zellen. Dissertation, University of Regensburg (1997)
38. H. Schweikl, G. Spagnuolo, G. Schmalz, Genetic and cellular toxicology of dental resin monomers. J. Dent. Res. **85**, 870–877 (2006)
39. M. Goldberg, In vitro and in vivo studies on the toxicity of dental resin components: A review. Clin. Oral. Invest. **12**, 1–8 (2008)
40. A. Uhl, R.W. Mills, K.D. Jandt, Polymerization and light-induced heat of dental composites cured with LED and halogen technology. Biomaterials **24**, 1809–1820 (2003)
41. G. Ergün, F. Eğilmez, M.B. Üctaşli et al., Effect of light curing type on cytotoxicity of dentine-bonding agents. Int. Endod. J. **40**, 216–223 (2007)
42. D. Yang, H. Li, R. Niu et al., Photocrosslinkable tissue adhesives based on dextrans. Carbohydr. Polym. **86**, 1578–1585 (2011)
43. D. Yang, T. Wang, J. Nie, Dextran and gelatin based photocrosslinkable tissue adhesive. Carbohydr. Polym. **90**, 1428–1436 (2012)
44. D. Yang, T. Wang, X. Mu et al., The photocrosslinkable tissue adhesive based on copolymeric dextran/HEMA. Carbohydr. Polym. **91**, 1423–1431 (2013)
45. M. Beck, UV-LED lamps: A viable alternative for UV inkjet applications. Radtech Rep November/December 39–45 (2009)
46. R. Chartoff, M. Pilkenton, J. Lewman, Effect of oxygen on the crosslinking and mechanical properties of a thermoset formed by free-radical photocuring. J. Appl. Polym. Sci. **119**, 2359–2370 (2011)
47. E. Kumacheva, Z. Nie, Patterning surfaces with functional polymers. Nat. Mater. **7**, 277–290 (2008)

48. Z.G. Yang, C. Yang, Synthesis of low viscosity, fast UV curing solder resist based on epoxy resin for ink-jet printing. J. Appl. Polym. Sci. **129**, 187–192 (2013)
49. S. Zankovych, T. Hoffmann, J. Seekamp et al., Nanoimprint lithography: Challenges and prospects. Nanotechnology **12**, 91–95 (2001)
50. C.C. Wu, S.L. Hsu, W.C. Liao, A photo-polymerization resist for UV nanoimprint lithography. Microelectron. Eng. **86**, 325–329 (2009)
51. I. Vasiev, A.I.M. Greer, A.Z. Khokhar et al., Self-folding nano- and micropatterned hydrogel tissue engineering scaffolds by single step photolithographic process. Microelectron. Eng. **108**, 76–81 (2013)
52. R. Schubert, T. Scherzer, M. Hinkefuss et al., VUV-induced micro-folding of acrylate-based coatings 1. Real-time methods for the determination of the micro-folding kinetics. Surf. Coat. Technol. **203**, 1844–1849 (2009)
53. R. Schubert, F. Frost, M. Hinkefuss et al., VUV-induced micro-folding of acrylate-based coatings 2. Characterization of surface properties. Surf. Coat. Technol. **203**, 3734–3740 (Corrigendum: Surf. Coat. Technol. **204**, 748) (2009)
54. A.J. Crosby, D. Chandra, Self-wrinkling of UV-cured polymer films. Adv. Mater. **23**, 3441–3445 (2011)
55. V. Landry, B. Riedl, P. Blanchet, Nanoclay dispersion effects on UV coatings curing. Prog. Org. Coat. **62**, 400–408 (2008)
56. C. Decker, L. Keller, K. Zahouily et al., Synthesis of nanocomposite polymers by UV-radiation curing. Polymer **46**, 6640–6648 (2005)
57. S.U. Pang, G. Li, D. Jerro et al., Fast joining of composite pipes using UV curing FRP composites. Polym. Compos. **25**, 298–306 (2004)
58. R. Dilg, Schlauchlining im Sammler. Verfahren, Regelwerke, Materialien, Einbau-/Aushärtetechniken und Entwicklungen. 3R Int. **46**, 621–627 (2010)
59. F.P.W. Melchels, J. Feijen, D.W. Grijpma, A review on stereolithography and its applications in biomedical engineering. Biomaterials **31**, 6121–6130 (2010)
60. S.H. Park, D.Y. Yang, K.S. Lee, Two-photon stereolithography for realizing ultraprecise three-dimensional nano/microdevices. Laser Photon. Rev. **3**, 1–12 (2009)
61. A. Spangenberg, N. Hobeika, F. Stehlin et al., Recent advances in two-photon stereolithography, in *Updates in Advanced Lithography,* ed. by S. Hosaka. InTech, pp. 35–63
62. T. Billiet, M. Vandenhaute, J. Schelfhout et al., A review of trends and limitations in hydrogel-rapid prototyping for tissue engineering. Biomaterials **33**, 6020–6041 (2012)
63. P.M. Puri, H. Khajuria, B. Prakash et al., Stereolithography: Potential applications in forensic science. Res. J. Eng. Sci. **1**, 47–50 (2012)
64. B.H. Kang, S.Y. Shin, Experiment of solidifying photo sensitive polymer by using UV LED, in *Proceedings of the SPIE 7266, Optomechatronic Technologies, San Diego* (2008)
65. R. Xie, D. Li, S. Chao, An inexpensive stereolithography technology with high power UV-LED light. Rapid Prototyping J. **17**, 441–450 (2011)
66. R. Xie, D. Li, Research on the curing performance of UV-LED light based stereolithography. Opt. Laser Technol. **44**, 1163–1171 (2012)

Index

A
Absorption, 151, 153
Absorption cell, 325
Absorption cross section, 326
Absorption mechanism, 324
Absorption sensors, 339
Advantages of UV LEDs, 288
A-excitons of (Γ_5-symmetry), 121
Air gaps, 162
AlGaN, 6, 75, 322
AlGaN cladding, 198
AlN bulk growth, 31
AlN bulk material, 58
AlN ceramics, 28
AlN ELOG coalescence, 52
AlN ELOG offcut, 52
AlN epitaxial template, 125
AlN pillar arrays, 109
AlN source material, 33
AlN substrate production, 29
Al partial pressure over AlN, 30
Aluminum nitride (AlN), 75, 171
$Al_xGa_{1-x}N$, 116, 176
Ambient and increased UV-B radiation, 395
American conference of governmental industrial hygienist (ACGIH), 191
Ammonia, 82
Angular emission distribution, 149
Anisotropic growth, 35
Anisotropy, 140
Anti-Stokes luminescence, 353
Apoptosis, 306
Applications, 3
Atomic-force microscope, 84
Atomic step lines, 118
Atopic dermatitis, 307
Auger recombination, 8
Autofluorescence, 182, 352, 365, 370, 373, 375–377

B
Ballistic energy transfer of high-energy electrons, 212
Band crossing, 142
Band-edge emission, 147
Band-pass filtered fluorescence, 373
Barrier composition, 146, 147
Basal cell carcinoma (BCC), 376
Beer–Lambert law, 278
Below band-gap luminescence, 40
Bench-scale apparatus, 274
Better overlapping of electron and hole wavefunctions, 132
Bimolecular recombination coefficient, 9
Bioanalytical testing, 287
Biocompatibility and degradability, 426
Biodosimetry, 273
Biodosimetry trials, 275
Biofilm, 372
Bioimaging, 352
Biomarkers, 365
Biosensors, 363, 370
Bisacylphosphine oxides, 424
Bone-shape error, 430
Bouguer–Lambert–Beer's law, 325
Broadband UVB, 302
B. subtilis spores, 269
Buffer layer, 91
Bulk AlN substrates, 10
Burns, 301

C
Camphorquinone, 417
Cancer, 390
Carbon, 39
Carrier density, 147
Carrier leakage, 205
Carrier transport, 204
Cathodoluminescence, 88

© Springer International Publishing Switzerland 2016

M. Kneissl and J. Rass (eds.), *III-Nitride Ultraviolet Emitters*,
Springer Series in Materials Science 227, DOI 10.1007/978-3-319-24100-5

Cationic polymerization, 421
Chemical activity of N_2, 30
Chemical sensing, 361
Chemometrics, 358
Chip size, 16
Chronic diseases, 390
Clinical studies, 310
Coalescence, 83, 161
Coherent length, 99
Co-initiator, 420
Collagen, 375
Collisional quenching, 355, 363
Commercial markets, 17
Commercial sources, 16
Compact UV laser source, 213
Companies, 5
Composition-graded, 206
Compressive in-plane strain, 145
Compressively strained, 210
Computational fluid dynamics (CFD), 186
Concentration measurements, 324, 327
Conductivity, 41, 178
Constitutively photomorphogenic 1 (COP1), 392
Contact resistivity, 153
Counterfeit detection, 360
Coupling coefficient, 106
C-plane, 179
Crack-free, 82
Cracking, 50
Critical angle, 138
Critical thickness, 50
Cross-interfering, 329
Crosslinked polymer, 415
Cross-sectional TEM, 99
Crucible, 33
Crystal field splitting, 140, 209
Crystal growth, 181
Crystal habit, 34
Current crowding, 156
Current density, 203
Current spreading length, 155
Current–voltage characteristics, 277
Cutaneous T-cell lymphomas, 308

D
Deactivation, 117
Dead sea region, 295
Deep curing, 419
Deep-level emissions, 92
Deep-state emission, 131
Deep-ultraviolet (DUV), 75, 116, 324
Deep-UV transparency, 39
Deep etched angled mesa sidewall, 158
Defect densities, 10
Defect formation, 36
Defense advanced research projects agency (DARPA), 214
Defense threat reduction agency (DTRA), 214
Degradation, 14
Degradation of the emission power, 278
Degree of polarization, 142, 149
Dentin bond agents, 424
Deuterium lamp, 174
Device lifetime, 103
Dielectric barrier discharge, 297
Different chemical glucosinolate structures, 399
Digital mirror device (DMD), 430
Disease-preventing functions, 389
Disinfection, 172, 189
Disinfection capacity, 286
Disinfection of *B. subtilis* spores, 282
Disinfection tests, 278, 284
Dislocation density, 176, 195
Dislocation reduction, 51, 52
Dislocations, 36, 176
Dissolved organic matter, 360
Distributed Bragg reflector, 156
DNA, 174
DNA and RNA, 269
DNA damage, 280
DNA microarrays, 364
DNA repair, 280
DNA/RNA replication, 269
Doping reactants, 130
Doppler-broadening, 120
3D-printing, 3
DUV LED module, 103
DUV-TRPL, 133
Dynamic quenching, 355

E
Edge-and screw-type dislocation, 85
Edge components, 118
Edge-type emitting laser diodes, 194
e^+-e^- annihilating (γ-rays), 120
Effective absorption coefficient, 326
Effective barrier height, 98
Effective radiative lifetime, 123
Efficiency, 180
Elastic collisions, 123
Electrodeless excimer lamp, 298
Electroluminescence, 92, 323
Electron beam, 119
Electron-beam excitation, 213
Electron-beam pumping, 212
Electron-blocking height, 93

Electron blocking layer (EBL), 7, 13, 90, 205
Electron-hole pairs, 88
Electron injection efficiency, 75
Electron overflow, 94
Ellipsometry, 202
Emission bandwidth Δλ, 338
Emission distribution, 150
Emission spectrum, 277, 333
Encapsulant, 105, 164
Environment, 388
Environmental protection agency (EPA), 189
Enzyme-linked immunosorbent assays (ELISA), 364
Epifluorescence, 365
Epitaxial lateral overgrowth (ELOG), 66, 161
Epoxy, 164
Equivalent electric circuit, 339
Equivalent values for η_{int}(T), 128
Erythema, 302
Escape cone, 138
Etching, 158
Evanescent field, 330
Excellent radiative performance, 133
Excimer lamps, 298, 310
Excimer lasers, 299
Excitation-emission matrix (EEM), 358
Excitonic luminescence, 40
Exciton-polariton bottleneck, 123
Exciton polaritons, 123
Excitons bound, 122
Exploring intrinsic influences of point defects, 117
Exposure time, 273
Extended defects, 198
External quantum efficiency, 5, 7, 48, 76, 138, 337
Extracorporeal photochemotherapy, 304

F
Fabry-Perot resonator, 194
Far-field radiation pattern, 151, 152
Fermi-level control, 132
Fermi-level effect, 39, 116, 119
Fermi-level pinning, 154
Filler, 425
Finite-difference time-domain, 106
Flavines, 370
Flavonoid biosynthesis genes, 395
Flavonoids, 395
Flip-chip, 15
Flip chip bonding, 166
Flow cell, 186
Flow cytometry, 368
Flow rate, 189, 286
Flow-through reactor, 276
Flow-through tests, 275, 279, 286
Fluence, 269, 278
Fluence-inactivation response curve, 283
Fluence-inactivation response curve of *B. subtilis* spores, 280
Fluorescence-activated cell sorting (FACS), 368
Fluorescence chemical sensor, 362
Fluorescence correlation spectroscopy (FCS), 367
Fluorescence diagnosis, 374
Fluorescence emissions, 333
Fluorescence in situ hybridization (FISH), 367
Fluorescence lifetime, 354
Fluorescence lifetime imaging microscopy (FLIM), 367
Fluorescence microscopy, 365
Fluorescence quantum yield, 354
Fluorescence resonance energy transfer (FRET), 355, 363
Fluorescence resonance energy transfer microscopy (FRETM), 367
Fluorescent lamp, 296
Fluorescent probe, 352
Fluorescent reporters, 365
Fluorometer, 358
Fluorophores, 352, 356
Fouling, 191
Fraunhofer absorption, 295
Free A-excitons of Γ1-symmetry [$FX_A(\Gamma_1)$], 121
Free-standing single crystals, 34
Frequency-quadrupled (4ω) mode-locked Al_2O_3 Ti laser, 119
Frequency-tripled (3ω) pulses of the Al_2O_3 Ti laser, 119
Full-width at half-maximum (FWHM), 119
Fully strained, 199
Future development, 41
Future device performance, 16

G
Gas discharge, 296
Gas discharge lamps, 333
Gas-sensing, 321
German procedure of UV reactor, 287
Germicidal efficiency, 285
Glucosinolates, 399
Goeckerman, 293
Gradual polarization switching, 147
Graft-versus-host disease, 309
Grain selection, 34

Green fluorescent protein (GFP), 362
Group III-nitride material system, 194
Grown on SiC seeds, 34
Growth atmosphere, 30
Growth procedure, 32
Growth rate, 31

H
H-bulb, 418
Health-promoting functions, 390
Heat extraction, 156
Hermetically, 182
Heteroepitaxial growth, 175
Hetero-interfaces, 85
Heterostructure, 5
High chemical stability, 28
High-aspect-ratio, 109
High-performance liquid chromatography (HPLC), 359
High-pressure mercury discharge, 297
High-throughput screening, 352
Hole concentration, 207
Home therapy, 310, 313
Homoepitaxial growth, 35
Homoepitaxially grown AlN, 197
Hot-zone geometry, 32
H_3SiNH_2, 130
Hybrid polymers, 422
Hydride vapor phase epitaxy (HVPE)
  HVPE AlGaN XRD FWHM, 65
  HVPE AlGaN AlN/sapphire templates, 63
  HVPE AlGaN chemical reactions, 55
  HVPE AlGaN CL-spectrum, 64
  HVPE AlGaN dislocation density, 68
  HVPE AlGaN growth conditions, 59
  HVPE AlGaN homogeneity, 61, 64
  HVPE AlGaN nitridation, 63
  HVPE AlGaN parameter studies, 59
  HVPE AlGaN sample rotation, 61
  HVPE AlGaN sapphire pretreatment, 63
  HVPE AlGaN semipolar growth, 66, 67
  HVPE-grown AlN, 40
  HVPE growth simulation, 57
  HVPE reactor design, 54, 59
  HVPE sources, 55
  HVPE thermodynamic model, 56
Hydrogels, 428

I
Impacts of point defects, 116
Improvement in performance, 207
Impurities, 38
Inactivation, 184
Inactivation curves, 284
Inactivation of *B. subtilis* spores, 280, 287
Inactivation rate constants k, 284
InAlGaN, 6
Incandescence emitters, 294
Inductively coupled plasma (ICP), 109
Inflammatory disorders, 306
Influencing UV fluence, 271
Initiation, propagation, and termination, 419
Injection efficiency, 8, 206
Ink-jet printing, 428
In-segregation, 88
Instantaneously, 174
Instrumental analysis, 359
Interaction, 388
Interdigitated finger contact, 12
Interface shape, 35
Internal conversion, 354
Internal electric fields, 146
Internal quantum efficiency, 75, 162, 337
Intersystem crossing, 354
Intrinsic defects, 38
Inversion domains, 37
Inverting the axial temperature gradient, 32
Ionisation energy, 12
Irradiance, 417
Isotropic distribution, 162
Isotropic emission, 151
Isotropic in-plane strain, 144

J
Jablonski diagram, 353
Junction temperature, 186

K
Kaempferol, 398
Kinetic chain length, 423
k·p theory, 211

L
Lasers, 298
Laser scanning microscopy (LSM), 367
Laser threshold power densities, 209
Lateral conductivity, 202
Lateral overgrowth, 52
Lattice mismatch, 49
LED-based spectroscope, 321
Lichen planus, 309
Lifetime, 15, 80
Light absorptions spectroscopy, 324
Light-emitting diodes (LEDs), 1, 75, 116, 171, 299
Light extraction efficiency, 8, 75
Light scattering, 162
Light sources, 174, 322

Low pressure discharge, 296
Low-pressure mercury lamps, 271
Luminescence, 353
Luminescence emitters, 294
Luminophores, 356

M
Major V_{III}-defect in $Al_xGa_{1-x}N$ is assigned to V_{Al}, 127
Malignant melanoma, 377
Mass transport in the gas phase, 31
Medium-pressure lamps, 271
Melanocytes, 308
Mercury lamp, 174
Mercury vapor, 296
Metal contacts, 13
Metal halide lamps, 296
Metal-organic chemical vapor deposition (MOCVD), 180
Metalorganic vapor phase epitaxy (MOVPE), 6, 118
Metal work function, 153
Mg acceptor, 12
Micro frustrum array, 159
Microarray readers, 364
Microbe, 187
Microlense array, 159
Microorganism detection, 369
Microorganisms, 174
Micro-pixel, 14
Micro pixel LEDs, 157
Microscopic inclusions, 37
Migration, 83
Minimal defect formation, 116
Minimal erythema dose (MED), 302
Minimal phototoxic dosage (MPD), 300
Minority carrier diffusion lengths, 10
Mirror facets, 209
Misfit dislocations, 49
Moderate UV-B radiation, 396
Monoenergetic e^+-beam, 120
MOVPE AlN, 50
M-plane substrates, 148
MQW active zone, 198
Multi-finger contacts, 156
Multiple quantum well, 6
Multi-quantum-barriers, 13, 75
Multi-reflection effects, 99
Multispectral analysis, 377
Multi-wavelength fluorimeter, 373

N
NADH, NADPH, 370, 371, 373, 375
Nakamura, 194
Nanocomposites, 429
Nano-imprinting, 109
Nano-particles, 425
Nanopixel contact design, 155
Narrow-band UV-B radiation, 302, 402
Narrow ridge, 194
Natural fluorophores, 356
N-contact, 152
Niels Ryberg Finsen, 293
Λ = 336 nm, 195
No escape zone, 139
Nonlinear crystal, 213
Nonmelanoma skin cancer (NMSC), 376, 377
Nonpolar substrates, 147
Non-radiative centers, 88, 201
Non-radiative recombination, 10, 87
N-polar directions, 34
NSF 55, 185
Nucleation layer, 83
Nucleic acid staining, 364

O
Ohmic contact, 153
Ohmic metal contact, 12
Omnidirectional reflector, 156
Onium salts, 421
Operating voltages, 9
Optical absorption, 39
Optical brightener, 360
Optically pumped UV lasers, 208
Optical polarization, 14
Optical properties, 199
Optical reference detector, 331
Optical spectroscopy, 321
Optical transmission, 326
Optimized lighting spectrum, 402
Optometer, 191
Orbitals, 149
Order of the valence bands, 209
O_3, SO_2, and NO_2, 321
Overcompensation, 117, 127, 131
Overshoot, 205
O^0X, 122
Oxygen, 39
Oxygen scavengers, 422

P
Packaging, 14
Packaging materials, 14
Particular sugar moiety, 398
Pathogen, 184
Pathogen detection, 369
Patterned AlN templates, 52
Patterned sapphire substrates (PSS), 66

Patterns sapphire substrate, 105
P-contact, 152
Peak emission wavelength, 323
Peak wavelength λ, 338
Phenolic acid, 398
Phosphors, 356
Photobleaching, 424
Photocleavage, 420
Photo-electrochemical etching, 158
Photoelectron gun (PE-gun), 119
Photoinitiator, 415
Photolithography, 428
Photoluminescence, 79, 353
Photomultiplier tube (PMT), 358, 372
Photonic crystal, 160
Photonic structure, 105
Photosensitizer, 300
Phototherapy, 3, 293
Physico-chemical water quality, 272
Piezo-electric fields, 95
Piezoelectric and spontaneous, 28, 201
Pillar buffer, 109
Planck's law, 294, 333
Plants, 388
Plasma frequency, 163
Plasmonic effects, 163
PL lifetime, 201
Point-of-use, 175, 183
Polarization-activated, 202
Polarization-induced 3D hole generation, 206
Polarization doping, 12
Polarization fields, 6
Polarization selection rules, 142
Polishing, 158
Polycrystalline boule, 34
Polycrystalline growth, 63
Polydimethylsiloxane, 166
Polygonization, 37
Polymers, 165
Polymorphic light eruption, 310
Porphyrins, 375
Positron annihilation spectroscopy (PAS), 116
Power conversion efficiency, 7
Power–current characteristics, 277
Power output, 186
Pressure, 324
Principal component analysis (PCA), 373
Proliferation, 375
Protoporphyrin IX (PpIX), 374
Pseudomorphic, 176
Psoralen, 293, 300
Psoralen plus UVA (PUVA) therapy, 300
Psoriasis, 307
Psoriasis area and severity index (PASI), 301
Psoriasis severity index (PSI), 311
p-SPSL, 203
PSS columns, 68
PSS honeycomb, 69
PSS isotropy, 68
PSS trenches, 66
P-type, 201
Pulsed current injection, 195
Pulsed-flow, 82

Q
Quantum confinement, 146
Quantum efficiency, 119
Quantum well thickness, 146
Quantum wells, 78, 178
Quaternary InAlGaN, 78
Quercetin, 398

R
Rabbit ears, 151, 162
Radiation, 174
Radiation angle, 95
Radiative and nonradiative lifetimes, 116
Radiative recombination efficiency, 8
Radical photopolymerization, 421
Rapid prototyping (RP), 430
Real-time infrared spectroscopy (RT-IR), 423
Rear-excitation configuration, 119
Recognition element, 362
Recombination rate, 163
Reduction equivalent fluence, 273
Reflectance, 184
Reflective contacts, 153
Reflective p-type electrode, 105
Reflectivity, 154
Reflow method, 159
Reproducibility, 103
Reproducibility of the test module, 282
Residence time, 184
Roughness, 179

S
Saltwater, 302
Sapphire substrates, 5, 48, 79
Scaling deposits, 272
Schottky barrier height, 154
Secondary-ion-mass spectrometry (SIMS), 118
Secondary plant metabolites, 388
Second harmonic generation (SHG), 213
Seed backside evaporation, 35
Seeded growth of AlN crystals, 35
Semiconductor, 172
Semi-insulating behaviour, 41
Semipolar substrates, 147

Sensing, 3
Sensitivity of *B. subtilis* spores, 280
Shaped semiconductor chip, 157
Shockley-Read-Hall recombination, 8
Short period superlattice layer, 7
Shrinkage, 425
Sidewalls, 151
Si-doped AlN interlayers, 52
Signaling molecules, 392
Signaling pathways, 392
Signal-processing, 329
Silicone, 164
Single-crystal AlN substrates, 196
Si substrate, 110
Si^0X, 122
Skin cancer, 302
Skin cancer diagnosis, 375
Slanted sidewalls, 157
Sol–gel immobilization, 364
Solid freeform fabrication (SFF), 430
Solvatochromism, 354
Sources, 324
Space-averaged time-of-flight, 123
S parameter, 120
Spatio-time-resolved cathodoluminescence (STRCL), 119
Spectral fluctuation, 331
Spectral resolution, 324
Spectral responsiveness, 322
Spore inactivation, 284
Squamous cell carcinoma (SCC), 376
SP–QW coupling, 164
Static disinfection tests, 276
Static tests, 275, 279
Sterilization, 77
Stoichiometric sublimation, 30
Stokes shift, 353
Strain, 14
Strain state, 144
Stress-induced changes, 393
Stretched exponential decay, 124
Structural perfection, 36
Sublimation growth models, 30
Sublimation–recondensation, 30
Sub-picosecond, 123
Substrate edge emission zone, 139
Substrate removal, 158
Substrates, 58
Substrate surface pretreatment, 50
Sun, 295
Superlattice, 81, 201
Surface contamination, 372
Surface emission zone, 139
Surface plasmon, 163
Surface plasmon polariton, 163
Surface roughening, 158
Surfactant, 130
Susceptor, 32
Switching of polarization characteristics, 143
Systemic sclerosis, 309

T
Tantalum carbide (TaC), 33
Targeted phototherapy, 303
TE and TM polarization, 211
Temperature, 324
Tensile strain, 145
TE polarized, 209
TE-polarized emission, 14
TE-polarized light, 143
Thermal activation energy, 201
Thermal annealing, 164
Thermal expansion coefficient, 110
Thermal gradients, 32
Thermal light sources, 333
Thermal management, 14
Thermal resistance, 15
Thermal roll over, 157
Thin layers, 418
Threading dislocation density, 48, 75
Threading dislocations, 10, 198
Tilted domains, 37
Time-correlated single photon counting (TCSPC), 358
Time-resolved cathodoluminescence (TRCL), 117, 119, 133
Time-resolved fluorescence, 358
Time-resolved photoluminescence (TRPL), 116, 199
Tissue adhesives, 426
Tissue engineering, 428
TM-polarized light, 143, 209
TO-39, 180
Total internal reflection, 105, 138
Total internal reflection fluorescence microscopy (TIRFM), 366
Total output power, 16
Transduction elements, 362
Transition matrix element, 141
Transmission, 325
Transmission electron microscope, 84
Transparent contact layer, 105
Trimethylaluminum, 83
Tryptophan, 370, 373, 375
Tunable diode laser absorption spectroscopy (TDLAS), 328
Tungsten, 33
Tunnel injection, 153

Tunnel junction, 160
Two-photon polymerization, 430

U
Ultraviolet (UV)
UVA (400–320 nm), 2
UVA-1 (340–400 nm), 296, 303
UV absorption, 281
UVB (320–280 nm), 2
UV-B exposure, 389
UV-B radiation, 391
UV-B specific, 392
UVC (280–200 nm), 2, 171
UVC absorption bands, 11
UV curing, 3
UV discharge lamps, 334
UV disinfection, 268
UV Dose, 184
UV-LEDs, 3, 17, 268, 271, 299, 312
UV LEDs for water disinfection, 287
UV LEDs for water disinfection applications, 274
UV light, 267, 268, 324
UV light absorption, 269
UV light available, 272
UV light source, 271
UV nanoimprint lithography (UV-NIL), 428
UV purification module, 286
UV reactor performance, 273
UV-reflective contacts, 14
UV-response locus 8 (UVR8), 392
UV sensitive microorganisms, 274
UV transmissivity (UVT), 183
UV-triggered processes, 402
Uniformity, 103

V
Vacancies, 116
Valence band, 95
Valence subbands, 141
V_{Al}-impurity complexes, 120
Vertical carrier transport, 202
Vertical-external-cavity surface-emitting laser (VECSEL), 213
Vertical LED, 106
Vitiligo, 308
Voltage drop, 155

W
Wall plug efficiency, 7, 186
Water, 172
Water factor, 278
Water purification, 3
Water qualities, 183, 281
Waveguide layers, 198
Waveguide zone, 139
Wavelength ratiometric fluorescent indicators, 363
Wetting conditions, 130
Woods lamp, 375
Wurtzite crystal structure, 140

X
Xenon flash lamp, 174
X-ray diffraction (XRD), 84, 179
X-ray rocking curves, 51

Y
Yellowish coloration, 39

Z
Zonar structure, 37